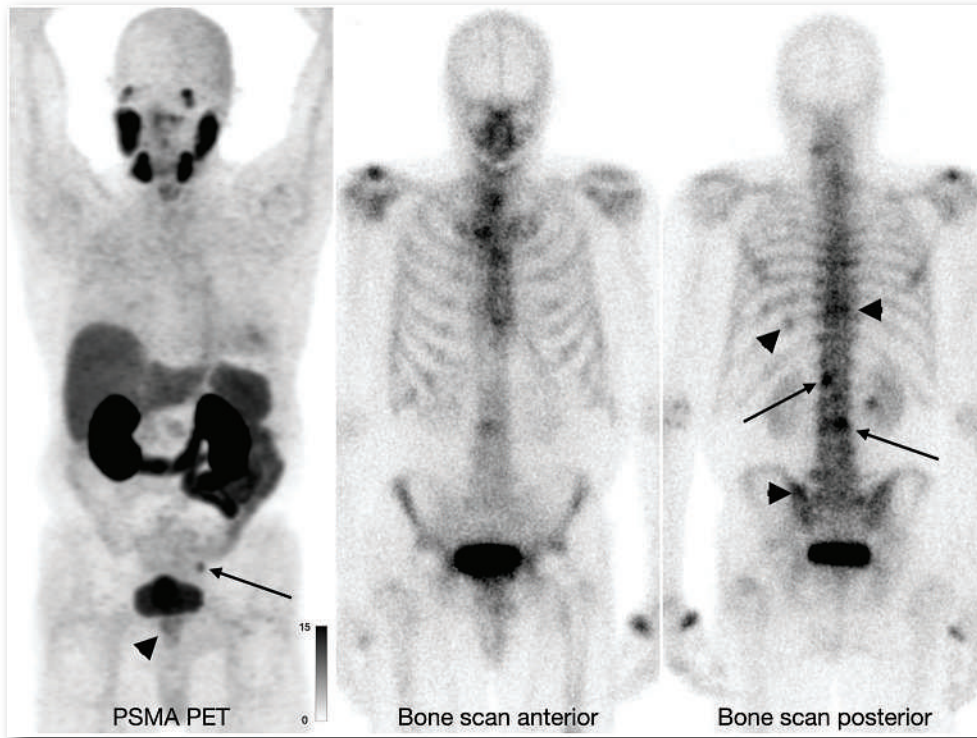


**FEATURED  
ARTICLE**

Do Bone Scans Overstage Disease Compared with PSMA PET at Initial Staging? An International Multicenter Retrospective Study with Masked Independent Readers. Thomas Hope et al. See page 1744.



**Immuno-PET biomarkers in IBD:** Noninvasive interleukin targeting of inflammation for diagnosis and management. Farzaneh Rezazadeh et al. See page 1806.

# The most powerful words you'll ever hear. “Thank You.”

With your contribution, our profession can continue efforts leading to critical advances in cancer treatments and care.

The **Mars Shot Research Fund** is the cornerstone for making these efforts a reality for patients of all ages.

**The world needs more “thank you’s.”**

Help improve the life of a patient. Lend your support today.



Help support the  
SNMMI Mars Shot Research Fund:  
[WWW.SNMMI.ORG/MARSSHOT](http://WWW.SNMMI.ORG/MARSSHOT)

**SNM** SOCIETY OF  
**MI** NUCLEAR MEDICINE &  
MOLECULAR IMAGING

# NEUROLITE®

KIT FOR THE PREPARATION OF TECHNETIUM  
Tc99m BICISATE FOR INJECTION

## Critical information when you need it

### High Contrast Perfusion Images

- Rapid brain uptake<sup>1</sup>
- Rapid blood clearance<sup>1,2,3</sup>
- Rapid washout from facial muscles<sup>2,4</sup>
- Negligible intracerebral redistribution<sup>1,3,5</sup>

### Extended *In Vitro* stability in syringe or vial

- Greater patient scheduling flexibility<sup>1,5,6</sup>
- Facilitates use in multiple settings<sup>1,5,6</sup>
- May result in fewer doses<sup>6</sup>



#### INDICATIONS:

NEUROLITE® single photon emission computerized tomography (SPECT) is indicated as an adjunct to conventional CT or MRI imaging in the localization of stroke in patients in whom stroke has already been diagnosed. NEUROLITE® is not indicated for assessment of functional viability of brain tissue or for distinguishing between stroke and other brain lesions.

#### CONTRAINDICATIONS:

None known.

#### IMPORTANT SAFETY INFORMATION:

In clinical trials, NEUROLITE® has been administered to 1063 subjects (255 normals, 808 patients). In the 808 patients with neurologic events, there were 11 (1.4%) deaths, none of which were clearly attributed to NEUROLITE®. The following adverse effects were observed in ≤ 1% of the subjects: headache, dizziness, seizure, agitation/anxiety, malaise/somnolence, parosmia, hallucinations, rash, nausea, syncope, cardiac failure, hypertension, angina, and apnea/cyanosis.

#### WARNINGS:

None known.

#### PRECAUTIONS:

##### General

USE WITH CAUTION IN PATIENTS WITH RENAL OR HEPATIC IMPAIRMENT. TECHNETIUM Tc99m BICISATE IS ELIMINATED PRIMARILY BY RENAL EXCRETION. WHETHER TECHNETIUM Tc99m BICISATE IS DIALYZABLE IS NOT KNOWN. DOSE ADJUSTMENTS IN PATIENTS WITH RENAL OR HEPATIC IMPAIRMENT HAVE NOT BEEN STUDIED.

Patients should be encouraged to drink fluids and to void frequently during the 2-6 hours immediately after injection to minimize radiation dose to the bladder and other target organs. As with any other radioactive material, appropriate shielding should be used to avoid unnecessary radiation exposure to the patient, occupational workers, and other people. Radiopharmaceuticals should be used only by physicians who are qualified by specific training in the safe use and handling of radionuclides.

Please see following page(s) for brief Prescribing Information. Full Prescribing Information may be accessed at [https://www.lantheus.com/assets/NEUROLITE\\_513073-0719mktg.pdf](https://www.lantheus.com/assets/NEUROLITE_513073-0719mktg.pdf)

#### References:

1. NEUROLITE® [package insert]. N. Billerica, MA: Lantheus Medical Imaging, Inc. 2. Leveille, J, Demonceau, G, Walovitch, R, Intraject Comparison Between Technetium-99m-ECD and Technetium-99m-HMPAO in Healthy Human Subjects, *JNM*, 1992;33(4):480-484 3. Vallabhajosula, S, Zimmerman, R, Picard, M, et al, Technetium-99m ECD: A New Brain Imaging Agent: In Vivo Kinetics and Biodistribution Studies in Normal Human Subjects, *JNM*, 1989; 30(5):599-604 4. Castagnoli, A, Borsato, N, Brung, A, et al, Cerebral Ischemia and Dementia. Springer-Verlag;1991: Chapter 39: SPECT Brain Imaging in Chronic Stroke and Dementia: A Comparison of <sup>99m</sup>Tc-ECD and <sup>99m</sup>Tc-HMPAO; 327-333 5. Siennicki-Lantz, A, Lijla, B, Elmstahl, S, How to interpret differing cerebral blood flow patterns estimated with <sup>99m</sup>Tc-HMPAO and <sup>99m</sup>Tc-ECD SPECT in a healthy population, *Nuclear Medicine Communications*, 1999;20:219-226 6. Koslowsky, I, Brake, S, Bitner, S, Evaluation of the Stability of <sup>99m</sup>Tc-ECD and Stabilized <sup>99m</sup>Tc-HMPAO Stored in Syringes, *J Nucl Med Technol*, 2001;29(4):197-200



LANTHEUS™

Trademarks, registered or otherwise, are the properties of their respective owner(s).  
©2022 Lantheus Medical Imaging, Inc. All rights reserved. July 2022 PM-US-NE-0003

# NEUROLITE<sup>®</sup>

KIT FOR THE PREPARATION OF TECHNETIUM  
Tc99m BICISATE FOR INJECTION

FOR DIAGNOSTIC USE

## BRIEF SUMMARY

Please see Full Prescribing Information available at [https://www.lantheus.com/assets/NEUROLITE\\_513073-0719mktg.pdf](https://www.lantheus.com/assets/NEUROLITE_513073-0719mktg.pdf) for complete information.

## INDICATIONS

Neurolite single photon emission computerized tomography (SPECT) is indicated as an adjunct to conventional CT or MRI imaging in the localization of stroke in patients in whom stroke has already been diagnosed.

Neurolite is not indicated for assessment of functional viability of brain tissue. Also, Neurolite is not indicated for distinguishing between stroke and other brain lesions.

## CONTRAINDICATIONS

None known

## WARNINGS

None known

## PRECAUTIONS

### General

USE WITH CAUTION IN PATIENTS WITH RENAL OR HEPATIC IMPAIRMENT. TECHNETIUM Tc99m BICISATE IS ELIMINATED PRIMARILY BY RENAL EXCRETION. WHETHER TECHNETIUM Tc99m BICISATE IS DIALYZABLE IS NOT KNOWN. DOSE ADJUSTMENTS IN PATIENTS WITH RENAL OR HEPATIC IMPAIRMENT HAVE NOT BEEN STUDIED.

Patients should be encouraged to drink fluids and to void frequently during the 2-6 hours immediately after injection to minimize radiation dose to the bladder and other target organs.

Contents of the vials are intended only for use in the preparation of Technetium Tc99m Bicisate and are not to be administered directly to the patient without first undergoing the preparation procedure.

The contents of each vial are sterile and non-pyrogenic. To maintain sterility, aseptic technique must be used during all operations in the manipulations and administration of Neurolite.

Technetium Tc99m Bicisate should be used within six hours of the time of preparation.

As with any other radioactive material, appropriate shielding should be used to avoid unnecessary radiation exposure to the patient, occupational workers, and other people.

Radiopharmaceuticals should be used only by physicians who are qualified by specific training in the safe use and handling of radionuclides.

## ADVERSE REACTIONS

In clinical trials, Neurolite has been administered to 1063 subjects (255 normals, 808 patients). Of these, 566 (53%) were men and 494 (47%) were women. The mean age was 58 years (range 17 to 92 years). In the 808 patients, who had experienced neurologic events, there were 11 (1.4%) deaths, none of which were clearly attributed to Neurolite.

A total of 60 subjects experienced adverse reactions; the adverse reaction rates were comparable in the <65 year, and the <65 year age groups.

The following adverse effects were observed in ≤ 1% of the subjects: headache, dizziness, seizure, agitation/anxiety, malaise/somnolence, parosmia, hallucinations, rash, nausea, syncope, cardiac failure, hypertension, angina, and apnea/cyanosis.

In clinical trials of 197 patients, there were inconsistent changes in the serum calcium and phosphate levels. The cause of the changes has not been identified and their frequency and magnitude have not been clearly characterized. None of the changes required medical intervention.

**To report SUSPECTED ADVERSE REACTIONS, contact Lantheus Medical Imaging, Inc. at 1-800-362-2668 or FDA at 1-800-FDA-1088 or [www.fda.gov/medwatch](http://www.fda.gov/medwatch).**

### Distributed by:

Lantheus Medical Imaging<sup>®</sup>

331 Treble Cove Road

N. Billerica, Massachusetts 01862 USA

For Ordering Tel: Toll Free: 800-299-3431

All Other Business: 800-362-2668



**LANTHEUS<sup>™</sup>**



## DISCUSSIONS WITH LEADERS

- 1671 Advancing Nuclear Medicine at the Multiomics Intersection: Johannes Czernin Discusses Innovation and Translation with Kalevi Kairemo**  
Kalevi Kairemo and Johannes Czernin

## HOT TOPICS

- 1674 FAPI PET/CT Immune-Fibrosis Imaging for New Insights into Rheumatologic Disorders**  
Christian Schmidkonz, Armin Atzinger, Andreas Ramming, and Torsten Kuwert

## FOCUS ON MOLECULAR IMAGING

- 1676 The Development and Validation of Radiopharmaceuticals Targeting Bacterial Infection**  
Alberto Signore, Alvaro A. Ordonez, Chanda Arjun, Gurpreet Kaur Aulakh, Nicolas Beziere, Ekaterina Dadachova, Thomas Ebenhan, Ulises Granados, Aruna Korde, Amirreza Jalilian, et al.

## ONCOLOGY

### Clinical

- 1683 Predictive IDH Genotyping Based on the Evaluation of Spatial Metabolic Heterogeneity by Compartmental Uptake Characteristics in Preoperative Glioma Using <sup>18</sup>F-FET PET**  
Johannes Lohmeier, Helena Radbruch, Winfried Brenner, Bernd Hamm, Anna Tietze, and Marcus R. Makowski
- 1690 Correlation of SUV on Early Interim PET with Recurrence-Free Survival and Overall Survival in Primary Operable HER2-Positive Breast Cancer (the TBCRC026 Trial)**  
Maeve A. Hennessy, Jeffrey P. Leal, Chiung-Yu Huang, Lilja B. Solnes, Rita Denbow, Vandana G. Abramson, Lisa A. Carey, Minetta C. Liu, Mothaffar Rimawi, Jennifer Specht, et al.
- 1697 ■ INVITED PERSPECTIVE. <sup>18</sup>F-FDG PET “Metabolic Response” to Neoadjuvant Systemic Therapy for Breast Cancer: Quo Vadis?**  
Geraldine Gebhart
- 1699 High Tumor Uptake on <sup>18</sup>F-FDOPA PET/CT Indicates Poor Prognosis in Patients with Metastatic Midgut Neuroendocrine Tumors: A Study from the Groupe d'étude des Tumeurs Endocrines and ENDOCAN-RENATEN Network**  
Ophélie De Rycke, Marine Perrier, Éric Ouvrard, Clément Menntrey, Choaib Lachachi, Aurélie Bando-Delaunay, David Morland, Bernard Goichot, David Taieb, Thomas Walter, et al.
- 1706 Validation of the  $\Delta$ SUV<sub>max</sub> for Interim PET Interpretation in Diffuse Large B-Cell Lymphoma on the Basis of the GAINED Clinical Trial**  
Emmanuel Itti, Paul Blanc-Durand, Alina Berriolo-Riedinger, Salim Kanoun, Françoise Kraeber-Bodéré, Michel Meignan, Elodie Gat, Steven Le Gouill, René-Olivier Casanovas, and Caroline Bodet-Milin

- 1712 Impact of <sup>68</sup>Ga-FAPI PET/CT on Staging and Oncologic Management in a Cohort of 226 Patients with Various Cancers**

Stefan A. Koerber, Manuel Röhrich, Leon Walkenbach, Jakob Liermann, Peter L. Choyke, Christoph Fink, Cathrin Schroeter, Anna-Maria Spektor, Klaus Herfarth, Thomas Walle, et al.

## THERANOSTICS

### Clinical

- 1721 ■ BRIEF COMMUNICATION. Prediction of Resistance to <sup>177</sup>Lu-PSMA Therapy by Assessment of Baseline Circulating Tumor DNA Biomarkers**  
Oliver Sartor, Elisa Ledet, Minqui Huang, Jennifer Schwartz, Alex Lieberman, Brian Lewis, Jodi Layton, Pedro Barata, Albert Jang, Madeline Hawkins, et al.
- 1726 ■ BRIEF COMMUNICATION. [<sup>177</sup>Lu]Lu-PSMA-617 Versus Docetaxel in Chemotherapy-Naïve Metastatic Castration-Resistant Prostate Cancer: Final Survival Analysis of a Phase 2 Randomized, Controlled Trial**  
Swayamjeet Satapathy, Bhagwant Rai Mittal, Ashwani Sood, Chandan Krushna Das, Ravimohan Suryanarayan Mavuduru, Shikha Goyal, Jaya Shukla, and Shrawan Kumar Singh
- 1730 Antihormonal-Treatment Status Affects <sup>68</sup>Ga-PSMA-HBED-CC PET Biodistribution in Patients with Prostate Cancer**  
Kilian Kluge, David Haberl, Holger Einspieler, Sazan Rasul, Sebastian Gutschmayer, Lukas Kenner, Gero Kramer, Bernhard Grubmüller, Shahrokh Shariat, Alexander Haug, et al.
- 1737 Prognostic Value of End-of-Treatment PSMA PET/CT in Patients Treated with <sup>177</sup>Lu-PSMA Radioligand Therapy: A Retrospective, Single-Center Analysis**  
Vishnu Murthy, Andrei Gafita, Pan Thin, Kathleen Nguyen, Tristan Grogan, John Shen, Alexandra Drakaki, Matthew Rettig, Johannes Czernin, and Jeremie Calais
- 1744 ■ FEATURED ARTICLE OF THE MONTH. Do Bone Scans Overstage Disease Compared with PSMA PET at Initial Staging? An International Multicenter Retrospective Study with Masked Independent Readers**  
Thomas A. Hope, Matthias Benz, Fei Jiang, Daniel Thompson, Francesco Barbato, Roxana Juarez, Miguel Hernandez Pampaloni, Martin Allen-Auerbach, Pawan Gupta, Wolfgang P. Fendler, et al.
- 1748 ■ INVITED PERSPECTIVE. Out with the Old, in with the New: Can We Bridge the Gap Between Clinical Trial Results Based on Bone Scans and the Era of Modern Prostate Cancer Imaging?**  
Michal Eifer, Ramin Alipour, Michael S. Hofman, and Aravind S. Ravi Kumar
- 1750 A Prostate-Specific Membrane Antigen PET-Based Approach for Improved Diagnosis of Prostate Cancer in Gleason Grade Group 1: A Multicenter Retrospective Study**  
Jingliang Zhang, Fei Kang, Jie Gao, Jianhua Jiao, Zhiyong Quan, Shuaijun Ma, Yu Li, Shikuan Guo, Zeyu Li, Yuming Jing, et al.
- 1758 Prediction of Response to <sup>177</sup>Lu-PSMA Therapy Based on Tumor-to-Kidney Ratio on Pretherapeutic PSMA PET/CT and Posttherapeutic Tumor-Dose Evaluation in mCRPC**  
Melanie Hohberg, Manuel Reifegerst, Alexander Drzezga, Markus Wild, and Matthias Schmidt

## 1765 Improved Quality of Life in Metastatic Castration-Resistant Prostate Cancer Patients Receiving Consecutive Cycles of <sup>177</sup>Lu-PSMA I&T

Amir Karimzadeh, Paula Soeiro, Benedikt Feurecker, Charlotte-Sophie Hecker, Karina Knorr, Matthias M. Heck, Robert Tauber, Calogero D'Alessandria, Wolfgang A. Weber, Matthias Eiber, et al.

### Basic

## 1772 Tandem Isotope Therapy with <sup>225</sup>Ac- and <sup>177</sup>Lu-PSMA-617 in a Murine Model of Prostate Cancer

Catherine Meyer, Andreea Stuparu, Katharina Lueckerath, Jeremie Calais, Johannes Czernin, Roger Slavik, and Magnus Dahlbom

## RADIOBIOLOGY/DOSIMETRY

### Clinical

## 1779 Lesion Dosimetry for [<sup>177</sup>Lu]Lu-PSMA-617 Radiopharmaceutical Therapy Combined with Stereotactic Body Radiotherapy in Patients with Oligometastatic Castration-Sensitive Prostate Cancer

Milan Grkovski, Joseph A. O'Donoghue, Brandon S. Imber, George Andl, Cheng Tu, Daniel Lafontaine, Jazmin Schwartz, Maria Thor, Michael J. Zelefsky, John L. Humm, et al.

## 1788 ■ BRIEF COMMUNICATION. Second Symposium of the European Working Group on the Radiobiology of Molecular Radionuclide Therapy

Julie Nonnekens, Bart Cornelissen, and Samantha Y.A. Terry

## RADIOCHEMISTRY

### Basic

## 1791 Optimized Methods for the Production of High-Purity <sup>203</sup>Pb Using Electroplated Thallium Targets

Shefali Saini, Jennifer L. Bartels, Jean-Pierre K. Appiah, Jason H. Rider, Nicholas Baumhover, Michael K. Schultz, and Suzanne E. Lapi

## NEUROLOGY

### Clinical

## 1798 Biostatistical Estimation of Tau Threshold Hallmarks (BETTH) Algorithm for Human Tau PET Imaging Studies

Alexandra Gogola, Brian J. Lopresti, Dana Tudorascu, Beth Snitz, Davneet Minhas, Vincent Doré, Milos D. Ikonovic, C. Elizabeth Shaaban, Cristy Matan, Pierrick Bourgeat, et al.

## GASTROENTEROLOGY

### Basic

## 1806 ■ FEATURED BASIC SCIENCE ARTICLE. Detection of IL12/23p40 via PET Visualizes Inflammatory Bowel Disease

Farzaneh Rezazadeh, Nicholas Ramos, Allen-Dexter Saliganan, Najeeb Al-Hallak, Kang Chen, Bashar Mohamad, Wendy N. Wiesend, and Nerissa T. Viola

## PHYSICS AND INSTRUMENTATION

### Clinical

## 1815 Long Versus Short Axial Field of View Immuno-PET/CT: Semiquantitative Evaluation for <sup>89</sup>Zr-Trastuzumab

Philipp Mohr, Joyce van Sluis, Laura Providência, Johannes H. van Snick, Marjolijn N. Lub-de Hooge, Antoon T. Willemsen, Andor W.J.M. Glaudemans, Ronald Boellaard, Adriaan A. Lammertsma, Adrienne H. Brouwers, et al.

## 1821 Total-Body Multiparametric PET Quantification of <sup>18</sup>F-FDG Delivery and Metabolism in the Study of Coronavirus Disease 2019 Recovery

Yiran Wang, Lorenzo Nardo, Benjamin A. Spencer, Yasser G. Abdelhafez, Elizabeth J. Li, Negar Omidvari, Abhijit J. Chaudhari, Ramsey D. Badawi, Terry Jones, Simon R. Cherry, et al.

## 1831 Total-Body Perfusion Imaging with [<sup>11</sup>C]-Butanol

Elizabeth J. Li, Javier E. López, Benjamin A. Spencer, Yasser Abdelhafez, Ramsey D. Badawi, Guobao Wang, and Simon R. Cherry

## ILLUSTRATED POST

## 1839 Obstructive Sialadenitis from Oral Squamous Cell Carcinoma: [<sup>68</sup>Ga]Ga-FAPI-46 PET-Positive and [<sup>18</sup>F]FDG PET-Negative

Peter George Maliha, Abie H. Mendelsohn, Johannes Czernin, Taylor Howard, Jeremie Calais, and Masatoshi Hotta

## LETTERS TO THE EDITOR

## 1841 HER2-Low Breast Cancer Can Be Visualized by HER2 PET

Renske Altena, Siri af Burén, Thuy Tran, and Rimma Axelsson

## 1841 ■ REPLY. HER2-Low Breast Cancer Can Be Visualized by HER2 PET

Romain-David Seban

## DEPARTMENTS

### 10A This Month in JNM

The Official Publication of **SNMMI**

## Publications Committee

TODD E. PETERSON, PhD, FSNMMI  
*Chair*

CAROLYN J. ANDERSON, PhD, FSNMMI  
PAIGE B. BENNETT, MD  
JOYITA DUTTA, PhD  
MICHAEL M. GRAHAM, MD, PhD, FACR,  
FSNMMI  
HOSSEIN JADVAR, MD, PhD, MPH, MBA,  
FACNM, FSNMMI  
STEVEN M. LARSON, MD, FACNM  
ASHWIN SINGH PARIHAR, MBBS, MD  
HEINRICH R. SCHELBERT, MD, PhD, FSNMMI  
HEIKO SCHÖDER, MD, MBA, FSNMMI  
DAVID M. SCHUSTER, MD

## *Ex officio*

JOHANNES CZERNIN, MD, FSNMMI  
ARNOLD M. STRASHUN, MD, FSNMMI

## Associate Director of Communications

SUSAN ALEXANDER

## Senior Copyeditor

SUSAN NATH

## Senior Publications & Marketing Service Manager

STEVEN KLEIN

## Editorial Production Manager

AMY TURNER

## Editorial Project Manager

MARK SUMIMOTO

## Director of Communications

REBECCA MAXEY

## CEO

VIRGINIA PAPPAS

**MISSION STATEMENT:** *The Journal of Nuclear Medicine* advances the knowledge and practice of molecular imaging and therapy and nuclear medicine to improve patient care through publication of original basic science and clinical research.

*JNM* (ISSN 0161-5505 [print]; ISSN 2159-662X [online]) is published monthly by SNMMI, 1850 Samuel Morse Drive, Reston, VA 20190-5316. Periodicals postage is paid at Herndon, VA, and additional mailing offices. Postmaster, send address changes to *The Journal of Nuclear Medicine*, 1850 Samuel Morse Drive, Reston, VA 20190-5316. The costs of publication of all nonsolicited articles in *JNM* were defrayed in part by the payment of page charges. Therefore, and solely to indicate this fact, these articles are hereby designated "advertisements" in accordance with 18 USC section 1734.

**DISCLOSURE OF COMMERCIAL INTEREST:** Johannes Czernin, MD, editor-in-chief of *The Journal of Nuclear Medicine*, has indicated that he is a founder of Sofie Biosciences and holds equity in the company and in intellectual property invented by him, patented by the University of California, and licensed to Sofie Biosciences. He is also a founder and board member of Trethera Therapeutics and holds equity in the company and in intellectual property invented by him, patented by the University of California, and licensed to Triangle. He also serves on the medical advisory board of Actinium Pharmaceuticals and on the scientific advisory boards of POINT Biopharma, RayzeBio, and Jubilant Pharma and is a consultant for Amgen. No other potential conflicts of interest were reported. Manuscripts submitted to *JNM* with potential conflicts are handled by a guest editor.

**EDITORIAL COMMUNICATIONS** should be sent to: Editor-in-Chief, Johannes Czernin, MD, *JNM* Office, SNMMI, 1850 Samuel Morse Drive, Reston, VA 20190-5316. Phone: (703) 326-1185; Fax: (703) 708-9018. To submit a manuscript, go to <https://submit-jnm.snmjournals.org>.

**BUSINESS COMMUNICATIONS** concerning permission requests should be sent to the publisher, SNMMI, 1850 Samuel Morse Drive, Reston, VA 20190-5316; (703) 708-9000; home page address: [jnm.snmjournals.org](http://jnm.snmjournals.org). Subscription requests and address changes should be sent to Membership Department, SNMMI at the address above. Notify the Society of change of address and telephone number at least 30 days before date of issue by sending both the old and new addresses. Claims for copies lost in the mail are allowed within 90 days of the date of issue. Claims are not allowed for issues lost as a result of insufficient notice of change of address. For information on advertising, contact Team SNMMI (Kevin Dunn, Rich Devanna, and Charlie Meitner; (201) 767-4170; fax: (201) 767-8065; [TeamSNMMI@cunnasso.com](mailto:TeamSNMMI@cunnasso.com)). Advertisements are subject to editorial approval and are restricted to products or services pertinent to nuclear medicine. Closing date is the first of the month preceding the date of issue.

**INDIVIDUAL SUBSCRIPTION RATES** for the 2023 calendar year are \$633 within the United States and Canada; \$680 elsewhere. Make checks payable to the SNMMI. CPC IPM Sales Agreement No. 1415158. Sales of individual back copies from 1999 through the current issue are available for \$60 at <http://www.snmml.org/subscribe> ([subscriptions@snmml.org](mailto:subscriptions@snmml.org); fax: (703) 667-5134). Individual articles are available for sale online at <http://jnm.snmjournals.org>.

COPYRIGHT © 2023 by the Society of Nuclear Medicine and Molecular Imaging. All rights reserved. No part of this work may be reproduced or translated without permission from the copyright owner. Individuals with inquiries regarding permission requests, please visit <http://jnm.snmjournals.org/site/misc/permission.xhtml>. Because the copyright on articles published in *The Journal of Nuclear Medicine* is held by the Society, each author of accepted manuscripts must sign a statement transferring copyright (available for downloading at <http://jnm.snmjournals.org/site/misc/fora.xhtml>). See Information for Authors for further explanation (available for downloading at <http://www.snmjournals.org/site/misc/fora.xhtml>).

The ideas and opinions expressed in *JNM* do not necessarily reflect those of the SNMMI or the Editors of *JNM* unless so stated. Publication of an advertisement or other product mentioned in *JNM* should not be construed as an endorsement of the product or the manufacturer's claims. Readers are encouraged to contact the manufacturer with any questions about the features or limitations of the products mentioned. The SNMMI does not assume any responsibility for any injury or damage to persons or property arising from or related to any use of the material contained in this journal. The reader is advised to check the appropriate medical literature and the product information currently provided by the manufacturer of each drug to be administered to verify the dosage, the method and duration of administration, and contraindications.

**EDITOR-IN-CHIEF**

**Johannes Czernin, MD**  
University of California at Los Angeles  
Los Angeles, California

**IMMEDIATE PAST EDITOR**

**Dominique Delbecq, MD, PhD**  
Vanderbilt University Medical Center  
Nashville, Tennessee

**ASSOCIATE EDITORS, CONTINUING EDUCATION**

**Hossein Jadvar, MD, PhD, MPH, MBA, FACNM, FSNMMI**

University of Southern California  
Los Angeles, California

**Lale Kostakoglu, MD, MPH**  
University of Virginia Health System  
Charlottesville, Virginia

**ASSOCIATE EDITORS**

**Ramsey Derek Badawi, PhD**

UC Davis Medical Center  
Sacramento, California

**Henryk Barthel, MD, PhD**

Leipzig University  
Leipzig, Germany

**Frank M. Bengel, MD**

Hannover Medical School  
Hannover, Germany

**Lisa Bodei, MD, PhD**

Memorial Sloan Kettering Cancer Center  
New York, New York

**Irene Buvat, PhD**

Université Paris Sud  
Orsay, France

**Jérémie Calais, MD**

University of California at Los Angeles  
Los Angeles, California

**Sharmila Dorbala, MBBS**

Brigham and Women's Hospital  
Lexington, Massachusetts

**Alexander E. Drzezga, MD**

University Hospital of Cologne  
Cologne, Germany

**Jan Grimm, MD, PhD**

Memorial Sloan Kettering Cancer Center  
New York, New York

**Ken Herrmann, MD, MBA**

Universitätsklinikum Essen  
Essen, Germany

**Thomas A. Hope, MD**

University of California, San Francisco  
San Francisco, California

**Jason S. Lewis, PhD**

Memorial Sloan Kettering Cancer Center  
New York, New York

**David A. Mankoff, MD, PhD**

University of Pennsylvania  
Philadelphia, Pennsylvania

**Heiko Schöder, MD**

Memorial Sloan Kettering Cancer Center  
New York, New York

**Wolfgang Weber, MD**

Technical University of Munich  
München, Germany

**SERIES EDITOR, FOCUS ON MI**

**Carolyn J. Anderson, PhD**

University of Missouri  
Columbia, Missouri

**SERIES EDITOR, HOT TOPICS**

**Heinrich R. Schelbert, MD, PhD**

University of California at Los Angeles  
Los Angeles, California

**CONSULTING EDITORS**

**Nancy Knight, PhD**

University of Maryland School of Medicine  
Baltimore, Maryland

**Barry A. Siegel, MD**

Mallinckrodt Institute of Radiology  
St. Louis, Missouri

**Arnold M. Strashun, MD**

SUNY Downstate Medical Center  
Scarsdale, New York

**H. William Strauss, MD**

Memorial Sloan Kettering Cancer Center  
New York, New York

**ASSOCIATE EDITORS (INTERNATIONAL)**

**Gerald Antoch, MD**

Düsseldorf, Germany

**Richard P. Baum, MD, PhD**

Bad Berka, Germany

**Ambros J. Beer, MD**

Ulm, Germany

**François Bénard, MD, FRCPC**

Vancouver, Canada

**Thomas Beyer, PhD**

Vienna, Austria

**Andreas K. Buck, MD, PhD**

Würzburg, Germany

**Ignasi Carrió, MD**

Barcelona, Spain

**June-Key Chung, MD**

Seoul, Korea

**Stefano Fanti, MD**

Bologna, Italy

**Markus Hacker, MD**

Wien, Austria

**Rodney J. Hicks, MD, FRACP**

Melbourne, Australia

**Michael S. Hofman, MBBS, FRACP**

Melbourne, Australia

**Ora Israel, MD**

Haifa, Israel

**Andreas Kjaer, MD, PhD, DMSc**

Copenhagen, Denmark

**Adriaan A. Lammertsma, PhD**

Amsterdam, The Netherlands

**Michael Lassman, PhD**

Würzburg, Germany

**Helmut R. Mäcke, PhD**

Freiburg, Germany

**Wim J.G. Oyen, MD, PhD**

Milan, Italy

**John O. Prior, MD, PhD**

Lausanne, Switzerland

**Osman Ratib, MD, PhD**

Geneva, Switzerland

**Mike Sathekge, MBChB, MMed, PhD**

Pretoria, South Africa

**Markus Schwaiger, MD**

München, Germany

**Andrew M. Scott, MD**

Heidelberg, Australia

**Nagara Tamaki, MD, PhD**

Kyoto, Japan

**Jia-He Tian, PhD**

Beijing, China

**Mei Tian, MD, PhD**

Hangzhou, China

**EDITORIAL CONSULTANTS**

**Martin S. Allen-Auerbach, MD**

Los Angeles, California

**Magnus Dahlbom, PhD**

Los Angeles, California

**Andrew Quon, MD**

Los Angeles, California

**Christiaan Schiepers, MD, PhD**

Los Angeles, California

**Daniel H. Silverman, MD, PhD**

Los Angeles, California

**Roger Slavik, PhD**

Winterthur, Switzerland

**EDITORIAL BOARD**

**Diane S. Abou, PhD**

St. Louis, Missouri

**Hojjat Ahmadzadehfar, MD**

Dortmund, Germany

**Valentina Ambrosini, MD, PhD**

Bologna, Italy

**Norbert Avril, MD**

Cleveland, Ohio

**Shadfar Bahri**

Los Angeles, California

**Jacques Barbet, PhD**

Saint-Herbalin, France

**Bradley Jay Beattie, PhD**

New York, New York

**Matthias Richard Benz, MD**

Los Angeles, California

**Elie Besserer-Offroy, PhD, FACSc**

Los Angeles, California

**Pradeep Bhambhvani, MD**

Birmingham, Alabama

**Angelika Bischof-Delaloye, MD**

Lausanne, Switzerland

**Christina Bluemel, MD**

Würzburg, Germany

**Ronald Boellaard, PhD**

Groningen, The Netherlands

**Nicolaas Bohnen, MD**

Ann Arbor, Michigan

**Wesley E. Bolch, PhD**

Gainesville, Florida

**Elias H. Botvinick, MD**

San Francisco, California

**Winfried Brenner, MD, PhD**

Berlin, Germany

**Richard C. Brunken, MD**

Cleveland, Ohio

**Ralph Buchert, PhD**

Hamburg, Germany

**Alfred Buck, MD**

Menzingen, Switzerland

**Denis B. Buxton, PhD**

Bethesda, Maryland

**Weibo Cai, PhD**

Madison, Wisconsin

**Federico Caobelli, MD**

Basel, Switzerland

**Giuseppe Carlucci, PhD**

Los Angeles, California

**Richard E. Carson, PhD**

New Haven, Connecticut

**Paolo Castellucci, MD**

Bologna, Italy

**Francesco Ceci, MD, PhD**

Turin, Italy

**Juliano J. Cerchi**

Curitiba, Brazil

**Delphine Chen, MD**

Seattle, Washington

**Xiaoyuan Chen, PhD**

Singapore

**Simon R. Cherry**

Davis, California

**Arturo Chiti, MD**

Rozzano, Italy

**Peter M. Clark, PhD**

Los Angeles, California

**Christian Cohade, MD**

Montreal, Canada

**Ekaterina (Kate) Dadachova, PhD**

Saskatoon, Canada

**Issa J. Dahabreh, MD**

Boston, Massachusetts

**Heike Elisabeth Daldrop-Link, MD, PhD**

Stanford, California

**Farrokh Dehdashti, MD**

St. Louis, Missouri

**Robert C. Delgado-Bolton, MD, PhD**

Logroño, Spain

**Thorsten Derlin, MD**

Hannover, Germany

**Elisabeth G.E. de Vries, PhD**

Groningen, The Netherlands

**Marcelo F. Di Carli, MD**

Boston, Massachusetts

**David W. Dick, PhD**

Iowa City, Iowa

**Vasken Dilsizian, MD**

Baltimore, Maryland

**Jacob Dubroff, MD, PhD**

Philadelphia, Pennsylvania

**Janet F. Eary, MD**

Bethesda, Maryland

**W. Barry Edwards, PhD**

Columbia, Missouri

**Matthias Eiber, MD**

Munich, Germany

**David Eidelberg, MD**

Manhasset, New York

**Georges El Fakhr, PhD**

Boston, Massachusetts

**Peter J. Eil, MD**

London, United Kingdom

**Keigo Endo, MD**

Nantan, Japan

**Einat Even-Sapir, MD, PhD**

Tel Aviv, Israel

**Frederic H. Fahey, DSc**

Boston, Massachusetts

**Melpomeni Fani, PhD, MS**

Basel, Switzerland

**Andrea Farolfi, MD**

Bologna, Italy

**Wolfgang Peter Fendler, MD**

Essen, Germany



**EDITORIAL BOARD, continued**

**James W. Fletcher, MD**  
Indianapolis, Indiana  
**Amy M. Fowler, MD, PhD**  
Madison, Wisconsin  
**Kirk A. Frey, MD, PhD**  
Ann Arbor, Michigan  
**Andrei Gafita**  
Los Angeles, California  
**Victor H. Gerbaudo, PhD, MSHCA**  
Boston, Massachusetts  
**Frederik L. Giesel, MD, PhD, MBA**  
Düsseldorf, Germany  
**Karolien Goffin, MD, PhD**  
Leuven, Belgium  
**Serge Goldman, MD, PhD**  
Brussels, Belgium  
**Stanley J. Goldsmith, MD**  
New York, New York  
**Martin Gotthardt, MD, PhD**  
Nijmegen, The Netherlands  
**Michael Graham, MD, PhD**  
Iowa City, Iowa  
**David Groheux, MD, PhD**  
Paris, France  
**Uwe A. Haberkorn, MD**  
Heidelberg, Germany  
**Mathieu Hatt, PhD, HDR**  
Brest, France  
**Wolf-Dieter Heiss, MD**  
Cologne, Germany  
**Karl Herholz, MD**  
Manchester, United Kingdom  
**Thomas F. Heston, MD**  
Las Vegas, Nevada  
**John M. Hoffman, MD**  
Salt Lake City, Utah  
**Carl K. Hoh, MD**  
San Diego, California  
**Jason P. Holland, DPhil**  
Zurich, Switzerland  
**Roland Hustinx, MD, PhD**  
Liege, Belgium  
**Andrei H. Iagaru, MD**  
Stanford, California  
**Masanori Ichise, MD**  
Chiba, Japan  
**Heather A. Jacene, MD**  
Boston, Massachusetts  
**Francois Jamar, MD, PhD**  
Brussels, Belgium  
**Jaе Min Jeong, PhD**  
Seoul, Korea  
**John A. Katzenellenbogen, PhD**  
Urbana, Illinois  
**Zohar Keidar, MD, PhD**  
Haifa, Israel  
**Kimberly A. Kelly, PhD**  
Charlottesville, Virginia  
**Laura M. Kenny, MD, PhD**  
London, United Kingdom  
**Fabian Kiessling, MD**  
Aachen, Germany  
**E. Edmund Kim, MD, MS**  
Orange, California  
**Francoise Kraeber-Bodéré, MD, PhD**  
Nantes, France  
**Clemens Kratochwil, MD**  
Heidelberg, Germany  
**Kenneth A. Krohn, PhD**  
Portland, Oregon  
**Brenda F. Kurland, PhD**  
Pittsburgh, Pennsylvania  
**Constantin Lapa, MD**  
Augsburg, Germany  
**Suzanne E. Lapi, PhD**  
Birmingham, Alabama  
**Steven M. Larson, MD**  
New York, New York  
**Dong Soo Lee, MD, PhD**  
Seoul, Korea  
**Jeffrey Leyton, PhD**  
Sherbrooke, Canada  
**Xiang-Guo Li, PhD**  
Turku, Finland  
**Hannah M. Linden, MD**  
Seattle, Washington  
**Martin A. Lodge, PhD**  
Baltimore, Maryland  
**Katharina Luckerath, PhD**  
Los Angeles, California  
**Susanne Lütje, MD, PhD**  
Bonn, Germany  
**Umar Mahmood, MD, PhD**  
Boston, Massachusetts

**H. Charles Manning, PhD**  
Nashville, Tennessee  
**Giuliano Mariani, MD**  
Pisa, Italy  
**Chester A. Mathis, PhD**  
Pittsburgh, Pennsylvania  
**Alan H. Maurer, MD**  
Philadelphia, Pennsylvania  
**Jonathan McConathy, MD, PhD**  
Birmingham, Alabama  
**Alexander J.B. McEwan, MD**  
Edmonton, Canada  
**Yusuf Menda, MD**  
Iowa City, Iowa  
**Philipp T. Meyer, MD, PhD**  
Freiburg, Germany  
**Matthias Miederer, MD**  
Mainz, Germany  
**Jasna Mihailovic, MD, PhD**  
Sremska Kamenica, Serbia  
**Erik Mittra, MD, PhD**  
Portland, Oregon  
**Christine E. Mona, PhD**  
Los Angeles, California  
**Dae Hyuk Moon, MD**  
Seoul, Korea  
**Jennifer Murphy, PhD**  
Los Angeles, California  
**Helen Nadel, MD, FRCP**  
Stanford, California  
**Matthias Nahrendorf, MD, PhD**  
Boston, Massachusetts  
**Yuji Nakamoto, MD, PhD**  
Kyoto, Japan  
**David A. Nathanson, PhD**  
Los Angeles, California  
**Nghi C. Nguyen, MD, PhD**  
Dallas, Texas  
**Sridhar Nimmagadda, PhD**  
Baltimore, Maryland  
**Egbert U. Nitzsche, MD**  
Aarau, Switzerland  
**Daniela E. Oprea-Lager, MD, PhD**  
Amsterdam, The Netherlands  
**Medhat M. Osman, MD, PhD**  
Saint Louis, Missouri  
**Christopher J. Palestro, MD**  
New Hyde Park, New York  
**Miguel Hernandez Pampaloni, MD, PhD**  
San Francisco, California  
**Neeta Pandit-Taskar, MD**  
New York, New York  
**Ashwin Singh Parihar, MBBS, MD**  
Saint Louis, Missouri  
**Michael E. Phelps, PhD**  
Los Angeles, California  
**Gerold Porenta, MD, PhD**  
Vienna, Austria  
**Sophie Poty, PhD**  
Montpellier, France  
**Edwin (Chuck) Pratt, PhD, MS Eng**  
New York, New York  
**Daniel A. Pryma, MD**  
Philadelphia, Pennsylvania  
**Valery Radchenko, PhD**  
Vancouver, Canada  
**Caius G. Radu, MD**  
Los Angeles, California  
**Isabel Rauscher, MD**  
Munich, Germany  
**Nick S. Reed, MBBS**  
Glasgow, United Kingdom  
**Mark Rijpkema, PhD**  
Nijmegen, The Netherlands  
**Steven P. Rowe, MD, PhD**  
Baltimore, Maryland  
**Mehran Sadeghi, MD**  
West Haven, Connecticut  
**Orazio Schillaci, MD**  
Rome, Italy  
**Charles Ross Schmidlein, PhD**  
New York, New York  
**David M. Schuster, MD**  
Atlanta, Georgia  
**Travis Shaffer, PhD**  
Stanford, California  
**Sai Kiran Sharma, PhD**  
New York, New York  
**Anthony F. Shields, MD, PhD**  
Detroit, Michigan  
**Barry L. Shulkin, MD, MBA**  
Memphis, Tennessee  
**Yu Shyr, PhD**  
Nashville, Tennessee

**Albert J. Sinusas, MD**  
New Haven, Connecticut  
**Riener H.J.A. Slart, MD, PhD**  
Groningen, The Netherlands  
**Piotr Slomka, PhD, FACC**  
Los Angeles, California  
**Simon John Christoph Soerensen, MD**  
Stanford, California  
**Ida Sonni, MD**  
Los Angeles, California  
**Michael G. Stabin, PhD**  
Richland, Washington  
**Lisa J. States, MD**  
Philadelphia, Pennsylvania  
**Sven-Erik Strand, PhD**  
Lund, Sweden  
**Rathan M. Subramaniam, MD, PhD, MPH**  
Dunedin, New Zealand  
**John Sunderland, PhD**  
Iowa City, Iowa  
**Suleman Surti, PhD**  
Philadelphia, Pennsylvania  
**Julie Sutcliffe, PhD**  
Sacramento, California  
**David Taieb, MD, PhD**  
Marseille, France  
**Laura H. Tang, MD, PhD**  
New York, New York  
**Ukihide Tateishi, MD, PhD**  
Tokyo, Japan  
**James T. Thackeray, PhD**  
Hannover, Germany  
**Mathew L. Thakur, PhD**  
Philadelphia, Pennsylvania  
**Alexander Thiel, MD**  
Montreal, Canada  
**Daniel L.J. Thorek, PhD**  
St. Louis, Missouri  
**David W. Townsend, PhD**  
Singapore  
**Timothy Turkington, PhD**  
Durham, North Carolina  
**Gary A. Ulaner, MD, PhD**  
Irvine, California  
**David Ulmert, MD, PhD**  
Los Angeles, California  
**Lena M. Unterrainer, MD, MHBA**  
Munich, Germany  
**Christopher H. van Dyck, MD**  
New Haven, Connecticut  
**Douglas Van Nostrand, MD**  
Washington, District of Columbia  
**Patrick Veit-Haibach, MD**  
Toronto, Canada  
**Nerissa Viola-Villegas, PhD**  
Detroit, Michigan  
**John R. Votaw, PhD**  
Atlanta, Georgia  
**Richard L. Wahl, MD**  
St. Louis, Missouri  
**Anne Marie Wallace, MD**  
La Jolla, California  
**Martin A. Walter, MD**  
Geneva, Switzerland  
**Rudolf A. Werner, MD**  
Wuerzburg, Germany  
**Andreas G. Wibmer, MD**  
New York, New York  
**Anna M. Wu, PhD**  
Duarte, California  
**Randy Yeh, MD**  
New York, New York  
**Hyewon (Helen) Youn, PhD**  
Seoul, Korea  
**Pat B. Zanzonico, PhD**  
New York, New York  
**Brian M. Zeglis, PhD**  
New York, New York  
**Robert Zeiser, MD**  
Freiburg, Germany  
**Hong Zhang, MD, PhD**  
Hangzhou, China  
**Hongming Zhuang, MD, PhD**  
Philadelphia, Pennsylvania  
**Sibylle I. Ziegler, PhD**  
Munich, Germany

**ASSISTANT TO THE EDITOR**

**Joshua N. Wachtel**  
Los Angeles, California

**SNMMI** SOCIETY OF  
NUCLEAR MEDICINE &  
MOLECULAR IMAGING  
MID-WINTER MEETING

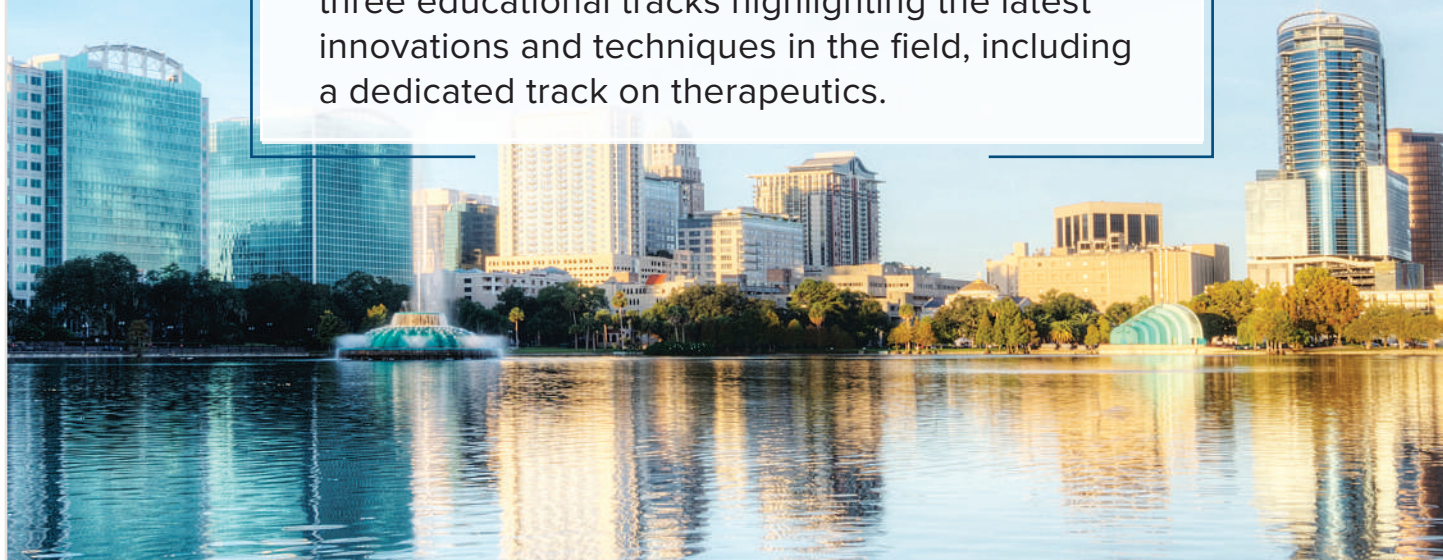
**ACNM**  
ANNUAL MEETING

**EARLY BIRD REGISTRATION DEADLINE:  
JANUARY 4, 2024**

**[WWW.SNMMI.ORG/MWM](http://WWW.SNMMI.ORG/MWM)**

**Feb. 1-3  
2024  
SNMMI Mid-Winter  
and ACNM Annual  
Meeting**  
Hilton Orlando Lake Buena Vista  
ORLANDO, FLORIDA

The 2024 SNMMI Mid-Winter and ACNM Annual Meeting—February 1-3 in Orlando, FL—will feature three educational tracks highlighting the latest innovations and techniques in the field, including a dedicated track on therapeutics.



# Don't Make This Your LAST Issue of The Journal of Nuclear Medicine

## Renew your SNMMI membership.

SNMMI members receive a complimentary subscription to *The Journal of Nuclear Medicine (JNM)*. Keep access to this world-renowned publication by renewing your SNMMI membership for the coming year!

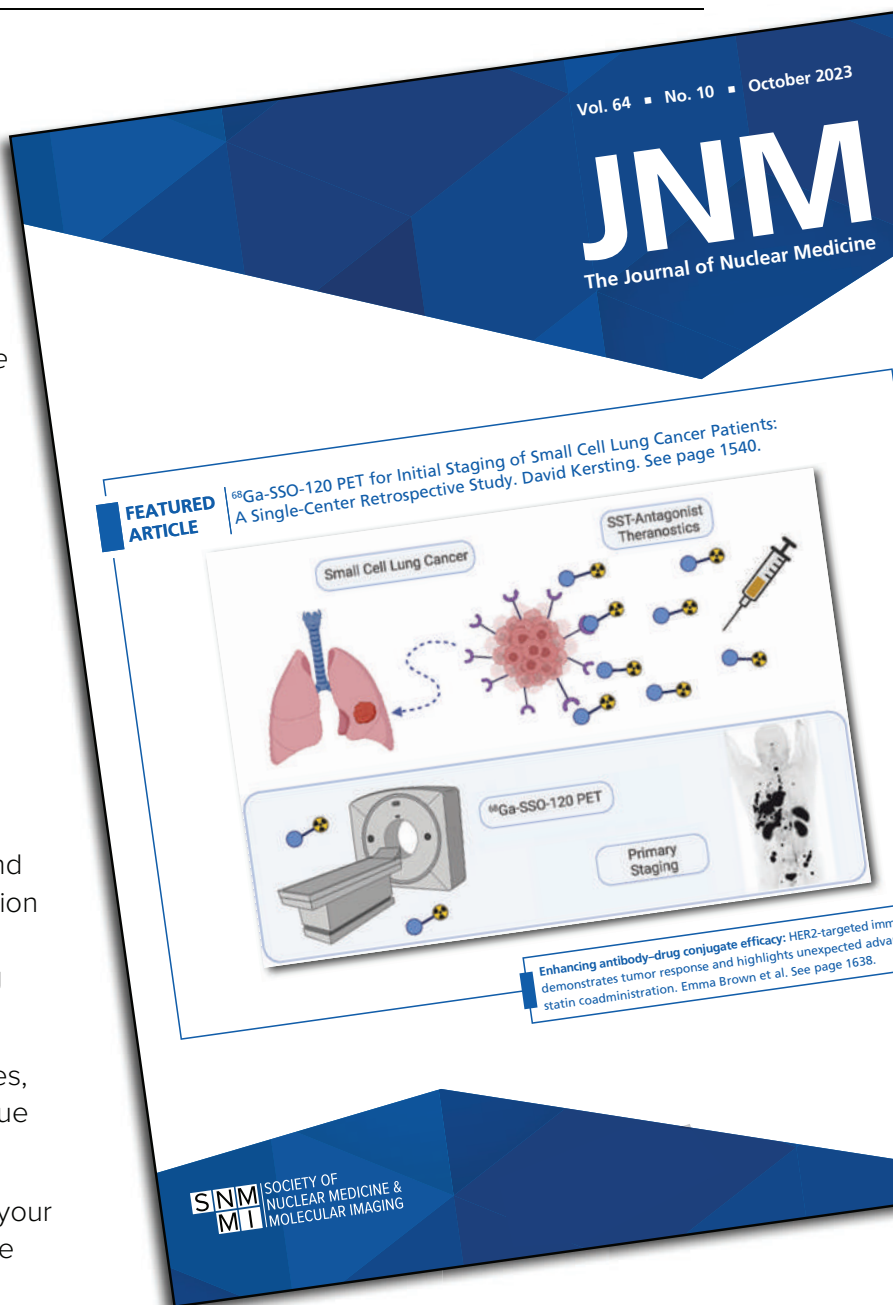
This past year, *The Journal of Nuclear Medicine* earned an impact factor of 9.3, ranking sixth in impact among 203 medical journals worldwide in the radiology, nuclear medicine and medical imaging category.

- Impact factor – 9.3
- Five-year impact factor – 9.0
- Immediacy index – 4.6
- Total citations – 31,896
- Eigenfactor Score – 0.02649
- Article Influence Score – 2.257

JNM offers readers around the globe clinical and basic science investigations, continuing education articles, state-of-the-art reviews, employment opportunities, and updates on rapidly changing issues in practice and research.

Your subscription includes full access to archives, SNMMI annual meeting abstracts, complete-issue PDFs, and online ahead-of-print articles.

Renew now to ensure uninterrupted access to your monthly JNM issues, as well as continued online access to years of archived research.



[www.snmami.org/RENEW](http://www.snmami.org/RENEW)

**SNMMI** SOCIETY OF  
NUCLEAR MEDICINE &  
MOLECULAR IMAGING



**Advancing innovation and translation:** Czernin interviews Kalevi Kairemo, president-elect of the World Association of Radiopharmaceutical and Molecular Therapy, about a diverse career in pioneering novel radiolabeled therapeutics. . . . . *Page 1671*

**FAPI in rheumatologic disorders:** Schmidkonz and colleagues offer perspective on the current and future potential of fibroblast-activation protein inhibitor PET in noninvasive characterization of rheumatoid arthritis, lung fibrosis, and IgG4-related disease. . . . . *Page 1674*

**Development of infection tracers:** Signore and participants summarize the consensus results of a 2022 International Atomic Energy Agency technical meeting focused on the use of radiolabeled agents for imaging of bacterial infection. . . . . *Page 1676*

**IDH mutation and metabolic heterogeneity:** Lohmeier and colleagues investigate metabolic reprogramming of glioma using compartmental uptake characteristics in  $^{18}\text{F}$ -FET PET and evaluate the diagnostic potential for isocitrate dehydrogenase genotyping. . . . . *Page 1683*

**Imaging biomarkers in breast cancer:** Hennessy and colleagues ask whether  $^{18}\text{F}$ -FDG PET/CT lean body mass parameters can predict recurrence-free and overall survival in patients with estrogen receptor-negative, HER2-positive breast cancer and neoadjuvant trastuzumab and pertuzumab therapy. . . . . *Page 1690*

**$^{18}\text{F}$ -FDG PET breast cancer therapy response:** Gebhart provides context and commentary on the potential of  $^{18}\text{F}$ -FDG PET assessment of metabolic response in neoadjuvant systemic therapy for breast cancer. . . . . *Page 1697*

**$^{18}\text{F}$ -FDOPA PET and prognosis in midgut NETs:** De Rycke and colleagues explore the prognostic role of  $^{18}\text{F}$ -FDOPA PET/CT tumor uptake in metastatic midgut neuroendocrine tumors. . . . . *Page 1699*

**$\Delta\text{SUV}_{\text{max}}$  for interim PET in DLBCL:** Itti and colleagues use phase 3 trial data from patients with diffuse large B-cell lymphoma to compare the prognostic value of PET protocol interpretation criteria with that of change in  $\text{SUV}_{\text{max}}$  alone. . . . . *Page 1706*

**$^{68}\text{Ga}$ -FAPI PET/CT impact on management:** Koerber and colleagues analyze the clinical impact of  $^{68}\text{Ga}$ -fibroblast-activation protein inhibitor PET/CT in staging and management in a large cohort of patients with various tumors. . . . . *Page 1712*

**ctDNA biomarkers and  $^{177}\text{Lu}$ -PSMA:** Sartor and colleagues investigate pretreatment circulating tumor DNA findings, including gene amplifications, in responders and nonresponders to  $^{177}\text{Lu}$ -PSMA-based therapies for metastatic castration-resistant prostate cancer. . . . . *Page 1721*

**$^{177}\text{Lu}$ -PSMA-617 vs docetaxel in mCRPC:** Satapathy and colleagues report on final analysis of overall survival for a phase 2 randomized trial of  $^{177}\text{Lu}$ -PSMA-617 and docetaxel in chemotherapy-naïve metastatic castration-resistant prostate cancer patients. . . . . *Page 1726*

**Antihormonal treatment and  $^{68}\text{Ga}$ -PSMA-11:** Kluge and colleagues explore the effects of androgen deprivation therapy on PSMA ligand biodistribution and discuss implications for treatment-optimizing and side-effect-minimizing strategies for PSMA radioligand therapies. . . . . *Page 1730*

**End-of-treatment PSMA PET:** Murthy and colleagues assess the prognostic value of end-of-treatment PSMA PET/CT in patients with metastatic castration-resistant prostate cancer treated with  $^{177}\text{Lu}$ -PSMA radioligand therapy. . . . . *Page 1737*

**Bone scan vs PSMA PET:** Hope and colleagues evaluate the ability of bone scans to detect osseous metastases from prostate cancer at initial staging using PSMA PET as a reference standard. . . . . *Page 1744*

**Redefining prostate cancer imaging:** Eifer and colleagues provide commentary on the current dynamic landscape of prostate cancer imaging and on the challenges and promise of integrating PSMA PET/CT findings into clinical treatment decision-making. . . . . *Page 1748*

**PSMA PET to predict csPca:** Zhang and colleagues introduce a PSMA PET-based model to improve the diagnostic accuracy of clinically significant prostate cancer in patients with preoperative Gleason grade group 1 biopsy. . . . . *Page 1750*

**Response prediction for PSMA therapy:** Hohberg and colleagues analyze  $^{177}\text{Lu}$ -PSMA absorbed doses in osseous versus lymphatic metastases in patients with metastatic castration-resistant prostate cancer across therapy cycles and relate those data, along with pretherapeutic PSMA PET, to therapeutic success. . . . . *Page 1758*

**HRQoL with mCRPC after PSMA RLT:** Karimzadeh and colleagues use the European Organization for Research and Treatment of Cancer quality-of-life questionnaire to assess health-related metrics for patients with metastatic castration-resistant prostate cancer receiving consecutive cycles of  $^{177}\text{Lu}$  therapy. . . . . *Page 1765*

**Tandem  $^{177}\text{Lu}/^{225}\text{Ac}$  PSMA RLT in mice:** Meyer and colleagues directly compare  $\alpha$ - and  $\beta$ -particle PSMA treatment, as well as a combination of the 2, at different stages of disease in a murine model of disseminated prostate cancer. . . . . *Page 1772*

**Combined [ $^{177}\text{Lu}$ ]Lu-PSMA-617 RPT and SBRT:** Grkovski and colleagues describe a pilot trial of the feasibility of combining [ $^{177}\text{Lu}$ ]Lu-PSMA-617 treatment with stereotactic body radiotherapy in patients with oligometastatic castration-sensitive prostate cancer. . . . . *Page 1779*

**MRT radiobiology symposium:** Nonnekens and participants summarize research and insights from the second International Workshop on Radiobiology of Molecular Radiotherapy, held in London in 2023. . . . . *Page 1788*

**$^{203}\text{Pb}$  production with electroplated  $^{205}\text{Tl}$ :** Saini and colleagues detail optimization of production and separation of high-specific-activity  $^{203}\text{Pb}$  using electroplated thallium targets and propose associated radiochemistry enhancements. . . . . *Page 1791*

**Tau threshold biostatistical estimation:** Gogola and colleagues compare multiple tau PET threshold-determining methods in study participants undergoing  $^{18}\text{F}$ -flortaucipir or  $^{18}\text{F}$ -MK-6240 imaging. . . . . *Page 1798*

**PET imaging of IL12/23p40 in IBD:** Rezazadeh and colleagues describe the potential of immuno-PET to image inflammation in a chemically induced mouse model of colitis by targeting IL12/23p40 with an  $^{89}\text{Zr}$ -radiolabeled anti-IL12/23p40 antibody. . . . . *Page 1806*

**LAFOV  $^{89}\text{Zr}$  immuno-PET:** Mohr and colleagues look at SUV differences between  $^{89}\text{Zr}$  immuno-PET scans obtained using PET/CT systems with long and standard axial fields of view and at how LAFOV PET scan duration affects image noise and SUV metrics. . . . . *Page 1815*

**Total-body dynamic PET and COVID recovery:** Wang and colleagues demonstrate quantification of glucose metabolism using total-body multiparametric  $^{18}\text{F}$ -FDG PET and assess specific glucose delivery and phosphorylation processes for studying COVID recovery. . . . . *Page 1821*

**[ $^{11}\text{C}$ ]-Butanol total-body perfusion:** Li and colleagues report on a pilot study using [ $^{11}\text{C}$ ]-butanol imaging on the uEXPLORER total-body PET/CT scanner for quantitative measurement of perfusion across the entire body. . . . . *Page 1831*

**Sialadenitis on PET:** Maliha and colleagues present findings from [ $^{68}\text{Ga}$ ]Ga-FAPI-46 PET and [ $^{18}\text{F}$ ]FDG PET in a case of obstructive sialadenitis from oral squamous cell carcinoma. . . . . *Page 1839*



# Advancing Nuclear Medicine at the Multiomics Intersection

## Johannes Czernin Discusses Innovation and Translation with Kalevi Kairemo

Kalevi Kairemo<sup>1</sup> and Johannes Czernin<sup>2</sup>

<sup>1</sup>*Docrates Cancer Center, Helsinki, Finland (retired); and* <sup>2</sup>*David Geffen School of Medicine at UCLA, Los Angeles, California*

**J**ohannes Czernin, MD, editor-in-chief of *The Journal of Nuclear Medicine* and a professor at the David Geffen School of Medicine at UCLA, talked with Kalevi Kairemo, MD, PhD, MSc (Eng), about his career in pioneering novel radiolabeled therapeutics. Dr. Kairemo is now retired as chief physician/professor, molecular radiotherapy and nuclear medicine, at the Docrates Cancer Center (Helsinki, Finland) and, since 2015, has served as a visiting professor in nuclear medicine at the University of Texas M.D. Anderson Cancer Center (Houston). His research is based on multiomics, making discoveries at the nexus of genomics, transcriptomics, proteomics, metabolomics, microbiomics, epigenomics, imaging, and precision medicine.

Dr. Kairemo graduated with an MSc (Eng) degree from the Helsinki University of Technology (Finland) in 1980 before completing his medical (1986) and doctorate (1993) degrees at the University of Helsinki. From 1989 to 1993 he held a postdoctoral research fellowship at the Memorial Sloan Kettering Cancer Center (MSKCC; New York, NY). He undertook specialist training in clinical chemistry (1994), nuclear medicine (1996), health care administration (2002), and pharmaceutical medicine (2006) at the Helsinki University Central Hospital. He has held faculty leadership positions at the Norwegian University of Science and Technology (Trondheim), Uppsala University Hospital (Sweden), and the Docrates Cancer Center. He has been active in transitioning new agents and techniques through the developmental pipeline and is the author of more than 250 peer-reviewed publications. Dr. Kairemo is the president-elect of the World Association of Radiopharmaceutical and Molecular Therapy (WARMTH).

**Dr. Czernin:** *You had a very diverse training and professional career. You were trained in chemical engineering but then switched to medicine, became chief physician of a big clinic, and are still a visiting professor at M.D. Anderson. You also were trained in health care administration. You ended up in nuclear medicine and were elected to serve as president of WARMTH. Can you briefly describe this unusual career trajectory?*

**Dr. Kairemo:** At the Helsinki University of Technology in the 1970s, I was majoring in physical chemistry and technical biochemistry. My thesis was about electrochemistry, and suddenly I realized that I did not know anything about human physiology or cellular electrolyte balance. Therefore, in the 1980s I started to study medicine. From the beginning I was interested in research. After various attempts, nuclear medicine became my research choice. While I was doing a summer job, I learned “the tracer principle” from, strangely enough, a pediatric patient. In 1986 a

preschool boy asked me very precise questions, and I was obliged to answer at a level that a child could understand—from the most basic perspective. The following summer I worked in the same place and embarked on a dissertation on radiolabeled monoclonal antibodies. I pursued a multidisciplinary career with a clear focus that required administrative skills and flexibility.

**Dr. Czernin:** *What attracted your interest in joining the lab of Steven Larson, MD, at MSKCC?*

**Dr. Kairemo:** I had heard his Georg de Hevesy Lecture about radiolabeled monoclonal antibodies at the European Association of Nuclear Medicine conference in Budapest, Hungary, in 1987. Then I met him personally at the 1988 SNMMI conference in San Francisco (CA), where I had 2 clinical posters about immunoscintigraphy. After discussions, he offered a fellowship at MSKCC.

**Dr. Czernin:** *You stayed at MSKCC for 4 years. What prompted you to return to Europe, and what did you learn from your time in New York? What did you take home to Finland?*

**Dr. Kairemo:** Those 4 years were spent in 2 phases. At that time there were 4 isotopes of radioiodine (<sup>123</sup>I, <sup>124</sup>I, <sup>125</sup>I, and <sup>131</sup>I) that could be given to patients. I first did nonclinical experiments and brought new methods back to Finland, such as radioimmuno-histochemistry and digital autoradiography. I also learned the theranostic concept, that one can use the same radioactive compound in vitro and in vivo in diagnostics and therapy and then confirm the results with ex vivo tissue sampling. The MSKCC period gave me courage to start new therapies, including radioimmunotherapy and Auger-chemotherapy in Helsinki in the early 1990s. At MSKCC I also learned how to build a team and that a critical mass is needed for team success.

**Dr. Czernin:** *Early in your career you developed a strong interest in industry-academia relationships. How did this interest develop?*

**Dr. Kairemo:** In 2000 I was introduced to Erkki Koivunen, PhD, from the lab of Erkki Ruoslahti, MD, PhD, who discovered the phage display technique and the RGD peptides. I briefly showed Dr. Koivunen some of the animal imaging and radiolabeling we were performing in Helsinki. We decided to join forces and introduced the idea of targeted nanoparticles. My role was in translational research, developing in silico/in vitro/ex vivo data to create new multidisciplinary compounds for in vivo research and to optimize their pharmacokinetic and -dynamic behavior. This idea was selected as “best business idea” in Finland in 2001, and



**Kalevi Kairemo, MD, PhD, MSc (Eng)**

Published online Oct. 19, 2023.

COPYRIGHT © 2023 by the Society of Nuclear Medicine and Molecular Imaging.  
DOI: 10.2967/jnumed.123.266793

we established the biotech CTT Cancer Targeting Technologies in Finland. Initially, I thought that it was impossible to develop nanoparticles that could contain cytotoxic molecules, gas bubbles, RNA strains, and other targeted loads at the good-manufacturing-practice level—but I was wrong.

**Dr. Czernin:** *With which companies were you involved, and what was the focus of your industry work?*

**Dr. Kairemo:** In industry, I worked as medical director of CTT Cancer Targeting Technologies, medical director of Imanext (2006–2008), and clinical director at Advanced Accelerator Applications (AAA; 2009) (now Novartis Co.). The CTT biotech company that we started in 2001 was a good example of success, going from laboratory bench to a phase I clinical trial in 5 years, with many contracts between multinational conglomerates and small spinoff biotech companies. We also grew quickly from 0 to 30 employees. In 2006, we founded Imanext as a contract research organization. Within 1 year, we had a large U.S. pharma customer that wanted us to conduct global clinical trials in radionuclide therapy in approximately 25 centers in 15 countries. The trials could not be finished because of the U.S. financial crisis in 2008.

When AAA started to develop its first theranostic compound in 2009, I created the regulatory environment and was involved in designing the phase 1/2 trial of Lutathera ( $^{177}\text{Lu}$ -DOTATATE), which received marketing authorization in 2017. The company was sold for €3.9 billion to Novartis.

**Dr. Czernin:** *How did your university view your industry relationships? Were they supportive?*

**Dr. Czernin:** *After your academic career you became involved in a private center that provided diagnostic and therapeutic services. Can you describe this clinic? How large was it?*

**Dr. Kairemo:** In 2009, the full-service private oncology Docrates Center was built in Helsinki. In the same building there was a radiopharmaceutical company that owned a cyclotron. The Docrates Cancer Center had PET/CT, SPECT/CT, 3-T MRI, and 2 linear accelerators, with about 50 employees. I started  $^{177}\text{Lu}$ -octreotate therapies in 2010 and soon treated Finnish residents and patients from other countries. We introduced voxel-based dosimetry to improve therapy planning. Our clinic also had many cancer patients, and we introduced imaging probes, including  $^{68}\text{Ga}$ -prostate-specific membrane antigen [PSMA]-11 and  $^{18}\text{F}$ -PSMA compounds,  $^{18}\text{F}$ -fluorestradiol, and  $^{18}\text{F}$ -Na for evaluating  $^{223}\text{Ra}$  therapy response. In the mid-2010s we started using  $^{177}\text{Lu}$ -PSMA-617 and  $^{177}\text{Lu}$ -PSMA-I&T. I introduced these radioligand therapies in neighboring countries such as Sweden, Norway, and Estonia. Later I helped many institutions to set up their own treatment protocols.

**Dr. Czernin:** *You set up mobile PET services. How did this work, and why was this necessary?*

**Dr. Kairemo:** Finland has 5 university hospitals for 5.5 million inhabitants. It is a large country with long distances outside the capital region. PET cameras initially were only in Turku and Helsinki (southern Finland). Mobile PET/CT trucks visited hospitals in different locations every day and also went to Sweden and Estonia. Today there is not much need for this, because all university hospitals and multiple regional hospitals have their own PET scanners.

---

Because of their sensitivity, specificity, time factors, and depth resolution in imaging, radionuclide methods cannot be replaced. Relevant therapy products can be designed for targeting and optimal kinetic constants. I have believed in this method for more than 30 years, and now we have products such as Pluvicto that have changed the treatment paradigm. Theranostics are here to stay.

---

**Dr. Kairemo:** When I first asked in the mid-1990s, the university hospital had no capabilities for supporting industry collaboration, so I could not patent anything. Later, in the early 2000s, my university had its own company to support this kind of development. We held 12 patents in our biotech portfolio.

**Dr. Czernin:** *You also started your own company? What was its focus?*

**Dr. Kairemo:** We founded Imanext in 2006 as a contract research organization, with a focus on providing imaging services for the pharmaceutical industry. Among the products were phase 0 trials (exploratory investigational new drugs), also using SPECT/CT. We designed a major clinical trial for big pharma globally, including Africa, Australia, and South America.

**Dr. Czernin:** *You were quite heavily involved in designing clinical trials. How did you learn about the regulatory landscape?*

**Dr. Kairemo:** I had collaborated with multiple radiopharmaceutical companies since the late 1980s, so I had to know the regulatory rules. In the CTT biotech we were aiming for clinical tracers, so I was forced to learn the regulatory environment. We collaborated with many contract research organizations. As clinical director of the AAA in France/Italy in 2009 I set up the regulatory environment. I was involved with initiating and designing the NETTER-1 study. I learned how regulatory requirements had grown to make large-scale physician-initiated trials almost impossible without massive institutional support.

**Dr. Czernin:** *How is nuclear medicine set up in Finland and other Scandinavian countries? Is it an independent specialty or part of radiology? You are aware that even in Europe some institutions merge radiology with nuclear medicine. What do you think about this?*

**Dr. Kairemo:** Briefly, nuclear medicine in Finland used to be a subspecialty (when I studied) within radiology, clinical physiology, or clinical chemistry. Later it became an independent specialty combined with clinical physiology (which used to be a main specialty in Finland, Sweden, and Denmark). In Norway, nuclear medicine could be combined with clinical chemistry as well. Therefore, in Scandinavia, the pressure to merge radiology with nuclear medicine has not been as high as in many other European countries (e.g., The Netherlands). It is fine that radiologists are fond of nuclear medicine and want to read scans. However, most radiologists are not interested in treating patients. Nuclear medicine is more than interpretation of images; it is also radiochemistry, pharmacology, nuclear physics, immunology, and more.

**Dr. Czernin:** *Can you describe briefly the Finnish health care system? Is it public only or public and private? What percentage of patients have private insurance?*

**Dr. Kairemo:** Public health care covers more than 90% of medical treatment, with no large regional differences in availability or quality. Private health care is often used in situations where there are long treatment waits or medical debt. Only a fourth of the

population (<1.3 million individuals) has private insurance, and almost half of these are children.

**Dr. Czernin:** *When you compare the health care systems in Europe with the ones in the United States in terms of quality of care for patients, accessibility, and availability, which system do you personally prefer? The question that I often ask Europeans in this series is: Do you prefer a system for everyone or a system for many that may leave out many?*

**Dr. Kairemo:** I absolutely prefer a system for everyone. We are almost there in many countries in Europe. However, the resources, including quality, accessibility, and availability, vary and will remain different despite national and international harmonization efforts.

**Dr. Czernin:** *Let's talk about theranostics. How did you get into theranostics? What is your view of the current state and future in Scandinavia and beyond?*

**Dr. Kairemo:** I started radioimmunotherapy in Finland in the mid-1990s and had to select patients by either in vivo or ex vivo imaging. In the next phase I became interested in peptide-receptor radionuclide therapy with somatostatin receptor ligands, first in Helsinki with an <sup>111</sup>In-labeled compound, then in Uppsala with a <sup>90</sup>Y-labeled compound. Then I worked with AAA and gained experience in France with <sup>177</sup>Lu-labeled compounds. At Docrates my own department was known as the “molecular radiotherapy” or “theranostics” department.

Because of their sensitivity, specificity, time factors, and depth resolution in imaging, radionuclide methods cannot be replaced. Relevant therapy products can be designed for targeting and optimal kinetic constants. I have believed in this method for more than 30 years, and now we have products such as Pluvicto that have changed the treatment paradigm. Theranostics are here to stay.

**Dr. Czernin:** *What are your treatment protocols like in Finland? In Germany, all patients must be inpatients. It's the same in Austria. In the United States, every patient is an outpatient.*

**Dr. Kairemo:** In our case, they can be either in- or outpatients. If they live nearby and the measured activity is less than 15  $\mu$ Sv/h

at a 1-m distance, they can leave the institution; others are inpatients in lead-shielded hotel rooms or in the hospital.

**Dr. Czernin:** *One important development is the emergence of dosimetry as a routine component of theranostics. How did you implement this and use it in your practice?*

**Dr. Kairemo:** I knew that patient dosimetry is very individual. I also knew that nephrotoxicity may exist and that individual values vary in this respect. Luckily, my physicist was specialized in nuclear physics and had mathematic skills. Together we created a voxel-based dosimetry program in 2010 that could routinely be applied in patients.

**Dr. Czernin:** *Your work has reached beyond Scandinavia. Can you tell us a little about your work for WARMTH and your outreach to African countries?*

**Dr. Kairemo:** I knew the key people in WARMTH even before it was established in 2009. I was present at the founding meeting of WARMTH's predecessor, the World Radiopharmaceutical Therapy Council, at the SNMMI meeting in 1999. My second contact with this group was at an International Atomic Energy Agency congress in 2002 in Beijing, China, where there were 150 participants from 72 countries.

WARMTH has arranged 2 world conferences in Africa: in Capetown, South Africa, in 2010 and Accra, Ghana, in 2023. During our last meeting in Ghana, the first therapy dose of <sup>177</sup>Lu-PSMA was given in Accra. In addition, we visited another hospital in Ghana that has been established by a European initiative. I am currently working with a research collaboration in Ghana.

**Dr. Czernin:** *Dr. Kairemo, yours has been an astonishingly diverse career encompassing research, industry-academia relationships, private health care experiences, leadership in international organizations, and much more. This may serve as an example of the near limitless opportunities in the fields of nuclear medicine, molecular imaging, and theranostics. I thank you very much for your time.*

# FAPI PET/CT Immune-Fibrosis Imaging for New Insights into Rheumatologic Disorders

Christian Schmidkonz<sup>1,2</sup>, Armin Atzinger<sup>1</sup>, Andreas Ramming<sup>3</sup>, and Torsten Kuwert<sup>1</sup>

<sup>1</sup>Department of Nuclear Medicine, Friedrich–Alexander University Erlangen–Nürnberg and University Hospital Erlangen, Erlangen, Germany; <sup>2</sup>Department of Industrial Engineering and Health, Technical University of Applied Sciences Amberg–Weiden, Weiden, Germany; and <sup>3</sup>Department of Internal Medicine 3 (Rheumatology and Immunology), Friedrich–Alexander University Erlangen–Nürnberg and University Hospital Erlangen, Erlangen, Germany

**I**mmune-mediated diseases are associated with substantial activation of tissue-resident fibroblasts resulting in fibrosis and organ damage (1). Despite the overall low incidence of fibrotic diseases, fibrotic tissue responses across different diseases have been estimated to account for up to 45% of deaths in high-income countries, causing socioeconomic costs of tens of billions of U.S. dollars per year (2). Although the detection of active inflammation by, for example, <sup>18</sup>F-FDG PET/CT is implemented in the clinical routine, the in vivo visualization of immune-mediated tissue remodeling has not been possible until recently (3,4). With the development of radiolabeled quinoline-based tracers suitable for PET that act as fibroblast-activation protein inhibitors (FAPIs), noninvasive characterization of rheumatologic disorders is now available. Clinical assessments of disease activity in immune-mediated rheumatologic disorders such as rheumatoid arthritis or systemic sclerosis (SSC)–associated interstitial lung disease usually include physical examinations and evaluation of functional parameters, as well as the patient’s self-reporting of disease activity and quality of life (5). Progression of disease is defined as tissue destruction between 2 patient examinations, meaning that disease activity is measured only indirectly by progression of existing tissue damage. Direct measurement of disease activity is not established in clinical practice. Instead, PET/CT imaging using FAPIs may serve as a reliable, reproducible, and objective indicator of disease activity (6). Activated fibroblasts that are located in the lining and sublining of the synovium contribute to pannus formation and bone destruction in rheumatoid arthritis, whereas fibroblasts in the lung tissue react to stimulation by an excessive release of extracellular matrix, resulting in progressive tissue fibrosis. To date, PET with <sup>18</sup>F-FDG or MRI is the method of choice for the detection and quantification of inflammation; however, this method does not allow for visualization of mesenchymal stromal activation and the subsequent process of tissue destruction.

## RHEUMATOID ARTHRITIS

An impressive example of the use of FAPI PET/CT for the detection and quantification of disease in rheumatoid arthritis was

given by Luo et al. (7). These authors performed a prospective dual-tracer PET/CT study using <sup>68</sup>Ga-FAPI and <sup>18</sup>F-FDG PET/CT in 20 patients with rheumatoid arthritis. They found that both imaging modalities were able to detect disease-affected joints; however, FAPI PET/CT was more sensitive in this regard than <sup>18</sup>F-FDG PET/CT. Furthermore, SUV<sub>max</sub> correlated with clinical and laboratory disease activity and radiographic progression of joint damage. Further studies that directly compare the use of FAPI PET/CT and the actual standard MRI are warranted to determine the potential role of this novel molecular medicine tool for therapy planning. A possible future therapeutic approach in patients with rheumatoid arthritis guided by FAPI PET/CT was evaluated by Dorst et al. (8). They used anti-fibroblast activation protein–targeted photodynamic therapy on rheumatoid synovial explants and found an upregulation of cell death markers, whereas no significant side effects were noted on the macrophages of neighboring fibroblasts. With this novel therapeutic approach, aberrant synovial cells previously identified using FAPI PET/CT could selectively be targeted without any systemic side effects.

## LUNG FIBROSIS

In contrast to rheumatoid arthritis, which is characterized by a strong inflammatory component, in SSC interstitial lung disease the activation of fibroblasts leads to excessive fibrosis of the lungs. Pulmonary fibrosis is often a severe and progressive condition, and despite the possibility of detecting interstitial lung diseases with the current standard imaging technique high-resolution CT and pulmonary function testing, monitoring of disease activity remains challenging, since the course of disease is highly variable (9). Furthermore, current diagnostic approaches do not predict the course of pulmonary fibrosis and do not enable appropriate risk stratification. In a single-center pilot study, Bergmann et al. studied a group of 21 patients with SSC interstitial lung disease who underwent FAPI PET/CT (6). Bergmann et al. could demonstrate that FAPI uptake was increased in patients with higher clinical activity scores and that the magnitude of tracer accumulation correlated with progression of disease independently of the extent of involvement on CT scans and lung function at baseline. Additionally, in consecutive FAPI PET/CT scans, changes in tracer uptake were concordant with response to the targeting antifibrotic drug nintedanib. These data demonstrated for the first time that fibroblast activation protein imaging is the only imaging method available that

Received Aug. 28, 2023; revision accepted Sep. 7, 2023.  
For correspondence or reprints, contact Christian Schmidkonz (christian.schmidkonz@uk-erlangen.de).  
Published online Sep. 21, 2023.  
COPYRIGHT © 2023 by the Society of Nuclear Medicine and Molecular Imaging.  
DOI: 10.2967/jnumed.123.266182



can directly assess the dynamics and potential treatment response in SSC interstitial lung disease. Besides pulmonary fibrosis, myocardial fibrosis is also a factor of poor prognosis in SSC. Treutlein et al. examined in a proof-of-concept trial patients with SSC-associated myocardial fibrosis who underwent FAPI PET/CT and MRI as well as clinical and serologic investigations (10). With FAPI PET/CT, dynamic changes in tracer uptake associated with changes in SSC-related myocardial fibrosis were observed that could not be detected by MRI. Further larger trials are warranted to evaluate the potential use of FAPI PET/CT to directly monitor cardiac fibroblast activity in vivo, which might enable 1-stop-shop imaging of patients with SSC with both heart and lung involvement. Since inflammatory processes in immune-mediated disease can already be detected by <sup>18</sup>F-FDG PET/CT, one may ask whether FAPI radioligands can provide additional information on the chronic inflammation process that often occurs in that kind of disease.

## IGG4-RELATED DISEASE

IgG4-related disease is a paradigm of the inflammation-versus-fibrosis dichotomy that affects the pancreas and biliary tree, the salivary glands, the kidneys, the aorta, and other organs. During the course of disease, there is a typical progression from a proliferative phenotype that is characterized by dense lymphoplasmacytic infiltrates to a fibrotic phenotype with a greater degree of fibrosis. Immune-targeted therapies effectively inhibit inflammation but may not be suited to tackle fibrotic tissue changes, requiring detection of whether IgG4-related disease is based primarily on inflammatory or fibrotic lesions in an individual patient. In a cross-sectional study, 27 patients with IgG4-related disease underwent both <sup>18</sup>F-FDG and FAPI PET/CT as well as MRI and histopathologic assessment (1). <sup>18</sup>F-FDG-positive lesions showed dense lymphoplasmacytic infiltrations of IgG4-positive plasma cells, whereas FAPI-positive lesions harbored abundant activated fibroblasts. Interestingly, dual-tracer follow-up imaging revealed that antiinflammatory treatment of IgG4 manifestations significantly reduced <sup>18</sup>F-FDG uptake whereas fibrotic lesions demonstrated only a partial reduction in uptake on <sup>68</sup>Ga-FAPI PET/CT. Furthermore, constant fibrotic activity resulted in progression of the fibrotic lesion mass, suggesting that patients with FAPI-positive lesions require different forms of treatment. In view of the development of specific treatments for fibrotic diseases—treatments such as pirfenidone or inhibitors of the transcription factor

purine-rich box1—FAPI-04 PET/CT might be an ideal tool for evaluating the treatment response in IgG4-related disease (11). In summary, FAPI PET/CT offers a completely new view on immune-fibrosis imaging in rheumatologic disorders. This novel imaging modality is the only noninvasive method available for the visualization and quantification of the tissue remodeling process and assessment of treatment response to antifibrotic therapies. To fully exploit the potential of FAPI PET/CT in rheumatologic disorders, further prospective high-quality trials that require the collaboration of the nuclear medicine community are needed.

## DISCLOSURE

No potential conflict of interest relevant to this article was reported.

## REFERENCES

1. Schmidkonz C, Rauber S, Atzinger A, et al. Disentangling inflammatory from fibrotic disease activity by fibroblast activation protein imaging. *Ann Rheum Dis*. 2020;79:1485–1491.
2. Gurtner GC, Werner S, Barrandon Y, Longaker MT. Wound repair and regeneration. *Nature*. 2008;453:314–321.
3. Kuwert T, Schmidkonz C, Prante O, Schett G, Ramming A. FAPI PET opens a new window to understanding immune-mediated inflammatory diseases. *J Nucl Med*. 2022;63:1136–1137.
4. Schmidkonz C. Perspective on fibroblast activation protein-specific PET/CT in fibrotic interstitial lung diseases: imaging fibrosis—a new paradigm for molecular imaging? *J Nucl Med*. 2022;63:125–126.
5. Anderson J, Caplan L, Yazdany J, et al. Rheumatoid arthritis disease activity measures: American College of Rheumatology recommendations for use in clinical practice. *Arthritis Care Res (Hoboken)*. 2012;64:640–647.
6. Bergmann C, Distler JH, Treutlein C, et al. <sup>68</sup>Ga-FAPI-04 PET-CT for molecular assessment of fibroblast activation and risk evaluation in systemic sclerosis-associated interstitial lung disease: a single-centre, pilot study. *Lancet Rheumatol*. 2021;3:e185–e194.
7. Luo Y, Pan Q, Zhou Z, et al. <sup>68</sup>Ga-FAPI PET/CT for rheumatoid arthritis: a prospective study. *Radiology*. 2023;307:e222052.
8. Dorst DN, Rijpkema M, Buitinga M, et al. Targeting of fibroblast activation protein in rheumatoid arthritis patients: imaging and ex vivo photodynamic therapy. *Rheumatology*. 2022;61:2999–3009.
9. Perelas A, Silver RM, Arrossi AV, Highland KB. Systemic sclerosis-associated interstitial lung disease. *Lancet Respir Med*. 2020;8:304–320.
10. Treutlein C, Distler JH, Tascilar K, et al. Assessment of myocardial fibrosis in patients with systemic sclerosis using [<sup>68</sup>Ga] Ga-FAPI-04-PET-CT. *Eur J Nucl Med Mol Imaging*. 2023;50:1629–1635.
11. Wohlfahrt T, Rauber S, Uebe S, et al. PU.1 controls fibroblast polarization and tissue fibrosis. *Nature*. 2019;566:344–349.

# The Development and Validation of Radiopharmaceuticals Targeting Bacterial Infection

Alberto Signore\*<sup>1</sup>, Alvaro A. Ordonez\*<sup>2</sup>, Chanda Arjun<sup>3</sup>, Gurpreet Kaur Aulakh<sup>4</sup>, Nicolas Beziere<sup>5</sup>, Ekaterina Dadachova<sup>6</sup>, Thomas Ebenhan<sup>7</sup>, Ulises Granados<sup>8</sup>, Aruna Korde<sup>9</sup>, Amirreza Jalilian<sup>9</sup>, Wening Lestari<sup>10</sup>, Archana Mukherjee<sup>11</sup>, Milos Petrik<sup>12</sup>, Tamer Sakr<sup>13</sup>, Clara L. Santos Cuevas<sup>14</sup>, Mick M. Welling<sup>15</sup>, Jan Rijn Zeevaart<sup>7</sup>, Sanjay K. Jain<sup>2</sup>, and David M. Wilson<sup>16</sup>

<sup>1</sup>Nuclear Medicine Unit, Department of Medical-Surgical Sciences and Translational Medicine, Faculty of Medicine and Psychology, University of Rome "Sapienza," Rome, Italy; <sup>2</sup>Center for Infection and Inflammation Imaging Research, Johns Hopkins University School of Medicine, Baltimore, Maryland; <sup>3</sup>Radiopharmaceutical Program, Board of Radiation and Isotope Technology, Mumbai, India; <sup>4</sup>Department of Small Animal Clinical Sciences, Western College of Veterinary Medicine, University of Saskatchewan, Saskatoon, Saskatchewan, Canada; <sup>5</sup>Werner Siemens Imaging Center, Department of Preclinical Imaging and Radiopharmacy, Eberhard Karls University of Tübingen, Tübingen, Germany; <sup>6</sup>College of Pharmacy and Nutrition, University of Saskatchewan, Saskatoon, Saskatchewan, Canada; <sup>7</sup>Nuclear Medicine, University of Pretoria, and Radiochemistry, Applied Radiation, South African Nuclear Energy Corporation, Pelindaba, South Africa; <sup>8</sup>Department of Nuclear Medicine, Hospital Internacional de Colombia–Fundación Cardiovascular de Colombia, Piedecuesta, Colombia; <sup>9</sup>Department of Nuclear Sciences and Applications, International Atomic Energy Agency, Vienna, Austria; <sup>10</sup>National Nuclear Energy Agency, South Tangerang, Indonesia; <sup>11</sup>Radiopharmaceuticals Division, Bhabha Atomic Research Centre, Mumbai, India; <sup>12</sup>Institute of Molecular and Translational Medicine and Czech Advanced Technology and Research Institute, Faculty of Medicine and Dentistry, Palacky University Olomouc, Olomouc, Czech Republic; <sup>13</sup>Radioactive Isotopes and Generator Department, Hot Labs Center, Egyptian Atomic Energy Authority, Cairo, Egypt; <sup>14</sup>Instituto Nacional de Investigaciones Nucleares, Ocoyoacac, Mexico; <sup>15</sup>Interventional Molecular Imaging Laboratory, Department of Radiology, Leiden University Medical Center, Leiden, The Netherlands; and <sup>16</sup>Department of Radiology and Biomedical Imaging, University of California San Francisco, San Francisco, California

The International Atomic Energy Agency organized a technical meeting at its headquarters in Vienna, Austria, in 2022 that included 17 experts representing 12 countries, whose research spanned the development and use of radiolabeled agents for imaging infection. The meeting focused largely on bacterial pathogens. The group discussed and evaluated the advantages and disadvantages of several radiopharmaceuticals, as well as the science driving various imaging approaches. The main objective was to understand why few infection-targeted radiotracers are used in clinical practice despite the urgent need to better characterize bacterial infections. This article summarizes the resulting consensus, at least among the included scientists and countries, on the current status of radiopharmaceutical development for infection imaging. Also included are opinions and recommendations regarding current research standards in this area. This and future International Atomic Energy Agency–sponsored collaborations will advance the goal of providing the medical community with innovative, practical tools for the specific image-based diagnosis of infection.

**Key Words:** infection; antibiotics; radiotracer; molecular imaging; development

**J Nucl Med 2023; 64:1676–1682**

DOI: 10.2967/jnumed.123.265906

Received Apr. 27, 2023; revision accepted Aug. 18, 2023.  
For correspondence or reprints, contact David M. Wilson (david.m.wilson@ucsf.edu).

\*Contributed equally to this work.

Published online Sep. 28, 2023.

COPYRIGHT © 2023 by the Society of Nuclear Medicine and Molecular Imaging.

**I**nfections remain a major threat to human health globally (1). The coronavirus disease 2019 pandemic has highlighted a pressing need to develop and translate innovative technologies to detect and treat infectious disease. Even before the onset of the pandemic, infections ranked third in mortality but first in morbidity among all human diseases in 2017, primarily affecting younger, healthier populations (2). There were an estimated 11 million sepsis-related deaths in 2017, accounting for about 20% of deaths globally, with the highest incidence reported in developing countries (3). By 2050, antimicrobial drug-resistant infections are expected to become the leading cause of death globally and surpass those due to cancer (4). The potential cost of drug-resistant infections has been estimated to be as high as \$100 trillion worldwide (5). We have also observed a dramatic rise in hospital-acquired (nosocomial) infections affecting at-risk patients during the pandemic. Enterobacterales pathogens, especially *K. pneumoniae*, and fungi including *Aspergillus* spp. are an important cause of secondary pneumonias in hospitalized patients with coronavirus disease 2019 (6).

Current diagnostic approaches to detecting bacterial infections, such as microscopy, microbiology, and molecular techniques (nucleic acid amplification and mass spectrometry), require clinical samples (blood, urine, stool, or cerebrospinal fluid) for culturing and sensitivity testing and infection-relevant assays. However, it is increasingly recognized that many different infectious foci with distinct bacterial burdens, antimicrobial exposures, and local biology can coexist in the same host (7–9). Clinical samples may not accurately represent the local biology at infectious sites and thus are either not sensitive to or not representative of the bacterial infection (10,11). Surgical resection or biopsy is often the last

resort for obtaining infected tissues, and because of the associated morbidity, these techniques are generally limited to the most accessible lesions identified at a single time point. Additionally, sampling methods fail to capture the heterogeneity of multiple lesions existing simultaneously in the same patient, as well as the temporal changes occurring over the course of the infection and its treatment.

Available imaging tools used in the clinic for detection of bacterial infections include radiography, ultrasonography, CT, and MRI, but these imaging tools are based on anatomic changes during disease, which are delayed compared with the biochemical events occurring within the affected tissues. Structural abnormalities are also nonspecific and reflect a combination of both the infectious agents and the host inflammatory response (12). Molecular hybrid imaging platforms have proven to efficiently localize pathology and assist in the clinical management of several diseases (13,14). These technologies, such as SPECT or PET, can measure molecular pathways in situ and are often used in combination with anatomic imaging (PET/CT, PET/MRI, or SPECT/CT). The use of radiolabeled leukocytes (white blood cells) is considered the gold standard technique for prosthetic (15), vascular graft (16), and diabetic foot (17) infections but requires skill and equipment for sterile blood manipulation. Radiolabeled antibodies against granulocyte antigens can induce human antimouse antibody production in approximately 4% of patients (18), limiting their use. The glucose analog [<sup>18</sup>F]FDG has also been used to image infection but lacks specificity for pathogens (19).

Despite these advanced tools, there is no universally accepted approach to the specific detection of bacterial infections. Therefore, there is an urgent, unmet need for the development of radiopharmaceuticals that can demonstrate the presence of living pathogens in vivo. However, because of bacterial diversity and the frequency of polymicrobial infections, developmental efforts have focused on both radiopharmaceuticals for panbacterial imaging and radiopharmaceuticals for type- or species-specific imaging. For potential clinical applications, there are advantages and disadvantages to both concepts. Given the breadth of research interests, in general all approaches have been hindered by a relative lack of funding (compared with oncology, for example), lack of uniformly reported data for imaging agents, misconceptions regarding radiation risks, and hurdles in the clinical translation and dissemination of promising radiopharmaceuticals (12).

In March 2022, the International Atomic Energy Agency (IAEA) organized a technical meeting titled “The Status of Radiolabeled Molecules for Infection and Inflammation Imaging” in Vienna, Austria, to evaluate and address these challenges. This summary should be used as a road map for advancing research in this field, understanding the potential clinical use of radiopharmaceuticals and their role in clinical decision-making, and most importantly motivating funding agencies and industry to support and develop pathogen-specific imaging technologies. Although the focus of this meeting was bacterial infection, the conclusions rendered may be expanded and tailored to nonbacterial pathogens whose detection via nuclear imaging is increasingly reported in the peer-reviewed literature.

## CLINICAL MOTIVATIONS

With the advance of medical imaging technologies, there has been a sustained interest in developing new tools to detect and monitor bacterial infections noninvasively—particularly in nuclear

medicine. Ideally, nuclear imaging probes should have high sensitivity and specificity for a wide range of pathogens, with enough tissue penetration to reach infected areas despite poor vascular supply while providing quantitative signals proportionate to the bacterial burden. They should also be chemically stable in blood and tissues; safe, with acceptable radiation exposure; and manufacturable at a reasonable expense (20,21). However, this magic bullet is not feasible for all imaging applications since disease location, type of pathogen, presence of comorbidities, chronicity of infection, and therapeutic interaction may influence the diagnostic accuracy of a given technique.

Therefore, analogous to the development of imaging agents in oncology, pathogen-specific imaging will greatly benefit from having multiple complementary agents with applicability to different clinical conditions. Several radiopharmaceuticals should be developed targeting variable pathways, allowing differentiation between infection and sterile inflammation and characterization of individual or classes of pathogens (e.g., gram-positive vs. gram-negative bacteria). A collaborative multidisciplinary environment with expert perspectives is essential, as is sharing information regarding how to best conduct imaging studies, interpret data, and include appropriate controls. A central agency (e.g., the IAEA) with a global focus represents an ideal platform to share this information and conduct multicenter comparisons. To allow replication of experiments at different sites, transparency in experimental methods for both pre-clinical and clinical studies is required, as well as willingness by the researchers to distribute data and standardize reporting.

The bacterial imaging field, both for SPECT and for PET, has grown significantly from 2000 to 2019, followed by a reduction in publications during the coronavirus disease 2019 pandemic, based on articles found via PubMed from 2001 to 2022 by searching “bacteria AND imaging AND scintigraphy/PET AND [year].” This refocusing of research effort may reflect a new focus on coronavirus disease 2019–related diagnostics, a pandemic-related loss of resources needed to conduct this type of research, or most likely both. Therefore, it is essential to reinvigorate this field, particularly with our new knowledge of infections—their transmission, morbidity, and mortality.

With respect to pathogen-specific imaging, it is important to learn from our previous mistakes. One of the first agents to be clinically translated for infection imaging was [<sup>99m</sup>Tc]ciprofloxacin, commercially known as Infected (Draxis). Although it was rapidly evaluated in hundreds of infected patients with promising results, these initial hopes were dashed when subsequent clinical studies (22–24) showed poor specificity of [<sup>99m</sup>Tc]ciprofloxacin for bacterial infections. The panel at the IAEA agreed that from the beginning [<sup>99m</sup>Tc]ciprofloxacin was a poorly chosen and validated tracer for numerous reasons, including its limited affinity for bacteria (reflected by fast efflux rates from affected tissues) and binding to both bacteria and mammalian cells (25,26). This was a valuable lesson in the need to thoroughly characterize bacteria-specific imaging agents to confirm their mechanism of action and specificity before investing extensive resources in their clinical translation. In this case, in vitro tests were not satisfactory (27–29) and heterogeneity of clinical studies limited their credibility. These studies had variable imaging indications, divergent gold standards, and poor controls and proved challenging to interpret (23,30–33).

To attract industry investment in new imaging technologies, attention should be paid to their potential profitability at all stages of development. For example, the preservation of intellectual property via patents is essential and often overlooked. Indeed,

patented radiotracers can be more easily acquired and produced by pharmaceutical companies, reducing the risk of competing technologies. A lack of intellectual protection will likely discourage industry investment, even if the science itself is promising.

## DEVELOPMENT OF PATHOGEN-SPECIFIC IMAGING METHODS

The discussion at the IAEA focused on the development of infection-targeted radiopharmaceuticals, including the basic *in vitro* and *in vivo* studies needed to validate their clinical relevance.

### Infrastructure Requirements

An important consideration in developing any imaging agents is the required infrastructure, with the safe handling of infectious agents representing a special challenge. For any radiopharmaceutical, relevant technologies include a cyclotron or radionuclide generator, shielded fume hoods (i.e., hot cells), a radioactivity-counting instrument (e.g., a  $\gamma$ -counter), high-performance liquid chromatography, and preclinical scanning equipment (PET or SPECT). For clinical translation, quality control evaluation including identity testing, pyrogen evaluation, radiochemical evaluation (yield, purity), and chemical stability is required. Staff with radiochemistry and regulatory expertise imply potentially high costs, which can be a limitation for the development of new agents. Considerations for handling pathogens and biosafety training are critical for conducting these studies. However, groups focused on radiochemistry are not familiar with regulations surrounding pathogens, as they have traditionally focused on cancer and neurologic disorders. Additional infrastructure challenges are related to infections with drug-resistant pathogens requiring special regimes for patient care and cleaning of hospital spaces (waste management) and hospital beds (isolation areas).

### Conception and Planning—Identifying the Target

Infectious diseases are widely heterogeneous illnesses associated with microorganisms that cause disease in humans. Although there is considerable overlap in the pathogenic mechanisms of these microorganisms and the host response to them, the intrinsic characteristics of these pathogens are highly variable. Bacteria, viruses, fungi, and parasites are genetically, biochemically, and metabolically different. Additionally, reference laboratory strains can be significantly different from pathogenic strains. For example, reference laboratory *E. coli* strains—the uropathogenic CFT073, enterohemorrhagic EDL933, and laboratory strain MG1655—all display a mosaic genome structure that can compose up to 40% of their genes (34). Therefore, it is fundamental to identify the target pathogen and its clinical presentation when planning to develop pathogen-specific imaging agents. The specific characteristics of the agent will vary depending on the target, and the use of clinical strains during the initial studies may be crucial.

Developing new infection-targeted agents depends both on the clinical need and on understanding of the mechanism the technology uses to generate image contrast. Bacteria (prokaryotes) are evolutionary and phylogenetically distinct from eukaryotic cells. These basic differences provide opportunities to leverage fundamental biochemical differences between bacteria and

mammalian cells—that is, energetic pathways, nucleic acid use, and cell surface components for the discovery of novel molecules that could be developed into pathogen-specific agents. Although initial efforts to develop pathogen-specific radiopharmaceuticals were based on radiolabeled antibiotics, recent approaches have focused on radiopharmaceuticals that are incorporated by the cell wall or are metabolized by microbe-specific pathways. For example, *D*-methyl- $^{11}\text{C}$ methionine and other positron-labeled *D*-amino acids have targeted bacterial peptidoglycan (Fig. 1) (35–38), whereas 2-deoxy-2- $^{18}\text{F}$ fluoro-*D*-sorbitol detects bacteria via the unique metabolism of sorbitol by Enterobacteriaceae (Fig. 2) (39,40). For a more thorough understanding of the target, collaboration with microbiologists and infectious disease physicians is helpful. Generally, attention to the literature and careful screening (including *in silico*) can identify the targets most relevant to probe design (41). Using an artificial intelligence approach in the selection of potentially pathogen-specific radiopharmaceuticals can make radiopharmaceutical agent development more efficient (42).

### Compound Screening and Radiochemistry

Once the bacterial target has been identified, the next step is to obtain lead molecules, which may require a conventional compound screen, structure-based design, modification of molecular probes developed for other imaging techniques, or radiosynthesis of metabolite analogs (43,44). Using an unbiased screening approach is essential to the discovery of candidates for pathogen-specific imaging. Screening of candidate compounds should be performed in whole bacterial cell cultures since working with an isolated target ignores critical determinants of clinical performance, such as cell wall penetration.

Multiple comprehensive reviews have been published on the radiochemistry of pathogen-specific imaging radiopharmaceuticals (43,45,46). However, many publications in this field lack the minimal requirements to allow validation and reproducibility of the described radiochemistry methodology. When a new agent is described, information regarding its radiochemical purity, radiochemical yield, molar activity, stability, and metabolism is necessary to allow other researchers to evaluate the presented approach and potentially reproduce it. Molar activity is particularly important to report and evaluate to address the presence of competing cold materials in a radiopharmaceutical sample. Numerous other considerations are relevant to the chemical specifics of the probe.

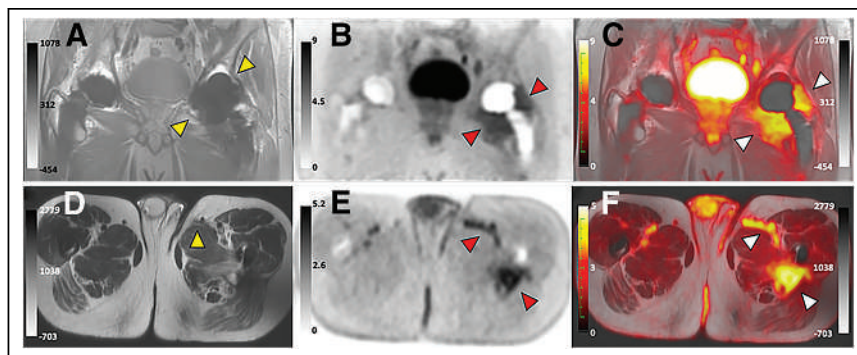


**FIGURE 1.** *D*-methyl- $^{11}\text{C}$ methionine PET/MR images of 61-y-old man with bilateral hip prostheses and confirmed *C. acnes* infection of left hip. Left bar represents SUV color scale, and right bar represents MRI color scale. (A, B, and C) Coronal MR, PET, and PET/MR images, respectively. Arrows indicate infected joint in A and area of radiotracer uptake surrounding joint in B and C. (D–F) Axial MR, PET, and PET/MR images. Arrows depict sinus tract communicating with skin in D and regions of radiotracer uptake in E and F. (Adapted from (35).)

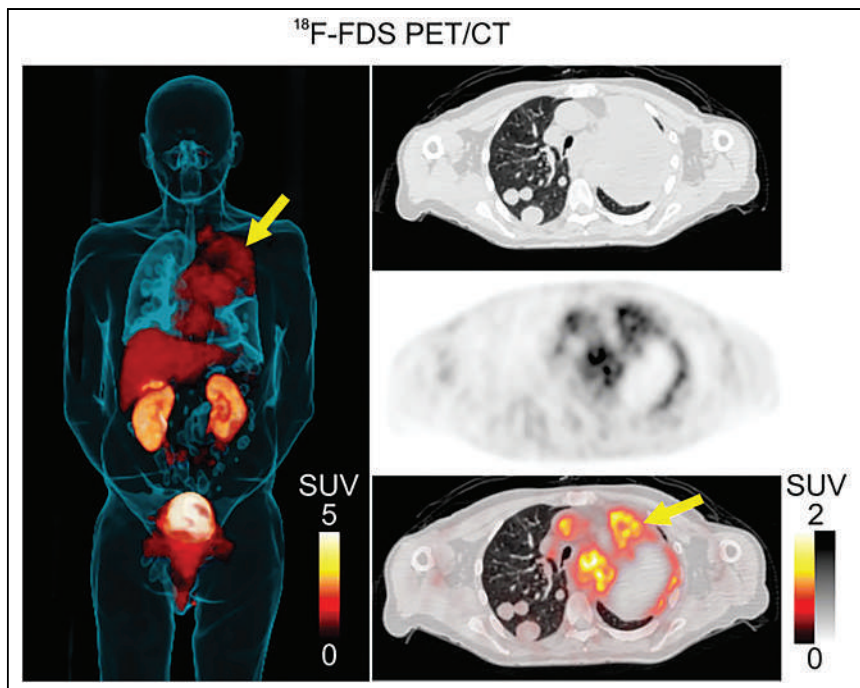


**FIGURE 2.** [ $^{18}\text{F}$ ]FDS PET study of 67-y-old man with squamous cell carcinoma of lung and *K. pneumoniae* pneumonia. On left, 3-dimensional minimum-intensity projection is shown, with arrow indicating [ $^{18}\text{F}$ ]FDS signal in infected tissues. On right, transverse CT, PET, and PET/CT images (from top to bottom) indicate minimal [ $^{18}\text{F}$ ]FDS signal in right-sided cancerous lesions (arrow). (Adapted from (40).)

For example, with radiometal modification of antibodies or related protein formats (i.e., single-domain antibodies), stoichiometry should be evaluated and reported. Both retention of activity and stability of conjugated antibodies should be determined. To rule out in vivo transchelation of  $^{99\text{m}}\text{Tc}$ , a cysteine challenge study may be considered. Basic radiopharmaceutical design criteria are beyond the scope of this discussion, but a summary has been provided in a previous review (47).

### In Vitro Testing

Evaluating uptake of radiopharmaceuticals by bacteria in vitro is a critical aspect of their validation. Since certain radionuclides both are costly and have short half-lives (e.g.,  $^{11}\text{C}$  for PET), the in vitro study of radiopharmaceutical analogs can begin with  $\beta$ -emitting nuclei ( $^{14}\text{C}$ ,  $^3\text{H}$ ) and scintillation counting (41), stable isotope MR spectroscopy (48) (e.g.,  $^{13}\text{C}$ ,  $^1\text{H}$ ,  $^2\text{H}$ , and  $^{19}\text{F}$ ), or mass spectroscopy (49). The essential validation of a new radiotracer concept is when it has been successfully labeled and incubated with bacterial cultures to detect specific incorporation (37). These studies are usually conducted with bacterial cultures in the growth or exponential phase, although of course other assessments are possible. After bacterial washing and detection of retained radioactive signals, a gross assessment of tracer retention can be made by the percentage of tracer retained, that is, the percentage uptake. However, these data should be normalized to bacterial count, which is not obtained via an estimate (e.g., an *E. coli* culture with an optical density of 1 measured at a wavelength of 600 nm represents  $8 \times 10^8$  organisms) but by serial dilutions and plating to determine the number of colony-forming units to be reported. The most relevant controls include the use of heat-killed organisms and blocking using a nonradiolabeled version of the radiopharmaceutical. These blocking, or competition, studies

can be used to explore the effect of molar activity on radiotracer performance. Finally, several pathogenic species, as well as multiple strains of the same species, should be included in these analyses. In addition to clinical isolates, commercially available bacteria should be used to allow reproduction of results by other groups.

Several in vitro studies are infrequently performed or use variable experimental conditions. For example, some investigators perform efflux studies whereby after bacterial radioactivity retention, the cells are washed and the subsequent loss of radioactivity over time is determined (50). There is also variability in the medium used, and some components may compete with exogenous radiopharmaceuticals for bacterial incorporation. At this point, there is no standard medium used although investigators should consider appropriate mimicry of the nutrient makeup of the human body.

### In Vivo Validation

Once the in vitro characterization of a probe has been completed, subsequent validations in animal models are frequently performed. Regulatory requirements for the development of animal models of infections vary considerably across different countries

and institutions. If excessive, these can be an additional burden to researchers (51). Animal models and relevant controls are well summarized in the consensus report by Signore et al. (52). When choosing an animal model, it is important to thoroughly understand the human infection that is being studied, as well as the strengths and limitations of a given model. The European Association of Nuclear Medicine recently published useful guidelines for choosing the appropriate animal model for preclinical experiments (53). In most cases, the models used should recapitulate human pathologies. When tracer sensitivity to different pathogens is being compared, a dual infection model (e.g., a mouse infected with 2 pathogens) (38) or separate carefully generated cohorts (e.g., in comparing [ $^{99\text{m}}\text{Tc}$ ]hydrazinonicotinamide polymyxin B accumulation in *Pseudomonas aeruginosa* and *Staphylococcus aureus*) may be used (Fig. 3) (54). The volume of distribution, metabolism, excretion, vascular leakage, etc., are also key variables that should be considered before choosing a specific model.

Determining and standardizing the readouts used to quantify signals from pathogen-specific agents in animal models are also key to comparing different agents and reproducing the reported findings. For example, for PET imaging of bacterial infections, the agent should be injected at a time point when the infection has been allowed to incubate for a sufficient time (e.g., 8–24 h) to resemble human pathology when inflammatory response peaks and bacteria are in different metabolic states. Determination of the stability of the agent in blood (or tissues if applicable) at the time of imaging should also be reported. Because of replication, the bacterial burden injected at a given site is much lower than found hours later. Therefore, the bacterial burden at the site evaluated should be determined immediately after imaging has been performed.



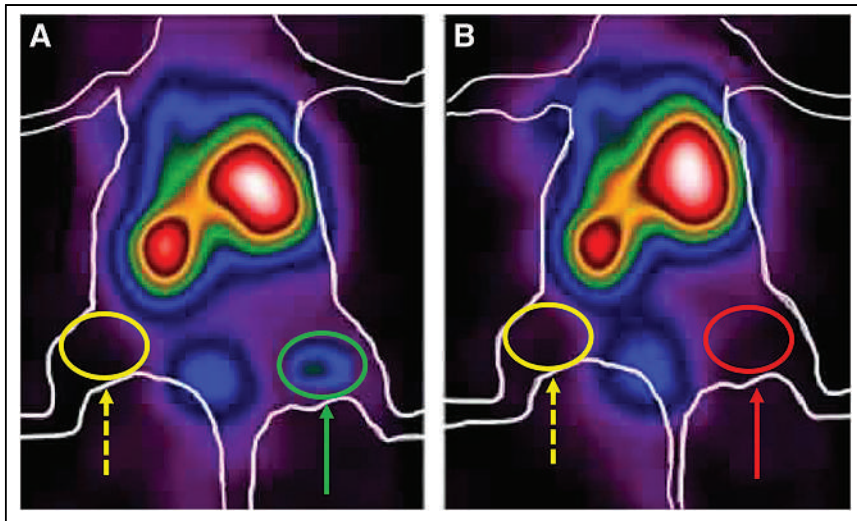


**FIGURE 3.** Representative planar  $\gamma$ -camera images of 2 mice infected with  $10^9$  colony-forming units of *P. aeruginosa* (A) (green arrow and circle) and *S. aureus* (B) (red arrow and circle) vs. contralateral thigh, injected with only hydrogel (yellow arrows and circles) as control. Images were acquired 6 h after injection of 3.7 MBq of [ $^{99m}\text{Tc}$ ]-hydrazinonicotinamide polymyxin B. Radiolabeled antibiotic binds only to gram-negative bacteria, thus highlighting presence of *P. aeruginosa* but not of gram-positive *S. aureus*. (Adapted from (54).)

The use of animal models beyond rodents in development of imaging research has also been suggested (53,55). The rabbit stands out among nonrodent mammals used in research because of its relatively small size, short gestation period (29–31 d), and potential for timed mating and superovulation (56). Myriad imaging studies have reported the successful use of rabbit infection models (57–59). Given ethical concerns, using nonhuman primates (macaques, baboons, marmosets, and African green monkeys) in biomedical research is usually allowed only in research areas for which no alternative is available (60,61); however, research on nonhuman primates regularly necessitates special facilities and expertise. Although expensive, nonhuman primates are invaluable tools to study complex infection pathogenesis (simian HIV or tuberculosis) (62) and are suitable for preclinical imaging studies (63,64), in particular for tracer biodistribution or radiation dosimetry (65–67), translational research on human respiratory infections, and pharmaceutical drug development (68–70). Beyond these common animals, the study of species-specific diseases might involve pigs, cats, dogs, cattle, horses, fish, and birds (71,72).

Distinguishing infection from inflammation depends on the typical host response via initiation of the innate immune system followed by an adaptive response targeting the pathogen (19,73). Frequently, inflammation may persist despite infection control (74). Inclusion of appropriate controls is an important determinant when developing specific infectious imaging agents. Whenever possible, contralateral limb or skin site controls, as demonstrated by the tissue cage model (75), can be used to test the specificity of the agent and further distinguish between infectious and sterile inflammation. Therefore, a rational preclinical screen should be designed to, first, understand the kinetics of the test molecular imaging agent in sterile (76–78) as well as infectious (39,79) animal inflammation models and, second, understand target organ function to compare the sensitivity of the imaging agent in animal models of infection and sterile inflammation. The imaging agents should be validated with the capability for dual or hybrid imaging platforms such as SPECT/CT, PET/CT, and PET/MRI (80).

An accurate analysis of the preclinical images is fundamental to determine the viability of the candidate agent for pathogen-specific imaging. The most used approach to determining the region (or volume) of interest via images is intrinsically operator-dependent. Therefore, efforts should be made to minimize bias (e.g., using the CT instead of the PET images to determine the region of interest). A frequently used unit to represent imaging results in PET/SPECT is  $\text{SUV}_{\text{mean}}$ , which considers average signals in a region of interest, corrected for the dose-decay-adjusted injected dose and the weight of the animal. Other methods of data quantification are available, and researchers should explain the methodology used for the analysis. Careful dissection and ex vivo analyses of all tissues should be performed via a radiation-detecting instrument (i.e.,  $\gamma$ -counter). Accurate identification of infected and noninfected tissues can be used to generate an uptake value, normalized to mass (i.e., percentage injected dose per gram). The tissues can be subsequently homogenized and plated to normalize the data for the number of viable bacteria (colony-forming units); this type of analysis is essential for evaluating the sensitivity of a radiopharmaceutical or comparing the sensitivity of different tracers.

## TRANSLATION AND THE FUTURE

The general process of translating new nuclear medicine technologies has been explored in numerous reviews (81,82) and in the context of dedicated workshops, such as that organized by the National Institute of Biomedical Imaging and Bioengineering (National Institutes of Health) (83). The basic approach involves the approval of both government and institutional regulatory bodies, toxicology studies as required, radiochemical optimization, and first-in-humans studies usually initiated for dosimetry evaluation. For any tracer, a major challenge is securing the funding to accomplish this work, given administrative expenses and the high cost of radiopharmaceutical production. Many researchers at the meeting felt these costs diminished the number of patients who could reasonably be scanned using a new tracer—thus limiting the conclusions obtained. A second challenge is the difficulty of proving the utility of infection-targeted radiopharmaceuticals in rigorous, multicenter studies. Even for researchers who wish to share and collaborate, securing the funding required for this effort is difficult. Finally, infection-targeted tracers face particular barriers to widespread clinical adoption, described below.

### There Is Currently Limited Engagement of Stakeholders

To be successful, physicians in numerous disciplines need to consider infection imaging essential to clinical practice. The collaboration of radiologists, nuclear medicine physicians, infectious disease doctors, surgeons (especially orthopedic surgeons and neurosurgeons), and other specialists will be essential in driving this field forward. In addition, partnerships with industry, including commercial radiopharmacies, are crucial to rendering these technologies profitable and sustainable.

## Current Patient Studies Are Not Sufficiently Convincing

The latest generation of microbe-specific tracers is highly compelling, but few carefully conducted patient studies support their use. Infectious disease is a broad topic, requiring time for researchers to produce relevant data in patients.

## Infection-Targeted Nuclear Medicine Tools Do Not Fit into an Existing Clinical Workflow

Access to nuclear medicine tools may be limited for the diagnosis of infection in the acute care setting. Most radiotracers cannot be synthesized on demand even during the regular operating hours of a radiopharmaceutical facility and, as a result, can often be used only when the patient is already undergoing antimicrobial therapy due to the urgency of treatment in acute infections. This is a significant limitation to first-in-humans studies, as imaging results can be confounded by the effects of the therapeutic regimen.

## CONCLUSION

Meetings such as that recently sponsored by the IAEA are essential in identifying ways for researchers and physicians to better diagnose and treat bacterial infections. The remarkable progress made over the last decade indicates that the successful application of new molecular imaging tools in the clinic will profoundly impact patient care.

## DISCLOSURE

No potential conflict of interest relevant to this article was reported.

## REFERENCES

1. GBD 2019 Antimicrobial Resistance Collaborators. Global mortality associated with 33 bacterial pathogens in 2019: a systematic analysis for the Global Burden of Disease Study 2019. *Lancet*. 2022;400:2221–2248.
2. GBD 2017 Causes of Death Collaborators. Global, regional, and national age-sex-specific mortality for 282 causes of death in 195 countries and territories, 1980–2017: a systematic analysis for the Global Burden of Disease Study 2017. *Lancet*. 2018;392:1736–1788.
3. Rudd KE, Johnson SC, Agesa KM, et al. Global, regional, and national sepsis incidence and mortality, 1990–2017: analysis for the Global Burden of Disease Study. *Lancet*. 2020;395:200–211.
4. O'Neill J. Tackling drug-resistant infections globally: final report and recommendations. Review on Antimicrobial Resistance website. [https://amr-review.org/sites/default/files/160518\\_Final%20paper\\_with%20cover.pdf](https://amr-review.org/sites/default/files/160518_Final%20paper_with%20cover.pdf). Published May 2016. Accessed August 30, 2023.
5. Dadgostar P. Antimicrobial resistance: implications and costs. *Infect Drug Resist*. 2019;12:3903–3910.
6. Dhesi Z, Enne VI, Brealey D, et al. Organisms causing secondary pneumonias in COVID-19 patients at 5 UK ICUs as detected with the FilmArray test. medRxiv website. <https://www.medrxiv.org/content/10.1101/2020.06.22.20131573v1>. Published June 23, 2020. Accessed August 31, 2023.
7. Cassat JE, Moore JL, Wilson KJ, et al. Integrated molecular imaging reveals tissue heterogeneity driving host-pathogen interactions. *Sci Transl Med*. 2018;10:eaan6361.
8. Ordóñez AA, Tucker EW, Anderson CJ, et al. Visualizing the dynamics of tuberculosis pathology using molecular imaging. *J Clin Invest*. 2021;131:e145107.
9. Ordóñez AA, Wang H, Magombedze G, et al. Dynamic imaging in patients with tuberculosis reveals heterogeneous drug exposures in pulmonary lesions. *Nat Med*. 2020;26:529–534.
10. Tucker EW, Guglieri-Lopez B, Ordóñez AA, et al. Noninvasive  $^{11}\text{C}$ -rifampin positron emission tomography reveals drug biodistribution in tuberculous meningitis. *Sci Transl Med*. 2018;10:eaa0965.
11. Ruiz-Bedoya CA, Mota F, Tucker EW, et al. High-dose rifampin improves bactericidal activity without increased intracerebral inflammation in animal models of tuberculous meningitis. *J Clin Invest*. 2022;132:e155851.
12. Jain SK, Andronikou S, Goussard P, et al. Advanced imaging tools for childhood tuberculosis: potential applications and research needs. *Lancet Infect Dis*. 2020;20:e289–e297.

13. Strosberg J, El-Haddad G, Wolin E, et al. Phase 3 trial of  $^{177}\text{Lu}$ -dotatate for midgut neuroendocrine tumors. *N Engl J Med*. 2017;376:125–135.
14. Rowe SP, Gorin MA, Pomper MG. Imaging of prostate-specific membrane antigen with small-molecule PET radiotracers: from the bench to advanced clinical applications. *Annu Rev Med*. 2019;70:461–477.
15. Romanò CL, Petrosillo N, Argento G, et al. The role of imaging techniques to define a peri-prosthetic hip and knee joint infection: multidisciplinary consensus statements. *J Clin Med*. 2020;9:2548.
16. Lauri C, Signore A, Glaudemans AWJM, et al. Evidence-based guideline of the European Association of Nuclear Medicine (EANM) on imaging infection in vascular grafts. *Eur J Nucl Med Mol Imaging*. 2022;49:3430–3451.
17. Lauri C, Tamminga M, Glaudemans AWJM, et al. Detection of osteomyelitis in the diabetic foot by imaging techniques: a systematic review and meta-analysis comparing MRI, white blood cell scintigraphy, and FDG-PET. *Diabetes Care*. 2017;40:1111–1120.
18. Steinträsser A, Oberhausen E. Granulocyte labelling kit BW 250/183: results of the European multicenter trial. *Nuklearmedizin*. 1996;35:1–11.
19. Jamar F, Buscombe J, Chiti A, et al. EANM/SNMMI guideline for  $^{18}\text{F}$ -FDG use in inflammation and infection. *J Nucl Med*. 2013;54:647–658.
20. Welling M, Stokkel M, Balter J, Sarda-Mantel L, Meulemans A, Le Guldec D. The many roads to infection imaging. *Eur J Nucl Med Mol Imaging*. 2008;35:848–849.
21. Polvoy I, Flavell RR, Rosenberg OS, Ohliger MA, Wilson DM. Nuclear imaging of bacterial infection: the state of the art and future directions. *J Nucl Med*. 2020;61:1708–1716.
22. Langer O, Brunner M, Zeitlinger M, et al. In vitro and in vivo evaluation of  $^{18}\text{F}$  ciprofloxacin for the imaging of bacterial infections with PET. *Eur J Nucl Med Mol Imaging*. 2005;32:143–150.
23. Sarda L, Crémieux A-C, Lebellec Y, et al. Inability of  $^{99\text{m}}\text{Tc}$ -ciprofloxacin scintigraphy to discriminate between septic and sterile osteoarticular diseases. *J Nucl Med*. 2003;44:920–926.
24. Dumarey N, Blocklet D, Appelboom T, Tant L, Schoutens A. Infection is not specific for bacterial osteo-articular infective pathology. *Eur J Nucl Med Mol Imaging*. 2002;29:530–535.
25. Pauwels EK, Welling MM, Lupetti A, Paulusma-Annema A, Nibbering PH, Balter HS. Concerns about  $^{99\text{m}}\text{Tc}$ -labelled ciprofloxacin for infection detection. *Eur J Nucl Med*. 2000;27:1866.
26. Welling MM, Nibbering PH, Paulusma-Annema A, Hiemstra PS, Pauwels EK, Calame W. Imaging of bacterial infections with  $^{99\text{m}}\text{Tc}$ -labeled human neutrophil peptide-1. *J Nucl Med*. 1999;40:2073–2080.
27. Auletta S, Baldoni D, Varani M, et al. Comparison of  $^{99\text{m}}\text{Tc}$ -UBI 29-41,  $^{99\text{m}}\text{Tc}$ -ciprofloxacin,  $^{99\text{m}}\text{Tc}$ -ciprofloxacin dithiocarbamate and  $^{111}\text{In}$ -biotin for targeting experimental *Staphylococcus aureus* and *Escherichia coli* foreign-body infections: an ex-vivo study. *Q J Nucl Med Mol Imaging*. 2019;63:37–47.
28. Larikka MJ, Ahonen AK, Niemelä O, Junila JA, Hämäläinen MM, Syrjälä HP. Specificity of  $^{99\text{m}}\text{Tc}$ -ciprofloxacin imaging [letter]. *J Nucl Med*. 2003;44:1368.
29. Alexander K, Drost WT, Mattoon JS, Kowalski JJ, Funk JA, Crabtree AC. Binding of ciprofloxacin labelled with technetium Tc 99m versus  $^{99\text{m}}\text{Tc}$ -pertechnetate to a live and killed equine isolate of *Escherichia coli*. *Can J Vet Res*. 2005;69:272–277.
30. Dutta P, Bhansali A, Mittal BR, Singh B, Masoodi SR. Instant  $^{99\text{m}}\text{Tc}$ -ciprofloxacin scintigraphy for the diagnosis of osteomyelitis in the diabetic foot. *Foot Ankle Int*. 2006;27:716–722.
31. De Winter F, Gemmel F, Van Laere K, et al.  $^{99\text{m}}\text{Tc}$ -ciprofloxacin planar and tomographic imaging for the diagnosis of infection in the postoperative spine: experience in 48 patients. *Eur J Nucl Med Mol Imaging*. 2004;31:233–239.
32. Fuster D, Soriano A, Garcia S, et al. Usefulness of  $^{99\text{m}}\text{Tc}$ -ciprofloxacin scintigraphy in the diagnosis of prosthetic joint infections. *Nucl Med Commun*. 2011;32:44–51.
33. Gemmel F, De Winter F, Van Laere K, Vogelaers D, Uyttendaele D, Dierckx RA.  $^{99\text{m}}\text{Tc}$  ciprofloxacin imaging for the diagnosis of infection in the postoperative spine. *Nucl Med Commun*. 2004;25:277–283.
34. Welch RA, Burland V, Plunkett G, et al. Extensive mosaic structure revealed by the complete genome sequence of uropathogenic *Escherichia coli*. *Proc Natl Acad Sci USA*. 2002;99:17020–17024.
35. Polvoy I, Seo Y, Parker M, et al. Imaging joint infections using D-methyl- $^{11}\text{C}$ -methionine PET/MRI: initial experience in humans. *Eur J Nucl Med Mol Imaging*. 2022;49:3761–3771.
36. Neumann KD, Villanueva-Meyer JE, Mutch CA, et al. Imaging active infection in vivo using D-amino acid derived PET radiotracers. *Sci Rep*. 2017;7:7903.
37. Stewart MN, Parker MFL, Jivan S, et al. High enantiomeric excess in-loop synthesis of D-[methyl- $^{11}\text{C}$ ]methionine for use as a diagnostic positron emission tomography radiotracer in bacterial infection. *ACS Infect Dis*. 2020;6:43–49.
38. Parker MFL, Luu JM, Schulte B, et al. Sensing living bacteria in vivo using D-alanine-derived  $^{11}\text{C}$  radiotracers. *ACS Cent Sci*. 2020;6:155–165.

39. Weinstein EA, Ordonez AA, DeMarco VP, et al. Imaging Enterobacteriaceae infection in vivo with <sup>18</sup>F-fluorodeoxyisobutyl positron emission tomography. *Sci Transl Med.* 2014;6:259ra146.
40. Ordonez AA, Wintaco LM, Mota F, et al. Imaging *Enterobacteriales* infections in patients using pathogen-specific positron emission tomography. *Sci Transl Med.* 2021;13:eabe9805.
41. Ordonez AA, Weinstein EA, Bamberger LE, et al. A systematic approach for developing bacteria-specific imaging tracers. *J Nucl Med.* 2017;58:144–150.
42. Webb EW, Scott PJH. Potential applications of artificial intelligence and machine learning in radiochemistry and radiochemical engineering. *PET Clin.* 2021;16:525–532.
43. Mota F, Ordonez AA, Firth G, Ruiz-Bedoya CA, Ma MT, Jain SK. Radiotracer development for bacterial imaging. *J Med Chem.* 2020;63:1964–1977.
44. Parker MFL, Flavell RR, Luu JM, Rosenberg OS, Ohliger MA, Wilson DM. Small molecule sensors targeting the bacterial cell wall. *ACS Infect Dis.* 2020;6:1587–1598.
45. Gouws AC, Kruger HG, Gheysens O, et al. Antibiotic-derived radiotracers for positron emission tomography: nuclear or “unclear” infection imaging? *Angew Chem Int Ed.* 2022;61:e202204955.
46. Lawal I, Zeevaert J, Ebenhan T, et al. Metabolic imaging of infection. *J Nucl Med.* 2017;58:1727–1732.
47. Vermeulen K, Vandamme M, Bormans G, Cleeren F. Design and challenges of radiopharmaceuticals. *Semin Nucl Med.* 2019;49:339–356.
48. Halouska S, Zhang B, Gaupp R, et al. Revisiting protocols for the NMR analysis of bacterial metabolomes. *J Integr OMICS.* 2013;3:120–137.
49. Bauermeister A, Mannocho-Russo H, Costa-Lotuffo LV, Jarmusch AK, Dorrestein PC. Mass spectrometry-based metabolomics in microbiome investigations. *Nat Rev Microbiol.* 2022;20:143–160.
50. Namavari M, Gowrishankar G, Srinivasan A, Gambhir SS, Haywood T, Beinat C. A novel synthesis of 6''-<sup>18</sup>F-fluoromaltootriose as a PET tracer for imaging bacterial infection. *J Labelled Comp Radiopharm.* 2018;61:408–414.
51. Everitt JI, Berridge BR. The role of the IACUC in the design and conduct of animal experiments that contribute to translational success. *ILAR J.* 2017;58:129–134.
52. Signore A, Artiko V, Conserva M, et al. Imaging bacteria with radiolabelled probes: is it feasible? *J Clin Med.* 2020;9:2372.
53. Aarntzen EHJG, Noriega-Álvarez E, Artiko V, et al. EANM recommendations based on systematic analysis of small animal radionuclide imaging in inflammatory musculoskeletal diseases. *EJNMMI Res.* 2021;11:85.
54. Auletta S, Galli F, Varani M, et al. In vitro and in vivo evaluation of <sup>99m</sup>Tc-poly-myxin B for specific targeting of gram-bacteria. *Biomolecules.* 2021;11:232.
55. Madeja ZE, Pawlak P, Piliszek A. Beyond the mouse: non-rodent animal models for study of early mammalian development and biomedical research. *Int J Dev Biol.* 2019;63:187–201.
56. Esteves PJ, Abrantes J, Baldauf H-M, et al. The wide utility of rabbits as models of human diseases. *Exp Mol Med.* 2018;50:1–10.
57. Via LE, Schimmel D, Weiner DM, et al. Infection dynamics and response to chemotherapy in a rabbit model of tuberculosis using [<sup>18</sup>F]2-fluoro-deoxy-D-glucose positron emission tomography and computed tomography. *Antimicrob Agents Chemother.* 2012;56:4391–4402.
58. Ordonez AA, Parker MF, Miller RJ, et al. <sup>11</sup>C-para-aminobenzoic acid PET imaging of *S. aureus* and MRSA infection in preclinical models and humans. *JCI Insight.* 2022;7:e154117.
59. Elgazzar AH, Dannoon S, Sarikaya I, Farghali M, Junaid TA. Scintigraphic patterns of indium-111 oxine-labeled white blood cell imaging of gram-negative versus gram-positive vertebral osteomyelitis. *Med Princ Pract.* 2017;26:415–420.
60. Walker RL, Eggel M. From mice to monkeys? Beyond orthodox approaches to the ethics of animal model choice. *Animals (Basel).* 2020;10:77.
61. Hart BA, Abbott DH, Nakamura K, Fuchs E. The marmoset monkey: a multi-purpose preclinical and translational model of human biology and disease. *Drug Discov Today.* 2012;17:1160–1165.
62. Hatzioannou T, Evans DT. Animal models for HIV/AIDS research. *Nat Rev Microbiol.* 2012;10:852–867.
63. Coleman MT, Maiello P, Tomko J, et al. Early changes by <sup>18</sup>F-fluorodeoxyglucose positron emission tomography coregistered with computed tomography predict outcome after *Mycobacterium tuberculosis* infection in cynomolgus macaques. *Infect Immun.* 2014;82:2400–2404.
64. Mattila JT, Maiello P, Sun T, Via LE, Flynn JL. Granzyme B-expressing neutrophils correlate with bacterial load in granulomas from *Mycobacterium tuberculosis*-infected cynomolgus macaques. *Cell Microbiol.* 2015;17:1085–1097.
65. Toyohara J, Sakata M, Tago T, Colabufo NA, Luurtsema G. Automated synthesis, preclinical toxicity, and radiation dosimetry of [<sup>18</sup>F]MC225 for clinical use: a tracer for measuring P-glycoprotein function at the blood-brain barrier. *EJNMMI Res.* 2020;10:84.
66. Prado C, Kazi A, Bennett A, MacVittie T, Prado K. Mean organ doses resulting from non-human primate whole thorax lung irradiation prescribed to mid-line tissue. *Health Phys.* 2015;109:367–373.
67. Ebenhan T, Sathegke MM, Lengana T, et al. <sup>68</sup>Ga-NOTA-functionalized ubi-quidin: cytotoxicity, biodistribution, radiation dosimetry, and first-in-human PET/CT imaging of infections. *J Nucl Med.* 2018;59:334–339.
68. Tanner R, White AD, Boot C, et al. A non-human primate in vitro functional assay for the early evaluation of TB vaccine candidates. *NPJ Vaccines.* 2021;6:3.
69. Uno Y, Uehara S, Yamazaki H. Utility of non-human primates in drug development: comparison of non-human primate and human drug-metabolizing cytochrome P450 enzymes. *Biochem Pharmacol.* 2016;121:1–7.
70. Orsi A, Rees D, Andreini I, Venturella S, Cinelli S, Oberto G. Overview of the marmoset as a model in nonclinical development of pharmaceutical products. *Regul Toxicol Pharmacol.* 2011;59:19–27.
71. Seyedmousavi S, Bosco S de MG, de Hoog S, et al. Fungal infections in animals: a patchwork of different situations. *Med Mycol.* 2018;56(suppl 1):165–187.
72. Vamathevan JJ, Hall MD, Hasan S, et al. Minipig and beagle animal model genomes aid species selection in pharmaceutical discovery and development. *Toxicol Appl Pharmacol.* 2013;270:149–157.
73. Signore A, Casali M, Lauri C. An easy and practical guide for imaging infection/inflammation by [<sup>18</sup>F]FDG PET/CT. *Clin Transl Imaging.* 2021;9:283–297.
74. Corrales-Medina VF, deKemp RA, Chirinos JA, et al. Persistent lung inflammation after clinical resolution of community-acquired pneumonia as measured by <sup>18</sup>F-FDG-PET/CT imaging. *Chest.* 2021;160:446–453.
75. Baldoni D, Waibel R, Bläuenstein P, et al. Evaluation of a novel Tc-99m labelled vitamin B12 derivative for targeting *Escherichia coli* and *Staphylococcus aureus* in vitro and in an experimental foreign-body infection model. *Mol Imaging Biol.* 2015;17:829–837.
76. Aulakh GK, Brocos Duda JA, Guerrero Soler CM, Snead E, Singh J. Characterization of low-dose ozone-induced murine acute lung injury. *Physiol Rep.* 2020;8:e14463.
77. Aulakh GK, Kaur M, Brown V, Ekanayake S, Khan B, Fonge H. Quantification of regional murine ozone-induced lung inflammation using [<sup>18</sup>F]F-FDG microPET/CT imaging. *Sci Rep.* 2020;10:15699.
78. Duda JAB, Kaur M, Aulakh GK. Visualizing lung cellular adaptations during combined ozone and LPS induced murine acute lung injury. *J Vis Exp.* 2021;(169).
79. Henneberg S, Hasenberg A, Maurer A, et al. Antibody-guided in vivo imaging of *Aspergillus fumigatus* lung infections during antifungal azole treatment. *Nat Commun.* 2021;12:1707.
80. Welling MM, Duszynko N, van Willigen DM, et al. Cyclodextrin/adamantane-mediated targeting of inoculated bacteria in mice. *Bioconjug Chem.* 2021;32:607–614.
81. Cho SY, Pomper MG. Clinical translation of molecular imaging probes. In: Chen A, ed. *Molecular Imaging Probes for Cancer Research.* World Scientific; 2012: 1041–1065.
82. Wester H-J. Nuclear imaging probes: from bench to bedside. *Clin Cancer Res.* 2007;13:3470–3481.
83. Liu CH, Sastre A, Conroy R, Seto B, Pettigrew RI. NIH workshop on clinical translation of molecular imaging probes and technology: meeting report. *Mol Imaging Biol.* 2014;16:595–604.

# Predictive IDH Genotyping Based on the Evaluation of Spatial Metabolic Heterogeneity by Compartmental Uptake Characteristics in Preoperative Glioma Using $^{18}\text{F}$ -FET PET

Johannes Lohmeier<sup>1</sup>, Helena Radbruch<sup>2</sup>, Winfried Brenner<sup>3</sup>, Bernd Hamm<sup>1</sup>, Anna Tietze<sup>\*4</sup>, and Marcus R. Makowski<sup>\*5</sup>

<sup>1</sup>Department of Radiology, Charité–Universitätsmedizin Berlin, Berlin, Germany; <sup>2</sup>Department of Neuropathology, Charité–Universitätsmedizin Berlin, Berlin, Germany; <sup>3</sup>Department of Nuclear Medicine, Charité–Universitätsmedizin Berlin, Berlin, Germany; <sup>4</sup>Institute of Neuroradiology, Charité–Universitätsmedizin Berlin, Berlin, Germany; and <sup>5</sup>Department of Radiology, Technical University Munich, Munich, Germany

Molecular markers are of increasing importance for classifying, treating, and determining the prognosis for central nervous system tumors. Isocitrate dehydrogenase (IDH) is a critical regulator of glucose and amino acid metabolism. Our objective was to investigate metabolic reprogramming of glioma using compartmental uptake (CU) characteristics in O-(2- $^{18}\text{F}$ -fluoroethyl)-L-tyrosine (FET) PET and to evaluate its diagnostic potential for IDH genotyping. **Methods:** Between 2017 and 2022, patients with confirmed glioma were preoperatively investigated using static  $^{18}\text{F}$ -FET PET. Metabolic tumor volume (MTV), MTV for 60%–100% uptake (MTV<sub>60</sub>), and T2-weighted and contrast-enhancing lesion volumes were automatically segmented using U-Net neural architecture and isocontouring. Volume intersections were determined using the Dice coefficient. Uptake characteristics were determined for metabolically defined compartments (central [80%–100%] and peripheral [60%–75%] areas of  $^{18}\text{F}$ -FET uptake). CU ratio was defined as the fraction between the peripheral and central compartments. Mean target-to-background ratio was calculated. Comparisons were performed using parametric and nonparametric tests. Receiver-operating-characteristic curves, regression, and correlation were used for statistical analysis. **Results:** In total, 52 participants (male, 27, female, 25; mean age  $\pm$  SD, 51  $\pm$  16 y) were evaluated. MTV<sub>60</sub> was greater and distinct from contrast-enhancing lesion volume ( $P = 0.046$ ). IDH-mutated tumors presented a greater volumetric CU ratio and SUV CU ratio than IDH wild-type tumors ( $P < 0.05$ ). Volumetric CU ratio determined IDH genotype with excellent diagnostic performance (area under the curve [AUC], 0.88;  $P < 0.001$ ) at more than 5.49 (sensitivity, 86%, specificity, 90%), because IDH-mutated tumors presented a greater peripheral metabolic compartment than IDH wild-type tumors ( $P = 0.045$ ). MTV<sub>60</sub> and MTV were not suitable for IDH classification ( $P > 0.05$ ). SUV CU ratio (AUC, 0.72;  $P = 0.005$ ) and target-to-background ratio (AUC, 0.68;  $P = 0.016$ ) achieved modest diagnostic performance—inferior to the volumetric CU ratio. Furthermore, the classification of loss of heterozygosity of chromosomes 1p and 19q (AUC, 0.75;  $P = 0.019$ ), MGMT promoter methylation (AUC, 0.70;  $P = 0.011$ ), and ATRX loss (AUC, 0.73;  $P = 0.004$ ) by amino acid PET was evaluated. **Conclusion:** We proposed parametric  $^{18}\text{F}$ -FET

PET as a noninvasive metabolic biomarker for the evaluation of CU characteristics, which differentiated IDH genotype with excellent diagnostic performance, establishing a critical association between spatial metabolic heterogeneity, mitochondrial tricarboxylic acid cycle, and genomic features with critical implications for clinical management and the diagnostic workup of patients with central nervous system cancer.

**Key Words:**  $^{18}\text{F}$ -FET PET/MRI; amino acid metabolism; IDH genotyping; biomarker; spatial metabolic heterogeneity

**J Nucl Med 2023; 64:1683–1689**

DOI: 10.2967/jnumed.123.265642

**G**liomas are the most common primary malignant neoplasms of the central nervous system (CNS) in adults and comprise a large spectrum of molecular subtypes with intricate pathophysiology. Molecular stratification is essential for diagnosis, treatment planning, and individual prognosis. In recent years, the World Health Organization (WHO) classification of tumors of the CNS has undergone several updates (1) introducing several important changes, such as the incorporation of molecular and genetic information. One important molecular marker that has gained significant attention is the mutation status of the isocitrate dehydrogenase (IDH) gene (2–4). IDH gene mutations play a central role in glioma pathophysiology, occurring early in the glioma genesis and characterizing a group of tumors that is molecularly distinct from primary glioblastoma. Because IDH mutations are associated with a more favorable prognosis (5), the IDH genotype has become a central feature in the diagnosis and management of patients with CNS cancer. In recent years, considerable progress in understanding the molecular mechanisms and pathophysiology underlying IDH mutations has been made. IDH genes encode a key enzyme in the tricarboxylic acid cycle, which is a central cellular pathway for energy production. When IDH genes are altered, a profound disruption in the tricarboxylic acid cycle with dysregulation of the amino acid metabolism is induced—a hallmark of CNS cancer—which is leveraged for bioenergetic processes and protein synthesis. By a gain-of-function mutation, the physiologic conversion of isocitrate to  $\alpha$ -ketoglutarate, an important intermediate metabolite in the Krebs cycle, is inhibited, whereas the production of D-2-hydroxyglutarate is propagated. High levels of the oncometabolite D-2-hydroxyglutarate mediate global DNA and histone hypermethylation, impairment of DNA break repair mechanisms, and a decrease in hypoxia-inducible factors through competitive inhibition

Received Feb. 27, 2023; revision accepted Jun. 13, 2023.

For correspondence, contact Johannes Lohmeier (johannes.lohmeier@charite.de).

\*Contributed equally to this work.

Published online Aug. 31, 2023.

Immediate Open Access: Creative Commons Attribution 4.0 International License (CC BY) allows users to share and adapt with attribution, excluding materials credited to previous publications. License: <https://creativecommons.org/licenses/by/4.0/>. Details: <http://jnm.snmjournals.org/site/misc/permission.xhtml>.

COPYRIGHT © 2023 by the Society of Nuclear Medicine and Molecular Imaging.



of tumor suppressors in the  $\alpha$ -ketoglutarate-dependent dioxygenase family that contribute to glioma pathogenesis and progression through alteration of cellular differentiation, proliferation, and gene expression (2,3).

In the surgical management of patients with preoperative IDH-mutated glioma, supramaximal resection was shown to improve overall survival (5–8). However, the IDH genotype is typically unknown before surgery, and a preceding (stereotactic or open) biopsy involves the hazards of perioperative complications. To date, there are few reliable means for noninvasive and predictive genotyping of IDH mutation status in clinical practice (5).

On the basis of the hypothesis that specific genetic alterations are linked with distinct metabolic phenotypes, we introduced the compartmental uptake (CU) ratio as a noninvasive metabolic imaging biomarker characterizing the spatially heterogeneous glioma metabolism by differentiating the metabolic tumor core from its periphery. Predictive genotyping of IDH mutation status was then investigated using *O*-(2-<sup>18</sup>F-fluoroethyl)-L-tyrosine (FET) PET, as an established marker for amino acid metabolism, in a patient cohort with preoperative glioma.

## MATERIALS AND METHODS

### Study Design and Patients

This retrospective clinical cohort study was conducted according to the principles of the Helsinki Declaration. Approval from the institutional ethics board was obtained (EA2/019/23). Informed consent was obtained from all participants. From 200 consecutive suspected-glioma patients evaluated using a simultaneous <sup>18</sup>F-FET PET/MRI approach between 2017 and 2022, 52 participants with hybrid imaging before resection (Fig. 1) were included according to the eligibility criteria.

### Neuropathologic Analysis

The molecular status of IDH mutation (IDH-mutated or wild-type), 1p/19q codeletion (loss of heterozygosity of chromosomes 1p and 19q [LOH1p/19q]-positive, codeleted; LOH1p/19q-negative, nondeleted), MGMT promoter methylation (MGMT-positive, methylated; MGMT-negative, unmethylated), and ATRX loss (ATRX-positive, deficient; ATRX-negative, retention) were determined from formalin-fixed paraffin-embedded tissue specimens during routine diagnostic workup procedures using fluorescence in situ hybridization analysis, pyrosequencing, EPIC DNA methylation arrays (Illumina), or immunostainings according to the requirements of the WHO classification of tumors of the CNS (1). When pyrosequencing of MGMT promoter methylation was used, a cutoff of 10% was defined to classify MGMT methylated versus unmethylated cases, a cutoff that is commonly applied and has been validated for routine clinical diagnostics (9). Gliomas were classified using the 2021 WHO classification (1) according to the molecular data available at that time point.

### PET/MRI Acquisition

Simultaneous PET/MRI was performed on a Magnetom Biograph mMR scanner (Siemens Healthcare) with an averaged axial spatial

resolution of 6 mm in full width at half maximum, which was determined in a 3-dimensional Hoffman brain phantom measurement (ordered-subsets expectation maximization, 3 iterations and 21 subsets, postfiltering by a 3-dimensional gaussian kernel of 3 mm in full width at half maximum, as in patient data) following the method by Joshi et al. (10). PET and clinical high-field (3-T) MRI were performed in list mode for up to 60 min after intravenous administration of <sup>18</sup>F-FET (mean  $\pm$  SD, 163  $\pm$  23 MBq; 180-MBq standard dose and individually calculated dose for body weight < 60 kg). Fasting for at least 4 h before PET acquisition was recommended. A gadolinium-based contrast agent (Gadovist; Bayer Pharma AG) was administered according to the patient's total body weight (0.1 mmol/kg). The MRI acquisition protocol included a transversal T1-weighted ultrashort echo time sequence for attenuation and scatter correction, a T2-weighted sequence (repetition time/echo time, 5,320/88 ms; matrix size, 230  $\times$  230  $\times$  230; voxel size, 0.4  $\times$  0.4  $\times$  3.0 mm), and a postcontrast T1-weighted magnetization-prepared rapid gradient echo sequence (repetition time/echo time/inversion time, 2,400/2.26/900 ms; flip angle, 8°; matrix size, 256  $\times$  256  $\times$  256; voxel size, 1.0  $\times$  1.0  $\times$  1.0 mm; thickness, 1 mm; slices, 192). Vendor-based attenuation correction (software versions MR B20P and MR E11P) using ultrashort echo time was performed. The PET acquisition was reconstructed into transaxial slices using an iterative ordered-subset expectation maximization algorithm (ordered-subsets expectation maximization, 3 iterations and 21 subsets; matrix size, 344  $\times$  344  $\times$  127; voxel size, 1.0  $\times$  1.0  $\times$  2.3 mm; gaussian filter, 3 mm). Emission data were corrected for decay, randoms, dead time, scatter, and attenuation.

### PET and MRI Analysis

Quantitative analysis was performed using OsiriX MD 12 (Pixmeo SARL). Contrast-enhancing and T2-weighted lesion volumes were determined in an automated manner using an attention-based U-Net architecture with postcontrast T1-weighted magnetization-prepared rapid gradient echo and T2-weighted/fluid-attenuated inversion recovery images as input (11). When applicable, regions of interest (ROIs) of T2-weighted and contrast-enhancing lesion volumes were slightly adapted. <sup>18</sup>F-FET uptake was measured in an automated manner using isocontouring based on attenuation-corrected <sup>18</sup>F-FET tracer uptake, yielding an uptake-based total (60%–100%, MTV<sub>60</sub>), peripheral (60%–75%, ROI<sub>60</sub>), and central (80%–100%, ROI<sub>80</sub>) metabolic compartment (thresholds were iteratively determined in a pilot experiment, differentiating uptake pattern into a central and peripheral compartment based on visual assessment). Segmentations were marginally adapted to exclude large intracranial blood vessels (when applicable). For definition of metabolic tumor volume, both a percentage method (60%–100%, MTV<sub>60</sub>) and an absolute threshold method (1.8 times the mean uptake of the healthy contralateral background, MTV) were used. CU ratio was defined as the fraction between ROI<sub>60</sub> and ROI<sub>80</sub>, yielding a volumetric CU ratio for the uptake-based volume or SUV CU ratio for the mean SUV. Mean target-to-background ratio was determined from SUV<sub>mean</sub> on the basis of a 3-dimensional VOI (ROI<sub>80</sub>) from an <sup>18</sup>F-FET-active lesion compared with the mean unaffected contralateral background to account for nonspecific and regional uptake behavior. In multifocal tumor manifestations, the most prominent <sup>18</sup>F-FET-active lesion was chosen as the target lesion.

Mean background tracer uptake was computed from a contralateral 2-dimensional ROI of similar size in unaffected brain tissue on a representative slice with the highest mean uptake within the tumor volume. Three-dimensional ROIs from magnetization-prepared rapid gradient echo and <sup>18</sup>F-FET PET were then transformed to a structural T2-weighted image using rigid deformation (ANTs, version 2.3.4).

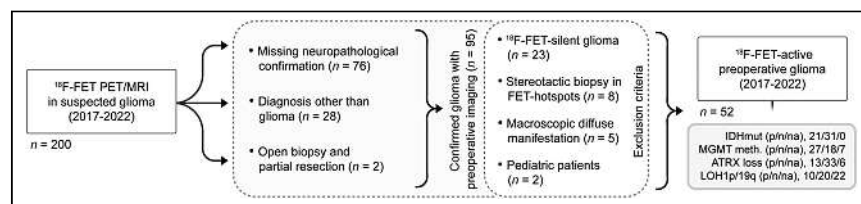


**FIGURE 1.** Study selection flowchart. ATRX =  $\alpha$ -thalassemia/mental retardation syndrome, X-linked; MGMT = *O*<sup>6</sup>-methylguanine DNA methyltransferase. p/n/na = positive/negative/not applicable.

## Statistics

Statistical analysis was performed using Prism version 9 (GraphPad Software) and MedCalc version 20.104 (MedCalc Software Ltd.). Mann–Whitney *U* (2-tailed) tests (with Holm–Šidák multiple-comparison testing) were used for comparisons between 2 groups. Wilcoxon signed-rank (1-tailed) testing was used for matched pairs. Kruskal–Wallis testing (with Dunn multiple-comparison testing) was used for comparisons among 3 groups. Receiver-operating-characteristic analysis was performed using the DeLong method reporting area under the curve (AUC), 95% CIs, and *P* value. Sensitivity and specificity were reported for the best cutoff point independent of the prevalence determined using the Youden index. Logistic regression was used to model binary outcome (predictive accuracy based on a *P* value cutoff of 0.5). Measurements were correlated and evaluated using the nonparametric Spearman correlation coefficient (2-tailed). Intersections between volumes were computed on the basis of the Dice coefficient (Eq. 1) and the Jaccard index. In all tests, a *P* value of less than 0.05 was considered statistically significant.

$$2 \times \frac{|X \cap Y|}{|X| + |Y|} \quad \text{Eq. 1}$$

## RESULTS

### Patient Population

Overall, the patient cohort comprised 52 participants (male, 27, female, 25; age, mean  $\pm$  SD, 51  $\pm$  16 y) with preoperative  $^{18}\text{F}$ -FET–active glioma (high-grade glioma, 45; low-grade glioma, 5; not applicable, 2) and available neuropathologic classification (Fig. 1; Table 1). Molecular data of IDH mutation (IDH-mutated,

**TABLE 1**  
Characteristics of Patient Cohort

Characteristic	Data
Participants	52
Age (mean $\pm$ SD in y)	51 $\pm$ 16
Sex	
Male	27
Female	25
IDH mutation status	
Positive	21
Negative	31
Not applicable	0
MGMT promoter methylation status	
Positive	27
Negative	18
Not applicable	7
ATRX loss	
Positive	13
Negative	33
Not applicable	6
LOH1p/19q	
Positive	10
Negative	20
Not applicable	22

Data are number, except for age.

40%, IDH wild-type, 60%), MGMT promoter methylation (MGMT-positive, 52%; MGMT-negative, 35%; unknown, 13%), LOH1p/19q (LOH1p/19q-positive, 19.2%; LOH1p/19q-negative, 38.5%; unknown, 42.3%), and ATRX loss (ATRX-positive, 25%; ATRX-negative, 63%; unknown, 12%) were determined. CNS WHO grade 4 tumors were predominantly IDH wild-type (93%), whereas most WHO CNS grade 2–3 tumors were IDH-mutated (86%). IDH-mutated gliomas included both astrocytoma (48%) and oligodendroglioma (52%). The study cohort comprised a case of diffuse pediatric-type high-grade glioma in an adult patient. A detailed overview of the

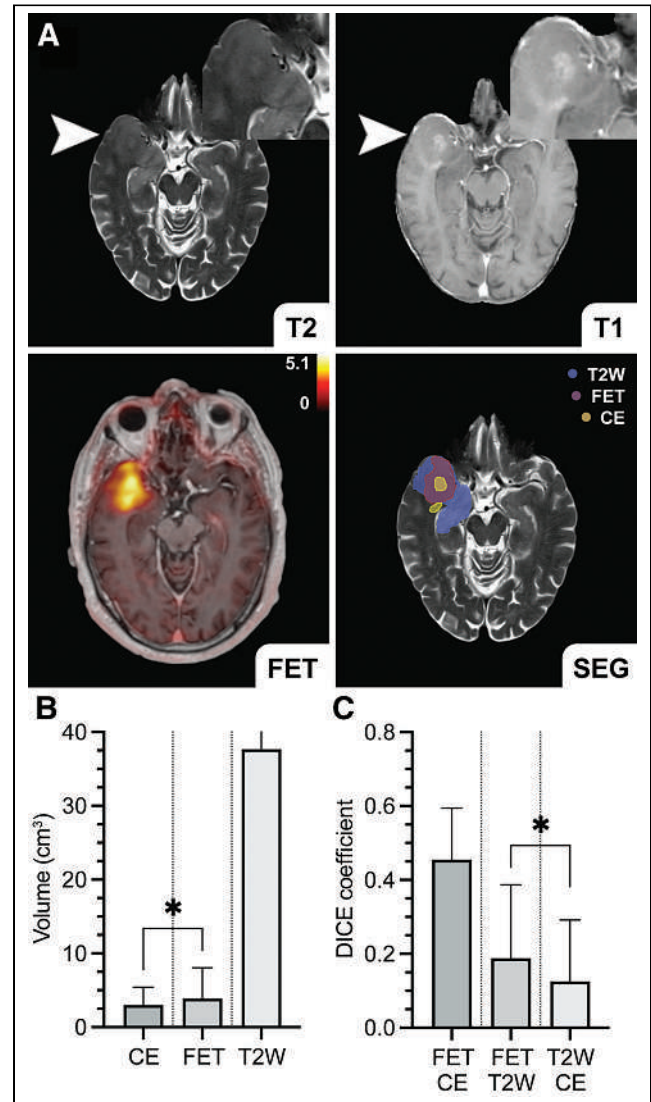


**FIGURE 2.** Volumetric analysis in multimodal  $^{18}\text{F}$ -FET PET/contrast-enhanced MRI. (A) Automated segmentation based on  $^{18}\text{F}$ -FET PET, contrast-enhancing, and T2-weighted lesion volume in multimodal dataset of patient with glioblastoma IDH wild-type (CNS WHO grade 4, MGMT-negative, ATRX-negative; arrowheads) is illustrated. (B and C) In intrasubject comparison, MTV<sub>60</sub> was greater than contrast-enhancing lesion volume (*P* = 0.046, *n* = 30). Furthermore, intersection or overlap between T2-weighted lesion volume and MTV<sub>60</sub> was greater than its overlap with contrast-enhanced MRI (*P* = 0.038, *n* = 30). Dice coefficients presented low to moderate degree of overlap or similarity between respective volumes, although MTV<sub>60</sub> and contrast-enhancing lesion volume showed highest concordance (C). Data are median  $\pm$  IQR. \**P* < 0.05. SEG = segmentation.

molecular stratification is available in Supplemental Table 1 (supplemental materials are available at <http://jnm.snmjournals.org>).

### Comparison of Volumetric Attributes in Preoperative Glioma

MTV<sub>60</sub> from <sup>18</sup>F-FET PET was greater than contrast-enhancing lesion volume (median, 3.87 cm<sup>3</sup> [interquartile range (IQR), 5.47] vs. 3.00 cm<sup>3</sup> [IQR, 4.66], *P* = 0.046, *n* = 30, Kendall W statistic, -165) in intrasubject comparison (Fig. 2). Correspondingly, the intersection of T2-weighted lesion volume with MTV<sub>60</sub> was greater than its overlap with contrast-enhancing lesion volume (median, 0.189 [IQR, 0.327] vs. 0.125 [IQR, 0.262], *P* = 0.038, *n* = 30, Kendall W statistic, -173) as determined by the Dice coefficient. T2-weighted lesion volume showed the greatest dimensions and variability because of perilesional edema and diffuse infiltration. Volume intersections between MTV<sub>60</sub>, contrast-enhancing lesion volume, and T2-weighted lesion volume presented a low to moderate degree of overlap or similarity (Fig. 2C), although MTV<sub>60</sub> and contrast-enhancing lesion volume (Dice coefficient; median, 0.455 [IQR, 0.372]) presented the greatest concordance and were weakly correlated (Spearman rank correlation coefficient, 0.38; *P* = 0.038).

### Association Between Molecular Status and CU Characteristics

IDH-mutated tumors presented a greater volumetric CU ratio (median, 7.84 [IQR, 5.20, *n* = 21] vs. 3.92 [IQR, 2.32, *n* = 31], *P* < 0.001, *U* = 76) and SUV CU ratio (median, 0.781 [IQR, 0.024, *n* = 21] vs. 0.768 [IQR, 0.022, *n* = 31], *P* = 0.032, *U* = 185) than IDH wild-type, as demonstrated in Table 2. For further evaluation of the volumetric CU ratio, the clinical cohort was randomly split into an independent model-building-and-assessment dataset based on neuropathologic IDH classification. Excellent diagnostic performance for the differentiation between IDH genotype (Fig. 3E) was apparent in the model-building dataset (AUC ± SE, 0.86 ± 0.09; *P* < 0.001; 95% CI, 0.66–0.96; IDH wild-type, 16; IDH-mutated, 10), which determined an optimal threshold of 5.43 (sensitivity, 80%; specificity, 88%; accuracy, 81%) based on the Youden index. This was then confirmed in the independent evaluation dataset (AUC ± SE, 0.89 ± 0.06; *P* < 0.001; 95% CI, 0.70–0.98; IDH wild-type, 15; IDH-mutated, 11) applying the previously determined threshold of 5.43 for IDH-mutated (sensitivity, 91%; specificity, 87%; accuracy, 88%) with similar results for the entire cohort (AUC ± SE, 0.88 ± 0.05; *P* < 0.001; 95% CI, 0.76–0.96). As shown in Figures 3A–3D, IDH-mutated tumors presented a greater peripheral metabolic compartment (corresponding to

ROI<sub>60</sub>) than IDH wild-type (median, 5.33 [IQR, 7.47, *n* = 21] vs. 2.78 [IQR, 4.94, *n* = 31], *P* = 0.045, *U* = 218), whereas no difference for the central metabolic compartment was apparent (*P* > 0.05). MTV<sub>60</sub> and MTV were not suitable for IDH classification (*P* > 0.05). A low correlation between volumetric CU ratio was observed for MTV<sub>60</sub> (Spearman rank correlation coefficient, 0.356; *P* = 0.01) but not for MTV (*P* > 0.05). With a more conservative thresholding method, MTV<sub>60</sub> underestimated the total tumor volume compared with the clinically established MTV (median, 4.95 cm<sup>3</sup> [IQR, 7.46] vs. 7.75 cm<sup>3</sup> [IQR, 10.77]; *P* = 0.018; *n* = 52; Kendall W statistic, 460). SUV CU ratio (AUC ± SE, 0.72 ± 0.08; *P* = 0.005; accuracy, 67%) and target-to-background ratio (AUC ± SE, 0.68 ± 0.07; *P* = 0.016; accuracy, 63%) achieved modest diagnostic power, although the performance of target-to-background ratio was inferior to that of volumetric CU ratio (difference in AUC ± SE, 0.203 ± 0.080; *P* = 0.01).

Comparisons between IDH-mutated oligodendroglioma (*n* = 11), IDH-mutated astrocytoma (*n* = 8), and IDH wild-type glioblastoma (*n* = 25) with regard to target-to-background ratio (*P* > 0.05; Kruskal–Wallis test, 4.125), SUV CU ratio (*P* = 0.028; Kruskal–Wallis test, 7.163; adjusted *P* > 0.05), and volumetric CU ratio (*P* < 0.001; Kruskal–Wallis test, 18.55) demonstrated that IDH wild-type glioblastoma presented lower volumetric CU ratios than IDH-mutated oligodendroglioma (median, 3.88 [IQR, 1.97] vs. 8.75 [IQR, 7.21]; *P* < 0.001; mean rank difference, 17.40) with a classification threshold (AUC ± SE, 0.88 ± 0.07; *P* < 0.001; 95% CI, 0.73–0.96; sensitivity, 82%; specificity 88%; accuracy, 81%) at 5.26 (based on the Youden index) and IDH-mutated astrocytoma (median, 3.88 [IQR, 1.97] vs. 7.89 [IQR, 2.17]; *P* = 0.007; mean rank difference, 16.01) with the same classification threshold (AUC ± SE, 0.89 ± 0.09; *P* < 0.001; 95% CI, 0.73–0.97; sensitivity, 88%; specificity 88%; accuracy, 82%) at 5.26 (based on the Youden index). No differences between IDH-mutated astrocytoma and oligodendroglioma were apparent (*P* > 0.05). Supplemental Table 2 provides further details.

Molecular classification of LOH1p/19q (AUC ± SE, 0.75 ± 0.11; *P* = 0.019; accuracy, 67%), MGMT promoter methylation (AUC ± SE, 0.70 ± 0.08; *P* = 0.011; accuracy, 64%), and ATRX loss (AUC ± SE, 0.73 ± 0.08; *P* = 0.004; accuracy, 74%) were additionally evaluated using volumetric CU ratio (Fig. 3F).

## DISCUSSION

We introduced a noninvasive metabolic imaging biomarker for the assessment of metabolic reprogramming in gliomas and

**TABLE 2**  
Diagnostic Measures from <sup>18</sup>F-FET PET for IDH Classification

Metric	Mann–Whitney <i>U</i> test			ROC				Sensitivity (%)	Specificity (%)
	Adjusted <i>P</i>	Mean rank difference	<i>U</i>	<i>P</i>	AUC ± SE	95% CI	Threshold		
Volumetric CU ratio	<0.001	-19.93	76	<0.001	0.88 ± 0.05	0.76–0.96	>5.49	86	90
MTV <sub>60</sub>	>0.05	-6.430	245	>0.05	0.62 ± 0.08	0.48–0.75	—		
MTV	>0.05	-1.717	304	>0.05	0.53 ± 0.09	0.39–0.67	—		
SUV CU ratio	0.032	-11.22	185	0.005	0.72 ± 0.08	0.57–0.83	>0.77	76	71
Target-to-background ratio	>0.05	9.386	208	0.016	0.68 ± 0.07	0.54–0.80	≤2.73	76	58

ROC = receiver operating characteristic.

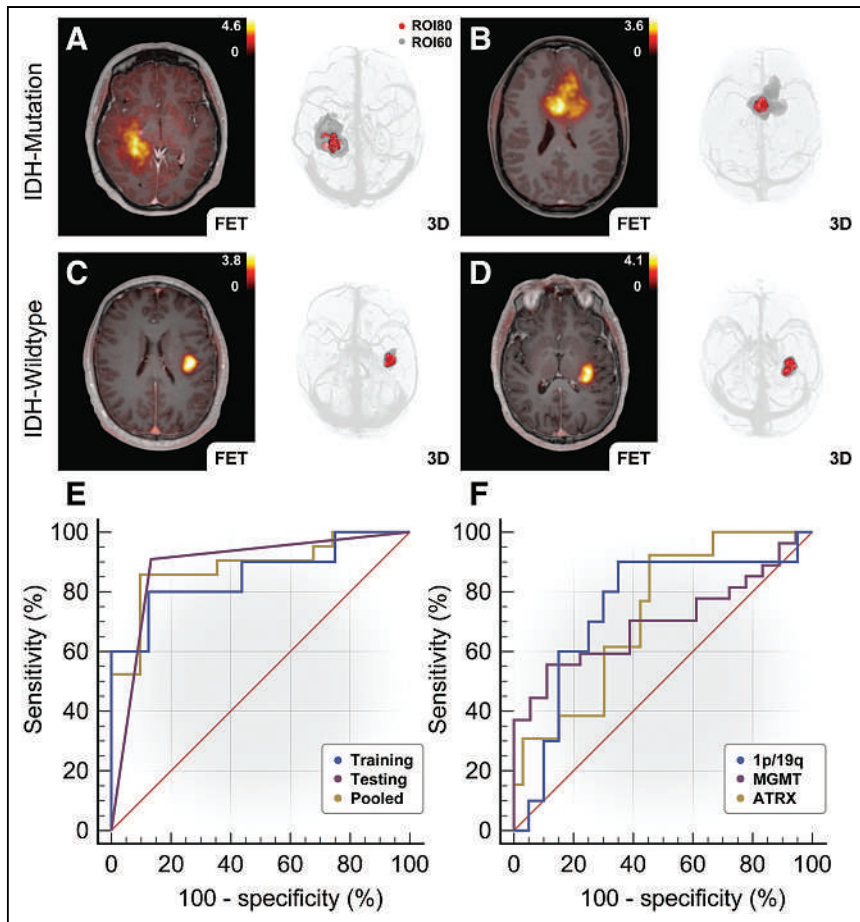


**FIGURE 3.** Evaluation of volumetric CU ratio for differentiation between IDH mutation status. (A and B) Representative cases of IDH-mutated high-grade astrocytoma (CNS WHO grade 3) (A) and IDH-mutated low-grade oligodendroglioma 1p/19q codeleted (CNS WHO grade 2) (B) are illustrated with  $^{18}\text{F}$ -FET PET/magnetization-prepared rapid gradient echo fusion image and 3-dimensional rendering, respectively, demonstrating increased volumetric CU ratio (ROI<sub>60</sub>/ROI<sub>80</sub>). (C and D) In contrast, IDH wild-type presented low volumetric CU ratio as shown in glioblastoma IDH wild-type (CNS WHO grade 4). (E and F) Genotyping of IDH mutation status using CU ratio based on receiver-operating-characteristic analysis: volumetric CU ratio demonstrated robust diagnostic performance for differentiation between IDH-mutated and IDH wild-type tumors in independent model-building (training) dataset (AUC,  $0.86 \pm 0.09$ ;  $P < 0.001$ ; 95% CI, 0.66–0.96; IDH wild-type, 16; IDH-mutated, 10) with threshold  $> 5.43$  (sensitivity, 80%, specificity, 88%) and evaluation (testing) dataset (AUC,  $0.89 \pm 0.06$ ;  $P < 0.001$ ; 95% CI, 0.70–0.98; IDH wild-type, 15; IDH-mutated, 11) as well as in entire study cohort (AUC,  $0.88 \pm 0.05$ ;  $P < 0.001$ ; 95% CI, 0.76–0.96) (E); in addition, differentiation between LOH1p/19q status, MGMT promoter methylation status, and ATRX loss was evaluated, presenting moderate diagnostic performance ( $P < 0.05$ ) (F).

demonstrated its diagnostic potential for the predictive genotyping of IDH mutation status by characterizing the spatially heterogeneous amino acid metabolism in a patient cohort with preoperative glioma. First, we showed that the MTV<sub>60</sub> in  $^{18}\text{F}$ -FET PET is distinct from contrast-enhanced MRI, which is the clinical standard for the initial diagnosis, biopsy targeting, and surveillance of brain tumors. Furthermore, MTV<sub>60</sub> presented greater dimensions than contrast-enhanced MRI, which is known to underestimate tumor margins because of diffuse infiltration beyond areas of blood–brain barrier impairment (12,13). Exploiting the cancer amino acid metabolism, we proposed the volumetric CU ratio as a biologic determinant for the assessment of CU characteristics, which determined IDH mutation status in this cohort of treatment-naïve glioma patients with excellent diagnostic accuracy, suggesting a central role for non-invasive genotyping before surgical intervention.

corresponded to a visually apparent heterogeneous uptake observed in some tumors.

#### IDH Genotyping Using Advanced Imaging

Determination of the IDH mutation status from conventional MRI is difficult, although IDH-mutated, LOH1p/19q-negative low-grade gliomas were reported to present T2-weighted or fluid-attenuated inversion recovery mismatch (20), which has low sensitivity (42%) but high specificity (nearly 100%) for this distinct entity. It must, however, be noted that dysembryoplastic neuroepithelial tumors were also reported to exhibit this imaging characteristic (21). Previous research efforts focused predominantly on measurement of D-2-hydroxyglutarate using MR spectroscopy (22–26), but its clinical implementation has been limited by low spatial resolution (voxel size  $> 1 \text{ cm}^3$ ) and signal-to-noise ratio,

Gene expression in glioma is known to be spatially distinct, for example, presenting differential upregulation of tyrosine aminotransferase—where increased expression in the tumor core as opposed to the periphery was reported—and a corresponding activation of the tyrosine metabolism (14). Because of this differential expression and metabolism, the IDH genotype, which is a critical regulator of both glucose and amino acid metabolism (15), was determined in an indirect bottom-up approach in the current study. Interestingly, LOH1p/19q, MGMT promoter methylation, and ATRX loss were differentiated by spatial metabolic patterns—although diagnostic performance was moderate—suggesting indirect associations. Similar to results from previous metabolic imaging studies (16–18), the averaged  $^{18}\text{F}$ -FET uptake differentiated IDH genotype with modest diagnostic performance—inferior to the volumetric CU ratio. MTV<sub>60</sub> and MTV were not suitable for differentiation between IDH genotypes, but a weak correlation between MTV<sub>60</sub> and volumetric CU ratio was observed. CU characteristics may also be determined as a ratio of total (summed) uptake (instead of volume) or may be accessible from histogram analysis. Although IDH-mutated astrocytoma and oligodendroglioma are considered distinct tumor entities, both could be independently differentiated from IDH wild-type glioblastoma at the same threshold, further suggesting that the volumetric CU ratio reflects metabolic reprogramming dependent on the IDH genotype. We could not observe increased uptake in IDH-mutated oligodendroglioma compared with IDH-mutated astrocytoma, as suggested in previous studies (17,19)—likely because of the relatively low number of these tumors in the cohort. When metabolic compartments were compared between IDH-mutated and IDH wild-type glioma, only the peripheral compartment was increased in IDH-mutated tumors, which



as well as the propensity to artifacts, particularly in the posttreatment setting. Moreover, D-2-hydroxyglutarate MR spectroscopy requires off-line postprocessing, currently impeding more widespread implementation. Of note is that single-voxel MR spectroscopy depends on the accuracy of the voxel placement in often heterogeneous tumors. Diffusion MRI was shown to correspond to the IDH genotype in CNS WHO 2 and 3 gliomas (27); however, modest diagnostic power for the differentiation of IDH mutation status was apparent using both single- and multiple-shell imaging. A study by Lohmann et al. (28) using  $^{18}\text{F}$ -FET PET radiomics suggested that the combined biparametric analysis of conventional uptake parameters with additional textural features can achieve a similar diagnostic accuracy (as reported here); nonetheless, textural feature analysis is a complex and time-demanding approach, which suffers from well-known issues of restricted generalizability, overfitting, or other methodologic flaws (29). Experimental advanced imaging techniques, such as chemical exchange saturation transfer (30) or hyperpolarized  $^{13}\text{C}$ -MRI (31), were also demonstrated to show correspondence to the IDH genotype, but clinical implementation is currently challenging. In contrast, the current study's approach demonstrated robust IDH classification based on static  $^{18}\text{F}$ -FET PET without the need for complex analysis.

### Clinical Relevance of Biomarker-Driven IDH Classification

The IDH genotype is a clinically important marker for molecular targeting, surgical planning, and individual prognosis (5). With the paradigm shift to molecular markers in clinical management of CNS cancer, there is a great clinically unmet need for noninvasive biomarker-driven classification. In clinical settings where limited tissue specimens are obtained, such as in stereotactic minimally invasive MRI-guided laser ablation or laser interstitial thermal therapy (32), an additional clinical benefit is expected. Molecular stratification before surgical intervention provides opportunities for more effective individualized neoadjuvant therapeutic strategies, an important topic in multimodal cytoreductive therapy because IDH-mutated gliomas are associated with better outcomes from radiochemotherapy (2,3). Furthermore, an imaging biomarker-driven classification aids the identification of patients with an increased risk of recurrence, allowing for earlier and more aggressive treatment regimens.

### Limitations

General conclusions should be drawn with caution because of the retrospective nature of this study. Further research with larger multicenter cohorts (with different scanners and reconstruction settings) and a prospective study design is required. The CU ratio using isocontouring may be sensitive to spatial image resolution and PET scanner variability. Subsequent investigations should evaluate the impact of different spatial resolutions and PET scanners, incorporating harmonization techniques (e.g., scanner-specific calibration phantoms or image postprocessing methods) and sensitivity analyses, thereby improving generalizability and clinical applicability.

Findings from the current study are restricted to  $^{18}\text{F}$ -FET-active tumors (76% of confirmed preoperative glioma with available imaging in the current study). In PET photopenic CNS cancer, advanced imaging techniques, such as MR spectroscopy, chemical exchange saturation transfer, or diffusion MRI, would certainly provide supplementary information, which should also be investigated in multimodal and multiparametric research for IDH genotyping—with potential to obviate a preceding biopsy. Furthermore, diffuse and multifocal tumor manifestations may result in divergent

metabolic and molecular signatures. The current cohort comprised a mixed patient population, which is reflective of the situation in clinical practice. A study population with the same histologic subtype could provide greater comparability at the cost of restricted generalizability; nonetheless, our results suggest that the CU ratio reflects metabolic reprogramming independent of tumor entity. Of particular note is that former IDH-mutated glioblastomas are classified as astrocytoma CNS WHO grade 4 and that oligodendrogliomas are genetically defined by IDH mutation and LOH1p/19q according to the 2021 WHO classification (1). Although the determined isocontouring thresholds achieve plausible segmentation into central and peripheral metabolic compartments, an immunohistochemical correlation and further optimization of thresholds based on tissue specimens merit further research. Future studies should investigate response assessment of IDH-targeted therapy, as well as CU characteristics in other IDH mutation-associated tumors, including acute myeloid leukemia, cholangiocarcinoma, or chondrosarcoma. Multilateral interactions between cancer metabolism, oncogenic pathways, and the tumor microenvironment, particularly interactions between cancer, immune, and neuronal cells, are further areas for future studies.

### CONCLUSION

The IDH genotype has a significant impact on the diagnosis and treatment of glioma. We proposed parametric  $^{18}\text{F}$ -FET PET as a noninvasive metabolic biomarker for the classification of IDH genotype—with critical implications for clinical management and the diagnostic workup of patients with CNS cancer.

### DISCLOSURE

This research project was funded by the “Deutsche Forschungsgemeinschaft” (DFG, German Research Foundation) (SFB1340/1 2018, SFB1315, and SFB295RETUNE). The PET/MRI scanner was cofunded by the “Deutsche Forschungsgemeinschaft” (INST 335/543-1 FUGG 2015). No other potential conflict of interest relevant to this article was reported.

### KEY POINTS

**QUESTION:** Is the IDH genotype—a critical regulator of glucose and amino acid metabolism—associated with a distinct metabolic phenotype in amino acid PET?

**PERTINENT FINDINGS:** Fifty-two patients with preoperative glioma were retrospectively investigated using static  $^{18}\text{F}$ -FET PET. Metabolic tumor volume was distinct and presented greater dimensions than contrast enhancement, which is known to underestimate tumor margins. Evaluation of compartmental  $^{18}\text{F}$ -FET uptake characteristics determined IDH genotype with excellent diagnostic performance, establishing a critical association between spatial metabolic heterogeneity, mitochondrial tricarboxylic acid cycle, and genomic features. Molecular classification of LOH1p/19q, MGMT promoter methylation, and ATRX loss by spatial metabolic patterns was possible, suggesting indirect associations with tyrosine metabolism.

**IMPLICATIONS FOR PATIENT CARE:** We proposed parametric  $^{18}\text{F}$ -FET PET as a noninvasive metabolic biomarker for the classification of IDH genotype before surgical intervention, with implications for clinical management and the diagnostic workup of patients with glioma.

## REFERENCES

1. Louis DN, Perry A, Wesseling P, et al. The 2021 WHO Classification of Tumors of the Central Nervous System: a summary. *Neuro Oncol.* 2021;23:1231–1251.
2. Gagné L, Boulay K, Topisirovic I, Huot MÉ, Mallette FA. Oncogenic activities of IDH1/2 mutations: from epigenetics to cellular signaling. *Trends Cell Biol.* 2017; 27:738–752.
3. Waitkus MS, Diplas BH, Yan H. Isocitrate dehydrogenase mutations in gliomas. *Neuro Oncol.* 2016;18:16–26.
4. Pirozzi CJ, Yan H. The implications of IDH mutations for cancer development and therapy. *Nat Rev Clin Oncol.* 2021;18:645–661.
5. Miller JJ, Gonzalez Castro LN, McBrayer S et al. Isocitrate dehydrogenase (IDH) mutant gliomas: a Society for Neuro-Oncology (SNO) consensus review on diagnosis, management, and future directions. *Neuro Oncol.* 2023;25:4–25.
6. Motomura K, Chalise L, Ohka F, et al. Impact of the extent of resection on the survival of patients with grade II and III gliomas using awake brain mapping. *J Neurooncol.* 2021;153:361–372.
7. Rossi M, Gay L, Ambrogi F, et al. Association of supratotal resection with progression-free survival, malignant transformation, and overall survival in lower-grade gliomas. *Neuro Oncol.* 2021;23:812–826.
8. Beiko J, Suki D, Hess KR, et al. IDH1 mutant malignant astrocytomas are more amenable to surgical resection and have a survival benefit associated with maximal surgical resection. *Neuro Oncol.* 2014;16:81–91.
9. Xie H, Tubbs R, Yang B. Detection of MGMT promoter methylation in glioblastoma using pyrosequencing. *Int J Clin Exp Pathol.* 2015;8:1790–1796.
10. Joshi A, Koeppe RA, Fessler JA. Reducing between scanner differences in multi-center PET studies. *Neuroimage.* 2009;46:154–159.
11. Bouget D, Pedersen A, Hosainy SAM, Solheim O, Reinertsen I. Meningioma segmentation in T1-weighted MRI leveraging global context and attention mechanisms. *Front Radiol.* 2021;1:711514.
12. Song S, Cheng Y, Ma J, et al. Simultaneous FET-PET and contrast-enhanced MRI based on hybrid PET/MR improves delineation of tumor spatial biodistribution in gliomas: a biopsy validation study. *Eur J Nucl Med Mol Imaging.* 2020;47: 1458–1467.
13. Lohmann P, Stavrinou P, Lipke K, et al. FET PET reveals considerable spatial differences in tumour burden compared to conventional MRI in newly diagnosed glioblastoma. *Eur J Nucl Med Mol Imaging.* 2019;46:591–602.
14. Yamashita D, Bernstock JD, Elsayed G, et al. Targeting glioma-initiating cells via the tyrosine metabolic pathway. *J Neurosurg.* 2020;134:721–732.
15. Bi J, Chowdhry S, Wu S, Zhang W, Masui K, Mischel PS. Altered cellular metabolism in gliomas: an emerging landscape of actionable co-dependency targets. *Nat Rev Cancer.* 2020;20:57–70.
16. Kudulaiti N, Zhang H, Qiu T, et al. The relationship between IDH1 mutation status and metabolic imaging in nonenhancing supratentorial diffuse gliomas: a <sup>11</sup>C-MET PET study. *Mol Imaging.* 2019;18:1536012119894087.
17. Verger A, Stoffels G, Bauer EK, et al. Static and dynamic <sup>18</sup>F-FET PET for the characterization of gliomas defined by IDH and 1p/19q status. *Eur J Nucl Med Mol Imaging.* 2018;45:443–451.
18. Lopci E, Riva M, Olivari L, et al. Prognostic value of molecular and imaging biomarkers in patients with supratentorial glioma. *Eur J Nucl Med Mol Imaging.* 2017; 44:1155–1164.
19. Kim D, Chun JH, Kim SH, et al. Re-evaluation of the diagnostic performance of <sup>11</sup>C-methionine PET/CT according to the 2016 WHO classification of cerebral gliomas. *Eur J Nucl Med Mol Imaging.* 2019;46:1678–1684.
20. Park SI, Suh CH, Guenette JP, Huang RY, Kim HS. The T2-FLAIR mismatch sign as a predictor of IDH-mutant, 1p/19q-noncodeleted lower-grade gliomas: a systematic review and diagnostic meta-analysis. *Eur Radiol.* 2021;31:5289–5299.
21. Onishi S, Amata VJ, Kolakshyapati M, et al. T2-FLAIR mismatch sign in dysembryoplasticneuroepithelial tumor. *Eur J Radiol.* 2020;126:108924.
22. Choi C, Ganji SK, DeBerardinis RJ, et al. 2-hydroxyglutarate detection by magnetic resonance spectroscopy in IDH-mutated patients with gliomas. *Nat Med.* 2012;18:624–629.
23. Andronesi OC, Arrillaga-Romany IC, Ly KI, et al. Pharmacodynamics of mutant-IDH1 inhibitors in glioma patients probed by in vivo 3D MRS imaging of 2-hydroxyglutarate. *Nat Commun.* 2018;9:1474.
24. Choi C, Raisanen JM, Ganji SK, et al. Prospective longitudinal analysis of 2-hydroxyglutarate magnetic resonance spectroscopy identifies broad clinical utility for the management of patients with IDH-mutant glioma. *J Clin Oncol.* 2016; 34:4030–4039.
25. Bumke E, Wirtz FP, Fellner C, et al. Non-invasive prediction of IDH mutation in patients with glioma WHO II/III/IV based on F-18-FET PET-guided in vivo <sup>1</sup>H-magnetic resonance spectroscopy and machine learning. *Cancers (Basel).* 2020;12:3406.
26. Tietze A, Choi C, Mickey B, et al. Noninvasive assessment of isocitrate dehydrogenase mutation status in cerebral gliomas by magnetic resonance spectroscopy in a clinical setting. *J Neurosurg.* 2018;128:391–398.
27. Figini M, Riva M, Graham M, et al. Prediction of isocitrate dehydrogenase genotype in brain gliomas with MRI: single-shell versus multishell diffusion models. *Radiology.* 2018;289:788–796.
28. Lohmann P, Lerche C, Bauer EK, et al. Predicting IDH genotype in gliomas using FET PET radiomics. *Sci Rep.* 2018;8:13328.
29. Gidwani M, Chang K, Patel JB et al. Inconsistent partitioning and unproductive feature associations yield idealized radiomic models. *Radiology.* 2023;307:e220715.
30. Paech D, Windschuh J, Oberhollenzer J, et al. Assessing the predictability of IDH mutation and MGMT methylation status in glioma patients using relaxation-compensated multipool CEST MRI at 7.0 T. *Neuro Oncol.* 2018;20:1661–1671.
31. Chaumeil MM, Larson PE, Woods SM, et al. Hyperpolarized [<sup>13</sup>C] glutamate: a metabolic imaging biomarker of IDH1 mutational status in glioma. *Cancer Res.* 2014;74:4247–4257.
32. Schupper AJ, Chanenchuk T, Racanelli A, Price G, Hadjipanayis CG. Laser hyperthermia: past, present, and future. *Neuro Oncol.* 2022;24(suppl 6):S42–S51.

---

---

# Correlation of SUV on Early Interim PET with Recurrence-Free Survival and Overall Survival in Primary Operable HER2-Positive Breast Cancer (the TBCRC026 Trial)

Maeve A. Hennessy<sup>1</sup>, Jeffrey P. Leal<sup>2</sup>, Chiung-Yu Huang<sup>2,3</sup>, Lilja B. Solnes<sup>2</sup>, Rita Denbow<sup>2</sup>, Vandana G. Abramson<sup>4</sup>, Lisa A. Carey<sup>5</sup>, Minetta C. Liu<sup>6</sup>, Mothaffar Rimawi<sup>7</sup>, Jennifer Specht<sup>8</sup>, Anna Maria Storniolo<sup>9</sup>, Vicente Valero<sup>10</sup>, Christos Vaklavas<sup>11</sup>, Eric P. Winer<sup>12</sup>, Ian E. Krop<sup>12</sup>, Antonio C. Wolff<sup>2</sup>, Ashley Cimino-Mathews<sup>2</sup>, Richard L. Wahl<sup>13</sup>, Vered Stearns<sup>2</sup>, and Roisin M. Connolly<sup>1,2</sup>

<sup>1</sup>Cancer Research @UCC, Cork, Ireland; <sup>2</sup>Sidney Kimmel Comprehensive Cancer Center, Johns Hopkins, Baltimore, Maryland;

<sup>3</sup>University of California, San Francisco, California; <sup>4</sup>Vanderbilt University, Nashville, Tennessee; <sup>5</sup>University of North Carolina,

Chapel Hill, North Carolina; <sup>6</sup>Mayo Clinic, Rochester, Minnesota; <sup>7</sup>Baylor College of Medicine, Houston, Texas; <sup>8</sup>University of Washington, Seattle, Washington; <sup>9</sup>Melvin and Bren Simon Comprehensive Cancer Center, Indiana University, Indianapolis, Indiana;

<sup>10</sup>M.D. Anderson Cancer Center, Houston, Texas; <sup>11</sup>University of Alabama, Birmingham, Alabama; <sup>12</sup>Yale Cancer Center, New Haven, Connecticut; and <sup>13</sup>Washington University, St. Louis, Missouri

---

Predictive biomarkers of response to human epidermal growth factor receptor 2 (HER2)-directed therapy are essential to inform treatment decisions. The TBCRC026 trial reported that early declines in tumor SUVs corrected for lean body mass (SUL<sub>max</sub>) on <sup>18</sup>F-FDG PET/CT predicted a pathologic complete response (pCR) to HER2 therapy with neoadjuvant trastuzumab and pertuzumab (HP) without chemotherapy in estrogen receptor (ER)-negative, HER2-positive breast cancer. We hypothesized that <sup>18</sup>F-FDG PET/CT SUL<sub>max</sub> parameters would predict recurrence-free survival (RFS) and overall survival (OS). **Methods:** Patients with stage II/III ER-negative, HER2-positive breast cancer received neoadjuvant HP (*n* = 88). pCR after HP alone was 22% (18/83), additional nonstudy neoadjuvant therapy was administered in 28% (25/88), and the majority received adjuvant therapy per physician discretion. <sup>18</sup>F-FDG PET/CT was performed at baseline and at cycle 1, day 15 (C1D15). RFS and OS were summarized using the Kaplan-Meier method and compared between subgroups using logrank tests. Associations between <sup>18</sup>F-FDG PET/CT (≥40% decline in SUL<sub>max</sub> between baseline and C1D15, or C1D15 SUL<sub>max</sub> ≤ 3) and pCR were evaluated using Cox regressions, where likelihood ratio CIs were reported because of the small numbers of events. **Results:** Median follow-up was 53.7 mo (83/88 evaluable), with 6 deaths and 14 RFS events. Estimated RFS and OS at 3 y was 84% (95% CI, 76%–92%) and 92% (95% CI, 87%–98%), respectively. A C1D15 SUL<sub>max</sub> of 3 or less was associated with improved RFS (hazard ratio [HR], 0.36; 95% CI, 0.11–1.05; *P* = 0.06) and OS (HR, 0.14; 95% CI, 0.01–0.85; *P* = 0.03), the latter statistically significant. The association of an SUL<sub>max</sub> decline of at least 40% (achieved in 59%) with RFS and OS did not reach statistical significance. pCR was associated with improved RFS (HR, 0.25; 95% CI, 0.01–1.24; *P* = 0.10) but did not reach statistical significance. **Conclusion:** For the first time, we report a potential association between a C1D15 SUL<sub>max</sub> of 3 or less on <sup>18</sup>F-FDG PET/CT and RFS and OS outcomes in patients with ER-negative, HER2-positive breast cancer receiving neoadjuvant HP alone. If confirmed in future

studies, this imaging-based biomarker may facilitate early individualization of therapy.

**Key Words:** FDG PET/CT; HER2-positive; breast cancer; biomarkers; neoadjuvant

**J Nucl Med 2023; 64:1690–1696**

DOI: 10.2967/jnumed.123.265853

---

**T**he current standard of care for patients with stage II–III human epidermal growth factor receptor 2 (HER2)-positive breast cancer is neoadjuvant chemotherapy in combination with HER2-directed therapy. This approach has resulted in improved surgical outcomes and high rates of pathologic complete response (pCR), an accepted surrogate endpoint for survival outcomes (1–4). Additionally, this strategy offers the opportunity to adapt postoperative treatment based on the response to the therapy (5–7). Excellent progress has undoubtedly been made in the treatment of this disease; however, the neoadjuvant approach is not without potential adverse effects. It is recognized that there may be subgroups of patients who need this aggressive standard approach and others who may be cured with less intensive regimens with fewer short- and long-term toxicities. Thus, predictive biomarkers of response to therapy are urgently needed to help tailor treatment recommendations.

Ongoing efforts are investigating a more individualized approach to care. The use of early <sup>18</sup>F-FDG PET/CT to predict breast cancer treatment response has been of increasing interest (8,9). The TBCRC026 study examined dual HER2 therapy with neoadjuvant trastuzumab and pertuzumab (HP) without chemotherapy in primary operable estrogen receptor (ER)-negative, HER2-positive breast cancer and reported pCR rates of 22%. Early changes in tumor SUVs corrected for lean body mass (SUL<sub>max</sub>) on <sup>18</sup>F-FDG PET/CT predicted pCR to neoadjuvant HP alone, suggesting that this may serve as a potential imaging biomarker of response to therapy (10). Indeed, the preoperative period has been recognized as an ideal setting for evaluating surrogate biomarkers for the

---

Received Apr. 12, 2023; revision accepted Jul. 6, 2023.

For correspondence or reprints, contact Roisin Connolly (roisin.connolly@ucc.ie) or Maeve Hennessy (122108045@umail.ucc.ie).

Published online Aug. 31, 2023.

COPYRIGHT © 2023 by the Society of Nuclear Medicine and Molecular Imaging.

prediction of treatment response, and there is a growing body of evidence to support imaging biomarkers in HER2-positive disease (11–13). Few studies, however, have examined the relationship between metabolic response on  $^{18}\text{F}$ -FDG PET/CT after neoadjuvant dual HER2 therapy and long-term patient outcomes.

We thus hypothesized that predefined  $^{18}\text{F}$ -FDG PET/CT  $\text{SUL}_{\text{max}}$  parameters would be associated with improved recurrence-free survival (RFS) and overall survival (OS) in patients with primary operable ER-negative, HER2-positive breast cancer receiving neoadjuvant HER2-directed therapy. To test this hypothesis, we performed a secondary planned biomarker analysis of the TBCRC026 clinical trial dataset.

## MATERIALS AND METHODS

### Study Design

TBCRC026 was a single-arm multicenter trial investigating biomarkers of response to preoperative HER2-directed therapy without chemotherapy (Supplemental Fig. 1; supplemental materials are available at <http://jnm.snmjournals.org>) (10). The primary objective was to correlate baseline and early percentage change (by cycle 1, day 15 [C1D15]) in  $\text{SUL}_{\text{max}}$  on  $^{18}\text{F}$ -FDG PET/CT of the primary breast cancer with pCR after 4 cycles of neoadjuvant HP, without chemotherapy. The institutional review board approved this study, and all patients gave written informed consent.

Pertuzumab (840-mg loading dose, then 420 mg) and trastuzumab (8 mg/kg loading dose, then 6 mg/kg) were administered intravenously

every 3 wk.  $^{18}\text{F}$ -FDG PET/CT was performed at baseline and at 15 d after commencement of HP (C1D15). Further neoadjuvant nonstudy therapy (chemotherapy or HER2-directed therapy) was administered as per physician discretion, if there was an incomplete response or disease progression on initial therapy (10). Tumor biopsy was undertaken to histologically confirm residual disease, before additional treatment. Any patient who received additional systemic therapy by definition was classified as not achieving pCR after HP alone, per the study protocol. Postoperative systemic therapy and radiation per the standard of care were recommended. All patients regardless of pCR status were recommended to undergo adjuvant chemotherapy if this was not received preoperatively, as per the standard of care.

Eligibility criteria included women 18 y or older with untreated, histologically confirmed infiltrating carcinoma of the breast, clinical stage T2–4(a–c), any N, M0, and tumors expressing ER of no more than 10% and being HER2-positive, by local pathology review (14,15). The participants agreed to study-specific procedures including 2 serial  $^{18}\text{F}$ -FDG PET/CT scans.

### $^{18}\text{F}$ -FDG PET/CT Procedures

$^{18}\text{F}$ -FDG PET/CT was performed at baseline and at C1D15, with a 3-d window permitted, according to a detailed imaging manual published previously (10). Administration of intravenous  $^{18}\text{F}$ -FDG was followed by a 60-min uptake phase, with subsequent  $^{18}\text{F}$ -FDG PET/CT imaging from the mid skull to the mid femur. All procedures were conducted in conformance with the  $^{18}\text{F}$ -FDG PET/CT uniform protocol for imaging in clinical trials and the profile of the Radiologic Society of

North America Quantitative Imaging Biomarkers Alliance (16,17). Images were assessed centrally, with reviewers masked to clinical information.

$\text{SUL}_{\text{max}}$  rather than SUV was recorded, as the former is less weight-dependent than the latter and has been shown to be more consistent in normal tissues among individuals. The primary breast cancer lesions were measured by placing a spheric volume over the target area, with avoidance of surrounding normal tissue, and recording the  $\text{SUL}_{\text{max}}$ .

### Statistical Analysis

The secondary preplanned endpoints reported here include the correlation of, first, at least a 40% decline in  $\text{SUL}_{\text{max}}$  between baseline and C1D15 and, second, a C1D15  $\text{SUL}_{\text{max}}$  of 3 or less on  $^{18}\text{F}$ -FDG PET/CT with RFS and OS. RFS was defined as the interval from the date of the first cycle of treatment to ipsilateral invasive breast tumor recurrence, locoregional recurrence, distant recurrence, or death of any cause, whichever occurred first. OS was defined as the interval from the date of the first cycle of treatment to death (18). Both RFS and OS were censored at the last study contact if no events were observed.

To be evaluable for this analysis, participants had to have both baseline and C1D15  $^{18}\text{F}$ -FDG PET/CT performed;  $\text{SUL}_{\text{max}}$ , RFS, and OS data collected; and pCR status after HP (without chemotherapy) evaluated. pCR was determined in the surgical specimen and defined as no viable invasive cancer in the breast and axilla (local pathology review)

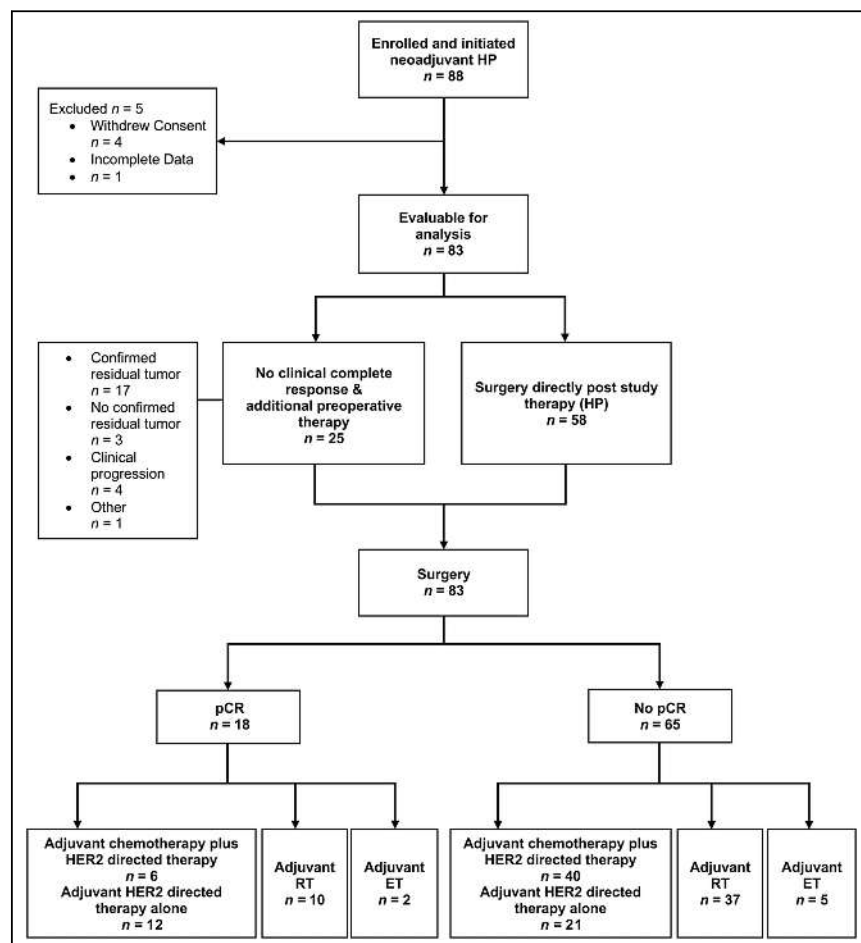


**FIGURE 1.** Study flowchart indicating therapies received. RT = radiotherapy; ET = endocrine therapy.



**TABLE 1**  
Patient Characteristics (Evaluable Population,  $n = 83$ )

Characteristic	Data
Age (y)	
Median	58
Range	29–82
Race	
White	70 (84)
Black	7 (8)
Other	6 (7)
Menopausal status	
Premenopausal	27 (33)
Postmenopausal	56 (67)
ECOG performance status	
0	72 (87)
1	11 (13)
Tumor size (cm)	
Median	3.9
Range	2–15
Baseline clinical stage	
II	71 (86)
III	12 (14)
Tumor grade	
2	20 (24)
3	63 (76)
Baseline ER status	
<1%	72 (87)
1%–10%	11 (13)
Additional neoadjuvant therapy	25 (30)
Taxane-based	7 (28)
Carboplatin/taxane	15 (60)
Anthracycline-based	2 (8)
HER2-directed	1 (4)
Surgery	
Mastectomy	46 (55)
Breast-conserving therapy	29 (35)
Not applicable	8 (10)
pCR	
Yes	18 (22)
No	65 (78)
Adjuvant chemotherapy	46 (55)
Taxane-based	21 (46)
Carboplatin/taxane	17 (40)
Anthracycline-based	8 (17)
Adjuvant HER2-targeted therapy	79 (95)
Trastuzumab	56 (67)
HP	22 (27)
Trastuzumab emtansine	1 (1)
Adjuvant radiotherapy	
Yes	47 (57)
No	36 (43)
Adjuvant endocrine therapy	
Yes	7 (8)
No	76 (92)

ECOG = Eastern Cooperative Oncology Group.  
Data are number and percentage, except for age and tumor size.

after HP without chemotherapy. Participants with residual disease after 12 wk of HP or clinical progression on HP were classified as non-pCR.

RFS and OS were summarized using the Kaplan–Meier methods and were compared between subgroups using logrank tests. Their associations with  $^{18}\text{F}$ -FDG PET/CT ( $\geq 40\%$  decline in  $\text{SUL}_{\text{max}}$  between baseline and C1D15, or C1D15  $\text{SUL}_{\text{max}} \leq 3$ ) and pCR were evaluated using Cox regressions, with likelihood ratio CIs being reported because of small event numbers.

## RESULTS

### Patient and Treatment Characteristics

Patient clinicopathologic characteristics were previously described and are available in Supplemental Table 1 (10). In summary, 88 women were enrolled from January 2014 to August 2017; 83 were evaluable for the survival analysis. Eighty-five percent of participants completed all 4 cycles of neoadjuvant HP. Twenty-five patients (28%) received additional nonstudy therapy neoadjuvantly and were classified as not obtaining pCR (Table 1). In 22% (18/83) of patients, pCR was observed after 4 cycles of HP alone.

Adjuvant therapy was advised as per the standard of care, and a summary of treatments received is available in Figure 1 and Table 1. There were 22 patients who received no adjuvant or neoadjuvant chemotherapy because of patient or physician preference. Most participants received adjuvant HER2-directed therapy (79/83; 95%), including trastuzumab ( $n = 56$ ; 67%), HP ( $n = 22$ ; 27%), and, in 1 patient with residual disease, adjuvant trastuzumab emtansine, which was not available for this indication in the earlier years of the study. Adjuvant radiation was completed by 57% (47/83), and adjuvant endocrine therapy by 8% (7/83) (Table 1). This was in keeping with the study eligibility criteria, which permitted enrollment of patients with tumors expressing ER of no more than 10%.

### RFS and OS Analyses

The median follow-up was 53.7 mo, with 6 deaths and 14 RFS events occurring. The estimated RFS at 3 y was 84% (95% CI, 76%–92%), and the estimated OS at 3 y was 92% (95% CI, 87%–98%).

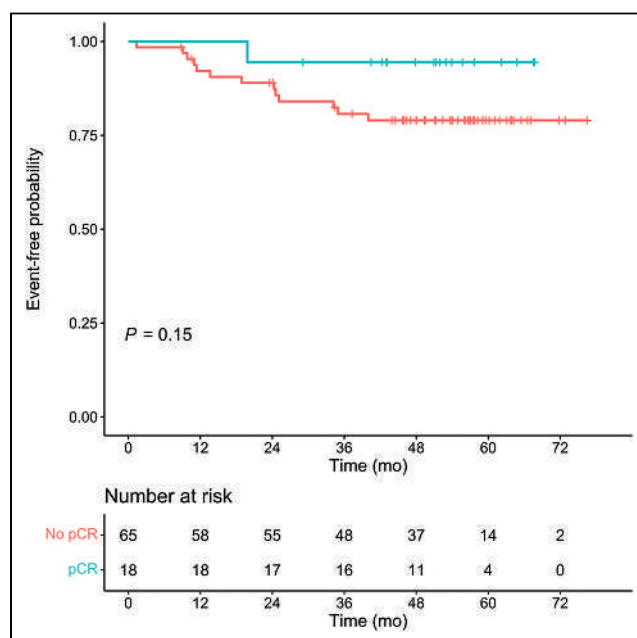


**FIGURE 2.** RFS by pCR.

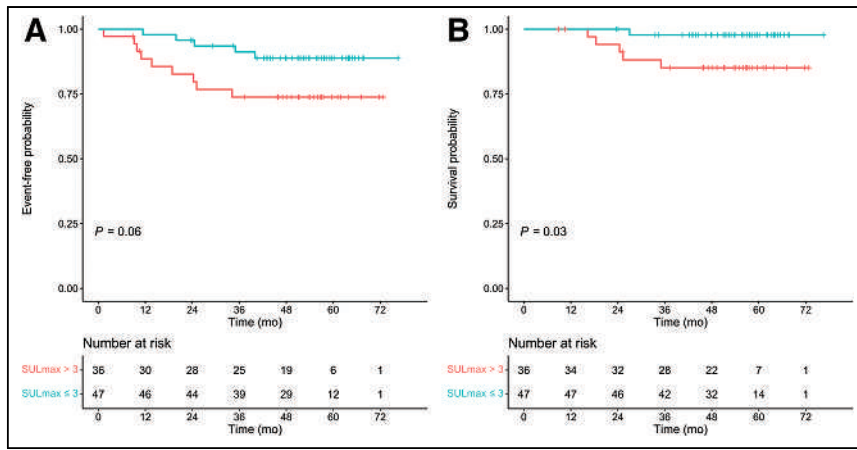


**FIGURE 3.** (A) RFS by C1D15 SUL<sub>max</sub> (≤3 vs. >3). (B) OS by C1D15 SUL<sub>max</sub> (≤3 vs. >3).

RFS events included 1 locoregional recurrence and 13 distant recurrences. The most common sites of distant relapse were lung ( $n = 4$ ) and liver ( $n = 2$ ). One patient relapsed with intracranial disease and with liver and bone involvement, and 1 patient developed bone-only disease. Of patients experiencing an RFS event, most (8/14, 57%) were lymph node-positive at baseline and all had at least T2 tumors with a median size of 3.5 cm—tumor characteristics indicating a higher-risk disease. Most events were in patients who did not achieve pCR (13/14, 93%) and occurred despite the majority's (10/14, 71%) receiving a complete course of adjuvant or neoadjuvant chemotherapy in addition to study therapy (HP). In terms of HER2-targeted therapy, most patients with RFS events received trastuzumab monotherapy in the adjuvant setting (8/14, 57%), with the addition of pertuzumab to trastuzumab in 3 patients and trastuzumab emtansine in 1 patient. Only one of these recurrence events, and subsequent death, occurred in a patient who had achieved a pCR after HP alone.

In keeping with the prognostic value of obtaining a pCR in published neoadjuvant breast cancer studies, pCR was associated with improved RFS (hazard ratio [HR], 0.25; 95% CI, 0.01–1.24;  $P = 0.10$ ) and OS (HR, 0.65; 95% CI, 0.03–4.06;  $P = 0.69$ ), although the observed trends did not reach statistical significance at this early point in the study (Fig. 2).

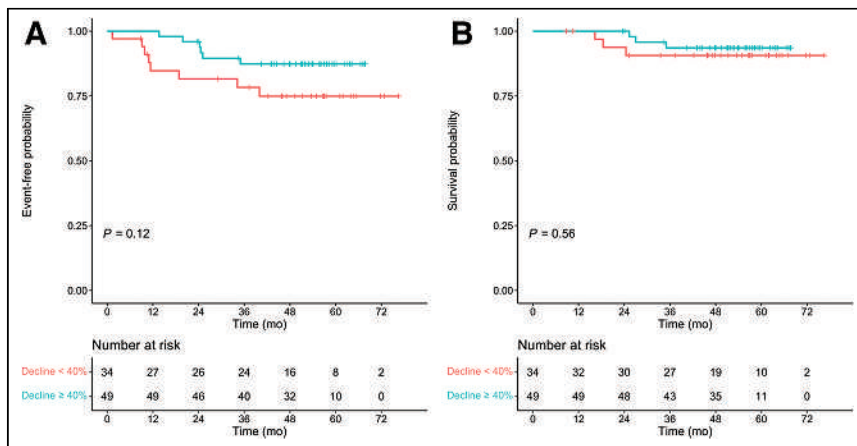


**FIGURE 4.** (A) RFS by SUL<sub>max</sub> decline (≥40% vs. <40%). (B) OS by SUL<sub>max</sub> decline (≥40% vs. <40%).

### Correlation of SUL<sub>max</sub> with OS and RFS

A summary of baseline and C1D15 SUL<sub>max</sub> has been previously reported and is available for reference in Supplemental Table 1. Regarding the association of SUL<sub>max</sub> on <sup>18</sup>F-FDG PET/CT and survival outcomes, achieving an SUL<sub>max</sub> of 3 or less by C1D15 was associated with an improved RFS, although not statistically significant (HR, 0.36; 95% CI, 0.11–1.05;  $P = 0.06$ ). The 3-y RFS probability was 91% (95% CI, 83%–100%) in those with a C1D15 SUL<sub>max</sub> of 3 or less, versus 74% (95% CI, 60%–90%) in those who did not achieve an SUL<sub>max</sub> of 3 or less. Interestingly, this biomarker parameter, achieved in 57% of patients, was associated with a statistically significant improvement in OS (HR, 0.14; 95% CI, 0.01–0.85;  $P = 0.03$ ). The 3-y OS was 98% (95% CI, 94%–100%), versus 85% (95% CI, 74%–98%) in those who failed to achieve an SUL<sub>max</sub> of 3 or less (Figs. 3A and 3B).

A similar proportion of patients (59%) achieved an SUL<sub>max</sub> decline of at least 40% between baseline and C1D15 after starting therapy. The association between an SUL<sub>max</sub> decline of at least 40% and RFS (HR, 0.45; 95% CI, 0.15–1.28;  $P = 0.13$ ) and OS (HR, 0.62; 95% CI, 0.12–3.37;  $P = 0.56$ ) did not reach statistical significance (Figs. 4A and 4B). Finally, the adjusted effect of a C1D15 SUL<sub>max</sub> of more than 3 on RFS did not reach statistical significance in the multivariable Cox regression that included the clinical variables of age, tumor grade, and tumor size (Table 2).

### DISCUSSION

In this updated analysis of the TBCRC026 trial, we have demonstrated an association between a C1D15 SUL<sub>max</sub> of 3 or less on <sup>18</sup>F-FDG PET/CT and improved survival outcomes in patients with ER-negative, HER2-positive breast cancer receiving neoadjuvant HER2-directed therapy. Patients receiving HP alone who achieved an SUL<sub>max</sub> of 3 or less on their C1D15 <sup>18</sup>F-FDG PET/CT experienced improved RFS (HR, 0.36; 95% CI, 0.11–1.05;  $P = 0.06$ ) and statistically significantly improved OS (HR, 0.14; 95% CI, 0.01–0.85;  $P = 0.03$ ), when compared with those who did not achieve this SUL<sub>max</sub>. This C1D15 SUL<sub>max</sub> was achieved in almost 60% of patients, suggesting that it may be a clinically useful biomarker.

One of the earliest reports suggesting that <sup>18</sup>F-FDG PET/CT may be a promising biomarker in HER2-positive early breast cancer was from the NeoALTTO PET substudy, which prospectively evaluated whether changes in SUV could predict response to neoadjuvant anti-HER2 therapy comprising trastuzumab and lapatinib (13). Metabolic responders (>15% reduction in SUV as determined by the study protocol) had higher pCR rates than nonresponders (42% vs. 21% at week 2; 44% vs. 19% at week 6) (13). More recently, studies have focused on neoadjuvant regimens incorporating more modern HER2-directed regimens including

**TABLE 2**  
Univariable and Multivariable Analysis of Association of C1D15 SUL<sub>max</sub> of 3 or Less with RFS

Variable	Univariable analysis		Multivariable analysis	
	HR	P	HR	P
C1D15 15 SUL <sub>max</sub> ≤3	0.36 (0.11–1.05)	0.06	0.41 (0.12–1.22)	0.1
Age	1.02 (0.98–1.07)	0.3	1.04 (0.99–1.1)	0.16
Grade III	0.81 (0.27–2.94)	0.7	0.68 (0.22–2.58)	0.55
Baseline tumor size (cm)	1.21 (0.97–1.45)	0.09	1.23 (0.96–1.5)	0.09

Data in parentheses are 95% CIs.

HP and the antibody–drug conjugate trastuzumab emtansine. The PHERGain phase II trial ( $n = 356$ ) randomized patients to neoadjuvant docetaxel, carboplatin, and HP ( $n = 71$ , group A) or HP alone ( $n = 285$ , group B). <sup>18</sup>F-FDG PET/CT was performed at baseline and after 2 cycles of treatment (11). The investigators defined metabolic response after 2 cycles as an SUV decline of at least 40% from baseline. Approximately 40% of patients who were designated as metabolic responders and continued dual anti-HER2 therapy achieved a pCR without the addition of chemotherapy, whereas non-responders in group B switched to neoadjuvant chemotherapy combined with HP. The study met its first coprimary endpoint (11). The phase II PREDIX HER2 trial found that neoadjuvant therapy with docetaxel and HP had pCR rates similar to those of the single agent trastuzumab emtansine. <sup>18</sup>F-FDG PET/CT was performed initially and after cycles 2 and 6 of neoadjuvant treatment. In a secondary analysis, a decrease in the SUV<sub>max</sub> by at least 68.7% (the median SUV<sub>max</sub> decline from baseline to cycle 2) was used as a cutoff and was associated with pCR in 57% of patients, versus 17% for patients with an SUV<sub>max</sub> less than the median (12).

The aforementioned studies differed from TBCRC026 in their design, with heterogeneous treatment regimens administered, varying eligibility criteria with regard to ER status, and SUV thresholds generally ranging from 40% to 60% assessed at varying times after initiation of therapy. Only the TBCRC026 trial was designed prospectively to determine the optimum <sup>18</sup>F-FDG PET/CT threshold for response as its primary objective (10). It is thus clear that further prospective studies are required to validate <sup>18</sup>F-FDG PET/CT as a biomarker across several standard treatment regimens. If confirmed, this noninvasive biomarker may be incorporated in future clinical trials aiming to determine the clinical utility of this approach in treatment decision-making. This paradigm of biomarker development has led to the successful clinical implementation of interim <sup>18</sup>F-FDG PET/CT scanning in lymphoma, with an escalated treatment approach being recommended for patients not achieving the desired <sup>18</sup>F-FDG PET/CT response (19,20). The EA1211/DIRECT trial (NCT05710328), led by the ECOG-ACRIN research group, will aim to prospectively validate the 40% SUL<sub>max</sub> decline threshold at 15 d after initiation of therapy as the optimum cut point across standard-of-care HER2-directed neoadjuvant regimens. If this threshold is validated, future trials may consider a response-guided treatment strategy, with the goal of changing practice.

Ultimately, for those with early-stage, curable HER2-positive breast cancer, long-term survival outcomes are the most important endpoint. We found that pCR after HP alone was associated with numerically improved RFS; however, this difference did not reach

statistical significance. Whether the prognostic value of pCR in HER2-positive breast cancer is equivalent if obtained with or without chemotherapy has been debated (21). In addition to our single-arm study results, others have observed acceptable long-term outcomes with HER2-directed therapy alone, suggesting that achieving a pCR translates into improved outcomes irrespective of the type of neoadjuvant treatment received (21,22). That a subset of patients can achieve a pCR and have excellent long-term outcomes without conventional chemotherapy highlights the need for identification of robust biomarkers and a careful study design to select this cohort. This approach is indeed appealing but will require further validation and clinical utility studies before it can be incorporated into routine clinical practice.

We acknowledge the limitations of this study, which include the heterogeneity in the postoperative therapy received and the possible effect of this heterogeneity on evaluating long-term outcomes. The C1D15 SUL<sub>max</sub> of 3 or less was associated with significantly improved OS in the univariable analysis but did not reach statistical significance in the multivariable analysis. Because this was a secondary analysis, the study was not adequately powered for the endpoints of RFS and OS, and we therefore await confirmatory studies with larger patient numbers. We used the absolute SUL<sub>max</sub> and its change as our markers of PET metabolic activity, rather than PERCIST 1.0. This study was designed before PERCIST was widely deployed and has identified a larger percentage change for response evaluation (specific to a breast cancer population) than PERCIST 1.0. In addition, some tumors that were small and not <sup>18</sup>F-FDG-avid in TBCRC026 might not have been metabolically assessable by PERCIST 1.0 at baseline. Additional studies using PERCIST 1.0 or a modified PERCIST threshold are warranted, as the PERCIST 1.0 responders across a wide range of tumor types appear to have outcomes superior to nonresponders. The change in SUV or SUL<sub>max</sub> appears to be a more reliable technical metric than absolute SUL<sub>max</sub>, which can vary by manufacturer and reconstruction method. Thus, the absolute SUL<sub>max</sub> threshold would be more difficult to apply routinely than the relative change metric. Further studies and technical standardization could help address this concern.

## CONCLUSION

To our knowledge, this is the first report of a potential association between a C1D15 SUL<sub>max</sub> of 3 or less on <sup>18</sup>F-FDG PET/CT after 2 wk of neoadjuvant HP alone and RFS and OS outcomes. If confirmed in larger studies, early neoadjuvant interim PET/CT may become a key tool used to adapt therapy for patients with breast cancer in the coming years. Patients demonstrating an early metabolic

response could potentially be spared additional chemotherapy, whereas nonresponders could go on to receive intensification of treatment. The ultimate goal will be to facilitate PET biomarker-informed early individualization of therapy to maximize efficacy and minimize toxicity for patients with early-stage HER2-positive breast cancer. We believe such an approach would be SMART in that it would allow us to “Scan More And Reduce Therapies.”

## DISCLOSURE

Research support was received from TBCRC and foundation partners (the AVON Foundation, the Breast Cancer Research Foundation, and Susan G. Komen for the Cure), an SKCCC core grant (P30-CA006973), an NCI Quantitative Imaging Network (QIN) contract (SU01CA140204), and Genentech Inc., including supply of pertuzumab and trastuzumab. Grant funding was obtained from the American Society of Clinical Oncology (ASCO) Conquer Cancer Foundation Career Development Award (2013) and the AVON Center of Excellence. Maeve Hennessy received salary support from Breakthrough Cancer Research and support for meetings and travel from Roche and MSD. Vandana Abramson received grants (to the institution) from Pfizer, Genentech, Gilead, AstraZeneca, and Zentalis and consulting fees from FirstThought, Daiichi Sankyo, SeaGen, AstraZeneca, and Eisai. Lisa Carey received research funding (to the institution) from Nanostring, SeaGen, AstraZeneca, and Veracyte and has uncompensated relationships with Lily, SeaGen, Novartis, Genentech/Roche, and GlaxoSmithKline. Minetta Liu received grants (to the institution) from Eisai, Exact Sciences, Genentech, Genomic Health, GRAIL, Menarini Silicon Biosystems, Merck, Novartis, Seattle Genetics, and Tesaro; honoraria (to the institution) from AstraZeneca, Celgene, Roche/Genentech, Genomic Health, GRAIL, Ionis, Merck, Pfizer, SeaGen, and Syndax (ad hoc advisory boards through June 20, 2022); and support for meetings and travel from AstraZeneca, Genomic Health, and Ionis. In addition, she is on the advisory board for NSABP/GBG; has a leadership role (unpaid) with the Alliance for Clinical Trials in Oncology and TBCRC; owns stock in Natera; and has been employed by Natera since June 2022. Mothaffar Rimawi received support for the present article from Genentech; grants from Pfizer; and consulting fees from Macro-genics, SeaGen, Novartis, and AstraZeneca and is coinventor on patent PCT/US21/70543 (Methods for Breast Cancer Treatment and Prediction of Therapeutic Response), filed and owned by the Baylor College of Medicine. Jennifer Specht received support for the present article from the Breast Cancer Foundation, TBCRC026, and Genentech (institutional grant) and has a leadership role with TBCRC (institutional principal investigator). Anna Maria Storniolo received funding from TBCRC (to the institution) for the present article. Vicente Valero received honoraria from Roche and Genentech; received support for meetings and travel from Roche; and is on the advisory board for AstraZeneca. Christos Vaklavas received grants (to the institution) from Pfizer, SeaGen, H3 Biomedicine/Eisai, AstraZeneca, and CytomX; consulting fees from Guidepoint, Novartis, SeaGen, Daiichi Sankyo, AstraZeneca, and Gilead; and honoraria from Gilead and AstraZeneca. He has a pending patent (63/133,678: Breast Cancer Diagnostic) and a leadership role (unpaid board member) with the Society of Utah Medical Oncologists. He is on a Think Tank (unpaid) for Genentech, and his spouse is employed by Flatiron. Ian Krop received grants (to the institution) from Pfizer, Macro-genics, and Genentech/Roche; consulting fees from AstraZeneca, Daiichi Sankyo, Genentech/Roche,

BMS, Macro-genics, Taiho Oncology, and SeaGen; and honoraria from AstraZeneca. He is on the advisory board for Novartis and Merck, and his spouse is employed by PureTech. Antonio Wolff is on the Data and Safety Monitoring Board for ALEXANDRA/IMPpassion030 (a Roche trial led by the Breast International Group) and honoraria from the Breast International Group. Ashley Cimino-Mathews received payments (to the institution) from BMS. Richard Wahl is on the advisory board for Clarity Pharmaceuticals, Voximetry, and Seno Medical; owns stock in Clarity Pharmaceuticals; has stock options in Voximetry; receives honoraria from BMS, Actinium Pharmaceuticals, Jubilant Draximage, Siemens, Abderra, Radiopharm Therapeutics, and ITM; and receives research support from Actinium Pharmaceuticals, BMS, Bayer, ITM, Siemens, and White Rabbit AI. Vered Stearns received research grants (to the institution) from Abbvie, Biocept, Novartis, Pfizer, Puma Biotechnology, and QUE Oncology; became a member of the advisory board for Novartis on October 25, 2021; is chair of the Data and Safety Monitoring Board for AstraZeneca; and received nonfinancial support from Foundation Medicine. Roisin Connolly received salary support from Breakthrough Cancer Research; an educational grant from Pfizer; and research funding (to the institution) from MSD, Pfizer, Daiichi Sankyo, and AstraZeneca. She has a consultancy (unpaid) with SeaGen and AstraZeneca/Daiichi; receives support for meetings and travel from Novartis; is on the advisory board (unpaid) for Roche and, as the chair, for SeaGen; received financial aid from AstraZeneca/Daiichi Sankyo and Gilead; and is a member of the steering committee (paid) for AstraZeneca/Daiichi and (unpaid) for Develop Med-UCD, ACRI, and Decrescendo. No other potential conflict of interest relevant to this article was reported.

## ACKNOWLEDGMENTS

We thank Martin Lodge for imaging assistance and Zhe Zhang, Susan Hilsenbeck, Stacie Jeter, and Bridget Walsh for valuable contributions during study design and conduct. This work was presented as a poster at the 2022 congress of the European Society for Medical Oncology (abstract 2551).

## KEY POINTS

**QUESTION:** We hypothesized that  $^{18}\text{F}$ -FDG PET/CT  $\text{SUL}_{\text{max}}$  parameters would predict RFS and OS in patients with early-stage ER-negative, HER2-positive breast cancer receiving HP without chemotherapy.

**PERTINENT FINDINGS:** Patients underwent  $^{18}\text{F}$ -FDG PET/CT at baseline and at C1D15. The metabolic endpoint of a C1D15  $\text{SUL}_{\text{max}}$  of 3 or less was associated with a statistically significant improvement in OS (HR, 0.14;  $P = 0.03$ ).

**IMPLICATIONS FOR PATIENT CARE:** If validated in future studies, this noninvasive imaging biomarker may facilitate early adoption of therapy for patients with early-stage HER2-positive breast cancer, resulting in improved efficacy and reduced toxicity.

## REFERENCES

1. Gianni L, Pienkowski T, Im YH, et al. Efficacy and safety of neoadjuvant pertuzumab and trastuzumab in women with locally advanced, inflammatory, or early HER2-positive breast cancer (NeoSphere): a randomised multicentre, open-label, phase 2 trial. *Lancet Oncol*. 2012;13:25–32.



2. Harbeck N, Gluz O, Christgen M, et al. De-escalation strategies in human epidermal growth factor receptor 2 (HER2)-positive early breast cancer (BC): final analysis of the West German Study Group Adjuvant Dynamic Marker-Adjusted Personalized Therapy Trial optimizing risk assessment and therapy response prediction in early BC HER2- and hormone receptor-positive phase II randomized trial—efficacy, safety, and predictive markers for 12 weeks of neoadjuvant trastuzumab emtansine with or without endocrine therapy (ET) versus trastuzumab plus ET. *J Clin Oncol*. 2017;35:3046–3054.
3. Schneeweiss A, Chia S, Hickish T, et al. Pertuzumab plus trastuzumab in combination with standard neoadjuvant anthracycline-containing and anthracycline-free chemotherapy regimens in patients with HER2-positive early breast cancer: a randomized phase II cardiac safety study (TRYPHAENA). *Ann Oncol*. 2013;24:2278–2284.
4. Cortazar P, Zhang L, Untch M, et al. Pathological complete response and long-term clinical benefit in breast cancer: the CTNeoBC pooled analysis. *Lancet*. 2014;384:164–172.
5. Loibl S, Poortmans P, Morrow M, Denkert C, Curigliano G. Breast cancer. *Lancet*. 2021;397:1750–1769.
6. Thomssen C, Balic M, Harbeck N, Gnant M. Gallen/Vienna 2021: a brief summary of the consensus discussion on customizing therapies for women with early breast cancer. *Breast Care (Basel)*. 2021;16:135–143.
7. von Minckwitz G, Huang C-S, Mano MS, et al. Trastuzumab emtansine for residual invasive HER2-positive breast cancer. *N Engl J Med*. 2019;380:617–628.
8. Wahl RL, Zasadny K, Helvie M, Hutchins GD, Weber B, Cody R. Metabolic monitoring of breast cancer chemohormonotherapy using positron emission tomography: initial evaluation. *J Clin Oncol*. 1993;11:2101–2111.
9. Han S, Choi JY. Prognostic value of <sup>18</sup>F-FDG PET and PET/CT for assessment of treatment response to neoadjuvant chemotherapy in breast cancer: a systematic review and meta-analysis. *Breast Cancer Res*. 2020;22:119.
10. Connolly RM, Leal JP, Solnes L, et al. Updated results of TBCRC026: phase II trial correlating standardized uptake value with pathological complete response to pertuzumab and trastuzumab in breast cancer. *J Clin Oncol*. 2021;39:2247–2256.
11. Pérez-García JM, Gebhart G, Ruiz Borrego M, et al. Chemotherapy de-escalation using an <sup>18</sup>F-FDG-PET-based pathological response-adapted strategy in patients with HER2-positive early breast cancer (PHERGain): a multicentre, randomised, open-label, non-comparative, phase 2 trial. *Lancet Oncol*. 2021;22:858–871.
12. Bergh JCS, Andersson A, Bjohle J, et al. Docetaxel, trastuzumab, pertuzumab versus trastuzumab emtansine as neoadjuvant treatment of HER2-positive breast cancer: results from the Swedish PREDIX HER2 trial identifying a new potential de-escalation standard? *J Clin Oncol*. 2019;37(suppl):501.
13. Gebhart G, Gámez C, Holmes E, et al. <sup>18</sup>F-FDG PET/CT for early prediction of response to neoadjuvant lapatinib, trastuzumab, and their combination in HER2-positive breast cancer: results from Neo-ALTTO. *J Nucl Med*. 2013;54:1862–1868.
14. Wolff AC, Hammond ME, Hicks DG, et al. Recommendations for human epidermal growth factor receptor 2 testing in breast cancer: American Society of Clinical Oncology/College of American Pathologists clinical practice guideline update. *J Clin Oncol*. 2013;31:3997–4013.
15. Hammond ME, Hayes DF, Dowsett M, et al. American Society of Clinical Oncology/College of American Pathologists guideline recommendations for immunohistochemical testing of estrogen and progesterone receptors in breast cancer. *J Clin Oncol*. 2010;28:2784–2795.
16. Graham MM, Wahl RL, Hoffman JM, et al. Summary of the UPICT protocol for <sup>18</sup>F-FDG PET/CT imaging in oncology clinical trials. *J Nucl Med*. 2015;56:955–961.
17. Kinahan PE, Perlman ES, Sunderland JJ, et al. The QIBA profile for FDG PET/CT as an imaging biomarker measuring response to cancer therapy. *Radiology*. 2020;294:647–657.
18. Tolaney SM, Garrett-Mayer E, White J, et al. Updated Standardized Definitions for Efficacy End Points (STEEP) in adjuvant breast cancer clinical trials: STEEP version 2.0. *J Clin Oncol*. 2021;39:2720–2731.
19. Cheson BD, Fisher RI, Barrington SF, et al. Recommendations for initial evaluation, staging, and response assessment of Hodgkin and non-Hodgkin lymphoma: the Lugano classification. *J Clin Oncol*. 2014;32:3059–3068.
20. Hoppe RT, Advani RH, Ai WZ, et al. Hodgkin lymphoma, version 2.2020, NCCN clinical practice guidelines in oncology. *J Natl Compr Canc Netw*. 2020;18:755–781.
21. Matikas A, Johansson H, Grybäck P, et al. Survival outcomes, digital TILs, and on-treatment PET/CT during neoadjuvant therapy for HER2-positive breast cancer: results from the randomized PREDIX HER2 trial. *Clin Cancer Res*. 2023;29:532–540.
22. Nitz U, Gluz O, Graeser M, et al. De-escalated neoadjuvant pertuzumab plus trastuzumab therapy with or without weekly paclitaxel in HER2-positive, hormone receptor-negative, early breast cancer (WSG-ADAPT-HER2+/HR-): survival outcomes from a multicentre, open-label, randomised, phase 2 trial. *Lancet Oncol*. 2022;23:625–635.

# $^{18}\text{F}$ -FDG PET “Metabolic Response” to Neoadjuvant Systemic Therapy for Breast Cancer: Quo Vadis?

Geraldine Gebhart

*Department of Nuclear Medicine, Institut Jules Bordet, Hôpital Universitaire de Bruxelles, Université Libre de Bruxelles, Brussels, Belgium*

**L**n their article in *The Journal of Nuclear Medicine*, Hennessy et al. (1) provide mature overall survival data on their neoadjuvant chemotherapy-free regimen of pertuzumab plus trastuzumab given to patients with localized human epidermal growth factor receptor type 2 (HER2)-positive breast cancer, monitored by  $^{18}\text{F}$ -FDG PET/CT, for which they previously reported a 34% pathologic response rate linked to an SUV (normalized by lean body mass) decline by at least 40% after 15 d of exposure to dual HER2 blockade.

The paper offers a unique opportunity to discuss the excitement of the oncology community about neoadjuvant trials, the importance of evaluating overall survival in addition to pathologic complete response (pCR), and the interest in this approach to explore treatment deescalation using molecular imaging.

Neoadjuvant systemic therapy has been initially applied as a downstaging procedure in patients presenting with surgically nonresectable breast tumors or tumors deemed unsuitable for breast conservation. The interest of the oncology community in this approach started to grow markedly when it became clear that the magnitude of response to neoadjuvant chemotherapy was associated with relapse-free survival (2) and when the seminal NSABP-B18 trial demonstrated similar outcomes for 4 cycles of doxorubicin-cyclophosphamide given before or after surgery (3).

At the turn of the century, many investigators embarked on the design and conduct of chemotherapy-based neoadjuvant trials with the choice of pCR as the primary endpoint for the comparison of newer, more sophisticated drug regimens. These efforts culminated in a pooled analysis of 12 trials involving 11,955 patients, all treated with preoperative cytotoxic drugs (few trials used targeted agents) (4). This analysis robustly confirmed a positive correlation, at the patient level, between pCR and event-free and overall survival. It also demonstrated that the best definition of pCR was the lack of invasive tumor in the breast and in the nodes. Disappointingly, however, pCR could not be proposed as a surrogate endpoint for event-free or overall survival, since at the trial level, there was only a marginal association between them. The dream of an accelerated new drug development for early breast cancer based on incremental gains in pCR, which can be achieved in a short time frame contrary to adjuvant trials, was not abandoned: trialists

remained convinced that with powerful targeted drugs, such as the anti-HER2 monoclonal antibody trastuzumab, given on top of chemotherapy, larger differences in pCR would be predictive of better long-term outcomes at a population level. They embarked on a second pooled analysis, this time of 11 trials and 3,710 patients, all with HER2-positive breast cancer, but again, a weak association was found between pCR and long-term outcome at the trial level (5). An important finding, however, was that tumor burden (e.g., tumor size and nodal status) remains prognostic, even in patients reaching pCR, who can still experience relapse.

All this historical background has important implications for the new field of excitement in breast oncology: namely the identification of biomarkers able to predict, early on (e.g., after 2–6 wk of therapy), whether a patient will benefit from the selected drug regimen administered preoperatively: the hope, here, is a truly individualized approach, which will consist either of treatment escalation or of treatment deescalation based on observed biomarker changes.

$^{18}\text{F}$ -FDG PET is the most studied noninvasive and dynamic biomarker in this field, but so far, many trials such as Neoalto (6) have suffered from the selection of a suboptimal endpoint, pCR, and from weak statistical power preventing robust correlations with long-term survival: the latter is what matters to patients, who will certainly welcome the news of complete tumor disappearance locally but who will continue to worry about their risk of distant relapse and death.

Two recent trials for HER2-positive breast cancer represent a step forward on the path toward chemotherapy deescalation based on early  $^{18}\text{F}$ -FDG PET metabolic responses.

The first is the single-arm U.S. trial TBCRC026 presented by Hennessy et al. (1). A strength of this trial is that it enrolled a relatively homogeneous population of 88 patients with HER2-positive/hormone receptor-negative tumors, known to be more addicted to the HER2 pathway than tumors coexpressing HER2 and hormone receptors and treated with dual HER2 blockade, namely trastuzumab plus pertuzumab, without chemotherapy and without endocrine therapy. With additional follow up, the study demonstrated that a maximum SUV (normalized by lean body mass) of no more than 3 at 2 wk was associated with improved relapse-free survival and overall survival, with the latter being statistically significant. Although this result is encouraging and underscores the potential role of molecular imaging in identifying a subgroup of patients who may safely forego chemotherapy, the trial has weaknesses: relapse-free survival and overall survival were only secondary endpoints, and postsurgical adjuvant therapy was left at the discretion of the oncologist; as a result, one third of patients who achieved

Received Jul. 31, 2023; revision accepted Sep. 27, 2023.  
For correspondence or reprints, contact Geraldine Gebhart (geraldine.gebhart@hubruxelles.be).  
Published online Nov. 1, 2023.  
COPYRIGHT © 2023 by the Society of Nuclear Medicine and Molecular Imaging.  
DOI: 10.2967/jnumed.123.266303

pCR (6/18) nevertheless went on to receive adjuvant chemotherapy combined with HER2-directed therapy. This leaves some uncertainty regarding the robustness of the  $^{18}\text{F}$ -FDG PET response to predict which patients may indeed be spared chemotherapy.

The second trial (PHERGAIN), conducted in Europe, also chose  $^{18}\text{F}$ -FDG PET as an early, dynamic biomarker for the selection of patients suitable for dual HER2 blockade without chemotherapy (7). After 2 cycles of combined trastuzumab and pertuzumab given over 6 wk, 356 patients were randomized 1 to 4 to receive either standard chemotherapy with trastuzumab-pertuzumab or a biomarker response adaptive regimen in which a 40% or greater decline in  $\text{SUV}_{\text{max}}$  at 6 wk would allow for the continuation of targeted therapy (trastuzumab-pertuzumab) without chemotherapy until surgery: not only did these patients achieve an impressive pCR rate of almost 40% (86/227), but with longer follow up, only one local relapse was documented at a median follow-up of 3 y (8). Here, the strengths include a strict policy for adjuvant therapy, which did not authorize chemotherapy in pCR patients, and the selection of invasive disease-free survival as a coprimary endpoint together with pCR, but a particular feature is that the primary focus is the entire response-guided arm, which includes patients who went on to receive chemotherapy in view of their insufficient biomarker response. Nevertheless, the null hypothesis set by the investigators could be rejected given the excellent 95.4% invasive disease-free survival observed in the response-adapted arm (it was required to be  $\geq 95\%$ ). Of note, the 3-y invasive disease-free survival was 98.3% in the biomarker-ignorant arm in which all patients received chemotherapy.

Can we derive lessons from these experiences and foresee new avenues of progress?

With the need to focus on truly important endpoints, namely event-free and overall survival, future trials will need to be large and therefore will require more extensive international collaboration. Standardization of PET imaging techniques among trial centers should not be a barrier in the 21st century, with the medical community claiming an ambition of delivering precision oncologic therapies.

Further progress could also emerge from the adjunct of circulating tumor DNA molecular responses to molecular imaging: indeed, a lack of circulating tumor DNA eradication in the neoadjuvant setting has been shown to predict a poor outcome (9). However, less than 50% of patients undergoing neoadjuvant chemotherapy have detectable circulating tumor DNA in their serum (10). Another potentially informative biomarker is represented by tumor-infiltrating lymphocytes,

which have been reported to complement the value of metabolic response (11).

With some extra collaborative efforts, early response assessment with molecular imaging should soon leave the scene of clinical trials and enter routine clinical care.

## DISCLOSURE

No potential conflict of interest relevant to this article was reported.

## REFERENCES

1. Hennessy MA, Leal JP, Huang C-Y, et al. Correlation of SUV on early interim PET with recurrence-free survival and overall survival in primary operable HER2-positive breast cancer (the TBCRC026 trial). *J Nucl Med*. 2023;64:1690–1696.
2. Bonadonna G, Valagussa P, Brambilla C, et al. Primary chemotherapy in operable breast cancer: eight-year experience at the Milan Cancer Institute. *J Clin Oncol*. 1998;16:93–100.
3. Wolmark N, Wang J, Mamounas E, et al. Preoperative chemotherapy in patients with operable breast cancer: nine-year results from National Surgical Adjuvant Breast and Bowel Project B-18. *J Natl Cancer Inst Monogr*. 2001;(30):96–102.
4. Cortazar P, Zhang L, Untch M, et al. Pathological complete response and long-term clinical benefit in breast cancer: the CTNeoBC pooled analysis. *Lancet*. 2014;384:164–172.
5. Squifflet P, Saad ED, Loibl S, et al.; CTNeoBC Project. Re-evaluation of pathologic complete response as a surrogate for event-free and overall survival in human epidermal growth factor receptor 2-positive, early breast cancer treated with neoadjuvant therapy including anti-human epidermal growth factor receptor 2 therapy. *J Clin Oncol*. 2023;41:2988–2997.
6. Gebhart G, Gámez C, Holmes E, et al.  $^{18}\text{F}$ -FDG PET/CT for early prediction of response to neoadjuvant lapatinib, trastuzumab, and their combination in HER2-positive breast cancer: results from Neo-ALTTO. *J Nucl Med*. 2013;54:1862–1868.
7. Cortes J, Pérez-García JM, Ruiz-Borrego M, et al. 3-year invasive disease-free survival (iDFS) of the strategy-based, randomized phase II PHERGain trial evaluating chemotherapy (CT) de-escalation in human epidermal growth factor receptor 2-positive (HER2[+]) early breast cancer (EBC) [abstract]. *J Clin Oncol*. 2023;41(suppl):LBA506.
8. Pérez-García JM, Gebhart G, Ruiz Borrego M et al. Chemotherapy de-escalation using an  $^{18}\text{F}$ -FDG-PET-based pathological response-adapted strategy in patients with HER2-positive early breast cancer (PHERGain): a multicentre, randomised, open-label, non-comparative, phase 2 trial. *Lancet Oncol*. 2021;22:858–971.
9. Ignatiadis M, Sledge GW, Jeffrey SS. Liquid biopsy enters the clinic: implementation issues and future challenges. *Nat Rev Clin Oncol*. 2021;18:297–312.
10. Rothé F, Silva MJ, Venet D, et al. Circulating tumor DNA in HER2-amplified breast cancer: a translational research substudy of the NeoALTTO phase III trial. *Clin Cancer Res*. 2019;25:3581–3588.
11. Matikas A, Johansson H, Grybäck P, et al. Survival outcomes, digital TILs, and on-treatment PET/CT during neoadjuvant therapy for HER2-positive breast cancer: results from the randomized PREDIX HER2 trial. *Clin Cancer Res*. 2023;29:532–540.

---

---

# High Tumor Uptake on $^{18}\text{F}$ -FDOPA PET/CT Indicates Poor Prognosis in Patients with Metastatic Midgut Neuroendocrine Tumors: A Study from the Groupe d'étude des Tumeurs Endocrines and ENDOCAN-RENATEN Network

Ophélie De Rycke<sup>1,2</sup>, Marine Perrier<sup>3</sup>, Éric Ouvrard<sup>4</sup>, Clément Menetrey<sup>5</sup>, Choib Lachachi<sup>6</sup>, Aurélie Bando-Delaunay<sup>2,7</sup>, David Morland<sup>8,9</sup>, Bernard Goichot<sup>10</sup>, David Taieb<sup>5</sup>, Thomas Walter<sup>11</sup>, Guillaume Cadiot<sup>3</sup>, Jérôme Cros<sup>2,12</sup>, Olivia Hentic<sup>1</sup>, Philippe Ruszniewski<sup>1,2</sup>, Rachida Lebtahi<sup>2,7</sup>, Alessio Imperiale<sup>4</sup>, and Louis de Mestier<sup>1,2</sup>

<sup>1</sup>Department of Pancreatology and Digestive Oncology, Beaujon Hospital, Université Paris-Cité, AP-HP.Nord, Clichy, France; <sup>2</sup>INSERM UMR 1149, Centre de Recherche sur l'Inflammation, Paris, France; <sup>3</sup>Department of Hepato-Gastroenterology and Digestive Oncology, CHU Reims, Université de Reims Champagne-Ardenne, Reims, France; <sup>4</sup>Department of Nuclear Medicine, Hautepierre University Hospital, Strasbourg, France; <sup>5</sup>Department of Nuclear Medicine, La Timone University Hospital, Université d'Aix-Marseille, Marseille, France; <sup>6</sup>Department of Nuclear Medicine, Edouard-Herriot University Hospital, Lyon, France; <sup>7</sup>Department of Nuclear Medicine, Beaujon Hospital, Université Paris-Cité, AP-HP.Nord, Clichy, France; <sup>8</sup>Department of Nuclear Medicine, Institut Godinot, Reims, France; <sup>9</sup>Université de Reims Champagne Ardenne, CReSTIC, EA 3804, Reims, France; <sup>10</sup>Department of Endocrinology, Hautepierre University Hospital, Strasbourg, France; <sup>11</sup>Department of Digestive Oncology, Edouard-Herriot University Hospital, Lyon, France; and <sup>12</sup>Department of Pathology, Beaujon Hospital, AP-HP.Nord, Université Paris-Cité, Clichy, France

---

PET/CT with 6- $^{18}\text{F}$ -fluoro-L-dopa ( $^{18}\text{F}$ -FDOPA) has high diagnostic performance for midgut neuroendocrine tumors (NETs). We explored the prognostic role of  $^{18}\text{F}$ -FDOPA PET/CT uptake in metastatic midgut NETs. **Methods:** We included, in a test cohort ( $n = 166$ ) and a full external validation cohort ( $n = 86$ ), all consecutive patients with metastatic midgut NETs who underwent  $^{18}\text{F}$ -FDOPA PET/CT in 5 expert centers from 2010 to 2021. We measured the maximal uptake ( $\text{SUV}_{\text{max}}$  and  $\text{SUV}_{\text{peak}}$ ) of the tumor and nontumor liver on each  $^{18}\text{F}$ -FDOPA PET/CT scan. We measured overall survival (OS) from the time of PET/CT and assessed prognostic factors using Kaplan-Meier and multivariable Cox proportional-hazards analyses in the test cohort, with replication in the validation cohort. **Results:** Patients had similar characteristics in both cohorts. In the test cohort, median follow-up was 60.3 mo. Patients with an  $\text{SUV}_{\text{peak}}$  tumor-to-liver (T/L) ratio of more than 4.2 had significantly shorter survival than those with a ratio of 4.2 or less ( $P = 0.01$ ), with a 5-y OS rate of  $74.1\% \pm 4.5\%$  versus  $95\% \pm 3.4\%$ , respectively. On multivariable analysis, an  $\text{SUV}_{\text{peak}}$  T/L ratio of more than 4.2 remained associated with shorter OS (hazard ratio, 2.30; 95% CI, 1.02–5.22;  $P = 0.046$ ) after adjustment for age, grade, number of previous lines, number of metastatic sites, and presence of carcinoid syndrome. In the validation cohort, the 5-y OS rate was 100% versus  $57.8\% \pm 12.5\%$  in patients with an  $\text{SUV}_{\text{peak}}$  T/L ratio  $\leq 4.2$  or  $> 4.2$ , respectively ( $P = 0.075$ ). An increasing  $\text{SUV}_{\text{peak}}$  T/L ratio over time tended to have a pejorative prognostic impact. **Conclusion:** Tumor uptake on  $^{18}\text{F}$ -FDOPA PET/CT is an independent prognostic factor in patients with metastatic midgut NETs.

**Key Words:** neuroendocrine tumors; small intestine; metastases;  $^{18}\text{F}$ -FDOPA PET/CT; prognosis

**J Nucl Med 2023; 64:1699–1705**  
DOI: 10.2967/jnumed.123.265584

---

Received Feb. 10, 2023; revision accepted Jul. 17, 2023.  
For correspondence or reprints, contact Louis de Mestier (louis.demestier@aphp.fr).  
Published online Aug. 31, 2023.  
COPYRIGHT © 2023 by the Society of Nuclear Medicine and Molecular Imaging.

**N**euroendocrine tumors (NETs) are a heterogeneous group of rare neoplasms with an increasing incidence (1). Midgut NETs are among the most frequent localizations of NETs and encompass NETs arising from the jejunum, ileum, appendix, and cecum (1). They derive from enterochromaffin cells able to produce serotonin and other hormones and peptides, whose hypersecretion can cause carcinoid syndrome (2). Apart from appendiceal NETs, 50%–65% of patients with midgut NETs have distant metastases, mainly in the liver (3). Nevertheless, because of their relatively slow evolution, overall survival (OS) is generally prolonged even in cases of metastases (1). The main prognostic factors for patients with metastatic midgut NETs include metastatic extension, notably extrahepatic; tumor volume, including liver involvement; tumor grade determined by the Ki-67 index; and hormone complications such as carcinoid heart disease (4,5).

Nuclear medicine plays an important role in the diagnosis, characterization, follow-up, and treatment of metastatic midgut NETs.  $^{68}\text{Ga}$ -labeled somatostatin analogs used for somatostatin receptor PET/CT have achieved consensus among expert panels as a forefront radiopharmaceutical for midgut NETs (6,7). Besides, midgut NETs have the ability to metabolize the dopamine precursor 3,4-dihydroxyphenylalanine (DOPA), whose amino acid analog 6- $^{18}\text{F}$ -fluoro-L-dopa ( $^{18}\text{F}$ -FDOPA) is a radiotracer available for PET imaging.  $^{18}\text{F}$ -FDOPA PET/CT has excellent diagnostic performance for midgut NETs—superior to that of morphologic imaging and somatostatin-receptor scintigraphy—and yields a significant clinical impact (8–10). In addition, several recent head-to-head comparisons reported that  $^{18}\text{F}$ -FDOPA PET/CT has a higher sensitivity than  $^{68}\text{Ga}$ -DOTATOC PET/CT at the lesion scale (11–15).

Whereas the diagnostic role of  $^{18}\text{F}$ -FDOPA PET/CT is now well described, its prognostic impact has never, to our knowledge, been explored. The objective of this study was to assess the prognostic value of tumor uptake on  $^{18}\text{F}$ -FDOPA PET/CT in patients with metastatic midgut NETs.



## MATERIALS AND METHODS

### Patients

We performed a retrospective multicentric study under the auspices of the Groupe d'étude des Tumeurs Endocrines.  $^{18}\text{F}$ -FDOPA PET/CT has been approved and available in France since 2007, whereas  $^{68}\text{Ga}$ -DOTATOC PET/CT was approved in 2017. Because of the superior performance of  $^{18}\text{F}$ -FDOPA PET/CT compared with somatostatin-receptor scintigraphy ( $^{111}\text{In}$ -chloride [Octreoscan; Curium]) in patients with metastatic small-intestine NETs (9,10), it has been used routinely for diagnosis, staging, and restaging.

We reviewed the medical records of all consecutive patients with midgut NETs and liver metastases who underwent at least one  $^{18}\text{F}$ -FDOPA PET/CT scan between January 1, 2010, and January 1, 2021, in 1 of 5 centers of the French NET expert network (ENDOCAN-RENATEN). We excluded patients with poorly differentiated neuroendocrine carcinoma and those without a  $^{18}\text{F}$ -FDOPA PET/CT scan available for review, without metastases visible on a  $^{18}\text{F}$ -FDOPA PET/CT scan, or without clinical data available. This study was performed according to the Helsinki convention. Data collection was anonymous after patient consent and institutional review board approval (CEERB Paris-Nord University approval 00006477-15-073).

### Data Collection and $^{18}\text{F}$ -FDOPA PET/CT Analysis

We retrospectively collected the main characteristics of patients at baseline (date of the first  $^{18}\text{F}$ -FDOPA PET/CT scan) using a standardized chart. Anonymized data collection included epidemiologic variables, detailed tumor staging, pathologic characterization, prior treatments, and survival.

All  $^{18}\text{F}$ -FDOPA PET/CT examinations were performed on hybrid PET/CT devices equipped with 3-dimensional time-of-flight technology and without iodinated contrast-medium administration. Patients in a given center were scanned on the same instrument. Patients were injected with an  $^{18}\text{F}$ -FDOPA dose of 3–4 MBq/kg.  $^{18}\text{F}$ -FDOPA (Dopacis; Cisbio International) was used in the setting of marketing authorization. The PET/CT protocol included an acquisition from the upper thigh to the top of the skull (3–5 min/step or continuous bed motion when available), starting approximately 60 min after injection of  $^{18}\text{F}$ -FDOPA. Carbidopa premedication (200 mg orally) 60–90 min before  $^{18}\text{F}$ -FDOPA injection was used in 24 patients in the validation cohort. PET image datasets were reconstructed iteratively (ordered-subsets expectation maximization algorithm) using non-contrast-enhanced data for attenuation correction. All  $^{18}\text{F}$ -FDOPA PET/CT scans were reviewed at each site by 1 expert nuclear physician, masked to clinical and survival data, after an initial central study board meeting was held to define the methodology of measurements in order to homogenize data collection.

The SUV was determined as a measure of  $^{18}\text{F}$ -FDOPA uptake using the region-of-interest technique. The maximum voxel ( $\text{SUV}_{\text{max}}$ ) and a 1-mL sphere at the region of highest uptake ( $\text{SUV}_{\text{peak}}$ ) were measured, as well as normal liver parenchyma, in each patient. To reduce potential partial-volume effects, the reference region of interest in the liver was kept consistently at 2 cm in diameter. We calculated the tumor-to-liver (T/L) ratios for  $\text{SUV}_{\text{max}}$  and  $\text{SUV}_{\text{peak}}$ .

### Statistical Analyses

We divided the study population between a test cohort, including all patients from Beaujon Hospital, and a full external validation cohort, including all patients from the other centers. Quantitative variables were described using median and interquartile range (IQR) and compared using the Mann–Whitney test. Qualitative variables were described using frequency and percentage and compared using the  $\chi^2$  test. Correlations between quantitative data were assessed using the Spearman test.

The primary endpoint was OS, measured between the date of the first  $^{18}\text{F}$ -FDOPA PET/CT scan and the date of death from any cause. Patients were censored if they were alive at the last follow-up. OS was estimated using the Kaplan–Meier method, expressed as median and 95% CI, and compared using the log-rank test. We determined the threshold of the  $\text{SUV}_{\text{peak}}$  or  $\text{SUV}_{\text{max}}$  T/L ratio corresponding to the highest prognostic value in the test cohort using receiver operating characteristic curves and the Youden index method. Then, independent prognostic factors were explored in the test cohort using univariate and backward-stepwise multivariate Cox proportional-hazards analyses. The prognostic impact of the best SUV ratio threshold was confirmed in the full external validation cohort using log-rank and univariate Cox proportional-hazards analyses.

Finally, in patients (whole cohort) who underwent an additional  $^{18}\text{F}$ -FDOPA PET/CT scan during their follow-up, we explored the prognostic impact of the best SUV ratio threshold on the last  $^{18}\text{F}$ -FDOPA PET/CT scan, and that of the increase in the best SUV ratio between the first and the last  $^{18}\text{F}$ -FDOPA PET/CT scans. A *P* value of less than 0.05 was considered significant.

The results of this study were reported in accordance with the STROBE (Strengthening the Reporting of Observational Studies in Epidemiology)/REMARK (Reporting Recommendations for Tumor Marker Prognostic Studies) guidelines (Supplemental Table 1; supplemental materials are available at <http://jnm.snmjournals.org>). In the absence of previous publications reporting on the prognostic role of  $^{18}\text{F}$ -FDOPA PET/CT in patients with NETs, no prognostic hypothesis could be formulated, hence hampering calculation of a specific sample size. All the analyses were performed using Prism (version 6; Graph-Pad) and SPSS (version 20; IBM) software.

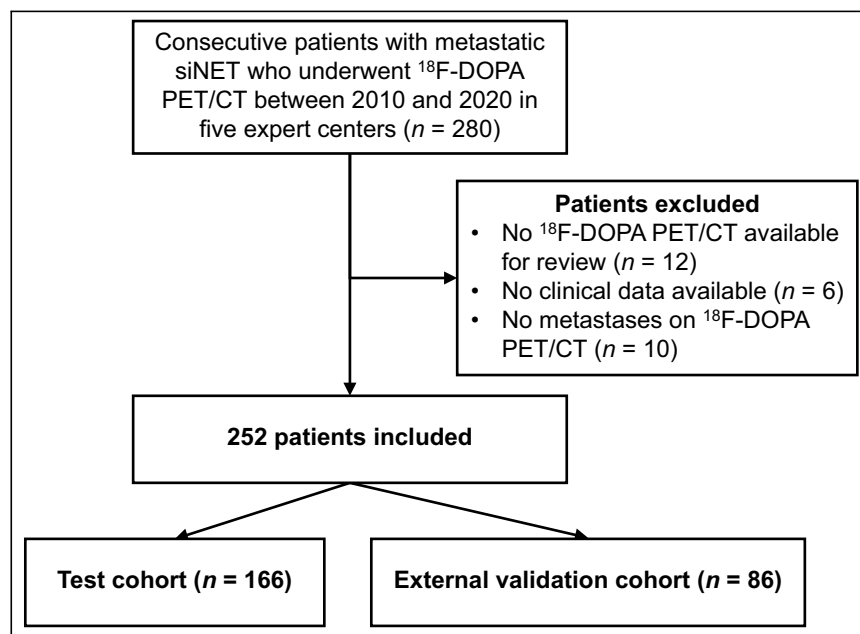


FIGURE 1. Flowchart of study. siNET = small-intestine NET.

## RESULTS

### Characteristics of Patients

We identified 280 consecutive patients in total. After we excluded 28 patients, 252 were finally included in the study: 166 managed in Beaujon University Hospital, composing the test cohort, and 86 from the 4 other expert centers, composing the full external validation cohort (Fig. 1).

The main characteristics of the test cohort are displayed in Table 1. Midgut NETs originated from the ileum in 91% of cases and were mostly classified as grade 1. At baseline, one third of patients had carcinoid syndrome. Hepatic and extrahepatic metastases were present in

88% and 73.5% of patients, respectively. Most patients (69.9%) had previously undergone surgical resection of the primary NET or metastatic lesions, and 54.8% of patients had received nonsurgical antitumor treatments, mostly somatostatin analogs.

Of note, the 166 patients included in the test cohort accounted for 59.1% of all patients managed in the same institution during the same period for a metastatic small-intestine NET. In comparison, the 112 patients with a metastatic small-intestine NET who did not undergo <sup>18</sup>F-FDOPA PET/CT had similar survival, indicating that our test cohort was representative of the whole consecutive population of patients (Supplemental Fig. 1).

**TABLE 1**  
Baseline Characteristic of Patients at Time of <sup>18</sup>F-FDOPA PET/CT, in Test and Validation Cohorts

Characteristic	Test cohort (n = 166)	Validation cohort (n = 86)	P
Age (y)	64.1 (56.5–71.3)	65 (57.8–71)	0.64
Male sex	88 (53)	44 (51)	0.78
Ki-67 (%)*	2 (1–5)	2 (1–5)	0.92
2019 WHO grade*			0.38
Grade 1	88 (56.4)	42 (53)	
Grade 2	65 (41.7)	37 (27)	
Grade 3	3 (1.9)	0	
Carcinoid syndrome	54 (32.5)	26 (30)	0.71
Urinary 5-HIAA (×ULN) <sup>†</sup>	1.3 (1–4)	1.3 (1–2.1)	0.12
Plasmatic chromogranin A (×ULN) <sup>‡</sup>	1.40 (1–7)	1.8 (1–3.7)	0.51
Carcinoid heart disease	12 (7.2)	3 (4)	0.28
Metachronous metastases	41 (24.7)	20 (23)	0.80
Metastatic sites			
Liver metastases	146 (88)	69 (80)	0.101
Liver involvement > 25%	41 (24.7)	20 (23)	0.80
Peritoneal metastases	69 (41.6)	41 (48)	0.35
Distant lymph-node metastases	72 (43.4)	32 (37)	0.35
Bone metastases	41 (24.7)	23 (27)	0.72
Extrahepatic metastases	122 (73.5)	61 (71)	0.67
Metastatic sites > 2	49 (29.5)	25 (29)	1
Previous surgical treatments			
Previous primary NET surgery	116 (69.9)	60 (70)	0.99
Metastases surgery	31 (18.7)	29 (34)	0.008
Previous nonsurgical treatments			
Somatostatin analogs	83 (50)	33 (38)	0.079
Liver transarterial embolization	21 (12.7)	11 (13)	0.97
Targeted therapies	10 (6)	7 (8)	0.56
<sup>177</sup> Lu-DOTATATE	7 (4)	3 (3)	1
Chemotherapy	10 (6)	7 (8)	0.56
Treatment-naive	75 (45.2)	51 (59)	0.034

\*Ki-67 index was missing for 10 patients and 7 patients from test and validation cohorts, respectively.

<sup>†</sup>5-HIAA value was missing for 82 patients and 25 patients from test and validation cohorts, respectively.

<sup>‡</sup>Chromogranin A value was missing for 80 patients and 23 patients from test and validation cohorts, respectively.

WHO = World Health Organization; 5-HIAA = 5-hydroxyindolacetic acid; ULN = upper limit of normal value.

Qualitative data are number and percentage; continuous data are median and IQR.

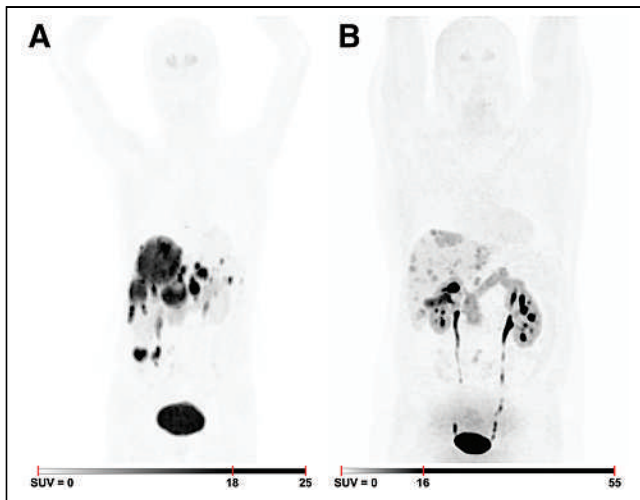


**FIGURE 2.** Examples of whole-body  $^{18}\text{F}$ -FDOPA PET images in patients with metastatic midgut NET and high tumor  $\text{SUV}_{\text{peak}}$  (T/L ratio, 17) (A) or low tumor  $\text{SUV}_{\text{peak}}$  (T/L ratio, 2.3) (B).

### Prognostic Impact of $\text{SUV}_{\text{peak}}$ T/L Ratio in Test Cohort

The median  $\text{SUV}_{\text{peak}}$  T/L ratio was 7.3 (IQR, 4.0–11.5), and the median  $\text{SUV}_{\text{max}}$  T/L ratio was 8.5 (IQR, 5.3–12.8). The correlation between the  $\text{SUV}_{\text{peak}}$  and  $\text{SUV}_{\text{max}}$  T/L ratios was excellent ( $r = 0.93$ ,  $P < 0.001$ ). The lesion with the highest uptake, that is, used to measure  $\text{SUV}_{\text{peak}}$  and  $\text{SUV}_{\text{max}}$ , was more frequently a liver metastasis (54.8%) or another distant metastasis (lymph node, peritoneal, bone, or lung in 12.7%, 10.2%, 5.4%, and 0.6%, respectively) than a primary midgut NET (1.8%) or a regional lymph node (14.5%).

The median follow-up after the  $^{18}\text{F}$ -FDOPA PET/CT scan was 60.3 mo (95% CI, 55.9–65.1), during which 47 patients died. We determined that an  $\text{SUV}_{\text{peak}}$  T/L ratio of more than 4.2 best predicted survival. Examples are displayed in Figure 2. Patients with an  $\text{SUV}_{\text{peak}}$  T/L ratio of more than 4.2 had significantly shorter survival than those with a ratio of 4.2 or less ( $P = 0.01$ ), with a 5-y OS rate of  $74.1\% \pm 4.5\%$  versus  $95\% \pm 3.4\%$ , respectively (Fig. 3A). On univariate Cox proportional-hazards analysis, an  $\text{SUV}_{\text{peak}}$  T/L ratio of more than 4.2 was associated with a 2.62-fold increased risk of death (95% CI, 1.22–5.62;  $P = 0.014$ ).

On multivariate Cox proportional-hazards analysis (Table 2), an  $\text{SUV}_{\text{peak}}$  T/L ratio of more than 4.2 was independently associated with a significantly increased risk of death (hazard ratio, 2.30;

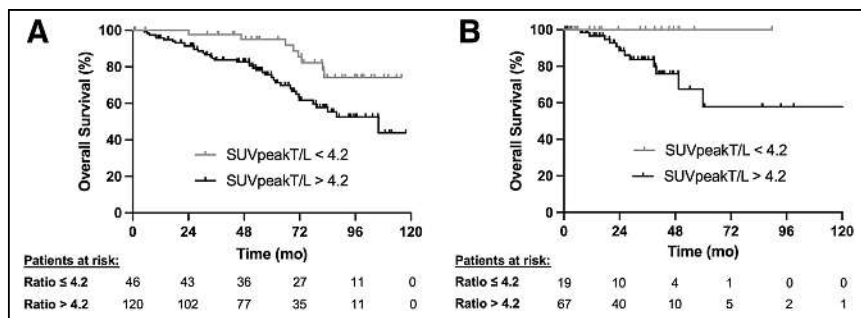


**FIGURE 3.** Impact of  $\text{SUV}_{\text{peak}}$  T/L ratio on OS in patients with midgut NETs who underwent  $^{18}\text{F}$ -FDOPA-PET/CT. (A) Test cohort ( $n = 166$ ,  $P = 0.01$ ). (B) External validation cohort ( $n = 86$ ,  $P = 0.075$ ).

95% CI, 1.02–5.22;  $P = 0.046$ ), after adjustment for age, grade, number of previous lines, number of metastatic sites, and presence of carcinoid syndrome.

### Prognostic Impact of $\text{SUV}_{\text{peak}}$ T/L Ratio in External Validation Cohort

The full external validation cohort included 86 patients from 4 expert centers. Baseline characteristics were similar to those of the test cohort, except that higher proportions of these patients had undergone prior metastasis surgery (34% vs. 18.7%,  $P = 0.008$ ) and no prior nonsurgical antitumor treatment (59.3% vs. 45%,  $P = 0.034$ ) (Table 1).

The median  $\text{SUV}_{\text{max}}$  T/L ratio was 9.2 (IQR, 5.4–12.1), and the median  $\text{SUV}_{\text{peak}}$  T/L ratio was 8.0 (IQR, 4.5–11)—without significant differences from the test cohort ( $P = 0.94$  and  $P = 0.57$ , respectively).

The  $\text{SUV}_{\text{peak}}$  T/L ratio maintained its prognostic impact in the full external validation cohort. The 5-y OS rate was 100% for an  $\text{SUV}_{\text{peak}}$  T/L ratio of 4.2 or less versus  $57.8\% \pm 12.5\%$  ( $P = 0.075$ ) for more than 4.2 (Fig. 3B). The prognostic impact of the  $\text{SUV}_{\text{peak}}$  T/L ratio was not different when studied in the subgroup of patients who received carbidopa premedication (Supplemental Fig. 2).

### Prognostic Impact of Tumor Uptake on Subsequent $^{18}\text{F}$ -FDOPA PET/CT

Overall, 104 patients underwent an additional  $^{18}\text{F}$ -FDOPA PET/CT scan during their follow-up. The median interval between scans was 28.5 mo (11.4–61.3). Patients with an  $\text{SUV}_{\text{peak}}$  T/L ratio of more than 4.2 on the additional  $^{18}\text{F}$ -FDOPA PET/CT scan had shorter survival than those with a ratio of 4.2 or less, with 5-y OS rates of  $45.5\% \pm 15.8\%$  versus  $74.5\% \pm 17.1\%$ , respectively (Fig. 4A). However, this difference was not statistically significant ( $P = 0.183$ ).

Similarly, patients for which the  $\text{SUV}_{\text{peak}}$  T/L ratio increased between scans had shorter survival than patients for which it decreased, with 5-y OS rates of  $41.8\% \pm 19\%$  versus  $70.5\% \pm 13.3\%$ , respectively (Fig. 4B). However, this difference was not statistically significant ( $P = 0.175$ ).

### Correlation Between $\text{SUV}_{\text{peak}}$ T/L Ratio and Disease Characteristics

We assessed whether  $\text{SUV}_{\text{peak}}$  T/L ratio correlates with clinical features among all patients. This ratio correlated with the urine 5-hydroxyindolacetic acid concentration (available for 145 patients,  $r = 0.436$ ,  $P < 0.001$ ) and, to a lesser extent, with plasma chromogranin A (available for 149 patients,  $r = 0.22$ ,  $P = 0.007$ ). Accordingly, the ratio was higher in patients with carcinoid syndrome (9.8; IQR, 6.3–12.7, vs. 6.6; IQR, 3.5–10.3;  $P < 0.001$ ). The ratio did not correlate with Ki-67 index ( $r = -0.05$ ,  $P = 0.42$ ) or age ( $r = 0.06$ ,  $P = 0.33$ ). Conversely, it tended to be higher in patients with extrahepatic metastases (7.8; IQR, 4.4–11.6, vs. 7.0; IQR, 3.3–10.3;  $P = 0.06$ ).

## DISCUSSION

We demonstrated that  $^{18}\text{F}$ -FDOPA PET/CT has a significant prognostic impact in patients with metastatic midgut NETs. To the best of our knowledge, this was the first

**TABLE 2**  
Univariate and Multivariate Cox Proportional-Hazard Models of Factors Associated with OS

Factor	Univariate			Multivariate		
	HR	95% CI	P	HR	95% CI	P
SUV <sub>max</sub> T/L ratio > 9	1.46	0.82–2.60	0.198			
SUV <sub>peak</sub> T/L ratio > 4.2	2.62	1.22–5.62	0.014	2.30	1.02–5.22	0.046
Age > 70 y	2.29	1.27–4.15	0.006	3.12	1.63–6.00	0.001
Grade 2 or 3	1.68	0.93–3.04	0.086	1.67	0.90–3.08	0.104
Number of previous lines (each additional line)	1.55	1.10–2.20	0.013	1.64	1.12–2.41	0.011
Number of metastatic sites > 2	2.03	1.14–3.62	0.017	1.83	0.99–3.36	0.053
Carcinoid syndrome	2.13	1.20–3.79	0.010	1.41	0.73–2.71	0.31

HR = hazard ratio.

study showing the prognostic value of <sup>18</sup>F-FDOPA PET/CT, in addition to its already known diagnostic impact, in a large multicentric cohort of patients with metastatic midgut NETs. Therefore, SUV<sub>peak</sub> T/L ratio measured on <sup>18</sup>F-FDOPA PET/CT could contribute, along with other known prognostic factors (e.g., tumor grade, number of metastatic sites, and tumor burden), to a better assessment of the prognosis of patients with metastatic midgut NETs and better choice of the most appropriate management.

In the test cohort comprising 166 patients with metastatic midgut NETs, an SUV<sub>peak</sub> T/L ratio of more than 4.2, which relies on the lesion with highest uptake, was determined as the threshold with the highest prognostic impact on univariable analysis ( $P = 0.01$ ). This prognostic impact remained statistically significant (hazard ratio, 2.3; 95% CI, 1.02–5.22;  $P = 0.046$ ) after adjustment for classic prognostic factors related to the patient (age), disease extension (metastatic sites), biologic aggressiveness (grade), evolution (previous lines), or presence of carcinoid syndrome, the last of which was biologically associated with <sup>18</sup>F-FDOPA uptake. Then, this result was replicated in the full external validation cohort containing 86 patients. Although the significance threshold was not reached in that cohort ( $P = 0.075$ ), the reason was likely a lack of power since the prognosis of patients with an SUV<sub>peak</sub> T/L ratio of 4.2 or less could not be improved further (100% survival)—which is by itself a strong argument supporting the prognostic impact of <sup>18</sup>F-FDOPA uptake.

A prognostic factor is all the more relevant if it remains prognostic when measured at different time points of disease evolution, as illustrated by the prognostic impact of the Ki-67 index increase on new biopsies in patients with NETs (16). Hence, we performed sensitivity analyses among patients who underwent an additional <sup>18</sup>F-FDOPA PET/CT scan during their follow-up and found that an SUV<sub>peak</sub> T/L ratio of more than 4.2 on the second scan, as well as an increase in the ratio between the 2 scans, were associated with shorter survival. Although the differences did not reach significance, this finding strengthens the prognostic relevance of <sup>18</sup>F-FDOPA PET/CT. Of note, whereas our study was not designed to identify the optimal SUV<sub>peak</sub> T/L ratio threshold on subsequent scans, future studies should explore the dynamic prognostic role of <sup>18</sup>F-FDOPA PET/CT over time.

The mechanisms underlying the prognostic impact of <sup>18</sup>F-FDOPA PET/CT are unclear. <sup>18</sup>F-FDOPA enters NET cells through the L-type neutral amino acid transporters LAT1 and LAT2, which are activated on their heterodimerization with the surface glycoprotein CD98/4F2hc (17,18). Then, intracellular metabolism is ensured through intracellular vesicular monoamine transporters and decarboxylation by the aromatic L-amino acid decarboxylase. This is the rate-limiting enzyme of serotonin and catecholamine biosynthesis and is highly active in midgut NETs, explaining high <sup>18</sup>F-FDOPA retention in these neoplasms (19,20). Therefore, higher <sup>18</sup>F-FDOPA uptake may reflect higher metabolism and biologic aggressiveness

of NET cells, reflected by increased nutrient supply. Accordingly, increased expression of LAT1 and CD98/4F2hc were found to be associated with higher biologic aggressiveness and poorer prognosis in different malignancies (18), including digestive and lung NETs (21–24). Besides, LAT1 mediates the influx of essential amino acids, including tryptophan, a necessary substrate for the biosynthesis of serotonin, whose hypersecretion can lead to carcinoid syndrome (25). Hence, it is not surprising that high <sup>18</sup>F-FDOPA uptake correlated with the presence of carcinoid syndrome and the level of 5-hydroxyindolacetic acid, as reported before (15,26). Finally, LAT1 and

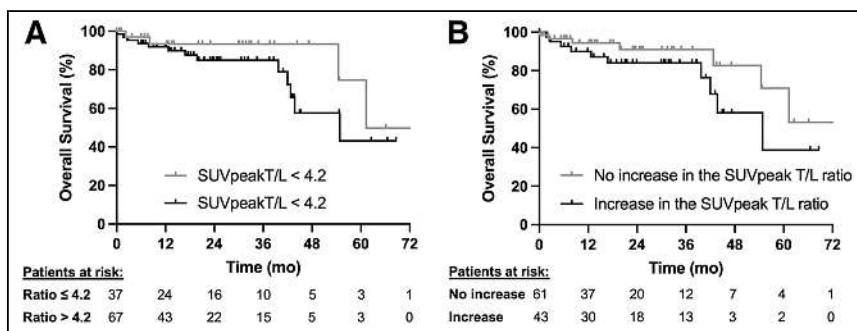


**FIGURE 4.** Prognostic impact of subsequent <sup>18</sup>F-FDOPA-PET/CT. (A) Prognostic impact of SUV<sub>peak</sub> T/L ratio measured on subsequent <sup>18</sup>F-FDOPA PET/CT scan ( $P = 0.183$ ). (B) Prognostic impact of variation of SUV<sub>peak</sub> T/L ratio between initial and subsequent <sup>18</sup>F-FDOPA-PET/CT scans ( $P = 0.175$ ).

CD98/4F2hc expression is associated with activation of the mammalian-target-of-rapamycin pathway (23,27). Future studies should explore whether  $^{18}\text{F}$ -FDOPA uptake could serve as a predictive marker for mammalian-target-of-rapamycin inhibitors, which have demonstrated efficacy in NETs (28,29).

Future investigation should focus on specifying the ranking of  $^{18}\text{F}$ -FDOPA PET/CT in comparison with other nuclear imaging techniques available for NETs, especially PET/CT using  $^{68}\text{Ga}$ -DOTA-peptides. Both techniques have high diagnostic performance, whereas  $^{68}\text{Ga}$ -DOTA-peptide PET/CT has an exclusive theranostic impact because it predicts the efficacy of peptide-radiation therapy targeting somatostatin receptors. In addition, the prognostic role of  $^{68}\text{Ga}$ -DOTA-peptide PET/CT has been reported, with higher tumor uptake indicating better prognosis (30,31). Conversely, higher uptake on  $^{18}\text{F}$ -fluorodesoxyglucose PET/CT is associated with poorer prognosis in patients with digestive NETs (32). Hence, noninvasive prognostic assessment using nuclear medicine would likely benefit from a multiparametric approach using several radioisotopes, among which the precise role of  $^{18}\text{F}$ -FDOPA should be better specified.

The main limitation of our study was its retrospective design, although there was a low proportion of missing data and there were protocolized clinical collection and  $^{18}\text{F}$ -FDOPA PET/CT measurements. We present here the largest comprehensive cohort of patients with metastatic midgut NETs and  $^{18}\text{F}$ -FDOPA PET/CT imaging available, to the best of our knowledge. Although some patients had to be excluded, mainly because they lacked available  $^{18}\text{F}$ -FDOPA PET/CT scans or a liver metastatic target, exclusions were limited and were unlikely to induce a selection bias. Several factors can influence SUVs, including the machine type, injected activity, and acquisition time (26). Notably, the fact that no early PET acquisition was done may influence the sensitivity with which liver metastatic lesions are detected. These potential biases were minimized by normalizing tumor uptake for the nontumor liver on the same PET scan, as the  $^{18}\text{F}$ -FDOPA biodistribution data show a relatively constant hepatic uptake intensity (6). Finally, we split patients into a test cohort composed of all patients from Beaujon Hospital ( $n = 166$ , 66%) and a validation cohort composed of all patients from the 4 other centers ( $n = 86$ , 34%), because it was the only way to perform a full external validation cohort, which is the methodologic reference, and because, otherwise, the separation of all patients into two thirds (test) and one third (validation) would have caused patients from one center to represent 66% of each cohort, hence resulting in a major center-effect bias.

## CONCLUSION

We demonstrated in a large comprehensive cohort that  $\text{SUV}_{\text{peak}}$  T/L ratio measured on  $^{18}\text{F}$ -FDOPA PET/CT had a significant prognostic impact in patients with metastatic midgut NETs. This result was confirmed in a multivariable analysis and was replicated in a full external validation cohort. Future translational studies should explore the molecular bases of this prognostic impact and aim at identifying potential related therapeutic targets.

## DISCLOSURE

This study was financed by an academic research grant from the Groupe d'étude des Tumeurs Endocrines (Fonds de Recherche 2020). Marine Perrier receives support from Adacap and Ipsen for attending meetings. Aurélie Bando-Delaunay is a consultant for

Adacap, Boston Scientific, and SIRTex. Bernard Goichot is a consultant for Adacap and Ipsen and receives support from Ipsen for attending meetings. David Taieb is a lecturer and consultant for Adacap and receives support from Adacap for attending meetings. Thomas Walter receives research support from Ipsen and Roche SAS; is a consultant or on the advisory board for Adacap, Ipsen, Terumo, and Servier; and receives support from Ipsen and Servier for attending meetings and from Adacap, Bayer, Bristol-Myers Squibb, Incyte, and Ipsen for attending educational events. Guillaume Cadiot is a consultant for Adacap and Ipsen and receives honoraria from Esteve. Jérôme Cros receives honoraria from Adacap for presentations. Olivia Hentic is a consultant for Adacap and Ipsen and receives support from Esteve and Ipsen for attending meetings. Philippe Ruzsiewicz is an advisor to Adacap, Ipsen, and ITM Solucin. Rachida Lebtahi is a consultant to Adacap, Ipsen, and SIRTex. Louis de Mestier is a consultant to Adacap, Esteve, Ipsen, Mayoli, and SIRTex; receives research support from Esteve; and receives support from Ipsen for attending meetings. No other potential conflict of interest relevant to this article was reported.

## ACKNOWLEDGMENTS

We thank the patients and their organization (Association des Patients Porteurs de Tumeurs Endocrines Diverses) for their participation. We also thank the ENDOCAN-RENATEN clinical network, a French Organization for Neuroendocrine Neoplasm Management constructed and supported by the Groupe d'étude des Tumeurs Endocrines.

## KEY POINTS

**QUESTION:** What is the prognostic role of tumor uptake on  $^{18}\text{F}$ -FDOPA PET/CT in patients with metastatic midgut NETs?

**PERTINENT FINDINGS:** We studied 252 consecutive patients with metastatic midgut NETs who underwent  $^{18}\text{F}$ -FDOPA PET/CT, and we measured  $\text{SUV}_{\text{max}}$  and  $\text{SUV}_{\text{peak}}$ . A T/L  $\text{SUV}_{\text{peak}}$  ratio of less than 4.2 was associated with good prognosis in a test cohort, on multivariable analysis and in a full external validation cohort.

**IMPLICATIONS FOR PATIENT CARE:** In addition to its high diagnostic performances, the independent prognostic impact of  $^{18}\text{F}$ -FDOPA PET/CT encourages its use for the evaluation of patients with metastatic midgut NETs, to improve case-by-case management.

## REFERENCES

1. Dasari A, Shen C, Halperin D, et al. Trends in the incidence, prevalence, and survival outcomes in patients with neuroendocrine tumors in the United States. *JAMA Oncol*. 2017;3:1335–1342.
2. Grozinsky-Glasberg S, Davar J, Hofland J, et al. European Neuroendocrine Tumor Society (ENETS) 2022 guidance paper for carcinoid syndrome and carcinoid heart disease. *J Neuroendocrinol*. 2022;34:e13146.
3. Strosberg JR, Weber JM, Feldman M, Coppola D, Meredith K, Kvols LK. Prognostic validity of the American Joint Committee on Cancer staging classification for midgut neuroendocrine tumors. *J Clin Oncol*. 2013;31:420–425.
4. Modlin IM, Gustafsson BI, Pavel M, Svejda B, Lawrence B, Kidd M. A nomogram to assess small-intestinal neuroendocrine tumor ('carcinoid') survival. *Neuroendocrinology*. 2010;92:143–157.
5. de Mestier L, Lepage C, Baudin E, et al. Digestive neuroendocrine neoplasms (NEN): French Intergroup clinical practice guidelines for diagnosis, treatment and follow-up (SNFGE, GTE, RENATEN, TENPATH, FFCD, GERCOR, UNICANCER, SFCD, SFED, SFRO, SFR). *Dig Liver Dis*. 2020;52:473–492.



6. Bozkurt MF, Virgolini I, Balogova S, et al. Guideline for PET/CT imaging of neuroendocrine neoplasms with <sup>68</sup>Ga-DOTA-conjugated somatostatin receptor targeting peptides and <sup>18</sup>F-DOPA. *Eur J Nucl Med Mol Imaging*. 2017;44:1588–1601.
7. Sundin A, Arnold R, Baudin E, et al. ENETS consensus guidelines for the standards of care in neuroendocrine tumors: radiological, nuclear medicine and hybrid imaging. *Neuroendocrinology*. 2017;105:212–244.
8. Becherer A, Szabó M, Karanikas G, et al. Imaging of advanced neuroendocrine tumors with <sup>18</sup>F-FDOPA PET. *J Nucl Med*. 2004;45:1161–1167.
9. Montravers F, Grahek D, Kerrou K, et al. Can fluorodihydroxyphenylalanine PET replace somatostatin receptor scintigraphy in patients with digestive endocrine tumors? *J Nucl Med*. 2006;47:1455–1462.
10. Montravers F, Kerrou K, Nataf V, et al. Impact of fluorodihydroxyphenylalanine-<sup>18</sup>F positron emission tomography on management of adult patients with documented or occult digestive endocrine tumors. *J Clin Endocrinol Metab*. 2009;94:1295–1301.
11. Ansquer C, Toucheffeu Y, Faivre-Chauvet A, et al. Head-to-head comparison of <sup>18</sup>F-DOPA PET/CT and <sup>68</sup>Ga-DOTANOC PET/CT in patients with midgut neuroendocrine tumors. *Clin Nucl Med*. 2021;46:181–186.
12. Ouvrard E, Chevalier E, Addeo P, et al. Intraindividual comparison of <sup>18</sup>F-FDOPA and <sup>68</sup>Ga-DOTATOC PET/CT detection rate for metastatic assessment in patients with ileal neuroendocrine tumours. *Clin Endocrinol (Oxf)*. 2021;94:66–73.
13. Ouvrard E, Mestier LD, Boursier C, et al. <sup>18</sup>F-DOPA PET/CT at the forefront of initial or presurgical evaluation of small-intestine neuroendocrine tumors. *J Nucl Med*. 2022;63:1865–1870.
14. Piccardo A, Fiz F, Bottoni G, Ugolini M, Noordzij W, Trimboli P. Head-to-head comparison between <sup>18</sup>F-DOPA PET/CT and <sup>68</sup>Ga-DOTA peptides PET/CT in detecting intestinal neuroendocrine tumours: a systematic review and meta-analysis. *Clin Endocrinol (Oxf)*. 2021;95:595–605.
15. Veenstra EB, de Groot DJA, Brouwers AH, Walenkamp AME, Noordzij W. Comparison of <sup>18</sup>F-DOPA versus <sup>68</sup>Ga-DOTATOC as preferred PET imaging tracer in well-differentiated neuroendocrine neoplasms. *Clin Nucl Med*. 2021;46:195–200.
16. Botling J, Lamarca A, Bajic D, et al. High-grade progression confers poor survival in pancreatic neuroendocrine tumors. *Neuroendocrinology*. 2020;110:891–898.
17. del Amo EM, Urtti A, Yliperttula M. Pharmacokinetic role of L-type amino acid transporters LAT1 and LAT2. *Eur J Pharm Sci*. 2008;35:161–174.
18. Häfliger P, Charles R-P. The L-type amino acid transporter LAT1: an emerging target in cancer. *Int J Mol Sci*. 2019;20:2428.
19. Santhanam P, Taïeb D. Role of <sup>18</sup>F-FDOPA PET/CT imaging in endocrinology. *Clin Endocrinol (Oxf)*. 2014;81:789–798.
20. Fargette C, Imperiale A, Taïeb D. Molecular imaging of endocrine neoplasms with emphasis on <sup>18</sup>F-DOPA PET: a practical approach for well-tailored imaging protocols. *Q J Nucl Med Mol Imaging*. 2022;66:141–147.
21. Kaira K, Oriuchi N, Imai H, et al. Expression of L-type amino acid transporter 1 (LAT1) in neuroendocrine tumors of the lung. *Pathol Res Pract*. 2008;204:553–561.
22. Sampedro-Núñez M, Bouthelier A, Serrano-Somavilla A, et al. LAT-1 and GLUT-1 carrier expression and its prognostic value in gastroenteropancreatic neuroendocrine tumors. *Cancers (Basel)*. 2020;12:2968.
23. Kaira K, Ohde Y, Endo M, et al. Expression of 4F2hc (CD98) in pulmonary neuroendocrine tumors. *Oncol Rep*. 2011;26:931–937.
24. Horita Y, Kaira K, Kawasaki T, et al. Expression of LAT1 and 4F2hc in gastroenteropancreatic neuroendocrine neoplasms. *In Vivo*. 2021;35:2425–2432.
25. Clement D, Ramage J, Srirajaskanthan R. Update on pathophysiology, treatment, and complications of carcinoid syndrome. *J Oncol*. 2020;2020:8341426.
26. Fiebrich H-B, de Jong JR, Kema IP, et al. Total <sup>18</sup>F-dopa PET tumour uptake reflects metabolic endocrine tumour activity in patients with a carcinoid tumour. *Eur J Nucl Med Mol Imaging*. 2011;38:1854–1861.
27. Ganapathy V, Thangaraju M, Prasad PD. Nutrient transporters in cancer: relevance to Warburg hypothesis and beyond. *Pharmacol Ther*. 2009;121:29–40.
28. Yao JC, Shah MH, Ito T, et al. Everolimus for advanced pancreatic neuroendocrine tumors. *N Engl J Med*. 2011;364:514–523.
29. Yao JC, Fazio N, Singh S, et al. Everolimus for the treatment of advanced, non-functional neuroendocrine tumours of the lung or gastrointestinal tract (RADIAN-4): a randomised, placebo-controlled, phase 3 study. *Lancet*. 2016;387:968–977.
30. Campana D, Ambrosini V, Pezzilli R, et al. Standardized uptake values of <sup>68</sup>Ga-DOTANOC PET: a promising prognostic tool in neuroendocrine tumors. *J Nucl Med*. 2010;51:353–359.
31. Sharma P, Naswa N, Kc SS, et al. Comparison of the prognostic values of <sup>68</sup>Ga-DOTANOC PET/CT and <sup>18</sup>F-FDG PET/CT in patients with well-differentiated neuroendocrine tumor. *Eur J Nucl Med Mol Imaging*. 2014;41:2194–2202.
32. Bahri H, Laurence L, Edeline J, et al. High prognostic value of <sup>18</sup>F-FDG PET for metastatic gastroenteropancreatic neuroendocrine tumors: a long-term evaluation. *J Nucl Med*. 2014;55:1786–1790.

---

---

# Validation of the $\Delta\text{SUV}_{\text{max}}$ for Interim PET Interpretation in Diffuse Large B-Cell Lymphoma on the Basis of the GAINED Clinical Trial

Emmanuel Itti<sup>1</sup>, Paul Blanc-Durand<sup>1</sup>, Alina Berriolo-Riedinger<sup>2</sup>, Salim Kanoun<sup>2</sup>, Françoise Kraeber-Bodéré<sup>3</sup>, Michel Meignan<sup>†1</sup>, Elodie Gat<sup>4</sup>, Steven Le Guill<sup>5</sup>, René-Olivier Casasnovas<sup>6</sup>, and Caroline Bodet-Milin<sup>3</sup>

<sup>1</sup>Nuclear Medicine, CHU Henri Mondor, Paris-Est University, Créteil, France; <sup>2</sup>Nuclear Medicine, Georges-François Leclerc Center, Dijon, France; <sup>3</sup>Nantes University, Angers University, CHU Nantes, INSERM, CNRS, CRCI2NA, Nantes, France; <sup>4</sup>Lymphoma Study Association Recherche Clinique (LYSARC), Pierre-Bénite, France; <sup>5</sup>Hematology, CHU de Nantes, Nantes, France; and <sup>6</sup>Hematology, CHU Dijon Bourgogne, Dijon, France

The GAINED phase 3 trial (ClinicalTrials.gov identifier: NCT01659099) evaluated a PET-driven consolidative strategy in patients with diffuse large B-cell lymphoma. In this post hoc analysis, we aimed to compare the prognostic value of the per-protocol PET interpretation criteria (Menton 2011 consensus) with the change in the  $\text{SUV}_{\text{max}}$  ( $\Delta\text{SUV}_{\text{max}}$ ) alone. **Methods:** Real-time central review of <sup>18</sup>F-FDG PET/CT was performed in 581 patients after 2 cycles (PET2) and 4 cycles (PET4) of immunochemotherapy using the Menton 2011 criteria, combining the  $\Delta\text{SUV}_{\text{max}}$  (cutoffs of 66% and 70% at PET2 and PET4, respectively) and the Deauville scale. In “special cases,” when the baseline  $\text{SUV}_{\text{max}}$  was less than 10.0 or the interim residual tumor  $\text{SUV}_{\text{max}}$  was greater than 5.0, the Menton 2011 experts’ consensus agreed that the  $\Delta\text{SUV}_{\text{max}}$  may not be reliable and that the Deauville score is preferable. Prognostic values of Menton 2011 and  $\Delta\text{SUV}_{\text{max}}$  were evaluated by Kaplan–Meier analyses in terms of progression-free survival (PFS). **Results:** Seventeen percent of patients at PET2 (100/581) and 8% at PET4 (49/581) had PET-negative results by  $\Delta\text{SUV}_{\text{max}}$  but were considered to have PET-positive results according to Menton 2011 with residual  $\text{SUV}_{\text{max}}$  of greater than 5.0. For the population with PET2-positive results, 2-y PFS was 70% (range, 58%–80%) with  $\Delta\text{SUV}_{\text{max}}$  alone, whereas the outcome tended to be better for those who were considered to have PET-positive results by Menton 2011, 81% (range, 72%–87%). Conversely, all 10 patients with baseline  $\text{SUV}_{\text{max}}$  of less than 10.0 had PET2-positive results by  $\Delta\text{SUV}_{\text{max}}$  but were considered to have PET2-negative results by Menton 2011. These patients had the same 2-y PFS as patients with PET2-negative/PET4-negative results, indicating that the  $\Delta\text{SUV}_{\text{max}}$  yielded false-positive results in this situation. **Conclusion:** We recommend the use of the  $\Delta\text{SUV}_{\text{max}}$  alone rather than the Menton 2011 criteria for assessing the interim metabolic response in patients with diffuse large B-cell lymphoma, except when the baseline  $\text{SUV}_{\text{max}}$  is less than 10.0.

**Key Words:** diffuse large B-cell lymphoma;  $\Delta\text{SUV}_{\text{max}}$ ; Deauville scale; interim <sup>18</sup>F-FDG PET; central review

**J Nucl Med 2023; 64:1706–1711**  
DOI: 10.2967/jnumed.123.265871

**E**valuation of the metabolic response in lymphoma by <sup>18</sup>F-FDG PET relies on the Deauville 5-point scale (1). For diffuse large B-cell lymphoma (DLBCL), several independent studies have demonstrated that semiquantitative assessment of the early response by computation of the change in the  $\text{SUV}_{\text{max}}$  ( $\Delta\text{SUV}_{\text{max}}$ ) between baseline and interim PET scans is more reproducible than visual assessment and allows the reduction of false-positive interpretation in patients with minimal residual uptake (2–8). The best cutoff for distinguishing good from bad responders is greater than 66% reduction of the  $\text{SUV}_{\text{max}}$  after 2 cycles of chemotherapy and greater than 70%–92% after 4 cycles. However, these cutoffs have been defined from retrospective studies. In some instances when the baseline  $\text{SUV}_{\text{max}}$  is relatively low (<10.0) or the interim residual tumor  $\text{SUV}_{\text{max}}$  is relatively high (>5.0), experts agree that  $\Delta\text{SUV}_{\text{max}}$  may not be appropriate for evaluating the response and that the Deauville 5-point scale is preferable (9). This approach, referred to as the Menton 2011 consensus, was recently used in a large prospective trial (10).

The GAINED (GA In NEwly diagnosed Diffuse large B-cell lymphoma) randomized phase 3 trial (ClinicalTrials.gov identifier: NCT01659099), comparing obinutuzumab (GA101) and rituximab in association with chemotherapy as an induction treatment followed by a PET-driven consolidative strategy (10), was recently conducted by the Lymphoma Study Association (Fig. 1). Patients underwent <sup>18</sup>F-FDG PET/CT at baseline (PET0), after 2 cycles of immunochemotherapy (PET2), and after 4 cycles of immunochemotherapy (PET4). Induction treatment was based on 14 d of anthracycline-containing chemotherapy in association with either rituximab or GA101. The consolidation treatment was driven by an early metabolic response at PET2 and PET4 using the Menton 2011 criteria (9): patients were assigned to receive standard immunochemotherapy, high-dose therapy followed by autologous stem cell transplantation (ASCT), or salvage therapy (Fig. 1). The results of this trial demonstrated that obinutuzumab was not superior to rituximab in transplant-eligible patients and that PET-driven treatment escalation using ASCT enabled patients with PET2-positive (PET2+)/PET4-negative (PET4–) results to achieve similar outcomes as patients with PET2-negative (PET2–)/PET4– results (10).

Considering these results, we conducted a post hoc analysis to compare the prognostic value of the per-protocol Menton 2011 criteria with the  $\Delta\text{SUV}_{\text{max}}$  alone and to make recommendations for quantitative evaluation of the metabolic response by <sup>18</sup>F-FDG PET/CT.

---

Received Apr. 14, 2023; revision accepted Aug. 18, 2023.  
For correspondence or reprints, contact Emmanuel Itti (emmanuel.itti@aphp.fr).

<sup>†</sup>Deceased.

Published online Sep. 21, 2023.

COPYRIGHT © 2023 by the Society of Nuclear Medicine and Molecular Imaging.

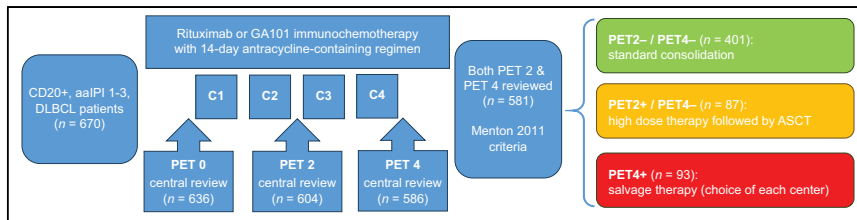


**FIGURE 1.** Study design and flowchart of PET central review. Patients were randomized to receive induction treatment with either rituximab or obinutuzumab (GA101) immunochemotherapy. Consolidation treatment was driven by PET metabolic response at PET2 and PET4 using Menton 2011 criteria. aalPI = age-adjusted International Prognostic Index.

## MATERIALS AND METHODS

### Imaging Review Process

Imaging was performed between September 2013 and December 2015. Scans were interpreted by the local investigator using on-site image viewers and remotely by independent reviewers from a panel of 10 available readers at 3 French institutions located in Créteil, Dijon, and Nantes. An online central review platform was set up for this purpose (11), and all readers were automatically notified by e-mail each time a scan was uploaded on the platform (Imagys; Keosys). Images were automatically deidentified and controlled by a research engineer. All PET/CT datasets that did not pass the quality control guidelines (incomplete datasets, calibration errors preventing  $SUV_{max}$  calculation, or attenuation maps generated from contrast-enhanced CT) were omitted and not reviewed.

At baseline (PET0), in addition to the local interpretation, 2 independent reviewers were asked to identify the tumor with the most intense uptake using a maximum-intensity projection display with a graded color scale, with red indicating the  $SUV_{max}$  (2,7); in case of discrepancy among these 3 interpretations, with regard to either the location or the  $SUV_{max}$  of the target lesion ( $\geq 10\%$  difference between the lowest and the highest measured values), a choice among the interpretations available on the platform was made by an adjudicator. At interim evaluations, in addition to the local interpretation, 2 independent reviewers were asked to measure the whole-body  $SUV_{max}$  on the most intense tumor lesion if residual uptake was present, even though its location differed from that at PET0; if no lesions were identifiable, then the  $SUV_{max}$  was measured in the area of the initially most active tumor at PET0 or, alternatively, was set to 1.0. At all time points, mediastinal blood-pool  $SUV_{max}$  and liver  $SUV_{max}$  were also measured to ensure quality control (12).

### Determination of Metabolic Response

The metabolic response using the Menton 2011 consensus criteria was determined by majority agreement of the 3 readings.  $\Delta SUV_{max}$  cutoffs of 66% and 70% were used at PET2 and PET4, respectively (4,13). In “special cases,” when the baseline  $SUV_{max}$  was less than 10.0 or the interim residual tumor  $SUV_{max}$  was greater than 5.0, the Deauville 5-point scale was used (9). This interpretation was used per protocol to allocate patients to the different consolidation arms (continuing immunochemotherapy, high-dose chemotherapy plus ASCT, or salvage therapy). In a post hoc analysis, the  $\Delta SUV_{max}$  alone was used to evaluate the metabolic response and classify patients as responders or nonresponders, regardless of special cases and without using the Deauville score.

### Statistical Analysis

Concordance between local reading and central review was assessed using Cohen  $\kappa$ -statistics. Progression-free survival (PFS) according to PET2 and PET4 interpretations was estimated using the Kaplan–Meier method and compared using the log-rank test. A *P* value of less than

0.05 indicated significance. Statistical analyses were performed by the statistical department of the Lymphoma Study Association using SAS 9.3 software (SAS Institute Inc.).

## RESULTS

### Population Characteristics

Among the 670 patients included in GAINED, the scans for 636 at PET0, 604 at PET2, and 586 at PET4 were centrally reviewed (Fig. 1). Locally interpreted scans failing quality control were not reviewed.

When the quality control of a PET0 examination failed, interpretation of the interim PET scans was not possible on the platform. Therefore, 581 patients (87%) had an interpretable baseline PET scan and centrally reviewed PET2 and PET4 scans. Patient characteristics are presented in Table 1. For the remaining 89 patients, treatment allocation relied on the local interpretation.

### Metabolic Response by Different Interpretation Criteria

The median delay between image upload and final interpretation of PET0 scans was 6 d (range, 0–47 d). The median PET0  $SUV_{max}$  was 23.4 (range, 1.9–100.7) by local reading and 24.1 (range, 3.0–78.4) by central reviewing. An adjudication consecutive to an  $SUV_{max}$  discrepancy of greater than or equal to 10% was required in 131 of the 636 PET0 scans (21%); in 97% of them ( $n = 127$ ), the adjudicator chose the  $SUV_{max}$  of 1 of the central reviewers. The median number of days between image upload and final interpretation of PET2 or PET4 scans was 0 d (range, 0–44 d; interquartile range, 0–4 d). For 92% of interim PET scans, interpretation of the first reviewer was concordant with the local interpretation and sufficient to draw a conclusion, whereas a second review was necessary for 8%. Finally, the local interpretation was concordant with the final result in 95% of cases, whereas it differed from the conclusion of the reviewers in 5% of cases.

Table 2 summarizes the per-protocol and post hoc PET interpretations for the 581 patients whose PET2 and PET4 scans were both centrally reviewed. Supplemental Table 1 details the interpretations of all scans uploaded on the online platform, including those for patients who had only PET2 or PET4 scans centrally reviewed but not both. PET2 scan results were positive for 28% of patients ( $n = 164$ ). In 81% of cases ( $n = 471$ ), a PET2 scan result was directly given by the  $\Delta SUV_{max}$ , whereas in 19% ( $n = 110$ ), a special case was identified and interpretation relied on the Deauville score. In all instances, the Menton 2011 interpretation changed the final conclusion. In 100 cases, a PET2 scan result that was negative by  $\Delta SUV_{max}$  was considered positive (Deauville score of  $\geq 4$ ) because the residual  $SUV_{max}$  was greater than 5.0, whereas in 10 patients, a PET2 scan result that was positive by  $\Delta SUV_{max}$  was considered negative (Deauville score of  $\leq 3$ ) because the PET0  $SUV_{max}$  was less than 10.0. PET4 scan results were positive in 16% of patients ( $n = 93$ ). In 90% of cases ( $n = 524$ ), a PET4 scan result was directly given by the  $\Delta SUV_{max}$ , whereas in 10% ( $n = 57$ ), a special case was identified. Again, in all instances, the Menton 2011 interpretation changed the final conclusion. In 49 cases, a PET4 scan result that was negative by  $\Delta SUV_{max}$  was considered positive, whereas in 8 patients, a PET4 scan result that was positive by  $\Delta SUV_{max}$  was considered negative. When the  $\Delta SUV_{max}$  alone was used, PET2 and PET4 scan results were positive for only 13% ( $n = 73$ ) and 9% ( $n = 54$ ) of patients,

**TABLE 1**  
Population Characteristics of GAINED Study Participants and Patients Who Had PET Central Review

Characteristic	GAINED trial ( <i>n</i> = 670)	This study ( <i>n</i> = 581)	Patients with PET2+ scan results ( <i>n</i> = 164)	Patients with PET2- scan results ( <i>n</i> = 417)
Age (y)*	48 (18–61)	48 (18–60)	47 (18–60)	49 (19–60)
Men, <i>n</i> (%)	373 (56)	327 (56)	95 (58)	232 (56)
<b>aalPI</b>				
0 or 1, <i>n</i> (%)	282 (42)	252 (44)	74 (45)	178 (43)
2 or 3, <i>n</i> (%)	383 (57)	325 (56)	89 (55)	236 (57)
Missing, <i>n</i>	5	4	1	3
<b>Ann Arbor stage</b>				
I or II, <i>n</i> (%)	118 (18)	110 (19)	37 (23)	73 (18)
III or IV, <i>n</i> (%)	552 (82)	471 (81)	127 (77)	344 (82)
<b>Extranodal involvement</b>				
<2, <i>n</i> (%)	315 (47)	277 (48)	70 (43)	207 (50)
≥2, <i>n</i> (%)	355 (53)	304 (52)	94 (57)	210 (50)
<b>Performance status</b>				
0 or 1, <i>n</i> (%)	575 (86)	503 (87)	139 (85)	364 (87)
>1, <i>n</i> (%)	94 (14)	77 (13)	25 (15)	52 (13)
Missing, <i>n</i>	1	1	0	1
<b>Lactate dehydrogenase levels</b>				
≤Upper limit, <i>n</i> (%)	180 (27)	160 (28)	43 (26)	117 (28)
>Upper limit, <i>n</i> (%)	487 (73)	418 (72)	120 (74)	298 (72)
Missing, <i>n</i>	3	3	1	2
<b>Treatment arm</b>				
GA101, <i>n</i> (%)	336 (50)	292 (50)	72 (44)	220 (53)
Rituximab, <i>n</i> (%)	334 (50)	289 (50)	92 (56)	197 (47)
<b>Induction treatment</b>				
GA101-CHOP, <i>n</i> (%)	169 (25)	148 (26)	38 (23)	110 (26)
Rituximab-CHOP, <i>n</i> (%)	170 (25)	155 (27)	54 (33)	101 (24)
GA101-ACVBP, <i>n</i> (%)	163 (25)	144 (25)	34 (21)	110 (26)
Rituximab-ACVBP, <i>n</i> (%)	161 (25)	134 (23)	38 (23)	96 (23)

\*Reported as means, with ranges in parentheses.

aalPI = age-adjusted International Prognostic Index; ACVBP = doxorubicin, cyclophosphamide, vindesine, bleomycin, prednisone; CHOP = cyclophosphamide, doxorubicin, vincristine, prednisone.

respectively, instead of 28% (*n* = 164) and 16% (*n* = 93) when the Menton 2011 interpretation was used, respectively.

The Cohen  $\kappa$ -value between local reading and central reviewing was 0.80 at PET2, reaching 0.84 between the 2 central reviewers; at PET4, these values were quite similar, 0.81 and 0.78, respectively. The median relative SUV<sub>max</sub> difference between the 2 central reviewers was 0% (range, 0%–333%; interquartile range, 0%–13%), and the locations of the target tumor were identical in 70% of cases. Identical PET interpretations (PET positive or PET negative) were reached between central reviewers in 97% and 94% of cases when  $\Delta$ SUV<sub>max</sub> and Menton 2011 were used, respectively. In contrast, the median relative SUV<sub>max</sub> difference between the local investigator and the central review was 3% (range, 0%–5,190%; interquartile range, 0.7%–74%), and the locations of the target tumor were identical in 66% of cases. Interestingly, the  $\Delta$ SUV<sub>max</sub> led to the same conclusion (PET positive or

PET negative) between the local investigator and the central reviewer in 97% of cases, whereas this result occurred in only 32% of special cases when Menton 2011 was used.

#### Survival Analyses

Kaplan–Meier estimates of PFS using the 2 methods of PET interpretation are presented in Figure 2. They were calculated for 581 patients whose PET2 and PET4 scans were both centrally reviewed and for whom 110 events occurred (disease progression). When per-protocol Menton 2011 criteria were used, the 2-y PFS estimates were 90% (range, 87%–93%) in patients with PET2–/PET4– scan results, 84% (range, 74%–90%) in patients with PET2+/PET4– scan results, and 62% (range, 51%–71%) in patients with PET4+ scan results (*P* < 0.0001). When the  $\Delta$ SUV<sub>max</sub> alone was used, the 2-y PFS estimates were 88% (range, 85%–90%), 77% (range, 60%–88%), and 60% (range, 46%–72%), respectively (*P* < 0.0001).

**TABLE 2**  
 PET Results According to Central Review Using Per-Protocol Menton 2011 Criteria and Post Hoc Analysis with  $\Delta\text{SUV}_{\text{max}}$  Alone

Conclusion	PET2	PET4
Final conclusion using Menton 2011 per-protocol criteria (no. of patients)	581	581
PET positive*	164 (28.2)	93 (16.0)
PET negative*	417 (71.8)	488 (84.0)
Conclusion obtained by $\Delta\text{SUV}_{\text{max}}$ *	471 (81.1)	524 (90.2)
$\Delta\text{SUV}_{\text{max}}$ positive	64 (13.6)	44 (8.4)
$\Delta\text{SUV}_{\text{max}}$ negative	407 (86.4)	480 (91.6)
Conclusion obtained by Deauville score (special cases)*	110 (18.9)	57 (9.8)
$\Delta\text{SUV}_{\text{max}}$ positive but baseline $\text{SUV}_{\text{max}} < 10.0^*$	10 (9.1)	8 (14.0)
PET positive converted to PET negative	All patients	All patients
$\Delta\text{SUV}_{\text{max}}$ negative but interim $\text{SUV}_{\text{max}} > 5.0^*$	100 (90.9)	49 (86.0)
PET negative converted to PET positive	All patients	All patients
Final conclusion using post hoc analysis with $\Delta\text{SUV}_{\text{max}}$ alone (no. of patients)	581	581
PET positive*	73 (12.6)	54 (9.3)
PET negative*	508 (87.4)	527 (90.7)

\*Reported as numbers of patients, with percentages in parentheses.

#### Focus on Special Cases of Menton 2011 Criteria

As stated earlier, 17% of patients at PET2 (100/581) and 8% at PET4 (49/581) had PET scan results that were negative by  $\Delta\text{SUV}_{\text{max}}$  but that were considered positive by Menton 2011 (residual tumor uptake with  $\text{SUV}_{\text{max}}$  of  $>5.0$ ). Interestingly, when we focused on survival analyses for the population with PET2+ scan results, the 2-y PFS estimate was 70% (range, 58%–80%) in patients with PET scan results that were positive by  $\Delta\text{SUV}_{\text{max}}$ , whereas the outcome tended to be better for those with PET scan results that were considered positive by Menton 2011, 81% (range, 72%–87%) ( $P = 0.099$ ) (Fig. 3A). This finding reached significance at PET4, with 2-y PFS estimates of 51% (range, 36%–65%) and 71% (range, 57%–82%), respectively ( $P = 0.043$ ) (Fig. 3B), suggesting that Menton 2011 yields false-positive results when

residual tumor  $\text{SUV}_{\text{max}}$  is greater than 5.0. On the contrary, 10 patients at PET2 and 8 patients at PET4 with  $\text{SUV}_{\text{max}}$  of less than 10.0 at baseline had PET scan results that were positive by  $\Delta\text{SUV}_{\text{max}}$  but that were considered PET negative by Menton 2011. These specific 10 patients had the same 2-y PFS estimates as patients with PET2–/PET4– scan results, that is, 90% (range, 47%–99%) versus 90% (range, 87%–93%), respectively, indicating that  $\Delta\text{SUV}_{\text{max}}$  yields false-positive results when the baseline  $\text{SUV}_{\text{max}}$  is less than 10.0.

#### DISCUSSION

The GAINED study demonstrates that interim PET/CT can identify slow metabolic-responders (PET2+/PET4–) who gain benefit from a therapy escalation. Menton 2011 criteria are quite reproducible, with Cohen  $\kappa$ -values ranging from 0.78 (substantial agreement) to 0.84 (almost perfect agreement) between local and central readers as well as between the 2 independent central reviewers (14). Local interpretation was concordant with the final conclusion of the central review in 95% of cases, which suggests that Menton 2011 criteria can be used in routine practice. However, accurate determination of the baseline  $\text{SUV}_{\text{max}}$  (most hypermetabolic target) may be problematic, as a  $\text{SUV}_{\text{max}}$  discrepancy of greater than or equal to 10% was noted in 21% of PET0 interpretations. In these situations, an adjudication was performed, and the adjudicator chose the same  $\text{SUV}_{\text{max}}$  as a central reviewer in 97% of cases, whereas he agreed with the local reader in only 3%. This finding emphasizes that  $\text{SUV}_{\text{max}}$  identification on baseline

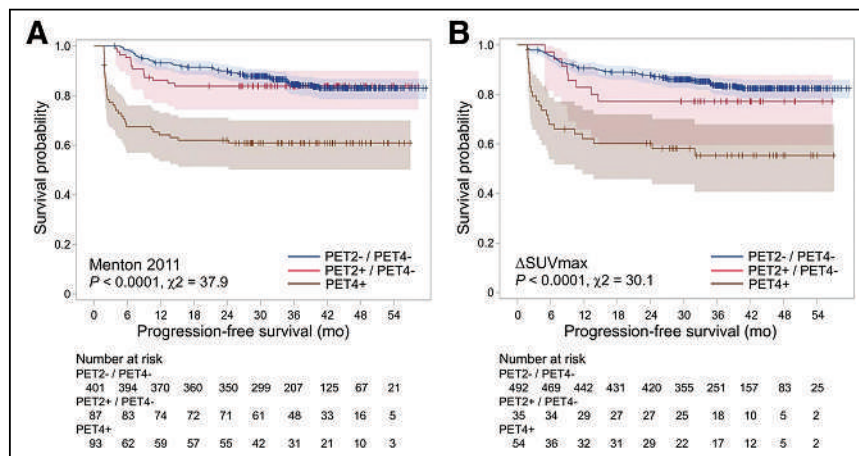


**FIGURE 2.** Kaplan-Meier estimates of progression-free survival according to metabolic response at PET2 and PET4 using Menton 2011 criteria (per protocol) (A) and  $\Delta\text{SUV}_{\text{max}}$  alone (post hoc analysis) (B).



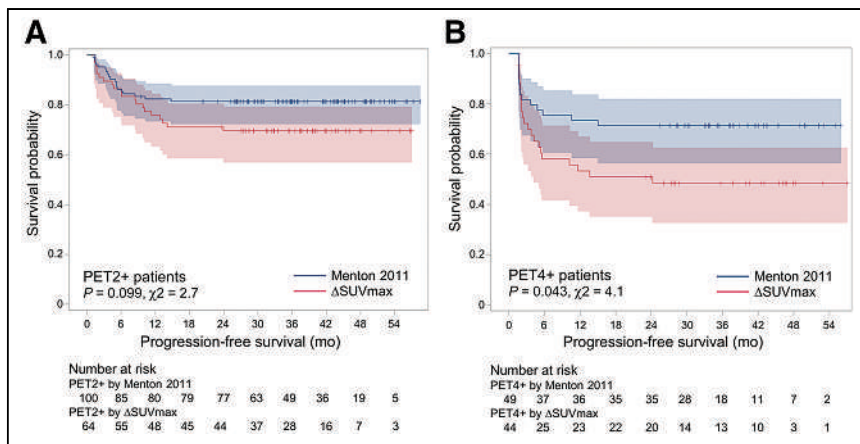


**FIGURE 3.** Kaplan–Meier estimates of progression-free survival in subgroup of patients with PET-positive scan results at PET2 (A) and PET4 (B) according to interpretation criteria: Menton 2011 (i.e., “special cases” consecutive to interim  $SUV_{max}$  of  $>5.0$ ) or  $\Delta SUV_{max}$  alone.

PET is more reliable when using a dedicated software and strict rules to identify the target lesion (maximum intensity projection display, use of a graded color scale and a spheric volume of interest), as previously proposed (2,7).

When comparing  $\Delta SUV_{max}$  alone with Menton 2011 criteria for the assessment of interim metabolic response, we emphasize that  $\Delta SUV_{max}$  alone could be preferentially used in DLBCL patients when a PET-driven escalation strategy is planned. Indeed,  $\Delta SUV_{max}$  led to the same conclusion (PET positive or PET negative) between the local investigator and the central review in 97% of cases, whereas this finding occurred in only 32% in the special cases of Menton 2011 interpretations, pointing out the variability of visual interpretation. When evaluating outcomes (Fig. 3), we found that patients with PET scan results that were positive by  $\Delta SUV_{max}$  alone tended to have a lower PFS than patients with PET scan results that were negative by  $\Delta SUV_{max}$  but that were considered positive by Menton 2011 (interim  $SUV_{max}$  of  $>5.0$ ). This finding may have affected the PET-driven escalation scheme, as some PET2+ scan results were intensified with ASCT, although the patients would have received standard consolidation if the  $\Delta SUV_{max}$  alone had been used. Although it is possible that ASCT intensification was beneficial for a small proportion of these patients, it may have also slightly overestimated the beneficial prognostic impact of ASCT in patients with PET2+/PET4– scan results.

In a retrospective analysis of 189 DLBCL patients homogeneously treated with rituximab + cyclophosphamide, doxorubicin, vincristine, prednisone, Mikhaeel et al. demonstrated that patients with a  $\Delta SUV_{max}$  of less than 66% after 2 rituximab + cyclophosphamide, doxorubicin, vincristine, prednisone treatments had worse PFS than those with  $\Delta SUV_{max}$  of greater than or equal to 66%, whereas the Deauville criteria (1, 2, 3 vs. 4, 5 and 1, 2, 3, 4 vs. 5) were not predictive (15). Recently, Michaud et al. demonstrated in a 166 DLBCL patients who underwent a PET-driven escalation strategy, that the combination of  $\Delta SUV_{max}$  and Deauville criteria after 4 cycles of chemotherapy (according to the recommendation of the Menton 2011 consensus) could improve risk stratification for patients with extremely poor prognosis, compared with the Deauville classification alone (16). However, they did not analyze the prognostic value of the  $\Delta SUV_{max}$  alone, which in our series of 581 patients, suggests an even better prognostic value.

With regard to the special cases consecutive to a baseline  $SUV_{max}$  of less than 10.0, 10 patients at PET2 (and 8 patients at PET4) had PET scan results that were positive by  $\Delta SUV_{max}$  but that were considered PET negative by the Menton 2011 interpretation (Deauville score of  $\leq 3$ ). These specific patients had the same 2-y PFS estimates as patients with PET2–/PET4– scan results, suggesting that  $\Delta SUV_{max}$  calculation is prone to generate false-positive results when baseline  $SUV_{max}$  is less than 10.0. As of today, only the PETAL trial (17) has relied on the  $\Delta SUV_{max}$  alone to evaluate the interim metabolic response. However, the PETAL study design was different to ours and the benefits of the PET-driven strategy in terms of PFS was not comparable with the benefits seen in the GAINED

trial, not due to interim PET issues, but to an inappropriate experimental arm in terms of tumor control.

Our study has several limitations. Because the GAINED trial was a PET-driven escalation strategy in which all patients with PET2+/PET4– scan results received ASCT intensification, it remains difficult to definitively evaluate the prognostic impact of the  $\Delta SUV_{max}$  alone. In addition, semiquantitative data provided here are available for the generation of PET/CT scanners between 2013 and 2015. Newer generations of digital detectors with improved sensitivity/spatial resolution and image reconstruction methods using resolution or point spread function (PSF) modeling or statistical recovery of partial-volume effects to improve SUV calculation (18), typically result in 2-fold-higher values than with older scanners. The special cases, in which PET results that were negative by  $\Delta SUV_{max}$  are considered PET positive because residual uptake is greater than 5.0 will probably be more frequent in the future. To overcome this bias, the current recommendation is to perform an EANM Research Ltd.–compliant reconstruction to interpret interim PET/CT, either visually or semiquantitatively (19).

## CONCLUSION

Assessment of interim metabolic response by –Menton 2011 criteria is quite reproducible and translatable to routine practice. However, we recommend the use of the  $\Delta SUV_{max}$  alone for interim PET evaluation in DLBCL as many patients with PET-negative scan results and interim  $SUV_{max}$  of greater than 5.0 are considered to have PET-positive scan results when Menton 2011 is used. These special cases demonstrate similar or better outcome when using the  $\Delta SUV_{max}$  alone and better agreement between local and central readers. The only situation where  $\Delta SUV_{max}$  should be interpreted with caution is when baseline  $SUV_{max}$  is less than 10.0.

## DISCLOSURE

This work was supported in part by grants from the French National Agency for Research “France 2030 Investment Plan,” Labex IRON (ANR-11-LABX-18-01), and INCa-DGOS-Inserm\_12558 (SIRIC ILIAD). Steven Le Gouill reports grants, personal fees, or nonfinancial support from Roche Genentech during the conduct of the study; personal fees from Celgene; and

grants and personal fees from Janssen-Cilag, GILEAD/kite, and Servier outside the submitted work. René-Olivier Casasnovas reports grants, personal fees, and nonfinancial support from Roche Genentech during the conduct of the study; personal fees from MSD, BMS, Abbvie, Amgen, Celgene, Janssen, and Astra Zeneca; and grants and personal fees from Takeda and GILEAD/kite outside the submitted work. No other potential conflict of interest relevant to this article was reported.

## ACKNOWLEDGMENTS

We thank Romain Ricci, Flavie Corbin, and Bastien Lesne for their support with data analysis and the associate central readers Thomas Eugène, Axel Van Der Gucht, and Myriam Sasanelli.

## KEY POINTS

**QUESTION:** Is the prognostic value of the  $\Delta\text{SUV}_{\text{max}}$  alone as efficient as the use of both  $\Delta\text{SUV}_{\text{max}}$  and the Deauville score for early metabolic response evaluation in DLBCL?

**PERTINENT FINDINGS:**  $\Delta\text{SUV}_{\text{max}}$  is reproducible and can identify early slow metabolic responders for whom a therapy escalation scheme can be proposed. The only situation in which the Deauville score is preferable for evaluating the interim metabolic response is when the baseline  $\text{SUV}_{\text{max}}$  is less than 10.0.

**IMPLICATIONS FOR PATIENT CARE:** We recommend the use of the  $\Delta\text{SUV}_{\text{max}}$  alone in routine practice for interim PET evaluation of the therapeutic response in DLBCL to identify patients for whom therapy escalation can be proposed, according to the GAINED trial.

## REFERENCES

- Cheson BD, Fisher RI, Barrington SF, et al. Recommendations for initial evaluation, staging, and response assessment of Hodgkin and non-Hodgkin lymphoma: the Lugano classification. *J Clin Oncol*. 2014;32:3059–3068.
- Lin C, Itti E, Haioun C, et al. Early  $^{18}\text{F}$ -FDG PET for prediction of prognosis in patients with diffuse large B-cell lymphoma: SUV-based assessment versus visual analysis. *J Nucl Med*. 2007;48:1626–1632.
- Itti E, Lin C, Dupuis J, et al. Prognostic value of interim  $^{18}\text{F}$ -FDG PET in patients with diffuse large B-cell lymphoma: SUV-based assessment at 4 cycles of chemotherapy. *J Nucl Med*. 2009;50:527–533.
- Casasnovas RO, Meignan M, Berriolo-Riedinger A, et al.  $\text{SUV}_{\text{max}}$  reduction improves early prognosis value of interim positron emission tomography scans in diffuse large B-cell lymphoma. *Blood*. 2011;118:37–43.
- Safar V, Dupuis J, Itti E, et al. Interim [ $^{18}\text{F}$ ]fluorodeoxyglucose positron emission tomography scan in diffuse large B-cell lymphoma treated with anthracycline-based chemotherapy plus rituximab. *J Clin Oncol*. 2012;30:184–190.
- Yang DH, Ahn JS, Byun BH, et al. Interim PET/CT-based prognostic model for the treatment of diffuse large B cell lymphoma in the post-rituximab era. *Ann Hematol*. 2013;92:471–479.
- Itti E, Meignan M, Berriolo-Riedinger A, et al. An international confirmatory study of the prognostic value of early PET/CT in diffuse large B-cell lymphoma: comparison between Deauville criteria and  $\Delta\text{SUV}_{\text{max}}$ . *Eur J Nucl Med Mol Imaging*. 2013;40:1312–1320.
- Nols N, Mounier N, Bouazza S, et al. Quantitative and qualitative analysis of metabolic response at interim positron emission tomography scan combined with International Prognostic Index is highly predictive of outcome in diffuse large B-cell lymphoma. *Leuk Lymphoma*. 2014;55:773–780.
- Meignan M, Gallamini A, Itti E, Barrington S, Haioun C, Polliack A. Report on the third international workshop on interim positron emission tomography in lymphoma held in Menton, France, 26–27 September 2011, and Menton 2011 consensus. *Leuk Lymphoma*. 2012;53:1876–1881.
- Le Gouill S, Ghesquieres H, Oberic L, et al. Obinutuzumab vs rituximab for advanced DLBCL: a PET-guided and randomized phase 3 study by LYSA. *Blood*. 2021;137:2307–2320.
- Meignan M, Itti E, Bardet S, et al. Development and application of a real-time on-line blinded independent central review of interim PET scans to determine treatment allocation in lymphoma trials. *J Clin Oncol*. 2009;27:2739–2741.
- Itti E, Juweid ME, Haioun C, et al. Improvement of early  $^{18}\text{F}$ -FDG PET interpretation in diffuse large B-cell lymphoma: importance of the reference background. *J Nucl Med*. 2010;51:1857–1862.
- Casasnovas RO, Ysebaert L, Thieblemont C, et al. FDG-PET-driven consolidation strategy in diffuse large B-cell lymphoma: final results of a randomized phase 2 study. *Blood*. 2017;130:1315–1326.
- Landis JR, Koch GG. The measurement of observer agreement for categorical data. *Biometrics*. 1977;33:159–174.
- Mikhaeel NG, Cunningham D, Counsell N, et al. FDG-PET/CT after two cycles of R-CHOP in DLBCL predicts complete remission but has limited value in identifying patients with poor outcome: final result of a UK National Cancer Research Institute prospective study. *Br J Haematol*. 2021;192:504–513.
- Michaud L, Bantilan K, Mauguen A, Moskowitz CH, Zelenetz AD, Schoder H. Prognostic value of  $^{18}\text{F}$ -FDG PET/CT in diffuse large B-cell lymphoma treated with a risk-adapted immunochemotherapy regimen. *J Nucl Med*. 2023;64:536–541.
- Dührsen U, Müller S, Hertenstein B, et al. Positron emission tomography-guided therapy of aggressive non-Hodgkin lymphomas (PETAL): a multicenter, randomized phase III trial. *J Clin Oncol*. 2018;36:2024–2034.
- van der Vos CS, Koopman D, Rijnsdorp S, et al. Quantification, improvement, and harmonization of small lesion detection with state-of-the-art PET. *Eur J Nucl Med Mol Imaging*. 2017;44:4–16.
- Barrington SF, Sulkin T, Forbes A, Johnson PWM. All that glitters is not gold: new reconstruction methods using Deauville criteria for patient reporting. *Eur J Nucl Med Mol Imaging*. 2018;45:316–317.

---

---

# Impact of $^{68}\text{Ga}$ -FAPI PET/CT on Staging and Oncologic Management in a Cohort of 226 Patients with Various Cancers

Stefan A. Koerber\*<sup>1-4</sup>, Manuel Röhrich\*<sup>5,6</sup>, Leon Walkenbach<sup>1</sup>, Jakob Liermann<sup>1,2</sup>, Peter L. Choyke<sup>7</sup>, Christoph Fink<sup>1,2</sup>, Cathrin Schroeter<sup>5</sup>, Anna-Maria Spektor<sup>5</sup>, Klaus Herfarth<sup>1-3</sup>, Thomas Walle<sup>8-10</sup>, Jeremie Calais<sup>11</sup>, Hans-Ulrich Kauczor<sup>12</sup>, Dirk Jaeger<sup>6</sup>, Juergen Debus<sup>1-3,10</sup>, Uwe Haberkorn<sup>5,13</sup>, and Frederik L. Giesel<sup>5,8,14,15</sup>

<sup>1</sup>Department of Radiation Oncology, Heidelberg University Hospital, Heidelberg, Germany; <sup>2</sup>National Center of Radiation Oncology, Heidelberg Institute of Radiation Oncology, Heidelberg, Germany; <sup>3</sup>Clinical Cooperation Unit Radiation Oncology, German Cancer Research Center, Heidelberg, Germany; <sup>4</sup>Department of Radiation Oncology, Barmherzige Brüder Hospital Regensburg, Regensburg, Germany; <sup>5</sup>Department of Nuclear Medicine, Heidelberg University Hospital, Heidelberg, Germany; <sup>6</sup>Department of Nuclear Medicine, Mainz University Hospital, Mainz, Germany; <sup>7</sup>Molecular Imaging Program, Center for Cancer Research, National Cancer Institute, National Institutes of Health, Bethesda, Maryland; <sup>8</sup>Department of Medical Oncology, National Center for Tumor Diseases, Heidelberg University Hospital, Heidelberg, Germany; <sup>9</sup>Clinical Cooperation Unit Virotherapy, German Cancer Research Center, Heidelberg, Germany; <sup>10</sup>German Cancer Consortium, Heidelberg, Germany; <sup>11</sup>Ahmanson Translational Theranostics Division, Department of Molecular and Medical Pharmacology, David Geffen School of Medicine at UCLA, Los Angeles, California; <sup>12</sup>Department of Diagnostic and Interventional Radiology, Heidelberg University Hospital, Heidelberg, Germany; <sup>13</sup>Clinical Cooperation Unit Nuclear Medicine, German Cancer Research Center, Heidelberg, Germany; <sup>14</sup>Department of Nuclear Medicine, Medical Faculty, Heinrich-Heine University, University Hospital Düsseldorf, Düsseldorf, Germany; and <sup>15</sup>Institute for Radiation Sciences, Osaka University, Osaka, Japan

---

Since the development of fibroblast activation protein–targeted radiopharmaceuticals,  $^{68}\text{Ga}$ -fibroblast activation protein inhibitor (FAPI) PET/CT has been found to be suitable for detecting primary and metastatic lesions in many types of tumors. However, there is currently a lack of reliable data regarding the clinical impact of this family of probes. To address this gap, the present study aimed to analyze the clinical impact of  $^{68}\text{Ga}$ -FAPI PET/CT by examining a large cohort of patients with various tumors. **Methods:** In total, 226 patients (137 male and 89 female) were included in this retrospective analysis. Pancreatic cancer and head and neck cancers were the most common tumor types in this cohort. TNM stage and oncologic management were initially determined with gold standard imaging, and these results were compared with  $^{68}\text{Ga}$ -FAPI PET/CT. Changes were classified as major and minor. **Results:** For 42% of all patients, TNM stage was changed by  $^{68}\text{Ga}$ -FAPI PET/CT results. Most of these changes resulted in upstaging. A change in clinical management occurred in 117 of 226 patients. Although a major change in management occurred in only 12% of patients, there was a significant improvement in the ability to accurately plan radiation therapy. In general, the highest clinical impact of  $^{68}\text{Ga}$ -FAPI PET/CT imaging was found in patients with lung cancer, pancreatic cancer, and head and neck tumors. **Conclusion:**  $^{68}\text{Ga}$ -FAPI PET/CT is a promising imaging probe that has a significant impact on TNM stage and clinical management.  $^{68}\text{Ga}$ -FAPI PET/CT promises to be a crucial new technology that will improve on

conventional radiologic imaging methods such as contrast-enhanced CT and contrast-enhanced MRI typically acquired for cancer staging.

**Key Words:** FAPI; PET/CT; management; staging; radiation therapy

**J Nucl Med 2023; 64:1712–1720**

DOI: 10.2967/jnumed.123.266046

---

**I**ndividualized treatment approaches and personalized medicine play a crucial role in modern oncology. Accurate staging and re-staging are essential for making informed clinical decisions in oncology. Over 40 y ago,  $^{18}\text{F}$ -FDG PET/CT emerged as an integral imaging probe for various tumors, such as lung cancer. In 1999, Nestle et al. reported a reduction in the size of radiotherapy portals based on  $^{18}\text{F}$ -FDG PET/CT information in a small retrospective cohort of lung cancer patients (1). Since then,  $^{18}\text{F}$ -FDG PET–based radiotherapy planning has demonstrated improved treatment efficacy, reduced observer variation, and improved local control without increasing toxicity rates (2–4). Although  $^{18}\text{F}$ -FDG has sufficient sensitivity and specificity, it has some well-known limitations. Physiologic  $^{18}\text{F}$ -FDG uptake in organs such as the brain or pharyngeal lymphoid tissue can hinder tumor detection in these anatomic regions (5). Additionally, false-positive uptake can be observed in activated brown fat and inflammation (6). Moreover, certain tumor types with low glucose transporter or hexokinase activity are not suitable for  $^{18}\text{F}$ -FDG PET/CT (7). Therefore, there is a need for novel tracers that can be widely used for patients with malignant tumors.

Considering that fibroblast activation protein (FAP) is highly expressed by stromal fibroblasts in more than 90% of epithelial cancers, radiolabeled FAP inhibitor (FAPI) tracers have shown promising diagnostic performance for oncologic imaging (8). Initial clinical results have demonstrated high uptake and image contrast in several

---

Received May 23, 2023; revision accepted Aug. 1, 2023.

For correspondence or reprints, contact Manuel Röhrich (manuel.roehrich@med.uni-heidelberg.de).

\*Contributed equally to this work.

Published online Sep. 7, 2023.

Immediate Open Access: Creative Commons Attribution 4.0 International License (CC BY) allows users to share and adapt with attribution, excluding materials credited to previous publications. License: <https://creativecommons.org/licenses/by/4.0/>. Details: <http://jnm.snmjournals.org/site/misc/permission.xhtml>.

COPYRIGHT © 2023 by the Society of Nuclear Medicine and Molecular Imaging.

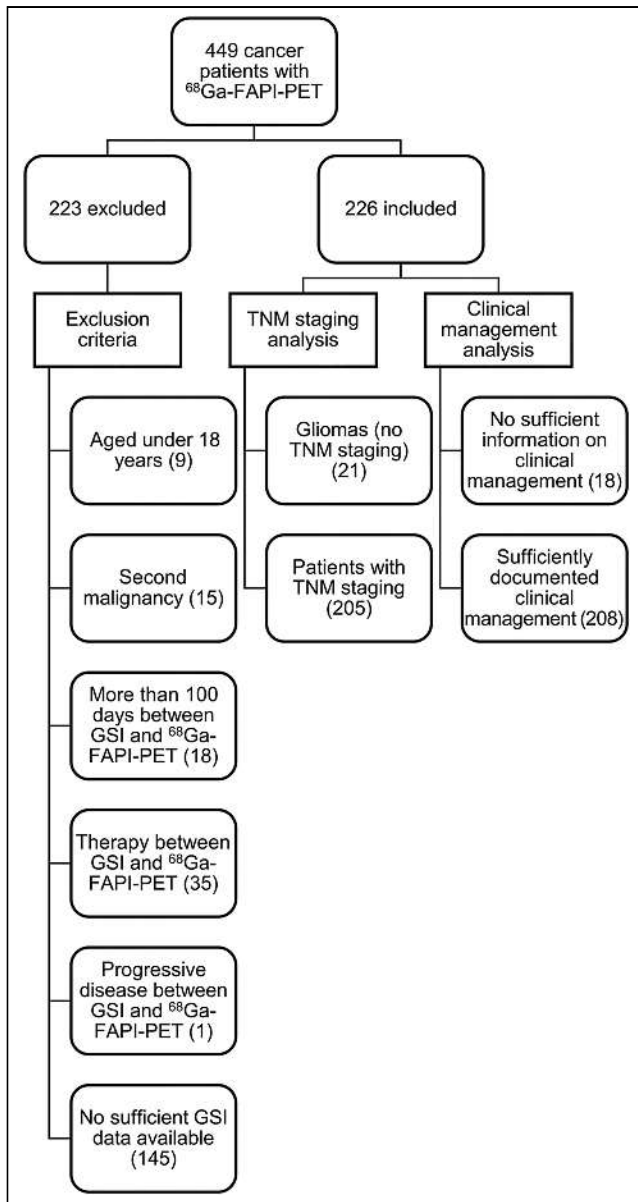


**FIGURE 1.** Flowchart displaying distribution of exclusion criteria among 449 cancer patients who underwent  $^{68}\text{Ga}$ -FAPI PET/CT at University Hospital Heidelberg between June 2017 and February 2022 (left side) and fractions of included patients who could be analyzed with regard to TNM staging and clinical management.

tumor types, detecting many more lesions than conventional imaging (9,10). Numerous trials have confirmed the efficacy of  $^{68}\text{Ga}$ -FAPI PET/CT as an efficient imaging probe and have suggested its superiority over  $^{18}\text{F}$ -FDG for certain tumors (7,11,12). However, the impact of  $^{68}\text{Ga}$ -FAPI PET/CT on clinical practice remains unclear, with only a few small trials assessing the impact on staging and oncologic management (13,14). Here, we evaluated the role of  $^{68}\text{Ga}$ -FAPI PET/CT on TNM staging and oncologic management in a large retrospective patient cohort across multiple types of solid tumors.

## MATERIALS AND METHODS

### Data Collection

Between June 2017 and February 2022, 449 patients with various cancers were referred for  $^{68}\text{Ga}$ -FAPI PET/CT imaging. All patients

**TABLE 1**  
GSI Modalities According to Type of Cancer

Entity	Patients (n)	GSI
Pancreatic ductal adenocarcinoma	77	ceCT or ceMRI
Head and neck cancer	29	ceCT or ceMRI
Lung cancer	23	ceCT (supplementary $^{18}\text{F}$ -FDG PET/CT for 5 patients)
Gliomas	21	ceMRI
Colorectal cancer	20	ceCT or ceMRI (supplementary $^{18}\text{F}$ -FDG PET/CT for 5 patients)
Sarcomas	11	ceCT or ceMRI
Esophageal cancer	10	ceCT (supplementary $^{18}\text{F}$ -FDG PET/CT for 1 patient)
Prostate cancer	3	ceCT and ceMRI (1) or $^{18}\text{F}$ -PSMA PET/CT (2)
Thyroid cancer	5	ceCT or ceMRI (supplementary $^{18}\text{F}$ -FDG PET/CT for 3 patients, supplementary $^{68}\text{Ga}$ -DOTATOC PET/CT for 1 patient)
Ovarian cancer	4	$^{18}\text{F}$ -FDG PET/CT and supplementary ceCT or ceMRI
Breast cancer	2	ceCT (supplementary $^{18}\text{F}$ -FDG PET/CT for 1 patient)
Hepatic cancer	4	ceCT or ceMRI
Cancer of unknown primary	1	ceCT
Melanoma	1	ceCT and ceMRI
Gastric cancer	1	ceCT
Cervical cancer	2	ceCT or ceMRI
Thymus cancer	1	ceCT
Lymphoma	1	ceCT
Gallbladder cancer	2	ceCT
Chordoma	1	ceCT
Renal cancer	1	ceCT
Esthesioneuroblastoma	1	ceCT
Cholangiocellular carcinoma	4	ceCT or ceMRI
Appendix cancer	1	ceCT
Total	226	

ceCT = contrast-enhanced CT; ceMRI = contrast-enhanced MRI.

underwent conventional gold standard imaging (GSI).  $^{68}\text{Ga}$ -FAPI PET was also performed to address issues such as inconclusive findings on other imaging modalities or to assist in radiotherapy planning. Of the 449 patients initially referred, 226 were selected for this retrospective

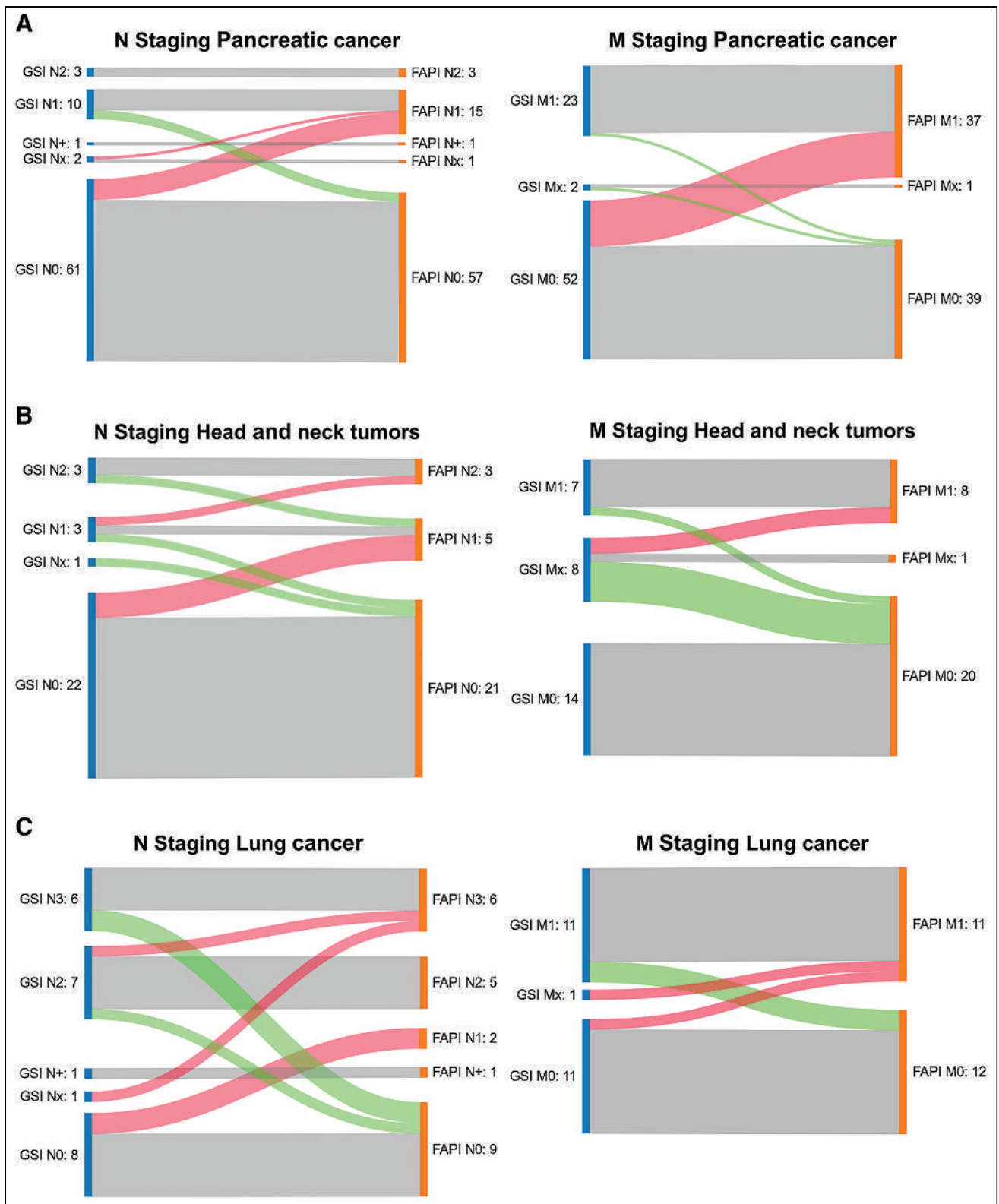


**FIGURE 2.** Sankey plots displaying  $^{68}\text{Ga}$ -FAPI PET/CT-related changes in N and M staging of pancreatic cancer (A), head and neck tumors (B), and lung cancer (C). Gray boxes indicate identical staging based on GSI and  $^{68}\text{Ga}$ -FAPI PET/CT. Red curves indicate upstaging based on  $^{68}\text{Ga}$ -FAPI PET/CT compared with GSI. Green curves indicate downstaging based on  $^{68}\text{Ga}$ -FAPI PET/CT compared with GSI.



**TABLE 2**  
Changes in TNM Staging

Entity	Patients (n)	Staging					Explanatory note
		Unchanged	Major up	Major down	Minor up	Minor down	
PDAC	77	44	26	6	1	0	
HNC	29	19	6	2	1	1	
Lung cancer	23	10	5	9	2	0	In 2 cases, major upstaging and major downstaging at same time; in 1 case, major downstaging and minor upstaging at same time
Gliomas	21						
Colorectal cancer	20	10	6	3	1		
Sarcomas	11	6	2	3			
Esophageal cancer	10	5	1	2	1	1	
Thyroid cancer	5	3	1	1			
Others*	30	22	6	3	0	0	In 1 case, major up- and downstaging at same time
Total number	226	119	53	29	6	2	

\*Prostate cancer, ovarian cancer, breast cancer, hepatic cancer, cancer of unknown primary, melanoma, gastric cancer, cervical cancer, thymus cancer, lymphoma, gallbladder cancer, chordoma, renal cancer, esthesioneuroblastoma, cholangiocellular carcinoma, appendix cancer.

PDAC = pancreatic ductal adenocarcinoma; HNC = head and neck cancer.

analysis on the basis of the following inclusion criteria: an age of 18 y or older, adequate GSI data available, no secondary malignancy within 5 y, and an interval of less than 100 d between GSI and <sup>68</sup>Ga-FAPI PET, with no intervening therapy and no evidence of progression between GSI and <sup>68</sup>Ga-FAPI PET (Fig. 1). The local institutional review board approved this retrospective analysis (study S-430/2022). A subgroup of patients analyzed here were included in previous projects with small and midsize patient cohorts, in which we evaluated

the impact of <sup>68</sup>Ga-FAPI PET/CT on the staging and clinical management of pancreatic ductal adenocarcinomas (15) and adenoid cystic carcinomas (16) but not the impact on staging or clinical management of <sup>68</sup>Ga-FAPI PET/CT for various cancer diseases (9,17–21).

#### <sup>68</sup>Ga-FAPI PET/CT Imaging

Four tracer variants of <sup>68</sup>Ga-FAPI were used in this study: <sup>68</sup>Ga-FAPI-02 (21 patients), <sup>68</sup>Ga-FAPI-04 (63 patients), <sup>68</sup>Ga-FAPI-46

**TABLE 3**  
Changes in Oncologic Management

Entity	Patients (n)	Clinical management			
		Unchanged	Major	Minor	Unknown
PDAC	77	34	7	23	13
HNC	29	4	1	24	
Lung cancer	23	8	1	13	1
Gliomas	21	6		15	
CRC	20	9	3	7	1
Sarcomas	11	5	0	5	1
Esophageal cancer	10	2		8	
Thyroid cancer	5	4			1
Others*	30	19	2	8	1
Total number	226	91	14	103	18

\*Prostate cancer, ovarian cancer, breast cancer, hepatic cancer, cancer of unknown primary, melanoma, gastric cancer, cervical cancer, thymus cancer, lymphoma, gallbladder cancer, chordoma, renal cancer, esthesioneuroblastoma, cholangiocellular carcinoma, appendix cancer.

PDAC = pancreatic ductal adenocarcinoma; HNC = head and neck cancer; CRC = colorectal cancer.

**TABLE 4**  
Cohort Divided into 3 Subgroups: Primary Staging, Follow-up or Adjuvant Therapy, and Progressive Disease or Recurrence

Subgroup	Patients (n)	TNM staging					Oncologic management				
		No change	Downstaging	Mixed	Upstaging	Gliomas	No change	Minor change	Major change	No sufficient data	
Primary staging	48	26	5	2	8	7	11	34	2	1	
Follow-up	91	54	13	0	19	5	42	32	4	13	
Progressive disease	84	36	9	2	28	9	37	37	8	2	
Unclear	3	3	0	0	0	0	1	0	0	2	
Total	226										

(101 patients), and  $^{68}\text{Ga}$ -FAPI-74 (41 patients). All tracers were synthesized and labeled as previously described (22–24). A Siemens Biograph mCT Flow scanner was used for PET imaging, according to previously published protocols (10). Briefly, a low-dose CT scan with or without contrast medium was first obtained, followed by a 3-dimensional PET acquisition (matrix,  $200 \times 200$ ). After image reconstruction, emission data were corrected for attenuation, scatter, and decay. All PET scans were acquired 60 min after administration of  $200 \pm 50$  MBq of  $^{68}\text{Ga}$ -labeled FAPI tracers.

#### TNM Staging Based on $^{68}\text{Ga}$ -FAPI PET Compared with GSI

Staging guidelines were based on the eighth edition of the TNM classification of malignant tumors of the Union for International Cancer Control based on GSI and  $^{68}\text{Ga}$ -FAPI PET/CT findings by 1 board-certified radiologist, 1 board-certified radiation oncologist, and 2 board-certified nuclear medicine physicians in consensus. Staging was based on reviewing clinical imaging records, but if the written record was inadequate, images were reviewed by three of the authors.

Table 1 lists GSI modalities according to the types of cancer. Changes in TNM stage, numeric changes, and the location of metastases were recorded. Staging changes comparing  $^{68}\text{Ga}$ -FAPI PET with GSI were considered major according to the following criteria: T, any change in T stage or evidence of invasion of other organs by the

primary tumor; N, a change from N0 to N+ or vice versa; and M, a change from M0 to M+ or detection of new metastases in other organs or vice versa. Minor staging changes were classified according to the following criteria: N, detection of additional lymph node metastases in N+-positive patients if not affecting N stage; and M, detection of additional distant metastases in the same organ or vice versa. Sankey plots for Figure 2 were produced using the freeware tool SankeyMATIC (www.sankeymatic.com).

#### Evaluation of Impact of $^{68}\text{Ga}$ -FAPI PET on Oncologic Management

Changes in clinical management related to additional findings on  $^{68}\text{Ga}$ -FAPI PET were recorded after retrospective review of patient charts by three of the authors. Changes in oncologic management (management based on  $^{68}\text{Ga}$ -FAPI PET/CT vs. management based on GSI) were classified as follows: fundamental alterations in the type or intent of treatment type were classified as major, whereas changes within an already prescribed treatment regime were classified as minor.

#### Statistical Analysis

Data were analyzed descriptively by comparing numeric results and percentages of TNM changes and changes in oncologic management.

## RESULTS

#### Patient Characteristics

Our cohort consisted of 137 male and 89 female patients with a mean age of 62 y (range, 20–86 y). In 48 patients imaging was performed at initial diagnosis, whereas in 50 patients imaging was performed for assessing metastatic disease. In 34 patients imaging was obtained for progressive disease, in 77 patients it was obtained for follow-up, and in 14 patients it was obtained in the adjuvant setting after surgery. In 3 cases the clinical situation could not be determined. The most common tumor site was pancreatic cancer (77 patients), head and neck tumors (29 patients), and lung cancer (23 patients). The cohort also included some rare tumors such as uterine sarcoma, appendiceal carcinoma, and thymus cancer. Oncologic diagnoses and clinical characteristics are listed by tumor type in Supplemental Table 1 (supplemental materials are available at <http://jnm.snmjournals.org>).

#### Impact of $^{68}\text{Ga}$ -FAPI PET on TNM Staging

Among 205 patients, 86 (42%) experienced a TNM change after  $^{68}\text{Ga}$ -FAPI PET/CT. For most (91%) of these cases, a major change was observed, and upstaging (53 major, 6 minor) was more frequent than downstaging (29 major, 2 minor). The most frequent reason for upstaging was the detection of new metastases on  $^{68}\text{Ga}$ -FAPI PET/CT compared with GSI. Three patients with

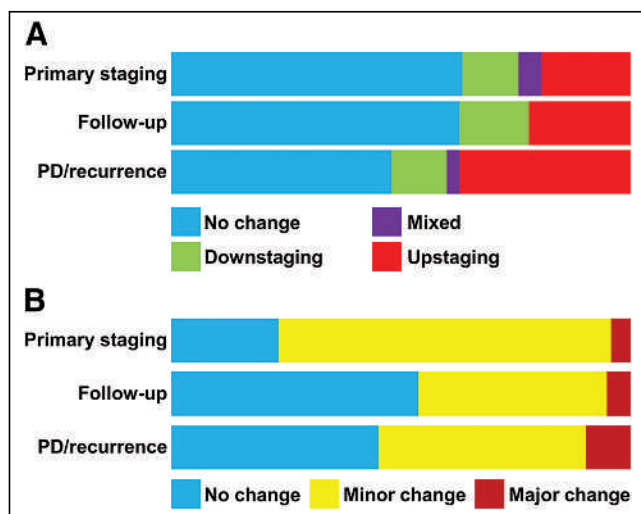


**FIGURE 3.** Relative distribution of  $^{68}\text{Ga}$ -FAPI PET-related changes in TNM staging (A) and clinical management (B) in different clinical settings (primary staging, follow-up, and progressive disease [PD]/recurrence). Bars are scales to 100% of patients analyzed per group.

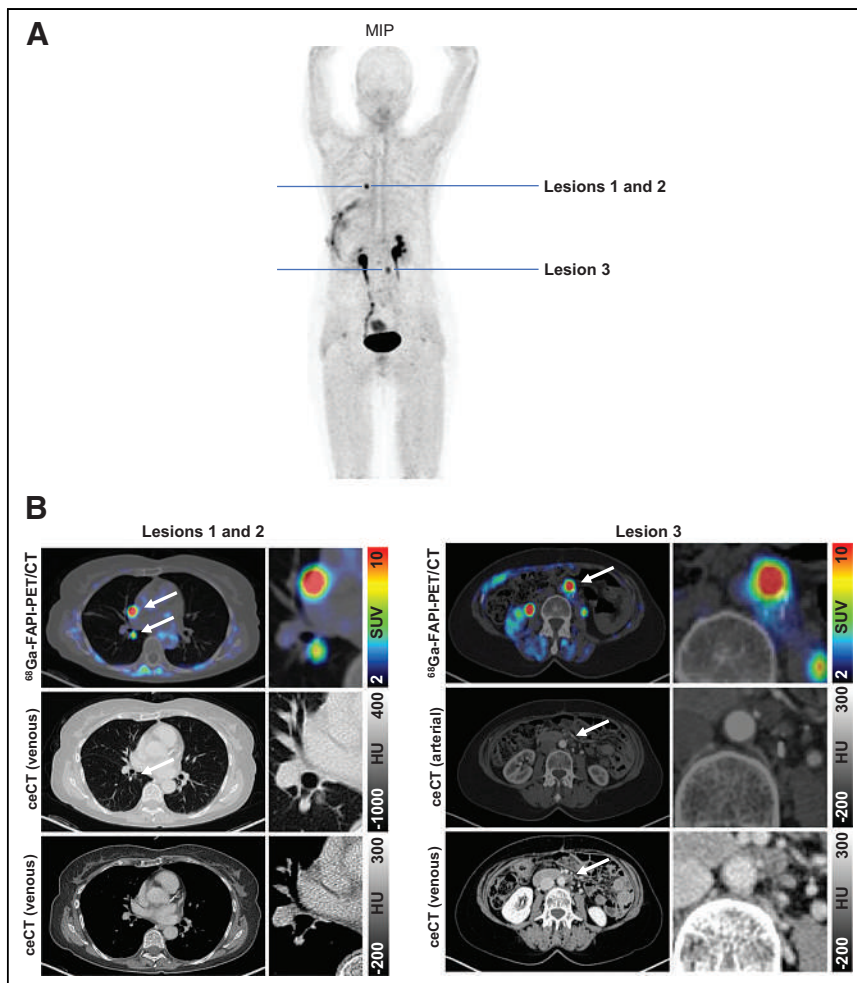


**FIGURE 4.** Example images of 64-y-old woman with recurrent pancreatic ductal adenocarcinoma. (A) Maximum-intensity projection (MIP) of  $^{68}\text{Ga}$ -FAPI PET. (B) Axial  $^{68}\text{Ga}$ -FAPI PET/CT images and contrast-enhanced CT (ceCT) images of suggestive lesions (arrows: lesions 1 and 2, pulmonary metastasis and mediastinal lymph node metastasis; lesion 3, paraaortic lymph node metastasis) detected by  $^{68}\text{Ga}$ -FAPI PET. HU = Hounsfield units.

carcinoma of the gallbladder (1) and lung cancer (2) had both major upstaging and major downstaging after  $^{68}\text{Ga}$ -FAPI PET/CT. In addition, 1 patient with lung cancer showed major downstaging and minor upstaging. Major changes occurred most frequently for pancreatic cancer patients (26 upstaged, 6 downstaged) and lung cancer (5 upstaged, 9 downstaged). Table 2 provides an overview of changes in TNM staging for all patients, and Supplemental Table 5 provides changes in TNM staging of rare entities. Figure 2 depicts changes in N and M staging of the 3 most common entities—pancreatic cancer, head and neck tumors, and lung cancer—in Sankey plots. Supplemental Tables 2–4 provide an overview of the locations of the additional findings on  $^{68}\text{Ga}$ -FAPI PET/CT compared with GSI, as well as  $^{68}\text{Ga}$ -FAPI-negative lesions, which led to staging changes in these 3 entities. For 21 patients with glioma, there were no TNM staging guidelines.

#### Impact of $^{68}\text{Ga}$ -FAPI PET on Patient Management

Among the 226 patients who underwent  $^{68}\text{Ga}$ -FAPI PET/CT for staging or restaging, 18 had no further clinical information available. Of the remaining 208 patients, 117 (56.3%) had a change in clinical management; however, major changes in management

occurred in only 14 patients (12%). The major changes in management after  $^{68}\text{Ga}$ -FAPI PET/CT included irradiation of a new organ,  $^{68}\text{Ga}$ -FAPI radioligand therapy, chemotherapy in place of radiation therapy, additional treatments such as surgery or chemotherapy, or a change in treatment intent (curative vs. palliative). Major treatment changes due to  $^{68}\text{Ga}$ -FAPI PET/CT more frequently led to systemic therapy in place of local treatment (4 cases) or local treatment in place of systemic treatment (1 case). Among the minor changes caused by findings on  $^{68}\text{Ga}$ -FAPI PET/CT, the most frequent was adjustment of the target volume for patients undergoing radiation therapy. Clinical management changed most frequently for pancreatic cancer (7 major, 23 minor), lung cancer (1 major, 13 minor), and head and neck tumors (1 major, 24 minor). Table 3 shows the changes in oncologic management for all cancer types, and Supplemental Table 6 shows changes in oncologic management for each of the rare entities.

#### Differences Between Clinical Settings

To evaluate the potential influence of disease state on the impact of  $^{68}\text{Ga}$ -FAPI PET/CT, we divided our cohort into 3 subgroups: primary staging ( $n = 48$ ), follow-up or adjuvant therapy ( $n = 91$ ), and progressive disease or recurrence ( $n = 84$ ). Three patients for whom the clinical setting remained unclear were excluded (Table 4).  $^{68}\text{Ga}$ -FAPI PET/CT led to changes in TNM staging less frequently in the primary and follow-up settings than in the progressive disease/recurrence setting. However, the impact on oncologic management was high-

est in the primary setting, followed by progressive disease/recurrence and finally follow-up, mostly because of  $^{68}\text{Ga}$ -FAPI PET/CT-related changes in radiotherapy planning (Fig. 3).

#### Case Vignettes

*Case 1.* A 64-year-old woman with pancreatic ductal adenocarcinoma achieved a complete remission after resection of the tail of the pancreas, with splenectomy, lymphadenectomy, and adjuvant chemotherapy (FOLFIRINOX [fluorouracil, leucovorin, irinotecan, and oxaliplatin] and oxaliplatin) and resection of the paraaortic lymph nodes and pulmonary metastases (Fig. 4). The tumor marker CA 19.9 had increased from 960 to 1,600 ng/mL, but restaging with contrast-enhanced CT did not reveal any sites of recurrence. A  $^{68}\text{Ga}$ -FAPI PET/CT scan revealed pulmonary metastases with mediastinal and paraaortic lymph node metastases. Retrospectively, we observed faint radiologic correlates for these metastases on previous CT scans, which were not prospectively interpreted as positive. Thus,  $^{68}\text{Ga}$ -FAPI PET/CT restaged the patient from cT0cN0cM0 to cTxN1cM1, leading to a major change in oncologic management. Previously, the patient was being observed, but after the  $^{68}\text{Ga}$ -FAPI PET/CT scan, systemic



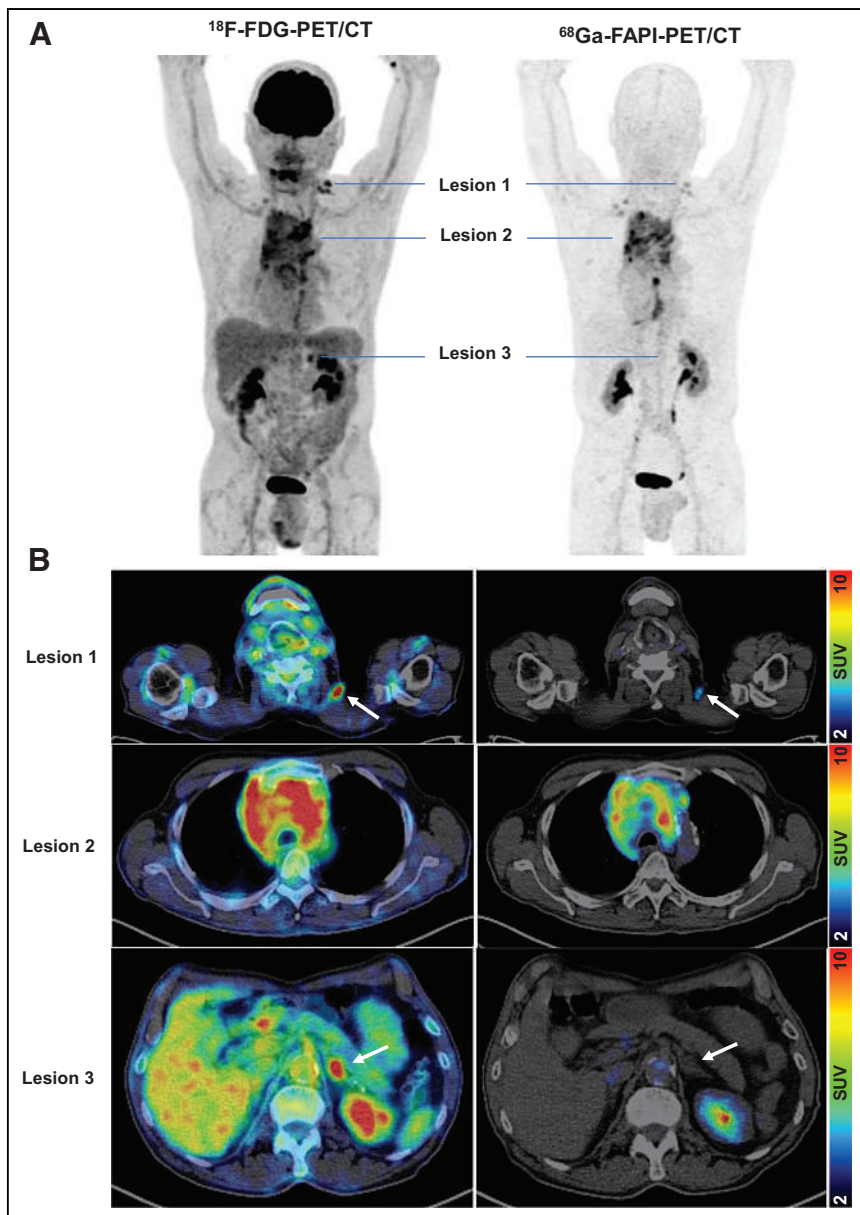


**FIGURE 5.** Example images of 78-y-old man with primary non-small cell lung cancer. (A) Maximum-intensity projection of  $^{18}\text{F}$ -FDG PET and  $^{68}\text{Ga}$ -FAPI PET. (B) Axial  $^{18}\text{F}$ -FDG PET/CT and  $^{68}\text{Ga}$ -FAPI PET/CT of suggestive lesions (arrows: lesion 1, cervical lymph node metastasis; lesion 2, non-small cell lung cancer with involvement of mediastinal lymph nodes; lesion 3, left adrenal mass). Although lesions 1 and 2 were clearly detectable by both PET scans, lesion 3 was  $^{18}\text{F}$ -FDG-avid but not confirmed by  $^{68}\text{Ga}$ -FAPI PET.

chemotherapy (FOLFIRINOX followed by 5-fluorouracil) was administered and resulted in regression of the pulmonary and lymphatic tumor lesions.

**Case 2.** A 78-y-old man presented with primary non-small cell lung cancer. GSI with  $^{18}\text{F}$ -FDG PET/CT showed extensive mediastinal involvement, with cervical lymph node and adrenal metastases (Fig. 5).  $^{68}\text{Ga}$ -FAPI PET/CT confirmed the primary and cervical lymph node disease, but the adrenal mass did not demonstrate uptake and was therefore reassessed as more likely benign. Before the  $^{68}\text{Ga}$ -FAPI PET/CT, the patient was to undergo selective irradiation of the left adrenal gland, but this was cancelled after the scan. The patient

underwent definitive irradiation of the mediastinum and cervical lymph nodes.

## DISCUSSION

Although the sensitivity for detecting cancers with  $^{68}\text{Ga}$ -FAPI PET/CT has been well reported, to date there is little information on the clinical impact of  $^{68}\text{Ga}$ -FAPI PET/CT on oncologic patients. Our large-cohort-based results substantiate smaller studies, in which the impact of  $^{68}\text{Ga}$ -FAPI PET on the staging and management of pancreatic ductal adenocarcinoma and on the staging of adenoid cystic carcinoma was reported (15,16). In the current analysis, we observed that  $^{68}\text{Ga}$ -FAPI PET/CT resulted in changes in TNM staging in about 40% of patients. The impact on TNM staging was particularly pronounced in clinical settings of progressive disease and recurrence, which is in line with our previous findings in pancreatic ductal adenocarcinoma staging (15). In this diverse group of cancers,  $^{68}\text{Ga}$ -FAPI PET/CT had the largest impact on pancreatic and lung cancer. Although  $^{18}\text{F}$ -FDG PET/CT is clinically well established in lung cancer,  $^{68}\text{Ga}$ -FAPI PET/CT appeared to surpass  $^{18}\text{F}$ -FDG PET/CT in detecting additional disease, thus altering TNM staging. For instance, whereas  $^{18}\text{F}$ -FDG PET/CT altered staging in 35% of patients with non-small cell lung cancer, compared with CT, in this study  $^{68}\text{Ga}$ -FAPI PET/CT altered staging in 56% of such patients. (25). Similar results were observed for  $^{18}\text{F}$ -FDG PET/CT for gastric adenocarcinoma, hepatic carcinoma, and pancreatic cancer (26–29). The PET-PANC trial demonstrated that  $^{18}\text{F}$ -FDG PET/CT correctly changed the staging of pancreatic cancer in only 56 of 550 patients. However,  $^{18}\text{F}$ -FDG PET/CT influenced management in 250 (45%) patients and stopped resection in 58 (20%) patients who were due to have surgery (30). In the current study, only a small percentage of patients had prior PET imaging ( $^{18}\text{F}$ -FDG,  $^{68}\text{Ga}$ -DOTATOC,  $^{68}\text{Ga}$ -PSMA) as part of their standard workup,

and therefore, no comparison between  $^{68}\text{Ga}$ -FAPI and other PET tracers can be made. However, a structured head-to-head comparison of staging based on  $^{68}\text{Ga}$ -FAPI PET/CT and  $^{18}\text{F}$ -FDG PET/CT would be of great interest, since the latter modality is so frequently performed as a standard of care.

The findings on  $^{68}\text{Ga}$ -FAPI PET/CT influencing TNM staging also had a direct impact on clinical management. More than half our cohort had a change in management due to findings on  $^{68}\text{Ga}$ -FAPI PET/CT that differed from GSI. A similar change of 30%–62% in patient management was seen after the introduction of PSMA PET/CT in prostate cancer, thus demonstrating the power of targeted PET agents to alter patient care (31–34). Interestingly, the

greatest impact was on radiation therapy planning—for both PSMA PET/CT and  $^{68}\text{Ga}$ -FAPI PET/CT—which underscores the additional value of PET imaging for radiotherapy planning. In our cohort, PET imaging was able to enhance target volume delineation, leading to reduced exposure of organs at risk and improved definition of the target volume. This finding is in line with findings from a large PET trial for patients with non-small cell lung cancer undergoing chemoradiation. Nestle et al. concluded that  $^{18}\text{F}$ -FDG PET-based planning was able to improve local control at no cost of added toxicity (4). Similarly,  $^{68}\text{Ga}$ -FAPI PET/CT also decreases off-target exposure and improves the target volume delineation, resulting in improved dosimetry for radiotherapy. As a side note,  $^{68}\text{Ga}$ -FAPI PET/CT appears to be superior to other modalities in detecting peritoneal carcinosis, which is often difficult to detect on imaging. Several prior studies have suggested that  $^{68}\text{Ga}$ -FAPI PET/CT has a higher sensitivity and specificity in the detection of peritoneal lesions in ovarian and colorectal cancer (35,36). Our data suggest that  $^{68}\text{Ga}$ -FAPI PET/CT is an extremely promising diagnostic approach for peritoneal disease and is more sensitive and specific than contrast-enhanced CT and contrast-enhanced MRI.

This study had several limitations. First, this retrospective trial was conducted at a single institution; however, the large size of the study counters, to some extent, potential patient selection biases. Most of the findings on  $^{68}\text{Ga}$ -FAPI PET/CT were not histologically verified, although false positives can occur. There was also no evidence that the prescribed changes in patient management resulted in improved patient outcomes. Instead of 1 unified type of  $^{68}\text{Ga}$ -FAPI PET/CT, 4 chemical variants were used, creating additional variables. However, most of the agents tested here appear to perform similarly, reducing the impact of this factor. Because the exclusion criteria allowed for a relatively long interval between GSI and  $^{68}\text{Ga}$ -FAPI PET/CT (<100 d), we cannot fully exclude the possibility that in some patients the differences in TNM staging might have been due to actual disease progression. Thus, the results of this study must be considered preliminary. Despite these limitations, these results provide a basis for prospective randomized trials that can provide level 1 evidence of the value of  $^{68}\text{Ga}$ -FAPI PET/CT.

## CONCLUSION

This study demonstrated that  $^{68}\text{Ga}$ -FAPI PET/CT impacts both TNM staging and oncologic management in a high percentage of cancer patients with a variety of cancer types.  $^{68}\text{Ga}$ -FAPI PET/CT detected numerous malignant lesions (in particular lung cancer, pancreatic cancer, and head and neck cancers) not visible on standard imaging and helped radiation therapy planning achieve superior target delineation. This innovative technology offers the potential to improve outcomes for patients by better defining the full extent of their disease.

## DISCLOSURE

Stefan Koerber reports research grants from Viewray Inc. and honoraria from IBA Dosimetry and Think Wired! (outside the submitted work). Frederik Giesel is an advisor at ABX, Telix, SOFIE Biosciences, and  $\alpha$ -Fusion and holds shares in the consultancy group iTheranostic. Jakob Liermann is funded by the Physician-Scientist Program of Heidelberg University, Faculty of Medicine. Thomas Walle reports stock ownership for Roche, Bayer, and Innate Pharma and research funding (outside the submitted work) from CanVirex AG, Basel, Switzerland, and the Institute of Clinical Cancer

Research IKF GmbH, Frankfurt, Germany. Dirk Jaeger reports consulting fees from CureVac AG, Definiens, F. Hoffmann-La Roche Ltd., Genmab A-S, Life Science Inkubator GmbH, VAXIMM AG, OncoOne Research & Development Research GmbH, Oncolytics Biotech Inc., Zelluna, HDIT GmbH, AYOXXA, Seattle Genetics, BreakBio Corp., and Roche Pharma AG; received honoraria from SKK Kliniken Heilbronn GmbH, Georg Thieme Verlag, Terrapinn, Touch Medical Media, BMS GmbH & Co. KGaA, MSD, Guppe 5 Filmproduktion GmbH, AstraZeneca GmbH, the Department of Radiation Medicine at the University of Kentucky, the Norwegian Cancer Society Oslo, Wilhem-Sander Stiftung, Else-Kröner-Fesenius Stiftung, Schering Stiftung, and NordForsk; and received support for attending meetings or travel from Amgen Inc., Oryx GmbH, Roche Glycart AG, Parexel.com, IKTZ HD GmbH, and BMS. Juergen Debus received grants from Accuray International Sàrl, Merck Serono GmbH, CRI—the Clinical Research Institute GmbH, View Ray Inc., Accuray Inc., RaySearch Laboratories AB, Vision RT Limited, Astellas Pharma GmbH, Astra Zeneca GmbH, Solution Akademie GmbH, Ergomed PLC Surrey Research Park, Siemens Healthcare GmbH, Quintiles GmbH, NovoCure, Pharmaceutical Research Associates GmbH, Boehringer Ingelheim Pharma GmbH Co., PTW-Freiburg Dr. Pychlau GmbH, Nanobiotix A.A., and IntraOP Medical (outside the submitted work). Uwe Haberkorn has a patent application for quinolone-based FAP-targeting agents for imaging and therapy in nuclear medicine and has shares of the consultancy group iTheranostics (outside the submitted work). No other potential conflict of interest relevant to this article was reported.

## KEY POINTS

**QUESTION:** Does the addition of  $^{68}\text{Ga}$ -FAPI PET/CT to GSI impact the TNM staging and clinical management of oncologic patients?

**PERTINENT FINDINGS:**  $^{68}\text{Ga}$ -FAPI PET/CT altered TNM stage in 42% of all patients and resulted in changes in clinical management in 52% of all patients, underscoring its potential utility in the diagnostic workup of cancers.

**IMPLICATIONS FOR PATIENT CARE:**  $^{68}\text{Ga}$ -FAPI PET/CT in addition to GSI impacts TNM staging and oncologic management in a high percentage of patients with various cancers, resulting in meaningful changes in treatment.

## REFERENCES

1. Nestle U, Walter K, Schmidt S, et al.  $^{18}\text{F}$ -deoxyglucose positron emission tomography (FDG-PET) for the planning of radiotherapy in lung cancer: high impact in patients with atelectasis. *Int J Radiat Oncol Biol Phys.* 1999;44:593–597.
2. De Ruyscher D, Wanders S, van Haren E, et al. Selective mediastinal node irradiation based on FDG-PET scan data in patients with non-small-cell lung cancer: a prospective clinical study. *Int J Radiat Oncol Biol Phys.* 2005;62:988–994.
3. Steenbakkens RJ, Duppen JC, Fitton I, et al. Reduction of observer variation using matched CT-PET for lung cancer delineation: a three-dimensional analysis. *Int J Radiat Oncol Biol Phys.* 2006;64:435–448.
4. Nestle U, Schimek-Jasch T, Kremp S, et al. Imaging-based target volume reduction in chemoradiotherapy for locally advanced non-small-cell lung cancer (PET-Plan): a multicentre, open-label, randomised, controlled trial. *Lancet Oncol.* 2020;21:581–592.
5. Yeh R, Am A, Johnson JM, Ginat DT. Pearls and pitfalls of  $^{18}\text{F}$ -FDG-PET head and neck imaging. *Neuroimaging Clin N Am.* 2022;32:287–298.
6. McKay MJ, Taubman KL, Foroudi F, Lee ST, Scott AM. Molecular imaging using PET/CT for radiation therapy planning for adult cancers: current status and expanding applications. *Int J Radiat Oncol Biol Phys.* 2018;102:783–791.



7. Giesel FL, Kratochwil C, Schlittenhardt J, et al. Head-to-head intra-individual comparison of biodistribution and tumor uptake of  $^{68}\text{Ga}$ -FAPI and  $^{18}\text{F}$ -FDG PET/CT in cancer patients. *Eur J Nucl Med Mol Imaging*. 2021;48:4377–4385.
8. Altmann A, Haberkorn U, Sivek J. The latest developments in imaging of fibroblast activation protein. *J Nucl Med*. 2021;62:160–167.
9. Kratochwil C, Flechsig P, Lindner T, et al.  $^{68}\text{Ga}$ -FAPI PET/CT: tracer uptake in 28 different kinds of cancer. *J Nucl Med*. 2019;60:801–805.
10. Röhrich M, Leitz D, Glatting FM, et al. Fibroblast activation protein-specific PET/CT imaging in fibrotic interstitial lung diseases and lung cancer: a translational exploratory study. *J Nucl Med*. 2022;63:127–133.
11. Chen H, Pang Y, Wu J, et al. Comparison of [ $^{68}\text{Ga}$ ]Ga-DOTA-FAPI-04 and [ $^{18}\text{F}$ ]FDG PET/CT for the diagnosis of primary and metastatic lesions in patients with various types of cancer. *Eur J Nucl Med Mol Imaging*. 2020;47:1820–1832.
12. Shi X, Xing H, Yang X, et al. Comparison of PET imaging of activated fibroblasts and  $^{18}\text{F}$ -FDG for diagnosis of primary hepatic tumours: a prospective pilot study. *Eur J Nucl Med Mol Imaging*. 2021;48:1593–1603.
13. Liermann J, Syed M, Ben-Josef E, et al. Impact of FAPI-PET/CT on target volume definition in radiation therapy of locally recurrent pancreatic cancer. *Cancers (Basel)*. 2021;13:796.
14. Zhao L, Chen S, Chen S, et al.  $^{68}\text{Ga}$ -fibroblast activation protein inhibitor PET/CT on gross tumour volume delineation for radiotherapy planning of oesophageal cancer. *Radiother Oncol*. 2021;158:55–61.
15. Röhrich M, Naumann P, Giesel FL, et al. Impact of  $^{68}\text{Ga}$ -FAPI PET/CT imaging on the therapeutic management of primary and recurrent pancreatic ductal adenocarcinomas. *J Nucl Med*. 2021;62:779–786.
16. Röhrich M, Syed M, Liew DP, et al.  $^{68}\text{Ga}$ -FAPI-PET/CT improves diagnostic staging and radiotherapy planning of adenoid cystic carcinomas: imaging analysis and histological validation. *Radiother Oncol*. 2021;160:192–201.
17. Röhrich M, Loktev A, Wefers AK, et al. IDH-wildtype glioblastomas and grade III/IV IDH-mutant gliomas show elevated tracer uptake in fibroblast activation protein-specific PET/CT. *Eur J Nucl Med Mol Imaging*. 2019;46:2569–2580.
18. Koerber SA, Staudinger F, Kratochwil C, et al. The role of  $^{68}\text{Ga}$ -FAPI PET/CT for patients with malignancies of the lower gastrointestinal tract: first clinical experience. *J Nucl Med*. 2020;61:1331–1336.
19. Syed M, Flechsig P, Liermann J, et al. Fibroblast activation protein inhibitor (FAPI) PET for diagnostics and advanced targeted radiotherapy in head and neck cancers. *Eur J Nucl Med Mol Imaging*. 2020;47:2836–2845.
20. Dendl K, Koerber SA, Finck R, et al.  $^{68}\text{Ga}$ -FAPI-PET/CT in patients with various gynecological malignancies. *Eur J Nucl Med Mol Imaging*. 2021;48:4089–4100.
21. Giesel FL, Adeberg S, Syed M, et al. FAPI-74 PET/CT using either  $^{18}\text{F}$ -AIF or cold-kit  $^{68}\text{Ga}$  labeling: biodistribution, radiation dosimetry, and tumor delineation in lung cancer patients. *J Nucl Med*. 2021;62:201–207.
22. Lindner T, Loktev A, Altmann A, et al. Development of quinoline-based theranostic ligands for the targeting of fibroblast activation protein. *J Nucl Med*. 2018;59:1415–1422.
23. Loktev A, Lindner T, Mier W, et al. A tumor-imaging method targeting cancer-associated fibroblasts. *J Nucl Med*. 2018;59:1423–1429.
24. Naka S, Watabe T, Lindner T, et al. One-pot and one-step automated radiosynthesis of [ $^{18}\text{F}$ ]AIF-FAPI-74 using a multi purpose synthesizer: a proof-of-concept experiment. *EJNMMI Radiopharm Chem*. 2021;6:28.
25. Taus Á, Aguilo R, Curull V, et al. Impact of  $^{18}\text{F}$ -FDG PET/CT in the treatment of patients with non-small cell lung cancer. *Arch Bronconeumol*. 2014;50:99–104.
26. Bosch KD, Chicklore S, Cook GJ, et al. Staging FDG PET-CT changes management in patients with gastric adenocarcinoma who are eligible for radical treatment. *Eur J Nucl Med Mol Imaging*. 2020;47:759–767.
27. Lee JW, O JH, Choi M, Choi JY. Impact of F-18 fluorodeoxyglucose PET/CT and PET/MRI on initial staging and changes in management of pancreatic ductal adenocarcinoma: a systemic review and meta-analysis. *Diagnostics (Basel)*. 2020;10:952.
28. Lin R, Lin Z, Chen Z, et al. [ $^{68}\text{Ga}$ ]Ga-DOTA-FAPI-04 PET/CT in the evaluation of gastric cancer: comparison with [ $^{18}\text{F}$ ]FDG PET/CT. *Eur J Nucl Med Mol Imaging*. 2022;49:2960–2971.
29. Shi X, Xing H, Yang X, et al. Fibroblast imaging of hepatic carcinoma with  $^{68}\text{Ga}$ -FAPI-04 PET/CT: a pilot study in patients with suspected hepatic nodules. *Eur J Nucl Med Mol Imaging*. 2021;48:196–203.
30. Ghaneh P, Hanson R, Titman A, et al. PET-PANC: multicentre prospective diagnostic accuracy and health economic analysis study of the impact of combined modality  $^{18}\text{F}$ fluoro-2-fluoro-2-deoxy-D-glucose positron emission tomography with computed tomography scanning in the diagnosis and management of pancreatic cancer. *Health Technol Assess*. 2018;22:1–114.
31. Koerber SA, Will L, Kratochwil C, et al.  $^{68}\text{Ga}$ -PSMA-11 PET/CT in primary and recurrent prostate carcinoma: implications for radiotherapeutic management in 121 patients. *J Nucl Med*. 2019;60:234–240.
32. Farolfi A, Ceci F, Castellucci P, et al.  $^{68}\text{Ga}$ -PSMA-11 PET/CT in prostate cancer patients with biochemical recurrence after radical prostatectomy and PSA <0.5 ng/ml. Efficacy and impact on treatment strategy. *Eur J Nucl Med Mol Imaging*. 2019;46:11–19.
33. Schmidt-Hegemann NS, Eze C, Li M, et al. Impact of  $^{68}\text{Ga}$ -PSMA PET/CT on the radiotherapeutic approach to prostate cancer in comparison to CT: a retrospective analysis. *J Nucl Med*. 2019;60:963–970.
34. Sonni I, Eiber M, Fendler WP, et al. Impact of  $^{68}\text{Ga}$ -PSMA-11 PET/CT on staging and management of prostate cancer patients in various clinical settings: a prospective single-center study. *J Nucl Med*. 2020;61:1153–1160.
35. Kömek H, Can C, Kaplan I, et al. Comparison of [ $^{68}\text{Ga}$ ]Ga-DOTA-FAPI-04 PET/CT and [ $^{18}\text{F}$ ]FDG PET/CT in colorectal cancer. *Eur J Nucl Med Mol Imaging*. 2022;49:3898–3909.
36. Zheng W, Liu L, Feng Y, Wang L, Chen Y. Comparison of  $^{68}\text{Ga}$ -FAPI-04 and fluorine-18-fluorodeoxyglucose PET/computed tomography in the detection of ovarian malignancies. *Nucl Med Commun*. 2023;44:194–203.

# Prediction of Resistance to <sup>177</sup>Lu-PSMA Therapy by Assessment of Baseline Circulating Tumor DNA Biomarkers

Oliver Sartor<sup>1,2</sup>, Elisa Ledet<sup>1</sup>, Minqui Huang<sup>1</sup>, Jennifer Schwartz<sup>1</sup>, Alex Lieberman<sup>1</sup>, Brian Lewis<sup>1</sup>, Jodi Layton<sup>1</sup>, Pedro Barata<sup>1</sup>, Albert Jang<sup>1</sup>, Madeline Hawkins<sup>1</sup>, Olivia Pocha<sup>1</sup>, Sree Lanka<sup>1</sup>, and Kendra Harris<sup>1,3</sup>

<sup>1</sup>Tulane Cancer Center, Tulane University School of Medicine, New Orleans, Louisiana; <sup>2</sup>Department of Medical Oncology, Mayo Clinic, Rochester, Minnesota; and <sup>3</sup>Department of Radiation Oncology, Orlando Health, Orlando, Florida

<sup>177</sup>Lu-PSMA-617 and <sup>177</sup>Lu-PSMA I&T (collectively termed <sup>177</sup>Lu-PSMA) are currently being used for the treatment of selected metastatic castration-resistant prostate cancer (mCRPC) patients with PSMA PET-positive disease, but biomarkers for these agents remain incompletely understood. **Methods:** Pretreatment circulating tumor DNA (ctDNA) samples were collected from 44 mCRPC patients receiving <sup>177</sup>Lu-PSMA treatment. Prostate-specific antigen responders and nonresponders were assessed relative to the ctDNA findings at baseline. **Results:** The ctDNA findings indicated that nonresponders were more likely to have gene amplifications than were responders (75% vs. 39.2%,  $P = 0.03$ ). In particular, amplifications in *FGFR1* (25% vs. 0%,  $P = 0.01$ ) and *CCNE1* (31.2% vs. 0%,  $P = 0.001$ ) were more likely to be present in nonresponders. *CDK12* mutations were more likely to be present in nonresponders (25% vs. 3.6%,  $P = 0.05$ ). **Conclusion:** Our analyses indicate that ctDNA assays may contain specific biomarkers predictive of response or resistance for <sup>177</sup>Lu-PSMA-treated mCRPC patients. Additional confirmatory studies are required before clinicians can use these findings to make personalized treatment decisions.

**Key Words:** radiopharmaceuticals; Lu-177; PSMA; biomarkers; ctDNA; prostate cancer

J Nucl Med 2023; 64:1721–1725

DOI: 10.2967/jnumed.123.266167

Two radioligand therapies being used for patients with metastatic castration-resistant prostate cancer (mCRPC) are <sup>177</sup>Lu-PSMA-617 and <sup>177</sup>Lu-PSMA-I&T (collectively termed <sup>177</sup>Lu-PSMA). In the phase III VISION trial, <sup>177</sup>Lu-PSMA prolonged radiographic progression-free survival and overall survival in PSMA-positive mCRPC patients (1). With supporting data from the phase III VISION trial, both the U.S. Food and Drug Administration and the European Commission approved <sup>177</sup>Lu-PSMA in 2022 for mCRPC patients previously treated with an androgen-receptor pathway inhibitor and taxane-based chemotherapy.

Many data have accumulated concerning the use of PSMA PET scans as a predictive biomarker for <sup>177</sup>Lu-PSMA therapy (2,3). Despite the importance of this image-based biomarker, additional factors such as chemotherapy status, baseline hemoglobin level, number of metastases, bone involvement, and liver metastases are

also associated with response and resistance to therapy (2). These biomarkers may play an important prognostic role for those being treated with this targeted radionuclide. Determining which prostate cancer patients will most benefit from <sup>177</sup>Lu-PSMA is of considerable interest given that this therapy is expensive and alternatives such as cabazitaxel might also be considered in therapeutic decision-making. The use of circulating tumor DNA (ctDNA) has emerged as an important noninvasive blood-based biomarker in prostate cancer therapeutics (4,5), and such approaches have now been approved by the Food and Drug Administration for therapeutic selection. Using ctDNA to assess somatic alterations in tumors is now established, and these somatic alterations have been shown to have prognostic significance. Despite the extensive body of evidence that has accumulated for a variety of diseases and therapies, to our knowledge no ctDNA data have been presented regarding the potential prognostic utility of ctDNA assays in mCRPC patients treated with <sup>177</sup>Lu-PSMA. Here, we present such experience.

## MATERIALS AND METHODS

Blood for ctDNA assays to assess selected somatic mutations, amplifications, deletions, and fusions was obtained less than 50 d before treatment with <sup>177</sup>Lu-PSMA, and all assays were performed using a commercial assay (Guardant360; Guardant) that has been widely referenced in the literature (6). This assay assesses 83 cancer-associated genes for mutations, 7 genes for deletions, 18 genes for amplifications, and 10 genes for various pathogenic fusions. The study included all consecutive patients with Guardant360 results who were treated at Tulane University. One additional patient was treated in Germany. No patients with ctDNA results were excluded.

All patients had mCRPC and PET-positive metastatic disease (>liver uptake). All patients had prior treatment with abiraterone, enzalutamide, or both. Most had at least 1 taxane-based chemotherapy. Standard-of-care therapies were used in combination with <sup>177</sup>Lu-PSMA. All but 4 patients were treated with <sup>177</sup>Lu-PSMA-617 (3 patients were treated with <sup>177</sup>Lu-PSMA I&T and 1 with <sup>177</sup>Lu-PSMA-R2).

Prostate-specific antigen (PSA) was assessed at baseline (before <sup>177</sup>Lu-PSMA treatment) and at every treatment cycle (every 6–8 wk). PSA declines at any point after treatment were assessed. Those with a PSA decline of more than 50% were classified as responders, and those with a lesser PSA decline were classified as nonresponders. This analysis compared responders and nonresponders relative to baseline ctDNA findings and demographics to assess differences in the 2 subsets using the Fisher exact methodology or the Mann–Whitney test (when appropriate). The comparisons in Table 2 and the  $P$  values reported there represent a direct comparison of the individual genetic alterations in the responder versus nonresponder groups. The institutional review board

Received Jun. 13, 2023; revision accepted Aug. 18, 2023.

For correspondence or reprints, contact Oliver Sartor (sartor.oliver@mayo.edu)

Published online Sep. 28, 2023.

COPYRIGHT © 2023 by the Society of Nuclear Medicine and Molecular Imaging.

**TABLE 1**  
Patient Demographics at Baseline

Demographic	Nonresponder	Responder	<i>P</i>
<b>Race</b>			
Black	3	1	0.12
White	12	26	
Hispanic	0	1	N/A
Other	1	0	N/A
<b>Prior treatments</b>			
<b>Abiraterone</b>			
No	4	3	0.39
Yes	12	25	
<b>Enzalutamide</b>			
No	5	5	0.46
Yes	11	23	
<b>Docetaxel</b>			
No	5	6	0.72
Yes	11	22	
<b>Cabazitaxel</b>			
No	8	16	0.76
Yes	8	12	
<b><sup>223</sup>Ra</b>			
No	15	23	0.39
Yes	1	5	
<b>Metastases</b>			
<b>Bone</b>			
No	0	6	0.07
Yes	16	22	
<b>Lymph node</b>			
No	7	16	0.53
Yes	9	12	
<b>Liver</b>			
No	12	27	0.05
Yes	4	1	
<b>Baseline labs</b>			
PSA (ng/mL)	71.5 (4.11–824)	88.9 (7.32–4,235.09)	0.61
Hemoglobin (g/dL)	11.15 (7.7–14)	11.45 (9.8–14.9)	0.16
Alkaline phosphatase (U/L)	163 (69–582)	81 (30–1,253)	0.003
Lactate dehydrogenase (U/L)	249.5 (163–613)	192 (87–695)	0.009

Qualitative data are number; continuous data are median and range.

approved this retrospective study, and the requirement to obtain informed consent was waived.

## RESULTS

As shown in Table 1, the population comprised 44 mCPRC patients, including 4 Black patients, 38 White patients, 1 Hispanic patient, and 1 “other.” The baseline PSA level was 71.5 and 88.9 ng/mL in the nonresponders and responders, respectively. The responders and nonresponders had several distinctions in their

baseline variables. Nonresponders were more likely to have liver metastases (25% vs. 3.6%,  $P = 0.05$ ), higher serum lactate dehydrogenase levels (median, 249.5 vs. 192.0;  $P = 0.009$ ), and higher serum alkaline phosphatase levels (median, 163 vs. 81;  $P = 0.003$ ).

The ctDNA findings were first assessed for amplifications, deletions, mutations, and splice variations (Table 2). No differences were noted between responders and nonresponders in the frequency of deletions, mutations, or splice variations reported by the Guardant360 testing. Amplifications, however, were distinct between the 2 groups. Those with no response to <sup>177</sup>Lu-PSMA were more

**TABLE 2**  
Guardant360 Results for All <sup>177</sup>Lu Responders and Nonresponders by Gene

Gene	Nonresponder				Responder				P
	No		Yes		No		Yes		
	n	%	n	%	n	%	n	%	
APC	15	93.75	1	6.25	28	100	0	0	0.36
AR	7	43.75	9	56.25	16	57.14	12	42.85	0.53
ARD1A	16	100	0	0	26	92.85	2	7.14	0.52
ATM	16	100	0	0	24	85.71	4	14.28	0.27
BRAF	16	100	0	0	27	96.42	1	3.57	1
BRCA2	15	93.75	1	6.25	26	92.85	2	7.14	1
CCND1	16	100	0	0	26	92.85	2	7.14	0.52
CCND2	14	87.5	2	12.5	28	100	0	0	0.12
CCNE1	11	68.75	5	31.25	28	100	0	0	0.004
CDH1	16	100	0	0	28	100	0	0	NA
CDK12	12	75	4	25	27	96.42	1	3.57	0.05
CDK4	15	93.75	1	6.25	28	100	0	0	0.36
CDK6	15	93.75	1	6.25	28	100	0	0	0.36
CHEK2	16	100	0	0	27	96.42	1	3.57	1
CTNNB1	16	100	0	0	25	89.28	3	10.71	0
EGFR	13	81.25	3	18.75	26	92.85	2	7.14	0.33
ERBB2	16	100	0	0	27	96.42	1	3.57	1
ESR1	15	93.75	1	6.25	26	92.85	2	7.14	1
FGFR1	12	75	4	25	28	100	0	0	0.01
GATA3	16	100	0	0	27	96.42	1	3.57	1
GNAS	16	100	0	0	25	89.28	3	10.71	0.28
HNF1A	16	100	0	0	28	100	0	0	NA
IDH2	16	100	0	0	27	96.42	1	3.57	1
JAK2	16	100	0	0	27	96.42	1	3.57	1
KIT	16	100	0	0	27	96.42	1	3.57	1
KRAS	14	87.5	2	12.5	28	100	0	0	0.12
MET	15	93.75	1	6.25	27	96.42	1	3.57	1
MSH6	16	100	0	0	28	100	0	0	NA
MYC	15	93.75	1	6.25	28	100	0	0	0.36
NF1	16	100	0	0	27	96.42	1	3.57	1
No ctDNA detected	15	93.75	1	6.25	25	89.28	3	10.71	1
PALB2	16	100	0	0	28	100	0	0	NA
PDGFRA	15	93.75	1	6.25	27	96.42	1	3.57	1
PIK3CA	14	87.5	2	12.5	26	92.85	2	7.14	0.07
PTEN	16	100	0	0	27	96.42	1	3.57	1
RAF1	16	100	0	0	28	100	0	0	N/A
RB1	15	93.75	1	6.25	28	100	0	0	0.36
TERT	16	100	0	0	26	92.85	2	7.14	0.52
TP53	8	50	8	50	12	42.85	16	57.14	0.75
Amplification	4	25	12	75	17	60.71	11	39.28	0.03
Deletion	15	93.75	1	6.25	26	92.85	2	7.14	1
Frameshift	13	81.25	3	18.75	22	78.57	6	21.42	1
Missense	8	50	8	50	11	39.28	17	60.71	0.54
Nonsense	13	81.25	3	18.75	23	82.14	5	17.85	0.65
Promoter SNV	16	100	0	0	26	92.85	2	7.14	0.52
Splice site SNV	13	81.25	3	18.75	26	92.85	2	7.14	0.33

NA = not applicable; SNV = single-nucleotide variant.

likely to have amplifications than were responders (75.0% vs. 39.2%,  $P = 0.03$ ). When examining the amplifications using a gene-by-gene analysis, we found that 2 specific amplifications were distinct between the 2 subsets. Nonresponders were more likely to have amplification in *CCNE1* (31.2% vs. 0%,  $P = 0.004$ ) or *FGFR1* (25% vs. 0%,  $P = 0.01$ ).

There was no difference between responders and nonresponders in the frequency of pathogenic mutations. However, a gene-by-gene analysis indicated that *CDK12* mutations were more frequent in the nonresponders than in the responders (25% vs. 3.7%,  $P = 0.05$ ).

## DISCUSSION

PSA nonresponders were significantly more likely to have amplifications in cancer-associated genes in the ctDNA. Though this might be viewed as an oversimplistic finding, it was a statistically significant finding in our analyses. Amplifications are well known in cancer biology and are clearly related to genomic instability, a quintessential hallmark of cancer. Of note, the methods used in these ctDNA assays may not distinguish between amplification of a specific gene and an alteration in chromosomal number (aneuploidy). Thus, the fact that the broad finding of amplifications is more common in PSA nonresponders may reflect genomic instability at a larger scale. Additional studies would be required to confirm or deny this possibility. Optimally, we would have multiple validation cohorts to confirm the findings reported here.

Two particular amplifications were distinct between these 2 groups, *CCNE1* and *FGFR1*. The *CCNE1* gene encodes for cyclin E, which has high oncogenic potential. *CCNE1* overexpression has been associated with worse overall survival, progression-free survival, and distant metastasis-free survival in multiple malignancies (7). *CCNE1* upregulation has been associated with platinum-based therapy resistance as shown in ovarian, endometrial, and bladder cancers (8–11). There is a significant association between *CCNE1* amplification and primary platinum-based treatment resistance in ovarian cancer (10). Given that both platinum and  $^{177}\text{Lu}$ -PSMA are DNA damage-inducing therapies, the link between  $^{177}\text{Lu}$ -PSMA treatment and resistance seems particularly plausible. More studies are needed to verify the validity of these findings.

*FGFR1* amplification is associated with upregulation of fibroblast growth factor receptor 1, which is responsible for the activation of multiple downstream oncogenic pathways, such as those associated with *MAPK*, *AKT*, and *STAT* signaling (12). Overexpression of fibroblast growth factor receptor 1 correlates with resistance to letrozole and cyclin-dependent kinase inhibitors in breast cancer (13,14). The utility of *FGFR1* amplification as a marker of therapeutic resistance in prostate cancer needs additional exploration.

*CDK12* mutations are well known to have adverse effects on prognosis in mCRPC (15). In addition, *CDK12* mutations are known to be deleterious for those prostate cancer patients treated with a variety of agents, including hormonal therapies, taxane chemotherapy, and poly(adenosine diphosphate ribose) polymerase inhibitors (16,17). Thus, perhaps it is not surprising that *CDK12* mutations are linked to  $^{177}\text{Lu}$ -PSMA resistance. Patients with *CDK12* mutations do poorly after a wide variety of treatments, not just  $^{177}\text{Lu}$ -PSMA. Several serum clinical and laboratory variables were predictive of no PSA decline in this small series. Higher alkaline phosphatase and lactate dehydrogenase levels have been adverse prognostic factors in multiple prostate cancer studies (18,19). Liver metastatic disease is a well-known adverse prognostic factor in advanced prostate cancer (2,18). Thus, despite being a

small series, the fact that adverse prognostic findings previously reported were independently detected here suggests that our series has similarities to other larger datasets.

It is important to emphasize that our data are likely prognostic and not predictive with regard to  $^{177}\text{Lu}$ -PSMA-based therapies. These data should not be used to make therapeutic choices at this time. First and most importantly, these data should be regarded as preliminary, and further validation is needed. Second with regard to therapeutic choices for  $^{177}\text{Lu}$ -PSMA versus other alternative therapies for mCRPC is that, clearly, these data do not adequately address clinical decision-making. Additional prospective trials would be required to make conclusions regarding predictive versus prognostic attributes of the biomarkers reported here.

There were several limitations to this study, including its small sample size and the fact that it took place at a single institution in which patients were treated with various PSMA agents. Although PSA changes are a well-accepted response biomarker, the more important and clinically relevant parameters related to radiographic response, time to radiographic progression, and overall survival were not assessed. Further, the sample size precluded multivariate analyses, which are most appropriate to ascertain. Interactions between PSMA PET parameters and ctDNA were not assessed. Given the degree of genetic heterogeneity, it is difficult to draw conclusions about many of the ctDNA abnormalities noted, and much larger studies would be required to better understand the prognostic and predictive importance of the individual genetic mutations in these mCRPC patients. The lack of multiple-hypothesis testing represents a limitation, and different statistical methods could potentially lead to different conclusions.

We also note that the genetic landscape assessed by Guardant360 assays is incomplete (20). This particular assay does not assess all the prostate cancer-relevant genes and furthermore has distinct limitations with regard to the detection of genetic deletions. More depth to the ctDNA analyses, or tissue-based biopsies, may yield distinct answers. Ideally, one would ascertain the importance of these findings in the context of multiple clinical and laboratory variables and use much larger patient series.

Taken together, despite these limitations, the role of ctDNA as a biomarker for response when using  $^{177}\text{Lu}$ -PSMA-based therapies is important to assess. Such analyses are important in the prognosis for a variety of cancers and a variety of treatments. The alterations identified here seem plausible on the basis of outcomes in other cancers and when using other therapies. Clearly, larger studies are justified to better understand the relationships between PSMA-targeted radioligand therapy and somatic genetics as assessed by ctDNA.

## CONCLUSION

In this small series of mCRPC patients treated with  $^{177}\text{Lu}$ -PSMA therapy, baseline ctDNA distinctions were found between those with and without PSA declines of 50% or more. These ctDNA abnormalities included mutations in *CDK12* or amplifications in *CCNE1* and *FGFR1*. In addition, higher levels of lactate dehydrogenase and alkaline phosphatase and the presence of liver metastases were associated with a lower probability of PSA response. Additional confirmatory studies are required before these data can be used for personalized treatment decisions in the clinic.

## DISCLOSURE

Oliver Sartor is a consultant to ArtBio, Point, Fusion, Telix, Bayer, Novartis, Pfizer, Merck, ITM, Sanofi, Eisai, Lantheus, and



AstraZeneca and receives research support from Telix, Bayer, Novartis, AstraZeneca, and Merck. Pedro Barata is a consultant or on the speakers' bureau for Astellas, AstraZeneca, Eisai, Exelixis, Janssen, EMD Serono, Dendreon, Pfizer, Seattle Genetics, BMS, Bayer, Guardant Health, Caris Life Sciences, and Sanofi and receives research support from AstraZeneca, Merck, Caris, Essa, Blue Earth, Merck, Exelixis, and Merus. No other potential conflict of interest relevant to this article was reported.

## KEY POINTS

**QUESTION:** What molecular factors are associated with resistance to  $^{177}\text{Lu}$ -PSMA therapy for patients with metastatic castration-resistant prostate cancer?

**PERTINENT FINDINGS:** Using circulating tumor DNA, we have determined that amplifications in *CCNE1* and *FGFR1* as well as pathogenic mutations in *CDK12* are associated with resistance to  $^{177}\text{Lu}$ -PSMA therapies.

**IMPLICATIONS FOR PATIENT CARE:** Determination of factors associated with resistance to  $^{177}\text{Lu}$ -PSMA may help clinicians make better treatment decisions for patients with advanced prostate cancer.

## REFERENCES

1. Sartor O, de Bono J, Chi KN, et al. Lutetium-177-PSMA-617 for metastatic castration-resistant prostate cancer. *N Engl J Med*. 2021;385:1091–1103.
2. Gafita A, Calais J, Grogan TR, et al. Nomograms to predict outcomes after  $^{177}\text{Lu}$ -PSMA therapy in men with metastatic castration-resistant prostate cancer: an international, multicentre, retrospective study. *Lancet Oncol*. 2021;22:1115–1125.
3. Buteau JP, Martin AJ, Emmett L, et al. PSMA and FDG-PET as predictive and prognostic biomarkers in patients given [ $^{177}\text{Lu}$ ]Lu-PSMA-617 versus cabazitaxel for metastatic castration-resistant prostate cancer (TheraP): a biomarker analysis from a randomised, open-label, phase 2 trial. *Lancet Oncol*. 2022;23:1389–1397.
4. Mehra N, Dolling D, Sumanasuriya S, et al. Plasma cell-free DNA concentration and outcomes from taxane therapy in metastatic castration-resistant prostate cancer from two phase III trials (FIRSTANA and PROSELICA). *Eur Urol*. 2018;74:283–291.
5. Kwan EM, Wyatt AW, Chi KN. Towards clinical implementation of circulating tumor DNA in metastatic prostate cancer: opportunities for integration and pitfalls to interpretation. *Front Oncol*. 2022;12:1054497.
6. Odegaard JI, Vincent JJ, Mortimer S, et al. Validation of a plasma-based comprehensive cancer genotyping assay utilizing orthogonal tissue- and plasma-based methodologies. *Clin Cancer Res*. 2018;24:3539–3549.
7. Zhao H, Wang J, Zhang Y, et al. Prognostic values of CCNE1 amplification and overexpression in cancer patients: a systematic review and meta-analysis. *J Cancer*. 2018;9:2397–2407.
8. Xu H, George E, Kinose Y, et al. CCNE1 copy number is a biomarker for response to combination WEE1-ATR inhibition in ovarian and endometrial cancer models. *Cell Rep Med*. 2021;2:100394.
9. Patch AM, Christie EL, Etemadmoghadam D, et al. Whole-genome characterization of chemoresistant ovarian cancer. *Nature*. 2015;521:489–494.
10. Etemadmoghadam D, deFazio A, Beroukhi R, et al. Integrated genome-wide DNA copy number and expression analysis identifies distinct mechanisms of primary chemoresistance in ovarian carcinomas. *Clin Cancer Res*. 2009;15:1417–1427.
11. Kim SH, Ho JN, Jin H, et al. Upregulated expression of BCL2, MCM7, and CCNE1 indicate cisplatin-resistance in the set of two human bladder cancer cell lines: T24 cisplatin sensitive and T24R2 cisplatin resistant bladder cancer cell lines. *Investig Clin Urol*. 2016;57:63–72.
12. Gallo LH. FGFR1, a novel biomarker for metastatic castration-resistant prostate cancer? *Oncotarget*. 2021;12:1026–1028.
13. Servetto A, Kollipara R, Formisano L, et al. Nuclear FGFR1 regulates gene transcription and promotes antiestrogen resistance in ER(+) breast cancer. *Clin Cancer Res*. 2021;27:4379–4396.
14. Formisano L, Lu Y, Servetto A, et al. Aberrant FGFR signaling mediates resistance to CDK4/6 inhibitors in ER+ breast cancer. *Nat Commun*. 2019;10:1373.
15. Rescigno P, Gurel B, Pereira R, et al. Characterizing CDK12-mutated prostate cancers. *Clin Cancer Res*. 2021;27:566–574.
16. Antonarakis ES, Isaacs Velho P, Fu W, et al. CDK12-altered prostate cancer: clinical features and therapeutic outcomes to standard systemic therapies, poly (ADP-ribose) polymerase inhibitors, and PD-1 inhibitors. *JCO Precis Oncol*. 2020;4:370–381.
17. Schweizer MT, Ha G, Gulati R, et al. CDK12-mutated prostate cancer: clinical outcomes with standard therapies and immune checkpoint blockade. *JCO Precis Oncol*. 2020;4:382–392.
18. Halabi S, Lin CY, Kelly WK, et al. Updated prognostic model for predicting overall survival in first-line chemotherapy for patients with metastatic castration-resistant prostate cancer. *J Clin Oncol*. 2014;32:671–677.
19. Sartor O, Coleman RE, Nilsson S, et al. An exploratory analysis of alkaline phosphatase, lactate dehydrogenase, and prostate-specific antigen dynamics in the phase 3 ALSYMPCA trial with radium-223. *Ann Oncol*. 2017;28:1090–1097.
20. Taavitsainen S, Annala M, Ledet E, et al. Evaluation of commercial circulating tumor DNA test in metastatic prostate cancer. *JCO Precis Oncol*. 2019;3:PO19.00014.

# [<sup>177</sup>Lu]Lu-PSMA-617 Versus Docetaxel in Chemotherapy-Naïve Metastatic Castration-Resistant Prostate Cancer: Final Survival Analysis of a Phase 2 Randomized, Controlled Trial

Swayamjeet Satapathy<sup>1</sup>, Bhagwant Rai Mittal<sup>1</sup>, Ashwani Sood<sup>1</sup>, Chandan Krushna Das<sup>2</sup>, Ravimohan Suryanarayan Mavuduru<sup>3</sup>, Shikha Goyal<sup>4</sup>, Jaya Shukla<sup>1</sup>, and Shrawan Kumar Singh<sup>3</sup>

<sup>1</sup>Department of Nuclear Medicine, Post Graduate Institute of Medical Education and Research, Chandigarh, India; <sup>2</sup>Department of Clinical Hematology and Medical Oncology, Post Graduate Institute of Medical Education and Research, Chandigarh, India; <sup>3</sup>Department of Urology, Post Graduate Institute of Medical Education and Research, Chandigarh, India; and <sup>4</sup>Department of Radiotherapy, Post Graduate Institute of Medical Education and Research, Chandigarh, India

The prostate-specific membrane antigen (PSMA) inhibitor [<sup>177</sup>Lu]Lu-PSMA-617 has been previously demonstrated to be noninferior to docetaxel in achieving a biochemical response in chemotherapy-naïve metastatic castration-resistant prostate cancer patients. Here, we report the final analysis of overall survival (OS) for a phase 2 randomized, controlled trial. **Methods:** Forty chemotherapy-naïve, PSMA-positive metastatic castration-resistant prostate cancer patients were randomly assigned to [<sup>177</sup>Lu]Lu-PSMA-617 ( $n = 20$ ) or docetaxel ( $n = 20$ ). Thirty-five patients received treatment per the protocol. Survival analysis was done using Kaplan–Meier curves and the Cox regression model. **Results:** The mean follow-up duration was 33.4 mo. In intention-to-treat analysis, the median OS for the [<sup>177</sup>Lu]Lu-PSMA-617 and docetaxel arms was 15.0 mo (95% CI, 9.5–20.5 mo) and 15.0 mo (95% CI, 8.1–21.9 mo), respectively ( $P = 0.905$ ). In per-protocol analysis, the median OS was 19.0 mo (95% CI, 12.3–25.7 mo) versus 15.0 mo (95% CI, 8.1–21.9 mo), respectively ( $P = 0.712$ ). No significant difference in OS was observed between the 2 arms across the analyzed subgroups. **Conclusion:** Long-term outcomes with [<sup>177</sup>Lu]Lu-PSMA-617 administered earlier in the prechemotherapy setting are comparable to those with docetaxel.

**Key Words:** mCRPC; [<sup>177</sup>Lu]Lu-PSMA-617; docetaxel; overall survival; randomized, controlled trial

J Nucl Med 2023; 64:1726–1729

DOI: 10.2967/jnumed.123.266141

Prostate cancer is the most common cancer in men, with a projected 288,300 new cases and 34,700 deaths in the United States in 2023 (1). Despite androgen deprivation, around 10%–20% of prostate cancer patients progress to a more aggressive castration-resistant state (2). Although a few drugs have been shown to improve survival outcomes in metastatic castration-resistant prostate cancer (mCRPC), it continues to remain a therapeutic challenge (3,4). [<sup>177</sup>Lu]Lu-PSMA-617 has recently emerged as a viable treatment option for mCRPC (5). Subsequent to the landmark TheraP and VISION trials, [<sup>177</sup>Lu]Lu-PSMA-617 has been recommended as

a third-line treatment for mCRPC patients after progression with at least one taxane and one androgen-receptor pathway inhibitor (6–8). However, data on earlier lines vis-à-vis other treatment options remain limited.

The use of [<sup>177</sup>Lu]Lu-PSMA-617 in the chemotherapy-naïve setting was evaluated previously in a randomized, phase 2 trial. In this trial, we randomized chemotherapy-naïve mCRPC patients with highly prostate-specific membrane antigen (PSMA)-expressing lesions to [<sup>177</sup>Lu]Lu-PSMA-617 or docetaxel. The trial demonstrated the noninferiority of [<sup>177</sup>Lu]Lu-PSMA-617 versus docetaxel for the primary endpoint of biochemical response rate in a per-protocol analysis (60% vs. 40%, respectively,  $P = 0.250$ ). Further, whereas the progression-free survival was also similar between the 2 interventions, [<sup>177</sup>Lu]Lu-PSMA-617 resulted in less frequent serious adverse events than docetaxel (9). Here, we report the results of the final overall survival (OS) analysis after a mean follow-up of about 3 y.

## MATERIALS AND METHODS

This investigator-initiated, randomized, parallel-group, open-label, phase 2 noninferiority trial was performed between December 2019 and March 2021. Chemotherapy-naïve patients with mCRPC and high PSMA expression were recruited. High PSMA expression was defined as tracer avidity in which at least 80% of the lesions were significantly ( $\geq 1.5$  times) more avid than normal liver on [<sup>68</sup>Ga]Ga-PSMA-11 PET/CT and none of the lesions had uptake less than that of the liver. The full inclusion and exclusion criteria have been described previously and briefly outlined in Supplemental Table 1 (supplemental materials are available at <http://jnm.snmjournals.org>) (9). Informed written consent was obtained from the patients before inclusion. The study was approved by the Institute Ethics Committee (INT/IEC/2019/001972) and followed the Helsinki Declaration guidelines. The trial was prospectively registered at the Clinical Trials Registry–India (CTRI/2019/12/022282).

Forty eligible patients were randomly assigned in a 1:1 ratio to either [<sup>177</sup>Lu]Lu-PSMA-617 (6.0–7.4 GBq/cycle intravenously, up to 4 cycles, 8–12 wk apart) or docetaxel (75 mg/m<sup>2</sup>/cycle intravenously, up to 10 cycles, 3 wk apart). The primary endpoint of best prostate-specific antigen response rate, and secondary endpoints comprising best objective response rate, molecular response rate, progression-free survival, toxicity, and quality-of-life outcomes, have been reported previously (9). The final endpoint, that is, OS, was planned to be analyzed after 70% data maturity, that is, at least 28 events. OS was estimated from the time of treatment initiation to death due to any cause.

Received Jun. 7, 2023; revision accepted Aug. 18, 2023.  
For correspondence or reprints, contact Bhagwant Rai Mittal (brmittal@yahoo.com).

Published online Sep. 14, 2023.

COPYRIGHT © 2023 by the Society of Nuclear Medicine and Molecular Imaging.

The primary analysis was by intention to treat and included all randomized patients. A per-protocol sensitivity analysis was also done by including only those patients who underwent at least half the allocated treatment—that is, received at least 2 cycles of  $^{177}\text{Lu}$ -PSMA-617 or at least 5 cycles of docetaxel. Statistical analyses were done using IBM SPSS Statistics (version 20.0 for Microsoft Windows) and Stata (version 14.2). Categorical variables were expressed as numbers and percentages, and the  $\chi^2$  test was used for intergroup comparison. Survival analysis was done using the Kaplan–Meier curve method and the Cox proportional-hazards model. The proportional-hazards assumption was checked by the Schoenfeld residuals test. Mean follow-up was calculated using the reverse Kaplan–Meier method. The log-rank test was used to compare the median OS between groups. A 2-tailed  $P$  value of less than 0.05 was considered statistically significant.

## RESULTS

Between December 2019 and March 2021, 40 chemotherapy-naïve mCRPC patients underwent randomization. Twenty patients each were assigned to the  $^{177}\text{Lu}$ -PSMA-617 and docetaxel arms, with similar characteristics at baseline (Supplemental Table 2). Of these, 35 patients received treatment per the protocol: 15 of 20 patients in the  $^{177}\text{Lu}$ -PSMA-617 arm and 20 of 20 patients in the docetaxel arm (Supplemental Fig. 1). Five patients in the  $^{177}\text{Lu}$ -PSMA-617 arm could not complete 2 cycles—because of disease progression in 2 patients, disease-related death in 2 patients, and treatment-related severe myelosuppression in 1 patient.

As of May 31, 2023, the patients had a mean follow-up of 33.4 mo (95% CI, 28.0–38.9 mo). Further posttrial treatments were received by 9 of 20 (45%) patients in the  $^{177}\text{Lu}$ -PSMA-617 arm, compared with 12 of 20 (60%) patients in the docetaxel arm ( $P = 0.342$ ) (Table 1). Notably, 30% of the patients in the  $^{177}\text{Lu}$ -PSMA-617 arm could switch over to docetaxel, in contrast to 5% of the patients in the docetaxel arm who could receive  $^{177}\text{Lu}$ -PSMA-617 subsequently ( $P = 0.038$ ).

Twenty-nine of the 40 (72.5%) patients died in the course of follow-up. Two patients each in the  $^{177}\text{Lu}$ -PSMA-617 and docetaxel arms were alive at the last cutoff date; however, 7 patients (3 in the  $^{177}\text{Lu}$ -PSMA-617 arm and 4 in the docetaxel arm) were lost to follow-up. The proportional-hazards assumption was met with a nonsignificant Schoenfeld residuals test ( $P = 0.638$ ). In intention-to-treat analysis, the median OS for the  $^{177}\text{Lu}$ -PSMA-617 and docetaxel arms was 15.0 mo (95% CI, 9.5–20.5 mo) and 15.0 mo

(95% CI, 8.1–21.9 mo), respectively ( $P = 0.905$ ) (Fig. 1). In the per-protocol analysis, the median OS for the  $^{177}\text{Lu}$ -PSMA-617 arm was 19.0 mo (95% CI, 12.3–25.7 mo), versus 15.0 mo (95% CI, 8.1–21.9 mo) for the docetaxel arm ( $P = 0.712$ ) (Fig. 2). No significant difference in OS was observed between the 2 arms across the analyzed subgroups (Table 2).

## DISCUSSION

$^{177}\text{Lu}$ -PSMA-617 has been previously shown to improve survival outcomes in the postchemotherapy mCRPC setting (6,7). To the best of our knowledge, this is one of the first trials evaluating  $^{177}\text{Lu}$ -PSMA-617 in the chemotherapy-naïve space. An important highlight of this study was the use of docetaxel as an active comparator. This is in contrast to other upcoming trials with  $^{177}\text{Lu}$ -PSMA radioligand therapy in the prechemotherapy setting (but after one line of androgen-receptor pathway inhibitor) wherein control group patients are switched over to another drug of the same class (PSMAfore and SPLASH). The fact that a second-line androgen-receptor pathway inhibitor often has limited activity (especially in the presence of a first-line novel androgen-receptor inhibitor such as enzalutamide) was the reason why we compared  $^{177}\text{Lu}$ -PSMA-617 and docetaxel in a noninferiority design in our trial (10). We have demonstrated earlier that  $^{177}\text{Lu}$ -PSMA-617 is not inferior to docetaxel in terms of the short-term outcome, that is, biochemical response rate (9). The current results indicate that even the long-term outcome with  $^{177}\text{Lu}$ -PSMA-617 administered earlier in the prechemotherapy setting is comparable to that with docetaxel.

The toxicity profiles of both arms in this trial have been extensively reported. Briefly, adverse events of grade 3 or higher occurred less frequently with  $^{177}\text{Lu}$ -PSMA-617 (30%) than with docetaxel (50%). This finding was also accompanied by an improvement in the quality of life of the patients receiving  $^{177}\text{Lu}$ -PSMA-617 (9).

**TABLE 1**  
Posttrial Treatments

Treatment option	$^{177}\text{Lu}$ -PSMA-617 arm* (n = 20)	Docetaxel arm (n = 20)
Docetaxel	6 (30)	0 (0)
Abiraterone	1 (5)	3 (15)
Enzalutamide	5 (25)	9 (45)
Rucaparib	1 (5)	0 (0)
Carboplatin	1 (5)	0 (0)
$^{177}\text{Lu}$ -PSMA-617	0 (0)	1 (5)
$^{225}\text{Ac}$ -PSMA-617	1 (5)	0 (0)

\*Few patients received more than one subsequent treatment. Data are number followed by percentage in parentheses.

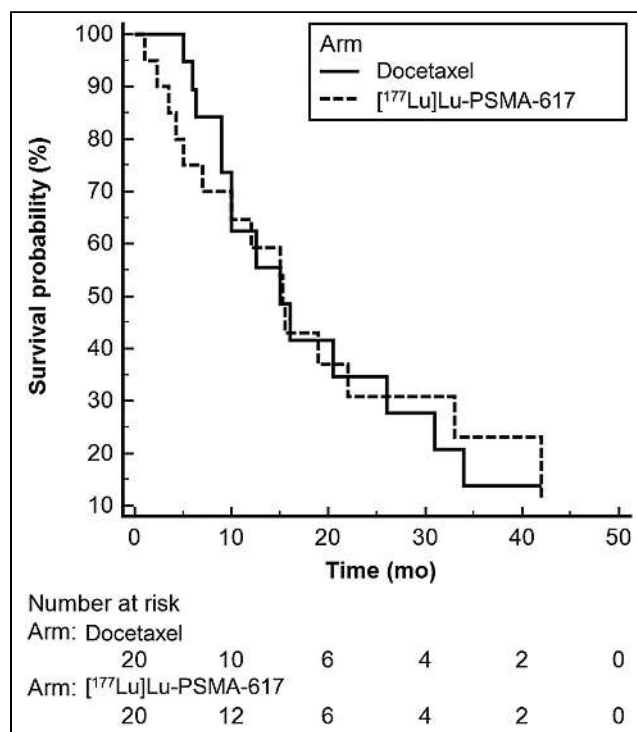


**FIGURE 1.** Kaplan–Meier curves for OS in intention-to-treat analysis.

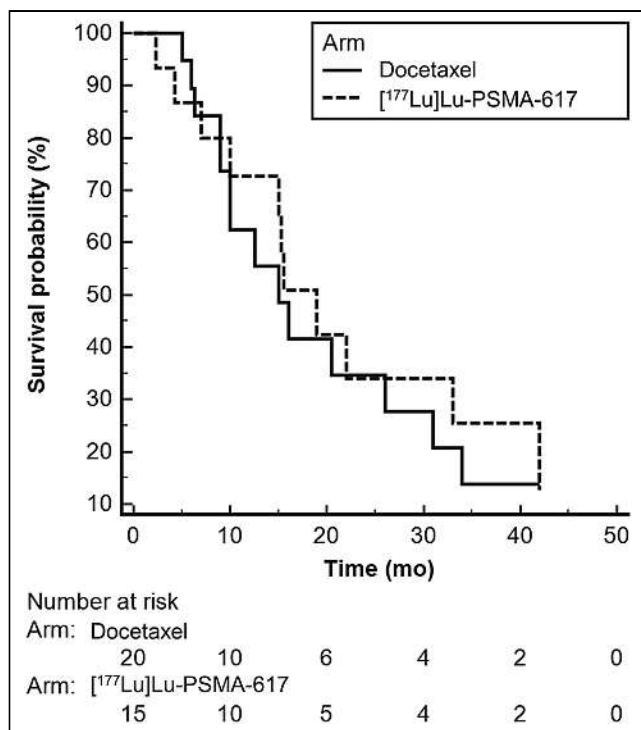


**FIGURE 2.** Kaplan–Meier curves for OS in per-protocol analysis.

Further, whereas a similar number of patients received subsequent therapies in both arms, the better safety with [177Lu]Lu-PSMA-617 allowed a higher proportion of patients to cross over to docetaxel. In contrast, only one patient in the docetaxel arm could receive [177Lu]Lu-PSMA-617 subsequently. These results indicate that contrary to the previous perception, early institution of

[177Lu]Lu-PSMA-617 does not significantly impair the ability to tolerate future treatments. Given its comparable efficacy over the short term as well as the long term, administration of [177Lu]Lu-PSMA-617 in the prechemotherapy setting therefore has the added advantages of less frequent treatment cycles, less toxicity, and preservation of patients' quality of life.

In the current trial, we observed a median OS of 15 mo in both the [177Lu]Lu-PSMA-617 arm and the docetaxel arm. However, this OS was similar to that reported with the [177Lu]Lu-PSMA-617 arm in the phase 3 VISION trial in the postchemotherapy setting (7). Given that our trial was conducted in the prechemotherapy space, a longer OS was expected. A few factors could have adversely impacted our results: a higher percentage of patients with extensive skeletal metastases, more frequent prior treatments with both abiraterone and enzalutamide in the [177Lu]Lu-PSMA-617 arm, a higher percentage of patients with extrapulmonary visceral metastases, lack of a baseline 2-[18F]FDG PET/CT scan to exclude patients with discordant PSMA-negative/2-[18F]FDG-positive lesions, and a treatment delay due to the coronavirus disease 2019 pandemic (9). Despite these factors, the comparability of the outcomes with [177Lu]Lu-PSMA-617 and docetaxel adds value to our study.

The OS results with [177Lu]Lu-PSMA-617 in our chemotherapy-naïve patients need to be seen further in the context of our other patients who were previously treated with chemotherapy. In a separate analysis comprising such heavily pretreated patients, we observed a median OS of 9.0 mo (11). The longer median OS in our chemotherapy-naïve patients therefore roughly translates to a hazard ratio of 0.60, that is, a 40% reduction in the risk of death. This is in agreement with the findings of a recent metaanalysis comparing [177Lu]Lu-PSMA radioligand therapy efficacy outcomes in chemotherapy-naïve versus chemotherapy-treated patients. In this pooled analysis comprising more than 2,000 patients, taxane-naïve patients had a 1.8 times improved odds of a biochemical response, a 40% reduced risk of progression, and a 46% reduced

**TABLE 2**  
Subgroup Regression Analyses for OS in [177Lu]Lu-PSMA-617 Versus Docetaxel Arms

Variable	HR	95% CI	P
<b>Age</b>			
<70 y (n = 24)	0.99	0.39–2.52	0.976
≥70 y (n = 16)	1.09	0.33–3.64	0.882
<b>Gleason score</b>			
<8 (n = 14)	1.77	0.47–6.61	0.397
≥8 (n = 26)	0.70	0.28–1.78	0.454
<b>Prior androgen-receptor pathway inhibitor</b>			
No (n = 14)	0.37	0.09–1.48	0.159
Yes (n = 26)	1.94	0.75–4.99	0.172
<b>Extent of skeletal disease</b>			
<10 lesions (n = 8)	2.54	0.35–18.45	0.357
≥10 lesions (n = 32)	0.77	0.33–1.78	0.540
<b>Visceral metastasis</b>			
No (n = 31)	0.86	0.36–2.08	0.744
Yes (n = 9)	2.47	0.57–10.69	0.226

HR = hazard ratio.

risk of death after [<sup>177</sup>Lu]Lu-PSMA radioligand therapy compared with their taxane-treated counterparts (12).

The current analysis has one key limitation. The study sample size was based on the primary endpoint of prostate-specific antigen response rate and was not adequately powered for other analyses. Nevertheless, this remains one of the first trials reporting final survival outcomes with [<sup>177</sup>Lu]Lu-PSMA-617 in the chemotherapy-naïve setting. The use of an active comparator agent, a prolonged follow-up, and mature data for OS constitute major strengths of this study.

## CONCLUSION

On the basis of the results of this phase 2 study, long-term outcomes with [<sup>177</sup>Lu]Lu-PSMA-617 administered earlier in the pre-chemotherapy setting are comparable to those with docetaxel. Further trials powered for survival analyses are required to validate our observations.

## KEY POINTS

**QUESTION:** How does [<sup>177</sup>Lu]Lu-PSMA-617 impact OS vis-à-vis docetaxel in chemotherapy-naïve mCRPC patients?

**PERTINENT FINDINGS:** This randomized, controlled phase 2 trial assigned 40 chemotherapy-naïve, PSMA-positive mCRPC patients in a 1:1 ratio to [<sup>177</sup>Lu]Lu-PSMA-617 or docetaxel. Over a mean follow-up of 33.4 mo, the median OS for the [<sup>177</sup>Lu]Lu-PSMA-617 and docetaxel arms was 15.0 mo (95% CI, 9.5–20.5 mo) and 15.0 mo (95% CI, 8.1–21.9 mo), respectively ( $P = 0.905$ ). No significant difference in OS was observed between the 2 arms across the analyzed subgroups.

**IMPLICATIONS FOR PATIENT CARE:** Showing long-term outcomes comparable to those of docetaxel in the chemotherapy-naïve mCRPC setting, [<sup>177</sup>Lu]Lu-PSMA-617 can be a potential alternative earlier in the disease course.

## DISCLOSURE

No potential conflict of interest relevant to this article was reported.

## ACKNOWLEDGMENT

We thank Ashish Kumar for his assistance in updating the patients' records.

## REFERENCES

1. Siegel RL, Miller KD, Wagle NS, Jemal A. Cancer statistics, 2023. *CA Cancer J Clin.* 2023;73:17–48.
2. Vellky JE, Ricke WA. Development and prevalence of castration-resistant prostate cancer subtypes. *Neoplasia.* 2020;22:566–575.
3. Cornford P, Bellmunt J, Bolla M, et al. EAU-ESTRO-SIOG guidelines on prostate cancer. Part II: treatment of relapsing, metastatic, and castration-resistant prostate cancer. *Eur Urol.* 2017;71:630–642.
4. Ingrosso G, Detti B, Scartoni D, et al. Current therapeutic options in metastatic castration-resistant prostate cancer. *Semin Oncol.* 2018;45:303–315.
5. Sartor O, Herrmann K. Prostate cancer treatment: <sup>177</sup>Lu-PSMA-617 considerations, concepts, and limitations. *J Nucl Med.* 2022;63:823–829.
6. Hofman MS, Emmett L, Sandhu S, et al. [<sup>177</sup>Lu]Lu-PSMA-617 versus cabazitaxel in patients with metastatic castration-resistant prostate cancer (TheraP): a randomised, open-label, phase 2 trial. *Lancet.* 2021;397:797–804.
7. Sartor O, de Bono J, Chi KN, et al. Lutetium-177-PSMA-617 for metastatic castration-resistant prostate cancer. *N Engl J Med.* 2021;385:1091–1103.
8. Garje R, Rumble RB, Parikh RA. Systemic therapy update on <sup>177</sup>lutetium-PSMA-617 for metastatic castration-resistant prostate cancer: ASCO rapid recommendation. *J Clin Oncol.* 2022;40:3664–3666.
9. Satapathy S, Mittal BR, Sood A, et al. <sup>177</sup>Lu-PSMA-617 versus docetaxel in chemotherapy-naïve metastatic castration-resistant prostate cancer: a randomized, controlled, phase 2 non-inferiority trial. *Eur J Nucl Med Mol Imaging.* 2022;49:1754–1764.
10. Khalaf DJ, Annala M, Taavitsainen S, et al. Optimal sequencing of enzalutamide and abiraterone acetate plus prednisone in metastatic castration-resistant prostate cancer: a multicentre, randomised, open-label, phase 2, crossover trial. *Lancet Oncol.* 2019;20:1730–1739.
11. Satapathy S, Das CK, Aggarwal P, et al. Genomic characterization of metastatic castration-resistant prostate cancer patients undergoing PSMA radioligand therapy: a single-center experience. *Prostate.* 2023;83:169–178.
12. Satapathy S, Sahoo RK, Bal C. [<sup>177</sup>Lu]Lu-PSMA-radioligand therapy efficacy outcomes in taxane-naïve versus taxane-treated patients with metastatic castration-resistant prostate cancer: a systematic review and metaanalysis. *J Nucl Med.* 2023; 64:1266–1271.



# Antihormonal-Treatment Status Affects $^{68}\text{Ga}$ -PSMA-HBED-CC PET Biodistribution in Patients with Prostate Cancer

Kilian Kluge<sup>1,2</sup>, David Haberl<sup>1,2</sup>, Holger Einspieler<sup>1</sup>, Sazan Rasul<sup>1</sup>, Sebastian Gutschmayer<sup>3</sup>, Lukas Kenner<sup>2,4</sup>, Gero Kramer<sup>5</sup>, Bernhard Grubmüller<sup>5,6,7</sup>, Shahrokh Shariat<sup>5,8-12</sup>, Alexander Haug<sup>1,2</sup>, and Marcus Hacker<sup>1</sup>

<sup>1</sup>Department of Biomedical Imaging and Image-Guided Therapy, Division of Nuclear Medicine, Medical University of Vienna, Vienna, Austria; <sup>2</sup>Christian Doppler Laboratory for Applied Metabolomics, Medical University of Vienna, Vienna, Austria; <sup>3</sup>QIMP Team, Medical University of Vienna, Vienna, Austria; <sup>4</sup>Department of Pathology, Medical University of Vienna, Vienna, Austria; <sup>5</sup>Department of Urology, Medical University of Vienna, Vienna, Austria; <sup>6</sup>Department of Urology and Andrology, University Hospital Krems, Krems, Austria; <sup>7</sup>Karl Landsteiner University of Health Sciences, Krems, Austria; <sup>8</sup>Karl Landsteiner Institute of Urology and Andrology, Vienna, Austria; <sup>9</sup>Department of Urology, University of Texas Southwestern Medical Center, Dallas, Texas; <sup>10</sup>Division of Urology, Department of Special Surgery, University of Jordan, Amman, Jordan; <sup>11</sup>Department of Urology, Second Faculty of Medicine, Charles University, Prague, Czech Republic; and <sup>12</sup>Department of Urology, Weill Cornell Medical College, New York, New York

J Nucl Med 2023; 64:1730–1736  
DOI: 10.2967/jnumed.123.265980

Androgen deprivation therapy (ADT) is known to influence the prostate-specific membrane antigen (PSMA) expression of prostate cancer, potentially complicating the interpretation of PSMA ligand PET findings and affecting PSMA radioligand therapy. However, the impact of ADT on PSMA ligand biodistribution in nontumorous organs is not well understood. **Methods:** Men ( $n = 112$ ) with histologically proven prostate cancer who underwent  $^{68}\text{Ga}$ -PSMA-HBED-CC ( $^{68}\text{Ga}$ -PSMA-11) PET/CT between November 2015 and July 2021 at the Medical University Vienna with known ADT status were retrospectively recruited. Fifty-six patients were on gonadotropin-releasing hormone–interfering ADT at the time of imaging (ADT group), whereas 56 patients with no history of ADT served as a control group. Physiologically PSMA-expressing organs (salivary glands, kidneys, liver, and spleen) were delineated, and their uptake was compared according to their data distributions. Multivariate regression analysis assessed the relationship between renal, hepatic, splenic, and salivary gland uptake and the explanatory variables metabolic tumor volume, glomerular filtration rate, and ADT status. **Results:** ADT was associated with lower levels of PSMA uptake in the kidneys ( $\text{SUV}_{\text{mean}}: \Delta[\text{ADT} - \text{control}] = -7.89$ ; 95% CI,  $-10.73$  to  $-5.04$ ;  $P < 0.001$ ), liver ( $\text{SUV}_{\text{peak}}: \Delta[\text{ADT} - \text{control}] = -2.3$ ; 95% CI,  $-5.72$  to  $-0.93$ ;  $P = 0.003$ ), spleen ( $\text{SUV}_{\text{peak}}: \Delta[\text{ADT} - \text{control}] = -1.27$ ; 95% CI,  $-3.61$  to  $-0.16$ ;  $P = 0.033$ ), and salivary glands ( $\text{SUV}_{\text{mean}}: \Delta[\text{ADT} - \text{control}] = -1.04$ ; 95% CI,  $-2.48$  to  $-0.13$ ;  $P = 0.027$ ). In a multivariate analysis, ADT was found to be associated with lower renal ( $\text{SUV}_{\text{mean}}: \beta = -7.95$ ; 95% CI,  $-11.06$  to  $-4.84$ ;  $P < 0.0001$ ), hepatic ( $\text{SUV}_{\text{peak}}: \beta = -7.85$ ; 95% CI,  $-11.78$  to  $-3.91$ ;  $P < 0.0001$ ), splenic ( $\text{SUV}_{\text{peak}}: \beta = -5.83$ ; 95% CI,  $-9.95$  to  $-1.7$ ;  $P = 0.006$ ), and salivary gland ( $\text{SUV}_{\text{mean}}: \beta = -1.47$ ; 95% CI,  $-2.76$  to  $-0.17$ ;  $P = 0.027$ ) uptake. A higher glomerular filtration rate was associated with a higher renal  $\text{SUV}_{\text{mean}}$  ( $\beta = 0.16$ ; 95% CI,  $0.05$  to  $0.26$ ;  $P = 0.0034$ ). **Conclusion:** These findings suggest that ADT systemically modulates PSMA expression, which may have implications for treatment-optimizing and side-effect-minimizing strategies for PSMA radioligand therapies, particularly those using more potent  $^{225}\text{Ac}$ -labeled PSMA conjugates.

**Key Words:** androgen deprivation therapy; prostate cancer; biodistribution; PSMA PET

**M**olecular imaging and targeted radioligand therapy (RLT) with prostate-specific membrane antigen (PSMA) ligands have been major diagnostic and therapeutic advances in the management of men with prostate cancer (PCA).

In various preclinical and clinical studies (1), the expression of PSMA, a type II membrane glycoprotein found on most PCA cells (2) and physiologically on various organs (3), has been shown to be modulated by androgen signaling.

Although the exact underlying mechanism remains to be fully elucidated, early work hypothesized that the PSMA enhancer (4–6), 1 of 2 crucial regulatory elements of the PSMA gene *FOLH1* (7), is, inter alia, inversely and indirectly regulated through sequestration of PSMA enhancer regulating transcription factors (i.e., *SOX*, *SOX7*, *SRY*) by activated and nuclear-translocated androgen receptors (4).

Since then, various preclinical and clinical studies (1) have investigated the effects of androgen deprivation therapy (ADT), a long-established therapeutic cornerstone of PCA management, on PSMA expression of tumorous lesions in an effort to unfold androgen-induced clinical caveats of diagnostic and therapeutic PSMA radioligand use.

Although these studies yielded partly heterogeneous (8) and conflicting results (9), there is a growing body of evidence suggesting a time-dependent early upregulation (10,11) followed by a decrease in PSMA expression of PCA cells after long-term ADT exposure (12,13).

Although previous studies focused on ADT influences on tumoral tissue or short-term impact on physiologic PSMA-expressing organs (14), literature on physiologic organ uptake after sustained ADT exposure, a commonly encountered clinical scenario in advanced disease before RLT, is currently lacking.

Yet, understanding the influences of ADT on PSMA uptake in nontumorous organs such as the salivary glands and kidneys might have important implications for PSMA RLT, since common side effects such as xerostomia, as well as dose-limiting renal radiotoxicity (15), are functions of the PSMA ligand biodistribution.

Received May 3, 2023; revision accepted May 31, 2023.  
For correspondence or reprints, contact Marcus Hacker (marcus.hacker@medunivien.ac.at).  
Published online Sep. 21, 2023.  
COPYRIGHT © 2023 by the Society of Nuclear Medicine and Molecular Imaging.

The present study is meant to address this gap in knowledge.

We hypothesized that the PSMA expression of healthy organs would differ in men with PCA depending on their hormonal treatment status.

The objective of this study was to retrospectively compare the  $^{68}\text{Ga}$ -PSMA-HBED-CC ( $^{68}\text{Ga}$ -PSMA-11) PET uptake of the salivary glands, kidneys, liver, and spleen between patients on ADT and patients without any history of ADT.

## MATERIALS AND METHODS

### Study Design and Cohort Selection

The data of men with histologically proven PCA who underwent  $^{68}\text{Ga}$ -PSMA-11 imaging between November 2015 and July 2021 were screened retrospectively.

Patients with conclusive ADT history data were considered for inclusion. Patients on gonadotropin-releasing hormone analogs or antagonists (16) during imaging for at least 1 mo or with no history of any ADT were included.

Men on androgen-receptor,  $5\alpha$ -reductase, or CYP17A1 inhibitors were excluded to minimize confounding by heterogeneous treatment regimens.

Scans with metabolic tumor volumes (MTVs) greater than  $25\text{ cm}^3$  were excluded to avoid an influence on  $^{68}\text{Ga}$ -PSMA-11 biodistribution by the tumor sink effect (17).

All scans were performed after written informed consent was obtained for application of the nonapproved imaging compound  $^{68}\text{Ga}$ -PSMA-11, and the need for written informed consent for retrospective data collection and analysis was waived (ethics committee identification number 1745/2021).

The primary endpoint of this study was the  $\text{SUV}_{\text{mean}}$  and  $\text{SUV}_{\text{peak}}$  of organs with physiologic PSMA expression, namely the submandibular glands, kidneys, liver, and spleen. The secondary endpoints were the  $\text{SUV}_{\text{mean}}$  of organs according to midterm (1–6 mo) and long-term (>6 mo) ADT exposure when the primary endpoint was met.

### Imaging Protocol

All scans were obtained on a Biograph TruePoint PET/CT scanner (Siemens Healthineers). The patients were intravenously injected with a mean of  $182.6\text{ MBq}$  ( $\pm 18.7$  [SD]) of  $^{68}\text{Ga}$ -PSMA-11. Sixty minutes after injection, static, whole-body scans were obtained from the skull base to the upper femur. First, CT scans were acquired at 120 kV and 230 mAs with intravenous contrast medium (CT matrix size,  $512 \times 512$ ) unless contraindications for contrast application existed. Afterward, PET scans were acquired at 3–4 bed positions, reconstructed iteratively using a point-spread-function-based algorithm, and subsequently corrected for scatter and attenuation on the basis of the CT scan (PET matrix size,  $168 \times 168$ ).

### Image Analysis

Physiologically PSMA-expressing organs were assessed, namely the submandibular glands, kidneys, liver, and spleen. The submandibular glands were chosen as a surrogate for overall salivary gland PSMA uptake since they were fully included in most fields of view (except in 2 scans). The organs were delineated in a 2-step process. First, the deep-learning-based Multi-Organ Objective Segmentation framework (18) was used to obtain CT-defined organ delineations of the liver, spleen, and kidneys. Next, the framework-derived segmentations were reviewed and, if necessary, adjusted manually to the PET component using Slicer3D software (version 4.11) (19) by a nuclear medicine physician. The submandibular glands were delineated on the PET component using the semiautomated Slicer3D extension PETtumorSegmentation (20). Two nuclear medicine physicians delineated tumor lesions manually on a dedicated workstation using Hybrid 3D

software (version 4.17; Hermes Medical Solutions).  $\text{SUV}_{\text{mean}}$  and  $\text{SUV}_{\text{peak}}$  not corrected for lean body mass and MTV were extracted from the regions of interest.

### Statistical Analysis

Numeric variables were expressed as mean ( $\pm$ SD), and discrete outcomes were expressed as absolute ( $n$ ) and relative (%) frequencies. The group comparability of the control and ADT groups was assessed by comparing baseline demographic data. The normality and heteroskedasticity of continuous data were assessed with the Shapiro–Wilk and Levene tests, respectively. Continuous outcomes were compared using the unpaired Student  $t$  test, Welch  $t$  test, and Mann–Whitney  $U$  test according to the data distribution. Discrete outcomes were compared using the  $\chi^2$  or Fisher exact test accordingly. All tests were 2-tailed.

Statistical tests for differences in visceral organ metastasis PSMA uptake could not be computed because of the sample size ( $n = 1$  in the ADT group).

Differences between renal, hepatic, splenic, and salivary gland uptake were assessed according to prior cytotoxic treatments with chemotherapy or  $^{177}\text{Lu}$ -PSMA RLTs.

Additionally, differences between renal, hepatic, splenic, and salivary gland PSMA uptake were assessed according to midterm (1–6 mo) and long-term (>6 mo) ADT runtimes with ANOVA and the Kruskal–Wallis test according to the data distribution. If the null hypothesis of the ANOVA and the Kruskal–Wallis test was rejected, post hoc pairwise analyses were performed with the Tukey honestly significant difference test and the Dunn–Bonferroni test, respectively.

### Multivariate Regression Analysis

Multivariate regression analysis was performed to assess the relationship between renal and salivary gland  $\text{SUV}_{\text{mean}}$ , as well as the relationship of hepatic and splenic  $\text{SUV}_{\text{peak}}$  with the following explanatory variables: MTV, glomerular filtration rate, and ADT status. Data were checked for multicollinearity with the Belsley–Kuh–Welsch technique. The heteroskedasticity and normality of residuals were assessed by, respectively, the Breusch–Pagan test and the Shapiro–Wilk test. The  $\alpha$ -risk was set for all statistical analyses to 5% ( $\alpha = 0.05$ ).

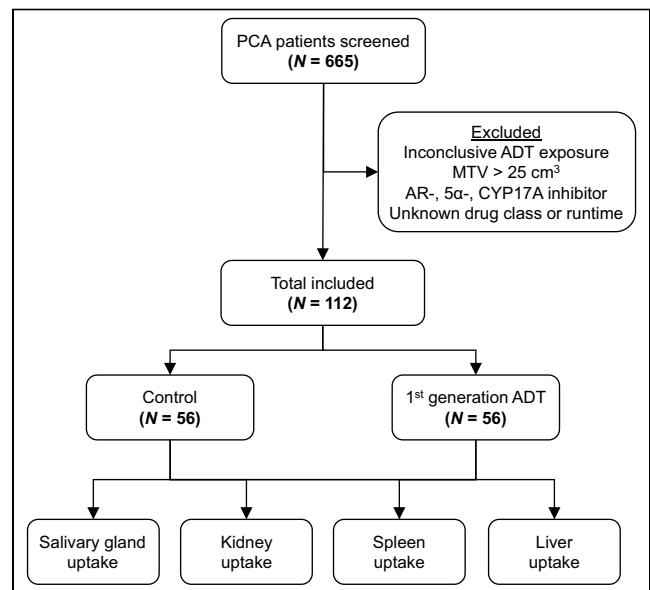


FIGURE 1. CONSORT (Consolidated Standards of Reporting Trials) diagram. AR = androgen receptor;  $5\alpha$ - =  $5\alpha$ -reductase.

Statistical analysis was performed with EasyMedStat software (version 3.24; EasyMedStat).

## RESULTS

### Clinical Cohort

Of 665 screened men with PCA and available PSMA PET/CT, 112 (17%) with a conclusive ADT treatment history at the time of imaging were entered into this study according to the inclusion criteria (Fig. 1). The demographic and clinical characteristics are summarized in Table 1.

### Organ PSMA Uptake Measurements

Differences in organ uptake between the ADT and control groups are summarized in Table 2.

There was a significantly lower mean renal  $SUV_{mean}$  ( $\Delta[ADT - control] = -7.89$ ; 95% CI,  $-10.73$  to  $-5.04$ ;  $P < 0.001$ ) and  $SUV_{peak}$  ( $\Delta[ADT - control] = -14.12$ ; 95% CI,  $-19.85$  to  $-8.39$ ;  $P < 0.001$ ) in the ADT group than in the control group. Similarly, median hepatic  $SUV_{peak}$  ( $\Delta[ADT - control] = -2.3$ ; 95% CI,  $-5.72$  to  $-0.93$ ;  $P = 0.003$ ), median splenic  $SUV_{peak}$  ( $\Delta[ADT - control] = -1.27$ ; 95% CI,  $-3.61$  to  $-0.16$ ;  $P = 0.033$ ), and median salivary gland  $SUV_{mean}$  ( $\Delta[ADT - control] = -1.04$ ; 95% CI,  $-2.48$  to  $-0.13$ ;  $P = 0.027$ ) and mean  $SUV_{peak}$  ( $\Delta[ADT - control] = -3.31$ ; 95% CI,  $-5.3$  to  $-1.31$ ;  $P = 0.001$ ) were significantly lower in the ADT group (Fig. 2).

### Secondary Endpoint Analysis According to ADT Runtime Length

The mean renal  $SUV_{mean}$  was 29.5 (SD, 7.2), 21.6 (SD, 8.37), and 21.61 (SD, 7.61) for the control group, patients on 1–6 mo of

**TABLE 1**  
Demographic and Clinical Patient Data

Variable	Control (n = 56)	ADT (n = 56)	P
Age (y)	69.6 ( $\pm 7.2$ )	70.4 ( $\pm 8.0$ )	0.58
Weight (kg)	86.2 ( $\pm 12.6$ )	83.4 ( $\pm 13.6$ )	0.31
Tracer dose (MBq)	181.8 ( $\pm 18.1$ )	183.4 ( $\pm 19.4$ )	0.59
PSA ( $\mu\text{g/dL}$ )*	13.0 ( $\pm 46.1$ )	7.1 ( $\pm 12.6$ )	0.06
GFR (mL/min) <sup>†</sup>	78.4 ( $\pm 15.5$ )	81.0 ( $\pm 14.2$ )	0.39
MTV (cm <sup>3</sup> )	3.3 ( $\pm 5.3$ )	5.0 ( $\pm 6.2$ )	0.20
PSMA-positive lesions			
Prostate	21 (37.5%)	21 (37.5%)	>0.99
Lymph nodes	19 (33.9%)	14 (25.0%)	0.41
Bone	8 (14.3%)	18 (32.1%)	0.04
Viscera (lung)	2 (3.6%)	1 (1.8%)	>0.99
Mean lesional $SUV_{mean}$			
Prostate	13.1 ( $\pm 11.4$ )	10.8 ( $\pm 8.4$ )	0.43
Lymph nodes	7.5 ( $\pm 4.3$ )	10.39 ( $\pm 6.3$ )	0.13
Bone	4.9 ( $\pm 2.2$ )	9.4 ( $\pm 12.5$ )	0.84
Viscera (lung)	4.79 (4.0–5.6)	7.7	— <sup>‡</sup>
Mean ADT runtime (m)	—	24.0 $\pm$ 34.9	
Runtimes binned (m)			
1–6	—	15 (26.8%)	
>6	—	41 (73.2%)	
ADT drug class			
GnRH analog			
Leuprorelin	—	38 (67.9%)	
Triptorelin	—	2 (3.6%)	
GnRH antagonist			
Degarelix	—	16 (28.6%)	
Previous cytotoxic treatments			
CHT	—	19 (33.9%)	
<sup>177</sup> Lu-PSMA	—	3 (5.3%)	

\*Missing data for control (n = 8) and ADT group (n = 4).

<sup>†</sup>Missing data for control (n = 9) and ADT group (n = 8).

<sup>‡</sup>Statistical testing not feasible because of sample size in control group (n = 2; data as mean and range) and ADT group (n = 1).

PSA = prostate-specific antigen; GFR = glomerular filtration rate; GnRH = gonadotropin-releasing hormone; CHT = chemotherapy. Qualitative data are number and percentages; continuous data are mean and SD.

**TABLE 2**  
PSMA Uptake Levels of Normal Organs According to Antihormonal Treatment Status

Variable	Control (n = 56)	ADT (n = 56)	Difference	P
Kidney SUV <sub>mean</sub> *†	29.5 ± 7.2; 95% CI, 27.57–31.42; range, 16.59–52.12	21.61 ± 8.1; 95% CI, 19.44–23.78; range, 5.18–37.36	Δyes – no = –7.89; 95% CI, –10.73 to –5.04	<0.001
Kidney SUV <sub>peak</sub> *	54.76 ± 14.29; 95% CI, 50.94–58.59; range, 26.65–93.75	40.64 ± 16.49; 95% CI, 36.23–45.06; range, 6.82–77.99	Δyes – no = –14.12; 95% CI, –19.85 to –8.39	<0.001
Liver SUV <sub>mean</sub> ‡	4.8 ± 1.31; 95% CI, 4.45–5.15; range, 2.15–8.63	4.44 ± 1.65; 95% CI, 3.99–4.88; range, 0.92–10.39	ΔADT – control = –0.14; 95% CI, –0.86 to 0.10	0.12
Liver SUV <sub>peak</sub> ‡	18.06 ± 14.75; 95% CI, 14.11–22.01; range, 3.81–55.8	11.18 ± 8.97; 95% CI, 8.78–13.58; range, 1.19–37.64	ΔADT – control = –2.3; 95% CI, –5.72 to –0.93	0.003
Spleen SUV <sub>mean</sub> ‡	6.08 ± 2.04; 95% CI, 5.53–6.62; range, 2.55–11.59	5.86 ± 2.42; 95% CI, 5.21–6.51; range, 0.782–14.56	Δyes – no = –0.49; 95% CI, –1.5 to 0.99	0.46
Spleen SUV <sub>peak</sub> ‡	14.76 ± 11.15; 95% CI, 11.78–17.75; range, 4.81–53.79	11.56 ± 9.61; 95% CI, 8.99–14.13; range, 1.14–52.34	ΔADT – control = –1.27; 95% CI, –3.61 to –0.16	0.033
Salivary gland SUV <sub>mean</sub> ‡§	11.34 ± 2.69; 95% CI, 10.62–12.06; range, 4.41–17.05	9.93 ± 3.17; 95% CI, 9.07–10.8; range, 1.18–18.02	ΔADT – control = –1.04; 95% CI, –2.48 to –0.13	0.027
Salivary gland SUV <sub>peak</sub> *	20.0 ± 5.02; 95% CI, 18.65–21.34; range, 7.53–34.76	16.69 ± 5.61; 95% CI, 15.16–18.22; range, 1.7–30.42	ΔADT – control = –3.31; 95% CI, –5.3 to –1.31	0.001

\*t test data as mean ± SD.

†Two patients underwent unilateral nephrectomy.

‡Mann–Whitney test data as median and IQR.

§Two scans (2/56, 4%) did not include salivary glands in field of view.

ADT, and patients on more than 6 mo of ADT, respectively ( $P < 0.001$ ). Post hoc pairwise analysis revealed significant differences between the control group and the 1- to 6-mo ADT group (mean difference: 95% CI, –13.2 to –2.56;  $P = 0.002$ ) and between the control group and the group receiving more than 6 mo of ADT (95% CI, –11.65 to –4.13;  $P < 0.001$ ). No significant difference between the 2 ADT groups was observed (95% CI, –5.51 to 5.53;  $P > 0.999$ ).

The median hepatic SUV<sub>peak</sub> was 9.9 (interquartile range [IQR], 19.43), 6.64 (IQR, 8.74), and 7.61 (IQR, 5.17) in the control group, the group receiving 1–6 mo of ADT, and the group receiving more than 6 mo of ADT, respectively ( $P = 0.012$ ). After post hoc adjustment, only the difference between the control group and the group receiving more than 6 mo of ADT remained significant (95% CI, –13.46 to –1.07;  $P = 0.006$ ).

The mean salivary gland SUV<sub>mean</sub> was 11.34 (SD, 2.69), 10.2 (SD, 3.8), and 9.83 (SD, 2.94) for the control group, the group receiving 1–6 mo of ADT, and the group receiving more than 6 mo of ADT, respectively ( $P = 0.043$ ). Pairwise analysis showed significant differences between the control group and the group receiving more than 6 mo of ADT (95% CI, –2.97 to –0.053;  $P = 0.041$ ) (Fig. 3).

#### Subgroup Analysis of ADT Group According to Previous Systemic Treatments

There was no statistical difference in mean renal or salivary gland SUV<sub>mean</sub> or median hepatic or splenic SUV<sub>peak</sub> between patients who underwent prior additional systemic therapies, namely taxane-based

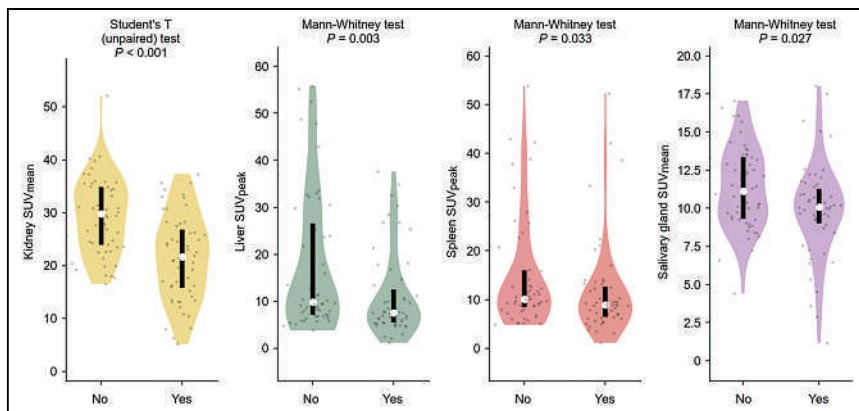


**FIGURE 2.** Violin plots of significantly different exemplary PSMA uptake levels of normal organs according to ADT treatment status. White dots indicate median value. No = control; Yes = ADT.

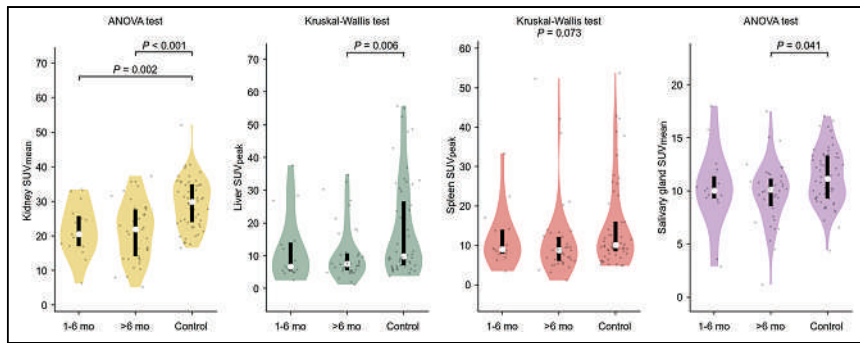


**FIGURE 3.** Violin plots of PSMA uptake levels of normal organs in ADT group according to different ADT runtimes and control group. Only significant values after post hoc testing are displayed as bars on figures. Nonsignificant *P* values are displayed in figure heading. White dots indicate median values.

chemotherapies,  $^{177}\text{Lu}$ -PSMA-617, or I&T RLT (24.93 [SD, 6.82], 10.02 [SD, 2.01], 7.8 [IQR, 6.16], and 8.54 [IQR, 2.96], respectively) and patients who did not receive prior additional systemic therapies (25.69 [SD, 8.97], 10.79 [SD, 3.18], 8.82 [IQR, 17.47], and 9.72 [IQR, 6.36], respectively) (Fig. 4).

### Multivariate Analysis of PSMA Organ Uptake

In the multivariate analysis, ADT was identified as an independent predictor of lower renal  $\text{SUV}_{\text{mean}}$  ( $\beta = -7.95$ ; 95% CI,  $-11.06$  to  $-4.84$ ;  $P < 0.0001$ ), hepatic  $\text{SUV}_{\text{peak}}$  ( $\beta = -7.85$ ; 95% CI,  $-11.78$  to  $-3.91$ ;  $P < 0.0001$ ), splenic  $\text{SUV}_{\text{peak}}$  ( $\beta = -5.83$ ; 95% CI,  $-9.95$  to  $-1.7$ ;  $P = 0.0062$ ), and salivary glandular  $\text{SUV}_{\text{mean}}$  ( $\beta = -1.47$ ; 95% CI,  $-2.76$  to  $-0.17$ ;  $P = 0.0274$ ). In addition, a high glomerular filtration rate was predictive only of a high renal  $\text{SUV}_{\text{mean}}$  ( $\beta = 0.16$ ; 95% CI, 0.05 to 0.26;  $P = 0.0034$ ) (Table 3).

### DISCUSSION

This study presents the first evidence that PCA patients on sustained ADT exhibit significantly lower  $^{68}\text{Ga}$ -PSMA-11 uptake in the salivary glands, liver, spleen, and kidneys than do hormonal therapy-naïve patients.

Although it is widely appreciated that ADT influences the PSMA expression of cancerous lesions, most likely in a time-dependent dichotomous manner (1), the effect of ADT on physiologically

PSMA-expressing organs such as the salivary glands, kidneys, liver, and spleen has been assessed only in a short-term setting (14).

This report therefore advances our understanding of the physiologic PSMA biodistribution in patients on sustained ADT and corroborates earlier findings (14) that hormonal changes exert a systemic influence on PSMA expression also in nontumorous tissues, holding possible implications for optimization strategies for PSMA RLTs.

Ettala et al. (14) investigated the short-term (pretreatment till a maximum of 8 wk after initiation) time-course effect of gonadotropin-releasing hormone–modulating ADT on the  $^{68}\text{Ga}$ -PSMA-11  $\text{SUV}_{\text{max}}$  of cancer lesions and physiologic PSMA-avid organs (salivary glands, kidneys, liver, and spleen) in newly diagnosed men with high-risk PCA ( $n = 9$ ) and observed heterogeneous and time-dependent uptake changes in tumorous and nontumorous tissues alike. Although they observed an initial heterogeneous uptake increase in all physiologically PSMA-avid organs, which peaked at around week 4, most patients who continued imaging beyond 1 mo started exhibiting stabilizing or falling PSMA organ uptake trajectories, which were most pronounced in the salivary glands and kidneys.

Analogously, several authors (12,21) have reported decreasing PSMA expression in tumorous lesions after long-term exposure to different classes of ADT. Although Vallabhajosula et al. (21) observed an initial increase in PSMA-expressing PCA lesions after 2 wk of abiraterone or enzalutamide ( $n = 4$ ), followed by a decrease in uptake after 3 mo, Afshar-Oromieh et al. (12) reported decreased PSMA uptake in roughly two thirds of PCA lesions after sustained gonadotropin-releasing hormone antagonist or analog exposure (median ADT runtime,  $\sim 7$  mo) in a retrospective, longitudinal cohort of 10 patients.

In summary with the abovementioned studies (12,14,21), the found association between midterm or, predominantly, long-term ADT and significantly lower PSMA uptake in the submandibular glands, liver, spleen, and kidneys (Fig. 3) suggests that not just tumorous but also nontumorous tissues might be subject to androgen-induced, time-dependent, dichotomous PSMA expression changes in early upregulation and late downregulation (1).

Surprisingly, we did not observe any PSMA uptake level differences of cancerous lesions between patients on ADT and those without a history of ADT, as repeatedly reported in the literature (10–12). We hypothesize that this might be due to the cross-sectional study design incorporating patients at different stages. Although patients on ADT have more advanced disease (22), as signified by a higher number of osseous bone lesions on imaging, the reported effects of hormonal therapy on cancer lesions could be blurred by ADT-induced PSMA downregulation of yet more advanced lesions in our cohort.

Since PSMA biodistribution in itself is a complex function of uptake, retention,

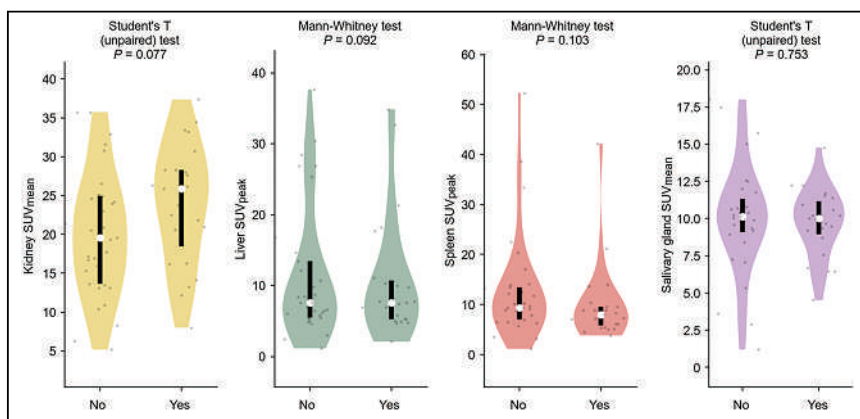


**FIGURE 4.** Violin plots of PSMA uptake levels according to prior cytotoxic treatments ( $^{177}\text{Lu}$ -PSMA RLT or chemotherapy) in normal organs. White dots indicate median value. Yes = prior systemic therapies; No = no prior systemic therapy.



TABLE 3

Multivariate Regression Analysis of Relationship Between Renal, Hepatic, Splenic, and Salivary Gland PSMA Uptake and Explanatory Variables MTV, Glomerular Filtration Rate, and ADT Status

Predicted endpoint	Variable	Odds ratio	P
Kidney SUV <sub>mean</sub>	Intercept	17.78; 9.28 to 26.27	<0.0001
	MTV (cm <sup>3</sup> )	-0.218; -0.495 to 0.0585	0.121
	GFR (mL/min)	0.156; 0.0531 to 0.259	0.0034
	ADT (0 = no, 1 = yes)	-7.95; -11.06 to -4.84	<0.0001
Liver SUV <sub>peak</sub>	Intercept	10.94; -1.06 to 22.94	0.0735
	MTV (cm <sup>3</sup> )	0.0389; -0.301 to 0.379	0.821
	GFR (mL/min)	0.09; -0.0606 to 0.241	0.238
	ADT (0 = no, 1 = yes)	-7.85; -11.78 to -3.91	<0.0001
Spleen SUV <sub>peak</sub>	Intercept	6.36; -5.73 to 18.45	0.299
	MTV (cm <sup>3</sup> )	0.295; -0.114 to 0.704	0.156
	GFR (mL/min)	0.104; -0.0615 to 0.27	0.214
	ADT (0 = no, 1 = yes)	-5.83; -9.95 to -1.7	0.006
SM SUV <sub>mean</sub>	Intercept	12.2; 8.67 to 15.73	<0.0001
	MTV (cm <sup>3</sup> )	-0.0679; -0.183 to 0.0472	0.244
	GFR (mL/min)	-0.00771; -0.0506 to 0.0352	0.722
	ADT (0 = no, 1 = yes)	-1.47; -2.76 to -0.167	0.0274

GFR = glomerular filtration rate; SM = Submandibular gland.  
Odds ratio is followed by 95% CI.

and excretion (17,23) in tumorous and nontumorous tissues, a multivariate regression analysis was performed to exclude the confounding effects of renal function and tumor tissue.

The MTV was not associated with salivary gland, hepatic, splenic, or renal uptake in the ADT group, most likely since the potential influence of the tumor sink effect (17), a sequestration phenomenon that occurs when extensive tumor masses reduce tracer accumulation in healthy tissues, was excluded by design (Fig. 1).

Interestingly, renal function was positively associated with renal PSMA uptake levels. We hypothesize that although there is a physiologic renal baseline PSMA expression, primarily in the proximal tubular cells (3), increased PSMA excretion in the case of higher glomerular filtration led to higher overall renal radioligand signal caused by count summation during static image acquisition.

Since sustained ADT is a commonly encountered clinical scenario in patients with advanced disease, a deeper understanding of the hormonal influences on PSMA biodistribution might have important implications for PSMA RLTs because common side effects, such as xerostomia and dose-limiting renal radiotoxicity (15), are functions of PSMA ligand biodistribution.

Even though dosimetric estimates of absorbed organ doses are the gold standard, <sup>68</sup>Ga-PSMA-11 PET has been shown to provide robust estimates of therapeutic PSMA ligand biodistributions (24,25) in that regard.

Our study had several limitations, and the findings should therefore be interpreted with caution.

First, as a retrospective, cross-sectional, and monocentric study, it was prone to selection bias, recall bias, inaccuracies in record keeping, and incomplete data, which could negatively affect the generalizability of the findings. We tried to minimize this potential bias by focusing on a narrow definition of ADT treatment and including only patients with complete hormonal treatment data, as well as by ensuring balanced groups according to possible confounders such as renal function, MTV (17), and previous systemic treatments (Fig. 4). Furthermore, multivariate regression analysis was performed to discover potential confounders, which, however, cannot fully be excluded.

Second, as a cross-sectional study, no causal relationships can be inferred. However, a cross-sectional study is a suitable design to assess nontemporal relationships between variables and to generate hypotheses. Therefore, we envision that groups with longitudinal or dosimetric datasets are able to establish a cause-effect relationship between gonadotropin-releasing hormone-modulating ADT and more potent antiandrogens such as androgen receptor inhibitors, 5 $\alpha$ -reductase, and CYP17a inhibitors on the PSMA biodistribution, as an understanding of hormonal influences might have important implications for efficacy-maximizing and side-effect-minimizing strategies for RLT.

## CONCLUSION

These findings suggest that long-term ADT modulates PSMA expression in a systemic fashion, which may have implications for

treatment-optimizing and side-effect-minimizing strategies for PSMA RLTs. Further, longitudinal studies also incorporating second-generation ADT are warranted to establish a cause-effect relationship and effect magnitude.

## DISCLOSURE

This study was partially funded by the Austrian Federal Ministry for Digital and Economic Affairs; the National Foundation for Research, Technology, and Development; the Christian Doppler Research Association; and Siemens Healthineers. No other potential conflict of interest relevant to this article was reported.

## KEY POINTS

**QUESTION:** Is ADT associated with the biodistribution of  $^{68}\text{Ga}$ -PSMA-11?

**PERTINENT FINDINGS:** In this monocentric, retrospective study, the  $^{68}\text{Ga}$ -PSMA-11 uptake of physiologically PSMA-avid organs was compared between patients on midterm and long-term ADT ( $n = 56$ ) and a control group ( $n = 56$ ). The ADT cohort had significantly lower PSMA uptake in the salivary glands, liver, spleen, and kidneys.

**IMPLICATIONS FOR PATIENT CARE:** These findings suggest that long-term ADT modulates PSMA expression in a systemic fashion, which may have implications for treatment-optimizing and side-effect-minimizing strategies for PSMA RLTs, particularly those using more potent  $^{225}\text{Ac}$ -labeled PSMA conjugates.

## REFERENCES

1. Vaz S, Hadaschik B, Gabriel M, Herrmann K, Eiber M, Costa D. Influence of androgen deprivation therapy on PSMA expression and PSMA-ligand PET imaging of prostate cancer patients. *Eur J Nucl Med Mol Imaging*. 2020;47:9–15.
2. Sweat SD, Pacelli A, Murphy GP, Bostwick DG. Prostate-specific membrane antigen expression is greatest in prostate adenocarcinoma and lymph node metastases. *Urology*. 1998;52:637–640.
3. Uhlén M, Fagerberg L, Hallström BM, et al. Proteomics. Tissue-based map of the human proteome. *Science*. 2015;347:1260419.
4. Ghosh A, Heston WDW. Tumor target prostate-specific membrane antigen (PSMA) and its regulation in prostate cancer. *J Cell Biochem*. 2004;91:528–539.
5. Watt F, Martorana A, Brookes DE, et al. A tissue-specific enhancer of the prostate-specific membrane antigen gene, FOLH1. *Genomics*. 2001;73:243–254.
6. Noss KR, Wolfe SA, Grimes SR. Upregulation of prostate-specific membrane antigen/folate hydrolase transcription by an enhancer. *Gene*. 2002;285:247–256.
7. O’Keefe DS, Bacich DJ, Heston WDW. Prostate specific membrane antigen. In: Chung LWK, Isaacs WB, Simons JW, eds. *Prostate Cancer: Biology, Genetics, and the New Therapeutics*. Humana Press; 2001:307–326.
8. Aggarwal R, Wei X, Kim W, et al. Heterogeneous flare in prostate-specific membrane antigen positron emission tomography tracer uptake with initiation of androgen pathway blockade in metastatic prostate cancer. *Eur Urol Oncol*. 2018;1:78–82.
9. Chang SS, Reuter VE, Heston WD, Hutchinson B, Grauer LS, Gaudin PB. Short-term neoadjuvant androgen deprivation therapy does not affect prostate-specific membrane antigen expression in prostate tissues. *Cancer*. 2000;88:407–415.
10. Emmett L, Yin C, Crumbaker M, et al. Rapid modulation of PSMA expression by androgen deprivation: serial  $^{68}\text{Ga}$ -PSMA-11 PET in men with hormone-sensitive and castrate-resistant prostate cancer commencing androgen blockade. *J Nucl Med*. 2019;60:950–954.
11. Hope TA, Truillet C, Ehman EC, et al.  $^{68}\text{Ga}$ -PSMA-11 PET imaging of response to androgen receptor inhibition: first human experience. *J Nucl Med*. 2017;58:81–84.
12. Afshar-Oromieh A, Debus N, Uhrig M, et al. Impact of long-term androgen deprivation therapy on PSMA ligand PET/CT in patients with castration-sensitive prostate cancer. *Eur J Nucl Med Mol Imaging*. 2018;45:2045–2054.
13. Liu T, Wu LY, Fulton MD, Johnson JM, Berkman CE. Prolonged androgen deprivation leads to downregulation of androgen receptor and prostate-specific membrane antigen in prostate cancer cells. *Int J Oncol*. 2012;41:2087–2092.
14. Ettala O, Malaspina S, Tuokkola T, et al. Prospective study on the effect of short-term androgen deprivation therapy on PSMA uptake evaluated with  $^{68}\text{Ga}$ -PSMA-11 PET/MRI in men with treatment-naïve prostate cancer. *Eur J Nucl Med Mol Imaging*. 2020;47:665–673.
15. Okamoto S, Thieme A, Allmann J, et al. Radiation dosimetry for  $^{177}\text{Lu}$ -PSMA 1&T in metastatic castration-resistant prostate cancer: absorbed dose in normal organs and tumor lesions. *J Nucl Med*. 2017;58:445–450.
16. Crawford ED, Schellhammer PF, McLeod DG, et al. Androgen receptor targeted treatments of prostate cancer: 35 years of progress with antiandrogens. *J Urol*. 2018;200:956–966.
17. Gafita A, Wang H, Robertson A, et al. Tumor sink effect in  $^{68}\text{Ga}$ -PSMA-11 PET: myth or reality? *J Nucl Med*. 2022;63:226–232.
18. Shiyam Sundar LK, Yu J, Muzik O, et al. Fully automated, semantic segmentation of whole-body 18F-FDG PET/CT images based on data-centric artificial intelligence. *J Nucl Med*. 2022;63:1941–1948.
19. Fedorov A, Beichel R, Kalpathy-Cramer J, et al. 3D Slicer as an image computing platform for the Quantitative Imaging Network. *Magn Reson Imaging*. 2012;30:1323–1341.
20. Beichel RR, Van Tol M, Ulrich EJ, et al. Semiautomated segmentation of head and neck cancers in  $^{18}\text{F}$ -FDG PET scans: a just-enough-interaction approach. *Med Phys*. 2016;43:2948–2964.
21. Vallabhajosula S, Jhanwar Y, Tagawa S, et al.  $^{99\text{m}}\text{Tc}$ -MIP-1404 planar and SPECT scan: imaging biomarker of androgen receptor (AR) signaling and prostate specific membrane antigen (PSMA) expression [abstract]. *J Nucl Med*. 2016;57(suppl 2):1541.
22. Afshar-Oromieh A, Avtzi E, Giesel FL, et al. The diagnostic value of PET/CT imaging with the  $^{68}\text{Ga}$ -labelled PSMA ligand HBED-CC in the diagnosis of recurrent prostate cancer. *Eur J Nucl Med Mol Imaging*. 2015;42:197–209.
23. Pfob CH, Ziegler S, Graner FP, et al. Biodistribution and radiation dosimetry of  $^{68}\text{Ga}$ -PSMA HBED CC: a PSMA specific probe for PET imaging of prostate cancer. *Eur J Nucl Med Mol Imaging*. 2016;43:1962–1970.
24. Wang J, Zang J, Wang H, et al. Pretherapeutic  $^{68}\text{Ga}$ -PSMA-617 PET may indicate the dosimetry of  $^{177}\text{Lu}$ -PSMA-617 and  $^{177}\text{Lu}$ -EB-PSMA-617 in main organs and tumor lesions. *Clin Nucl Med*. 2019;44:431–438.
25. Violet J, Jackson P, Ferdinandus J, et al. Dosimetry of Lu-PSMA-617 in metastatic castration-resistant prostate cancer: correlations between pretherapeutic imaging and whole-body tumor dosimetry with treatment outcomes. *J Nucl Med*. 2019;60:517–523.

---

---

# Prognostic Value of End-of-Treatment PSMA PET/CT in Patients Treated with <sup>177</sup>Lu-PSMA Radioligand Therapy: A Retrospective, Single-Center Analysis

Vishnu Murthy\*<sup>1</sup>, Andrei Gafita\*<sup>1</sup>, Pan Thin<sup>1</sup>, Kathleen Nguyen<sup>1</sup>, Tristan Grogan<sup>2</sup>, John Shen<sup>3</sup>, Alexandra Drakaki<sup>3</sup>, Matthew Rettig<sup>3</sup>, Johannes Czernin<sup>1</sup>, and Jeremie Calais<sup>1</sup>

<sup>1</sup>Ahmanson Translational Theranostics Division, Department of Molecular and Medical Pharmacology, David Geffen School of Medicine at UCLA, Los Angeles, California; <sup>2</sup>Department of Medicine Statistics Core, David Geffen School of Medicine at UCLA, Los Angeles, California; and <sup>3</sup>Division of Hematology/Oncology, Department of Medicine, David Geffen School of Medicine at UCLA, Los Angeles, California

Our objective was to evaluate the prognostic value of end-of-treatment prostate-specific membrane antigen (PSMA) PET/CT (PSMA-PET) in patients with metastatic castration-resistant prostate cancer (mCRPC) treated with <sup>177</sup>Lu-PSMA radioligand therapy (PSMA-RLT). **Methods:** This was a single-center retrospective study. mCRPC patients who underwent PSMA-RLT with available baseline PSMA-PET (bPET) and end-of-treatment PSMA-PET (ePET) within 6 mo of the last PSMA-RLT cycle were eligible. Overall survival (OS) and prostate-specific antigen (PSA) progression status at the time of ePET (by Prostate Cancer Clinical Trials Working Group 3 criteria) were collected. PSMA-PET tumor segmentation was performed to obtain whole-body PSMA tumor volume (PSMA-VOL) and define progressive ( $\geq 20\%$  increase) versus nonprogressive disease. Pairs of bPET and ePET were interpreted for appearance of new lesions. Response Evaluation Criteria in PSMA-PET/CT (RECIP) 1.0 were also applied to define progressive versus nonprogressive disease. The associations between changes in PSMA-VOL, new lesions, RECIP 1.0, and PSA progression status at the time of ePET with OS were evaluated by Kaplan–Meier analysis. **Results:** Twenty mCRPC patients were included. The median number of treatment cycles was 3.5 (interquartile range [IQR], 2–4). The median time between bPET and cycle 1 of PSMA-RLT was 1.0 mo (IQR, 0.7–1.8 mo). The median time between the last cycle of PSMA-RLT and ePET was 1.9 mo (IQR, 1.2–3.5 mo). Twelve of 20 patients (60%) had died at the last follow-up. The median follow-up time from ePET for survivors was 31.2 mo (IQR, 6.8–40.7 mo). The median OS from ePET was 11.4 mo (IQR, 6.8–30.7 mo). Patients with new lesions on ePET had shorter OS than those without new lesions (median OS, 10.7 mo [95% CI, 9.2–12.2] vs. not reached;  $P = 0.002$ ). Patients with progressive PSMA-VOL had shorter OS than those with nonprogressive PSMA-VOL (median OS, 10.7 mo [95% CI: 9.7–11.7 mo] vs. not reached;  $P = 0.007$ ). Patients with progressive RECIP had shorter OS than those with nonprogressive RECIP (median OS, 10.7 mo [95% CI, 9.7–11.7 mo] vs. not reached;  $P = 0.007$ ). PSA progression at the time of ePET was associated with shorter OS (median, 10.9 mo [95% CI, 9.4–12.4 mo] vs. not reached;  $P = 0.028$ ). **Conclusion:** In this retrospective study of 20 mCRPC patients treated with PSMA-RLT, progression on ePET by the appearance of new lesions, changes in PSMA-VOL, and RECIP

1.0 was prognostic for OS. Validation in larger, prospective multicentric clinical trials is warranted.

**Key Words:** metastatic castration-resistant prostate cancer; radioligand therapy; PSMA-PET; end-of-treatment PET; <sup>177</sup>Lu-PSMA

**J Nucl Med 2023; 64:1737–1743**

DOI: 10.2967/jnumed.122.265155

---

**T**he small-molecule inhibitor <sup>177</sup>Lu-PSMA binds with high affinity to prostate-specific membrane antigen (PSMA) and delivers  $\beta$ -radiation. In the phase III VISION trial, which led to approval by the Food and Drug Administration, <sup>177</sup>Lu-PSMA-617 prolonged overall survival (OS) and image-based progression-free survival when added to the standard of care for patients with metastatic castration-resistant prostate cancer (mCRPC) who had received prior taxane-based chemotherapy (1).

In metastatic prostate cancer, treatment response is typically evaluated using conventional imaging (CT and bone scanning) according to the Prostate Cancer Clinical Trials Working Group 3 criteria (2). The Food and Drug Administration approved PSMA PET/CT (PSMA-PET) for different clinical settings in men with prostate cancer (3). However, further research is necessary to evaluate the prognostic value of PSMA-PET for OS in mCRPC patients undergoing treatment with <sup>177</sup>Lu-PSMA radioligand therapy (PSMA-RLT) (4).

Progression on end-of-treatment PSMA-PET (ePET) by modified PSMA-PET progression criteria was reported to be prognostic for OS in mCRPC patients undergoing treatment with PSMA-RLT (5,6). Increased whole-body PSMA tumor volume (PSMA-VOL) on ePET was also reported to be prognostic for OS, independent of <sup>18</sup>F-FDG PET/CT parameters (7). Recently, Response Evaluation Criteria in PSMA-PET/CT (RECIP) 1.0 were introduced. Patients were classified as having progressive disease (PD) if they had at least a 20% increase in PSMA-VOL and the appearance of new lesions on interim PSMA-PET after the first 2 cycles of PSMA-RLT (4). Progression on interim PSMA-PET by RECIP 1.0 was also found to be prognostic for OS in mCRPC patients treated with PSMA-RLT. However, the prognostic value of progression on ePET by RECIP 1.0 has not, to our knowledge, been previously investigated.

In this retrospective study, we aimed to evaluate the prognostic value of progression on ePET by RECIP 1.0 in mCRPC patients treated with PSMA-RLT.

---

Received Nov. 7, 2022; revision accepted Jun. 21, 2023.

For correspondence or reprints, contact Andrei Gafita (agafita1@jhmi.edu).

\*Contributed equally to this work.

Guest Editor: Carolyn J. Anderson, University of Missouri

Published online Sep. 7, 2023.

COPYRIGHT © 2023 by the Society of Nuclear Medicine and Molecular Imaging.

**TABLE 1**  
**RECIP 1.0**

Criteria	Definition
New lesions	Any new focus of PSMA uptake higher than surrounding background, with tumor SUV <sub>max</sub> > blood-pool SUV <sub>max</sub> , not present on bPET (tumor SUV <sub>max</sub> < blood-pool SUV <sub>max</sub> ), and with tumor uptake not attributable to physiologic uptake or pitfalls; alternatively, any new malignant lesion detected on follow-up CT imaging independent of PSMA-ligand uptake
RECIP 1.0	
Complete response	Absence of any PSMA uptake on follow-up PET scan
Partial response	≥30% decrease in PSMA-VOL without appearance of new lesions
PD	≥20% increase in PSMA-VOL with appearance of new lesions
Stable disease	<30% decrease in PSMA-VOL with or without appearance of new lesions, ≥30% decrease in PSMA-VOL with appearance of new lesions, <20% increase in PSMA-VOL with or without appearance of new lesions, or ≥20% increase in PSMA-VOL without appearance of new lesions

## MATERIALS AND METHODS

### Patients and Study Design

In this single-center retrospective study, mCRPC patients who underwent PSMA-PET or PSMA-RLT between October 2016 and April 2022 at UCLA were retrospectively screened for inclusion. Eligible patients underwent PSMA-RLT, had available baseline PET (bPET) and ePET performed within 6 mo of the last PSMA-RLT cycle, and had available survival data. The cutoff date for follow-up was November 5, 2022. Patients who did not have a confirmed date of death and had a follow-up time of less than 3 mo were excluded. This retrospective analysis was approved by the Ethics Committee (UCLA institutional review board approval 20-000954), which waived the study-specific consent requirement. The primary outcome of the study was to evaluate the prognostic value of ePET for OS. The secondary outcome was to evaluate the correlation of prostate-specific antigen (PSA) changes with ePET.

### PSMA-PET Image Acquisition

Twenty pairs of PET scans (40 PET scans total) were used for this analysis. <sup>68</sup>Ga-PSMA-11 (Glu-NH-CO-NH-Lys-(Ahx)-[<sup>68</sup>Ga(H-BEDCC)]) was used as the PSMA ligand. PSMA-PET/CT images were acquired after intravenous injection of a median of 191 MBq of <sup>68</sup>Ga-PSMA-11 (interquartile range [IQR], 183–204 MBq) and a median uptake time of 63 min (IQR, 59–68 min). Thirty-six of 40 (90%) PET scans were done at UCLA, whereas 4 of 40 (10%) were done at outside institutions. Twenty-one of 40 (53%) PET scans were acquired on a Siemens Biograph 64 Truepoint scanner (image reconstruction parameters: no time of flight, ordered-subsets expectation maximization 2-dimensional [2 iterations, 8 subsets], 5-mm gaussian postreconstruction filter), 18 of 40 (45%) on a Siemens Biograph 64 mCT scanner (image reconstruction parameters: no time of flight, ordered-subsets expectation maximization 3-dimensional [2 iterations, 24 subsets], 5-mm gaussian postreconstruction filter), and 1 of 40 (2%) on a GE Healthcare Discovery VCT scanner (image reconstruction parameters: 3-dimensional, no time of flight).

### Image Analysis

*Changes in Tumor Burden.* The PSMA-positive tumor lesions on bPET and ePET were segmented by 1 nuclear medicine physician, who was masked to outcome data, using qPSMA software as described previously (8). PSMA-VOL was extracted, and percentage changes on ePET relative to bPET were calculated. Patients were classified as having PD (progressive PSMA-VOL, ≥20% increase) versus non-PD.

*New Lesions.* Pairs of bPET and ePET were interpreted by 1 nuclear medicine physician. The appearance of at least 1 new lesion on ePET was recorded.

*RECIP.* RECIP 1.0 were applied as previously described (4). Patients were classified as having PD if they had at least a 20% increase in PSMA-VOL with the appearance of new lesions on ePET versus non-PD. Table 1 summarizes RECIP 1.0 classifications (4).

### Statistical Analysis

OS was calculated in a landmark analysis from time of bPET (to permit comparisons with the VISION trial) and from time of ePET (for Kaplan–Meier analyses) to death or date of last follow-up alive. PSA progression status at the time of ePET was recorded and categorized according to Prostate Cancer Clinical Trials Working Group 3 criteria (2).

Patient characteristics and study variables were summarized overall and by group (progressive RECIP vs. nonprogressive RECIP) using frequencies (percentages) or medians (quarters 1–3) unless otherwise noted. To assess the association between OS and clinical parameters such as changes in PSMA-VOL, appearance of new lesions, RECIP 1.0, and PSA progression status at the time of ePET, we used the Kaplan–Meier method. The 95% CIs for the median OS (if it existed) were computed and the corresponding *P* values from the log-rank test were used to formally assess the associations of interest. The correlations between percentage changes in serum PSA and percentage changes in PSMA-VOL from bPET to ePET were assessed using Spearman rank correlation coefficients. The associations between PSMA-PET–derived parameters and PSA progression status at the time of ePET were evaluated using the Fisher exact test. Analyses were performed using Jamovi, and *P* values of less than 0.05 were considered statistically significant.

## RESULTS

### Patients

Retrospective data from 425 men with prostate cancer who underwent 2 PSMA-PET scans between October 2016 and April 2022 were screened. Of these, 20 mCRPC patients treated with PSMA-RLT with available bPET and ePET met the eligibility criteria and were included (Fig. 1). Patients were treated with PSMA-RLT at UCLA and other international sites. Seven of 20 (35%) patients were treated with PSMA-RLT under compassionate-access programs, 10 of 20 (50%) in a phase II clinical trial (NCT03042312), and 3 of 20 (15%) under an expanded-access protocol (NCT04825652) (9). Baseline characteristics are summarized in Table 2.

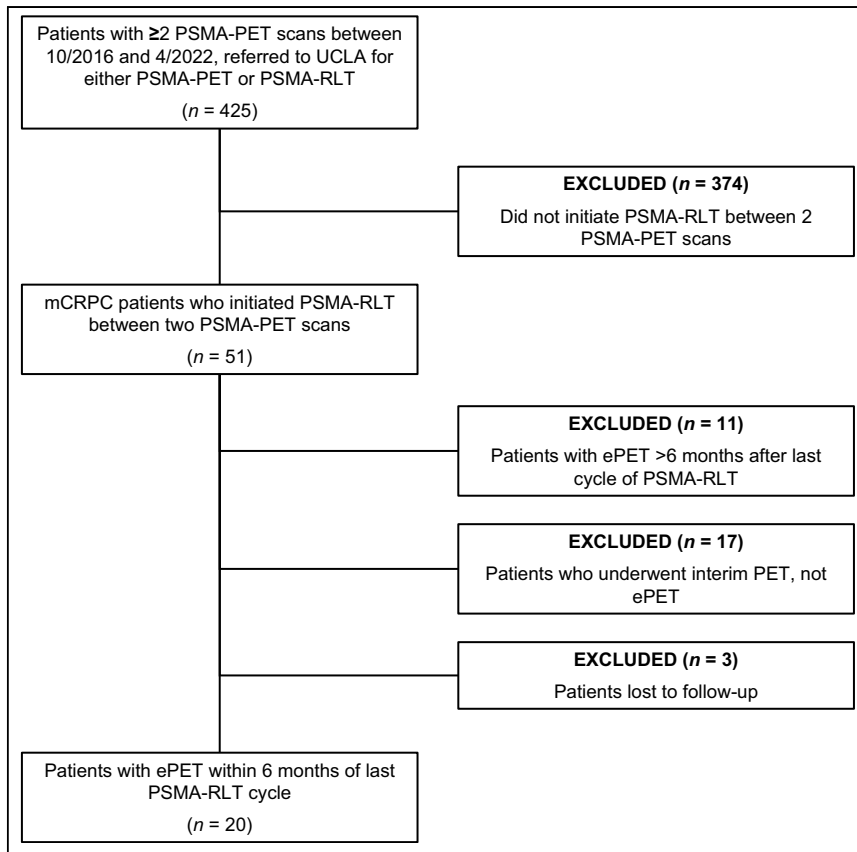


**FIGURE 1.** Study flowchart.

### PSMA-RLT

The median number of treatment cycles was 3.5 (IQR, 2–4). The median activity per cycle was 7.3 GBq (IQR, 6.6–7.4 GBq). Injected activity data were not available in 5 patients for 8 cycles. The median time between bPET and cycle 1 of PSMA-RLT was 1.0 mo (IQR, 0.7–1.8 mo), whereas the median time between the last cycle of PSMA-RLT and ePET was 1.9 mo (IQR, 1.2–3.5 mo).

### Clinical Outcomes

Twelve of 20 patients (60%) had died at last follow-up. The median follow-up time from ePET for survivors was 31.2 mo (IQR, 6.8–40.7 mo). The median OS was 19.5 mo from bPET (IQR, 16.3–36.6 mo) and 11.4 mo from ePET (IQR, 6.8–30.7 mo).

### Image Analysis

Case summary images for each patient are provided in the supplemental figures (supplemental materials are available at <http://jnm.snmjournals.org>). Four of 20 patients (20%) did not have sufficient PSA data to document changes during PSMA-RLT. Sample cases of PSMA-PET and PSA responders and nonresponders are also shown in Figure 2.

**New Lesions.** Eleven of 20 patients (55%) had new lesions on ePET and had a shorter OS than patients without new lesions (median OS, 10.7 mo [95% CI, 9.2–12.2] vs. not reached;  $P = 0.002$ ; Fig. 3).

**PSMA-VOL Changes.** The median change in PSMA-VOL on ePET relative to bPET was +21.5% (IQR, –76.9% to +266.5%). Ten of 20 patients (50%) had progressive PSMA-VOL at the time of ePET and had a shorter OS than patients with nonprogressive

PSMA-VOL (median OS, 10.7 mo [95% CI, 9.7–11.7 mo] vs. not reached;  $P = 0.007$ ; Fig. 3).

**RECIP.** Ten of 20 patients (50%) had progressive RECIP at the time of ePET and had a shorter OS than patients with nonprogressive RECIP (median OS, 10.7 mo [95% CI, 9.7–11.7] vs. not reached;  $P = 0.007$ ; Fig. 3).

**PSA and ePET.** Eighteen of 20 patients (90%) had available serum PSA values to assess PSA progression status at the time of ePET. Ten of 18 patients (55.6%) experienced PSA progression at the time of ePET. Two of 18 patients (11.1%) experienced PSA progression at the time of ePET but were classified as non-PD by RECIP 1.0. PSA progression at the time of ePET was associated with shorter OS (median, 10.9 mo [95% CI, 9.4–12.4] vs. not reached;  $P = 0.028$ ; Fig. 3). Associations between progression by PSMA-VOL, new lesions, and RECIP 1.0 with PSA progression status at ePET are summarized in Table 3. Changes in PSA and PSMA-VOL between bPET and ePET were strongly correlated (Spearman  $\rho = 0.776$ ;  $P < 0.001$ ).

### DISCUSSION

In this single-center retrospective cohort study of 20 mCRPC patients treated with PSMA-RLT, progression on ePET by

RECIP 1.0 was prognostic for OS. Changes in PSMA-VOL correlated with changes in PSA and were associated with PSA progression status.

These findings are consistent with Michalski et al., who found that progression on ePET using modified PSMA-PET progression criteria was prognostic for OS in mCRPC patients treated with PSMA-RLT (5). Our results are also consistent with Pathmanandavel et al., who demonstrated that changes in total tumor volume on ePET were prognostic for OS, independent of  $^{18}\text{F}$ -FDG parameters, in mCRPC patients who underwent PSMA-RLT (7). Although RECIP 1.0 was initially introduced using interim PSMA-PET, our analysis now suggests that response assessment on ePET using RECIP 1.0 can be prognostic for OS (4).

Because the extraction of quantitative, whole-body PSMA-PET parameters is not widely available in clinical practice, lesion-based response criteria still provide easily accessible prognostic information. Similar to prior reports, we found that the appearance of new lesions on ePET is prognostic for OS (4,5). However, it should also be noted that the appearance of new lesions on ePET as a single lesion assessment may not fully capture disease heterogeneity. In our analysis, among 11 of 20 patients who had new lesions on ePET, 1 (9%) patient (case 9, supplemental materials) was classified as non-PD by PSMA-VOL and RECIP 1.0 and had an OS of 9.7 mo after ePET. In the original RECIP 1.0 study, which analyzed 124 patients, 13% of patients had new lesions despite a decrease in tumor volume and were classified as having stable disease, with a different survival outcome from true



**TABLE 2**  
Baseline Characteristics

Characteristic	All patients (n = 20)	Progressive RECIP (n = 10)	Nonprogressive RECIP (n = 10)
Age (y)	71 (66–75)	74 (69–77)	68 (61–72)
Time since diagnosis of prostate cancer (y)	8 (5–13)	9 (7–16)	7 (4–12)
Gleason score at diagnosis*			
<8	6 (31.6)	5 (50)	1 (11.1)
≥8	13 (68.4)	5 (50)	8 (88.9)
M status at diagnosis†			
M0 (%)	11 (61.1)	7 (77.8)	4 (44.4)
M1 (%)	7 (38.9)	2 (22.2)	5 (55.6)
Primary treatment			
Prostatectomy ± lymphadenectomy	9 (45)	6 (60)	3 (30)
Local radiotherapy	1 (5)	1 (10)	0 (0)
Systemic treatment	10 (50)	3 (30)	7 (70)
Previous mCRPC treatments			
Previous chemotherapy			
Docetaxel	11 (55)	7 (70)	4 (40)
Cabazitaxel	6 (30)	3 (30)	3 (30)
Other chemotherapy	4 (20)	1 (10)	3 (30)
Androgen receptor-signaling inhibitor			
Abiraterone	16 (80)	8 (80)	8 (80)
Enzalutamide	14 (70)	8 (80)	6 (60)
<sup>223</sup> Ra	4 (20)	2 (20)	2 (20)
Other	14 (70)	8 (80)	6 (60)
Prior lines of mCRPC systemic treatment			
0	2 (10)	1 (10)	1 (10)
1	3 (15)	0	3 (30)
≥2	15 (75)	9 (90)	6 (60)
≥3	14 (70)	8 (80)	6 (60)
≥4	12 (60)	7 (70)	5 (50)
Baseline PSA (ng/mL), closest to cycle 1	19.5 (3.4–30.3)	20.0 (10.4–32.2)	5.3 (0.8–27.8)
Time between PSA and cycle 1 (d)	6 (3–11)	7 (4–11)	6 (2–12)
Baseline lactate dehydrogenase (U/L)‡	215 (178–224)	218.5 (206.8–271)	174 (167–200)
Baseline total alkaline phosphatase (U/L)§	94.5 (70–117.5)	113 (85–132)	81 (68–95)
Baseline hemoglobin (g/dL)¶	13.1 (11.6–13.5)	13.1 (11.4–13.4)	13.1 (11.6–13.6)
Baseline ECOG performance status¶			
0	10 (62.5)	5 (55.6)	5 (71.4)
1	5 (31.3)	3 (33.3)	2 (28.6)
2	1 (6.3)	1 (11.1)	0 (0)
Sites of disease on bPET			
Bone	2 (10)	2 (20)	0 (0)
Nodal	1 (5)	0 (0)	1 (10)
Bone + nodal	10 (50)	6 (60)	4 (40)
Visceral + bone	1 (5)	0 (0)	1 (10)
Visceral + nodal	2 (10)	1 (10)	1 (10)
Bone + nodal + visceral	4 (20)	1 (10)	3 (30)

\*Data missing 1 for patient overall, 0 for progressive RECIP cohort, and 1 for nonprogressive RECIP cohort.

†Data missing for 2 patients overall, 1 for progressive RECIP cohort, and 1 for nonprogressive RECIP cohort.

‡Data missing for 13 patients overall, 6 for progressive RECIP cohort, and 7 for nonprogressive RECIP cohort.

§Data missing for 2 patients overall, 1 for progressive RECIP cohort, and 1 for nonprogressive RECIP cohort.

¶Data missing for 1 patient overall, 0 for progressive RECIP cohort, and 1 for nonprogressive RECIP cohort.

¶Data missing for 4 patients overall, 1 for progressive RECIP cohort, and 3 for nonprogressive RECIP cohort.

ECOG = Eastern Cooperative Oncology Group.

Qualitative data are number and percentage of available data in cohort; continuous data are median and IQR.

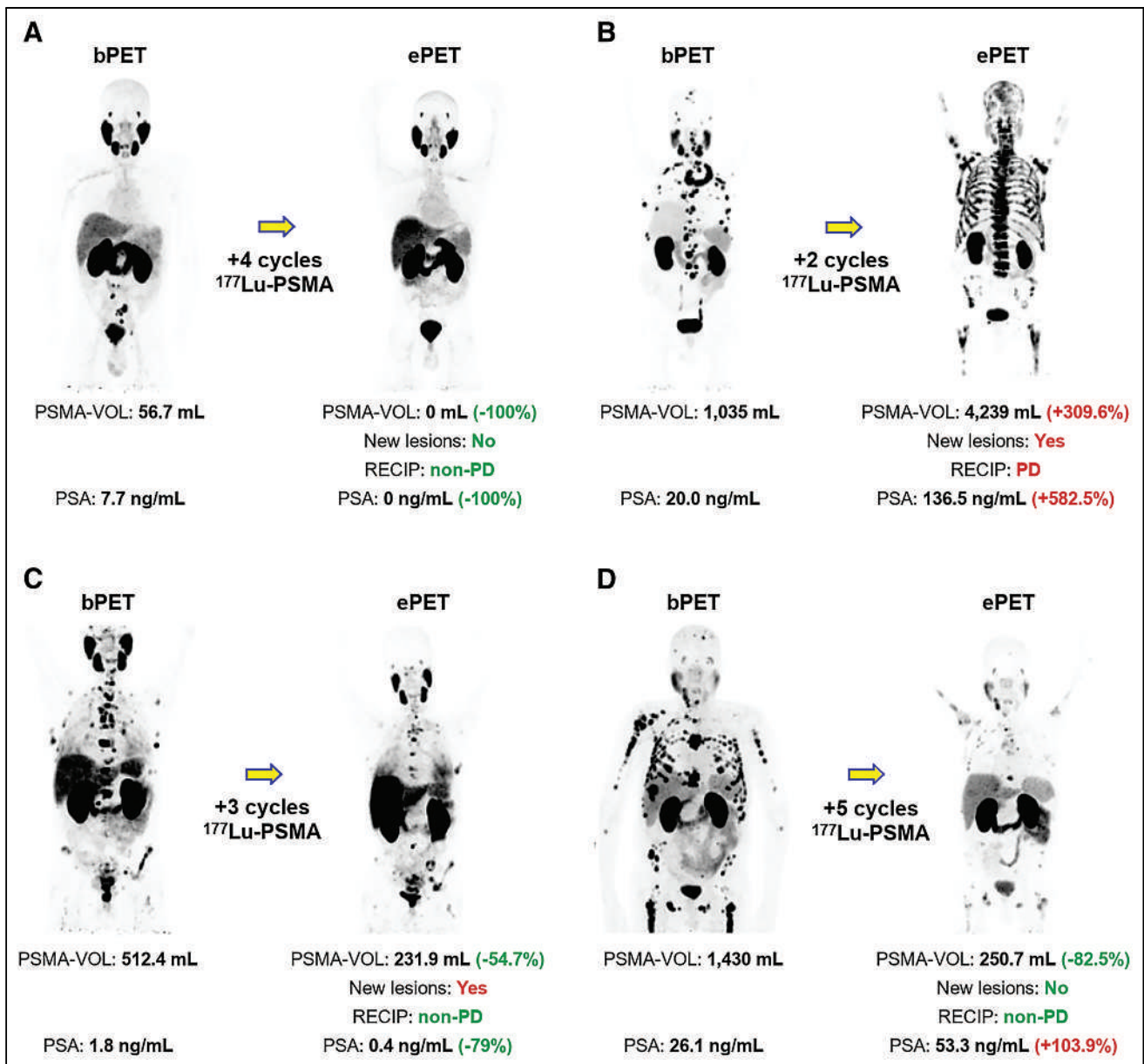


**FIGURE 2.** Sample cases. (A) 48-y-old man with mCRPC treated with 4 cycles of PSMA-RLT between bPET and ePET. Patient had no new lesions on ePET, was classified as non-PD on basis of PSMA-VOL and RECIP 1.0, and experienced PSA decrease of 100% from bPET to ePET. Patient had follow-up of 41.5 mo from ePET. (B) 77-y-old man with mCRPC treated with 2 cycles of PSMA-RLT between bPET and ePET. Patient had new lesions on ePET, was classified as PD on basis of PSMA-VOL and RECIP 1.0, and experienced PSA increase of 582.5% from bPET to ePET. Patient had OS of 5.0 mo from ePET. (C) 59-y-old man with mCRPC treated with 3 cycles of PSMA-RLT between bPET and ePET. Patient had new lesions on ePET but was classified as non-PD on basis of PSMA-VOL and RECIP 1.0 and experienced PSA decrease of 79% from bPET to ePET. Patient had OS of 9.7 mo from ePET. (D) 65-y-old man with mCRPC treated with 5 cycles of PSMA-RLT between bPET and ePET. Patient had no new lesions on ePET and was classified as non-PD on basis of PSMA-VOL and RECIP 1.0 but experienced PSA increase of 103.9% from bPET to ePET. Patient had OS of 11.8 mo from ePET.

progressors (4). This discrepancy illustrates the importance of incorporating quantitative, whole-body PSMA-PET parameters in response assessment. Furthermore, in a comparative analysis of criteria for therapy response assessment in mCRPC, RECIP 1.0 identified fewer patients with PD, and patients classified as PD had a higher risk of death than non-PD patients by RECIP 1.0 compared with PSMA PET Progression criteria (10). These findings suggest that the incorporation of changes in PSMA-VOL in response evaluation may be more informative than per-lesion analyses (10).

Automatic segmentation software is currently in development to provide fast and reproducible tools to extract whole-body quantitative PSMA-PET metrics and enable their widespread use in clinical practice (8,11). As an alternative to the extraction of whole-body quantitative PSMA-PET parameters, a recent study also demonstrated that RECIP 1.0 determined by visual reads had excellent interreader reliability and agreement with quantitative RECIP 1.0 as determined by semiautomatic segmentation software, and progression by visual RECIP 1.0 was prognostic for OS in mCRPC patients undergoing

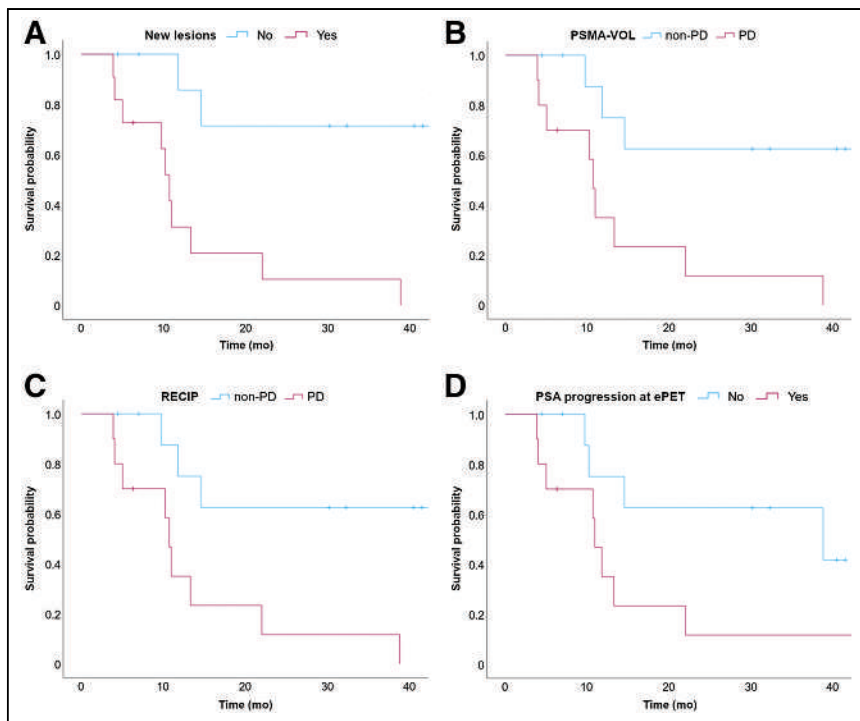


**FIGURE 3.** Kaplan-Meier curves. (A) Appearance of new lesions on ePET. (B) Progressive PSMA-VOL vs. nonprogressive PSMA-VOL on ePET. (C) Progressive RECIP vs. nonprogressive RECIP on ePET. (D) PSA progression status at time of ePET. PD = progressive disease.

PSMA-RLT (12). Visual RECIP can serve as an effective surrogate for quantitative changes derived from a tumor segmentation software.

The prognostic value of ePET has been extensively explored with <sup>18</sup>F-FDG in lymphoma both using visual scores (Deauville/IHC) and using quantitative parameters (changes in SUV<sub>max</sub> and metabolic tumor volume) (13–16). <sup>18</sup>F-FDG PET is a response assessment and surveillance tool routinely incorporated in the management of lymphoma patients. Response monitoring and prognostic assessments based on multiple PSMA-PET parameters including ePET may be considered in the management of mCRPC patients to guide treatment decisions in a more personalized manner. However, the value of ePET for clinical management may be more limited in mCRPC patients undergoing treatment with PSMA-RLT than is end-of-treatment <sup>18</sup>F-FDG PET in lymphoma patients, since mCRPC patients rarely have a complete response to PSMA-RLT. Still, changes in PSMA-PET parameters from baseline to end of treatment may be able to predict OS and progression-free survival in mCRPC patients.

If ePET is shown to be an independent predictor of OS and progression-free survival in large, prospective trials, it can serve as an expedited novel endpoint for clinical trials assessing novel drugs.

For other molecular targeted therapeutics, there are only limited series reporting on the prognostic value of end-of-treatment PET/CT with <sup>68</sup>Ga-DOTATATE in patients with neuroendocrine tumors undergoing treatment with somatostatin receptor-targeted RLT (17). In a retrospective analysis of 12 patients, decreases in the H-lesion SUV<sub>max</sub> on end-of-treatment DOTATATE PET indicated a lower risk for PD within 20 mo of therapy (18). In another retrospective analysis of 30 patients, increases in whole-body somatostatin receptor tumor volume on end-of-treatment DOTATATE PET were associated with lower OS (19). Future studies that investigate the prognostic value of whole-body targeted PET imaging metrics in patients undergoing targeted therapy are warranted.

The main limitation of this study is the selection bias inherent in its retrospective design. First, we only included patients who survived long enough to undergo ePET. Therefore, the OS from bPET in

our cohort was 19.5 mo, compared with 15.3 mo from randomization in the treatment arm of the VISION trial. This difference in OS can also be explained by the difference in patient populations: multiple patients in our cohort did not previously undergo taxane-based chemotherapy, which was a prerequisite for enrollment in the VISION trial. Second, patients were more likely to be referred to undergo a restaging PSMA-PET scan after their last PSMA-RLT cycle because of suspicion of disease progression based on PSA. Therefore, there was a general concordance between PSA progression status and characteristics on PSMA-PET. There were only 2 patients (cases 5 and 15, supplemental materials) who experienced PSA progression at ePET but were classified as non-PD on the basis of RECIP 1.0. Given the small size of our cohort, we were not able to directly compare the prognostic value of PSA with PSMA-PET in this analysis. In the original RECIP 1.0 study, among the patients without a PSA response at 12 wk (76/124, 61%), patients classified as RECIP-PR (10/76, 13%) had an OS

**TABLE 3**  
ePET and PSA Progression

Parameter	Total	PSA progression at ePET	No PSA progression at ePET	P
Total	18	10 (55.6)	8 (44.4)	NA
New lesions on ePET	9 (50)	8 (80)*	1 (12.5)	0.015
PSMA-VOL, PD	8 (44.4)	8 (80)*	0 (0)	0.001
RECIP, PD	8 (44.4)	8 (80)*	0 (0)	0.001

\*Significant by Fisher exact test.

NA = not applicable.

Data are number and percentage.

superior to that of patients without RECIP-PR (66/76, 87%): 22.7 versus 9.0 mo (4). These results demonstrate the potential added value of PSMA-PET to PSA for therapy response assessment.

Other limitations of this retrospective study include the small sample size, the use of a single PET reader, the heterogeneous number of PSMA-RLT cycles administered for each patient before ePET, and the heterogeneity of prior and concomitant mCRPC therapies. Five patients initiated other treatments in addition to PSMA-RLT between bPET and ePET (supplemental materials). Thus, the impact of PSMA-RLT on PSMA-PET findings could not be teased out in these patients.

Larger prospective trials are necessary to define the prognostic value of progression on ePET by RECIP 1.0 for progression-free survival and OS. These trials could provide data to support the use of PSMA-PET as a novel surrogate endpoint in clinical trials.

## CONCLUSION

In this retrospective cohort of 20 mCRPC patients treated with PSMA-RLT, progression on ePET by the appearance of new lesions, changes in PSMA-VOL, and RECIP 1.0 was prognostic for OS. These findings warrant validation in a larger, multicentric patient cohort.

## DISCLOSURE

Jeremie Calais reports prior consulting services for Advanced Accelerator Applications, Astellas, Blue Earth Diagnostics, Curium Pharma, DS Pharma, EXINI, GE Healthcare, Isoray, IBA RadioPharma, Janssen Pharmaceuticals, Lightpoint Medical, Lantheus, Monrol, Novartis, Progenics, POINT Biopharma, Radiomedix, Sanofi, and Telix Pharmaceuticals outside the submitted work. Johannes Czernin is the founder of Sofie Biosciences and Trethera Therapeutics and serves as a scientific advisor for Point Biopharma, RayzeBio, Jubilant Radiopharma, and Amgen. Matthew Rettig reports consulting services for Progenics, Amgen, INmune Bio, Bayer, Astra-Zeneca, and Myovant; receives research funding from Novartis, Merck, and Progenics; and is on the speakers' bureau for Bayer and Janssen. No other potential conflict of interest relevant to this article was reported.

## KEY POINTS

**QUESTION:** What is the prognostic value of ePET in mCRPC patients treated with PSMA-RLT?

**PERTINENT FINDINGS:** In this retrospective study of 20 mCRPC patients treated with PSMA-RLT, progression on ePET by the appearance of new lesions, changes in PSMA-VOL, and RECIP 1.0 was prognostic for OS.

**IMPLICATIONS FOR PATIENT CARE:** Progression on ePET by RECIP 1.0 is prognostic for OS and may be considered in the management of mCRPC patients to guide treatment decisions in a more personalized manner.

## REFERENCES

1. Sartor O, de Bono J, Chi KN, et al. Lutetium-177-PSMA-617 for metastatic castration-resistant prostate cancer. *N Engl J Med*. 2021;385:1091–1103.
2. Scher HI, Morris MJ, Stadler WM, et al. Trial design and objectives for castration-resistant prostate cancer: updated recommendations from the Prostate Cancer Clinical Trials Working Group 3. *J Clin Oncol*. 2016;34:1402–1418.
3. Henrich U, Eder M. [<sup>68</sup>Ga]Ga-PSMA-11: The first FDA-approved <sup>68</sup>Ga-radio-pharmaceutical for PET imaging of prostate cancer. *Pharmaceuticals (Basel)*. 2021;14:713.
4. Gafita A, Rauscher I, Weber M, et al. Novel framework for treatment response evaluation using PSMA PET/CT in patients with metastatic castration-resistant prostate cancer (RECIP 1.0): an international multicenter study. *J Nucl Med*. 2022;63:1651–1658.
5. Michalski K, Klein C, Brueggemann T, Meyer PT, Jilg CA, Ruf J. Assessing response to [<sup>177</sup>Lu]PSMA radioligand therapy using modified PSMA PET progression criteria. *J Nucl Med*. 2021;62:1741–1746.
6. Fanti S, Hadaschik B, Herrmann K. Proposal for systemic-therapy response-assessment criteria at the time of PSMA PET/CT imaging: the PSMA PET progression criteria. *J Nucl Med*. 2020;61:678–682.
7. Pathmanandavel S, Crumbaker M, Nguyen A, et al. The prognostic value of post-treatment <sup>68</sup>Ga-PSMA-11 PET/CT and <sup>18</sup>F-FDG PET/CT in metastatic castration-resistant prostate cancer treated with <sup>177</sup>Lu-PSMA-617 and NOX66 in a phase I/II trial (LuPIN). *J Nucl Med*. 2023;64:69–74.
8. Gafita A, Bieth M, Kronke M, et al. qPSMA: semiautomatic software for whole-body tumor burden assessment in prostate cancer using <sup>68</sup>Ga-PSMA11 PET/CT. *J Nucl Med*. 2019;60:1277–1283.
9. Calais J, Gafita A, Eiber M, et al. Prospective phase 2 trial of PSMA-targeted molecular Radiotherapy with <sup>177</sup>Lu-PSMA-617 for metastatic castration-resistant Prostate Cancer (RESIST-PC): efficacy results of the UCLA cohort. *J Nucl Med*. 2021;62:1440–1446.
10. Gafita A, Rauscher I, Fendler WP, et al. Measuring response in metastatic castration-resistant prostate cancer using PSMA PET/CT: comparison of RECIST 1.1, aPCWG3, aPERCIST, PPP, and RECIP 1.0 criteria. *Eur J Nucl Med Mol Imaging*. 2022;49:4271–4281.
11. Seifert R, Herrmann K, Kleesiek J, et al. Semiautomatically quantified tumor volume using <sup>68</sup>Ga-PSMA-11 PET as a biomarker for survival in patients with advanced prostate cancer. *J Nucl Med*. 2020;61:1786–1792.
12. Gafita A, Djaileb L, Rauscher I, et al. Practical RECIP: visual assessment of response evaluation criteria in PSMA-PET 1.0. *Med Nucl (Paris)*. 2023;47:41–42.
13. Albano D, Bosio G, Re A, Pagani C, Giubbini R, Bertagna F. Metabolic behavior and prognostic value of early and end of treatment <sup>18</sup>F-FDG PET/CT in adult Burkitt's lymphoma: the role of Deauville and IHP criteria. *Leuk Lymphoma*. 2019;60:326–333.
14. Wang H, Shen G, Jiang C, Li L, Cui F, Tian R. Prognostic value of baseline, interim and end-of-treatment <sup>18</sup>F-FDG PET/CT parameters in extranodal natural killer/T-cell lymphoma: a meta-analysis. *PLoS One*. 2018;13:e0194435.
15. Chang Y, Fu X, Sun Z, et al. Utility of baseline, interim and end-of-treatment <sup>18</sup>F-FDG PET/CT in extranodal natural killer/T-cell lymphoma patients treated with L-asparaginase/pegaspargase. *Sci Rep*. 2017;7:41057.
16. Jiang C, Su M, Kosik RO, Zou L, Jiang M, Tian R. The Deauville 5-point scale improves the prognostic value of interim FDG PET/CT in extranodal natural killer/T-cell lymphoma. *Clin Nucl Med*. 2015;40:767–773.
17. Chan DL, Clarke SJ, Diakos CI, et al. Prognostic and predictive biomarkers in neuroendocrine tumours. *Crit Rev Oncol Hematol*. 2017;113:268–282.
18. Opalińska M, Morawiec-Slawek K, Kania-Kuc A, Al Maraii I, Sowa-Staszczak A, Hubalewska-Dydejczyk A. Potential value of pre- and post-therapy [<sup>68</sup>Ga]Ga-DOTA-TATE PET/CT in the prognosis of response to PRRT in disseminated neuroendocrine tumors. *Front Endocrinol (Lausanne)*. 2022;13:929391.
19. Bello Martinez R, Ghesani M, Wolin E, Kim M, Ghesani N, Gavane S. Study evaluating the prognostic value of PET parameters after <sup>177</sup>Lu-DOTATATE peptide receptor therapy in NET patients [abstract]. *J Nucl Med*. 2021;62(suppl 1):77.

# Do Bone Scans Overstage Disease Compared with PSMA PET at Initial Staging? An International Multicenter Retrospective Study with Masked Independent Readers

Thomas A. Hope<sup>1,2</sup>, Matthias Benz<sup>3</sup>, Fei Jiang<sup>4</sup>, Daniel Thompson<sup>1</sup>, Francesco Barbato<sup>5</sup>, Roxana Juarez<sup>1</sup>, Miguel Hernandez Pampaloni<sup>1</sup>, Martin Allen-Auerbach<sup>3</sup>, Pawan Gupta<sup>3</sup>, Wolfgang P. Fendler<sup>5</sup>, and Jeremie Calais<sup>3</sup>

<sup>1</sup>Department of Radiology and Biomedical Imaging, University of California, San Francisco, San Francisco, California; <sup>2</sup>Helen Diller Family Comprehensive Cancer Center, University of California, San Francisco, San Francisco, California; <sup>3</sup>Ahmanson Translational Theranostics Division, Department of Molecular and Medical Pharmacology, David Geffen School of Medicine, UCLA, Los Angeles, California; <sup>4</sup>Department of Epidemiology and Biostatistics, University of California, San Francisco, San Francisco, California; and <sup>5</sup>Department of Nuclear Medicine, University of Duisburg-Essen and German Cancer Consortium, University Hospital Essen, Essen, Germany

Prostate-specific membrane antigen (PSMA) PET has a higher accuracy than CT and bone scans to stage patients with prostate cancer. We do not understand how to apply clinical trial data based on conventional imaging to patients staged using PSMA PET. Therefore, we aimed to evaluate the ability of bone scans to detect osseous metastases using PSMA PET as a reference standard. **Methods:** In this multicenter retrospective diagnostic study, 167 patients with prostate cancer, who were imaged with bone scans and PSMA PET performed within 100 d, were included for analysis. Each study was interpreted by 3 masked readers, and the results of the PSMA PET were used as the reference standard. Endpoints were positive predictive value (PPV), negative predictive value (NPV), and specificity for bone scans. Additionally, interreader reproducibility, positivity rate, uptake on PSMA PET, and the number of lesions were evaluated. **Results:** In total, 167 patients were included, with 77 at initial staging, 60 in the biochemical recurrence and castration-sensitive prostate cancer setting, and 30 in the castration-resistant prostate cancer setting. In all patients, the PPV, NPV, and specificity for bone scans were 0.73 (95% CI, 0.61–0.82), 0.82 (95% CI, 0.74–0.88), and 0.82 (95% CI, 0.74–0.88), respectively. In patients at initial staging, the PPV, NPV, and specificity for bone scans were 0.43 (95% CI, 0.26–0.63), 0.94 (95% CI, 0.85–0.98), and 0.80 (95% CI, 0.68–0.88), respectively. Interreader agreement for bone disease was moderate for bone scans (Fleiss  $\kappa$ , 0.51) and substantial for the PSMA PET reference standard (Fleiss  $\kappa$ , 0.80). **Conclusion:** In this multicenter retrospective study, the PPV of bone scans was low in patients at initial staging, with 57% of positive bone scans being false positives. This suggests that a large proportion of patients considered low-volume metastatic by the bone scan actually had localized disease, which is critical when applying clinical data from trials such as the STAMPEDE M1 radiation therapy trial to patients being staged with PSMA PET.

**Key Words:** oncology; radiopharmaceuticals; bone scans; initial staging; PSMA PET; prostate cancer

**J Nucl Med 2023; 64:1744–1747**  
DOI: 10.2967/jnumed.123.265916

**P**rostate-specific membrane antigen (PSMA) PET has become the standard imaging modality for patients with prostate cancer at initial staging and biochemical recurrence (1). Previous work has compared the results of PSMA PET with the results of bone scans for the detection of osseous metastases and has shown that PSMA PET has a sensitivity and specificity higher than that of bone scans (2,3). Nearly all prostate cancer trials have used conventional imaging (bone scans in combination with CT scans) for staging. However, how to apply the data from these clinical trials to patients staged with PSMA PET remains unclear.

In the CHAARTED trial, patients with high-volume disease, which is defined as having 4 or more bone lesions on a bone scan, were shown to have overall survival benefits with the addition of docetaxel compared with androgen-deprivation therapy alone (4). Given that PSMA PET has a detection sensitivity higher than that of bone scans, most believe that a larger number of lesions seen on PSMA PET are needed to meet the definition of high-volume disease.

More recently, a secondary analysis of the STAMPEDE M1 radiation therapy (RT) trial demonstrated that patients with low-volume disease, which is defined as having 3 or fewer lesions on a bone scan, benefit from prostate bed RT when combined with androgen-deprivation therapy and docetaxel (5). The results of this study have led to the use of prostate bed RT in patients with low-volume metastatic disease on bone scans. However, questions remain about the accuracy of bone scans for the assessment of metastatic burden and what number of lesions seen on PSMA PET would cause patients to be considered to have high-volume disease and thus not to benefit from prostate bed RT.

We therefore set forth to understand the positive predictive value (PPV), negative predictive value (NPV), and specificity of bone scans using PSMA PET as a reference standard in patients at various disease stages to help us understand how to use PSMA PET results in the setting of clinical trial data performed using conventional imaging.

## MATERIALS AND METHODS

This was an international multicenter retrospective head-to-head comparison imaging study. Databases from 3 institutions (University of California, San Francisco, UCLA, and Essen) were retrospectively

Received Apr. 21, 2023; revision accepted Jul. 5, 2023.

For correspondence or reprints, contact Thomas Hope (thomas.hope@ucsf.edu).

Guest Editor: Michael Hofman, Peter MacCallum Cancer Centre

Published online Aug. 17, 2023.

COPYRIGHT © 2023 by the Society of Nuclear Medicine and Molecular Imaging.

screened, and patients were included who had PSMA PET scans and bone scans performed within 100 d of one another. Patients with new interval treatment were excluded. Patients included in the analysis were those at initial staging, in a biochemical recurrence and castration-sensitive prostate cancer (BCR/CSPC) setting, and in a castration-resistant prostate cancer (CRPC) setting. This study was approved by each site's institutional review board; all data were deidentified, and informed consent was waived.

### Image Interpretation

Each bone scan was interpreted by 3 masked readers, and each PSMA PET scan was interpreted by 3 other masked readers. Anonymized datasets were provided to each reader. Readers were masked to all clinical information and did not have access to other imaging studies available for the patient. For bone scans, the presence of prostate cancer (positive vs. negative) was recorded for 17 osseous regions. For PSMA PET scans, in addition to the osseous regions used for bone scans, 4 other regions were recorded including prostate bed, pelvic nodes, extrapelvic nodes, and visceral metastases.  $SUV_{max}$  was recorded for the osseous lesion with the highest uptake. The total number of osseous lesions was also noted by each reader for both bone scans and PSMA PET scans. Their findings were entered by the readers directly into the central REDCap database (supplemental material, available at <http://jnm.snmjournals.org>). Per-region majority rule was used for the analysis.

### Statistical Analysis

The primary outcome was PPV, NPV, and specificity of bone scans using PSMA PET as a reference standard. The secondary outcomes were the comparison of patient-level positivity rates, the number of lesions detected with each modality, the interreader agreement, and the PSMA PET  $SUV_{max}$ . Results were broken down by clinical stage. Interreader agreement was evaluated using Fleiss  $\kappa$  and interpreted by criteria of Landis and Koch by region (6). CIs were calculated using the Wilson method (7). A 95% CI was calculated for the number of lesions visualized. A 2-sided Student *t* test was used to compare  $SUV_{max}$  and the number of lesions seen between cohorts. Statistical analyses were performed with R, version 3.5.1 (R Foundation).

## RESULTS

In total, 167 patients were included across 3 institutions (Supplemental Fig. 1). Seventy-seven patients were imaged at initial staging, 60 in the BCR/CSPC setting, and 30 in the CRPC setting (Table 1). The median time between the bone scan and the PSMA PET scan was 29 d (range, 1–100 d). PSMA PET was performed earlier than bone scanning in 117 patients (70%).

### Imaging Results

On the basis of the majority read, 66 (40%) patients had osseous region disease on bone scans and PSMA PET scans (Table 2). Of the 66 patients positive on bone scanning, 48 were positive on PSMA PET. The PPV and NPV for bone scans were 0.73 (95% CI, 0.61–0.82) and 0.82 (95% CI, 0.74–0.88), respectively, with a specificity of 0.82 (95% CI, 0.74–0.88).

When focusing on patients at the initial staging, we found that 13 (17%) patients had osseous region disease on PSMA PET, whereas 23 (30%) were identified as having osseous region disease on bone scanning. Of the 23 patients positive on bone scanning, only 10 were positive on PSMA PET (Fig. 1). The PPV and NPV for bone scans were 0.43 (95% CI, 0.26–0.63) and 0.94 (95% CI, 0.85–0.98), respectively, with a specificity of 0.80 (95% CI, 0.68–0.88). When we limited the data to patients who had imaging done within 30 d, the PPV and NPV for bone scans were 0.36 (95% CI, 0.16–0.61) and 0.90 (95% CI, 0.75–0.97), respectively, with a specificity of 0.76 (95% CI, 0.60–0.87). In the 16 patients with fewer than 4 lesions on bone scanning (i.e., low volume by CHARTED criteria), only 7 (44%) were positive on PSMA PET. Three patients were positive on PSMA PET and negative on bone scanning.

In the BCR/CSPC setting, the PPV, NPV, and specificity were 0.77 (95% CI, 0.57–0.90), 0.74 (95% CI, 0.58–0.85), and 0.85 (95% CI, 0.69–0.93), respectively. In CRPC patients, the PPV, NPV, and specificity were 1.0 (95% CI, 0.85–1.0), 0.56 (95% CI, 0.27–0.81), and 1.0 (95% CI, 0.57–1.0), respectively. Of the 16

**TABLE 1**  
Patient Demographics

Parameters	Initial staging	BCR/CSPC	CRPC	Overall
Patients	77	60	30	167
Age (y)	66.5 (42–86)	71.2 (53–85)	71.0 (52–88)	69.0 (42–88)
PSA at imaging (ng/mL)	12.2 (1.8–516)	4.7 (0.1–1164)	26.3 (0.9–1389)	10.5 (0.1–1389)
ISUP				
1–3	15 (19)	39 (65)	10 (33)	64 (38)
4	22 (29)	7 (12)	6 (20)	35 (21)
5	38 (49)	13 (22)	12 (40)	63 (38)
Prior treatments				
RP	0 (0)	40 (67)	19 (64)	59 (35)
RT	0 (0)	37 (62)	25 (83)	62 (37)
ARTT	1 (1)	4 (7)	9 (30)	14 (8)
Chemotherapy	0 (0)	9 (15)	10 (33)	19 (11)
Days between PSMA PET and bone scan	28.0 (1–85)	41.5 (1–100)	10.0 (1–87)	29.0 (1–100)
Number of patients with <30 d between imaging	43 (56)	23 (38)	18 (60)	84 (50)

PSA = prostate-specific antigen; ISUP = International Society of Urological Pathology; RP = radical prostatectomy; ARTT = androgen receptor-targeted therapy.

Qualitative data are number and percentage; continuous data are median and range.



**TABLE 2**  
Imaging Results

Parameter	Initial staging	BCR/CSPC	CRPC	Overall
<b>Bone scans</b>				
M1b positive	23 (30)	22 (37)	21 (70)	66 (40)
Low volume (1–3 lesions)	16 (70)	10 (45)	6 (29)	32 (48)
High volume ( $\geq 4$ lesions)	7 (30)	12 (55)	15 (71)	34 (52)
<b>PSMA PET</b>				
T-positive	69 (90)	17 (28)	6 (20)	92 (55)
N-positive	28 (36)	20 (33)	14 (47)	62 (37)
M1a-positive	9 (12)	20 (33)	16 (53)	45 (27)
M1b-positive	13 (17)	28 (47)	25 (83)	66 (40)
M1c-positive	0 (0)	6 (10)	3 (10)	9 (5)
<b>Bone scan vs. PSMA PET comparison</b>				
Both positive, TP	10 (13)	17 (28)	21 (70)	48 (29)
Both negative, TN	51 (66)	27 (45)	5 (17)	83 (50)
BS-positive/PSMA-negative, FP	13 (17)	5 (8)	0 (0)	18 (11)
PSMA-positive/BS-negative, FN	3 (4)	11 (18)	4 (13)	18 (11)

M1b = osseous regions; T = prostate bed; N = pelvic nodes; M1a = extrapelvic nodes; M1c = visceral metastases; TP = true-positive; TN = true-negative; FP = false-positive; FN = false-negative.  
Data are number and percentage.

patients in the BCR/CSPC and CRPC settings with fewer than 4 lesions on bone scanning, 12 (75%) were positive on PSMA PET.

In patients with positive osseous lesions on both PSMA PET and bone scanning by a majority read ( $n = 48$ ), there were  $4.4 \pm 0.6$  lesions on bone scanning and  $7.5 \pm 1.6$  lesions on

PSMA PET ( $P < 0.001$ ). In the subset of patients at initial staging, the number of lesions seen was smaller and the difference not significant, with  $2.8 \pm 1.1$  lesions on bone scanning and  $3.2 \pm 1.3$  lesions on PSMA PET ( $P = 0.5$ ). The mean  $SUV_{max}$  on PSMA PET in patients at initial staging was lower than that in patients in the BCR/CSPC and CRPC settings ( $10.3 \pm 6.9$  vs.  $36.3 \pm 42.5$ ,  $P = 0.049$ ).

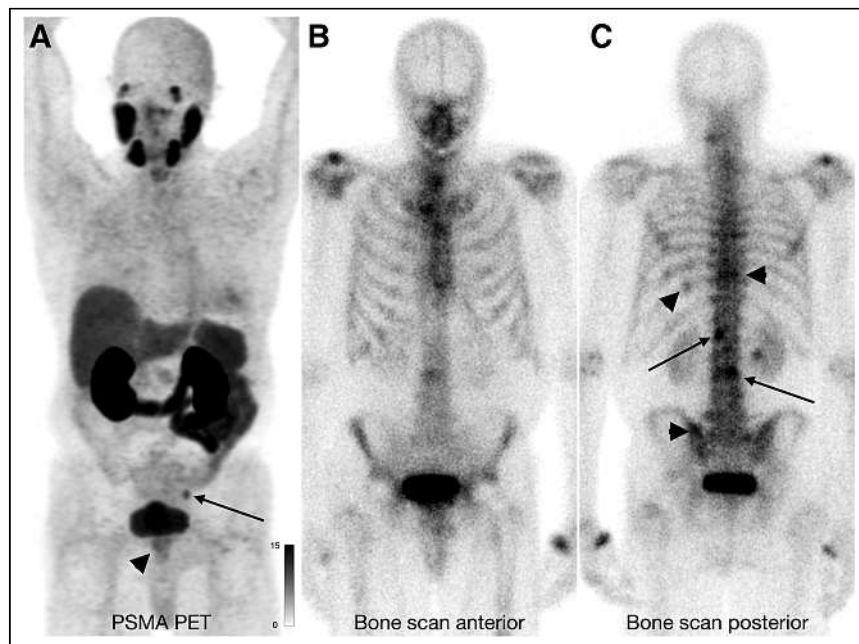


**FIGURE 1.** A 74-y-old man at initial staging with PSMA PET that demonstrates low uptake in primary tumor (A, arrowhead) and left pelvic side wall node (A, arrow). Bone scan was read as positive by 2 of 3 readers. One reader read 2 lesions in lumbar spine (C, arrows), and second reader read additional lesions in ribs, thoracic spine, and sacrum (C, arrowheads). This case is false-positive on bone scan.

#### Interreader Agreement

For osseous lesions, interreader agreement for bone scans was moderate (Fleiss  $\kappa$ , 0.51), whereas for PSMA PET, it was substantial (Fleiss  $\kappa$ , 0.80). For prostate bed, pelvic nodes, and extrapelvic nodes, the interreader agreement for PSMA PET was substantial: 0.73, 0.61, and 0.73, respectively. For other organs, the interreader agreement for PSMA PET was moderate (0.41).

#### DISCUSSION

In this multicenter retrospective head-to-head comparison diagnostic study using PSMA PET as a reference standard, we demonstrated that the specificity of bone scans is high and similar across disease states, but the PPV is lower in patients at initial staging than in the population as a whole (0.43 vs. 0.73). Overall, 27% of patients with osseous metastases on bone scanning were negative on PSMA PET, and this increased to 57% in patients at initial staging.

Prior work has demonstrated similar high specificities for bone scans, reporting values of approximately 0.82 (8). It is important to remember that in the initial staging population, where the prevalence of osseous metastases is lower, the false-positive rate is much higher. This can be seen in our data, in which the percentage of bone scans that were false positive was 57% at initial staging versus 0% in the CRPC setting. These results are nearly identical to prior work comparing the results of bone scanning with PSMA PET at initial staging (9).

These results bring into question how to define patients with low-volume disease using PSMA PET in light of the STAMPEDE M1 RT data. If one were to apply our initial staging data to the M1 RT trial, 56% of patients with low-volume disease based on bone scanning had localized disease by PSMA PET. Therefore, there is a greater likelihood that the overall survival benefit seen in the trial is not driven by preventing further development of metastatic disease but rather by providing definitive RT to nonmetastatic disease that was incorrectly classified as M1 by bone scanning. Although one typically thinks of bone scans as understaging disease relative to PSMA PET (as was shown in our study, because more lesions than on bone scans were seen in patients with positive PSMA PET scans), in the initial staging setting a bone scan overstages patients relative to PSMA PET because of its high false-positive rate.

This study has many limitations. First, using PSMA as a reference standard for evaluation of bone scans can be problematic, particularly given the false positives on PSMA PET in bone lesions. Of note, PSMA PET false positives would not impact the false-negative rate of bone scans in our analysis. Second, the bone scans and PSMA PET scans were not concurrent, although the difference in PPV was not impacted by limiting imaging studies done 30 d apart versus 100 d apart. Third, planar bone scans were used consistently with the STAMPEDE trial, but it is well established that the use of SPECT/CT would increase the specificity and PPV of bone scans (10). It should be noted that the STAMPEDE trial did not require SPECT/CT. Fourth, as the masked reads were performed retrospectively, readers may have been inclined to increase their sensitivity.

## CONCLUSION

In this multicenter retrospective diagnostic study using PSMA PET as the reference standard, the PPV of bone scans at initial staging was low (0.43). This results in incorrect staging (as having osseous metastasis) of more than half of patients in this group. This overstaging by bone scans is important when applying clinical data from trials such as the STAMPEDE M1 RT trial to patients being staged with PSMA PET. Before patients receive prostate bed RT in low-volume metastatic disease on PSMA PET, further work should be performed to understand if the results of the STAMPEDE M1 RT trial are generalizable.

## DISCLOSURE

Thomas Hope has grant funding to the institution from Clovis Oncology, Philips, GE Healthcare, Lantheus, the Prostate Cancer

Foundation, and the National Cancer Institute (R01CA235741 and R01CA212148); received personal fees from Ipsen, Bayer, and BlueEarth Diagnostics; and received fees from and has an equity interest in RayzeBio and Curium. Wolfgang Fendler reports fees from SOFIE Biosciences (research funding), Janssen (consultant, speaker), Calyx (consultant), Bayer (consultant, speaker, research funding), Parexel (image review), Novartis (speaker), and Telix (speaker) outside the submitted work. No other potential conflict of interest relevant to this article was reported.

## KEY POINTS

**QUESTION:** What is the PPV, NPV, and specificity of bone scans in prostate cancer patients using PSMA PET as a reference standard?

**PERTINENT FINDINGS:** Although the specificity of bone scans was similar in initial staging of patients versus the entire cohort (0.80 vs. 0.82), the PPV was markedly lower in the initial staging of patients (0.43 vs. 0.73).

**IMPLICATIONS FOR PATIENT CARE:** The lower PPV at the initial staging of patients means that more than half of patients staged as having metastatic disease on bone scans actually had no osseous metastasis. The observed overstaging by bone scans is important when applying clinical data from trials such as the STAMPEDE M1 RT trial to patients being staged with PSMA PET.

## REFERENCES

1. Jadvar H, Calais J, Fanti S, et al. Appropriate use criteria for prostate-specific membrane antigen PET imaging. *J Nucl Med*. 2022;63:59–68.
2. Pyka T, Okamoto S, Dahlbender M, et al. Comparison of bone scintigraphy and <sup>68</sup>Ga-PSMA PET for skeletal staging in prostate cancer. *Eur J Nucl Med Mol Imaging*. 2016;43:2114–2121.
3. Zhao G, Ji B. Head-to-head comparison of <sup>68</sup>Ga-PSMA-11 PET/CT and <sup>99m</sup>Tc-MDP bone scintigraphy for the detection of bone metastases in patients with prostate cancer: a meta-analysis. *AJR*. 2022;219:386–395.
4. Sweeney CJ, Chen Y-H, Carducci M, et al. Chemohormonal therapy in metastatic hormone-sensitive prostate cancer. *N Engl J Med*. 2015;373:737–746.
5. Ali A, Hoyle A, Haran AM, et al. Association of bone metastatic burden with survival benefit from prostate radiotherapy in patients with newly diagnosed metastatic prostate cancer: a secondary analysis of a randomized clinical trial. *JAMA Oncol*. 2021;7:555–563.
6. Landis JR, Koch GG. An application of hierarchical kappa-type statistics in the assessment of majority agreement among multiple observers. *Biometrics*. 1977;33:363–374.
7. Newcombe RG. Two-sided confidence intervals for the single proportion: comparison of seven methods. *Stat Med*. 1998;17:857–872.
8. Shen G, Deng H, Hu S, Jia Z. Comparison of choline-PET/CT, MRI, SPECT, and bone scintigraphy in the diagnosis of bone metastases in patients with prostate cancer: a meta-analysis. *Skeletal Radiol*. 2014;43:1503–1513.
9. Lengana T, Lawal IO, Boshomane TG, et al. <sup>68</sup>Ga-PSMA PET/CT replacing bone scan in the initial staging of skeletal metastasis in prostate cancer: a fait accompli? *Clin Genitourin Cancer*. 2018;16:392–401.
10. Simsek DH, Sanli Y, Civan C, et al. Does bone scintigraphy still have a role in the era of <sup>68</sup>Ga-PSMA PET/CT in prostate cancer? *Ann Nucl Med*. 2020;34:476–485.

# Out with the Old, in with the New: Can We Bridge the Gap Between Clinical Trial Results Based on Bone Scans and the Era of Modern Prostate Cancer Imaging?

Michal Eifer<sup>1-3</sup>, Ramin Alipour<sup>3,4</sup>, Michael S. Hofman<sup>3,4</sup>, and Aravind S. Ravi Kumar<sup>3,4</sup>

<sup>1</sup>Department of Diagnostic Imaging, Chaim Sheba Medical Centre, Ramat Gan, Israel; <sup>2</sup>Sackler Faculty of Medicine, Tel Aviv University, Tel Aviv, Israel; <sup>3</sup>Molecular Imaging and Therapeutic Nuclear Medicine, Peter MacCallum Centre, Melbourne, Victoria, Australia; and <sup>4</sup>Sir Peter MacCallum Department of Oncology, University of Melbourne, Melbourne, Victoria, Australia

**P**rostate cancer is a significant contributor to overall cancer-related morbidity and mortality (1). Accurate disease staging is a critical component in making informed therapeutic decisions (2). Prostate cancer imaging has witnessed noteworthy advancements in recent years, with a noticeable shift from traditional imaging techniques such as <sup>99m</sup>Tc bone scans and CT to PET/CT modalities, most notably using various tracers targeting prostate-specific membrane antigen (PSMA). The Food and Drug Administration has granted approval for 5 PET/CT tracers since 2012, namely, <sup>11</sup>C-choline (2012), <sup>18</sup>F-fluciclovine (2016), <sup>68</sup>Ga-PSMA-11 (2020), <sup>18</sup>F-piflufolastat (2021), and <sup>18</sup>F-flotufolastat (2023). The Food and Drug Administration–approved indications for these agents include biochemical recurrence (BCR) in prostate cancer, with the latter 3 agents also approved for initial staging.

Extensive research has been performed to ascertain the diagnostic accuracy of PET/CT tracers as well as their performance in relation to conventional imaging. In a prospective trial that compared the diagnostic efficacy of <sup>68</sup>Ga-PSMA-11 with that of <sup>18</sup>F-fluciclovine, the former demonstrated significantly higher detection rates (3). Moreover, the multicenter, randomized pro-PSMA trial evaluated CT and bone scanning versus <sup>68</sup>Ga-PSMA-11 PET in staging men with high-risk prostate cancer, with PSMA PET demonstrating a 27% greater accuracy (4). Furthermore, in comparison to conventional bone scanning or PET/CT with bone-seeking tracers, whole-body PSMA PET/CT offers the advantage of detecting additional sites of disease beyond skeletal metastases, providing the added benefit of a 1-stop shop in its staging. Indeed, the mounting body of evidence on the diagnostic accuracy of PSMA PET agents has led to their inclusion in the National Comprehensive Cancer Network prostate cancer guidelines. Specifically, the guidelines recommend that <sup>18</sup>F-piflufolastat or <sup>68</sup>Ga-PSMA-11 PET/CT or PET/MRI be considered as alternatives to conventional imaging at initial staging, BCR, and workup for progressive disease (<https://www.nccn.org>).

Appropriate-use criteria for PSMA PET/CT, published in this journal in 2022 (5), also suggest that PSMA PET/CT is appropriate for staging newly diagnosed unfavorable intermediate- to high-risk

prostate cancer, staging BCR after radical prostatectomy or definitive radiotherapy, and assessing nonmetastatic castration-resistant prostate cancer based on conventional imaging. However, in the context of evaluating therapy response and restaging in castration-resistant disease, there are limitations in the available data for PSMA PET and a lack of validated standardized criteria for assessing response using this modality. As a result, conventional imaging remains the gold standard modality, as recognized by the Prostate Cancer Clinical Trials Working Group 3 (6).

The study published by Hope et al. (7) in this issue of *The Journal of Nuclear Medicine* is a great attempt at translating clinical trial findings derived from bone scans to PSMA PET/CT. This international multicenter retrospective study was conducted to evaluate the diagnostic efficacy of bone scans in detecting osseous metastases using PSMA PET/CT as a reference standard. The study enrolled 167 patients with prostate cancer (77 at initial staging, 60 at BCR, and 30 in the setting of castration resistance) who underwent bone scanning and PSMA PET/CT within 100 d. Three independent masked readers evaluated each scan without access to clinical information or other imaging results. Overall, the bone scans had a positive predictive value, negative predictive value, and specificity of 0.73, 0.82, and 0.82, respectively. However, when only the initial staging cohort was considered, the positive predictive value, negative predictive value, and specificity were 0.43, 0.94, and 0.8, respectively. In total, 27% of patients with bone metastases detected on bone scanning were found to be negative on PSMA PET/CT. This (false-positive) percentage increased to 57% in the initial staging group. In the separate analysis for BCR and castration-resistant patients, the positive predictive value was 0.77 and 1, respectively. This suggests that the rate of false-positive bone scans decreased as the pretest probability for metastatic disease increased (positive and negative predictive values are directly related to disease prevalence).

Hope et al. further discussed their findings in relation to the secondary analysis of the STAMPEDE M1 radiation therapy trial (8), which demonstrated the effectiveness of prostate irradiation in combination with androgen-deprivation therapy and docetaxel for patients with low-volume disease on bone scans (fewer than 4 bone metastases). Discovering the disease overestimation by bone scanning compared with PSMA PET/CT, Hope et al. then extrapolated that it was highly likely that many patients classified as having low-volume metastatic disease at initial staging in the STAMPEDE

Received Jun. 4, 2023; revision accepted Jul. 11, 2023.  
For correspondence or reprints, contact Aravind Ravi Kumar ([aravind.ravikumar@petermac.org](mailto:aravind.ravikumar@petermac.org)).  
Published online Aug. 17, 2023.  
COPYRIGHT © 2023 by the Society of Nuclear Medicine and Molecular Imaging.  
DOI: 10.2967/jnumed.123.266025

M1 radiation therapy trial based on bone scanning ( $\leq 57\%$ ) would have had localized disease had they been staged by PSMA PET/CT. Therefore, the additional survival benefit derived from the trial intervention would realistically be attributed to treating only localized disease. However, it is not possible to totally dismiss the added benefit of the trial intervention in the subset of patients who truly had low-volume M1 metastatic disease on bone scans. Despite Hope et al. and other groups' best efforts, it remains unknown how low-volume disease on the bone scan translates to PSMA PET/CT and whether there still is a survival benefit from irradiation of the primary in the presence of a (yet undefined) low burden of PSMA PET-detected metastatic disease.

It is noteworthy that Hope et al. screened 10,807 patients who had a PSMA PET/CT scan, only to find 973 patients (9%) who also had a bone scan. After excluding studies with scans performed more than 100 d apart and patients who had treatment between the 2 imaging modalities, they included 167 patients (1.5% of the screened population) in their final cohort, 70% (117 patients) of whom underwent PSMA PET/CT before bone scanning. Although this observation is a true reflection of a real-world scenario where bone scanning has been replaced by PSMA PET/CT, this would unintentionally introduce a selection bias in this study population.

Hope et al. were also masked to clinical and correlative imaging information when interpreting bone scans and used planar imaging only, with no category for equivocal scan interpretation, which is far from the reality of modern imaging reporting. The retrospective nature of the study, inclusion of metastatic castration-resistant prostate cancer patients, and known higher accuracy of PSMA PET/CT than of bone scanning could have also potentially introduced an unconscious bias into this study and the way bone scans were interpreted compared with what was undertaken in the original STAMPEDE trial (8). Finally, it is not clear how comfortable the readers in this study were at interpreting planar bone scans without SPECT/CT.

The dynamic landscape of prostate cancer imaging is witnessing novel PSMA PET/CT agents replacing CT and bone scanning. Although the accuracy of PSMA PET/CT findings is now accepted, integrating these findings in clinical situations where the body of evidence for treatment decision-making is based on conventional imaging remains an ongoing challenge. Further research is warranted to elucidate these nuances and to ensure a seamless transition. Incorporation of PSMA PET/CT (or in broader terms, novel molecular

imaging techniques and tracers) in future clinical trials should become mandatory. Additionally, efforts should be directed toward standardization of PSMA PET/CT reporting, establishing it as the new modern benchmark in future clinical trials and practice.

## DISCLOSURE

Michael Hofman received philanthropic/government grant support from the Prostate Cancer Foundation (PCF) funded by CANICA Oslo Norway, Peter MacCallum Foundation, Medical Research Future Fund (MRFF), NHMRC Investigator Grant, Movember, and the Prostate Cancer Foundation of Australia (PCFA); received research grant support (to institution) from Novartis (including AAA and Endocyte), ANSTO, Bayer, Isotopia, and MIM; and received consulting fees for lectures or advisory boards from Astellas and AstraZeneca in the last 2 years and Janssen, Merck/MSD, and Mundipharma in the last 5 years. Aravind Ravi Kumar received a research grant from Varian Medical Systems unrelated to this work. No other potential conflict of interest relevant to this article was reported.

## REFERENCES

1. Siegel RL, Miller KD, Wagle NS, et al. Cancer statistics, 2023. *CA Cancer J Clin*. 2023;73:17–48.
2. Parker C, Castro E, Fizazi K, et al. Prostate cancer: ESMO clinical practice guidelines for diagnosis, treatment and follow-up. *Ann Oncol*. 2020;31:1119–1134.
3. Calais J, Ceci F, Eiber M, et al.  $^{18}\text{F}$ -fluciclovine PET-CT and  $^{68}\text{Ga}$ -PSMA-11 PET-CT in patients with early biochemical recurrence after prostatectomy: a prospective, single-centre, single-arm, comparative imaging trial. *Lancet Oncol*. 2019;20:1286–1294.
4. Hofman MS, Lawrentschuk N, Francis RJ, et al. Prostate-specific membrane antigen PET-CT in patients with high-risk prostate cancer before curative-intent surgery or radiotherapy (proPSMA): a prospective, randomised, multicentre study. *Lancet*. 2020;395:1208–1216.
5. Jadvar H, Calais J, Fanti S, et al. Appropriate use criteria for prostate-specific membrane antigen PET imaging. *J Nucl Med*. 2022;63:59–68.
6. Scher HI, Morris MJ, Stadler WM, et al. Trial design and objectives for castration-resistant prostate cancer: updated recommendations from the Prostate Cancer Clinical Trials Working Group 3. *J Clin Oncol*. 2016;34:1402–1418.
7. Hope TA, Benz M, Jiang F, et al. Do bone scans overstage disease compared with PSMA PET at initial staging? An international multicenter retrospective study with masked independent readers. *J Nucl Med*. 2023;64:1744–1747.
8. Ali A, Hoyle A, Haran AM, et al. Association of bone metastatic burden with survival benefit from prostate radiotherapy in patients with newly diagnosed metastatic prostate cancer: a secondary analysis of a randomized clinical trial. *JAMA Oncol*. 2021;7:555–563.

# A Prostate-Specific Membrane Antigen PET-Based Approach for Improved Diagnosis of Prostate Cancer in Gleason Grade Group 1: A Multicenter Retrospective Study

Jingliang Zhang<sup>\*1</sup>, Fei Kang<sup>\*2</sup>, Jie Gao<sup>\*3</sup>, Jianhua Jiao<sup>1</sup>, Zhiyong Quan<sup>2</sup>, Shuaijun Ma<sup>1</sup>, Yu Li<sup>1</sup>, Shikuan Guo<sup>1</sup>, Zeyu Li<sup>1</sup>, Yuming Jing<sup>1</sup>, Keying Zhang<sup>1</sup>, Fa Yang<sup>1</sup>, Donghui Han<sup>1</sup>, Weihong Wen<sup>4</sup>, Jing Zhang<sup>5</sup>, Jing Ren<sup>6</sup>, Jing Wang<sup>†2</sup>, Hongqian Guo<sup>†3</sup>, and Weijun Qin<sup>†1</sup>

<sup>1</sup>Department of Urology, Xijing Hospital, Fourth Military Medical University, Xi'an, China; <sup>2</sup>Department of Nuclear Medicine, Xijing Hospital, Fourth Military Medical University, Xi'an, China; <sup>3</sup>Department of Urology, Nanjing Drum Tower Hospital, Affiliated Hospital of Nanjing University Medical School, Institute of Urology, Nanjing University, Nanjing, China; <sup>4</sup>Institute of Medical Research, Northwestern Polytechnical University, Xi'an, China; <sup>5</sup>Department of Pathology, Xijing Hospital, Fourth Military Medical University, Xi'an, China; and <sup>6</sup>Department of Radiology, Xijing Hospital, Fourth Military Medical University, Xi'an, China

The preoperative Gleason grade group (GG) from transrectal ultrasound-guided prostate biopsy is crucial for treatment decisions but may underestimate the postoperative GG and miss clinically significant prostate cancer (csPCa), particularly in patients with biopsy GG1. In such patients, an SUV<sub>max</sub> of at least 12 has 100% specificity for detecting csPCa. In patients with an SUV<sub>max</sub> of less than 12, we aimed to develop a model to improve the diagnostic accuracy of csPCa.

**Methods:** The study retrospectively included 56 prostate cancer patients with transrectal ultrasound-guided biopsy GG1 and an SUV<sub>max</sub> of less than 12 from 2 tertiary hospitals. All [<sup>68</sup>Ga]Ga-PSMA-HBED-CC PET scans were centrally reviewed in Xijing Hospital. A deep learning model was used to evaluate the overlap of SUV<sub>max</sub> (size scale, 3 cm) and the level of Gleason pattern (size scale, 500 μm). A diagnostic model was developed using the PRIMARY score and SUV<sub>max</sub>, and its discriminative performance and clinical utility were compared with other methods. The 5-fold cross-validation (repeated 1,000 times) was used for internal validation. **Results:** In patients with GG1 and an SUV<sub>max</sub> of less than 12, significant prostate-specific membrane antigen (PSMA) histochemical score (H-score) H-score overlap occurred among benign gland, Gleason pattern 3, and Gleason pattern 4 lesions, causing SUV<sub>max</sub> overlap between csPCa and non-csPCa. The model of  $10 \times \text{PRIMARY score} + 2 \times \text{SUV}_{\text{max}}$  exhibited a higher area under the curve (AUC, 0.8359; 95% CI, 0.7233–0.9484) than that found using only the SUV<sub>max</sub> (AUC, 0.7353;  $P = 0.048$ ) or PRIMARY score (AUC, 0.7257;  $P = 0.009$ ) for the cohort and a higher AUC (0.8364; 95% CI, 0.7114–0.9614) than that found using only the Prostate Imaging Reporting and Data System (PI-RADS) score of 5–4 versus 3–1 (AUC, 0.7036;  $P = 0.149$ ) and the PI-RADS score of 5–3 versus 2–1 (AUC, 0.6373;  $P = 0.014$ ) for a subgroup. The model reduced the misdiagnosis of the PI-RADS score of 5–4 versus 3–1 by 78.57% (11/14) and the PI-RADS score of 5–3 versus 2–1 by 77.78% (14/18). The internal validation showed that the mean 5-fold cross-validated AUC was 0.8357 (95% CI, 0.8357–0.8358). **Conclusion:** We preliminarily suggest that the model of  $10 \times \text{PRIMARY score} + 2 \times \text{SUV}_{\text{max}}$  may enhance the diagnostic accuracy of csPCa in patients with biopsy GG1 and an SUV<sub>max</sub> of less than 12 by maximizing PSMA information use, reducing the misdiagnosis of the PI-RADS score, and thereby aiding in making appropriate treatment decisions.

**Key Words:** PET; PRIMARY score; PSMA; diagnosis; prostate cancer

**J Nucl Med 2023; 64:1750–1757**

DOI: 10.2967/jnumed.122.265001

The International Society of Urological Pathology Gleason grade group (GG) before radical prostatectomy (RP) is a key factor in determining the appropriate treatment for prostate cancer (PCa). Transrectal ultrasound (TRUS)-guided prostate biopsy is the standard of care for obtaining preoperative GG (1). However, this approach has the limitation that it can potentially underestimate the true GG because of biopsy undersampling, leading to the misclassification of clinically significant PCa (csPCa) as indolent PCa, especially in patients with TRUS-guided biopsy GG1. According to a large-scale study with 17,598 cases, 55.7% of biopsy GG1 patients have experienced GG upgrading after RP (2). It is important to differentiate between indolent PCa and csPCa to determine the most appropriate treatment. Active surveillance is typically recommended for patients with indolent PCa, whereas curative treatment is the preferred option for csPCa (1). Therefore, multiple previous studies have attempted to identify csPCa patients using clinical and biopsy GG parameters (3). However, studies with large sample sizes, including 7,643 patients (4) and 10,089 patients (5), have concluded that clinical and pathologic morphology information alone is insufficient to accurately predict csPCa. It is necessary to include additional imaging or molecular information to improve the diagnostic performance (6). Previous studies have reported that the Prostate Imaging Reporting and Data System (PI-RADS) score had a diagnostic area under the curve (AUC) of only 0.672–0.694 for detecting csPCa in patients with biopsy GG1 (7,8). Consistent with this, the European Association of Urology guideline pointed out that the MRI PI-RADS score has low specificity in very low-risk patients, which can result in a higher incidence of false-positive results and necessitate further optimization (1).

In recent years, [<sup>68</sup>Ga]Ga-PSMA-HBED-CC ([<sup>68</sup>Ga]PSMA) PET/CT has gained recognition as a precise molecular imaging approach for PCa detection (9). Studies have indicated that prostate-specific membrane antigen (PSMA) intensity positively correlated with GG (10) and tumorigenic molecular events (11). SUV<sub>max</sub> can

Received Jan. 15, 2023; revision accepted Jul. 11, 2023.

For correspondence or reprints, contact Weijun Qin (qinwj@fmmu.edu.cn).

\*†Contributed equally to this work.

Published online Aug. 31, 2023.

COPYRIGHT © 2023 by the Society of Nuclear Medicine and Molecular Imaging.

provide intraprostatic pathologic information and has the potential to improve the performance of existing nomograms for identifying csPCa. The PRIMARY study also demonstrated that an  $SUV_{max}$  of at least 12 had 100% specificity for csPCa (12).

However, the problem with using  $SUV_{max}$  for csPCa detection among patients with biopsy GG1 is the overlap of  $SUV_{max}$  between csPCa (mainly GG2 through GG3) and non-csPCa (benign prostate disease or GG1 PCa). This makes it difficult to accurately detect csPCa among patients with biopsy GG1 and an  $SUV_{max}$  of less than 12 (13). In addition, the diagnostic performance of the PRIMARY score for patients with biopsy GG1 warrants further research. Therefore, the aim of this study was to analyze the overlap of  $SUV_{max}$  (size scale, 3 cm) on Gleason pattern (GP, the basic component of GG) level (size scale, 500  $\mu$ m) and develop a csPCa-predicting model based on both the  $SUV_{max}$  and the PRIMARY score. This model aimed to improve the diagnostic accuracy of csPCa in patients with biopsy GG1 and an  $SUV_{max}$  of less than 12. In addition, the quantitative relationship among the PRIMARY score,  $SUV_{max}$ , and csPCa risk was presented using a contour plot.

## MATERIALS AND METHODS

### Participants

We performed a retrospective review of 1,003 consecutive patients who underwent [ $^{68}\text{Ga}$ ]PSMA PET/CT from June 2017 to June 2022 at Xijing Hospital and Nanjing Drum Tower Hospital in China. Patients were included if they were suspected to have PCa on the basis of a prostate-specific antigen test or digital rectal examination and underwent [ $^{68}\text{Ga}$ ]PSMA PET/CT. Patients were excluded if [ $^{68}\text{Ga}$ ]PSMA PET/CT was performed after pharmacotherapy or surgery, there was an absence of biopsy GG information, the  $SUV_{max}$  was at least 12, the biopsy result was not GG1, and there was an absence of RP GG information. Ultimately, 56 patients were included in the analysis. The institutional review board (Ethics Committees of Xijing Hospital, Fourth Military Medical University) approved this study, and all subjects signed a written informed consent form.

### PET Imaging Protocols and Image Interpretation

The [ $^{68}\text{Ge}$ ]/[ $^{68}\text{Ga}$ ] generator was from ITG Co., and the PSMA-HBED-CC ligand was from ABX Co. Patients were prepared and PET images were acquired according to the procedure guideline (Supplemental Table 1 [supplemental materials are available at <http://jnm.snmjournals.org>] (14). All [ $^{68}\text{Ga}$ ]PSMA PET/CT images were reviewed by 2 experienced nuclear medicine specialists according to the guideline (15) in Xijing Hospital. The PRIMARY scores were evaluated according to the previous PRIMARY study (13).

### MRI Acquisition Protocol and Imaging Evaluation

The protocol consisted of T1-weighted imaging, T2-weighted imaging, and diffusion-weighted imaging sequences. All MR images were analyzed according to PI-RADS version 2.1 (16) by 2 urologic radiologists. Interrater agreement was evaluated with Cohen  $\kappa$  and associated 95% CI.

## Histopathologic Examination

All patients underwent TRUS-guided prostate biopsy and RP. csPCa was diagnosed if malignancy of at least GG2 was present. All pathologic results were reported according to the International Society of Urological Pathology guideline (17). The descriptions for the deep learning model, immunohistochemistry analysis (18,19), and International Society of Urological Pathology grading system are provided in the supplemental materials (Supplemental Table 2).

## Statistical Analysis

In addition to basic descriptive statistics, a contour plot was used to depict csPCa probability according to PSMA PET  $SUV_{max}$  and the PRIMARY score. The methods for imputation of missing data (20), model development, and subgroup analysis (21–23) are provided in the supplemental materials. All tests were 2-sided, and statistical significance was set at a  $P$  value of less than 0.05. All statistical analyses were performed using R (version 4.1.1; R Foundation for Statistical Computing).

## RESULTS

### Baseline Characteristics

In total, 56 patients were included in the study (Fig. 1). The baseline characteristics of these patients are shown in Table 1. The mean time between [ $^{68}\text{Ga}$ ]PSMA PET/CT examination and RP was 13.4 d (range, 1–61 d).

### Performance of PI-RADS Score in Discrimination Between Non-csPCa and csPCa

MRI results were available for analysis for 47 of 56 (83.93%) patients in the study. In contrast to biopsy GG1, indicating non-csPCa, 51.06% (24/47; PI-RADS, 5–4) or 80.85% (38/47; PI-RADS, 5–3) of these patients had a positive PI-RADS result, indicating csPCa (Supplemental Table 3). Furthermore, the false-positive rate of the PI-RADS score ranged from 33.33% (8/24; PI-RADS, 5–4 vs. 3–1) to 44.74% (17/38; PI-RADS, 5–3 vs. 2–1), and the

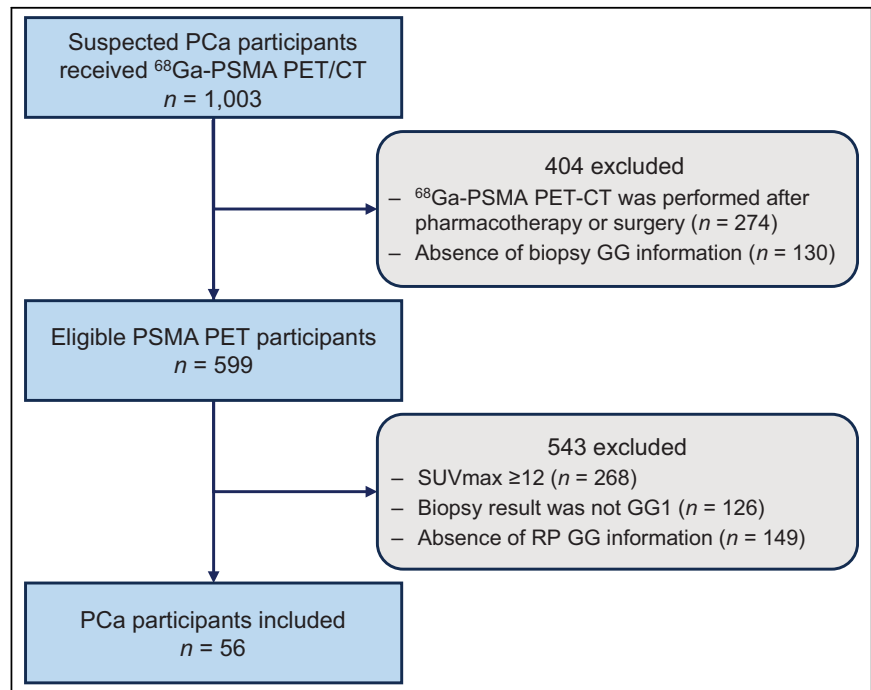


FIGURE 1. Flowchart of study design.



**TABLE 1**  
Demographic and Clinical Characteristics of 56 Patients Investigated in This Study

Baseline characteristic	Entire cohort, <i>n</i> = 56	Xijing cohort, <i>n</i> = 42	Nanjing cohort, <i>n</i> = 14
Age (y)	67 (62, 70)	65 (61, 70)	70 (67, 74)
PSA at PET/CT (ng/mL)	9.28 (6.10, 14.71)	9.66 (6.65, 15.18)	8.09 (5.86, 13.56)
PV (mL)	41.02 (26.46, 58.95)	39.49 (26.46, 52.02)	41.18 (27.85, 60.31)
SUV <sub>max</sub>	5.50 (3.63, 7.66)	4.86 (3.30, 6.44)	7.49 (6.43, 9.40)
PRIMARY score (%)			
1	5 (8.93)	4 (9.52)	1 (7.14)
2	15 (26.79)	13 (30.95)	2 (14.29)
3	7 (12.50)	4 (9.52)	3 (21.43)
4	29 (51.79)	21 (50.00)	8 (57.14)
RP ISUP GG (%)			
Benign	0 (0)	0 (0)	0 (0)
GG1	30 (53.57)	24 (57.14)	6 (42.86)
GG2	21 (37.50)	14 (33.33)	7 (50.00)
GG3	3 (5.36)	3 (7.14)	0 (0)
GG4	2 (3.57)	1 (2.38)	1 (7.14)
GG5	0 (0)	0 (0)	0 (0)
TRUS			
Normal	28	22	6
Abnormal	28	20	8
DRE			
Normal	26	19	7
Abnormal	30	23	7
PI-RADS score			
1	3 (6.38)	3 (9.09)	0 (0)
2	6 (12.77)	6 (18.18)	0 (0)
3	14 (29.79)	8 (24.24)	6 (42.86)
4	14 (29.79)	8 (24.24)	6 (42.86)
5	10 (21.28)	8 (24.24)	2 (14.29)

PSA, prostate-specific antigen; PV, prostate volume; ISUP, International Society of Urological Pathology; DRE, digital rectal examination.  
Qualitative data are number and percentage; continuous data are median and interquartile range.

false-negative rate ranged from 11.11% (1/9; PI-RADS, 5–3 vs. 2–1) to 26.09% (6/23; PI-RADS, 5–4 vs. 3–1). The AUC for detecting csPCa was only 0.7036 (95% CI, 0.5703–0.8370; PI-RADS, 5–4 vs. 3–1) and 0.6373 (95% CI, 0.5339–0.7407; PI-RADS, 5–3 vs. 2–1). Similar findings were reported in previous studies (Supplemental Table 3) (7,8,24,25). In addition, Cohen  $\kappa$  for the MRI evaluation was 0.763 (95% CI, 0.544–0.982) for a PI-RADS score of 5–4 versus 3–1 and 0.957 (95% CI, 0.875–1) for a PI-RADS score of 5–3 versus 2–1. For the 5-point PI-RADS, Cohen  $\kappa$  was 0.786 (95% CI, 0.650–0.920).

#### Overlap of SUV<sub>max</sub> in Discrimination Between Non-csPCa and csPCa

As shown in Figure 2, csPCa had a significantly higher SUV<sub>max</sub> than that of non-csPCa ( $7.52 \pm 3.13$  vs.  $4.91 \pm 1.96$ ,  $P = 0.002$ ). In addition, all lesions with an SUV<sub>max</sub> of less than 2.9 (dashed gray line) were non-csPCa, and all lesions with an SUV<sub>max</sub> of

greater than 9.2 (solid gray line) were csPCa. However, there was an overlap of SUV<sub>max</sub> between 2.9 and 9.2, which reduced the diagnostic performance of SUV<sub>max</sub>. The GG of the index lesion (size scale, 3 cm) was composed of different ratios of GPs (size scale, 500  $\mu$ m) (26). On the level of GP, we classified hematoxylin-eosin tiles into benign gland, GP3, and GP4 by the deep learning model (Supplemental Fig. 1) and found that the mean PSMA histochemical scores (H-scores) of benign gland, GP3, and GP4 were 132.03 ( $\pm 29.80$ ), 149.10 ( $\pm 33.77$ ), and 166.69 ( $\pm 38.70$ ), respectively (Fig. 2). There were significant overlaps of PSMA H-scores among tiles of benign gland, GP3, and GP4. Because of such overlaps, the AUC of SUV<sub>max</sub> was limited as 0.7353 (95% CI, 0.6006–0.8699).

#### Performance of PRIMARY Score in Discrimination Between Non-csPCa and csPCa

A tumor located in the anterior apex region was easily underestimated because the prostate needle biopsy had difficulty reaching into the anterior location in TRUS-guided biopsy, resulting in

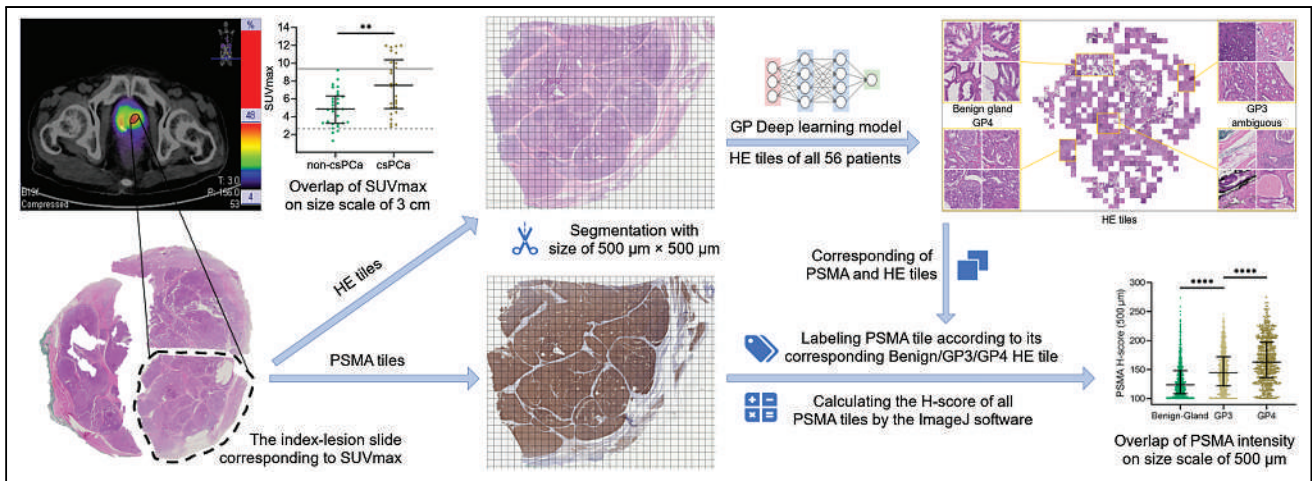


**FIGURE 2.** Overlap of  $SUV_{max}$  and overlap of PSMA intensity in patients with TRUS-guided biopsy GG1 and  $SUV_{max} < 12$ . Distribution of [ $^{68}\text{Ga}$ ]PSMA PET/CT  $SUV_{max}$  demonstrated higher  $SUV_{max}$  in csPca than in non-csPca. However, between values of 2.9 (dashed gray line) and 9.2 (solid gray line), there was  $SUV_{max}$  overlap between csPca and non-csPca. Subsequently, 56 patients' index-lesion slides corresponding to  $SUV_{max}$  were selected and made into 2 consecutive tissue sections. After this, 2 consecutive tissue sections were subjected to hematoxylin-eosin and PSMA immunohistochemistry staining and digital scanning. Resulting hematoxylin-eosin and PSMA images were segmented into  $500 \times 500 \mu\text{m}$  tiles. Deep learning was used to identify and cluster hematoxylin-eosin tiles, whereas PSMA tiles were matched with their corresponding hematoxylin-eosin tiles on basis of sample name and spatial coordinates of 2 consecutive tissue sections. Finally, according to categories of hematoxylin-eosin tiles, PSMA tiles were correspondingly labeled benign gland, GP3, and GP4 and randomly selected ( $n = 1,000$  for each category) to calculate PSMA H-score using ImageJ software (National Institutes of Health).  $**P < 0.01$  by Mann-Whitney test (overlap of  $SUV_{max}$ ) and Kruskal-Wallis test (overlap of PSMA intensity).  $****P < 0.0001$  by Mann-Whitney test (overlap of  $SUV_{max}$ ) and Kruskal-Wallis test (overlap of PSMA intensity). HE = hematoxylin-eosin.

prostatic evasive anterior tumors (27). In the current cohort, the  $SUV_{max}$  and PRIMARY score screened out 66.67% (2/3) and 100.00% (3/3) of prostatic evasive anterior cases, respectively. As shown in Figure 3, the representative case was previously classified as indolent PCa (prostate-specific antigen, 4.56 ng/mL; biopsy GG1; 1/13 positive core) and would be recommended for active surveillance on the basis of the guideline (1). Because of its PRIMARY score of 4 and  $SUV_{max}$  of 10.1, RP was finally performed and the RP pathologic result proved to be csPca (at least GG2).

However, the AUC of the PRIMARY score was limited to 0.7256 (95% CI, 0.6159–0.8354). Its false-negative rate was 15%

in the PRIMARY score of 1–2 and its false-positive rate was 86% and 25% in the PRIMARY scores of 3 and 4, respectively (Supplemental Fig. 2). It is necessary to develop a csPca-predicting model incorporating both the  $SUV_{max}$  and the PRIMARY score to further improve the diagnostic performance of [ $^{68}\text{Ga}$ ]PSMA PET/CT.

#### Development and Internal Validation of [ $^{68}\text{Ga}$ ]PSMA PET/CT-Based Diagnostic Model

We developed a diagnostic model based on the PRIMARY score ( $P = 0.010$ ), TRUS imaging result ( $P = 0.045$ ), and  $SUV_{max}$  ( $P = 0.147$ ), even though the  $SUV_{max}$  did not have a  $P$  value of less than 0.05 in the multivariate logistic analysis (Supplemental Table 4). The missing values were imputed (Supplemental Fig. 3).

The PRIMARY scores were treated as ordered categorical variables, whereas the  $SUV_{max}$  was treated as a continuous variable. Restricted cubic spline functions of the continuous variables showed  $SUV_{max}$  can be modeled as a continuous linear variable (nonlinearity,  $P = 0.2111$ ). Furthermore, in the subgroup analysis of the peripheral zone and transition zone of the study population, a linear relationship between  $SUV_{max}$  and csPca risk was maintained (Supplemental Fig. 4). No interaction terms were found by the interaction tests. The coefficients for the PRIMARY score,  $SUV_{max}$ , and TRUS imaging result were calculated using logistic analysis and multiplied by 10. Finally, 2 models were developed.

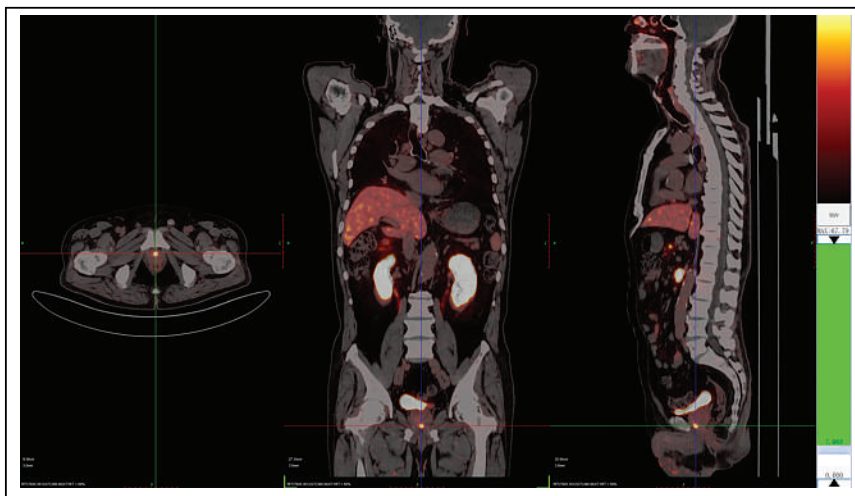


**FIGURE 3.** Representative case of prostatic evasive anterior tumor shown on [ $^{68}\text{Ga}$ ]PSMA PET/CT in axial, coronal, and sagittal views (from left to right). Representative case was previously underestimated as indolent PCa on basis of TRUS-guided biopsy result (biopsy GG1 and 1/13 positive core). [ $^{68}\text{Ga}$ ]PSMA PET/CT (PRIMARY score, 4;  $SUV_{max}$ , 10.1) identified case as csPca (RP GG2).

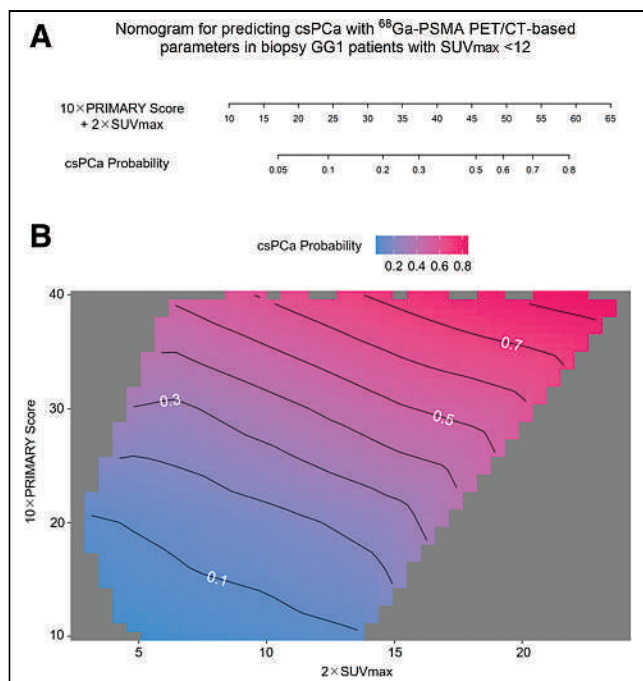


**FIGURE 4.** Relationships among  $SUV_{max}$ , PRIMARY score, and csPCa probability. (A) Nomogram of model of  $10 \times \text{PRIMARY score} + 2 \times SUV_{max}$  for individual csPCa prediction. (B) Contour plot of csPCa probability according to  $10 \times \text{PRIMARY score}$  and  $2 \times SUV_{max}$ .

**Model 1.** Linear predictor =  $10 \times \text{PRIMARY score} + 2 \times SUV_{max}$ . The coefficients were rounded to the nearest integer to create a user-friendly model.

**Model 2.** Linear predictor =  $8.4 \times \text{PRIMARY score} + 1.7 \times SUV_{max} + 15.1 \times \text{TRUS}$ . The coefficients were rounded to 1 decimal to improve accuracy.

The Akaike information criterion and AUC values for models 1 and 2 are shown in Supplemental Table 5. Compared with model 1 (AUC, 0.8359), model 2 (AUC, 0.8615) only slightly improved the Akaike information criterion and AUC values, with the TRUS

imaging result as the additional predictor ( $P = 0.367$ ) (Supplemental Table 5). To develop an easy-to-use risk assessment tool, model 1 was selected as the final model. A diagnostic model based on these findings was created for individual csPCa risk assessment (Fig. 4A). The relationship among the  $SUV_{max}$ , PRIMARY score, and csPCa probability was depicted in a contour plot (Fig. 4B). The calibration plot indicated that the model had good calibration, with a Hosmer–Lemeshow  $P$  value of 0.9115 and a Brier score of 0.162 (Supplemental Fig. 5). In internal validation, the mean 5-fold cross-validated AUC (repeated 1,000 times) was 0.8357 (95% CI, 0.8357–0.8358).

#### Comparison of Diagnostic Performance of Model 1 and Other Methods

The AUC of the model was significantly higher than that of the  $SUV_{max}$  (0.8359 vs. 0.7353,  $P = 0.048$ ) and PRIMARY score (0.8359 vs. 0.7257,  $P = 0.009$ ) (Table 2). As shown in Supplemental Figure 6A, decision curve analysis indicated that the net benefit of the model was similar to that of the PRIMARY score at low-risk thresholds (0%–40%). However, at high-risk thresholds (40%–90%), the net benefit of model 1 was superior to that of other methods. At a risk threshold of 50%, the difference of net benefit between model 1 and the PRIMARY score was 0.143 (0.268–0.125). Therefore, use of model 1 would lead to 14.3% (0.143/[0.50/0.50]) fewer false-positive csPCa reports with no increase in the number of false-negative csPCa reports compared with the PRIMARY score (Supplemental Fig. 6A).

In the MRI subgroup, model 1 also outperformed the PI-RADS score, with a higher AUC for a PI-RADS score of 5–4 versus 3–1 (AUC, 0.8364 vs. 0.7036;  $P = 0.149$ ) and a PI-RADS score of 5–3 versus 2–1 (AUC, 0.8364 vs. 0.6373;  $P = 0.014$ ) (Table 2) and with greater net benefit (Supplemental Fig. 6B). Figure 5 displays 2 typical cases in which model 1 corrected misdiagnoses in the PI-RADS score. Overall, model 1 reduced misdiagnoses of PI-RADS (5–4 vs. 3–1) by 78.57% (11/14) and PI-RADS (5–3 vs. 2–1) by 77.78% (14/18) (Supplemental Table 6). Furthermore, the discriminative performance and clinical utility of model 1 were better in almost all subgroups (Supplemental Tables 7–10; Supplemental Figs. 7 and 8).

**TABLE 2**

Comparison of Performance and Discriminative Ability of Model 1 and Other Diagnostic Methods

Cohort	Diagnostic method	AUC	AIC	$P$ value*
Entire cohort, $n = 56$	Model 1, cutoff value <sup>†</sup> = 45.25	0.8359 (0.7233–0.9484)	60.46	—
	$SUV_{max}$ , cutoff value = 7.3	0.7353 (0.6006–0.8699)	68.68	0.048
	PRIMARY score, 5–3 vs. 2–1	0.7257 (0.6159–0.8354)	68.00	0.009
MRI subgroup, $n = 47$	Model 1, cutoff value = 45.25	0.8364 (0.7114–0.9614)	52.02	—
	$SUV_{max}$ , cutoff value = 7.6	0.7555 (0.6112–0.8997)	56.68	0.127
	PRIMARY score, 5–3 vs. 2–1	0.6918 (0.5678–0.8158)	60.82	0.002
	PI-RADS score, 5–4 vs. 3–1	0.7036 (0.5703–0.8370)	60.96	0.149
	PI-RADS score, 5–3 vs. 2–1	0.6373 (0.5339–0.7407)	62.54	0.014

\*Difference compared with model 1.

<sup>†</sup>Cutoff value corresponding to highest level of accuracy (minimal false-negative and false-positive results) for model 1 and  $SUV_{max}$ .

AIC = Akaike information criterion.

AUC data in parentheses are 95% CI.



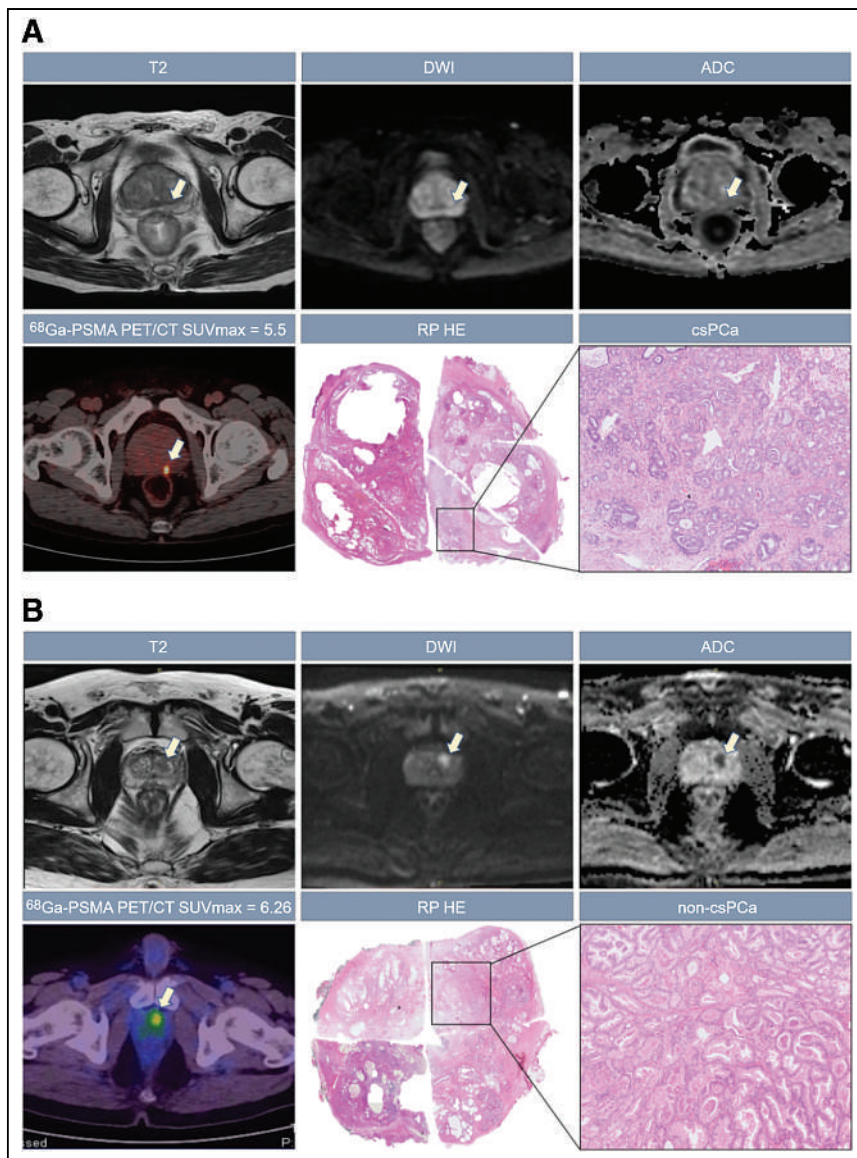


**FIGURE 5.** Correction of misdiagnoses by model 1. (A) Patient with PI-RADS score of 3, biopsy GG1, PRIMARY score of 4, SUV<sub>max</sub> of 5.5, and positive model 1 score of 51 (~60% csPCa probability). Lesion pointed at with arrow was missed by MRI but was detected by PRIMARY score and model 1. Postoperative pathology confirmed csPCa (GG2). (B) Patient with PI-RADS score of 4, PRIMARY score of 3, SUV<sub>max</sub> of 6.26, and negative model 1 score of 42.52 (~40% csPCa probability). Lesion pointed at with arrow was identified as csPCa by PI-RADS score and PRIMARY score but was suggested as non-csPCa by model 1. Postoperative pathology confirmed non-csPCa (type of benign prostatic disease called atypical adenomatous hyperplasia). ADC = apparent diffusion coefficient; DWI = diffusion-weighted imaging; HE = hematoxylin-eosin.

## DISCUSSION

In a cohort of 56 patients with TRUS-guided biopsy GG1 and a [<sup>68</sup>Ga]PSMA PET/CT SUV<sub>max</sub> of less than 12, we developed and internally validated the model of  $10 \times \text{PRIMARY score} + 2 \times \text{SUV}_{\text{max}}$  to predict the probability of csPCa with better diagnostic performance than the PRIMARY score, SUV<sub>max</sub>, and PI-RADS alone. The current study visualizes the relationships among the SUV<sub>max</sub>, PRIMARY score, and csPCa probability with a contour plot; analyzes SUV<sub>max</sub> overlap among patients (size scale, 3 cm)

based on the level of GP (size scale, 500 μm); and enhances the diagnostic accuracy of csPCa by developing a predictive model based on PSMA PET parameters for patients with biopsy GG1 and an SUV<sub>max</sub> of less than 12.

The European Association of Urology guideline recommended routine MRI for suspected PCa patients. PI-RADS demonstrated adequate diagnostic accuracy for csPCa detection, with pooled sensitivity of 0.91 (95% CI, 0.83–0.95) and specificity of 0.37 (95% CI, 0.29–0.46) (1). However, the guideline highlighted that MRI in very low-risk patients could lead to more false-positive reports because of low specificity. In this study, 33.33% (PI-RADS, 5–4 vs. 3–1) or 44.74% (PI-RADS, 5–3 vs. 2–1) of reports were false-positive. Previous studies reported similar false-positive rates of 25.87%–39.33%. Meanwhile, the false-negative rates in this study and prior research were between 11.11% and 54.65% (7,8). In addition, in this study, despite biopsy GG1 suggesting non-csPCa, 51.1% (PI-RADS, 5–4) and 80.85% (PI-RADS, 5–3) of patients had positive PI-RADS scores, indicating csPCa. Similarly, recent studies have reported that the positive rate of PI-RADS ranged from 13.21% to 50.71% in patients with biopsy GG1 (24,25). Because misdiagnoses of the PI-RADS score could lead to inappropriate treatment decisions, improving the diagnostic performance for csPCa in patients with biopsy GG1 was essential.

[<sup>68</sup>Ga]PSMA PET/CT is useful for evaluating the entire prostate, identifying the location of lesions, and providing additional pathologic information in the early stage of disease. This method may be particularly helpful in addressing the diagnostic challenges of TRUS-guided biopsy. Therefore, it is necessary to incorporate [<sup>68</sup>Ga]PSMA PET/CT parameters in the csPCa-predicting model for patients with TRUS-guided biopsy GG1. In previous research, a positive correlation had been found between SUV<sub>max</sub> and GG (10). A study that reviewed 419 patients with biopsy results of no more than GG2 demonstrated that only 10% of cases with an SUV<sub>max</sub> of no more than 5 were upgraded compared with 90% of cases with an SUV<sub>max</sub> of more than 11 (28). However, SUV<sub>max</sub> alone may not be sufficient for detecting csPCa in the current population because of significant overlap of SUV<sub>max</sub> among patients with GG2 through GG3 and GG1 or benign (13). The GG was reported on the basis of the whole tumor lesion (size scale, 3 cm) via the microscopic examination by pathologists, and the whole tumor lesion was composed of different ratios of benign prostate tissue, GP3, GP4, and Gleason pattern 5 tiles (size scale, 500 μm) (Fig. 2) (26).

On the GP level, we found significant overlap of PSMA H-scores among the tiles of benign gland, GP3, and GP4, resulting in the overlap of  $SUV_{max}$  between patients with GG2 through GG3 and GG1 or benign.

The anterior apex region often contains csPCa, but taking a TRUS-guided biopsy sample of this region can be painful and challenging because of its location. If not adequately sampled, it can lead to prostatic evasive anterior csPCa and GG upgrading (27). We found the PRIMARY score is effective in identifying such prostatic evasive anterior csPCa. However, further optimization is needed for the PRIMARY score method in csPCa detection. In patients with biopsy GG1, the false-positive rate of the PRIMARY scores (scores 3 and 4) was 38.5% (20/52) in the PRIMARY study (13) and 43.3% (13/30) in the current study. In addition, the false-negative rate of the PRIMARY scores (scores 1 and 2) was 11.5% (3/26) in the current study.

Considering that the  $SUV_{max}$  and PRIMARY score represent the level and anatomic location of PSMA expression, respectively, a comprehensive model is crucial for csPCa prediction instead of relying solely on either factor. As a result, we introduced a user-friendly model that integrates both the  $SUV_{max}$  and the PRIMARY score, maximizing PSMA information use and ultimately improving diagnostic accuracy for csPCa in patients with biopsy GG1.

Previous studies have suggested that the combined use of PSMA PET  $SUV_{max}$  and PI-RADS can accurately identify csPCa and potentially allow a biopsy-free strategy for specific patients (12,29). Similarly, when our model was used as a complementary diagnostic approach with PI-RADS, misdiagnosis was reduced.

This study had limitations, such as including only biopsy GG1 patients who underwent RP, which could introduce participation bias. PSMA PET/CT examinations were typically performed on patients with positive results from other tests, potentially causing verification bias and enhancing sensitivity of PSMA PET/CT-based parameters. In addition, the sample size remains small for developing a nomogram. To address this limitation, a prospective study or external validation is needed to confirm the conclusions of the current study.

## CONCLUSION

This study preliminarily suggests using the model of  $10 \times \text{PRIMARY score} + 2 \times SUV_{max}$  as a complementary diagnostic approach to PI-RADS for assessing csPCa risk. The approach can maximize the use of PSMA information and correct the misdiagnosis of the PI-RADS score, ultimately improving the diagnostic accuracy of csPCa and assisting in making appropriate treatment decisions.

## DISCLOSURE

This study was supported by the National Natural Science Foundation of China (82220108004, 82122033, 92259304, and 82103002), the Innovation Capability Support Program of Shaanxi (2021TD-39), the Clinical Research Project of AFMU (2021LC2111), and the China Postdoctoral Science Foundation (2022M711579). No other potential conflict of interest relevant to this article was reported.

## KEY POINTS

**QUESTION:** How can we improve csPCa diagnostic accuracy in patients with biopsy GG1 and an  $SUV_{max}$  of less than 12 to reduce the risk of inappropriate treatment decisions?

**PERTINENT FINDINGS:** In this patient group, the PI-RADS score demonstrated modest discriminative ability with an AUC of 0.704 (PI-RADS 5–4 vs. 3–1) and 0.637 (PI-RADS 5–3 vs. 2–1). A multicenter retrospective study led to a predictive model for csPCa, termed “ $10 \times \text{PRIMARY score} + 2 \times SUV_{max}$ ,” which outperformed individual  $SUV_{max}$ , PRIMARY score, and PI-RADS score, fully exploiting the advantages of both the  $SUV_{max}$  and the PRIMARY score.

**IMPLICATIONS FOR PATIENT CARE:** The model can identify misdiagnosis in PI-RADS score results, prompting clinicians to take necessary actions for accurate diagnosis and facilitating the selection of appropriate treatment decisions, such as RP to avoid delayed treatment or active surveillance to prevent overtreatment.

## REFERENCES

1. Mottet N, van den Bergh RCN, Briers E, et al. EAU-EANM-ESTRO-ESUR-SIOG guidelines on prostate cancer: 2020 update. Part 1: screening, diagnosis, and local treatment with curative intent. *Eur Urol*. 2021;79:243–262.
2. Bullock N, Simpkin A, Fowler S, Varma M, Kynaston H, Narahari K. Pathological upgrading in prostate cancer treated with surgery in the United Kingdom: trends and risk factors from the British Association of Urological Surgeons Radical Prostatectomy Registry. *BMC Urol*. 2019;19:94.
3. Iremashvili V, Manoharan M, Parekh DJ, Punnen S. Can nomograms improve our ability to select candidates for active surveillance for prostate cancer? *Prostate Cancer Prostatic Dis*. 2016;19:385–389.
4. Epstein JI, Feng Z, Trock BJ, Pierorazio PM. Upgrading and downgrading of prostate cancer from biopsy to radical prostatectomy: incidence and predictive factors using the modified Gleason grading system and factoring in tertiary grades. *Eur Urol*. 2012;61:1019–1024.
5. Yang DD, Mahal BA, Muralidhar V, et al. Risk of upgrading and upstaging among 10 000 patients with Gleason 3 + 4 favorable intermediate-risk prostate cancer. *Eur Urol Focus*. 2019;5:69–76.
6. Payton S. Prostate cancer: new nomogram predicts risk of Gleason upgrading. *Nat Rev Urol*. 2013;10:553.
7. Song W, Bang SH, Jeon HG, et al. Role of PI-RADS version 2 for prediction of upgrading in biopsy-proven prostate cancer with Gleason score 6. *Clin Genitourin Cancer*. 2018;16:281–287.
8. Seo JW, Shin SJ, Taik Oh Y, et al. PI-RADS version 2: detection of clinically significant cancer in patients with biopsy Gleason score 6 prostate cancer. *AJR*. 2017; 209:W1–W9.
9. Lawhn-Heath C, Salavati A, Behr SC, et al. Prostate-specific membrane antigen PET in prostate cancer. *Radiology*. 2021;299:248–260.
10. Rahbar K, Weckesser M, Huss S, et al. Correlation of intraprostatic tumor extent with  $^{68}\text{Ga}$ -PSMA distribution in patients with prostate cancer. *J Nucl Med*. 2016; 57:563–567.
11. Chu CE, Alshalalfa M, Sjostrom M, et al. Prostate-specific membrane antigen and fluciclovine transporter genes are associated with variable clinical features and molecular subtypes of primary prostate cancer. *Eur Urol*. 2021;79:717–721.
12. Emmett L, Buteau J, Papa N, et al. The additive diagnostic value of prostate-specific membrane antigen positron emission tomography computed tomography to multiparametric magnetic resonance imaging triage in the diagnosis of prostate cancer (PRIMARY): a prospective multicentre study. *Eur Urol*. 2021; 80:682–689.
13. Emmett L, Papa N, Buteau J, et al. The PRIMARY score: using intraprostatic  $^{68}\text{Ga}$ -PSMA PET/CT patterns to optimize prostate cancer diagnosis. *J Nucl Med*. 2022;63:1644–1650.
14. Fendler WP, Eiber M, Beheshti M, et al.  $^{68}\text{Ga}$ -PSMA PET/CT: joint EANM and SNMMI procedure guideline for prostate cancer imaging—version 1.0. *Eur J Nucl Med Mol Imaging*. 2017;44:1014–1024.

15. Fendler WP, Eiber M, Beheshti M, et al. PSMA PET/CT: joint EANM procedure guideline/SNMMI procedure standard for prostate cancer imaging 2.0. *Eur J Nucl Med Mol Imaging*. 2023;50:1466–1486.
16. Turkbey B, Rosenkrantz AB, Haider MA, et al. Prostate Imaging Reporting and Data System version 2.1: 2019 update of Prostate Imaging Reporting and Data System version 2. *Eur Urol*. 2019;76:340–351.
17. Iczkowski KA, van Leenders G, van der Kwast TH. The 2019 International Society of Urological Pathology (ISUP) consensus conference on grading of prostatic carcinoma. *Am J Surg Pathol*. 2021;45:1007.
18. Varghese F, Bukhari AB, Malhotra R, De A. IHC Profiler: an open source plugin for the quantitative evaluation and automated scoring of immunohistochemistry images of human tissue samples. *PLoS One*. 2014;9:e96801.
19. Zhang J, Shao S, Wu P, et al. Diagnostic performance of <sup>68</sup>Ga-PSMA PET/CT in the detection of prostate cancer prior to initial biopsy: comparison with cancer-predicting nomograms. *Eur J Nucl Med Mol Imaging*. 2019;46:908–920.
20. Zhang Z. Missing data exploration: highlighting graphical presentation of missing pattern. *Ann Transl Med*. 2015;3:356.
21. US Preventive Services Task Force, Grossman DC, Curry SJ, et al. Screening for prostate cancer: US Preventive Services Task Force recommendation statement. *JAMA*. 2018;319:1901–1913.
22. Yilmaz H, Ustuner M, Ciftci S, Yavuz U, Ozkan TA, Dillioglulil O. Prostate volume predicts high grade prostate cancer both in digital rectal examination negative (ct1c) and positive ( $\geq$ ct2) patients. *Int Braz J Urol*. 2014;40:613–619.
23. Vickers AJ, Sjoberg DD, Ulmert D, et al. Empirical estimates of prostate cancer overdiagnosis by age and prostate-specific antigen. *BMC Med*. 2014;12:26.
24. Olsson H, Nordstrom T, Jaderling F, et al. Incorporating magnetic resonance imaging and biomarkers in active surveillance protocols: results from the prospective Stockholm3 Active Surveillance Trial (STHLM3AS). *J Natl Cancer Inst*. 2021;113:632–640.
25. Hugosson J, Mansson M, Wallstrom J, et al. Prostate cancer screening with PSA and MRI followed by targeted biopsy only. *N Engl J Med*. 2022;387:2126–2137.
26. Tolkach Y, Dohmgörger T, Toma M, Kristiansen G. High-accuracy prostate cancer pathology using deep learning. *Nat Mach Intell*. 2020;2:411–418.
27. Lawrentschuk N, Haider MA, Daljeet N, et al. “Prostatic evasive anterior tumours”: the role of magnetic resonance imaging. *BJU Int*. 2010;105:1231–1236.
28. Raveenthiran S, Yaxley WJ, Franklin T, et al. Findings in 1,123 men with preoperative <sup>68</sup>Ga-prostate-specific membrane antigen positron emission tomography/computerized tomography and multiparametric magnetic resonance imaging compared to totally embedded radical prostatectomy histopathology: implications for the diagnosis and management of prostate cancer. *J Urol*. 2022;207:573–580.
29. Meissner VH, Rauscher I, Schwamborn K, et al. Radical prostatectomy without prior biopsy following multiparametric magnetic resonance imaging and prostate-specific membrane antigen positron emission tomography. *Eur Urol*. 2022;82:156–160.



---

---

# Prediction of Response to $^{177}\text{Lu}$ -PSMA Therapy Based on Tumor-to-Kidney Ratio on Pretherapeutic PSMA PET/CT and Posttherapeutic Tumor-Dose Evaluation in mCRPC

Melanie Hohberg, Manuel Reifegerst, Alexander Drzezga, Markus Wild, and Matthias Schmidt

Department of Nuclear Medicine and Cancer Center Cologne, University Hospital of Cologne, Cologne, Germany

---

The aim of this study was to analyze the absorbed dose of  $^{177}\text{Lu}$ -PSMA in osseous versus lymphatic metastases in patients with metastatic castration-resistant prostate cancer across therapy cycles and to relate those data to therapeutic success. In addition, pretherapeutic prostate-specific membrane antigen (PSMA) PET/CT was evaluated for its ability to predict response behavior. **Methods:** The study comprised 30 patients with metastatic castration-resistant prostate cancer, each receiving at least 3 cycles of  $^{177}\text{Lu}$ -PSMA therapy. Prostate-specific antigen (PSA) values between baseline and 6 wk after the third therapy cycle were used to classify the patients as responders (PSA decline  $\geq 50\%$ ) or nonresponders (unchanged or increasing PSA level). Quantitative SPECT/CT images were acquired 24, 48, and 168 h after application of  $^{177}\text{Lu}$ -PSMA. The absorbed dose for tumor lesions was calculated with dosimetry software. From the pretherapeutic PET/CT scan, the tumor-to-kidney uptake ratio was determined for different SUVs. **Results:** Regardless of patient response, the kidneys received a mean dose of  $0.55 \pm 0.20$  Gy/GBq per cycle. In the first therapy cycle, the lymph node lesions received a mean dose of  $3.73 \pm 1.65$  Gy/GBq in responders and  $1.86 \pm 1.25$  Gy/GBq in nonresponders ( $P < 0.01$ ). For bone lesions, the respective mean doses were  $3.47 \pm 2.00$  Gy/GBq and  $1.48 \pm 0.95$  Gy/GBq ( $P < 0.01$ ). When successive therapy cycles were compared, the mean dose was found to have been reduced from the first to the second cycle by 27% for lymph nodes and by 33% for bone lesions. A significant difference ( $P < 0.01$ ) in the ratio of lymph node and bone lesion uptake to kidney uptake between responders and nonresponders could be deduced from the pretherapeutic PET/CT scan. **Conclusion:** Significantly higher doses were achieved for lymph node and bone lesions in responders. The highest absorbed dose, for both lymphatic and osseous lesions, was achieved in the first cycle, decreasing in the second therapy cycle thereafter despite unchanged therapy activities. It may be possible to estimate the response to therapy from the ratio of tumor uptake to kidney uptake obtained from the pretherapeutic PSMA PET/CT scans.

**Key Words:** PSMA therapy; prediction of therapy response; dosimetry; prostate cancer

J Nucl Med 2023; 64:1758–1764  
DOI: 10.2967/jnumed.122.264953

---

Received Sep. 23, 2022; revision accepted Jul. 25, 2023.  
For correspondence or reprints, contact Melanie Hohberg (melanie.hohberg@uk-koeln.de).  
Published online Aug. 31, 2023.  
COPYRIGHT © 2023 by the Society of Nuclear Medicine and Molecular Imaging.

**P**eptide radioligand therapy with prostate-specific membrane antigen (PSMA) ligands is now accepted for the treatment of metastases of advanced, castration-resistant prostate cancer for which both hormonal therapy and chemotherapy are no longer effective (1,2). To date, the treatment has been found to deliver good results with low side effects. Various clinical studies have shown that tumor growth can be slowed or tumor size greatly reduced with the help of radioligand therapy (3–9). The therapy is able to reduce the tumor load, thus lowering the prostate-specific antigen (PSA) level, and also to reduce pain, thereby significantly improving the patient's quality of life. However, experience has shown that although some patients respond well to  $^{177}\text{Lu}$ -PSMA therapy, others respond poorly. The key may lie in individual differences in the degree to which the tracer accumulates in tumor lesions and hence differences in the absorbed tumor dose. A possible correlation between tumor dose and therapy outcome has already been explored in several papers (10–12). However, different methodologic approaches were taken. For example, some studies distinguished between responders and nonresponders but not between the different types of metastatic lesions, that is, lymph node or osseous involvement. In other studies, a distinction was made between lymph node and osseous metastases, but the patient group was not divided into responders and nonresponders. The aim of this work was to combine both approaches. The patients were divided into responders and nonresponders according to their response to therapy, as reflected in PSA decline, and at the same time differences between lymph node and bone lesions were evaluated. The correlation of tumor dose and therapy outcome is of course important, but even more valuable would be to predict the likelihood of response before radioligand therapy by means of a marker. This study investigated whether pretherapeutic PSMA PET/CT imaging could be used to predict therapy response (and hence the course of therapy).

## MATERIALS AND METHODS

### Study Population

Between March 2020 and February 2022, 30 patients with metastatic castration-resistant prostate cancer were enrolled in our study and underwent at least 3 cycles of  $^{177}\text{Lu}$ -PSMA therapy ( $^{177}\text{Lu}$ -PSMA-I&T).

All patients had undergone radical prostatectomy before  $^{177}\text{Lu}$ -PSMA therapy. Patients with a good treatment response received up to 6 cycles. Sufficient PSMA avidity for therapy was defined on  $^{18}\text{F}$ -PSMA-7 or  $^{68}\text{Ga}$ -PSMA PET/CT before the therapy. To minimize renal toxicity due to impaired renal function or excretory problems,  $^{99\text{m}}\text{Tc}$ -mercaptoacetyl-triglycine scintigraphy was performed before every therapy cycle.

This study was conducted in accordance with the requirements of the Institutional Review Board. All patients gave written informed consent to receive PSMA PET/CT and radioligand therapy and imaging and to have their data included in a retrospective analysis. All procedures were performed in compliance with the regulations of the responsible local authorities (District Administration of Cologne, Germany).

### Radiotracer

**Pretherapeutic Imaging.** Pretherapeutic PET imaging was performed using  $^{18}\text{F}$ -PSMA-7 ( $^{18}\text{F}$ -JK-PSMA-7) or  $^{68}\text{Ga}$ -PSMA ( $^{68}\text{Ga}$ -PSMA-HBED-CC). The preparations of both tracers have been described previously (13,14).  $^{18}\text{F}$ -PSMA-7 or  $^{68}\text{Ga}$ -PSMA was administered to patients on a weight-adjusted basis of 5.0 MBq/kg and 2.5 MBq/kg, respectively.

**Therapy.** High-purity lutetium chloride ( $^{177}\text{LuCl}_3$ ) was obtained from ITG, and PSMA-I&T was purchased from ABX.  $^{177}\text{Lu}$ -PSMA-I&T was synthesized and labeled according to a previously published protocol (15). Patients received a mean activity of  $7,209 \pm 379$  MBq of  $^{177}\text{Lu}$ -PSMA-I&T for each therapy cycle.

### Acquisition and Image Reconstruction

All PET/CT scans were obtained on a Biograph mCT device (mCT 128 Flow Edge; Siemens). Imaging started with a low-dose non-enhanced CT scan (120 kV, tube current modulation, pitch of 1.2, slice thickness of 5.0 mm) for attenuation correction followed by a whole-body PET scan from the base of the skull to the mid thigh. Reconstruction was conducted with an ordered-subset expectation maximization algorithm with 4 iterations and 12 subsets and gaussian-filtered to a transaxial resolution of 5 mm in full width at half maximum.

Quantitative SPECT/CT images (xSPECT; Siemens) were acquired at 24, 48, and 168 h after application of  $^{177}\text{Lu}$ -PSMA-I&T on a Symbya Intevo Bold system (Siemens). The same time points were chosen for each therapy cycle. If no lesions in the head region were of interest for dosimetry, images of the thorax and abdomen were acquired at 2 bed positions. For attenuation correction, a low-dose CT scan (110 kV, 30 mAs, pitch of 1.5, slice thickness of 3.0 mm) was acquired alongside each SPECT scan. The SPECT images were reconstructed with an ordered-subset conjugate gradient maximization algorithm. For quantitative imaging, the device was regularly calibrated for  $^{177}\text{Lu}$  according to the manufacturer's protocol.

### Image Evaluation

Radiation dosimetry was performed using dosimetry software (MIM SurePlan MRT; MIM Software). Lesions were contoured on the first SPECT scan of each cycle using a gradient-based segmentation algorithm (PET Edge+; MIM Software). Once the user clicks anywhere within the region of interest, the algorithm begins to move outward, like a balloon slowly expanding. As the balloon expands, the algorithm is checking the gradient of the proposed contour until it reaches the optimal condition. The accuracy of the PET Edge+ tool has already been verified for PET imaging in other studies (16,17). A maximum of 5 lymph node lesions or 5 bone lesions per patient that were visually suggestive of prostate cancer metastases were counted and analyzed. Lesions with a volume smaller than  $10\text{ cm}^3$  were not considered. In addition to the lesions, the kidneys were automatically segmented on the first CT image, using an artificial intelligence algorithm (Contour Protégé AI; MIM Software). Lesions and the kidneys were resegmented for each therapy cycle in the same way. All SPECT and CT datasets were automatically coregistered by multiple local rigid registrations for each region of interest. The spatially aligned images are then used to calculate time-activity curves and the absorbed doses. The MIM Software provides a voxel-by-voxel curve fitting and integration. Curves are fitted by minimizing the squared differences between the curve from the selected function and the

observed data points. The curve-fitting options are trapezoid plus exponential, monoexponential, biexponential, biexponential (fixed second  $\lambda$ ), biexponential (forced zero at uptake time 0), and automatically determined, which finds the best fitting model from the monoexponential and biexponential options. The metric used to evaluate each equation is the Akaike information criterion, which evaluates the loss of information when a model is used to approximate the true distribution. The lowest Akaike information criterion value corresponds to the lowest information loss, and the model with the lowest Akaike information criterion is chosen on a voxel-by-voxel basis. The automatically determined curve fitting was selected in each case. The calculation of absorbed dose is based on the voxel S-value convolution method according to MIRD pamphlet 17. The voxel S-value convolution kernel was derived from Monte Carlo simulations with MCNP 6.2.2. The voxel S-value convolution kernels are simulated assuming the density of water for the MIRD 17 kernels. Therefore, a correction is necessary for tissues with heterogeneous densities. The absorbed dose map was corrected for physical density by applying a physical density map derived from the CT scan, with Hounsfield units being mapped to physical density values using a bilinear fit curve. The Hounsfield units are derived by scanning a CT density phantom using the same CT protocol as will be used for the SPECT/CT image acquisition. The resulting dose maps are divided by the physical density map, providing a density-corrected absorbed dose calculation.

Time-activity curve and dose volume histograms were calculated for all segmented structures on a voxel-based level. The same lesions and the kidneys were segmented on the corresponding pretherapeutic PET/CT scans. From these segmented structures, the mean ratio of lesion uptake to kidney uptake was calculated for  $\text{SUV}_{\text{max}}$ ,  $\text{SUV}_{\text{peak}}$ ,  $\text{SUV}_{\text{mean}}$ , and  $\text{SUV}_{\text{median}}$ .

An in-house workflow was created to calculate the total tumor burden (TTB) and the distribution to lymph nodes and bone lesions for each patient. In this workflow, a bone mask containing the entire bone volume of the patient is generated on the CT scan. Using the PET Edge+ tool, all lesions larger than  $10\text{ cm}^3$  are segmented. The bone mask is used to separate the bone lesions from the lymph nodes. At the same time, all segmented standard organs are also separated from the TTB.

For all segmented lesions, partial-volume correction was based on 2 phantom measurements with the National Electrical Manufacturers Association-International Electrotechnical Commission PET body phantom. During the first measurement, all 6 spheres (diameters of 10, 13, 17, 22, 28, and 37 mm) were filled with an activity concentration of 1.35 MBq of  $^{177}\text{Lu}$ -PSMA per milliliter at a sphere-to-background ratio of 10:1. In a second measurement, the same activity concentration and sphere-to-background ratio were used for a 60-mm-diameter sphere. These measurements also served to evaluate the PET Edge+ tool for SPECT imaging. Calculation of recovery coefficients was based on the segmented and nominal activity in each sphere (18). The recovery curve was fitted to apply them to arbitrary volumes. Partial-volume correction was also applied for the kidneys.

The corresponding phantom measurements were also performed on the PET/CT scanner for  $^{18}\text{F}$  and  $^{68}\text{Ga}$  at an activity concentration of 20 kBq/mL.

### Response Assessment

Biochemical response assessment was based on PSA levels according to previously described protocols (19). Response was defined as a PSA decline of at least 50% and nonresponse as an unchanged PSA level or an increasing level. Baseline for the PSA value was acquired on the day of therapy or the day before. The last PSA value considered was 6 wk after the third therapy or on the day of the fourth therapy if this had taken place.

**TABLE 1**  
Patient Characteristics ( $n = 30$ )

Parameter	Age (y)	Weight (kg)	Initial PSA ( $\mu\text{g/L}$ )	Activity (MBq)		
				First cycle	Second cycle	Third cycle
Mean	72.4	81.4	315	7,209	7,191	7,128
SD	7.56	15.9	466	379	537	536
Range	56–87	60–169	7–2,480	6,463–8,009	6,107–8,263	6,014–7,805

### Statistical Analysis

The software package SPSS Statistics 29 (IBM) was used for statistical analysis. The mean absorbed doses in lymph node and bone lesions were compared between responders and nonresponders using a Mann–Whitney  $U$  test. Furthermore, the ratio of lesion to kidney uptake was compared between responders and nonresponders. Differences in absorbed dose among the 3 cycles of therapy were examined using a Wilcoxon test matched-pair signed-rank test. The Kolmogorov–Smirnov test and the Shapiro–Wilk test were used to test for normality of the distributions. A  $P$  value of less than 0.05 was considered statistically significant. All data are expressed as the mean and related SD.

### RESULTS

The patients had an average age of 72 y (range, 56–87 y) and an average weight of 81 kg (range, 60–169 kg). The initial PSA value ranged from 3 to 2,480  $\mu\text{g/L}$ . The mean time between the pretherapeutic PSMA PET/CT and the first radioligand therapy cycle was 34 d (range, 5–90 d). Follow-up analysis revealed no evidence of kidney, liver, or bone marrow toxicity between any 2 cycles of therapy in any patient. Patient characteristics are summarized in Table 1. Detailed information on treatments before the first therapy, as well the TTB and distribution among lymph nodes and bone lesions, is presented in Supplemental Table 1 (supplemental materials are available at <http://jnm.snmjournals.org>). The change in PSA value with each cycle of therapy for each patient is listed in Supplemental Table 2.

### Partial-Volume Correction

Results and details on the partial-volume correction and evaluation of the PET Edge+ tool for SPECT imaging can be found in

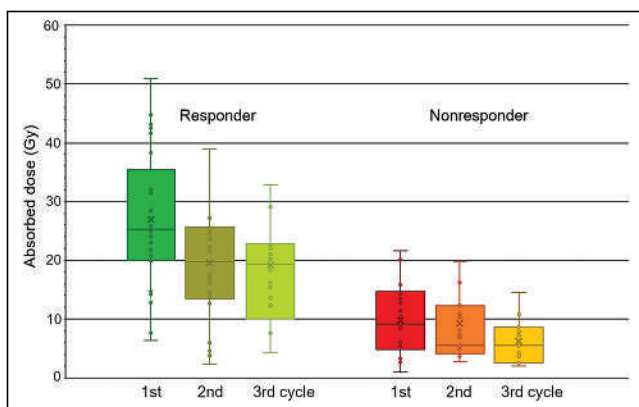


**FIGURE 1.** Mean dose for lymph node lesions differentiated between responders and nonresponders over 3 therapy cycles.

Supplemental Tables 3 and 4. Furthermore, the recovery coefficient curve can be found in Supplemental Figure 1.

### Kidney Dosimetry

The mean absorbed kidney dose did not differ significantly ( $Z = -0.73$ ;  $P = 0.47$ ) between responders ( $0.53 \pm 0.21$  Gy/GBq) and nonresponders ( $0.56 \pm 0.20$  Gy/GBq), nor did it change significantly between the separate therapy cycles ( $Z \geq -0.69$ ;  $P \geq 0.44$ ). All results for the individual therapy cycles are presented in Table 2 and Supplemental Table 5.

### Dosimetry for Lymph Node and Bone Lesions

In total, 77 suggestive lesions were analyzed, including 37 lymph node lesions and 40 bone lesions. The number of lesions was evenly distributed between responders and nonresponders. Individual tumor volumes used for analysis are summarized in Supplemental Table 6.

In the first therapy cycle, the responders received a mean dose of  $3.73 \pm 1.65$  Gy/GBq for lymph node lesions and the nonresponders  $1.86 \pm 1.25$  Gy/GBq. For the second therapy cycle, the mean absorbed dose for lymph nodes was reduced to  $2.73 \pm 1.48$  Gy/GBq for responders and to  $1.81 \pm 1.45$  Gy/GBq for nonresponders. In the third cycle, the dose dropped to  $2.71 \pm 1.55$  Gy/GBq for responders and to  $1.74 \pm 1.55$  Gy/GBq for nonresponders. The difference between the first and second therapy cycles and between responders and nonresponders was significant ( $P < 0.01$ ).

A similar pattern was found for bone lesions in responders and nonresponders. In the first cycle, a mean dose of  $3.47 \pm 2.00$  Gy/GBq was achieved for osseous metastases in responders, compared with a mean dose of  $1.48 \pm 0.95$  Gy/GBq in nonresponders. In the second and third cycles, responders received mean doses of  $2.32 \pm 0.96$  Gy/GBq and  $1.73 \pm 0.79$  Gy/GBq, respectively, whereas nonresponders received  $1.31 \pm 0.91$  Gy/GBq and  $1.31 \pm 0.94$  Gy/GBq, respectively. The difference between the first and second therapy cycles and between responders and nonresponders was significant ( $P < 0.01$ ).

**TABLE 2**  
Results for Mean Kidney Dose Divided into Responder and Nonresponder

Parameter	Mean dose (Gy/GBq)		
	First cycle	Second cycle	Third cycle
Responder	$0.53 \pm 0.21$	$0.55 \pm 0.22$	$0.56 \pm 0.12$
Nonresponder	$0.56 \pm 0.20$	$0.57 \pm 0.18$	$0.55 \pm 0.12$
$Z$	-0.73	-0.68	-0.61
$P$	0.47	0.45	0.43

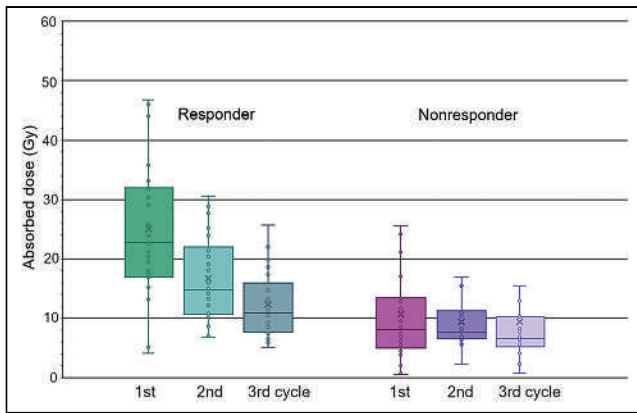


**FIGURE 2.** Mean dose for bone lesions differentiated between responders and nonresponders over 3 therapy cycles.

Over the course of the therapy cycles, the dose for responders decreased with each cycle, but only between the first and second cycles was the difference statistically significant ( $P = 0.001$  for lymph nodes and  $P = 0.003$  for bone lesions). There were no significant differences in absorbed dose between the second and third cycles for responders ( $P = 0.126$  for lymph nodes and  $P = 0.220$  for bone lesions). In nonresponders, the absorbed dose also decreased with each cycle of therapy, but none of the declines in dose was statistically significant ( $P > 0.400$ ). Similar to the decrease in dose, the residence time also decreased with each subsequent therapy cycle. Again, significant differences were observed only between the first and second cycles ( $P < 0.01$ ). Regardless of whether one considers lymph nodes or bone lesions in responders, the residence time halved from the first to the second therapy cycle. This halving of the residence time was not seen in nonresponders. However, the mean residence time in nonresponders was already 45% lower in lymph nodes and 54% lower in bone lesions in the first therapy cycle. An overview of the results is presented in Figures 1 and 2 and in Supplemental Tables 7–9.

In addition to the achieved dose, the TTB also changed over the course of therapy cycles. In patients who responded to therapy, the TTB decreased by  $52.3\% \pm 4.7\%$  on average. In the group of nonresponders, the TTB decreased less or even increased again overall. With regard to only the tumor volume of the lesions considered for dosimetry, responders were found to have a mean decrease of 54.5% and nonresponders a mean decrease of 30.8%. Already-treated lesions appeared to diminish in nonresponders

while new lesions appeared. The corresponding data are given in Supplemental Table 10.

### Ratio of Tumor to Kidney Uptake in Pretherapeutic PET/CT Scan

This evaluation was based on a total of 19 scans with  $^{18}\text{F}$ -PSMA-7 PET/CT and 11 with  $^{68}\text{Ga}$ -PSMA PET/CT.

Kidney uptake measured as  $\text{SUV}_{\text{max}}$ ,  $\text{SUV}_{\text{peak}}$ ,  $\text{SUV}_{\text{mean}}$ , and  $\text{SUV}_{\text{median}}$  was equal in responders and nonresponders. On average, the SUVs for  $^{68}\text{Ga}$  were 36% higher than those for  $^{18}\text{F}$ , but this applied to the kidneys and lesions alike. Detailed information on the individual SUVs for  $^{68}\text{Ga}$  and  $^{18}\text{F}$  is shown in Supplemental Table 11.

The pretherapeutic PSMA PET/CT was acquired on average 1 mo (mean,  $30.6 \pm 10.4$  d) before the first therapy cycle. There was a significant difference ( $P < 0.01$ ) in the ratio of tumor-to-kidney uptake between responders and nonresponders. This difference applied to both lymph node and bone lesions. Uptake in lesions was about a factor of 2 higher than kidney uptake in responders ( $P < 0.01$ ). The ratio of tumor uptake to kidney uptake correlated with the mean dose between responders and nonresponders. The mean dose was also 2 times higher for responders than for nonresponders. Again, this applied to lymph node and bone lesions in the same way. For the tumor-to-kidney uptake ratio, similar values were obtained, regardless of whether  $\text{SUV}_{\text{peak}}$ ,  $\text{SUV}_{\text{max}}$ ,  $\text{SUV}_{\text{mean}}$ , or  $\text{SUV}_{\text{median}}$  was used for the calculations. All results are summarized in Tables 3 and 4. Figures 3 and 4 show results from a responder and a nonresponder, respectively, including the tumor-to-kidney uptake ratio and the decrease or increase in TTB.

### DISCUSSION

Three main findings emerged from the study: responders to  $^{177}\text{Lu}$ -PSMA therapy achieved higher absorbed doses than nonresponders, absorbed doses decreased over the 3 therapy cycles, and tumor-to-kidney uptake ratio may serve as a parameter to identify potential responders on a pretherapeutic PSMA PET/CT scan.

The mean kidney dose did not differ significantly between responders and nonresponders, a total kidney dose of  $0.55 \pm 0.20$  Gy/GBq being measured in both groups. The calculated mean dose for the kidneys was comparable to previously published data (10,20–22). A threshold dose for the human kidneys (20 Gy) would thus be exceeded only after more than 6 therapy cycles (23). Partial-volume correction for the kidneys was based on the largest sphere, which does not correspond to the anatomic shape of the kidneys. This represents a limitation of the kidney dose thus determined.

**TABLE 3**  
Mean Dose for Lymph Node Lesions and Corresponding Lesion-to-Kidney Ratio

Parameter	Mean dose, first cycle (Gy/GBq)	Lesion-to-kidney ratio			
		$\text{SUV}_{\text{peak}}$	$\text{SUV}_{\text{mean}}$	$\text{SUV}_{\text{median}}$	$\text{SUV}_{\text{max}}$
Responder	$3.73 \pm 1.65$	$1.59 \pm 0.73$	$1.57 \pm 0.58$	$1.44 \pm 0.57$	$1.58 \pm 0.71$
Nonresponder	$1.86 \pm 1.25$	$0.74 \pm 0.47$	$0.85 \pm 0.43$	$0.78 \pm 0.39$	$0.80 \pm 0.58$
Ratio*	2.00	2.14	1.85	1.83	1.97
Z	-2.71	-4.75	-4.20	-4.75	-4.75
P	<0.01	<0.01	<0.01	<0.01	<0.01

\*Responder to nonresponder.

**TABLE 4**  
Mean Dose for Bone Lesions and Corresponding Lesion-to-Kidney Ratio

Parameter	Mean dose, first cycle (Gy/GBq)	Lesion-to-kidney ratio			
		SUV <sub>peak</sub>	SUV <sub>mean</sub>	SUV <sub>median</sub>	SUV <sub>max</sub>
Responder	3.47 ± 2.00	1.62 ± 0.79	1.59 ± 0.62	1.44 ± 0.61	1.61 ± 0.78
Nonresponder	1.48 ± 0.95	0.60 ± 0.35	0.79 ± 0.44	0.71 ± 0.39	0.78 ± 0.40
Ratio*	2.34	2.68	2.01	2.03	2.05
Z	-4.05	-5.18	-4.63	-5.10	-4.63
P	<0.01	<0.01	<0.01	<0.01	<0.01

\*Responder to nonresponder.

Other studies reported similar mean tumor doses (12) and higher tumor doses (11) for <sup>177</sup>Lu-PSMA-617. A direct comparison of our findings with those obtained in previous studies is not feasible because of the differing procedures and software products used. Furthermore, the composition of the study groups varied: some authors distinguished responders from nonresponders (10,11), others characterized only lymph node or bone lesions (12), and in one study only the course of the mean dose over several cycles was analyzed (24).

Our results for lymph node and bone lesions contrast with previous findings (12) in which no difference in absorbed doses was evident between the first and second therapy cycles. However, the focus there was on very small lesions less than 1 cm<sup>3</sup>. Furthermore, different activities were administered in the first (3 GBq) and second (6 GBq) therapy cycles, thus potentially compensating for a decrease in absorbed dose in subsequent cycles. Our data actually suggest the opposite, namely that patients might well benefit from a higher activity administered in the first cycle since the absorbed dose was found to decrease significantly from the first to the second cycle of therapy. A similar decrease in tumor dose over successive therapy cycles was observed by Okamoto et al. (24). Our data suggest that the observed decrease in absorbed dose may be related to a decrease in residence time. It remains unclear whether this decrease may be due to reduction or damage of PSMA receptors by the initial therapy. No further dose decrease could be observed between the second and third cycles. Rather, the dose achieved remained constant in both responders and nonresponders. Whether this also applies to subsequent therapy cycles will be investigated in a further study.

In our study, no distinction was made between unchanged PSA level and PSA increase. Defining an unchanged PSA value as the initial PSA value ± 10% deviation, we found that 50% of nonresponders belong to this group. This, too, may have influenced our measure of further disease progression.

Compared with other studies, only 3 measurement points were chosen for dosimetry. However, this number should be sufficiently accurate, as results with a root-mean-squared error below 10% have already been achieved in other studies with only one late measurement point (25,26).

The lesion-to-kidney ratio based on the pretherapeutic PSMA PET/CT scan revealed a significant difference between responders and nonresponders. This difference was also reflected in the tumor dose reached and the

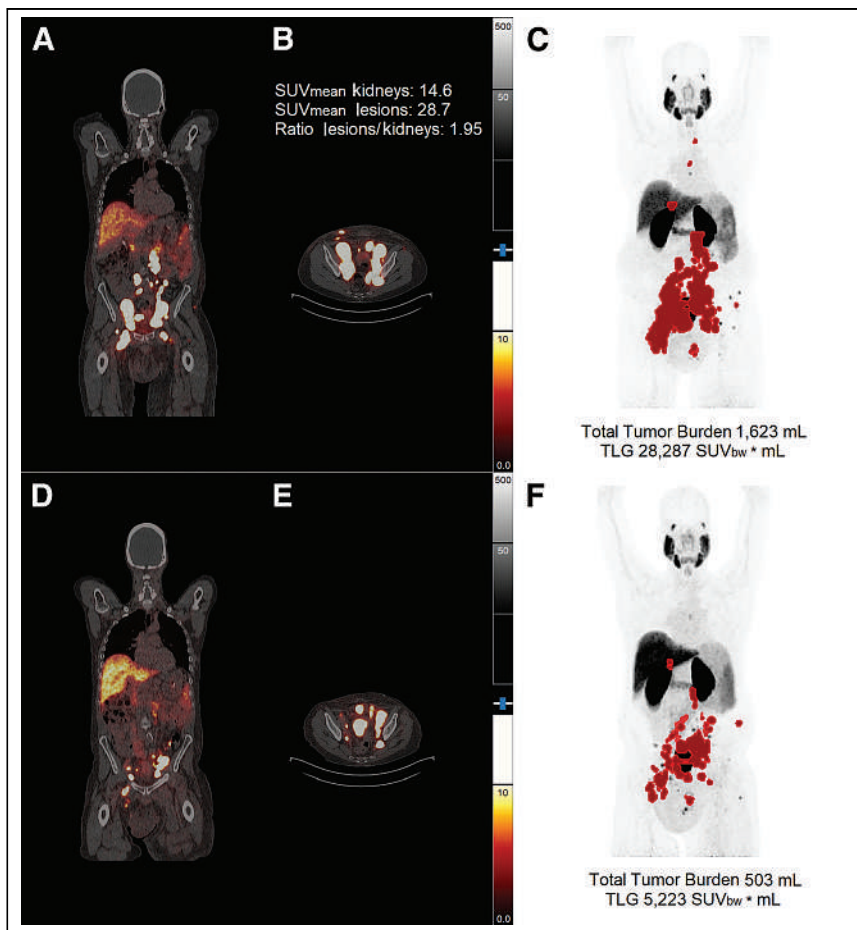


**FIGURE 3.** Results from one responder. (A–C) PET/CT imaging before first therapy cycle. (D–F) PET/CT imaging after 2 therapy cycles. (C and F) Maximum-intensity projections together with TTB and TLG. Lesions with SUV < 3.5 were not included. SUV<sub>bw</sub> = standardized uptake value based on body weight.



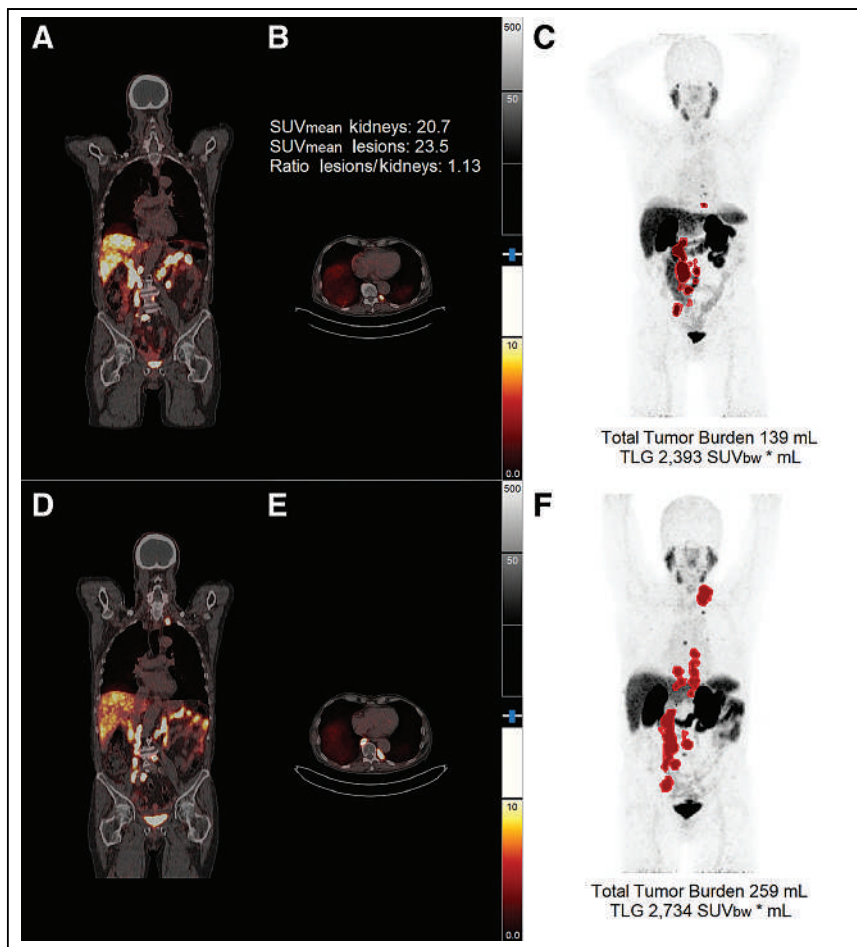


**FIGURE 4.** Results from one nonresponder. (A–C) PET/CT imaging before first therapy cycle. (D–F) PET/CT imaging after 2 therapy cycles. (C and F) Maximum-intensity projections together with TTB and TLG. Lesions with SUV < 3.5 were not included. SUV<sub>bw</sub> = standardized uptake value based on body weight.

PSA decline. The ratio of tumor uptake to kidney uptake in pretherapeutic PET/CT may therefore serve as a predictor of treatment response. This information would be available even before the first therapy cycle, thereby allowing other therapy options to be considered. These might include therapy with <sup>225</sup>Ac-PSMA (27,28) at an early stage for patients who are likely to have a poor response to treatment with <sup>177</sup>Lu-PSMA ligands. PET/CT images with <sup>18</sup>F and <sup>68</sup>Ga were used to assess the lesion-to-kidney ratio. However, since no absolute SUVs but only relative ratios were compared between kidney and lesion uptake, this limitation should affect the results only minimally.

There are multiple studies suggesting the importance of pretherapeutic PET/CT in predicting response to <sup>177</sup>Lu-PSMA therapies (29,30). In contrast to the work of Khreish et al. (29), we cannot confirm that SUV<sub>peak</sub> is less appropriate than SUV<sub>mean</sub> as a predictor of therapy response. However, the tumor-to-liver uptake ratio was compared with progression-free survival in the study of Khreish et al. The tumor-to-liver ratio was not available in our patient collective because some patients also had metastases in the liver.

In the work by Buteau et al. (30), an SUV<sub>mean</sub> of 10 or higher on PSMA PET was evaluated as a predictive biomarker for response to <sup>177</sup>Lu-PSMA-617. The cutoff proposed by Buteau et al. would not be transferable to our collective as the SUV<sub>mean</sub>

in tumor lesions was higher than 10 for responders and nonresponders.

So far, the response evaluation has been based on only biochemical response, with no long-term follow-up or survival data. Some patients reported here received up to 6 cycles. For now, the number of these patients is still too small for a valid statistical evaluation. However, even in this small group, a few tendencies are emerging for further treatment response, which will also be investigated together with overall survival in the future.

## CONCLUSION

In lymph node and bone lesions, a significantly higher dose is absorbed in responders than nonresponders during the course of radioligand therapy with <sup>177</sup>Lu-PSMA-I&T. This difference is also reflected in the therapeutic success. The absorbed dose was highest in the first cycle and then decreased significantly in the second cycle. There is a case, therefore, for increasing the applied activity in the first cycle to maximize therapy success. The significant difference in the tumor-to-kidney uptake ratio between responders and nonresponders may serve as a predictor of treatment response. Further studies will be needed to examine this possibility.

## DISCLOSURE

No potential conflict of interest relevant to this article was reported.

## KEY POINTS

**QUESTION:** Is there a clear difference between responders and nonresponders, and is it possible to predict the response to <sup>177</sup>Lu-PSMA therapy?

**PERTINENT FINDINGS:** In this study, 30 patients with metastatic castration-resistant prostate cancer undergoing <sup>177</sup>Lu-PSMA therapy were examined with regard to therapy response and the achieved dose for lymph nodes and bone metastases. A significant difference between responders and nonresponders was found. The response to therapy may be estimated from pretherapeutic PSMA PET/CT based on the lesion-to-kidney uptake ratio.

**IMPLICATIONS FOR PATIENT CARE:** An assessment of the therapy response allows other options to be considered or the applied activity to be adjusted.

## REFERENCES

1. Sartor O, de Bono J, Chi KN, et al.; VISION Investigators. Lutetium-177-PSMA-617 for metastatic castration-resistant prostate cancer. *N Engl J Med.* 2021;385:1091–1103.
2. Schneider CA, Täger P, Hammes J, et al. Treatment outcome and identification of factors influencing overall survival after Lu-177-PSMA-617 radioligand therapy in metastatic castration-resistant prostate cancer. *Nuklearmedizin.* 2022;61:25–32.



3. Bander NH, Milowsky MI, Nanus DM, Kostakoglu L, Vallabhajosula S, Goldsmith SJ. Phase I trial of <sup>177</sup>lutetium-labeled J591, a monoclonal antibody to prostate-specific membrane antigen, in patients with androgen-independent prostate cancer. *J Clin Oncol*. 2005;23:4591–4601.
4. Tagawa ST, Milowsky MI, Morris M, et al. Phase II study of lutetium-177-labeled antiprostate-specific membrane antigen monoclonal antibody J591 for metastatic castration-resistant prostate cancer. *Clin Cancer Res*. 2013;19:5182–5191.
5. Kratochwil C, Giesel FL, Eder M, et al. (<sup>177</sup>Lu)lutetium-labelled PSMA ligand-induced remission in a patient with metastatic prostate cancer. *Eur J Nucl Med Mol Imaging*. 2015;42:987–988.
6. Ahmadzadehfah H, Eppard E, Kurpig S, et al. Therapeutic response and side effects of repeated radioligand therapy with <sup>177</sup>Lu-PSMA-DKFZ-617 of castrate-resistant metastatic prostate cancer. *Oncotarget*. 2016;7:12477–12488.
7. Baum RP, Kulkarni HR, Schuchardt C, et al. Lutetium-177 PSMA radioligand therapy of metastatic castration-resistant prostate cancer: safety and efficacy. *J Nucl Med*. 2016;57:1006–1013.
8. Rahbar K, Ahmadzadehfah H, Kratochwil C, et al. German multicenter study investigating <sup>177</sup>Lu-PSMA-617 radioligand therapy in advanced prostate cancer patients. *J Nucl Med*. 2017;58:85–90.
9. Heck MM, Tauber R, Schwaiger S, et al. Treatment outcome, toxicity, and predictive factors for radioligand therapy with <sup>177</sup>Lu-PSMA-1&T in metastatic castration-resistant prostate cancer. *Eur Urol*. 2019;75:920–926.
10. Violet J, Jackson P, Ferdinandus J, et al. Dosimetry of <sup>177</sup>Lu-PSMA-617 in metastatic castration-resistant prostate cancer: correlations between pretherapeutic imaging and whole-body tumor dosimetry with treatment outcomes. *J Nucl Med*. 2019;60:517–523.
11. Völter F, Mittlmeier L, Gosewisch A, et al. Correlation of an index-lesion-based SPECT dosimetry method with mean tumor dose and clinical outcome after <sup>177</sup>Lu-PSMA-617 radioligand therapy. *Diagnostics (Basel)*. 2021;11:428.
12. Peters SMB, Privé BM, de Bakker M, et al. Intra-therapeutic dosimetry of (<sup>177</sup>Lu)Lu-PSMA-617 in low-volume hormone-sensitive metastatic prostate cancer patients and correlation with treatment outcome. *Eur J Nucl Med Mol Imaging*. 2022;49:460–469.
13. Hohberg M, Kobe C, Krapf P, et al. Biodistribution and radiation dosimetry of (<sup>18</sup>F)-JK-PSMA-7 as a novel prostate-specific membrane antigen-specific ligand for PET/CT imaging of prostate cancer. *EJNMMI Res*. 2019;9:66.
14. Eder M, Schäfer M, Bauder-Wüst U, et al. <sup>68</sup>Ga-complex lipophilicity and the targeting property of a urea-based PSMA inhibitor for PET imaging. *Bioconjug Chem*. 2012;23:688–697.
15. Weineisen M, Simecek J, Schottelius M, Schwaiger M, Wester H-J. Synthesis and preclinical evaluation of DOTAGA-conjugated PSMA ligands for functional imaging and endoradiotherapy of prostate cancer. *EJNMMI Res*. 2014;4:63.
16. Werner-Wasik M, Nelson AD, Choi W, et al. What is the best way to contour lung tumors on PET scans? Multiobserver validation of a gradient-based method using a NSCLC digital PET phantom. *Int J Radiat Oncol Biol Phys*. 2012;82:1164–1171.
17. Obara P, Liu H, Wroblewski K, et al. Quantification of metabolic tumor activity and burden in patients with non-small-cell lung cancer: is manual adjustment of semiautomatic gradient-based measurements necessary? *Nucl Med Commun*. 2015;36:782–789.
18. Hoffman EJ, Huang SC, Phelps ME. Quantitation in positron emission computed tomography: 1. Effect of object size. *J Comput Assist Tomogr*. 1979;3:299–308.
19. Scher HI, Morris MJ, Stadler WM, et al. Trial design and objectives for castration-resistant prostate cancer: updated recommendations from the Prostate Cancer Clinical Trials Working Group 3. *J Clin Oncol*. 2016;34:1402–1418.
20. Hohberg M, Eschner W, Schmidt M, et al. Lacrimal glands may represent organs at risk for radionuclide therapy of prostate cancer with (<sup>177</sup>Lu)DKFZ-PSMA-617. *Mol Imaging Biol*. 2016;18:437–445.
21. Delker A, Fendler WP, Kratochwil C, et al. Dosimetry for <sup>177</sup>Lu-DKFZ-PSMA-617: a new radiopharmaceutical for the treatment of metastatic prostate cancer. *Eur J Nucl Med Mol Imaging*. 2016;43:42–51.
22. Herrmann K, Rahbar K, Eiber M, et al. Dosimetry of <sup>177</sup>Lu-PSMA-617 for the treatment of metastatic castration-resistant prostate cancer: results from the VISION trial sub-study [abstract]. *J Clin Oncol*. 2022;40(suppl):97.
23. ICRP publication 118: ICRP statement on tissue reactions and early and late effects of radiation in normal tissues and organs—threshold doses for tissue reactions in a radiation protection context. *Ann ICRP*. 2012;41:1–322.
24. Okamoto S, Thieme A, Allmann J, et al. Radiation dosimetry for <sup>177</sup>Lu-PSMA 1&T in metastatic castration-resistant prostate cancer: absorbed dose in normal organs and tumor lesions. *J Nucl Med*. 2017;58:445–450.
25. Rinscheid A, Kletting P, Eiber M, Beer AJ, Glatting G. Influence of sampling schedules on (<sup>177</sup>Lu)Lu-PSMA dosimetry. *EJNMMI Phys*. 2020;17:7:41.
26. Kurth J, Heuschkel M, Tonn A, et al. Streamlined schemes for dosimetry of <sup>177</sup>Lu-labeled PSMA targeting radioligands in therapy of prostate cancer. *Cancers (Basel)*. 2021;13:3884.
27. Kratochwil C, Bruchertseifer F, Giesel FL, et al. <sup>225</sup>Ac-PSMA-617 for PSMA-targeted  $\alpha$ -radiation therapy of metastatic castration-resistant prostate cancer. *J Nucl Med*. 2016;57:1941–1944.
28. Tauber RL, Feuerecker B, Knorr K, et al. Safety and efficacy of Ac-225-PSMA-617 in metastatic castration resistant prostate cancer (mCRPC) after failure of Lu-177-PSMA [abstract]. *Ann Oncol*. 2019;30(suppl 5):V342.
29. Khreish F, Wiessner M, Rosar F, et al. Response assessment and prediction of progression-free survival by <sup>68</sup>Ga-PSMA-11 PET/CT based on tumor-to-liver ratio (TLR) in patients with mCRPC undergoing <sup>177</sup>Lu-PSMA-617 radioligand therapy. *Biomolecules*. 2021;11:1099.
30. Buteau JP, Martin AJ, Emmett L, et al.; TheraP Trial Investigators and the Australian and New Zealand Urogenital and Prostate Cancer Trials Group. PSMA and FDG-PET as predictive and prognostic biomarkers in patients given (<sup>177</sup>Lu)Lu-PSMA-617 versus cabazitaxel for metastatic castration-resistant prostate cancer (TheraP): a biomarker analysis from a randomised, open-label, phase 2 trial. *Lancet Oncol*. 2022;23:1389–1397.

---

---

# Improved Quality of Life in Metastatic Castration-Resistant Prostate Cancer Patients Receiving Consecutive Cycles of $^{177}\text{Lu}$ -PSMA I&T

Amir Karimzadeh<sup>1,2</sup>, Paula Soeiro<sup>3</sup>, Benedikt Feurecker<sup>4</sup>, Charlotte-Sophie Hecker<sup>1</sup>, Karina Knorr<sup>1</sup>, Matthias M. Heck<sup>5</sup>, Robert Tauber<sup>5</sup>, Calogero D'Alessandria<sup>1</sup>, Wolfgang A. Weber<sup>1</sup>, Matthias Eiber<sup>\*1</sup>, and Isabel Rauscher<sup>\*1</sup>

<sup>1</sup>Department of Nuclear Medicine, School of Medicine, Technical University of Munich, Munich, Germany; <sup>2</sup>Department of Diagnostic and Interventional Radiology and Nuclear Medicine, University Medical Center Hamburg-Eppendorf, Hamburg, Germany; <sup>3</sup>Centro Hospitalar Universitário de São João, Porto, Portugal; <sup>4</sup>Department of Radiology, University Hospital, LMU Munich, Munich, Germany; and <sup>5</sup>Department of Urology, School of Medicine, Technical University of Munich, Munich, Germany

The aim of this retrospective analysis was to evaluate health-related quality of life (HRQoL) for patients with metastatic castration-resistant prostate cancer (mCRPC) receiving consecutive cycles of  $^{177}\text{Lu}$ -prostate-specific membrane antigen (PSMA) radioligand therapy (RLT) using the reliable and validated European Organisation for Research and Treatment of Cancer core quality-of-life (QoL) questionnaire. In addition, differences in HRQoL between patients with early discontinuation of treatment because of disease progression and patients who were defined as eligible for treatment continuation were analyzed. **Methods:** In total, 60 mCRPC patients were included in this analysis. The European Organisation for Research and Treatment of Cancer core QoL questionnaire was completed at baseline, before each treatment cycle up to the sixth treatment cycle, and at the time of PSMA-ligand PET/CT scans after the second and fourth treatment cycles. QoL assessment included global health status, functional scales, and symptom burden during treatment. **Results:** Global health was significantly improved at the second and fourth cycles of  $^{177}\text{Lu}$ -PSMA RLT ( $P = 0.014$  and  $P = 0.039$ , respectively). In line with this, role and emotional functioning showed significant improvements at the second and fourth treatment cycles (role functioning,  $P = 0.045$  and  $P = 0.048$ , respectively, and emotional functioning,  $P = 0.035$  and  $P = 0.007$ , respectively). In addition, compared with baseline, fatigue and pain were significantly alleviated at the second and fourth treatment cycles (pain,  $P = 0.035$  and  $P = 0.034$ , respectively, and fatigue,  $P = 0.042$  and  $P = 0.041$ , respectively). Other aspects of HRQoL, even if not significantly improved, remained stable over time, except for deterioration of fatigue at the study's end ( $P = 0.014$ ) and reduction of dyspnea at the second treatment cycle ( $P = 0.012$ ). Patients with early discontinuation of treatment showed a concordant decline in HRQoL. **Conclusion:** mCRPC patients showed significant improvement in HRQoL in the course of treatment with  $^{177}\text{Lu}$ -PSMA RLT. Furthermore, patients with early discontinuation of treatment showed an analogous decline in HRQoL.

**Key Words:** prostate-specific membrane antigen radioligand therapy (PSMA RLT); metastatic castration-resistant prostate cancer (mCRPC); health-related quality of life (HRQoL); EORTC QLQ-C30

**J Nucl Med 2023; 64:1765–1771**  
DOI: 10.2967/jnumed.123.265878

---

Received Apr. 17, 2023; revision accepted Aug. 1, 2023.  
For correspondence or reprints, contact Amir Karimzadeh (amir.karimzadeh@uke.de).

\*Contributed equally to this work.

Published online Sep. 7, 2023.

COPYRIGHT © 2023 by the Society of Nuclear Medicine and Molecular Imaging.

In patients with metastatic castration-resistant prostate cancer (mCRPC), radioligand therapy (RLT) that targets  $^{177}\text{Lu}$ -prostate-specific membrane antigen (PSMA) has emerged as a promising treatment option and has recently received approval from the U.S. Food and Drug Administration and European Medicines Agency. Patients with metastatic prostate cancer commonly present with bone metastases that potentially lead to severe pain and impaired mobility, which might cause substantial deterioration in quality of life (QoL) (1,2).

Therefore, the assessment of health-related QoL (HRQoL) and its changes during therapy is of major interest when new treatment strategies are evaluated. The recently published prospective phase II and III trials investigated the influence of  $^{177}\text{Lu}$ -PSMA-617 RLT on HRQoL for mCRPC patients, reporting improvements in both QoL and symptom control (3–5). A potential tool for the evaluation of QoL in cancer patients is the European Organisation for Research and Treatment of Cancer (EORTC) core QoL questionnaire (QLQ-C30) (4–6). Since its introduction, the EORTC QLQ-C30 has been evaluated in several field studies and appeared as reliable and valid (7). The EORTC QLQ-C30 defines HRQoL as a multidimensional construct consisting of subjectively perceived global health status, different functional scales, and disease-related symptoms. However, despite recent publications investigating the impact of  $^{177}\text{Lu}$ -PSMA-617 RLT on HRQoL using small sample sizes over a short treatment period, data on the impact of repeated ( $\geq 2$ ) cycles of  $^{177}\text{Lu}$ -PSMA I&T RLT on HRQoL using a larger cohort of mCRPC patients are scarce and limited (8). Furthermore, on the basis of our clinical experience, we assumed that patients with treatment discontinuation because of disease progression after the first 2 cycles showed a concordant decline in HRQoL during treatment. Thus, the aims of this analysis were to assess changes in HRQoL with mCRPC during treatment with  $^{177}\text{Lu}$ -PSMA RLT and to evaluate potential differences in HRQoL between patients who discontinued treatment because of disease progression and patients who responded and could continue treatment.

## MATERIALS AND METHODS

### Patient Selection and $^{177}\text{Lu}$ -PSMA I&T RLT

Initially, 92 mCRPC patients with accessible EORTC QLQ-C30 responses who received  $^{177}\text{Lu}$ -PSMA I&T RLT in a compassionate-use program between 2014 and 2019 were screened for this retrospective

analysis. Of these, 60 patients fulfilled our study-related inclusion criteria and therefore were identified as eligible for our study. The following criteria were used for inclusion: at least 2 cycles of <sup>177</sup>Lu-PSMA I&T; completion of <sup>177</sup>Lu-PSMA I&T RLT; Eastern Cooperative Oncology Group (ECOG) 0–2; and completed EORTC QLQ-C30 before treatment initiation and at least 12 ± 4 wk after treatment initiation (at PSMA-ligand PET/CT imaging or before the third treatment cycle). The measured time points (e.g., 12 ± 4 wk) were defined retrospectively by the intervals (4- to 8-wk intervals) in which the patients received their treatment cycles or their interim PSMA-ligand PET/CT imaging.

All patients had previously received second-line hormonal therapy with abiraterone or enzalutamide and chemotherapy or were unfit for chemotherapy. Before treatment, sufficient PSMA expression was confirmed by PSMA-ligand PET imaging. Only patients with PSMA-ligand uptake in tumor lesions at least as high as liver background were treated. Data on treatment response and outcome after <sup>177</sup>Lu-PSMA RLT of these patients have been previously reported (9,10).

<sup>177</sup>Lu-PSMA I&T was prepared according to good manufacturing practice and the German Medicinal Products Act (AMG §13 2b). All patients signed informed consent forms and were treated under the conditions of Declaration of Helsinki article 37, “Unproven Interventions in Clinical Practice.” The retrospective analysis was approved by the local ethics committee under reference 115/18 S.

In total, 264 cycles of <sup>177</sup>Lu-PSMA RLT with a median of 4 cycles per patient (range, 2–20 cycles) were applied. Patients received intravenous treatment with a standard dose of approximately 7.4 GBq of <sup>177</sup>Lu-PSMA I&T every 4–10 wk (median, 6 wk). All patients received at least 2 treatment cycles (*n* = 60), 2 patients received 3 cycles, and 35 patients underwent at least 4 cycles of <sup>177</sup>Lu-PSMA RLT (Table 1). Median time on treatment was 4 mo (range, 2–20 mo).

#### QoL Analysis

HRQoL for mCRPC patients was evaluated using the German version of the EORTC QLQ-C30 (version 3.0) (6). The questionnaire was filled out before each <sup>177</sup>Lu-PSMA I&T cycle and at the time of PSMA-ligand PET/CT scans after 2 and potentially 4 treatment cycles. Specifically developed for cancer patients, the EORTC QLQ-C30 is a reliable and valid 30-item questionnaire of self-assessed HRQoL. It consists of 1 multiitem measured global health status; 5 multiitem measured functional scales, namely, physical functioning, role functioning (i.e., performance in daily activities and free-time activities or work), cognitive functioning, emotional functioning, and social functioning; 3 multiitem measured symptom scales (fatigue, pain, and nausea or vomiting); and 6 single items (constipation, diarrhea, insomnia, dyspnea, appetite loss, and financial difficulties). According to the standardized EORTC scoring procedure, scores for each multi- and single-item measure were linearly transformed to a score value from 0 to 100 (11). Although high score values in global health and functional scales represent high levels of health status and functional ability, high scores in symptom scales and single items represent worse symptom status.

#### Statistical Analysis

All analyses were performed using GraphPad Prism version 9.4.1(458) (GraphPad Software) for Mac (Apple). A mixed-effects model that allows missing values was performed to analyze repeated measures data of HRQoL for the total patient cohort and for patients stratified according to their ECOG performance status at baseline (ECOG 0, ECOG 1, or ECOG 2). Questionnaires with a response rate of less than 25% (15%, *n* = 9) after the sixth treatment cycle were excluded from further analysis. Results were presented as mean changes from baseline scores of HRQoL. A paired *t* test visualized in Tukey box-and-whisker plots was performed to evaluate differences in

**TABLE 1**  
Baseline Patient Characteristics

Characteristic	Data
Patients receiving <sup>177</sup> Lu-PSMA RLT	60
2 cycles	23
3 cycles	2
≥4 cycles	35
ECOG 0	19
ECOG 1	34
ECOG 2	7
Age (y)	72 (67–76)
PSA (ng/mL)	132.3 (29.2–267.6)
LDH (U/L)	252.5 (215.8–316.8)
AP (U/L)	118.5 (78.0–211.8)
Hb (g/dL)	11.5 (10.3–12.6)
Prior systemic therapies for mCRPC, <i>n</i> = 60 (%)	
Docetaxel	44 (73)
Cabazitaxel	12 (20)
Abiraterone	46 (77)
Enzalutamide	40 (67)
<sup>223</sup> Ra	12 (20)
Previous chemotherapy	44 (73)
Site of metastasis, <i>n</i> = 60	
Lymph node, overall	49
Lymph node, N1+/M1a	5
Bone, overall	54
Bone, M1b, without visceral metastases	38
Visceral, overall, M1c	19
Liver	3
Lung	11
Adrenal	7

PSA = prostate-specific antigen; LDH = lactate dehydrogenase; AP = alkaline phosphatase; Hb = hemoglobin.

Qualitative data are number and percentage; continuous data are median and interquartile range.

HRQoL between patients who were excluded after 2 or 4 treatment cycles (nonresponder) and those who continued treatment beyond 2 or 4 treatment cycles (responder). HRQoL deterioration-free survival was defined as the time between treatment initiation and first HRQoL score deterioration of at least 5 points compared with the baseline score (without subsequent improvement ≥5 points compared with baseline or improvement to ≥90 if the baseline score was ≥90) or death, whichever occurred first (12). Deterioration-free survival curves were estimated using the Kaplan–Meier method for estimation of event time distributions, and log-rank tests were used for group comparisons. Patients who were alive were censored at the last HRQoL follow-up (26 ± 4 wk) if deterioration of at least 5 points from baseline was not observed or if a decrease of at least 5 points was present but was followed by improvement of at least 5 points or improvement to at least 90 if the baseline score was at least 90. HRQoL for patients who were

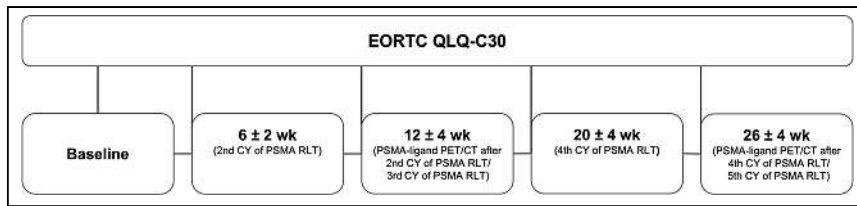


**FIGURE 1.** Study design. CY = cycle.

excluded from treatment (nonresponder) and in those who were defined as eligible for treatment continuation (responder) was analyzed on the basis of disease progression upon PSMA-ligand PET/CT imaging routinely performed after 2 treatment cycles (at  $12 \pm 4$  wk). The corresponding hazard ratio (HR) and 95% CI are presented. A *P* value of less than 0.05 was considered statistically significant.

## RESULTS

### QoL in the Entire Patient Cohort

Patient characteristics are shown in Table 1. Before treatment, 32% ( $n = 19$ ), 57% ( $n = 34$ ), and 11% ( $n = 7$ ) of the patients presented with ECOG 0, ECOG 1, and ECOG 2, respectively. At baseline and at  $12 \pm 4$  wk (PSMA-ligand PET/CT imaging after the second treatment cycle or before the third treatment cycle) the questionnaire was available for all 60 (100%) patients (Fig. 1). For 39 (65%), 18 (30%), 16 (27%), and 9 (15%) patients, the questionnaire was available at  $6 \pm 2$  wk (second treatment cycle),  $20 \pm 4$  wk (fourth treatment cycle),  $26 \pm 4$  wk (PSMA-ligand PET/CT imaging after the fourth treatment cycle or before the fifth treatment cycle), and  $34 \pm 4$  wk (sixth treatment cycle) after the first treatment cycle, respectively (Fig. 1).

Compared with baseline, HRQoL improved significantly, revealing elevated global health status at  $6 \pm 2$  wk ( $P = 0.014$ ) and at  $20 \pm 4$  wk ( $P = 0.039$ ) after treatment initiation (Fig. 2A; Table 2). In accordance with this, role functioning and emotional functioning demonstrated significant improvements after the first cycle of  $^{177}\text{Lu}$ -PSMA RLT and over time (role functioning,  $6 \pm 2$  wk [ $P = 0.045$ ] and  $20 \pm 4$  wk [ $P = 0.048$ ]; emotional functioning,  $6 \pm 2$  wk [ $P = 0.035$ ] and  $20 \pm 4$  wk [ $P = 0.007$ ]; Figs. 2C and 2D; Table 2). Other aspects of functional ability, namely, physical functioning, cognitive functioning, and social functioning, although not significantly improved, remained constant during treatment (Fig. 2B; Table 2). Moreover, compared with baseline, some symptom scales, such as fatigue and pain, were significantly alleviated at  $6 \pm 2$  and  $20 \pm 4$  wk (fatigue,  $P = 0.042$  and  $P = 0.041$ , respectively, and pain,  $P = 0.035$  and  $P = 0.034$ , respectively; Figs. 2E and 2F; Table 2). In addition, at  $26 \pm 4$  wk, significant deterioration ( $P = 0.014$ ) of fatigue was detected (Fig. 2E). Other symptoms, even if not significantly improved (except significant alleviation of dyspnea at  $6 \pm 2$  wk,  $P = 0.012$ ), showed no deterioration over time

(Table 2). Patients with ECOG 0 had higher HRQoL scores and less symptom burden in all domains during the course of treatment, whereas patients within the ECOG 1 and ECOG 2 group had worse HRQoL (Fig. 2; Supplemental Tables 1 and 2 [supplemental materials are available at <http://jnm.snmjournals.org>]). However, the presented significant effects of  $^{177}\text{Lu}$ -PSMA RLT on HRQoL for the total patient cohort were not

found within the ECOG-stratified groups (ECOG 0, ECOG 1, or ECOG 2; Fig. 2; Supplemental Tables 1 and 2).

### QoL for Patients with Early Exclusion from Treatment

Following PSMA-ligand PET/CT imaging after 2 treatment cycles (at  $12 \pm 4$  wk; Fig. 1), 23 patients discontinued treatment because of disease progression and were stratified as nonresponders, whereas 37 patients were defined as eligible for treatment continuation and were stratified as responders (Table 1).

The nonresponder group presented with a lower baseline HRQoL than did the responder group in most assessed domains (Table 3). In addition, significantly worse physical functioning ( $P = 0.0495$ ) and role functioning ( $P = 0.011$ ), deterioration of fatigue ( $P = 0.046$ ), and increased nausea and vomiting ( $P = 0.008$ ) were detectable at  $12 \pm 4$  wk in the nonresponder group (Figs. 3B, 3C, and 3E; Table 3). In contrast, patients in the responder group showed significantly improved global health status ( $P = 0.002$ ), alleviation of pain ( $P = 0.011$ ), and reduced dyspnea ( $P = 0.047$ ; Figs. 3A and 3F; Table 3). Other aspects of HRQoL, although not significantly improved, remained stable over time (Table 3).

In line with this, the nonresponder group had a significantly higher risk of HRQoL deterioration in global health status (HR,

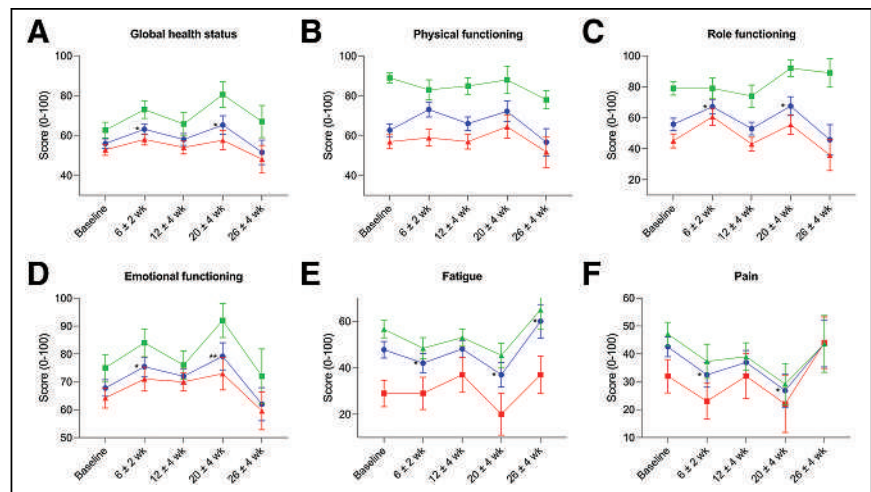


**FIGURE 2.** Changes in global health status, selected functional scales (physical functioning, role functioning, and emotional functioning), and selected symptom scales (fatigue and pain) for total patient cohort (blue) and for patients with ECOG 0 (green) and ECOG 1 or ECOG 2 (red) performance status during treatment with  $^{177}\text{Lu}$ -PSMA RLT, according to EORTC QLQ-C30. Results are presented as mean changes from baseline and SEM. (A) In total patient cohort, global health status was significantly improved at  $6 \pm 2$  wk ( $P = 0.014$ ) and  $20 \pm 4$  wk ( $P = 0.039$ ). (B–D) In total patient cohort, role functioning and emotional functioning were significantly improved at  $6 \pm 2$  wk ( $P = 0.045$  and  $P = 0.035$ ) and at  $20 \pm 4$  wk ( $P = 0.048$  and  $P = 0.007$ ), while physical functioning, although not significantly improved, remained constant during treatment. (E and F) In total patient cohort, fatigue and pain were significantly alleviated at  $6 \pm 2$  wk ( $P = 0.042$  and  $P = 0.035$ ) and at  $20 \pm 4$  wk ( $P = 0.041$  and  $P = 0.034$ ), whereas fatigue was significantly deteriorated at  $26 \pm 2$  wk ( $P = 0.014$ ). \* $P < 0.05$ . \*\* $P < 0.01$ .

**TABLE 2**  
EORTC QLQ-C30 Scores for Total Patient Cohort

Parameter	Category	EORTC QLQ-C30 score (0–100)				
		Baseline	6 ± 2 wk	12 ± 4 wk	20 ± 4 wk	26 ± 4 wk
Global health status		56.0 (51.3–60.6)	63.2* (58.0–68.3)	57.8 (52.0–63.5)	65.3* (56.2–74.4)	51.6 (39.6–63.6)
Functional scale	Physical functioning	67.1 (60.9–73.3)	67.2 (59.8–74.5)	65.8 (59.2–72.3)	72.2 (62.2–82.3)	56.7 (43.3–70.1)
	Role functioning	55.8 (48.1–63.6)	67.1* (58.2–76.0)	52.8 (44.7–60.9)	67.6* (55.7–79.5)	45.8 (26.6–65.1)
	Emotional functioning	67.8 (62.0–73.6)	75.4* (68.7–82.2)	71.8 (66.4–77.2)	79.2 <sup>†</sup> (69.6–88.7)	62.0 (50.3–73.6)
	Cognitive functioning	84.7 (79.6–89.9)	84.2 (77.9–90.5)	84.0 (78.7–89.1)	85.2 (76.0–94.4)	87.5 (80.1–94.9)
	Social functioning	65.3 (58.8–71.7)	70.6 (62.4–78.8)	61.9 (54.8–69.1)	75.0 (63.7–86.3)	56.3 (40.5–72.0)
Symptom scale	Fatigue	47.8 (40.8–54.7)	41.8* (33.8–49.9)	48.2 (41.0–55.3)	37.0* (26.6–47.4)	59.7* (45.3–74.1)
	Nausea and vomiting	6.7 (2.7–10.7)	11.8 (5.7–18.0)	9.2 (4.5–13.8)	3.7 (0.0–7.8)	8.3 (0.2–16.5)
	Pain	42.5 (23.6–43.1)	32.5* (23.6–43.1)	36.9 (26.7–43.4)	26.9* (15.8–39.8)	43.8 (25.4–59.1)
Single item	Dyspnea	40.0 (31.5–48.6)	28.1* (18.5–37.7)	30.6 (23.0–38.2)	25.9 (12.8–39.1)	35.4 (20.7–50.1)
	Insomnia	30.6 (21.4–39.7)	29.8 (19.0–40.6)	29.4 (20.5–38.4)	29.6 (17.2–42.1)	25.0 (11.5–38.5)
	Appetite loss	29.4 (17.1–31.8)	28.1 (17.6–38.5)	26.1 (17.8–34.4)	11.1 (2.2–20.0)	33.3 (15.1–51.6)
	Constipation	16.1 (9.7–22.6)	16.7 (8.3–25.0)	18.9 (12.1–25.7)	13.0 (2.5–23.4)	12.5 (0.0–25.3)
	Diarrhea	12.2 (6.3–18.2)	11.4 (3.6–19.2)	11.1 (5.4–16.8)	7.4 (0.0–15.6)	10.4 (2.9–18.0)
	Financial difficulties	10.0 (4.2–15.8)	13.2 (5.3–21.1)	13.3 (7.1–19.5)	18.5 (5.7–31.3)	20.8 (5.7–36.0)

\* $P < 0.05$ .

<sup>†</sup> $P < 0.01$ .

Data are baseline mean scores and 95% CIs before first <sup>177</sup>Lu-PSMA RLT cycle and for 6 ± 2 wk during second <sup>177</sup>Lu-PSMA RLT cycle, 12 ± 4 wk during PSMA-ligand PET/CT scan after second <sup>177</sup>Lu-PSMA RLT cycle or third <sup>177</sup>Lu-PSMA RLT cycle, and 20 ± 4 wk during fourth <sup>177</sup>Lu-PSMA RLT cycle after first cycle of <sup>177</sup>Lu-PSMA RLT for patients with mCRPC treated with <sup>177</sup>Lu-PSMA RLT.

2.9; 95% CI, 1.3–6.6;  $P = 0.002$ ), physical functioning (HR, 2.2; 95% CI, 1.1–4.8;  $P = 0.013$ ), role functioning (HR, 2.2; 95% CI, 1.0–5.2;  $P = 0.035$ ), cognitive functioning (HR, 2.4; 95% CI, 1.0–6.0;  $P = 0.035$ ), fatigue (HR, 2.7; 95% CI, 1.3–5.6;  $P = 0.001$ ), nausea and vomiting (HR, 4.5; 95% CI, 1.6–12.8;  $P = 0.001$ ), appetite loss (HR, 3.5; 95% CI, 1.3–9.7;  $P = 0.005$ ), and diarrhea (HR, 3.4; 95% CI, 1.1–10.1;  $P = 0.017$ ; Figs. 4A–4C and 4E; Supplemental Table 3). Similar trends were observed for most remaining aspects of HRQoL (Figs. 4D and 4F; Supplemental Table 3).

Differences in HRQoL between patients who discontinued treatment (nonresponder,  $n = 7$ ) because of relevant disease progression in PSMA-ligand PET/CT imaging after 4 treatment cycles (at 26 ± 4 wk; Fig. 1) and those who continued treatment (responder,  $n = 9$ ) are given in Supplemental Table 4.

## DISCUSSION

The results of our retrospective analysis indicate significant improvements in various aspects of HRQoL (e.g., global health status) during treatment with <sup>177</sup>Lu-PSMA I&T RLT in mCRPC. In contrast, patients who discontinued treatment after 2 treatment cycles because of disease progression had a concordant decline in HRQoL and a higher risk of deterioration in QoL than did patients who responded after the initial 2 cycles.

The most affected dimensions of HRQoL were global health status, role functioning, emotional functioning, fatigue, and pain. In these domains, significant improvements were detectable at the second (at 6 ± 2 wk) and fourth (at 20 ± 4 wk) treatment cycles. Our analysis might underline the beneficial impact of <sup>177</sup>Lu-PSMA I&T RLT on HRQoL—in contrast to a recently published analysis of mCRPC patients treated with new hormonal agents or first-line chemotherapy, which reported continuous and significant deterioration in, for example, physical functioning, fatigue, and pain (13). However, because our analysis evaluates the impact of <sup>177</sup>Lu-PSMA I&T RLT on HRQoL over only a short treatment period, further studies analyzing the long-term impact on HRQoL are warranted.

At PSMA-ligand PET/CT imaging after the second treatment cycle or before the third treatment cycle (12 ± 4 wk) and at PSMA-ligand PET/CT imaging after the fourth treatment cycle or before the fifth treatment cycle (26 ± 4 wk) a slight shift toward HRQoL deterioration was detectable. Similar trends were reported in a previously published prospective phase II trial (4,14). A potential hypothesis for this could be a concordant decline of QoL for patients with relevant disease progression, leading to negative affection of HRQoL at the measured time points. This is supported by our results, which revealed significant deterioration of HRQoL

**TABLE 3**

EORTC QLQ-C30 Scores at Baseline and 12 ± 4 Weeks After Treatment Initiation in Nonresponder Patients Receiving 2 Cycles and Responder Patients Receiving More Than 2 Cycles of <sup>177</sup>Lu-PSMA RLT

Parameter	Category	EORTC QLQ-C30 score (0–100)				
		Total patient cohort	Nonresponder		Responder	
		Baseline	Baseline	12 ± 4 wk	Baseline	12 ± 4 wk
Global health status		56.0 (51.3–60.6)	51.8 (44.4–59.3)	44.2 (35.3–53.1)	58.6 (52.1–65.1)	66.2 <sup>†</sup> (60.0–72.5)
Functional scale	Physical functioning	67.1 (60.9–73.3)	61.7 (51.5–72.0)	53.9* (43.7–64.1)	70.5 (62.8–78.1)	73.2 (65.2–81.1)
	Role functioning	55.8 (48.1–63.6)	50.7 (39.5–62.0)	37.0* (24.1–49.8)	59.0 (49.7–68.3)	62.6 (53.0–72.2)
	Emotional functioning	67.8 (62.0–73.6)	59.4 (49.7–69.2)	63.0 (55.7–70.4)	73.0 (65.8–80.1)	77.3 (70.1–84.4)
	Cognitive functioning	84.7 (79.6–89.9)	81.2 (72.1–90.2)	77.5 (68.6–86.4)	86.9 (80.7–93.1)	87.8 (81.3–94.4)
	Social functioning	65.3 (58.8–71.7)	54.4 (43.9–64.8)	48.6 (37.6–59.5)	72.1 (64.9–79.3)	70.3 (62.6–77.9)
Symptom scale	Fatigue	47.8 (40.8–54.7)	49.8 (39.1–60.5)	59.9* (48.8–71.0)	46.6 (37.7–55.4)	40.8 (33.3–48.4)
	Nausea and vomiting	6.7 (2.7–10.7)	7.3 (1.6–12.9)	19.6 <sup>†</sup> (9.6–29.5)	6.3 (0.0–12.8)	2.7 (0.0–6.0)
	Pain	42.5 (23.6–43.1)	51.5 (40.7–62.3)	54.4 (39.3–69.4)	36.9 (28.8–45.1)	26.1* (18.1–34.1)
Single item	Dyspnea	40.0 (31.5–48.6)	50.7 (35.2–66.2)	42.0 (28.6–55.5)	33.3 (24.4–42.4)	23.4* (15.1–31.8)
	Insomnia	30.6 (21.4–39.7)	46.4 (29.9–62.8)	44.9 (28.1–61.8)	20.7 (11.4–30.1)	19.8 (10.7–28.9)
	Appetite loss	29.4 (17.1–31.8)	21.7 (9.3–34.2)	36.2 (21.3–51.2)	26.1 (17.2–35.1)	19.8 (9.6–30.1)
	Constipation	16.1 (9.7–22.6)	18.8 (7.6–30.1)	23.2 (11.5–34.9)	14.4 (8.3–20.5)	16.2 (7.9–24.5)
	Diarrhea	12.2 (6.3–18.2)	11.6 (3.0–20.2)	13.0 (2.6–23.5)	12.6 (5.0–20.3)	9.9 (3.2–16.6)
	Financial difficulties	10.0 (4.2–15.8)	15.9 (4.7–27.2)	15.9 (6.2–25.7)	6.3 (0.0–13.5)	11.7 (2.3–21.1)

\**P* < 0.05.

<sup>†</sup>*P* < 0.01.

Data are baseline mean scores and 95% CIs before first <sup>177</sup>Lu-PSMA RLT cycle in total patient cohort and in nonresponder and responder patients, dichotomized according to number of received treatment cycles of <sup>177</sup>Lu-PSMA RLT at 12 ± 4 wk and at 12 ± 4 wk during PSMA-ligand PET/CT scan after second <sup>177</sup>Lu-PSMA RLT cycle or third <sup>177</sup>Lu-PSMA RLT cycle after first cycle of <sup>177</sup>Lu-PSMA RLT in nonresponder and responder patients with mCRPC treated with <sup>177</sup>Lu-PSMA RLT.

(e.g., physical functioning) for patients who discontinued <sup>177</sup>Lu-PSMA RLT after the second treatment cycle because of disease progression (at 12 ± 4 wk), whereas patients who continued treatment showed stabilization or improvement of HRQoL (e.g., global health status). In accordance with this, we could also demonstrate a significantly higher risk of HRQoL deterioration for patients with early treatment discontinuation. This is in line with results from van der Doelen et al., who reported stabilization of HRQoL for patients who completed <sup>223</sup>Ra treatment but observed decline in HRQoL for patients who discontinued treatment (15). The same was true for most assessed HRQoL domains for patients who discontinued treatment after 4 treatment cycles compared with those who received more than 4 treatment cycles. However, in this patient cohort, none of the detected differences were statistically significant, which is most likely because of the small sample size.

Two previously published prospective phase II trials analyzed HRQoL using the EORTC QLQ-C30 for mCRPC patients undergoing <sup>177</sup>Lu-PSMA-617 RLT (4,5,14). These trials reported higher HRQoL scores and lower symptom burden at baseline in most domains than found in our results (5). The worse HRQoL scores at

baseline reported in our analysis might be explained by the more advanced disease stage in our patient cohort, including visceral metastases in 32% of our patients (*n* = 19) versus, for example, 7% of TheraP patients (*n* = 7), given the known negative association of visceral metastases with outcome (5,16). In addition, 20% (*n* = 12) of our patients received pretreatment with cabazitaxel versus none of the TheraP patients, also illustrating their more advanced stage regularly associated with decreased QoL (17). Differences in administered therapies and disease stages should be considered when comparing HRQoL between studies. Furthermore, a recently published prospective phase III trial investigating the impact of <sup>177</sup>Lu-PSMA-617 RLT plus standard of care versus standard of care alone reported a beneficial HRQoL for the <sup>177</sup>Lu-PSMA-617 RLT group (18). However, because it used “Functional Assessment of Cancer Therapy: Prostate and the Brief Pain Inventory—Short Form” for the assessment of HRQoL and different outcome parameters, a direct comparison with the results of our analysis is not possible (3).

Patients with either slight impairment in physically demanding activities (ECOG 1) or total inability in work activities (ECOG 2) had concordantly lower HRQoL than did patients with fully active



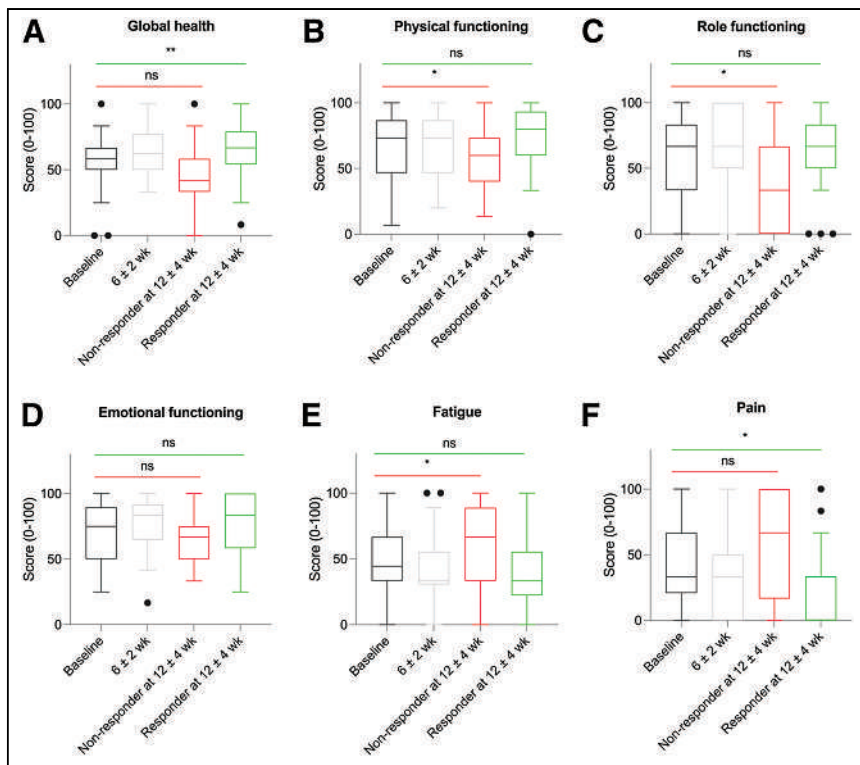


**FIGURE 3.** Tukey box plot display of global health status, selected functional scales (physical functioning, role functioning, and emotional functioning), and selected symptom scales (fatigue and pain) for total patient cohort at baseline (black) and at  $6 \pm 2$  wk (light gray) and for patients dichotomized according to number of received treatment cycles of  $^{177}\text{Lu}$ -PSMA RLT at  $12 \pm 4$  wk (nonresponder, red; responder, green). (A) Compared with baseline, global health status was significantly improved at  $12 \pm 4$  wk in responder group ( $P = 0.002$ ). (B–D) Compared with baseline, physical functioning and role functioning were significantly worse in nonresponder group ( $P = 0.0495$  and  $P = 0.011$ ), while no significant differences were detectable for emotional functioning. (E and F) Compared with baseline, fatigue was significantly deteriorated in nonresponder group ( $P = 0.046$ ) and pain was significantly alleviated in responder group ( $P = 0.011$ ). Outliers that differ significantly from rest of dataset were plotted as individual points beyond whiskers on box plot. \* $P < 0.05$ . \*\* $P < 0.01$ . ns = not significant.

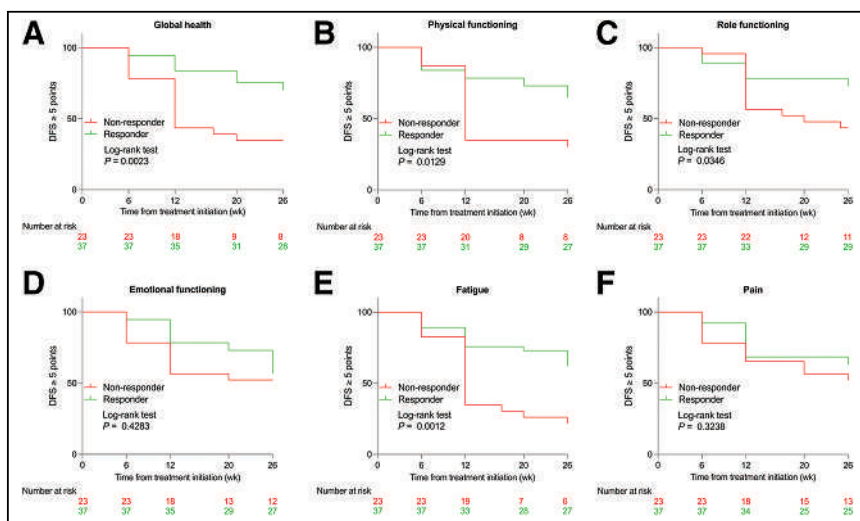


**FIGURE 4.** Kaplan–Meier survival curves for HRQoL deterioration-free survival for global health status (A), selected functioning scales (physical functioning, role functioning, and emotional functioning) (B–D), and selected symptom scales (fatigue and pain) (E and F) for patients dichotomized according to number of received treatment cycles of  $^{177}\text{Lu}$ -PSMA RLT at  $12 \pm 4$  wk (nonresponder, red; responder, green). DFS = deterioration-free survival.

performance status (ECOG 0) at all measuring points. This is in line with results from Marinova et al., who investigated HRQoL for patients with midgut neuroendocrine tumors after peptide receptor radionuclide therapy (19). However, the significant impact of  $^{177}\text{Lu}$ -PSMA RLT on HRQoL for our total patient cohort was not found within ECOG-divided groups (ECOG 0 vs. ECOG 1 or ECOG 2), although there was a similar tendency detectable (e.g., global health status). This might be explained by the relatively small sample size in each of the analyzed subgroups, which resulted in decreased power of the statistical test. Further studies are warranted to validate our results in larger patient cohorts.

Our study has several limitations, including the single-center retrospective nature of this analysis, which may limit the validity of our results. The small sample size may prevent our findings from being extrapolated and impede the visibility of small effects of  $^{177}\text{Lu}$ -PSMA RLT on HRQoL.

### CONCLUSION

The results of our analysis indicate a beneficial impact of  $^{177}\text{Lu}$ -PSMA RLT on QoL for mCRPC patients. Patients showed improvement in HRQoL and alleviation in relevant disease-related symptoms. In addition, we could demonstrate a significant decline in HRQoL for patients with unfavorable disease progression that resulted in early discontinuation of treatment.

### DISCLOSURE

Matthias Eiber reports fees from Blue Earth Diagnostics Ltd. (consulting and research funding), Novartis/AAA (consulting), Telix (consulting), Bayer (consulting and research funding), RayzeBio (consulting), Point Biopharma (consulting), Janssen Pharmaceuticals (consulting and speakers bureau), Parexel (image review), and Bioclinica (image review) outside the submitted work and a patent application for rhPSMA. Robert Tauber reports prior consulting activities for AstraZeneca, Bayer, BMS, Eisai, EUSA, Ipsen, Janssen, MSD, Philogen, Roche, and Sanofi and travel support from Bayer, BMS, Ipsen, Janssen, and Roche. Robert Tauber owns shares of Bayer. Wolfgang Weber is on the advisory boards and receives compensation from Blue Earth Diagnostics, ITG, and Pentixapharm. He has received research support from Blue Earth Diagnostics, BMS, and Pentixapharm. No other potential conflict of interest relevant to this article was reported.

## KEY POINTS

**QUESTION:** Does  $^{177}\text{Lu}$ -PSMA I&T RLT have a beneficial impact on HRQoL for mCRPC patients?

**PERTINENT FINDINGS:** In our analysis, we could demonstrate that  $^{177}\text{Lu}$ -PSMA I&T RLT is associated with a beneficial impact on HRQoL. Moreover, we could detect a significant decline in HRQoL for patients who discontinued treatment because of disease progression.

**IMPLICATIONS FOR PATIENT CARE:** HRQoL is important when it comes to the evaluation of new treatment strategies such as  $^{177}\text{Lu}$ -PSMA RLT.  $^{177}\text{Lu}$ -PSMA RLT demonstrates a beneficial impact on patients' HRQoL. However, for patients with early disease progression, the positive impact of  $^{177}\text{Lu}$ -PSMA RLT on QoL is limited.

## REFERENCES

- Gandaglia G, Abdollah F, Schiffmann J, et al. Distribution of metastatic sites in patients with prostate cancer: a population-based analysis. *Prostate*. 2014;74:210–216.
- Jenkins V, Solis-Trapala I, Payne H, et al. Treatment experiences, information needs, pain and quality of life in men with metastatic castrate-resistant prostate cancer: results from the EXTREQOL study. *Clin Oncol (R Coll Radiol)*. 2019;31:99–107.
- Sartor O, de Bono J, Chi KN, et al. Lutetium-177-PSMA-617 for metastatic castration-resistant prostate cancer. *N Engl J Med*. 2021;385:1091–1103.
- Hofman MS, Violet J, Hicks RJ, et al.  $^{177}\text{Lu}$ -PSMA-617 radionuclide treatment in patients with metastatic castration-resistant prostate cancer (LuPSMA trial): a single-centre, single-arm, phase 2 study. *Lancet Oncol*. 2018;19:825–833.
- Hofman MS, Emmett L, Sandhu S, et al.  $^{177}\text{Lu}$ -PSMA-617 versus cabazitaxel in patients with metastatic castration-resistant prostate cancer (TheraP): a randomised, open-label, phase 2 trial. *Lancet*. 2021;397:797–804.
- Aaronson NK, Ahmedzai S, Bergman B, et al. The European Organisation for Research and Treatment of Cancer QLQ-C30: a quality-of-life instrument for use in international clinical trials in oncology. *J Natl Cancer Inst*. 1993;85:365–376.
- Bjordal K, de Graeff A, Fayers PM, et al. A 12 country field study of the EORTC QLQ-C30 (version 3.0) and the head and neck cancer specific module (EORTC QLQ-H&N35) in head and neck patients. EORTC Quality of Life Group. *Eur J Cancer*. 2000;36:1796–1807.
- Marinova M, Alamdar R, Ahmadzadehfar H, et al. Improving quality of life in patients with metastatic prostate cancer following one cycle of  $^{177}\text{Lu}$ -PSMA-617 radioligand therapy: a pilot study. *Nuklearmedizin*. 2020;59:409–414.
- Karimzadeh A, Heck M, Tauber R, et al.  $^{177}\text{Lu}$ -PSMA-I&T for treatment of metastatic castration resistant prostate cancer: prognostic value of scintigraphic and clinical biomarkers. *J Nucl Med*. 2023;64:402–409.
- Karimzadeh A, Heck M, Tauber R, et al. The impact of PSMA PET-based eligibility criteria used in the prospective phase II TheraP trial in metastatic castration-resistant prostate cancer patients undergoing prostate-specific membrane antigen-targeted radioligand therapy. *J Nucl Med*. 2023;64:1252–1258.
- Fayers PM, Aaronson NK, Bjordal K, et al. *The EORTC QLQ-C30 Scoring Manual*. 3rd ed. European Organisation for Research and Treatment of Cancer; 2001.
- Osoba D, Rodrigues G, Myles J, Zee B, Pater J. Interpreting the significance of changes in health-related quality-of-life scores. *J Clin Oncol*. 1998;16:139–144.
- Kuppen MCP, Westgeest HM, van den Eertwegh AJM, et al. Health-related quality of life and pain in a real-world castration-resistant prostate cancer population: results from the PRO-CAPRI study in the Netherlands. *Clin Genitourin Cancer*. 2020;18:e233–e253.
- Violet J, Sandhu S, Irvani A, et al. Long-term follow-up and outcomes of retreatment in an expanded 50-patient single-center phase II prospective trial of  $^{177}\text{Lu}$ -PSMA-617 theranostics in metastatic castration-resistant prostate cancer. *J Nucl Med*. 2020;61:857–865.
- van der Doelen MJ, Oving IM, Wyndaele DNJ, et al. Health-related quality of life, psychological distress, and fatigue in metastatic castration-resistant prostate cancer patients treated with radium-223 therapy. *Prostate Cancer Prostatic Dis*. 2023;26:142–150.
- Manafi-Farid R, Harsini S, Saidi B, et al. Factors predicting biochemical response and survival benefits following radioligand therapy with  $^{177}\text{Lu}$ -PSMA in metastatic castrate-resistant prostate cancer: a review. *Eur J Nucl Med Mol Imaging*. 2021;48:4028–4041.
- Ahmadzadehfar H, Rahbar K, Baum RP, et al. Prior therapies as prognostic factors of overall survival in metastatic castration-resistant prostate cancer patients treated with  $^{177}\text{Lu}$ -PSMA-617: a WARMTH multicenter study (the 617 trial). *Eur J Nucl Med Mol Imaging*. 2021;48:113–122.
- Karim F, Herrmann K, Krause BJ, et al. Health-related quality of life (HRQoL), pain and safety outcomes in the phase III VISION study of  $^{177}\text{Lu}$ -PSMA-617 in patients with metastatic castration-resistant prostate cancer [abstract]. *Ann Oncol*. 2021;32(suppl 5):S626–S677.
- Marinova M, Mücke M, Fischer F, et al. Quality of life in patients with midgut NET following peptide receptor radionuclide therapy. *Eur J Nucl Med Mol Imaging*. 2019;46:2252–2259.

---

---

# Tandem Isotope Therapy with $^{225}\text{Ac}$ - and $^{177}\text{Lu}$ -PSMA-617 in a Murine Model of Prostate Cancer

Catherine Meyer<sup>1</sup>, Andreea Stuparu<sup>1</sup>, Katharina Lueckerath<sup>1,2</sup>, Jeremie Calais<sup>1</sup>, Johannes Czernin<sup>1</sup>, Roger Slavik<sup>1</sup>, and Magnus Dahlbom<sup>1</sup>

<sup>1</sup>Ahmanson Translational Theranostics Division, Department of Molecular and Medical Pharmacology, David Geffen School of Medicine, UCLA, Los Angeles, California; and <sup>2</sup>Clinic for Nuclear Medicine, University Hospital Essen, Essen, Germany

Radionuclide therapy targeting prostate-specific membrane antigen (PSMA) is a promising option for metastatic castration-resistant prostate cancer. Clinical experience using  $^{177}\text{Lu}$  or  $^{225}\text{Ac}$  has demonstrated encouraging treatment responses; however, responses are not durable. Dual-isotope combinations, or “tandem” approaches, may improve tolerability while retaining a high tumor dose. In this study, we directly compared  $\alpha$ - versus  $\beta$ -particle treatment, as well as a combination thereof, at different stages of disease in a murine model of disseminated prostate cancer. **Methods:** First, to determine comparable injected activities from  $^{177}\text{Lu}$ - and  $^{225}\text{Ac}$ -PSMA-617, *ex vivo* biodistribution studies were performed at 5 time points after treatment of C4-2 subcutaneous tumor-bearing NSG mice. To establish a more representative model of metastatic prostate cancer, NSG mice were inoculated with luciferase-expressing C4-2 cells in the left ventricle, leading to disseminated visceral and bone lesions. At either 3 or 5 wk after inoculation, the mice were treated with equivalent tumor dose-depositing activities of  $^{177}\text{Lu}$ - or  $^{225}\text{Ac}$ -PSMA-617 alone or in combination (35 MBq of  $^{177}\text{Lu}$ , 40 kBq of  $^{225}\text{Ac}$ , or 17 MBq of  $^{177}\text{Lu}$  + 20 kBq  $^{225}\text{Ac}$ ; 10/group). Disease burden was assessed by weekly bioluminescence imaging. Treatment efficacy was evaluated using whole-body tumor burden and overall survival. **Results:** The *ex vivo* biodistribution studies revealed that 35 MBq of  $^{177}\text{Lu}$  and 40 kBq of  $^{225}\text{Ac}$  yield equivalent absorbed tumor doses in a subcutaneous C4-2 model. The disease burden of mice treated at 3 wk after inoculation (microscopic disease) with  $^{177}\text{Lu}$  was not significantly different from that of untreated mice. However,  $^{225}\text{Ac}$ -PSMA-617 both as a single agent and in combination with  $^{177}\text{Lu}$  (17 MBq of  $^{177}\text{Lu}$  + 20 kBq of  $^{225}\text{Ac}$ ) were associated with significant whole-body tumor growth retardation and survival benefit (overall survival, 8.3 wk for nontreatment, 9.4 wk for  $^{177}\text{Lu}$ , 15.3 wk for  $^{225}\text{Ac}$  alone, and 14.1 wk for tandem therapy). When treated at 5 wk after inoculation (macroscopic disease), all treatment groups showed retarded tumor growth and improved survival, with no significant differences between  $^{225}\text{Ac}$  alone and administration of half the  $^{225}\text{Ac}$  activity in tandem with  $^{177}\text{Lu}$  (overall survival, 7.9 wk for nontreatment, 10.3 wk for  $^{177}\text{Lu}$ , 14.6 wk for  $^{225}\text{Ac}$  alone, and 13.2 wk for tandem therapy). **Conclusion:** Treatment of a disseminated model of prostate cancer with simultaneous  $^{225}\text{Ac}$ - and  $^{177}\text{Lu}$ -PSMA-617 results in significantly decreased tumor growth compared with  $^{177}\text{Lu}$ , which was ineffective as a single agent against

microscopic lesions. Mice treated later in the disease progression and bearing macroscopic, millimeter-sized lesions experienced significant tumor growth retardation and survival benefit in both monoisotopic and tandem regimens of  $^{177}\text{Lu}$  and  $^{225}\text{Ac}$ . Although the greatest benefits were observed with the single agent  $^{225}\text{Ac}$ , the tandem arm experienced no significant difference in disease burden or survival benefit, suggesting that the reduced activity of  $^{225}\text{Ac}$  was adequately compensated in the tandem arm. The superior therapeutic efficacy of  $^{225}\text{Ac}$  in this model suggests a preference for  $\alpha$ -emitters alone, or possibly in combination, in the microscopic disease setting.

**Key Words:** PSMA-617;  $^{177}\text{Lu}$ ;  $^{225}\text{Ac}$ ; mouse model; prostate cancer; RLT

**J Nucl Med 2023; 64:1772–1778**

DOI: 10.2967/jnumed.123.265433

**R**adionuclide therapy targeting the prostate-specific membrane antigen (PSMA) protein is a promising option for patients with metastatic castration-resistant prostate cancer. The most commonly used therapeutic isotope is  $^{177}\text{Lu}$ , a medium-energy  $\beta$ -emitter (0.5 MeV) with a 6.7-d half-life (*J*). Response rates to  $^{177}\text{Lu}$ -PSMA-617 (as measured by >50% decline in serum biomarker prostate-specific antigen) have varied from 30% to 70% across treatment studies and patient cohorts (2–7). With a tissue penetration range of less than 2 mm and the ensuing cross-fire effect,  $^{177}\text{Lu}$   $\beta$ -particles are best suited for treating lesions of a certain size (i.e., nonmicroscopic) (8–10). Although treatment with  $^{177}\text{Lu}$ -PSMA-617 is largely well tolerated, with a favorable dosimetry profile (11–13), in the setting of diffuse bone marrow infiltration, treatment with  $\beta$ -emitters may be limited by hematologic toxicity due to the irradiation of the surrounding healthy bone marrow tissues (10).  $^{225}\text{Ac}$ , an  $\alpha$ -emitter with a 9.9-d half-life, has emerged as an alternative isotope with favorable therapeutic decay properties.  $\alpha$ -particles are of interest in radionuclide therapy because of higher energy deposition over a much shorter tissue penetration range, causing more dense ionizations and localized dose profiles than for  $\beta$ -particles (14–16). The higher energy of  $^{225}\text{Ac}$   $\alpha$ -particles over a shorter tissue range (<0.1 mm) leads to a linear energy transfer on the order of 100 keV/ $\mu\text{m}$  (9,17–19). Decay schemes for  $^{177}\text{Lu}$  and  $^{225}\text{Ac}$  are shown in Figure 1.

Although fewer clinical studies have been conducted with  $^{225}\text{Ac}$ -PSMA-617, studies so far have reported biochemical response rates (>50% decline in prostate-specific antigen) ranging from 25% to over 90%, though patient cohorts, prior treatments, and treatment settings have varied widely (20–23). Additionally,  $\alpha$ -particle therapy may be favored in the treatment of microscopic metastatic disease and bone marrow infiltration because of the shorter range of

Received Jan. 13, 2023; revision accepted Jun. 17, 2023.

For correspondence or reprints, contact Magnus Dahlbom (mdahlbom@mednet.ucla.edu).

Guest editor: David Mankoff, University of Pennsylvania

Published online Oct. 5, 2023.

Immediate Open Access: Creative Commons Attribution 4.0 International License (CC BY) allows users to share and adapt with attribution, excluding materials credited to previous publications. License: <https://creativecommons.org/licenses/by/4.0/>. Details: <http://jnm.snmjournals.org/site/misc/permission.xhtml>.

COPYRIGHT © 2023 by the Society of Nuclear Medicine and Molecular Imaging.

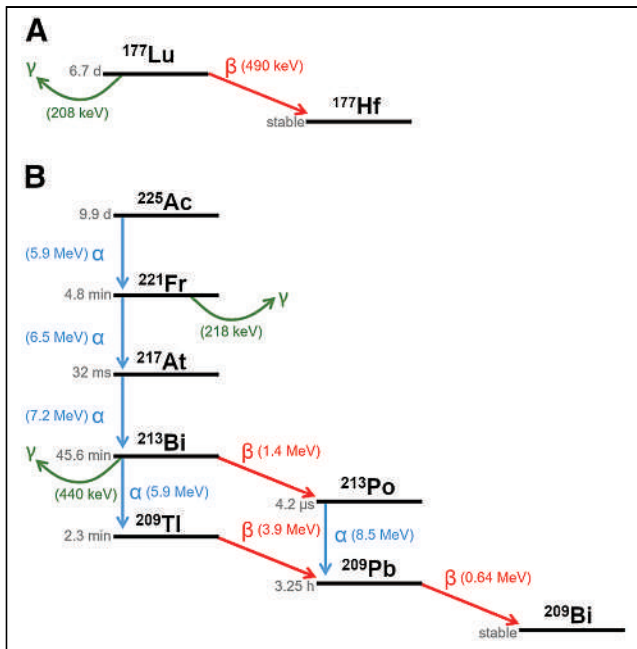


**FIGURE 1.** (A)  $^{177}\text{Lu}$  decay scheme. (B)  $^{225}\text{Ac}$  decay scheme.

$\alpha$ -radiation (24–27). However, the same radiobiologic features that make  $^{225}\text{Ac}$  attractive against tumors also present a tradeoff at the expense of higher-grade toxicities (22). The most significant adverse effect of  $\alpha$ -particle PSMA-targeted radionuclide therapy with small molecules (i.e., PSMA-617, PSMA-I&T) is xerostomia, making the salivary glands a key dose-limiting organ (28). Although the accumulation of PSMA ligands in the salivary glands is still not well understood, it is believed to be the result of both nonspecific (non-PSMA-related) and specific (PSMA-related) uptake mechanisms of PSMA ligands (29–31). Although xerostomia from  $^{177}\text{Lu}$  therapy is often temporary and reversible, with  $^{225}\text{Ac}$  there is a greater incidence of xerostomia, which can significantly diminish patient quality of life and lead to treatment discontinuation (22,32,33).

Overall, clinical experience using  $^{177}\text{Lu}$  or  $^{225}\text{Ac}$  has shown encouraging treatment responses; however, the responses have not been durable. Given that salivary gland toxicity limits the injected activity of  $^{225}\text{Ac}$ , simply using higher  $^{225}\text{Ac}$  treatment activities to increase tumor dose delivery is not an option. Dual-isotope combinations, or “tandem” approaches, may provide the benefits of both  $^{177}\text{Lu}$  and  $^{225}\text{Ac}$  to improve treatment tolerability while retaining high tumor dose delivery (10,34). Early clinical studies on both  $^{177}\text{Lu}$ -naïve patients and those who progressed after  $^{177}\text{Lu}$ -PSMA have shown that augmentation of  $^{177}\text{Lu}$ -PSMA therapy with a boost of  $^{225}\text{Ac}$  is an effective option with a more favorable side effects profile (35–37). No incidents of grade 3 or higher xerostomia were reported in these studies. A similar approach has been tested in peptide receptor radionuclide therapy against neuroendocrine tumors using tandem  $^{177}\text{Lu}/^{90}\text{Y}$ -DOTATATE, combining 2  $\beta$ -particle-emitting isotopes with different energies and tissue penetration ranges (38,39). In the preclinical setting, tandem  $^{177}\text{Lu}/^{90}\text{Y}$ -DOTATATE demonstrated an antitumor effect superior to that of either monotherapy alone (40). For PSMA-targeted therapies, clinical data are still limited by small patient cohort sizes, and to date, there have been no systematic preclinical investigations into the efficacy of dual-isotope combinations. In this work, we sought to directly compare  $\alpha$ - versus  $\beta$ -particle PSMA radionuclide therapy, as well as combinations of the two, in a

mouse model of prostate cancer. Our hypothesis was that the emitted particle pathlength can impact the radiation dose delivery, especially to microscopic disease. The objective was to compare the treatment efficacy of a scaled combination of  $^{225}\text{Ac}$  and  $^{177}\text{Lu}$  to single-isotope treatments, as measured by longitudinal tumor control and survival. First, we conducted an ex vivo  $\gamma$ -counting biodistribution and tumor dosimetry study to determine injected activities of  $^{177}\text{Lu}$  and  $^{225}\text{Ac}$  that yield comparable tumor doses. We then treated mice bearing disseminated prostate cancer lesions at 2 different stages of disease with  $^{177}\text{Lu}$ - and  $^{225}\text{Ac}$ -PSMA-617 as single agents, or in combination, to compare therapeutic efficacy and survival.

## MATERIALS AND METHODS

### Cell Culture and Animal Studies

In all studies, the human-derived, PSMA-expressing prostate cancer tumor cell line C4-2 was used (courtesy of Dr. George Thalmann, Inselspital Bern, Switzerland). Cells were maintained in RPMI 1640 medium supplemented with 10% fetal bovine serum (Omega Scientific) and grown at 37°C and 5%  $\text{CO}_2$ . Cells were monitored for *Mycoplasma* contamination using the Venor GeM *Mycoplasma* detection kit (Sigma Aldrich) and authenticated by short tandem repeat sequencing (Laragen). The parental cells were engineered to express firefly luciferase (C4-2-luc) to allow luciferase-mediated bioluminescence imaging to monitor tumor burden, as previously described (41).

All animal studies were approved by the UCLA Animal Research Committee (approval 2005-090). The mice were housed under pathogen-free conditions with food and water ad libitum and a 12 h–12 h light–dark cycle. Veterinary staff and investigators observed the mice daily to ensure animal welfare.

### Radiochemistry

PSMA-617 precursor was obtained from ABX Advanced Biochemical Compounds.  $^{177}\text{Lu}$  was obtained from Spectron MRC, and  $^{225}\text{Ac}$  was supplied by the U.S. Department of Energy’s Isotope Program within the Office of Science. Radiolabeling was performed as previously described with molar activities of 84  $\text{GBq}/\mu\text{mol}$  and 130  $\text{MBq}/\mu\text{mol}$  for  $^{177}\text{Lu}$ - and  $^{225}\text{Ac}$ -PSMA-617, respectively (41,42).

### Biodistribution and Tumor Dosimetry of $^{177}\text{Lu}$ - and $^{225}\text{Ac}$ -PSMA-617

Immunodeficient, 6- to 8-wk-old NOD SCID  $\gamma$  (NSG; The Jackson Laboratory) male mice were inoculated subcutaneously with  $5 \times 10^6$  C4-2 cells in 100  $\mu\text{L}$  of Matrigel (Corning) into the shoulder region (50 mice). After 3 wk, when the tumors reached about 300  $\text{mm}^3$  in volume, the mice were treated with either 30 MBq of  $^{177}\text{Lu}$ -PSMA-617 (25 mice) or 40 kBq of  $^{225}\text{Ac}$ -PSMA-617 (25 mice). The treatment activities were based on efficacious and well-tolerated activities in previous studies (43). The mice were euthanized at 1, 4, 24, 48, and 168 h after treatment (5 mice per time point for each nuclide). At the time of euthanasia, tumors and organs (including kidneys, liver, submandibular salivary glands, and intestines) were collected for ex vivo  $\gamma$ -counting for activity quantification ( $^{177}\text{Lu}$  energy window, 189–231 keV;  $^{225}\text{Ac}$  energy window, 170–260 keV for  $^{221}\text{Fr}$  daughter detection; Cobra II Auto-Gamma; Packard Instrument Co.). Actinium samples were counted after 24 h when secular equilibrium was reached (44). The multiple  $t$  test method with Welch correction was used for biodistribution statistical comparisons (statistical significance set to  $\leq 0.05$ ).

We estimated tumor self-doses (ignoring cross-dose contributions from neighboring organs) by first curve-fitting and integrating the tumor time–activity curves (NUKFIT Software) (45). The total number of disintegrations was multiplied by dose constants to yield tumor doses for  $^{177}\text{Lu}$  and  $^{225}\text{Ac}$  ( $5.934 \times 10^{-1}$  and  $2.838 \times 10^{-3}$   $\text{Gy}\cdot\text{g}/[\mu\text{Ci}\cdot\text{h}]$ , respectively). Dose constants are derived from nuclear data for energy



released per disintegration of each radionuclide, ignoring contributions with a decay yield of less than 1% (1,46). In this case of self-dose calculation, it is assumed that all radiation has an absorption fraction of 1.0 and that all disintegrations measured in the tumor deposit all energy in the tumor. We could thereby estimate the injected activities of  $^{177}\text{Lu}$ - and  $^{225}\text{Ac}$ -PSMA-617 that yield approximately equal tumor doses for subsequent studies directly comparing single- versus dual-isotope approaches.

### Tandem $^{177}\text{Lu}/^{225}\text{Ac}$ Therapy

All subsequent therapy studies were investigated in a mouse model of advanced metastatic prostate cancer. NSG mice were inoculated with C4-2-luc cells in the left ventricle, leading to disseminated visceral and bone lesions, as previously described (80 mice) (41). The mice were treated at 2 different stages of disease—either 3 or 5 wk after inoculation with equivalent tumor dose-depositing activities of  $^{177}\text{Lu}$ - or  $^{225}\text{Ac}$ -PSMA-617 or in scaled combination. Three weeks after inoculation, the disseminated lesions are approximately 200  $\mu\text{m}$  in size, increasing to millimeter scale by 5 wk, as previously characterized (41). The treatment activities were determined by the tumor biodistribution and dose-finding study as previously described. The treatment groups were as follows: 35 MBq of  $^{177}\text{Lu}$ -PSMA-617, 40 kBq of  $^{225}\text{Ac}$ -PSMA-617, a mixture of 17 MBq of  $^{177}\text{Lu}$ -PSMA-617 plus 20 kBq of  $^{225}\text{Ac}$ -PSMA-617, or untreated (10 mice per group per treatment time, intravenous administration; the chosen activities are justified in the Results section). The tandem-isotope treatment regimen was designed to halve the respective doses of  $^{225}\text{Ac}$  and  $^{177}\text{Lu}$  in combination.

Disease burden was assessed by weekly luciferase-mediated bioluminescence imaging (IVIS Lumina III; Perkin Elmer), and the mice were followed for overall survival. The mice were euthanized when their overall condition showed signs of deteriorating health based on the body conditioning score (47). Therapeutic efficacy data regarding tumor burden, as measured by whole-body radiance over time (Living Image; Perkin Elmer), were analyzed with 1-way ANOVA with Bonferroni adjustment using GraphPad Prism 8. The log-rank (Mantel-Cox) test was used for survival analysis.

## RESULTS

### Biodistribution and Tumor Dosimetry of $^{177}\text{Lu}$ - and $^{225}\text{Ac}$ -PSMA-617

The ex vivo biodistribution of  $^{177}\text{Lu}$ - and  $^{225}\text{Ac}$ -PSMA-617 in subcutaneous tumors and organs is shown in Figure 2. Tabulated biodistribution values for tumors and organs are available in Supplemental Tables 1 and 2 (supplemental materials are available at <http://jnm.snmjournals.org>). Kidney uptake at 1 h after injection was significantly greater for  $^{225}\text{Ac}$  than for  $^{177}\text{Lu}$  ( $25.9\% \pm 3.5\%$  and  $13.3\% \pm 1.6\%$  injected activity/g,  $P < 0.0005$ ), but no statistical difference was observed at later time points. Both  $^{177}\text{Lu}$ - and  $^{225}\text{Ac}$ -PSMA-617 rapidly localized to the tumor, with similar uptake ( $14.4\% \pm 4.1\%$  and  $14.1\% \pm 4.9\%$  injected activity/g, respectively) at 4 h after intravenous injection (not statistically significant;  $P = 0.89$ ). Tumor uptake peaked at 4 h after

injection, and by 168 h (7 d), tumor uptake was significantly greater in  $^{225}\text{Ac}$ -treated tumors than in  $^{177}\text{Lu}$ -treated tumors ( $9.3\% \pm 1.3\%$  vs.  $6.3\% \pm 0.9\%$  injected activity/g,  $P < 0.004$ , 5 mice per radionuclide). Tumor time-activity uptake curves in percentage injected activity were used for curve-fitting in NUKFIT (Figs. 2B and 2D). NUKFIT software selected the best curve-fitting model in both cases to be in the following form:  $A_1e^{-\lambda_1 t} + A_2e^{-\lambda_2 t}$ , where  $\lambda_1$  and  $\lambda_2$  represent the fitted decay constants. The best-fit curve parameters are shown in Figure 2. The resultant cumulated activities were multiplied by the respective dose constants and normalized by injected activity and average tumor masses. The tumor-absorbed doses for  $^{177}\text{Lu}$ - and  $^{225}\text{Ac}$ -PSMA-617 in the subcutaneous C4-2 model were 0.00758 and 65.03 cGy/kBq, respectively, or roughly 850 times greater for  $^{225}\text{Ac}$  than for  $^{177}\text{Lu}$ . Therefore, from this study we decided to use 35 MBq of  $^{177}\text{Lu}$  and 40 kBq of  $^{225}\text{Ac}$  to yield similar absorbed tumor doses in the therapeutic efficacy studies. Previous work demonstrated that 40 kBq of  $^{225}\text{Ac}$ -PSMA-617 is well tolerated (43). For the tandem treatment arm, we chose to halve the activity of each isotope in combination (17 MBq of  $^{177}\text{Lu}$  + 20 kBq of  $^{225}\text{Ac}$ ) to test a more tolerable activity regimen.

### Tandem $^{177}\text{Lu}/^{225}\text{Ac}$ Therapy

Whole-body bioluminescence imaging radiance over time and mouse survival curves for treatment 3 wk after inoculation are shown in Figures 3 and 4, respectively. Notably, the disease burden of mice treated at this earlier stage of disease with  $^{177}\text{Lu}$ -PSMA-617 was not significantly different from that of untreated mice at any time point ( $P = 0.932$ ). However,  $^{225}\text{Ac}$ -PSMA-617

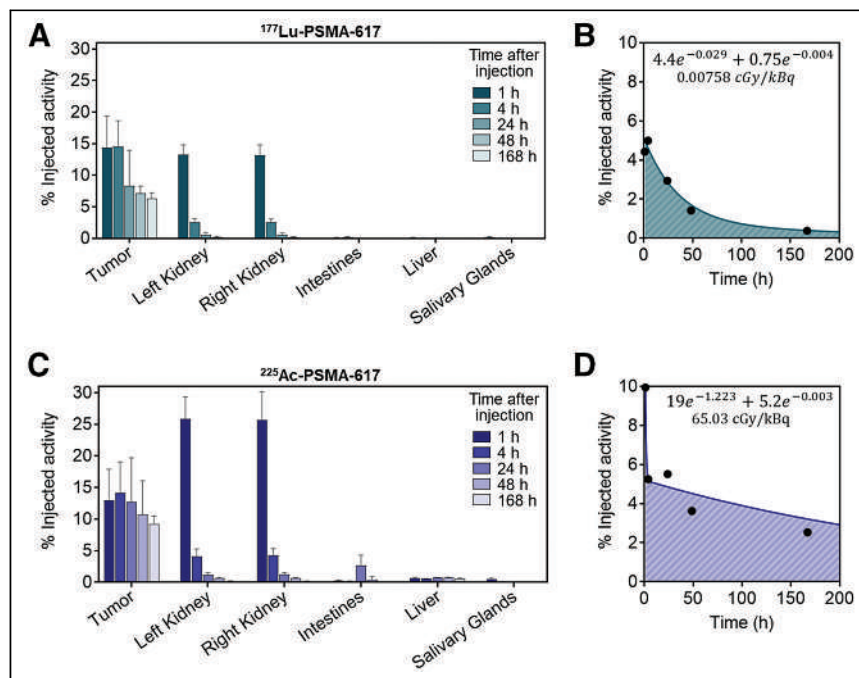


**FIGURE 2.** Ex vivo biodistribution and tumor time-activity curves for  $^{177}\text{Lu}$ - and  $^{225}\text{Ac}$ -PSMA-617. (A) Mean  $\pm$  SD percentage injected activity per gram of tissue for mice treated with 30 MBq of  $^{177}\text{Lu}$ -PSMA-617 (5 mice per time point). Tabulated values and additional organs are available in supplemental materials. (B) Mean percentage injected activity of  $^{177}\text{Lu}$ -PSMA-617 in tumors over time used for curve-fitting and dosimetry. Best-fit parameters are shown. (C) Mean  $\pm$  SD percentage injected activity per gram of tissue for mice treated with 40 kBq of  $^{225}\text{Ac}$ -PSMA-617 (5 mice per time point). Tabulated values and additional organs are available in supplemental materials. (D) Mean percentage injected activity of  $^{225}\text{Ac}$ -PSMA-617 in tumors over time used for curve-fitting and dosimetry. Best-fit parameters are shown.

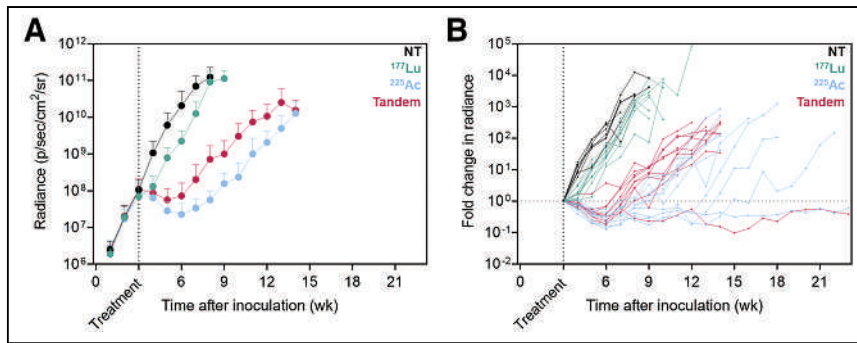


**FIGURE 3.** Therapeutic efficacy for mice treated 3 wk after inoculation with <sup>177</sup>Lu/<sup>225</sup>Ac-PSMA-617 or in tandem. (A) Mean  $\pm$  SD whole-body radiance over time (10 mice per group). Data are shown for time points with 5 or more remaining mice. (B) Individual mouse fold change in radiance over time relative to disease burden at time of treatment. NT = no treatment.

both as a single agent and in combination with <sup>177</sup>Lu-PSMA-617 was associated with significant tumor growth retardation ( $P = 0.009$  for tandem vs. <sup>177</sup>Lu;  $P = 0.0084$  for <sup>225</sup>Ac vs. <sup>177</sup>Lu;  $P > 0.999$  for tandem vs. <sup>225</sup>Ac measured 5 wk after treatment). If mice were left untreated, median survival was 8.3 wk. When mice were treated with 35 MBq of <sup>177</sup>Lu-PSMA-617, no significant survival benefit was observed (median survival, 9.4 wk;  $P = 0.337$ ). However, when treated with one of the <sup>225</sup>Ac regimens, the median survival increased to 14.1 wk for the tandem approach and 15.3 wk for <sup>225</sup>Ac-PSMA-617 alone ( $P < 0.0001$  for tandem vs. <sup>177</sup>Lu;  $P < 0.0001$  for <sup>225</sup>Ac vs. <sup>177</sup>Lu;  $P = 0.108$  for <sup>225</sup>Ac vs. tandem).

When mice were treated at a later time point of macroscopic disease (5 wk after inoculation), all treatment groups showed retarded tumor growth relative to untreated mice (Fig. 5). However, the greatest benefits were observed with <sup>225</sup>Ac-PSMA-617 monotherapy and tandem approaches ( $P < 0.0001$  for <sup>225</sup>Ac vs. <sup>177</sup>Lu;  $P < 0.0001$  for tandem vs. <sup>177</sup>Lu measured 5 wk after treatment). Median overall survival increased from 7.9 wk (untreated) to 10.3 wk for <sup>177</sup>Lu-PSMA-617, 13.2 wk for tandem therapy, and 14.6 wk for <sup>225</sup>Ac-PSMA-617 alone ( $P < 0.0001$  for NT vs. <sup>177</sup>Lu;  $P < 0.0001$  for

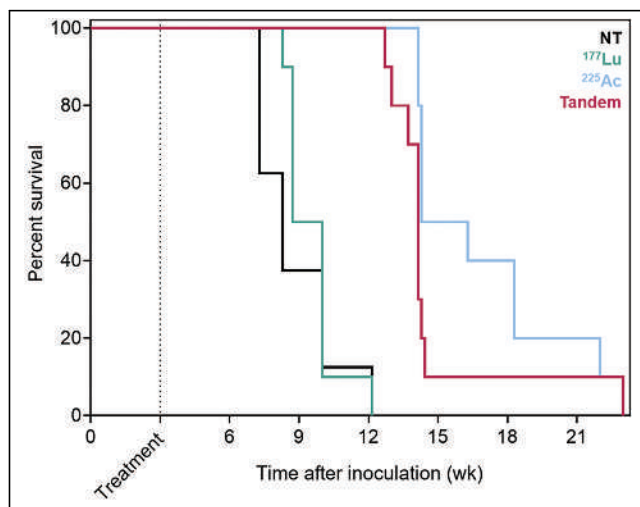


**FIGURE 4.** Survival curves for mice treated 3 wk after inoculation with <sup>177</sup>Lu/<sup>225</sup>Ac-PSMA-617 or in tandem. Median overall survival increased from 8.3 to 9.4 wk for <sup>177</sup>Lu-PSMA-617, 14.1 wk for tandem therapy, and 15.3 wk for <sup>225</sup>Ac-PSMA-617 alone ( $P = 0.337$  for NT vs. <sup>177</sup>Lu,  $P < 0.0001$  for tandem vs. <sup>177</sup>Lu;  $P < 0.0001$  for <sup>225</sup>Ac vs. <sup>177</sup>Lu;  $P = 0.108$  for <sup>225</sup>Ac vs. tandem). NT = no treatment.

tandem vs. <sup>177</sup>Lu;  $P < 0.0001$  for <sup>225</sup>Ac vs. <sup>177</sup>Lu) (Fig. 6). There were no significant differences in whole-body disease burden or survival benefit conferred between <sup>225</sup>Ac alone and halving the <sup>225</sup>Ac activity in tandem with <sup>177</sup>Lu ( $P = 0.171$  for <sup>225</sup>Ac vs. tandem survival and  $P > 0.999$  for <sup>225</sup>Ac vs. tandem whole-body radiance 5 wk after treatment).

## DISCUSSION

To our knowledge, this was the first study reporting on the efficacy of <sup>177</sup>Lu/<sup>225</sup>Ac-PSMA tandem-isotope combinations in a mouse model of prostate cancer. In this work, we sought to compare the treatment efficacy of the same tumor dose delivered by 3 different radiation mechanisms:  $\beta$ -particles (<sup>177</sup>Lu),  $\alpha$ -particles (<sup>225</sup>Ac), or both (<sup>177</sup>Lu + <sup>225</sup>Ac). To do so, we first determined comparable injected activities to yield comparable tumor doses by conducting a full ex vivo biodistribution study using both <sup>177</sup>Lu-PSMA-617 and <sup>225</sup>Ac-PSMA-617. It is important to note that the applied injected activities were chosen so as to expose the cancerous lesions to comparable absorbed radiation doses, without adjustment for the effectiveness of the type of radiation. Interestingly, there was no significant difference in peak tumor uptake of <sup>177</sup>Lu- or <sup>225</sup>Ac-PSMA-617 at 4 h after injection; however, increased tumor retention was observed at all subsequent time points for mice treated with <sup>225</sup>Ac-PSMA-617 compared with <sup>177</sup>Lu-PSMA-617. Although normal-organ biodistribution was not the primary objective of this report, all biodistribution data are available in the supplemental materials. In addition to the kidneys, liver, salivary glands, and intestines included in this report, uptake data for the following additional organs are available: blood, heart, lungs, spleen, stomach (with contents), prostate, testes, muscle, femur (with and without bone marrow), bone marrow, and brain.

In this work, we challenged a tandem-isotope approach against an advanced model of widespread disease to compare the dynamics of tumor control and overall survival. To more objectively compare the treatment arms against one another, we first determined injected activities for <sup>177</sup>Lu and <sup>225</sup>Ac that expose the tumors to similar absorbed doses in the subcutaneous C4-2 model. We then designed the tandem arm to be a combination of half of each respective single-agent activity. The tandem-isotope approach was tested with the intracardiac inoculation model of C4-2 cells, at 2 different stages of disease progression with different volumes of lesions. Although subcutaneous tumors allow for straightforward uptake quantification, and therefore interrogation into absorbed doses, they fail to recapitulate the metastatic state. Dosimetry was not feasible in the intracardiac inoculation model because the lesions are not easily isolated, especially in microscopic stages. Translating dosimetry findings from subcutaneous models is one approach toward standardizing the applied activity when the tumor burden is distributed throughout the mouse and direct dosimetry is not possible. Furthermore, we sought to investigate the performance of tandem therapy in a model that more faithfully represents the setting in which treatment with  $\alpha$ -particles (alone or in combination) would actually be clinically warranted.

The intracardiac inoculation model is an aggressive prostate cancer model in which mice, when left untreated, succumb to



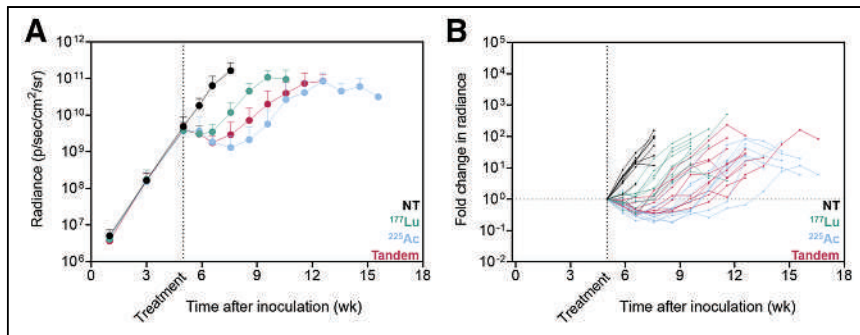


**FIGURE 5.** Therapeutic efficacy for mice treated 5 wk after inoculation with <sup>177</sup>Lu/<sup>225</sup>Ac-PSMA-617 or in tandem. (A) Mean ± SD whole-body radiance over time (10 mice per group). Data are shown for time points with 5 or more remaining mice. (B) Individual mouse fold change in radiance over time relative to disease burden at time of treatment. NT = no treatment.

extensive disseminated disease warranting euthanasia by 8 wk after inoculation (Figs. 4 and 6). This model has previously been shown to be sensitive to treatment with <sup>225</sup>Ac-PSMA-617 early in the disease, but this work is the first effort, to our knowledge, at challenging at a very advanced stage (5 wk after inoculation) (41). By treating at 2 different stages of disease, we can also seek to answer what size lesions most benefit from treatment with <sup>177</sup>Lu or tandem approaches. At the onset of the earlier treatment time investigated (3 wk after inoculation), the disseminated lesions are approximately 200 μm in size, increasing to millimeter scale by 5 wk, as previously characterized (41). When given at 3 wk, <sup>177</sup>Lu-PSMA-617 as a single agent did not significantly improve tumor control or survival relative to untreated mice (Fig. 4). However, when lesions were millimeters in size at the time of treatment, <sup>177</sup>Lu-PSMA-617 retarded tumor growth and the mice conferred a significant survival advantage. Failure of <sup>177</sup>Lu-PSMA-617 against micron-scale lesions in the earlier treatment setting can be explained by a mismatch between the target lesion size and the pathlength of the therapeutic radiation. With a mean tissue range of 600 μm (9), β-particles from <sup>177</sup>Lu travel a distance that

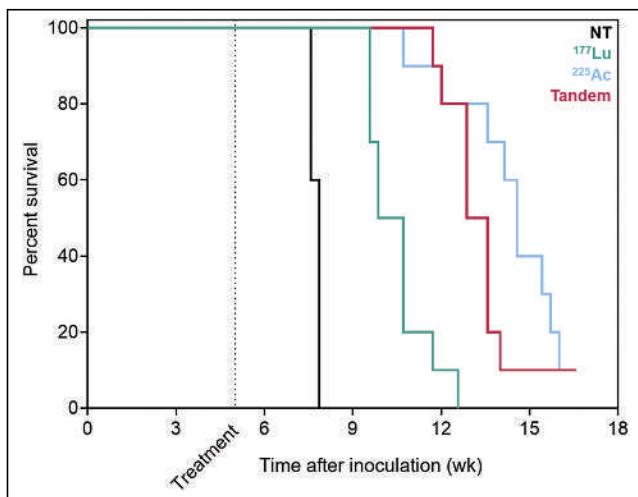


**FIGURE 6.** Survival curves for mice treated 5 wk after inoculation with <sup>177</sup>Lu/<sup>225</sup>Ac-PSMA-617 or in tandem. Median overall survival increased from 7.9 to 10.3 wk for <sup>177</sup>Lu-PSMA-617, 13.2 wk for tandem therapy, and 14.6 wk for <sup>225</sup>Ac-PSMA-617 alone ( $P < 0.0001$  for NT vs. <sup>177</sup>Lu,  $P < 0.0001$  for tandem vs. <sup>177</sup>Lu;  $P < 0.0001$  for <sup>225</sup>Ac vs. <sup>177</sup>Lu;  $P = 0.171$  for <sup>225</sup>Ac vs. tandem). NT = no treatment.

exceeds the lesion size at the time of early treatment (3 wk). This results in a loss of specificity to the targeted lesions and attenuates tumor response, as confirmed in this study.

Given the tissue range of less than 0.1 mm, α-particles from <sup>225</sup>Ac yield dense ionizing paths with little to no cross-fire effect. For treatment at both stages of disease, mice treated with <sup>225</sup>Ac-PSMA-617 as a single agent survived the longest and experienced the best tumor control (despite not reaching statistically significant differences at all time points). Even when challenged with lesions on the millimeter scale, the single agent <sup>225</sup>Ac-PSMA-617 outperformed <sup>177</sup>Lu-PSMA-617. Interestingly,

halving the <sup>225</sup>Ac activity in tandem with <sup>177</sup>Lu did not significantly increase the whole-body disease burden as measured 5 wk after treatment (Figs. 3A and 5A). In this model, the comparable tumor control and survival between the full <sup>225</sup>Ac dose and the tandem dose regimen suggest that a reduced administered activity of <sup>225</sup>Ac could be adequately compensated with <sup>177</sup>Lu without significantly sacrificing effectiveness. The superior therapeutic efficacy of <sup>225</sup>Ac in the microscopic setting studied in this work suggests a preference for α-emitters alone, or possibly in combination, for treatment of microscopic or minimal residual disease.

This work compares therapeutic isotopes using a fixed activity prescription for the tandem-isotope treatment arm. However, in the few published studies describing tandem treatment approaches of <sup>177</sup>Lu- and <sup>225</sup>Ac-PSMA-617 in the clinical setting, the applied injected activities have been heterogeneous. The mean reported activity of <sup>177</sup>Lu-PSMA-617 has ranged from 6 to 6.7 GBq, whereas the mean activity of <sup>225</sup>Ac-PSMA-617 has ranged from 2.7 to 4 MBq (35,37). Another study reported a median <sup>177</sup>Lu-PSMA-617 activity of 6.9 GBq (ranging from 5.0 to 11.6 GBq) and 5.3 MBq (ranging from 1.5 to 7.9 MBq) for <sup>225</sup>Ac-PSMA-617 (36). This wide range in applied activities precludes interpretation of a recommended activity scheme, and the heterogeneity underscores that, in practice, the treatment activities should reflect the individual patient condition. Additional studies are thereby needed to establish maximum tolerated doses in tandem-isotope schemes. One such prospective study examining the combination of <sup>177</sup>Lu-PSMA-I&T and <sup>223</sup>Ra (AlphaBet trial NCT05383079) is under way using a fixed 7.4 GBq of <sup>177</sup>Lu-PSMA administration followed by escalating activities of <sup>223</sup>Ra (48). Furthermore, prior treatments, including the cumulative injected activity of <sup>177</sup>Lu-PSMA-617 as a monotherapy if applicable, should also be considered in the activity prescription. Yet another factor to consider in the design of tandem-isotope treatments is the timing of the relative administrations. Although our preclinical work investigated the simultaneous administration of <sup>177</sup>Lu and <sup>225</sup>Ac, tandem treatment on consecutive days or in the first few days of each cycle also warrants investigation. Further work is required to understand the optimal conditions under which to prescribe tandem-isotope approaches, including how to adapt the treatment activities to reflect individual patient tumor burden, metastatic extent, and prior treatments.

One limitation of the mouse models used in these studies is the inability to recapitulate critical organ uptake as seen in patients (i.e., in the salivary glands and kidneys). In the subcutaneous tumor model, kidney uptake was higher with <sup>225</sup>Ac than with <sup>177</sup>Lu

at 1 h after injection; however, no significant difference was observed beyond the initial uptake phase. Clinically, kidney and salivary gland equivalent doses from  $^{177}\text{Lu}$ -PSMA-617 were reported in one study as 0.39 and 0.36–0.58 Sv/GBq, respectively (13). For  $^{225}\text{Ac}$ -PSMA-617, one dosimetry report calculated kidney and salivary gland doses to be 0.74 and 2.33 Sv/MBq, respectively (assuming a relative biologic effectiveness factor of 5 for  $^{225}\text{Ac}$ ) (49). However, our biodistribution study revealed no significant differences in submandibular gland uptake between  $^{177}\text{Lu}$ - and  $^{225}\text{Ac}$ -treated mice, and peak uptake was less than 0.5% of injected activity at all measured time points (Fig. 2). Given this inherent limitation in the translatability of salivary gland toxicity, it was not within the scope of this study to assess the preclinical feasibility of tandem-isotope treatment to improve the toxicity profile.

## CONCLUSION

Treatment of a microscopic model of prostate cancer with 40 kBq of  $^{225}\text{Ac}$ -PSMA-617 or 20 kBq of  $^{225}\text{Ac}$  in tandem with 17 MBq of  $^{177}\text{Lu}$  resulted in significantly decreased tumor growth compared with  $^{177}\text{Lu}$ , which was ineffective as a single agent against microscopic lesions, likely because of a mismatch of particle pathlength and lesion size. Mice treated later (when lesions were millimeter scale in size) experienced significant tumor growth retardation and survival benefit in both monotherapy and tandem regimes of  $^{177}\text{Lu}$ - and  $^{225}\text{Ac}$ -PSMA therapy. However, the greatest benefits were observed with  $^{225}\text{Ac}$ -PSMA-617 as a single agent and in tandem approaches. Further work is needed to identify the disease patterns and settings that most benefit from treatment with  $\beta$ -particles,  $\alpha$ -particles, or both.

## DISCLOSURE

Katharina Lueckerath reports paid consulting activities for Sofie Biosciences/iTheranostics and funding from AMGEN outside the submitted work. Jeremie Calais reports prior consulting activities for Advanced Accelerator Applications, Blue Earth Diagnostics, Curium Pharma, GE Healthcare, EXINI, IBA RadioPharma, Janssen Pharmaceuticals, Lantheus, POINT Biopharma, Progenics, Radiomedix, and Telix Pharmaceuticals. No other potential conflict of interest relevant to this article was reported.

## KEY POINTS

**QUESTION:** Does dual-isotope tandem  $^{177}\text{Lu}/^{225}\text{Ac}$ -PSMA radionuclide therapy improve treatment outcomes in a mouse model of disseminated prostate cancer?

**PERTINENT FINDINGS:** We determined equivalent tumor dose-depositing injected activities of  $^{177}\text{Lu}$ - and  $^{225}\text{Ac}$ -PSMA-617 and tested treatment as single agents versus in combination against different-sized lesions.  $^{225}\text{Ac}$  alone, and in tandem with  $^{177}\text{Lu}$ , was superior to  $^{177}\text{Lu}$  as a single agent against microscopic lesions. No significant difference was observed between the tandem and  $^{225}\text{Ac}$  treatment arms.

**IMPLICATIONS FOR PATIENT CARE:** This work provides efficacy data for  $^{177}\text{Lu}$ - and  $^{225}\text{Ac}$ -PSMA-617 as single agents and in combination against lesions of micron to millimeter scale. These data can be used as a basis for further investigations into the disease conditions best suited for treatment with  $\beta$ -particles,  $\alpha$ -particles, or both.

## REFERENCES

- Wong FC. MIRD: radionuclide data and decay schemes. *J Nucl Med.* 2009;50:2091.
- Awang ZH, Essler M, Ahmadzadehfar H. Radioligand therapy of metastatic castration-resistant prostate cancer: current approaches. *Radiat Oncol.* 2018;13:98.
- Rahbar K, Bode A, Weckesser M, et al. Radioligand therapy with  $^{177}\text{Lu}$ -PSMA-617 as a novel therapeutic option in patients with metastatic castration resistant prostate cancer. *Clin Nucl Med.* 2016;41:522–528.
- Kratochwil C, Giesel FL, Stefanova M, et al. PSMA-targeted radionuclide therapy of metastatic castration-resistant prostate cancer with  $^{177}\text{Lu}$ -labeled PSMA-617. *J Nucl Med.* 2016;57:1170–1176.
- Rahbar K, Ahmadzadehfar H, Kratochwil C, et al. German multicenter study investigating  $^{177}\text{Lu}$ -PSMA-617 radioligand therapy in advanced prostate cancer patients. *J Nucl Med.* 2017;58:85–90.
- Ahmadzadehfar H, Eppard E, Kürpig S, et al. Therapeutic response and side effects of repeated radioligand therapy with  $^{177}\text{Lu}$ -PSMA-DKFZ-617 of castrate-resistant metastatic prostate cancer. *Oncotarget.* 2016;7:12477–12488.
- Hofman MS, Violet J, Hicks RJ, et al. [ $^{177}\text{Lu}$ ]-PSMA-617 radionuclide treatment in patients with metastatic castration-resistant prostate cancer (LuPSMA trial): a single-centre, single-arm, phase 2 study. *Lancet Oncol.* 2018;19:825–833.
- Emmett L, Willowson K, Violet J, Shin J, Blanksby A, Lee J. Lutetium  $^{177}\text{Lu}$  PSMA radionuclide therapy for men with prostate cancer: a review of the current literature and discussion of practical aspects of therapy. *J Med Radiat Sci.* 2017;64:52–60.
- Sgouros G, Bodei L, McDevitt MR, Nedrow JR. Radiopharmaceutical therapy in cancer: clinical advances and challenges. *Nat Rev Drug Discov.* 2020;19:589–608.
- Haberkmorn U, Giesel F, Morgenstern A, Kratochwil C. The future of radioligand therapy:  $\alpha$ ,  $\beta$ , or both? *J Nucl Med.* 2017;58:1017–1018.
- Delker A, Fendler WP, Kratochwil C, et al. Dosimetry for  $^{177}\text{Lu}$ -DKFZ-PSMA-617: a new radiopharmaceutical for the treatment of metastatic prostate cancer. *Eur J Nucl Med Mol Imaging.* 2016;43:42–51.
- Kabasakal L, AbuQbeith M, Aygün A, et al. Pre-therapeutic dosimetry of normal organs and tissues of  $^{177}\text{Lu}$ -PSMA-617 prostate-specific membrane antigen (PSMA) inhibitor in patients with castration-resistant prostate cancer. *Eur J Nucl Med Mol Imaging.* 2015;42:1976–1983.
- Violet J, Jackson P, Ferdinandus J, et al. Dosimetry of  $^{177}\text{Lu}$ -PSMA-617 in metastatic castration-resistant prostate cancer: correlations between pretherapeutic imaging and whole-body tumor dosimetry with treatment outcomes. *J Nucl Med.* 2019;60:517–523.
- Sgouros G, Roeske JC, McDevitt MR, et al. MIRD pamphlet no. 22 (abridged): radiobiology and dosimetry of alpha-particle emitters for targeted radionuclide therapy. *J Nucl Med.* 2010;51:311–328.
- Mulford DA, Scheinberg DA, Jurcic JG. The promise of targeted  $\alpha$ -particle therapy. *J Nucl Med.* 2005;46(suppl 1):199S–204S.
- Birindelli G, Drobnjakovic M, Morath V, et al. In silico study on radiobiological efficacy of Ac-225 and Lu-177 for PSMA-guided radiotherapy. *Annu Int Conf IEEE Eng Med Biol Soc.* 2021;2021:4497–4500.
- Miederer M, Scheinberg DA, McDevitt MR. Realizing the potential of the actinium-225 radionuclide generator in targeted alpha particle therapy applications. *Adv Drug Deliv Rev.* 2008;60:1371–1382.
- Scheinberg DA, McDevitt MR. Actinium-225 in targeted alpha-particle therapeutic applications. *Curr Radiopharm.* 2011;4:306–320.
- McDevitt MR, Scheinberg DA. Ac-225 and her daughters: the many faces of Shiva. *Cell Death Differ.* 2002;9:593–594.
- Sathekge M, Bruchertseifer F, Knoesen O, et al.  $^{225}\text{Ac}$ -PSMA-617 in chemotherapy-naive patients with advanced prostate cancer: a pilot study. *Eur J Nucl Med Mol Imaging.* 2019;46:129–138.
- Yadav MP, Ballal S, Sahoo RK, Tripathi M, Seth A, Bal C. Efficacy and safety of  $^{225}\text{Ac}$ -PSMA-617 targeted alpha therapy in metastatic castration-resistant prostate cancer patients. *Theranostics.* 2020;10:9364–9377.
- Kratochwil C, Bruchertseifer F, Rathke H, et al. Targeted alpha-therapy of metastatic castration-resistant prostate cancer with  $^{225}\text{Ac}$ -PSMA-617: swimmer-plot analysis suggests efficacy regarding duration of tumor control. *J Nucl Med.* 2018;59:795–802.
- Kratochwil C, Bruchertseifer F, Giesel FL, et al.  $^{225}\text{Ac}$ -PSMA-617 for PSMA-targeted alpha-radiation therapy of metastatic castration-resistant prostate cancer. *J Nucl Med.* 2016;57:1941–1944.
- Kojima S, Cuttler JM, Shimura N, Koga H, Murata A, Kawashima A. Present and future prospects of radiation therapy using  $\alpha$ -emitting nuclides. *Dose Response.* 2018;16:1559325817747387.
- Morgenstern A, Apostolidis C, Kratochwil C, Sathekge M, Krolicki L, Bruchertseifer F. An overview of targeted alpha therapy with  $^{225}\text{Ac}$  actinium and  $^{213}\text{Bi}$  bismuth. *Curr Radiopharm.* 2018;11:200–208.

26. Chakravarty R, Siamof CM, Dash A, Cai W. Targeted  $\alpha$ -therapy of prostate cancer using radiolabeled PSMA inhibitors: a game changer in nuclear medicine. *Am J Nucl Med Mol Imaging*. 2018;8:247–267.
27. van der Doelen MJ, Mehra N, van Oort IM, et al. Clinical outcomes and molecular profiling of advanced metastatic castration-resistant prostate cancer patients treated with  $^{225}\text{Ac}$ -PSMA-617 targeted alpha-radiation therapy. *Urol Oncol*. 2021;39:729.e7–729.e16.
28. Heynickx N, Herrmann K, Vermeulen K, Baatout S, Aerts A. The salivary glands as a dose limiting organ of PSMA-targeted radionuclide therapy: a review of the lessons learnt so far. *Nucl Med Biol*. 2021;98-99:30–39.
29. Rupp NJ, Umbricht CA, Pizzuto DA, et al. First clinicopathologic evidence of a non-PSMA-related uptake mechanism for  $^{68}\text{Ga}$ -PSMA-11 in salivary glands. *J Nucl Med*. 2019;60:1270–1276.
30. Tönnemann R, Meyer PT, Eder M, Baranski A-C. [ $^{177}\text{Lu}$ ]Lu-PSMA-617 salivary gland uptake characterized by quantitative in vitro autoradiography. *Pharmaceuticals (Basel)*. 2019;12:18.
31. Roy J, Warner BM, Basuli F, et al. Comparison of prostate-specific membrane antigen expression levels in human salivary glands to non-human primates and rodents. *Cancer Biother Radiopharm*. 2020;35:284–291.
32. Taieb D, Foletti JM, Bardies M, Rocchi P, Hicks RJ, Haberkorn U. PSMA-targeted radionuclide therapy and salivary gland toxicity: why does it matter? *J Nucl Med*. 2018;59:747–748.
33. Feurecker B, Tauber R, Knorr K, et al. Activity and adverse events of actinium-225-PSMA-617 in advanced metastatic castration-resistant prostate cancer after failure of lutetium-177-PSMA. *Eur Urol*. 2021;79:343–350.
34. Kratochwil C, Haberkorn U, Giesel FL.  $^{225}\text{Ac}$ -PSMA-617 for therapy of prostate cancer. *Semin Nucl Med*. 2020;50:133–140.
35. Rosar F, Krause J, Bartholomä M, et al. Efficacy and safety of [ $^{225}\text{Ac}$ ]Ac-PSMA-617 augmented [ $^{177}\text{Lu}$ ]Lu-PSMA-617 radioligand therapy in patients with highly advanced mCRPC with poor prognosis. *Pharmaceutics*. 2021;13:722.
36. Khreish F, Ebert N, Ries M, et al.  $^{225}\text{Ac}$ -PSMA-617/ $^{177}\text{Lu}$ -PSMA-617 tandem therapy of metastatic castration-resistant prostate cancer: pilot experience. *Eur J Nucl Med Mol Imaging*. 2020;47:721–728.
37. Rosar F, Hau F, Bartholomä M, et al. Molecular imaging and biochemical response assessment after a single cycle of [ $^{225}\text{Ac}$ ]Ac-PSMA-617/ $^{177}\text{Lu}$ ]Lu-PSMA-617 tandem therapy in mCRPC patients who have progressed on [ $^{177}\text{Lu}$ ]Lu-PSMA-617 monotherapy. *Theranostics*. 2021;11:4050–4060.
38. Zemczak A, Kołodziej M, Gut P, et al. Effect of peptide receptor radionuclide therapy (PRRT) with tandem isotopes - [ $^{90}\text{Y}$ ]Y/ $^{177}\text{Lu}$ ]Lu-DOTATATE in patients with disseminated neuroendocrine tumours depending on [ $^{18}\text{F}$ ]FDG PET/CT qualification in Polish multicentre experience - do we need [ $^{18}\text{F}$ ]FDG PET/CT for qualification in PRRT? *Endokrynol Pol*. 2020;71:240–248.
39. Kunikowska J, Zemczak A, Kołodziej M, et al. Tandem peptide receptor radionuclide therapy using  $^{90}\text{Y}$ / $^{177}\text{Lu}$ ]Lu-DOTATATE for neuroendocrine tumors efficacy and side-effects: Polish multicenter experience. *Eur J Nucl Med Mol Imaging*. 2020;47:922–933.
40. de Jong M, Breeman WA, Valkema R, Bernard BF, Krenning EP. Combination radionuclide therapy using  $^{177}\text{Lu}$ - and  $^{90}\text{Y}$ -labeled somatostatin analogs. *J Nucl Med*. 2005;46(suppl 1):13S–17S.
41. Stuparu AD, Meyer CAL, Evans-Axelsson SL, et al. Targeted alpha therapy in a systemic mouse model of prostate cancer: a feasibility study. *Theranostics*. 2020;10:2612–2620.
42. Fendler WP, Stuparu AD, Evans-Axelsson S, et al. Establishing  $^{177}\text{Lu}$ -PSMA-617 radioligand therapy in a syngeneic model of murine prostate cancer. *J Nucl Med*. 2017;58:1786–1792.
43. Stuparu AD, Capri JR, Meyer CAL, et al. Mechanisms of resistance to prostate-specific membrane antigen-targeted radioligand therapy in a mouse model of prostate cancer. *J Nucl Med*. 2021;62:989–995.
44. Kruijff RM, Raavé R, Kip A, et al. The in vivo fate of  $^{225}\text{Ac}$  daughter nuclides using polymersomes as a model carrier. *Sci Rep*. 2019;9:11671.
45. Kletting P, Schimmel S, Kestler HA, et al. Molecular radiotherapy: the NUKFIT software for calculating the time-integrated activity coefficient. *Med Phys*. 2013;40:102504.
46. Jiang Z, Revskaya E, Fisher DR, Dadachova E. In vivo evaluation of free and chelated accelerator-produced actinium-225: radiation dosimetry and toxicity results. *Curr Radiopharm*. 2018;11:215–222.
47. Ullman-Culleré MH, Foltz CJ. Body condition scoring: a rapid and accurate method for assessing health status in mice. *Lab Anim Sci*. 1999;49:319–323.
48. Combination of radium-223 and lutetium-177 PSMA-I&T in men with metastatic castration-resistant prostate cancer. ClinicalTrials.gov website. <https://ClinicalTrials.gov/show/NCT05383079>. Updated September 28, 2022. Accessed August 22, 2023.
49. Kratochwil C, Bruchertseifer F, Rathke H, et al. Targeted alpha-therapy of metastatic castration-resistant prostate cancer with  $^{225}\text{Ac}$ -PSMA-617: dosimetry estimate and empiric dose finding. *J Nucl Med*. 2017;58:1624–1631.

---

---

# Lesion Dosimetry for [<sup>177</sup>Lu]Lu-PSMA-617 Radiopharmaceutical Therapy Combined with Stereotactic Body Radiotherapy in Patients with Oligometastatic Castration-Sensitive Prostate Cancer

Milan Grkovski<sup>1</sup>, Joseph A. O'Donoghue<sup>1</sup>, Brandon S. Imber<sup>2</sup>, George Andl<sup>3</sup>, Cheng Tu<sup>3</sup>, Daniel Lafontaine<sup>1</sup>, Jazmin Schwartz<sup>1</sup>, Maria Thor<sup>1</sup>, Michael J. Zelefsky<sup>2</sup>, John L. Humm<sup>1</sup>, and Lisa Bodei<sup>4</sup>

<sup>1</sup>Department of Medical Physics, Memorial Sloan Kettering Cancer Center, New York, New York; <sup>2</sup>Department of Radiation Oncology, Memorial Sloan Kettering Cancer Center, New York, New York; <sup>3</sup>Varian Medical Systems Inc., Palo Alto, California; and

<sup>4</sup>Department of Radiology, Memorial Sloan Kettering Cancer Center, New York, New York

A single-institution prospective pilot clinical trial was performed to demonstrate the feasibility of combining [<sup>177</sup>Lu]Lu-PSMA-617 radiopharmaceutical therapy (RPT) with stereotactic body radiotherapy (SBRT) for the treatment of oligometastatic castration-sensitive prostate cancer. **Methods:** Six patients with 9 prostate-specific membrane antigen (PSMA)-positive oligometastases received 2 cycles of [<sup>177</sup>Lu]Lu-PSMA-617 RPT followed by SBRT. After the first intravenous infusion of [<sup>177</sup>Lu]Lu-PSMA-617 (7.46 ± 0.15 GBq), patients underwent SPECT/CT at 3.2 ± 0.5, 23.9 ± 0.4, and 87.4 ± 12.0 h. Voxel-based dosimetry was performed with calibration factors (11.7 counts per second/MBq) and recovery coefficients derived from in-house phantom experiments. Lesions were segmented on baseline PSMA PET/CT (50% SUV<sub>max</sub>). After a second cycle of [<sup>177</sup>Lu]Lu-PSMA-617 (44 ± 3 d; 7.50 ± 0.10 GBq) and an interim PSMA PET/CT scan, SBRT (27 Gy in 3 fractions) was delivered to all PSMA-avid oligometastatic sites, followed by post-PSMA PET/CT. RPT and SBRT voxelwise dose maps were scaled (α/β = 3 Gy; repair half-time, 1.5 h) to calculate the biologically effective dose (BED). **Results:** All patients completed the combination therapy without complications. No grade 3+ toxicities were noted. The median of the lesion SUV<sub>max</sub> as measured on PSMA PET was 16.8 (interquartile range [IQR], 11.6) (baseline), 6.2 (IQR, 2.7) (interim), and 2.9 (IQR, 1.4) (post). PET-derived lesion volumes were 0.4–1.7 cm<sup>3</sup>. The median lesion-absorbed dose (AD) from the first cycle of [<sup>177</sup>Lu]Lu-PSMA-617 RPT (AD<sub>RPT</sub>) was 27.7 Gy (range, 8.3–58.2 Gy; corresponding to 3.7 Gy/GBq, range, 1.1–7.7 Gy/GBq), whereas the median lesion AD from SBRT was 28.1 Gy (range, 26.7–28.8 Gy). Spearman rank correlation, ρ, was 0.90 between the baseline lesion PET SUV<sub>max</sub> and SPECT SUV<sub>max</sub> (P = 0.005), 0.74 (P = 0.046) between the baseline PET SUV<sub>max</sub> and the lesion AD<sub>RPT</sub>, and -0.81 (P = 0.022) between the lesion AD<sub>RPT</sub> and the percent change in PET SUV<sub>max</sub> (baseline to interim). The median for the lesion BED from RPT and SBRT was 159 Gy (range, 124–219 Gy). ρ between the BED from RPT and SBRT and the percent change in PET SUV<sub>max</sub> (baseline to post) was -0.88 (P = 0.007). Two cycles of [<sup>177</sup>Lu]Lu-PSMA-617 RPT contributed approximately 40% to the maximum BED from RPT and SBRT. **Conclusion:** Lesional dosimetry in patients with oligometastatic castration-sensitive prostate cancer undergoing [<sup>177</sup>Lu]Lu-PSMA-617 RPT followed by SBRT is feasible. Combined RPT and SBRT may provide an

efficient method to maximize the delivery of meaningful doses to oligometastatic disease while addressing potential microscopic disease reservoirs and limiting the dose exposure to normal tissues.

**Key Words:** prostate cancer; oligometastasis; [<sup>177</sup>Lu]Lu-PSMA-617; dosimetry; SBRT; biologically effective dose

**J Nucl Med 2023; 64:1779–1787**

DOI: 10.2967/jnumed.123.265763

---

**P**rostate cancer is the most common and the second most lethal cancer among men in the United States, with 288,300 estimated new diagnoses and 34,700 estimated deaths in 2023 (1). An oligometastatic clinical state has been proposed as an intermediate point between local and widespread disease (2). Patients with more limited metastatic burden might thus benefit from aggressive metastasis-selective therapy. In a recent pooled analysis of prospective randomized phase II trials in oligometastatic castration-sensitive prostate cancer (omCSPC), median progression-free survival was prolonged with metastasis-selective therapy compared with observation (3).

Stereotactic body radiotherapy (SBRT) is an effective way of delivering high radiation doses for patients with oligometastases. It has been widely adopted (4) as a generally well-tolerated treatment strategy with high local control rates (5). Distant metastasis-free survival rates are, however, modest (6), as patients often develop metastatic cancer outside of the treated area (7). Targeted radiopharmaceutical therapy (RPT) with [<sup>177</sup>Lu]Lu-PSMA-617 (Pluvicto; Novartis AG) is an efficacious systemic treatment, delivering cytotoxic β-radiation to cells expressing prostate-specific membrane antigen (PSMA) without causing excessive normal-tissue toxicity (8–10). Outcomes for omCSPC may be improved by combining SBRT for focal therapy of bulk tumors with [<sup>177</sup>Lu]Lu-PSMA-617 RPT to address microscopic disease reservoirs (11). Because of nonoverlapping toxicities, these treatment strategies allow escalation of the combined absorbed dose (AD) of radiation in the tumor and may act synergistically (12,13). Because both use ionizing radiation, a quantitative metric combining the radiation ADs from each treatment into a biologically effective dose (BED) can be calculated, which in turn can be used in models to predict the response and toxicity (14,15). Combination therapies with radiopharmaceuticals are becoming a new

---

Received Mar. 21, 2023; revision accepted Jul. 11, 2023.

For correspondence or reprints, contact Milan Grkovski (grkovskm@mskcc.org) or Lisa Bodei (bodeil@mskcc.org).

Published online Aug. 31, 2023.

COPYRIGHT © 2023 by the Society of Nuclear Medicine and Molecular Imaging.

paradigm (11), with 2 currently ongoing clinical studies using external-beam radiotherapy (EBRT) and [<sup>177</sup>Lu]Lu-PSMA-617: PROQUIRE-1 phase I trial (16) and LUNAR phase II trial (17). The present study was performed to evaluate the feasibility of performing composite lesional dosimetry in PSMA-avid omCSPEC patients undergoing theranostic [<sup>177</sup>Lu]Lu-PSMA-617 RPT followed by SBRT.

## MATERIALS AND METHODS

### Patient Selection

The pilot clinical trial was approved by Memorial Sloan Kettering Cancer Center's Institutional Review Board (protocol 21-158; NCT05079698), and all patients gave written informed consent regarding the examination and use of anonymous data for research and publication purposes. Inclusion and exclusion criteria are available in the supplemental materials (available at <http://jnm.snmjournals.org>). Briefly, patients with a biopsy-confirmed adenocarcinoma of the prostate, a prostate-specific antigen (PSA) level between 0.5 and 50 ng/mL, and a primary tumor previously (>2 y) treated with surgery or definitive radiation were considered. The oligometastatic patient population was defined as oligorecurrence after definite prostate-directed therapy with 1–3 discrete sites of gross metastatic disease.

### PSMA PET/CT Imaging

PSMA PET/CT was used to identify patients, gauge response, and track efficacy (18–20). PSMA PET/CT scans were performed at baseline, after [<sup>177</sup>Lu]Lu-PSMA-617 RPT (interim), and after SBRT (post). Patients were injected with 208 ± 38 MBq (range, 167–266 MBq) of <sup>68</sup>Ga-PSMA-11 or 332 ± 34 MBq (range, 266–366 MBq) of <sup>18</sup>F-DCFPyL and imaged 71 ± 9 min after administration (range, 60–95 min). Whole-body (vertex of skull to proximal thigh) images were acquired on a GE Healthcare Discovery 710 PET/CT scanner. <sup>18</sup>F-DCFPyL was previously reported to result in an approximately 18% higher lesion SUV<sub>max</sub> (21); however, in that study, <sup>18</sup>F-DCFPyL PET images were acquired 2 h after injection versus 1 h after injection for <sup>68</sup>Ga-PSMA-11 PET. A separate study indicated that the <sup>18</sup>F-DCFPyL lesion SUV<sub>max</sub> increased by approximately 19% between 1 and 2 h (22). The CT images were acquired at 120 kVp, 56 mAs, and a 3.75-mm slice thickness. All PET emission data were corrected for attenuation, scatter, and random events and iteratively reconstructed into a 128 × 128 × 47 matrix (voxel dimensions, 5.47 × 5.47 × 3.27 mm) using an ordered-subset expectation maximization algorithm (2 iterations, 16 subsets) incorporating time-of-flight and point-spread-function modeling. A gaussian postprocessing filter of 6.4 mm in full width at half maximum was applied. All screening and posttreatment PSMA scans were reviewed by an experienced nuclear medicine physician, and lesions were scored using the structured PSMA reporting and data system, version 1.99, radiographic criteria (23). Treatable oligometastases were lesions scored as either 4 or 5 on this system.

### [<sup>177</sup>Lu]Lu-PSMA-617 SPECT/CT Imaging

After the first intravenous infusion of [<sup>177</sup>Lu]Lu-PSMA-617 (7.46 ± 0.15 GBq), patients were serially imaged on a Symbia Intevo Bold (Siemens Healthineers AG) γ-camera equipped with a medium-energy collimator and 9.5-mm-thick crystals. Imaging consisted of a whole-body planar scintigraphy (anterior and posterior; scan speed, 10 cm/min) followed by a single-field-of-view SPECT/CT scan. SPECT/CT start times were 3.2 ± 0.5, 23.9 ± 0.4, and 87.4 ± 12.0 h after infusion, with acquisition parameters as follows: 180° elliptic arc, step-and-shoot mode with 64 stops, 20 s/stop, 20% acquisition window at 208 keV with an adjacent 10% scatter windows, and a 128 × 128 × 79 matrix (4.8 × 4.8 × 4.8 mm voxels). SPECT image reconstruction was performed in HybridRecon version 3.0 (Hermes Medical Solutions) and incorporated motion, attenuation, resolution recovery, and

scatter corrections. An ordered-subset expectation maximization algorithm (48 iterations, 1 subset) without a postprocessing filter was used for image reconstruction (24,25). For SPECT quantification, a calibration factor (11.7 counts per minute/MBq) was derived from in-house experiments with a <sup>177</sup>Lu-filled American College of Radiology SPECT phantom without inserts. After the second [<sup>177</sup>Lu]Lu-PSMA-617 administration (7.50 ± 0.10 GBq; 44 ± 3 d after the beginning of cycle 1), whole-body planar scintigraphy (with same acquisition parameters as used during the first cycle) was performed on the day of injection only, with no SPECT imaging.

### SBRT

Patients underwent SBRT on a Varian TrueBeam linear accelerator to all PSMA-avid oligometastatic sites (prescription of 27 Gy in 3 fractions; institutional standard for extracranial lesions) at 5 ± 1 wk after the second [<sup>177</sup>Lu]Lu-PSMA-617 cycle and after simulation and radiation planning (Eclipse version 16; Varian Medical Systems Inc.) according to Memorial Sloan Kettering Cancer Center's Department of Radiation Oncology guidelines. Before the treatment, patients were immobilized in a reproducible position in a custom mold. A CT scan was acquired in the treatment-planning position (120 kVp, 56 mAs, and 3-mm slice thickness) on a Philips Big Bore CT simulator. The dose was prescribed to the 100% isodose line, which completely encompassed the planning tumor volume. SBRT was delivered with 6× flattening filter-free photon beam profiles. Hot spots were limited to less than 110% of the prescription dose. Normal tissues and lesions were contoured on the treatment-planning CT to determine dose–volume histograms. The Digital Imaging and Communications in Medicine dose, plans, structures, and CT data were subsequently imported from Eclipse version 16.

### Dosimetry

Voxel-based dosimetry was performed in Velocity version 4.2 Development Build (Varian Medical Systems Inc.). Lesions were segmented on the coregistered PSMA PET/CT (50% SUV<sub>max</sub> threshold) and subsequently copied to the [<sup>177</sup>Lu]Lu-PSMA-617 SPECT/CT. AD calculations were based on the time–activity data derived from each patient's set of 3 SPECT/CT images. Application of partial-volume correction was based on recovery coefficients (RCs) derived from in-house phantom experiments with a standard National Electrical Manufacturers Association Image Quality phantom with 6 spheric inserts (diameter, 10–37 mm). The phantom was imaged and analyzed using acquisition settings and reconstruction parameters identical to those used for the clinical protocol. Volumes of interest (VOIs) were drawn on the CT image and subsequently copied to the SPECT image. The fit to our RC versus sphere diameter data was

$$\text{SPECT RC} = 0.96 - 0.831 / \left( 1 + \left( s_d / 20.93 \right)^{4.05} \right), \quad \text{Eq. 1}$$

where  $s_d$  is the sphere diameter in millimeters. Comparison with RC obtained by other groups is presented in Supplemental Figure 1 (26,27). Voxel-based dosimetry was performed with the ACUROS Molecular Radiotherapy algorithm within Velocity, which uses a voxel-based fitting method that estimates a fitting function (sum of exponentials) for each voxel by automatically selecting the most appropriate model among a predetermined set via Akaike information criterion (28).

As a cross-check, the area-under-the-curve (MBq·h/mL) and time-integrated activity coefficients for lesions were also calculated according to the scheme defined by the committee on MIRD (29). Cumulated activity within the lesion VOI was determined by a trapezoid method between the end of the infusion and the third SPECT scan and a mono-exponential model without residual activity thereafter. Lesion ADs were subsequently calculated using the sphere model in OLINDA/EXM version 1.1 (Hermes Medical Solutions). A third method using multiple

concentric oversized VOIs to determine the activity of a source was also investigated (10,30). Unlike the first 2 approaches, the latter method does not require the use of RC.

BED scaling of both RPT and SBRT dose maps was performed in Velocity. BED is defined as

$$\text{BED} = D \cdot \text{RE}, \quad \text{Eq. 2}$$

where  $D$  is the total dose and RE is the relative effectiveness. For treatments with fractionated doses (i.e., SBRT),  $D$  and RE are calculated as

$$D = n \cdot d, \quad \text{Eq. 3}$$

$$\text{RE} = \left(1 + \frac{d}{\alpha/\beta}\right), \quad \text{Eq. 4}$$

where  $n$  and  $d$  are the number of fractions (3) and fraction size (9 Gy), respectively. The  $\alpha/\beta$  ratio was set to 3 Gy. For treatments with an exponentially decaying source integrated to infinity (i.e., [<sup>177</sup>Lu]Lu-PSMA-617 RPT) and a monoexponential dose-rate function, RE is defined as (14)

$$\text{RE} = 1 + \frac{R_0}{\mu + \lambda} \left(\frac{\beta}{\alpha}\right), \quad \text{Eq. 5}$$

$$R_0 = \lambda \cdot D, \quad \text{Eq. 6}$$

where  $R_0$  is the initial dose rate (Gy/h),  $\lambda$  is the effective decay rate, and  $\mu$  is the repair rate (set to  $0.462 \text{ h}^{-1}$ , corresponding to a commonly used repair half-time of 1.5 h). In this special case,  $\lambda/(\mu + \lambda)$  is the Lea-Catcheside time factor. BED-scaled dose maps were subsequently aligned (deformable multipass coregistration) and summed into a single resampled dose volume, from which dose-volume histograms were extracted. Note that the equieffective dose, EQD<sub>2 $\alpha/\beta$</sub>  (Gy), where 2 refers to 2-Gy daily fractions, can be calculated as

$$\text{EQD2} = D \left[ \frac{d + \alpha/\beta}{2 + \alpha/\beta} \right]. \quad \text{Eq. 7}$$

For an  $\alpha/\beta$  ratio of 3, an EQD<sub>2 $\alpha/\beta$</sub>  of 3 is equal to  $0.6 \times \text{BED}$  (BED is mathematically the same as a dose delivered in infinitely small 0-Gy fractions).

### Statistical Analysis

The Spearman rank-order correlation coefficient,  $\rho$ , was calculated to evaluate the strength of association between various investigated metrics. Metrics between different time points (baseline, post-RPT, post-SBRT) were compared with the Wilcoxon signed-rank test (2-tailed). Interquartile range (IQR) was used as a measure of statistical dispersion. A  $P$  value of less than 0.05 indicated statistical significance. The statistical analysis was performed in MATLAB R2020b (MathWorks Inc.) with Statistics and Machine Learning Toolbox version 12.0.

### RESULTS

Six patients (median age, 74 y; range, 51–78 y) with PSMA-positive metachronous oligometastases were included in the analysis (Table 1). The first cycle of [<sup>177</sup>Lu]Lu-PSMA-617 RPT was administered between December 2021 and September 2022. The time after the initial definite prostate-directed therapy was 7 y (range, 4–24 y). Baseline PSA levels were 2.0 ng/mL (IQR, 1.2 ng/mL). All patients underwent hematologic safety and adverse event monitoring for at least 4 wk after both cycles of [<sup>177</sup>Lu]Lu-PSMA-617 RPT. Two patients experienced grade 2 toxicities after the combined treatment: transient anemia and hyperbilirubinemia (the latter is probably unrelated; no patients had liver metastases). No grade 3+ toxicities were

noted. Nine PSMA-positive lesions were identified by the nuclear medicine physician. Lesion volume as measured on baseline PSMA PET/CT was  $0.8 \text{ cm}^3$  (range, 0.4–1.7  $\text{cm}^3$ ), resulting in a median SPECT RC of 0.20 (IQR, 0.01; range, 0.16–0.30). Median of the lesion SUV<sub>max</sub> as measured on PSMA PET was 16.8 (IQR, 11.6), 6.2 (IQR, 2.7), and 2.9 (IQR, 1.4) at baseline, interim (i.e., after completion of [<sup>177</sup>Lu]Lu-PSMA-617 RPT but before SBRT), and post (i.e., after completion of SBRT), respectively. Percentage change (% $\Delta$ ) in SUV<sub>max</sub> between baseline and interim PSMA PET (calculated as  $100\% \times (\text{interim SUV}_{\text{max}} - \text{baseline SUV}_{\text{max}}) / \text{baseline SUV}_{\text{max}}$ , that is, % $\Delta_1$ ) was  $-65\%$  (range,  $-82\%$  to  $44\%$ ;  $P < 0.05$ ). Corresponding % $\Delta$  between interim and post-PSMA PET (i.e., % $\Delta_2$ ) was  $-43\%$  (range,  $-74\%$  to  $31\%$ ; significance not reached), whereas % $\Delta$  between baseline and post-PSMA PET (i.e., % $\Delta_{\text{total}}$ ) was  $-74\%$  (range,  $-91\%$  to  $-30\%$ ;  $P < 0.05$ ). The % $\Delta_1$  in the PSMA PET-derived maximum tumor-to-liver ratio (calculated as lesion SUV<sub>max</sub>/liver SUV<sub>mean</sub>) was  $-59\%$  ( $P < 0.05$ ), whereas the corresponding % $\Delta_2$  and % $\Delta_{\text{total}}$  for the maximum tumor-to-liver ratios were  $-49\%$  and  $-77\%$ , respectively ( $P < 0.05$ ). The median % $\Delta$  in PSA between baseline and 3 mo after the combined therapy was  $-83\%$  (range,  $-97\%$  to  $58\%$ ; significance not reached because of paucity of data), closely resembling the relative decrease in PSMA SUV<sub>max</sub>.

Seven of 9 lesions remained PSMA-avid after [<sup>177</sup>Lu]Lu-PSMA-617 treatment, as assessed by a lesion uptake greater than the mean liver uptake on the interim PSMA PET/CT scan. Liver SUV and parotid SUV were not significantly different among the 3 PSMA PET scans (liver SUV = 5.4, 4.6, and 5.0, respectively; parotid SUV = 12.5, 12.4, and 10.5, respectively). Three of 9 lesions (33%; lesions 1, 2, and 4) were visible on the standard-of-care <sup>99m</sup>Tc-methylene diphosphonate planar bone scintigraphy (acquired 2.5–3 h after  $774 \pm 51 \text{ MBq}$  administration of <sup>99m</sup>Tc-methylene diphosphonate) at both baseline and post-SBRT imaging. The remaining lesions were lymph nodes ( $n = 5$ ) or visceral ( $n = 1$ ). No additional lesions were noted on the <sup>99m</sup>Tc-methylene diphosphonate scans that were not visualized by PSMA PET/CT.

In patient 1, the 2 lesions could not be visualized on the single-bed SPECT scan (380-cm axial field of view); therefore, dosimetric calculations were performed for only 1 ( $n = 8$  lesions in total). Median of the lesion SUV<sub>max</sub> as measured on [<sup>177</sup>Lu]Lu-PSMA-617 SPECT was 3.7 (IQR, 1.5), 9.4 (IQR, 7.2), and 7.3 (IQR, 4.5) on the first, second, and third SPECT, respectively. The highest lesion SUV<sub>max</sub> was reached on either the second or the third SPECT scan. The salivary glands were not within the SPECT field of view for 5 of 6 patients.

The summary of dosimetry results is presented in Table 2. The mean lesion AD from the first cycle of [<sup>177</sup>Lu]Lu-PSMA-617 RPT (AD<sub>RPT</sub>; calculated from voxels within the tumor volume as defined by the 50% threshold on PSMA PET) was 27.7 Gy (IQR, 17.5 Gy; range, 8.3–58.2 Gy), translating into 3.7 Gy/GBq (IQR, 2.4 Gy/GBq; range, 1.1–7.7 Gy/GBq). As  $\beta$  electrons emitted from <sup>177</sup>Lu have an approximate 0.6-mm range in soft tissue, most of the energy will be absorbed within 1  $\text{cm}^3$  lesions. The mean BED from RPT was 28.2 Gy (IQR, 18.5 Gy; range, 8.4–59.9 Gy; median RE from RPT, 1.02). The medians of the maximum AD<sub>RPT</sub> and maximum BED from RPT were 37.5 Gy (IQR, 24.2 Gy) and 38.5 Gy (IQR, 25.4 Gy), respectively.

The median AD<sub>RPT</sub> when recalculated using the MIRD formalism, and the sphere model in OLINDA was 32.7 Gy (IQR, 20.4 Gy; range, 7.7–70.5 Gy), translating into 4.3 Gy/GBq (IQR, 2.8 Gy/GBq; range, 1.0–9.6 Gy/GBq). The corresponding median



**TABLE 1**  
Summary of Patient Characteristics and Imaging Results

Patient	Age (y)	Gleason score	Stage	Location	PSMA PET											
					SUV <sub>max</sub> *					TLR <sub>max</sub> *					[ <sup>177</sup> Lu]Lu-PSMA-617	
					Baseline	Interim	Post	Baseline	Interim	Post	Baseline	Interim	Post	SUV <sub>max</sub>	TLR <sub>max</sub>	Lesion volume (cm <sup>3</sup> )
1 [1]	75	4 + 5	N1	Left transverse process of T7 vertebra	16.8	5.5	2.5	3.8	1.2	0.4	0.4	11.4	14.2	0.8	1.4	
1 [2]				Right femoral neck	27.2	9.6	2.5	6.2	2.0	0.4	NA	NA	NA	0.8	4.0	
2 [3]	78	3 + 4	cT2a	Right internal iliac node	12.1	6.2	4.1	2.2	1.9	1.0	0.7	8.4	7.8	0.7	0.6	
3 [4]	60	5 + 4	pT3bN1	Left transverse process of C6 vertebra	12.7	9.3	3.3	2.3	2.1	0.7	0.7	5.8	7.5	0.8	1.3	
4 [5]	72	4 + 3	pT3aN0	Lower retrocaval lymph node	23.7	4.2	2.4	3.2	0.8	0.4	0.4	11.7	10.5	0.4	1.7	
4 [6]				Right posterior common iliac lymph node	18.8	5.9	3.8	2.6	1.1	0.6	0.6	15.4	14.0	0.9	1.9	
4 [7]				Superior presacral lymph node	26.3	7.2	9.4	3.6	1.3	1.4	1.4	15.0	13.6	0.8	2.1	
5 [8]	77	4 + 3	pT4N0	Right posterior middle lobe periffissural nodule	2.7	1.9	1.9	0.7	0.5	0.4	0.4	3.3	2.2	1.7	2.4	
6 [9]	51	4 + 4	pT3aN0	Right obturator lymph node	5.7	8.2	3.4	0.8	1.4	0.7	0.7	3.3	2.7	0.8	15.0†	
Median	74 (14)				16.8 (11.6)	6.2 (2.7)	3.3 (1.3)	2.6 (1.4)	1.3 (0.8)	0.6 (0.3)	0.6 (0.3)	9.9 (7.3)	9.1 (7.4)	0.8 (0.0)	1.9 (1.0)	

\*Partial-volume correction not applied.  
 †Patient 6 had small pelvic lymph nodes that were in vicinity of PSMA-avid node. Clinical judgment was made to cover nonavid nearby nodes.  
 NA = not available; TLR<sub>max</sub> = maximum tumor-to-liver ratio; GTV = gross tumor volume.  
 Numbers in brackets are number of lesions; numbers in parentheses are IQR.

**TABLE 2**  
Summary of Dosimetry Results

Patient	Mean AD <sub>RPT</sub> (Gy/GBq)*	Mean AD delivered by SBRT (Gy) <sup>†</sup>	Mean total from RPT (Gy) <sup>‡</sup>	Mean BED from SBRT (Gy) <sup>†</sup>	Mean total BED (Gy) <sup>§</sup>	Maximum total BED (Gy) <sup>§</sup>
1 [1]	3.7	27.7	53	113	160	185
1 [2]	NA	27.9	NA	114	NA	NA
2 [3]	5.0	28.1	73	116	186	217
3 [4]	2.9	28.8	41	121	158	171
4 [5]	7.7	28.4	114	118	219	258
4 [6]	5.1	27.9	75	114	187	209
4 [7]	3.7	28.2	54	116	158	179
5 [8]	1.1	28.3	16	117	124	138
6 [9]	2.1	26.7	31	106	131	141
Median	3.7 (2.4)	28.1 (0.4)	58 (37)	116 (3)	159 (35)	182 (48)

\*As calculated from first-cycle serial SPECT/CT imaging.

<sup>†</sup>Mean within gross tumor volume.

<sup>‡</sup>Total dose from both cycles, assuming second cycle contributes 90% of dose from first cycle. Mean within VOI is as defined on PSMA PET/CT.

<sup>§</sup>Mean BED from RPT and SBRT within VOI as defined on PSMA PET/CT. Mean BED from RPT and SBRT within gross tumor volume was approximately 5% lower.

NA = not available.

Numbers in brackets are number of lesions; numbers in parentheses are IQR. Lesion 2 was not within SPECT field of view, assuming  $\alpha/\beta$  ratio of 3 Gy.

AD<sub>RPT</sub> calculated with a multiple concentric oversized VOI method was 27.3 Gy (IQR, 10.2 Gy; range, 16.1–42.9 Gy), translating into 4.1 Gy/GBq (IQR, 1.2 Gy/GBq; range, 2.1–5.8 Gy/GBq). AD<sub>RPT</sub> values calculated with both of these methods were strongly correlated with AD<sub>RPT</sub> derived in Velocity (Spearman  $\rho$  of 0.83 [ $P = 0.015$ ] and 0.86 [ $P = 0.011$ ], respectively); however, their correlation with baseline PSMA SUV<sub>max</sub> and  $\% \Delta_1$  was weaker.

Median gross, clinical, and planning tumor volumes for SBRT were 1.8, 4.6, and 8.8 cm<sup>3</sup>, respectively. The median of the mean lesion AD delivered by SBRT calculated from voxels within the gross tumor volume) was 28.1 Gy (IQR, 0.5 Gy), whereas the median of the mean BED from SBRT was 116.3 Gy (IQR, 3.8 Gy). The median RE from SBRT was 4.13, reflecting the 9.4 Gy delivered per fraction to the gross tumor volume. Corresponding values for maximum AD delivered by SBRT and maximum BED from SBRT were 29.7 Gy (IQR, 1.0 Gy) and 130.5 Gy (IQR, 6.8 Gy), respectively.

The normalized uptake as measured on planar images from the second cycle was approximately 85%–95% of the uptake measured from the first cycle (normalization with respect to background-corrected uptake in liver, kidneys, and parotid gland; uptake in these organs was assumed to remain unchanged between the 2 cycles). The same lesion regions of interest as drawn on the

planar images from the first cycle were used to measure the lesion counts from the second cycle. Lesion shrinkage between the 2 cycles was not accounted for (no significant lesion shrinkage was observed between baseline and interim PSMA PET/CT). If it is assumed that the second cycle delivers 90% of the dose from the first cycle, the

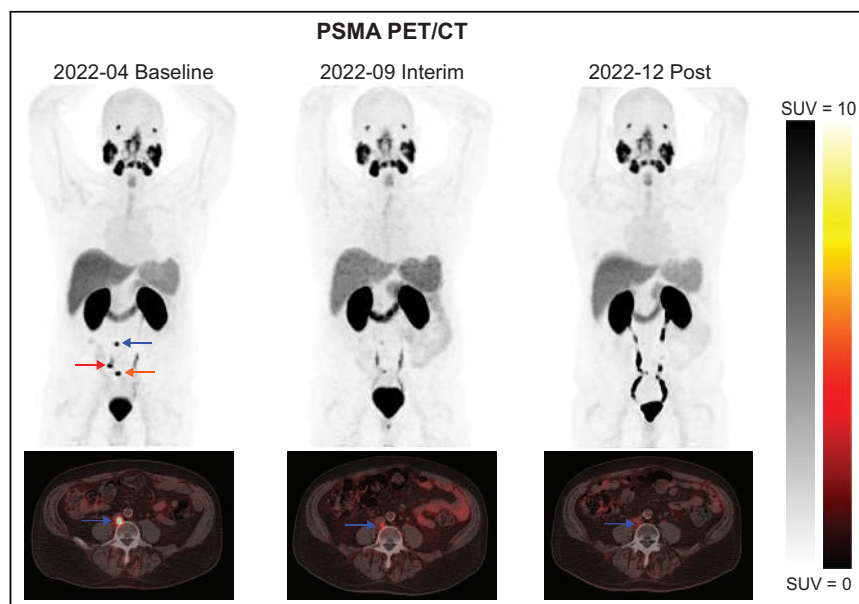


**FIGURE 1.** Top: Maximum-intensity projections for 3 PSMA PET/CT scans of 72-y-old patient initially treated with radical retropubic prostatectomy in 1998 (patient 4). Oligorecurrent lymph nodes in lower retrocaval (blue arrow), right posterior common iliac (red arrow), and superior presacral (orange arrow) regions. Bottom: Axial CT slices, centered on lower retrocaval lymph node.

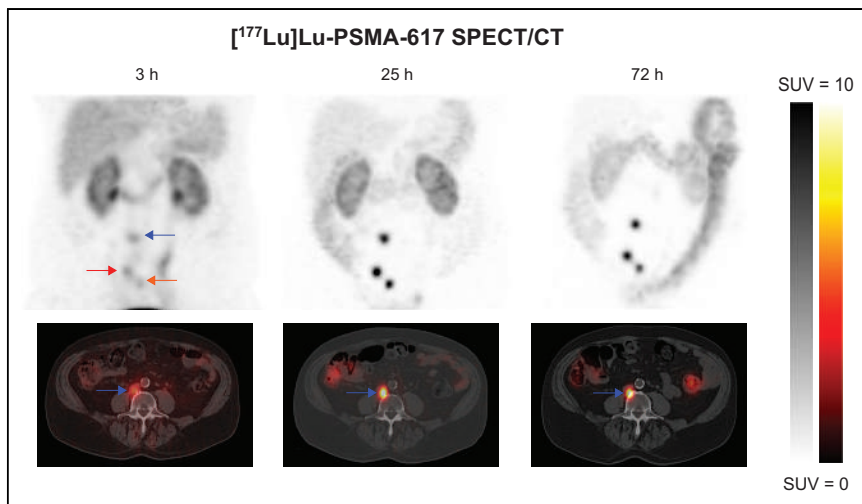


**FIGURE 2.** Top: Maximum-intensity projections for 3 [<sup>177</sup>Lu]Lu-PSMA-617 SPECT/CT scans of patient 4. Oligorecurrent lymph nodes in lower retrocaval (blue arrow), right posterior common iliac (red arrow), and superior presacral (orange arrow) regions. Bottom: Axial CT slices, centered on lower retrocaval lymph node.

median for the mean lesion BED from combined radiopharmaceutical and EBRT (BED from RPT and SBRT) was 159 Gy (IQR, 35 Gy; range, 124–219 Gy), corresponding to a prescription of 33.6 Gy in 3 fractions. The median of the maximum BED from RPT and SBRT was 182 Gy (IQR, 48 Gy; range, 138–258 Gy), corresponding to a prescription of 36.2 Gy in 3 fractions. The total contribution of 2 cycles of RPT to the mean and maximum BED from RPT and SBRT was 34% (range, 13%–52%) and 40% (range, 18%–61%), respectively. If an  $\alpha/\beta$  ratio of 3 is substituted with an  $\alpha/\beta$  ratio of 1.5, the total contribution of [<sup>177</sup>Lu]Lu-PSMA-617 RPT would decrease to 24% because of its low dose rate. The dosimetry workflow for a representative case is presented in Figures 1–3.

Correlations between various indices are presented in Figures 4 and 5. Neither  $AD_{RPT}$  nor interim PET  $SUV_{max}$  was significantly correlated with the  $\% \Delta_2$ , with a  $\rho$  of 0.12 and 0.29, respectively. Analysis was also repeated by substituting  $SUV_{max}$  with  $SUV_{peak}$  (supplemental materials).

## DISCUSSION

The sequential or concurrent combination of cancer therapies may act in an additive and possibly even a synergistic way to increase site-specific coverage of the overall cancer treatment.

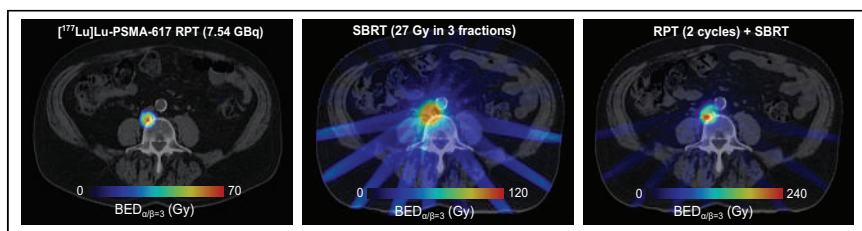


**FIGURE 3.** Axial views of voxelwise dose maps of patient 4, focused on lower retrocaval lymph node. From left to right: BED (assuming  $\alpha/\beta$  ratio of 3 [ $BED_{\alpha/\beta=3}$ ]) from first cycle of [<sup>177</sup>Lu]Lu-PSMA-617 RPT only, from SBRT, and from combined therapy. If second RPT cycle delivers 90% of AD from first cycle, total mean and maximum lesion  $BED_{\alpha/\beta=3}$  would be 219 and 258 Gy, respectively, corresponding to prescription of 40.1 Gy (mean) and 43.9 Gy (maximum) in 3 fractions or  $EQD2_{\alpha/\beta=3}$  of 131 Gy (mean) and 155 Gy (maximum). Two cycles of [<sup>177</sup>Lu]Lu-PSMA-617 RPT were estimated to contribute 52% and 61% to combined mean and maximum  $BED_{\alpha/\beta=3}$ , respectively.

Focal therapy remains important for omCSPC (3), as the gross sites of disease may be less responsive to complete elimination by systemic therapies. In the present work, a theranostic strategy was implemented in which patients with oligometastatic disease were identified by PSMA PET, which was in turn used to gauge the response and to track the treatment efficacy. This was a feasibility study, a precursor to a phase I trial that will be initiated soon ( $n = 27$  patients; same set of interventions as the current study). The decision to administer 2 cycles of [<sup>177</sup>Lu]Lu-PSMA-617 RPT was made up front given the increased bioavailability of the radiopharmaceutical in normal tissues due to low-volume metastatic disease in this cohort of patients compared with the VISION trial in which patients had significant castration-resistant disease (8). An effort to be conservative was made given

that it was not known how castration-sensitive patients with low-volume disease would tolerate the drug. The increased bioavailability of the radiopharmaceutical due to the limited absorption in small-volume disease needs to be factored in when treating earlier stages of disease. The combination of RPT and SBRT addresses this issue by intensifying the radiation on the target and limiting the exposure of normal tissues. It is likely that the clinical significance of late radiation damage, in particular, radiation nephropathy, is strongly linked to life expectancy. The dosimetry was exploratory and was not used to guide treatment in patients that exhibited lower [<sup>177</sup>Lu]Lu-PSMA-617 ADs, had a higher PSA doubling rate, or had a poor PSA response to cycles 1 and 2. Treatment intensification could be achieved by increasing the number of cycles (31), increasing the activity per cycle, decreasing the time gap between cycles, or some combination of these. The requirement for accurate dosimetry for optimizing combined-modality approaches is probably most relevant for normal-tissue toxicity. We expect that the importance of dosimetry will increase as RPT is applied earlier in the disease process, especially if the clinical results suggest there is a rationale for dose escalation.

In our previous study with 133 men who received salvage radiotherapy (median of 20 mo after radical prostatectomy), approximately 70% of PSMA PET–positive cases were oligorecurrent (32). The metastasis-selective combination of systemic targeted RPT, followed by focal EBRT, is a novel concept with a strong rationale: both modalities use ionizing radiation and can thus be quantified and compared in terms of BED; RPT with [<sup>177</sup>Lu]Lu-PSMA-617 enables tumor dose escalation without substantial toxicity to nearby organs; the combination of [<sup>177</sup>Lu]Lu-PSMA-617 RPT and SBRT allows for the intensification of therapeutic ADs to the target while limiting the exposure of the organs at risk more than if treating with [<sup>177</sup>Lu]Lu-PSMA-617 alone, escalated to provide similar tumor ADs; [<sup>177</sup>Lu]Lu-PSMA-617 has the potential to deliver a cytotoxic payload to disseminated

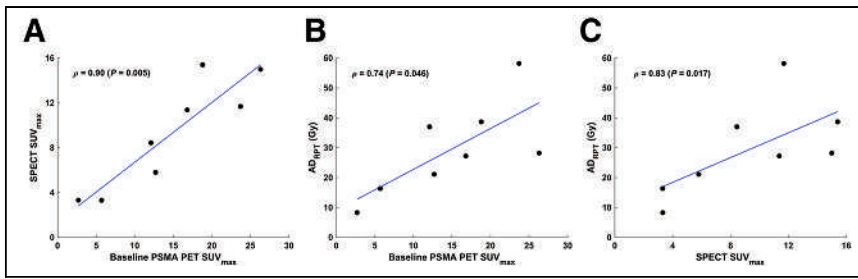


**FIGURE 4.** Correlations between imaging and dosimetry-based metrics: SPECT  $SUV_{max}$  vs. baseline PSMA PET  $SUV_{max}$  (A),  $AD_{RPT}$  vs. baseline PSMA PET  $SUV_{max}$  (B), and  $AD_{RPT}$  vs. SPECT  $SUV_{max}$  (C).

ocult PSMA-expressing microscopic disease that is below the resolution limits of modern PET scanners; SBRT can provide a high-radiation AD to the larger oligometastatic sites for which the RPT radiation dose might be subtherapeutic; and protracted low-dose radiation might serve as a primer dose that sensitizes cancer cells to subsequent high-dose-rate radiotherapy (33). In the omCSPC setting, the proposed combination therapy may result in the delay of castration resistance and the need for androgen-deprivation therapy. A recent prospective phase III trial concluded that a single-dose radiation therapy (24 Gy, corresponding to a BED [assuming an  $\alpha/\beta$  ratio of 3] of 216 Gy) for the treatment of omCSPC results in a lower 3-y cumulative incidence of local recurrence and distant metastatic progression than does a standard (27 Gy in 3 fractions, corresponding to a BED [assuming an  $\alpha/\beta$  ratio of 3] of 108 Gy) SBRT regimen ( $\sim 5\%$  compared with  $\sim 22\%$ , respectively) (34), indicating that comprehensive ablation of oligometastatic lesions, for which  $[^{177}\text{Lu}]\text{Lu-PSMA-617}$  RPT may help facilitate, is associated with significant mitigation of distant metastatic progression.

A PET-derived  $\Delta SUV_{max}$  of at least 75% has been suggested to strongly predict freedom from local failure in patients undergoing oligometastasis-directed ablative radiotherapy (35). The observed median lesion  $AD_{RPT}$  of 3.7 Gy/GBq is comparable to previously published results from 10 studies on lesion dosimetry of  $[^{177}\text{Lu}]\text{Lu-PSMA-617}$  (36). Correlations between aspects of screening PSMA PET and tumor and normal-tissue dose provide a rationale for patient-specific dosing (37). In patients with low-volume metastatic CSPC, the AD in organs appears to be similar or lower in the second  $[^{177}\text{Lu}]\text{Lu-PSMA-617}$  cycle, suggesting that the bioavailability does not increase in later treatment cycles (10). A trend of decreasing AD in lesions over cycles was previously observed for  $[^{177}\text{Lu}]\text{Lu-PSMA I\&T}$  (38).

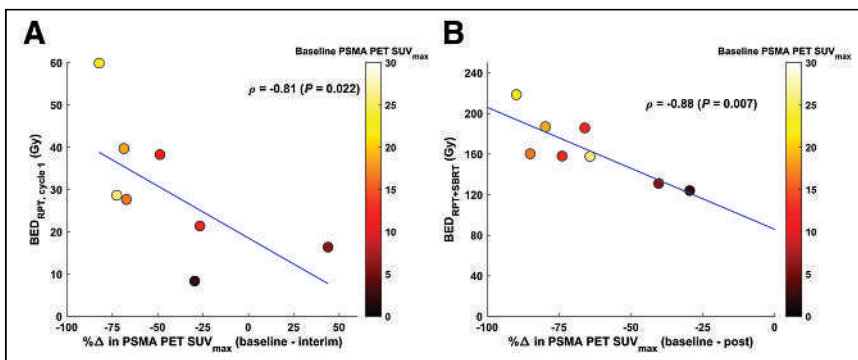


**FIGURE 5.** Relationship between lesion BED and PSMA PET-assessed response to  $[^{177}\text{Lu}]\text{Lu-PSMA-617}$  RPT before SBRT (i.e., interim) (A) and after SBRT (i.e., post) (B).

The 2 main components of the uncertainty in RPT dosimetry are the variability associated with contour delineation and the volume- and sphere-based RC (25,39). A 50% threshold on PET was chosen because it was previously reported to result in the smallest mean differences from morphologic volume measurements (Bland–Altman analysis (40)) and most closely corresponds to volumes delineated on a PSMA PET/MRI scan (41). PET-derived volumes also closely correspond in size to CT-derived volumes; however, in 2 cases, the lesions were not seen on the

CT. When lesions were segmented with a 40% or 30% threshold instead of a 50% threshold, the resulting  $AD_{RPT}$  was approximately 10% and 40% lower, respectively. Optimal threshold depends on multiple factors such as lesion size and lesion-to-background ratio (42). RCs also depend on factors other than the volume of the object, such as shape and activity distribution, with the dependence being largest for extreme departures from spheric geometry (43). No account was taken of nonuniform RPT dose distribution. Even for large tumors, assessing this issue is limited by the spatial resolution of SPECT, and derived quantities such as dose volume histograms may be more of a reflection of SPECT image limitations than underlying dosimetric nonuniformity. A limitation of the current study is that the inaccuracies associated with quantifying activity in small lesions with SPECT have not been validated via phantom experiments. For objects with sizes comparable to or smaller than the spatial resolution of emission tomographic imaging cameras, substantial underestimation in the apparent radioactivity concentration is observed, leading to, for example, an approximately  $50\times$  lower apparent calculated AD for  $0.25\text{ cm}^3$  lesions (44). However, the observed good agreement between lesion ADs calculated in Velocity and an additional method using multiple concentric oversized VOIs, which enables activity quantification without partial-volume correction (10,30), increases confidence in the quantification approach as implemented in Velocity.

Although BED does not have a definitive mechanistic underpinning that relates it to cellular biology and does not incorporate reoxygenation, it accounts for the effect of AD rate (14) and is shown to better correlate with toxicity than does AD (45). MIRD pamphlet no. 20 demonstrated equivalent BED response curves for both external-beam data and peptide-receptor data (46). The linear quadratic model is reasonably well validated up to 10 Gy/fraction (47); however, the upper limit of fraction sizes for which the model remains valid is uncertain (48). In ultra-high-dose radiation therapy ( $>12$  Gy fractions), a unique dual-target mechanism of action has been observed that is fundamentally distinct from the classic fractionation model, linking a transient microvascular vasoactive dysfunction to the repression of high-fidelity homologous recombinatory repair of radiation-induced DNA damage (49). Radiosensitivity may also differ within a lesion, between lesions, and among patients and is possibly influenced by prior therapy (50). Moreover, the fractionation

response (ratio of radiobiologic parameters  $\alpha$  and  $\beta$ , traditionally established from in vitro cell-colony experiments) of prostate cancers has yet to be rigorously defined. To combine the radiobiologic effect of different modalities, the same  $\alpha/\beta$  ratio must be used. Operationally, an  $\alpha/\beta$  ratio of 3 Gy was chosen because it is within the range of reported values for prostate cancer for low-dose-rate brachytherapy and relatively low-dose-per-fraction EBRT (we anticipate that these general findings are likely to be equally applicable to low-dose-rate RPT) and for hypofractionated SBRT (51). Currently, there is no consensus on what radiobiologic parameter values to use for RPT with [<sup>177</sup>Lu]Lu-PSMA-617 (and if those from EBRT apply) and what is the best approach for relating RPT to EBRT dose response (52). The tumor microenvironment, intratumor genomic heterogeneity, intercellular dose nonuniformity, inflammation- or immune-mediated effects, cell-cycle phase, and chemical factors such as tissue oxygen saturation also impact the biologic response; however, these were not considered in the current work.

## CONCLUSION

We demonstrate the feasibility of performing lesional dosimetry in patients with omCSPC undergoing [<sup>177</sup>Lu]Lu-PSMA-617 RPT followed by SBRT. Combined RPT and SBRT may provide an efficient method to maximize the delivery of meaningful doses to oligometastatic disease while addressing potential microscopic disease reservoirs and limiting the dose exposure of normal tissues.

## DISCLOSURE

This study was funded by a Department of Radiology seed grant of Memorial Sloan Kettering Cancer Center with support from Memorial Sloan Kettering Cancer Center's Radiochemistry and Molecular Imaging Probes Core (NIH/NCI Cancer Center support grant P30 CA008748). The study was also supported by a generous philanthropic gift from the Charles Greenberg Chair Fund. [<sup>177</sup>Lu]Lu-PSMA-617 was provided as a fully synthesized product from Advanced Accelerator Applications/Endocyte (a division of Novartis). No other potential conflict of interest relevant to this article was reported.

## KEY POINTS

**QUESTION:** Is combination therapy with [<sup>177</sup>Lu]Lu-PSMA-617 RPT and SBRT for the treatment of omCSPC feasible?

**PERTINENT FINDINGS:** The proposed combination therapy was well tolerated. Composite lesional dosimetry revealed a relatively high attainable maximum BED of more than 180 Gy, with 2 cycles of [<sup>177</sup>Lu]Lu-PSMA-617 RPT contributing approximately 40% to the combined maximum BED.

**IMPLICATIONS FOR PATIENT CARE:** Combined [<sup>177</sup>Lu]Lu-PSMA-617 RPT and SBRT may provide an efficient method to maximize the delivery of meaningful doses to omCSPC tumors while addressing potential microscopic disease reservoirs and limiting the dose exposure of normal tissues.

## REFERENCES

- Siegel RL, Miller KD, Wagle NS, Jemal A. Cancer statistics, 2023. *CA Cancer J Clin.* 2023;73:17–48.
- Hellman S, Weichselbaum RR. Oligometastases. *J Clin Oncol.* 1995;13:8–10.
- Deek MP, Van der Eecken K, Sutura P, et al. Long-term outcomes and genetic predictors of response to metastasis-directed therapy versus observation in oligometastatic prostate cancer: analysis of STOMP and ORIOLE trials. *J Clin Oncol.* 2022;40:3377–3382.
- Lewis SL, Porceddu S, Nakamura N, et al. Definitive stereotactic body radiotherapy (SBRT) for extracranial oligometastases: an international survey of >1000 radiation oncologists. *Am J Clin Oncol.* 2017;40:418–422.
- Tosoian JJ, Gorin MA, Ross AE, Pienta KJ, Tran PT, Schaeffer EM. Oligometastatic prostate cancer: definitions, clinical outcomes, and treatment considerations. *Nat Rev Urol.* 2017;14:15–25.
- Ost P, Jereczek-Fossa BA, As NV, et al. Progression-free survival following stereotactic body radiotherapy for oligometastatic prostate cancer treatment-naive recurrence: a multi-institutional analysis. *Eur Urol.* 2016;69:9–12.
- Kneebone A, Hruby G, Ainsworth H, et al. Stereotactic body radiotherapy for oligometastatic prostate cancer detected via prostate-specific membrane antigen positron emission tomography. *Eur Urol Oncol.* 2018;1:531–537.
- Sartor O, de Bono J, Chi KN, et al. Lutetium-177-PSMA-617 for metastatic castration-resistant prostate cancer. *N Engl J Med.* 2021;385:1091–1103.
- Privé BM, Peters SMB, Muselaers CHJ, et al. Lutetium-177-PSMA-617 in low-volume hormone-sensitive metastatic prostate cancer: a prospective pilot study. *Clin Cancer Res.* 2021;27:3595–3601.
- Peters SMB, Privé BM, de Bakker M, et al. Intra-therapeutic dosimetry of [<sup>177</sup>Lu]Lu-PSMA-617 in low-volume hormone-sensitive metastatic prostate cancer patients and correlation with treatment outcome. *Eur J Nucl Med Mol Imaging.* 2022;49:460–469.
- Suman SK, Subramanian S, Mukherjee A. Combination radionuclide therapy: a new paradigm. *Nucl Med Biol.* 2021;98–99:40–58.
- Gill MR, Falzone N, Du Y, Vallis KA. Targeted radionuclide therapy in combined-modality regimens. *Lancet Oncol.* 2017;18:e414–e423.
- Bodey RK, Evans PM, Flux GD. Application of the linear-quadratic model to combined modality radiotherapy. *Int J Radiat Oncol Biol Phys.* 2004;59:228–241.
- Sgouros G, Bolch WE, Chiti A, et al. ICRU REPORT 96, dosimetry-guided radio-pharmaceutical therapy. *J ICRU.* 2021;21:1–212.
- Hobbs RF, McNutt T, Baechler S, et al. A treatment planning method for sequentially combining radiopharmaceutical therapy and external radiation therapy. *Int J Radiat Oncol Biol Phys.* 2011;80:1256–1262.
- van der Sar ECA, Braat A, van der Voort-van Zyp JRN, et al. Tolerability of concurrent external beam radiotherapy and [<sup>177</sup>Lu]Lu-PSMA-617 for node-positive prostate cancer in treatment naïve patients, phase I study (PROQUIRE-I trial). *BMC Cancer.* 2023;23:268.
- Ma TM, Czernin J, Felix C, et al. LUNAR: a randomized phase 2 study of <sup>177</sup>lutetium-PSMA neoadjuvant to ablative radiotherapy for oligorecurrent prostate cancer (clinical trial protocol). *BJU Int.* 2023;132:65–74.
- Hope TA, Goodman JZ, Allen IE, Calais J, Fendler WP, Carroll PR. Metaanalysis of <sup>68</sup>Ga-PSMA-11 PET accuracy for the detection of prostate cancer validated by histopathology. *J Nucl Med.* 2019;60:786–793.
- Fendler WP, Calais J, Eiber M, et al. Assessment of <sup>68</sup>Ga-PSMA-11 PET accuracy in localizing recurrent prostate cancer: a prospective single-arm clinical trial. *JAMA Oncol.* 2019;5:856–863.
- Artigas C, Diamand R, Shagera QA, et al. Oligometastatic disease detection with <sup>68</sup>Ga-PSMA-11 PET/CT in hormone-sensitive prostate cancer patients (HSPC) with biochemical recurrence after radical prostatectomy: predictive factors and clinical impact. *Cancers (Basel).* 2021;13:4982.
- Dietlein M, Kobe C, Kuhnert G, et al. Comparison of [<sup>18</sup>F]DCFPyL and [<sup>68</sup>Ga]Ga-PSMA-HBED-CC for PSMA-PET imaging in patients with relapsed prostate cancer. *Mol Imaging Biol.* 2015;17:575–584.
- Lu M, Lindenberg L, Mena E, et al. A pilot study of dynamic <sup>18</sup>F-DCFPyL PET/CT imaging of prostate adenocarcinoma in high-risk primary prostate cancer patients. *Mol Imaging Biol.* 2022;24:444–452.
- Rowe SP, Pienta KJ, Pomper MG, Gorin MA. PSMA-RADS version 1.0: a step towards standardizing the interpretation and reporting of PSMA-targeted PET imaging studies. *Eur Urol.* 2018;73:485–487.
- Tran-Gia J, Lassmann M. Characterization of noise and resolution for quantitative <sup>177</sup>Lu SPECT/CT with xSPECT Quant. *J Nucl Med.* 2019;60:50–59.
- Dewaraja YK, Miranda DM, Peterson AB, et al. A pipeline for automated voxel dosimetry: application in patients with multi-SPECT/CT imaging after <sup>177</sup>Lu-peptide receptor radionuclide therapy. *J Nucl Med.* 2022;63:1665–1672.
- Ryu H, Meikle SR, Willowson KP, Eslick EM, Bailey DL. Performance evaluation of quantitative SPECT/CT using NEMA NU 2 PET methodology. *Phys Med Biol.* 2019;64:145017.
- Peters SMB, Meyer Viol SL, van der Werf NR, et al. Variability in lutetium-177 SPECT quantification between different state-of-the-art SPECT/CT systems. *EJNMMI Phys.* 2020;7:9.



28. Sarut D, Halty A, Badel JN, Ferrer L, Bardiès M. Voxel-based multimodel fitting method for modeling time activity curves in SPECT images. *Med Phys*. 2017;44:6280–6288.
29. Bolch WE, Eckerman KF, Sgouros G, Thomas SR. MIRD pamphlet no. 21: a generalized schema for radiopharmaceutical dosimetry—standardization of nomenclature. *J Nucl Med*. 2009;50:477–484.
30. Carnegie-Peake L, Taprogge J, Murray I, Flux GD, Gear J. Quantification and dosimetry of small volumes including associated uncertainty estimation. *EJNMMI Phys*. 2022;9:86.
31. Mader N, Nguyen Ngoc C, Kirkgöze B, et al. Extended therapy with [<sup>177</sup>Lu]Lu-PSMA-617 in responding patients with high-volume metastatic castration-resistant prostate cancer. *Eur J Nucl Med Mol Imaging*. 2023;50:1811–1821.
32. Imber BS, O'Dwyer E, Lobaugh S, et al. Failure patterns by PSMA PET for recurrent prostate cancer after prostatectomy and salvage radiation. *Urology*. 2022;170:146–153.
33. Murray D, McEwan AJ. Radiobiology of systemic radiation therapy. *Cancer Biother Radiopharm*. 2007;22:1–23.
34. Zelefsky MJ, Yamada Y, Greco C, et al. Phase 3 multi-center, prospective, randomized trial comparing single-dose 24 Gy radiation therapy to a 3-fraction SBRT regimen in the treatment of oligometastatic cancer. *Int J Radiat Oncol Biol Phys*. 2021;110:672–679.
35. Greco C, Pares O, Pimentel N, et al. Positron emission tomography-derived metrics predict the probability of local relapse after oligometastasis-directed ablative radiation therapy. *Adv Radiat Oncol*. 2021;7:100864.
36. Jackson P, Hofman M, McIntosh L, Buteau JP, Ravi Kumar A. Radiation dosimetry in <sup>177</sup>Lu-PSMA-617 therapy. *Semin Nucl Med*. 2022;52:243–254.
37. Violet J, Jackson P, Ferdinandus J, et al. Dosimetry of <sup>177</sup>Lu-PSMA-617 in metastatic castration-resistant prostate cancer: correlations between pretherapeutic imaging and whole-body tumor dosimetry with treatment outcomes. *J Nucl Med*. 2019;60:517–523.
38. Okamoto S, Thieme A, Allmann J, et al. Radiation dosimetry for <sup>177</sup>Lu-PSMA I&T in metastatic castration-resistant prostate cancer: absorbed dose in normal organs and tumor lesions. *J Nucl Med*. 2017;58:445–450.
39. Gear JI, Cox MG, Gustafsson J, et al. EANM practical guidance on uncertainty analysis for molecular radiotherapy absorbed dose calculations. *Eur J Nucl Med Mol Imaging*. 2018;45:2456–2474.
40. Reddy RP, Ross Schmidlein C, Giampoli RG, et al. The quest for an accurate functional tumor volume with <sup>68</sup>Ga-DOTATATE PET/CT. *J Nucl Med*. 2022;63:1027–1032.
41. Zhang YN, Lu ZG, Wang SD, et al. Gross tumor volume delineation in primary prostate cancer on <sup>18</sup>F-PSMA-1007 PET/MRI and <sup>68</sup>Ga-PSMA-11 PET/MRI. *Cancer Imaging*. 2022;22:36.
42. Hatt M, Lee JA, Schmidlein CR, et al. Classification and evaluation strategies of auto-segmentation approaches for PET: report of AAPM task group no. 211. *Med Phys*. 2017;44:e1–e42.
43. Carter LM, Krebs S, Marquis H, et al. Dosimetric variability across a library of computational tumor phantoms. *J Nucl Med*. 2023;64:782–790.
44. Marquis H, Willowson KP, Bailey DL. Partial volume effect in SPECT & PET imaging and impact on radionuclide dosimetry estimates. *Asia Ocean J Nucl Med Biol*. 2023;11:44–54.
45. Barone R, Borson-Chazot F, Valkema R, et al. Patient-specific dosimetry in predicting renal toxicity with <sup>90</sup>Y-DOTATOC: relevance of kidney volume and dose rate in finding a dose–effect relationship. *J Nucl Med*. 2005;46(suppl 1):99S–106S.
46. Wessels BW, Konijnenberg MW, Dale RG, et al. MIRD pamphlet no. 20: the effect of model assumptions on kidney dosimetry and response—implications for radionuclide therapy. *J Nucl Med*. 2008;49:1884–1899.
47. Brenner DJ. The linear-quadratic model is an appropriate methodology for determining isoeffective doses at large doses per fraction. *Semin Radiat Oncol*. 2008;18:234–239.
48. McMahon SJ. The linear quadratic model: usage, interpretation and challenges. *Phys Med Biol*. 2018;64:01TR01.
49. Bodo S, Campagne C, Thin TH, et al. Single-dose radiotherapy disables tumor cell homologous recombination via ischemia/reperfusion injury. *J Clin Invest*. 2019;129:786–801.
50. Baechler S, Hobbs RF, Prideaux AR, Wahl RL, Sgouros G. Extension of the biological effective dose to the MIRD schema and possible implications in radionuclide therapy dosimetry. *Med Phys*. 2008;35:1123–1134.
51. Cui M, Gao XS, Li X, Ma M, Qi X, Shibamoto Y. Variability of  $\alpha/\beta$  ratios for prostate cancer with the fractionation schedule: caution against using the linear-quadratic model for hypofractionated radiotherapy. *Radiat Oncol*. 2022;17:54.
52. Sgouros G, Dewaraja YK, Escorcía F, et al. Tumor response to radiopharmaceutical therapies: the knowns and the unknowns. *J Nucl Med*. 2021;62(suppl 3):12S–22S.



## Second Symposium of the European Working Group on the Radiobiology of Molecular Radionuclide Therapy

Julie Nonnekens<sup>1,2</sup>, Bart Cornelissen<sup>3,4</sup>, and Samantha Y.A. Terry<sup>5</sup>; on behalf of the European Working Group on the Radiobiology of Molecular Radiotherapy

<sup>1</sup>Department of Molecular Genetics, Erasmus MC Cancer Institute, Erasmus University Medical Center, Rotterdam, The Netherlands;

<sup>2</sup>Department of Radiology and Nuclear Medicine, Erasmus MC Cancer Institute, Erasmus University Medical Center, Rotterdam,

The Netherlands; <sup>3</sup>Department of Nuclear Medicine and Molecular Imaging, University Medical Center Groningen, University

of Groningen, Groningen, The Netherlands; <sup>4</sup>Department of Oncology, University of Oxford, Oxford, United Kingdom; and

<sup>5</sup>Department of Imaging Chemistry and Biology, School of Biomedical Engineering and Imaging Sciences, King's College London, London, United Kingdom

Molecular radionuclide therapy is a relatively novel anticancer treatment option using radiolabeled, tumor-specific vectors. On binding of these vectors to cancer cells, radioactive decay induces DNA damage and other effects, leading to cancer cell death. Treatments, such as with [<sup>177</sup>Lu]Lu-octreotate for neuroendocrine tumors and [<sup>177</sup>Lu]Lu-PSMA for prostate cancer, are now being implemented into routine clinical practice around the world. Nonetheless, research into the underlying radiobiologic effects of these treatments is essential to further improve them or formulate new ones. The purpose of the European Working Group on the Radiobiology of Molecular Radiotherapy is to promote knowledge, investment, and networking in this area. This report summarizes recent research and insights presented at the second International Workshop on Radiobiology of Molecular Radiotherapy, held in London, U.K., on March 13 and 14, 2023. The symposium was organized by members of the Cancer Research U.K. RadNet City of London and the European Working Group on the Radiobiology of Molecular Radiotherapy.

**Key Words:** cancer treatment; collaboration; external-beam radiotherapy; molecular radionuclide therapy; radiobiology

**J Nucl Med 2023; 64:1788–1790**

DOI: 10.2967/jnumed.123.265956

This second workshop (a hybrid meeting) on molecular radionuclide therapy was a follow-on from the call-to-arms editorial article published in 2019 (1) and the inaugural meeting in 2021 in Montpellier (2). The aim of this workshop was to update the community on the current state of the art and research on radiobiology in the field of molecular radionuclide therapy (MRT), to be inspired by research performed in the field of external-beam radiotherapy and cancer biology, and to network during dedicated times in the schedule. In total, 120 attendees (100 live and 20 online) from 11 countries participated in talks, debates, and poster sessions. Proffered talks, posters, and poster pitches were selected from more than 40 abstracts.

Jonathan Wadsley from the University of Sheffield, U.K., gave the first keynote lecture, highlighting the state of the art of MRT, and indicated where efforts are best invested for impactful clinical success. He started with an overview of current clinical indications for MRT such as <sup>131</sup>I for thyroid cancer, <sup>223</sup>Ra for prostate cancer bone metastases, radioembolization, [<sup>177</sup>Lu]Lu-octreotate for neuroendocrine tumors, and [<sup>177</sup>Lu]Lu-PSMA for prostate cancer. Future work, he proposed, should focus on novel tumor indications, novel radionuclides, and combination treatments. He discussed 6 gaps in our current knowledge, indicating the challenges in standardized dosimetry and poorly understood radiobiology: how we can personalize therapy to ensure that each patient receives the most effective absorbed dose to treat the tumor while maintaining safety and not damaging organs at risk; what absorbed doses are being delivered, and what the radiobiologic significance is of dose-rate effects; what the radiobiologic consequences are of different types of emissions with different energies and path-lengths; how tumor heterogeneity is managed; what the role of radiosensitizers is; and what the effect of immune interactions on therapeutic efficacy can be. Wadsley also discussed some lessons learned from clinical trials (e.g., the SELIMETRY trial) and where we as a community might best lay our efforts to achieve impactful clinical success, such as by focusing on personalizing treatment to ensure that every patient gets the maximum possible benefit from the activity delivered and by performing rigorous, multidisciplinary clinical trials addressing meaningful clinical questions such as dosimetry, radiobiology, and molecular biomarkers.

A series of proffered talks highlighted the best-scored abstracts that had been submitted. Simone Kleinendorst (Radboudumc, Nijmegen, The Netherlands) discussed the potential of combining carbonic anhydrase IX–targeted <sup>177</sup>Lu treatment with immune checkpoints inhibitors. Hanna Berglund (Uppsala University, Sweden) talked about how p53 stabilization potentiates [<sup>177</sup>Lu]Lu-octreotate therapy in neuroblastoma. Jordan Cheng (King's College London, U.K.) highlighted the option of using chemotherapeutics targeting replication to enhance [<sup>177</sup>Lu]Lu-octreotate therapy *in vitro*.

The second session focused on the role of the tumor microenvironment (TME) and immune response in MRT efficacy. The first talk was an invited lecture by Julie Constanzo from the Montpellier Cancer Research Institute, France, on the topic of MRT and vesicle signaling in the context of anticancer immunity. She showed how the TME plays a major role in the cellular response

Received May 1, 2023; revision accepted Jun 20, 2023.

For correspondence or reprints, contact Samantha Terry (samantha.terry@kcl.ac.uk).

Published online Jul. 13, 2023.

COPYRIGHT © 2023 by the Society of Nuclear Medicine and Molecular Imaging.

to radiotherapy (including MRT). MRT acts via induction of targeted effects (such as direct DNA breaks) and nontargeted effects (such as via excretion of cytokines, extracellular vesicles, danger-associated molecular patterns, or chemokines). The latter will lead to direct killing of surrounding cells or activation of the immune system. Furthermore, her work showed that membrane targeting with radionuclides can activate the cGAS-STING pathway (cyclic guanosine monophosphate–adenosine monophosphate synthase and stimulator of interferon genes). She also showed that extracellular vesicles play a role in enhancing the therapeutic effect via the immune system, since extracellular vesicles isolated from MRT-treated cells can effectively be used to treat immune-competent xenografted mice but not immunodeficient mice. Future work will focus on the combination of MRT with immune checkpoint inhibitors and when to use this combination. What would, for example, be the best treatment schedule and which patients would be eligible?

The session was continued with proffered talks on submitted abstracts. Yasmine Bouden (University of Montpellier, France) gave a talk on the role of double-stranded DNA contained in extracellular vesicles released by irradiated cells. Gemma Dias (University of Oxford, U.K.) talked about her work on the antitumor immune response induced by [<sup>177</sup>Lu]Lu-PSMA, and Sapna Lunj (University of Manchester, U.K.) showed her data on the systemic immune response induced by MRT in men with prostate cancer. The session was followed by poster pitches from the highest-ranked poster abstracts. Concluding the first day, participants were divided into groups and were asked to discuss 4 questions and upload their answers in Padlet, an online visual board for organizing and sharing content. Question 1 was, “My research in radionuclide therapy would progress if I could just . . . .” Question 2 was, “The next big thing should be . . . .” Question 3 was, “What other suggestions do you have on how to progress the field?” Question 4 was, “How will we fund this?” All answers were compiled and discussed during an audience-engaged discussion on day 2.

The second day started with an invited talk by Isabel Pires from the University of Manchester, U.K., who gave an extensive overview on how to target hypoxia biology as a radiosensitizing approach in breast cancer. Years of research by many groups has shown that hypoxia causes resistance to radiotherapy, as well as increased genomic instability, increased metastatic potential, metabolic and angiogenic switches, and stemness. Pires discussed her work on WSB-1, an E3 ligase associated with hypoxia signaling. WSB-1 is a HIF1 target and has a positive feedback loop with HIF1. High expression of WSB-1 is associated with poor prognosis (distant metastasis–free survival) for hormone receptor–negative breast cancer patients, and downregulation leads to decreased angiogenic and metastatic capacity *in vitro* and *in vivo*. More recent data indicate that WSB-1 could regulate the DNA damage response, which gives opportunities for combination treatment strategies. She concluded with the statement that WSB-1 could be a potential novel breast cancer gene biomarker for dysfunctional DNA damage response in hypoxic breast cancer. Similarly detailed radiobiologic studies should be on the horizon for MRT.

During the audience-engaged discussion, the outcomes of the group discussion of the first day were debated. The participants saw various promising developments both in the lab and in the clinic, including novel treatment options such as drug combinations and the use of Auger electron emitters. In addition, the participants indicated that more emphasis should be put on radiogenomics, dosimetry, and novel models such as 3-dimensional spheroids and animals.

Furthermore, they concluded that it is essential to include radiobiology and dosimetry in clinical practice—for example, to enable biomarker research and to develop quick and easy functional tests for patient selection and prediction of therapy efficacy. The audience showed a clear consensus on standardization of terminology (e.g., what is this therapy called: molecular radionuclide therapy, radiopharmaceutical therapy, or targeted radiotherapy?). The audience also found that it is essential to better report on experimental procedures and use appropriate controls to allow for standardization and increase reproducibility. Additionally, the participants believed there to be a great need for better interaction and knowledge exchange within the community. The working group is currently following up on these points.

The second keynote talk was by Fran Balkwill of Queen Mary University of London, U.K. She talked about how the TME might influence MRT success. Cancers are not just masses of malignant cells but complex organs, to which many other cells are recruited and are sometimes corrupted by the transformed cells. Interactions between those cells create the TME, which can vastly differ between different tumor types. Balkwill showed her team’s work on high-grade serous ovarian cancer, which often metastasizes to the omentum. Mouse models can be used to study this tumor type and its response to treatment since there are many common elements between mouse and human samples, such as the type of infiltrated immune cells. Her work showed that chemotherapy can stimulate the immune response and modulate the TME and that, to study this change, it is essential to obtain pre- and posttreatment samples. Very recent work showed live imaging of human tissue slices and cocultures of different types of cells to follow tumor and immune cell movement using antibodies (data not published).

The last 2 sessions of the conference comprised the last proffered talks. Paula Raposinho and Ana Belchior (both from the Technical University of Lisbon, Portugal) talked about cellular studies using <sup>67</sup>Ga- and <sup>177</sup>Lu-labeled nanoparticles for theranostics of glioblastoma and dosimetric challenges from nanoscopic patterns to biologic effectiveness, respectively. Emmanuel Deshayes (Montpellier Cancer Research Institute, France) gave a lecture on the dose–effect relationship in tumors and healthy organs for patients treated with [<sup>177</sup>Lu]Lu-DOTA-octreotate. The last 2 talks focused on drug screens to find novel combination treatments. Edward O’Neill (University of Oxford, U.K.) used a clonogenic assay–based drug screen to identify cyclin-dependent kinase 4/6 inhibitors as potential radiosensitizers for <sup>177</sup>Lu-based MRT, and Thom Reuvers (Erasmus University Medical Center Rotterdam, The Netherlands) performed a plate reader–based high-throughput screen and identified DNA–protein kinase catalytic subunit inhibitors as potent radiosensitizers of [<sup>177</sup>Lu]Lu-DOTA-octreotate.

Simone Kleinendorst was awarded first place for the best oral presentation, and Thom Reuvers and Sapna Lunj were jointly awarded second place. Isabella Strobel was awarded first place for the best poster, and Anthony Waked and Katarina Gleisner were jointly awarded second place.

The radiobiology of MRT is gaining much attention, and various studies are showing an important role for clinical MRT implementation. Symposia such as this are highly effective opportunities for networking and establishing novel collaborations. Although growing, the field is not yet overcrowded; in fact, we would go so far as to state that researching the biologic mechanisms that influence radionuclide therapy effectiveness would make an excellent niche for many early-career researchers, as well as more established

academics, to move into. At the workshop, follow-up meetings were also planned to identify concrete ways forward for the working group. Equally, the scholar-in-training committee will now be reinstated to increase the visibility of scholar-in-training members within the radiobiology-of-MRT community and will work to offer networking and community opportunities. Several recommendations were made to help the community move the field of MRT forward at a faster pace, including standardizing the name of MRT to aid visibility among other research areas, sharing protocols, collaborating more, and standardizing reporting of results. Additional information is available online ([www.mrtradiobiology.com](http://www.mrtradiobiology.com)).

#### DISCLOSURE

The symposium was generously sponsored by Artios, AstraZeneca, Mediso, MiLabs, RPS Service, and Viewpoint Molecular Targeting (now Perspective Therapeutics) and by the Radiation Research Unit at the Cancer Research U.K. City of London Centre (C7893/A28990). No other potential conflict of interest relevant to this article was reported.

#### ACKNOWLEDGMENTS

The local organization organizing committee included Hafiza Bibi, Vittorio de Santis, Jordan Cheng, and Samantha Terry. The scientific committee included Jordan Cheng, Paul Gape, and Mark Gaze, Jane Sosabowski, Bart Cornelissen, Julie Nonnekens, and

Samantha Terry. We thank all panel members, chairs, and others who helped make the symposium a success.

#### KEY POINTS

**QUESTION:** This symposium set out to enable a networking opportunity for biologic researchers working in MRT and ascertain how they as a group should best proceed.

**PERTINENT FINDINGS:** Several suggestions were made to help move the field of MRT forward at a faster pace, including creating a scientist-in-training committee, sharing protocols, collaborating more, and standardizing reporting of results.

**IMPLICATIONS FOR PATIENT CARE:** By moving the field of MRT forward through new connections and more in-depth biologic research, further highly effective therapeutic options will become available for patients.

#### REFERENCES

1. Terry SYA, Nonnekens J, Aerts A, et al. Call to arms: need for radiobiology in molecular radionuclide therapy. *Eur J Nucl Med Mol Imaging*. 2019;46:1588–1590.
2. Cornelissen B, Terry S, Nonnekens J, Pouget JP; European Working Group on the Radiobiology of Molecular Radiotherapy. First symposium of the European Working Group on the Radiobiology of Molecular Radiotherapy. *J Nucl Med*. 2021; 62(7):14N–15N.

---

---

# Optimized Methods for the Production of High-Purity $^{203}\text{Pb}$ Using Electroplated Thallium Targets

Shefali Saini<sup>1</sup>, Jennifer L. Bartels<sup>1</sup>, Jean-Pierre K. Appiah<sup>1</sup>, Jason H. Rider<sup>1</sup>, Nicholas Baumhover<sup>2</sup>, Michael K. Schultz<sup>2</sup>, and Suzanne E. Lapi<sup>1</sup>

<sup>1</sup>Department of Radiology, University of Alabama at Birmingham, Birmingham, Alabama; and <sup>2</sup>Perspective Therapeutics, Inc., Coralville, Iowa

$^{203}\text{Pb}$  is a surrogate imaging match for  $^{212}\text{Pb}$ . This elementally matched pair is emerging as a suitable pair for imaging and targeted radionuclide therapy in cancer care. Because of the half-life (51.9 h) and low-energy  $\gamma$ -rays emitted,  $^{203}\text{Pb}$  is suitable for the development of diagnostic radiopharmaceuticals. The aim of this work was to optimize the production and separation of high-specific-activity  $^{203}\text{Pb}$  using electroplated thallium targets. We further investigated the radiochemistry optimization using a suitable chelator, tetraazacyclododecane-1,4,7-triacetic acid (DO3A), and targeting vector, VMT- $\alpha$ -NET (lead-specific chelator conjugated to tyr3-octreotide via a polyethylene glycol linker). **Methods:** Targets were prepared by electroplating of natural or enriched ( $^{205}\text{Tl}$ ) thallium metal. Scanning electron microscopy was performed to determine the structure and elemental composition of electroplated targets. Targets were irradiated with 24-MeV protons with varying current and beam time to investigate target durability.  $^{203}\text{Pb}$  was purified from the thallium target material using an extraction resin (lead resin) column followed by a second column using a weak cation-exchange resin to elute the lead isotope as  $[\text{}^{203}\text{Pb}]\text{PbCl}_2$ . Inductively coupled plasma mass spectrometry studies were used to further characterize the separation for trace metal contaminants. Radiolabeling efficiency was also investigated for DO3A chelator and VMT- $\alpha$ -NET (a peptide-based targeting conjugate). **Results:** Electroplated targets were prepared at a high plating density of 76–114 mg/cm<sup>2</sup> using a plating time of 5 h. A reproducible separation method was established with a final elution in HCl (400  $\mu\text{L}$ , 1 M) suitable for radiolabeling. Greater than 90% recovery yields were achieved, with an average specific activity of  $37.7 \pm 5.4$  GBq/ $\mu\text{mol}$  ( $1.1 \pm 0.1$  Ci/ $\mu\text{mol}$ ). **Conclusion:** An efficient electroplating method was developed to prepare thallium targets suitable for cyclotron irradiation. A simple and fast separation method was developed for routine  $^{203}\text{Pb}$  production with high recovery yields and purity.

**Key Words:** lead-203; thallium-205; electroplating; DO3A; radiolabeling

**J Nucl Med 2023; 64:1791–1797**

DOI: 10.2967/jnumed.123.265976

**R**adiopharmaceuticals can be used for diagnostic or therapeutic applications based on the incorporated radionuclide. The term *theranostic* is a portmanteau word for *therapy* and *diagnostic*. In theranostics, an imaging surrogate is used to guide delivery of a personalized dosage for a disease condition (1,2). In nuclear medicine, theranostic radiopharmaceuticals use a common precursor to

diagnose and treat the disease condition using radionuclides with similar or identical chemistry but decay properties that are suitable for imaging and therapy (3). In this context,  $^{203}\text{Pb}$  and  $^{212}\text{Pb}$  represent an elementally identical radioisotope pair that is particularly well suited for the development of theranostics.

Food and Drug Administration approved agents such as NET-SPOT ( $[\text{}^{68}\text{Ga}]\text{Ga-DOTATATE}$ ; Advanced Accelerator Applications) and LUTATHERA ( $[\text{}^{177}\text{Lu}]\text{Lu-DOTATATE}$ ; Novartis) are routinely used in clinical settings for the diagnosis and therapy of somatostatin receptor positive neuroendocrine tumors (4,5). However, despite the potential of these theranostic agents, different radionuclides for imaging and therapy may often require different methods for chemistry optimization and different chelators. In addition, the in vivo biodistribution profiles of these radiopharmaceuticals labeled with  $^{68}\text{Ga}$  or  $^{177}\text{Lu}$  may be different (6,7). Therefore, to better match the diagnostic and therapeutic counterparts, elementally matched isotope pairs are highly desired. Elementally matched radiopharmaceuticals use the same radioactive element with isotopes that have decay properties making them suitable for diagnostic imaging ( $\beta^+$ / $\gamma$ -emitting) and therapeutic ( $\alpha/\beta^-$  emitting) applications. In this way, the in vivo biodistribution is identical and the imaging surrogate can be used to understand and predict the pharmacokinetics of the therapeutic. In addition, the use of an elementally matched isotope pair for theranostics adds confidence to dosimetry, thereby providing potentially more accurate treatment planning. Table 1 provides a list of elementally matched isotopes for theranostic matched pairs.

$^{203}\text{Pb}$  and  $^{212}\text{Pb}$  are an emerging, elementally matched pair of high interest.  $^{203}\text{Pb}$  decays to stable  $^{203}\text{Tl}$  by electron capture with the emission of a low-energy  $\gamma$ -photon (279 keV, 81%) and no radioactive daughter, making it suitable for SPECT imaging applications (8).  $^{212}\text{Pb}$  is a daughter of  $^{224}\text{Ra}$  and decays by emitting 2  $\beta^-$  and one  $\alpha$  particle, making it suitable for therapeutic applications (9–11).  $^{212}\text{Pb}$  is typically available from a  $^{224}\text{Ra}/^{212}\text{Pb}$  generator, but commercial-scale manufacturing is feasible because of relatively straightforward chemistry for purification.

The present study investigated the production of  $^{203}\text{Pb}$  via proton irradiation of thallium targets ( $^{205}\text{Tl}(p,3n)^{203}\text{Pb}$ ) and development of a robust separation method to obtain a final product of high specific activity. A simple 2-column separation method was developed that requires small elution volumes with a separation time of less than 2 h. The final product was eluted in HCl (400  $\mu\text{L}$ , 1 M), making it feasible for radiolabeling and shipping to other facilities. Further evaluation for radiolabeling was performed with a DO3A chelator to develop a standard operating procedure for apparent molar activity (AMA) analysis. Elemental analysis was determined using inductively coupled plasma mass spectrometry (ICP-MS) to analyze the impurities in the final product.

Received May 4, 2023; revision accepted Jul. 17, 2023.

For correspondence or reprints, contact Suzanne E. Lapi (lapi@uab.edu).

Published online Aug. 31, 2023.

COPYRIGHT © 2023 by the Society of Nuclear Medicine and Molecular Imaging.

**TABLE 1**  
Characteristic Properties of Elementally Matched Theranostic Isotope Pairs

Diagnostic				Therapeutic				Reference
Radionuclide	Half-life	Decay	Energy* (keV)	Radionuclide	Half-life	Decay	Energy* (keV)	
<sup>203</sup> Pb	51.8 h	EC (100%)	279 (81%)	<sup>212</sup> Pb	10.6 h	β <sup>-</sup> (100%)	β <sup>-</sup> : 40.9 (5%), 93.3 (81.5%), 171.4 (13.7%), γ: 238 (46.3%)	(8,22)
<sup>64</sup> Cu	12.7 h	β <sup>+</sup> (17.8%), EC (43.8%)	511 (35%), 1,345 (0.5%)	<sup>67</sup> Cu	61.9 h	β <sup>-</sup> (100%)	395 (45%), 484 (35%), 577 (20%)	(23,24)
<sup>86</sup> Y	14.7 h	β <sup>+</sup> (31.9%), EC (68.1%)	443 (16.9%), 628 (32.6%)	<sup>90</sup> Y	64 h	β <sup>-</sup> (100%)	932.4 (99.9%)	(25,26)
<sup>124</sup> I	4.2 d	β <sup>+</sup>	603 (61%), 1,691 (11%)	<sup>131</sup> I	8 d	β <sup>-</sup> (100%)	284 (6.14%), 365 (81.7%), 637 (7.17%)	(27,28)
<sup>152</sup> Tb	17.5 h	β <sup>+</sup> + EC (100%)	344 (63.5%)	<sup>149</sup> Tb	4.1 h	α (17.7%)	α: 3 967	(29,30)
<sup>149</sup> Tb	4.1 h	EC (82.3%)	165 (26.7%), 352 (29.8%), 388.6 (18.6%)	<sup>161</sup> Tb	6.9 d	β <sup>-</sup> (100%)	137.7 (25.7%), 157.4 (65%)	
<sup>155</sup> Tb	5.3 d	EC (100%)	86.5 (32%), 105.3 (25%), 180 (7.5%)					
<sup>43</sup> Sc	3.9 h	β <sup>+</sup> (98%),	373 (22.5%)	<sup>47</sup> Sc	3.3 d	β <sup>-</sup> (100%)	159.4 (68%)	(31–35)
<sup>44g</sup> Sc	3.9 h	β <sup>+</sup> (94%)	1,157 (100%)					

\*Intensity.

EC = electron capture.

## MATERIALS AND METHODS

All reagents were purchased from Sigma Aldrich unless otherwise noted. Additional details are provided in the supplemental materials (supplemental materials are available at <http://jnm.snmjournals.org>).

### Thallium Target Preparation by Electroplating

An electroplating bath was prepared following the procedure from Suparman with some modifications (12). Briefly, the electroplating bath was prepared by mixing 250 mg of [<sup>mab</sup>Tl]Tl<sub>2</sub>O<sub>3</sub> or [<sup>205</sup>Tl]Tl<sub>2</sub>O<sub>3</sub>, hydrazine hydrate (300 μL), NaOH (1 g), and ethylenediaminetetraacetic acid (1.5 g) in 10 mL of water. Copper (1.5-mm thickness) or gold (1-mm thickness) backings of 25-mm diameter were used as the cathodes. An electroplating station (Fig. 1) was designed and manufactured to help optimize uniform target mass deposition on a copper or gold coin. The details of the procedure are provided in the supplemental materials.

### Target Irradiation and Purification of <sup>203</sup>Pb

All target irradiations were performed on an Advanced Cyclotron Systems TR24 cyclotron. Using an Advanced Cyclotron Systems 90° solid target holder (13), electroplated target disks of <sup>205</sup>Tl were manually loaded in the target holder and irradiated at 24 MeV with varying currents from 5 to 40 μA and durations of 15 min to 3 h. The optimal beam profile and transmission were determined through maximization of the ion source injection system and the beamline vertical and horizontal focusing quadrupole magnet system settings on the cyclotron. With an effective beam energy of 24 MeV, the best transmission ratio was 93% with a 10%–15% beam spill on target collimators (top/bottom and left/right). A higher beam spill was chosen to help with cooling, provide better beam spread, and avoid a pinpoint beam spot

that leads to target failure. With a pneumatic release system, irradiated target disks were loaded into lead containers and transferred for further processing. Targets were left overnight to allow for decay of short-lived isotopes, including <sup>201</sup>Pb (half-life, 9.3 h) and <sup>204m</sup>Pb (half-life, 67.2 min).

For separation of <sup>203</sup>Pb from the thallium target material, irradiated targets were dissolved in HNO<sub>3</sub> (5–7 mL, 2 M) with gentle heating to 90°C. The dissolved target was loaded onto a solid-phase extraction column (1 mL) containing an extraction resin (lead resin; Eichrom) (50 mg), which was preconditioned with water (10 mL) and HNO<sub>3</sub> (10 mL, 2 M). The solution was pushed through the column at 0.5–0.8 mL/min using a syringe or peristaltic pump. The resin was washed with additional HNO<sub>3</sub> (10 mL, 2 M) to allow maximum removal of thallium target material from the resin bed. <sup>203</sup>Pb was eluted using sodium acetate (5 mL, 1 M, pH 5.5). This elution was loaded onto a second column containing 50 mg of weak cation-exchange resin previously preconditioned with water (5 mL) and NaOAc (5 mL, 1 M, pH 5.5). The resin was washed with HCl (1 mL, 0.01 M), and <sup>203</sup>Pb was eluted as [<sup>203</sup>Pb]PbCl<sub>2</sub> using HCl (400 μL, 1 M). The fractions were analyzed with γ-ray spectroscopy. The separation scheme is shown in Figure 2.

### ICP-MS

To investigate the trace metal impurities, ICP-MS analysis (Agilent 7700x) was performed for common contaminants including thallium, iron, copper, zinc, and stable lead in the final elution. Details of sample preparation are provided in the supplemental materials.

### AMA Evaluation

AMA (GBq/μmol) was calculated by titration of [<sup>203</sup>Pb]PbCl<sub>2</sub> with DO3A chelator (Supplemental Fig. 1B). The ratio of radiolabeling

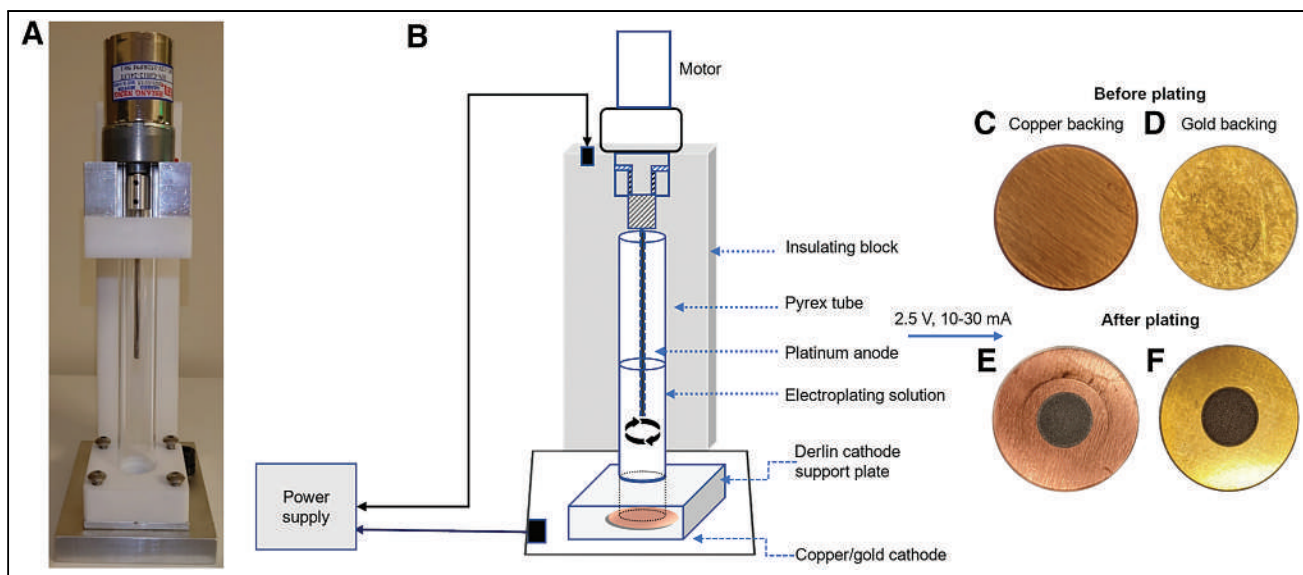


**FIGURE 1.** (A and B) Electroplating setup used for target preparation. (C–F) Copper and gold backings before (C and D) and after (E and F) electroplating.

yield (%) versus concentration of chelator ( $\log[\text{DO3A}]$  [ $\mu\text{mol}$ ]) was plotted using GraphPad Prism for the half-maximal effective concentration calculation. Results are reported as GBq (Ci)/ $\mu\text{mol}$ . Complexation was analyzed using instant thin-layer chromatography silica gel (iTLC-SG) using 50 mM ethylenediaminetetraacetic acid as the mobile phase.

#### Radiolabeling

The VMT- $\alpha$ -NET targeting conjugate (Supplemental Fig. 1B) was used for radiolabeling studies (14). Stocks were prepared in  $\text{NH}_4\text{OAc}$  (0.5 M, pH 5). Radiolabeling was performed using mass amounts from 100 to 0.5  $\mu\text{g}$  of the desired compound. Reactions were incubated for 20 min at 70°C. Instant thin-layer chromatography silica gel plates were used to confirm complexation using 50 mM ethylenediaminetetraacetic acid as the mobile phase. Results were analyzed using GraphPad Prism and reported as MBq (mCi)/mmol.

## RESULTS

### Electroplated Thallium Target Preparation

To produce  $^{203}\text{Pb}$ , thallium metal ( $^{205}\text{Tl}$ ) was used to prepare targets. Extreme toxicity, low melting point, and nonavailability

of thallium metal foils led us to explore an electroplating approach to target preparation (15,16). Electroplating conditions were optimized for electroplating periods extending from 1 to 5 h and solution pH ranging from 8 to 13. An approximately  $14.5 \pm 4$  mg/h plating rate with a plating density of 76–114 mg/cm<sup>2</sup> was achieved on a regular basis ( $n = 16$ ), and a pH of more than 12.5 was found to be most suitable for rapid deposition of thallium metal. The electroplating bath could be reused several times ( $\sim 7$ –8 reactions) with regular replenishing of target material, which eliminated the need to recycle the target material after every plating cycle. However, further investigation is required to develop a methodology for recycling the starting thallium metal. A schematic of the electroplating setup used for the plating process is shown in Figure 1. Targets were prepared on copper and gold backings.

To analyze the relationship between target density and plating time, targets were plated for 1 and 5 h. Scanning electron microscopy was performed on the electroplated targets to determine the structure and elemental composition of the target prepared. For thallium targets prepared on copper and gold backings, there were observable differences between the 1- and 5-h plating patterns in scanning electron microscopy analysis, indicating a nonuniform plating at 1 h whereas a uniform plating pattern was observed at the 5-h plating time point (Figs. 3A and 3B). However, gold backings showed uniform plating patterns at both the 1-h and the 5-h plating time points (Figs. 3D and 3E). Overall,  $75\% \pm 5\%$  of the thallium in the electroplating solution was deposited after 5 h. In addition, the percentage deposition of thallium in the final plating was found to be independent of plating time. Both gold and copper backings were observed to have approximately  $89.3\% \pm 1.6\%$  (by weight) thallium element deposited, with the remainder of the material composed of oxygen for both 1 h and 5 h as shown in the

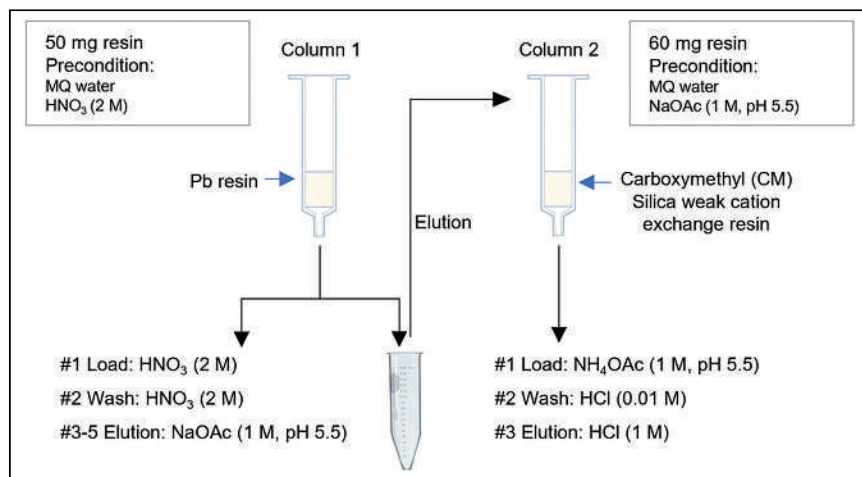


**FIGURE 2.** Separation scheme of  $^{203}\text{Pb}$  purification from thallium target material. MQ = Milli-Q (Millipore Sigma).



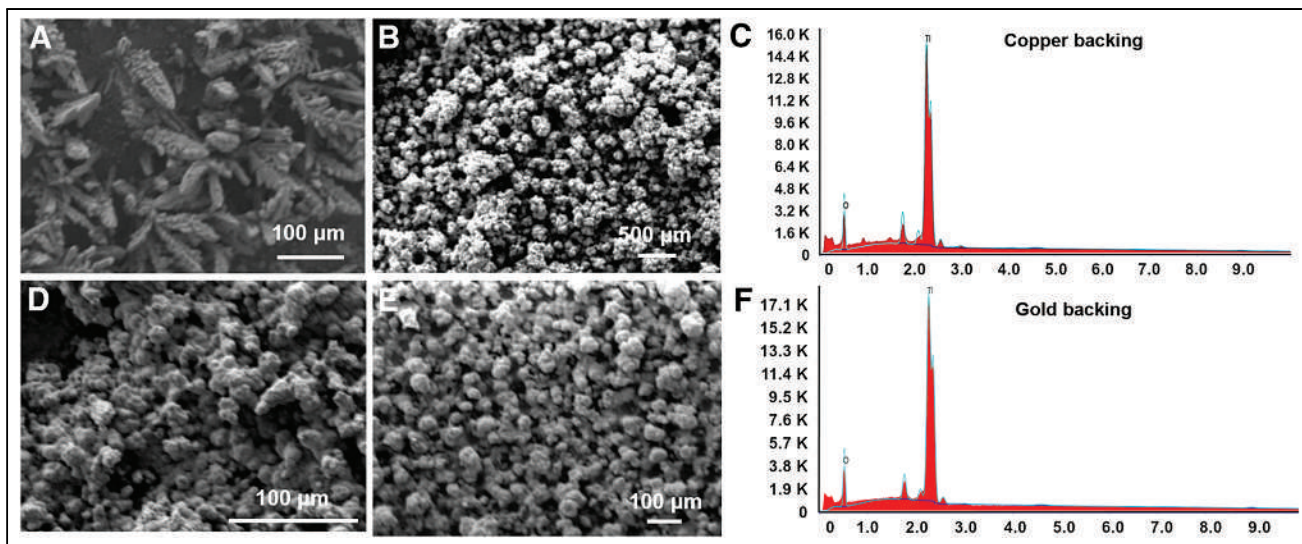


**FIGURE 3.** Representative scanning electron microscopy images of copper (top) and gold (bottom) backing. (A and B) Analysis at 1 h after plating. (D and E) Five-hour time point for copper and gold backing, respectively. (C and F) Energy-dispersive x-ray analysis spectra for both gold and copper backing, respectively.

energy-dispersive x-ray analysis spectra in Figures 3C and 3F. Since thallium has a very high propensity to oxidize (15), a significant amount of oxygen ( $10.6\% \pm 1.6\%$ ) was also observed in scanning electron microscopy analysis. No other elemental peaks were found in the energy-dispersive x-ray analysis spectra. To achieve the production of the highest-purity  $^{203}\text{Pb}$  possible, we explored the use of a 99.1% enriched  $^{205}\text{Tl}$  target material, which contained trace levels of other contaminants such as silver, zinc, boron, sodium, and silicon as described in the material's certificate of analysis (Supplemental Table 1). The elemental analysis of the plated target material by scanning electron microscopy confirmed the presence of only thallium and oxygen, suggesting that high-purity  $^{205}\text{Tl}$  targets are achievable if electroplating is used.

#### Target Irradiation and Purification of $^{203}\text{Pb}$

The complete separation scheme of  $^{203}\text{Pb}$  from thallium target material is as shown in Figure 4. We observed negligible ( $<2\%$ ) lead isotopes in the eluate and nitric acid wash, whereas the lead isotopes were eluted in NaOAc buffer (5 mL, 1 M, pH 5.5) in the first column. During optimization of the separation procedures, we observed inconsistency in the chemical behavior of  $^{203}\text{Pb}$  when stored in NaOAc for a longer period, which was most likely due to its hydrolyzation at this pH. In addition, to achieve more than 95% elution of  $^{203}\text{Pb}$ , a large volume of NaOAc buffer (5–6 mL) was required. Therefore, concentration and purification of the elution from buffer to a more suitable labeling concentration was required. To address these challenges, a second column was used to further purify the  $^{203}\text{Pb}$ . Final elution of  $^{203}\text{Pb}$  separation from the enriched thallium target ( $^{205}\text{Tl}$ ) was achieved in a small fraction of HCl ( $\sim 400\ \mu\text{L}$ , 1 M), with average recovery yields of  $92.3\% \pm 3.5\%$  ( $n = 3$ ). At the end of processing,  $4,477 \pm 444\ \text{MBq}$  ( $121 \pm 12\ \text{mCi}$ )  $^{203}\text{Pb}$  was obtained in the final elution (decay corrected to end of bombardment). The isotopic composition of the final elution product was found to be  $^{203}\text{Pb}$  ( $>99.5\%$ ) and  $^{201}\text{Pb}$  ( $<0.5\%$ ) as analyzed by  $\gamma$ -ray spectroscopy. The average production yields of  $32.9 \pm 6.3\ \text{MBq}/\mu\text{A}\cdot\text{h}$  ( $0.9 \pm 0.2\ \text{mCi}/\mu\text{A}\cdot\text{h}$ ) were achieved with a  $98 \pm 16\ \text{mg}$  target.

Our separation method required about 1 h from column loading to elution from the second column, with a very small final volume ( $<400\ \mu\text{L}$ ) and more than a 95% recovery yield.

#### ICP-MS

ICP-MS analysis was performed to further quantify the separation method and determine the presence of trace metal contamination. Results were compared for enriched  $^{205}\text{Tl}$  targets for copper and gold backings as shown in Table 2. The method developed indicated a good separation, with only a small amount of thallium

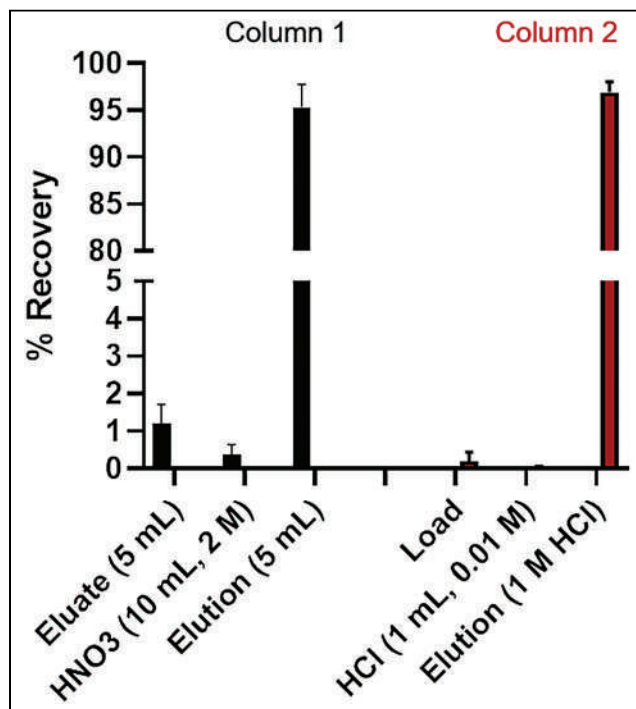


**FIGURE 4.** Separation results for column 1 and column 2, with percentage recovery of  $^{203}\text{Pb}$  ( $n = 3$ , enriched target material  $^{205}\text{Tl}$ ).

**TABLE 2**  
ICP-MS Results of Final  $^{203}\text{Pb}$  Elution to Determine Metal Contaminants

Backing	Target	Iron	Copper	Zinc	Thallium	Lead
Copper	$^{205}\text{Tl}$	$0.01 \pm 0.01$	$0.40 \pm 0.48$	$0.09 \pm 0.05$	$0.22 \pm 0.38$	$0.16 \pm 0.06$
Gold	$^{205}\text{Tl}$	$0.01 \pm 0.00$	$0.01 \pm 0.01$	$0.19 \pm 0.08$	Below LOD	$0.20 \pm 0.08$

LOD = limit of detection.  
Data are micrograms for final elution fraction of 400  $\mu\text{L}$ .

( $550 \pm 950$  ppb or  $0.2 \pm 0.4$   $\mu\text{g}$ ) and lead ( $400 \pm 150$  ppb or  $0.2 \pm 0.1$   $\mu\text{g}$ ) in the final 400  $\mu\text{L}$  elution fraction. Significant SDs were observed in the reported results and are likely due to process variabilities in different batches.

During optimization of the separation method for  $^{203}\text{Pb}$ , practical steps were taken to minimize the amount of residual trace metal contaminants in the product solution to improve the overall molar activity. For example, stable lead contamination is one of the primary concerns due to abundance of lead bricks in radiochemistry facilities. Therefore, the working station lead bricks were covered to reduce the amount of nonradioactive lead in the final elution and significantly reduced this contaminant. For copper backings, we found milligram amounts of copper in the dissolved target coming from dissolution of the backing in the  $\text{HNO}_3$ , whereas switching to a gold target material alleviated this issue as indicated in Supplemental Table 2. The extraction resin is highly selective for lead isotopes in 2 M  $\text{HNO}_3$ , which was confirmed during the separation because minimum breakthrough of lead (<2%) was observed in the flowthrough and the first wash of nitric acid as shown in Supplemental Table 3.

The molar activity of the final elution was also calculated using ICP-MS, and the average specific activity was about 5  $\text{TBq}/\mu\text{mol}$  ( $4,745 \pm 2,657$   $\text{TBq/g}$ ) for an average batch size of  $7.5 \pm 1.4$   $\text{GBq/mL}$  ( $202.5 \pm 38.7$   $\text{mCi/mL}$ ).

#### AMA Evaluation

To determine the AMA, the DO3A chelator was used for titration analysis. Figure 5B represents the instant thin-layer chromatography graph for radiolabeled DO3A. AMA was calculated using the amount of radiolabeled versus free radioisotope. The average AMA (Fig. 6) was  $37.7 \pm 5.4$   $\text{GBq}/\mu\text{mol}$  ( $1.1 \pm 0.1$   $\text{Ci}/\mu\text{mol}$ ) ( $n = 3$ ).

#### Radiolabeling Studies

Radiolabeling studies were optimized for the VMT- $\alpha$ -NET targeting conjugate, and a molar activity of  $40.6 \pm 11$   $\text{GBq}/\mu\text{mol}$

( $1.1 \pm 0.3$   $\text{Ci}/\mu\text{mol}$ ) was achieved, indicating a high molar activity of  $^{203}\text{Pb}$ . A representative instant thin-layer chromatography silica gel graph illustrating the radiolabeled [ $^{203}\text{Pb}$ ]Pb-VMT- $\alpha$ -NET is shown in Figure 5C. It was important to understand whether the final product remained stable with similar radiolabeling yields over time. Thus, radiolabeling studies were performed for 2 consecutive days, and no changes in labeling efficiency were observed in the final product.

#### DISCUSSION

This work represents a method of production and separation of  $^{203}\text{Pb}$  using an enriched  $^{205}\text{Tl}$  reaction route and electrochemistry for target preparation. Thallium metal has a very low melting point, which was initially a concern during targetry optimization. Electroplating of targets from dissolved  $\text{Tl}_2\text{O}_3$  was determined to be the preferred route. Targets were manufactured that could withstand irradiation times of up to 4 h and currents of 40  $\mu\text{A}$  when irradiated with a 24-MeV incident beam energy without melting. In addition, the electroplated target enabled irradiation at 24-MeV proton incident energy without any degradation, which was not feasible with a powder target.

Irradiated targets resulted in suitable yields with a small amount of target material (<100 mg). However, the plated targets were peeling off when plating density exceeded  $150$   $\text{mg}/\text{mm}^2$ , and no consistent plating results were observed above this density. Therefore, for routine production, the plating density was kept below  $150$   $\text{mg}/\text{mm}^2$ .

The cross section for  $^{203}\text{Pb}$  production via the  $^{205}\text{Tl}(p,3n)^{203}\text{Pb}$  reaction route is a maximum at 26 MeV ( $\sigma = 1,244$  mb), indicating that a 30-MeV cyclotron could produce higher yields. However, a significant amount of the high cross section could be captured with a TR-24 cyclotron. With enriched thallium target material, production yields were significantly higher ( $32.9 \pm 4.1$   $\text{MBq}/\mu\text{A-h}$  [ $0.9 \pm 0.1$   $\text{mCi}/\mu\text{A-h}$ ]) than previously published

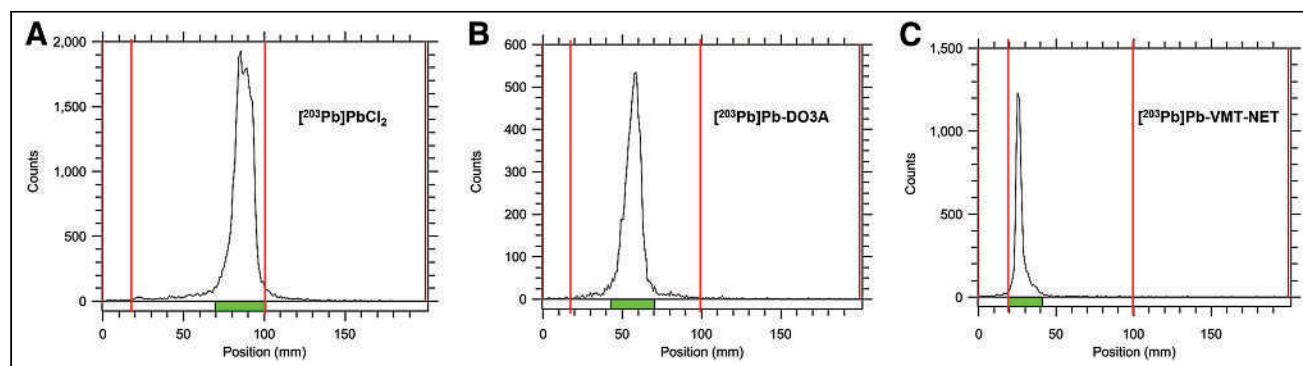


**FIGURE 5.** Instant thin-layer chromatography silica gel graph for unlabeled [ $^{203}\text{Pb}$ ]PbCl<sub>2</sub> (A), [ $^{203}\text{Pb}$ ]Pb-DO3A (B), and [ $^{203}\text{Pb}$ ]Pb-VMT-NET (C).

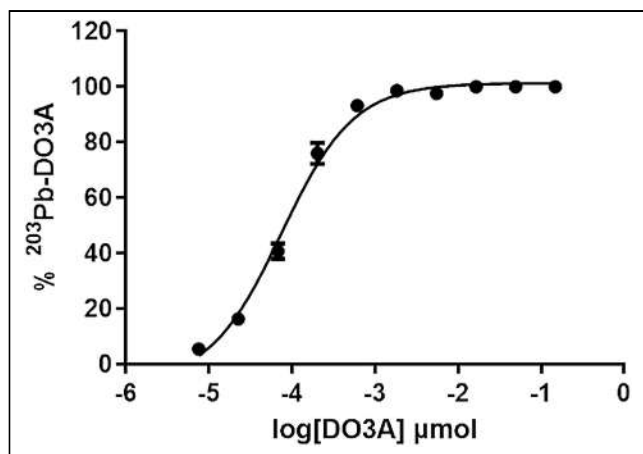


FIGURE 6. Representative AMA measurement for  $^{203}\text{Pb}$ Pb-DO3A ( $n = 3$ ).

production routes for  $^{203}\text{Tl}(d,2n)^{203}\text{Pb}$  (5.8 MBq/ $\mu\text{A}\cdot\text{h}$  [0.2 mCi/ $\mu\text{A}\cdot\text{h}$ ]) (17) and  $^{203}\text{Tl}(p,n)^{203}\text{Pb}$  (6.3 MBq/ $\mu\text{A}\cdot\text{h}$  [0.2 mCi/ $\mu\text{A}\cdot\text{h}$ ]) (11). Theoretic production yields were calculated to be 38.1 MBq/ $\mu\text{A}\cdot\text{h}$  (1.03 mCi/ $\mu\text{A}\cdot\text{h}$ ) for a 100-mg enriched target material with 24-MeV incident beam energy. The experimentally measured results ( $32.9 \pm 4.1$  MBq/ $\mu\text{A}\cdot\text{h}$  [ $0.9 \pm 0.1$  mCi/ $\mu\text{A}\cdot\text{h}$ ] [ $n = 3$ ]) were in close agreement with the theoretically predicted numbers for 24-MeV incident proton beam energy.

Isolation and purification of  $^{203}\text{Pb}$  from the postirradiation dissolved target using extraction resin chromatography were accomplished using a straightforward method that achieved high recovery yields after separation of more than 95% in the final elution. A small loading volume and controlled flow rate of 0.5 mL/min throughout the separation helped to minimize breakthrough of  $^{203}\text{Pb}$  in the loading and washing steps. A second column using weak cation-exchange resin was used to further concentrate and purify  $^{203}\text{Pb}$  from any residual Tl or trace metal contaminants and also enabled the final elution in a 400- $\mu\text{L}$  volume. These methods have been tested with up to 3 GBq (80 mCi) of  $^{203}\text{Pb}$ , confirming the successful separation. Previous work by Garmestani et al. (17) established separation methods for  $^{203}\text{Pb}$  using the  $^{203}\text{Tl}(d,2n)^{203}\text{Pb}$  reaction route. However, large elution volumes required additional drying steps resulting in production yields of 2.1 MBq/ $\mu\text{A}\cdot\text{h}$  (0.1 mCi/ $\mu\text{A}\cdot\text{h}$ ) for natural and 7.5 MBq/ $\mu\text{A}\cdot\text{h}$  (0.2 mCi/ $\mu\text{A}\cdot\text{h}$ ) for approximately 250-mg enriched  $^{203}\text{Tl}$  targets (17). Recent work by McNeil et al. (11) found a successful production method for  $^{203}\text{Pb}$  using  $^{nat}\text{Tl}$  and  $^{203}\text{Tl}$  targets. Although the separation yield was reported to be  $73.8\% \pm 2.1\%$ , a significant amount of  $^{203}\text{Pb}$  was lost in the initial load ( $8.7 \pm 0.3\%$ ) and wash ( $\sim 5\%$ ) steps (11). Recently, Nelson et al. (18) developed a production and separation method using  $^{205}\text{Tl}$  as a target material. Their separation method resulted in more than 83% recovery of  $^{203}\text{Pb}$  as  $^{203}\text{Pb}$ PbCl<sub>2</sub> in a 4-mL final volume in less than 4 h with production yields of 23.3 MBq/ $\mu\text{A}\cdot\text{h}$  (0.6 mCi/ $\mu\text{A}\cdot\text{h}$ ) using a 250-mg powder target (18). Previous studies reported in the literature also worked with a high amount of starting material—between 250 mg and 4 g (11,18,19). Comparing our results with previous literature, we optimized an electroplating method to produce  $^{203}\text{Pb}$  for fast and consistent results with a small amount of starting material ( $\sim 100$  mg).

Separation of  $^{203}\text{Pb}$  from enriched  $^{205}\text{Tl}$  using the extraction resin is very specific to lead, with minimum breakthrough in the initial load and wash (Supplemental Table 3 for complete separation).

The target material was dissolved in HNO<sub>3</sub> (5 mL, 2 M) at a temperature of 90°C and loaded on an extraction resin column. Overall, a very small amount of radioactive waste was generated while keeping the load and wash volumes small.

Gold coins were tested because of high amounts of measured copper ( $\sim$ tens of milligrams) in the dissolved target solution when using copper backings. Such high amounts of copper could make it difficult to recycle the enriched target material in the future and introduce a possibility for contamination in the final  $^{203}\text{Pb}$  elution. In addition to cold contaminants, the copper backing produces  $\gamma$ -ray emitting zinc isotopes (such as  $^{65}\text{Zn}$ ; half-life, 244 d), exposing personnel to potentially higher doses after bombardments. At the current bombardment angle, most of the 24-MeV incident energy is stopped on the copper backing, resulting in long-lived Zn radioisotopes emitting high-energy photons. Comparatively, gold is resistant to dissolution under harsh acid conditions with better heat conductivity. In addition, proton irradiation of gold backing produces mercury isotopes such as  $^{197\text{m}}\text{Hg}$  (23.8 h [133 keV (intensity of  $\gamma$ -rays ( $I_\gamma$ ), 33.5%), 279 keV ( $I_\gamma$ , 6%)],  $^{197\text{g}}\text{Hg}$  (64 h [77 keV ( $I_\gamma$ , 18.7%)]),  $^{195\text{m}}\text{Hg}$  (41.6 h [261 keV ( $I_\gamma$ , 31%), 387.8 keV ( $I_\gamma$ , 2.18%), 560 keV ( $I_\gamma$ , 7.1%)]), and  $^{195\text{g}}\text{Hg}$  (10.5 h [180 keV ( $I_\gamma$ , 1.9%), 207 keV ( $I_\gamma$ , 1.6%), 261 keV ( $I_\gamma$ , 1.6%), and 585 keV ( $I_\gamma$ , 2%)]). Although these radiocontaminants have a small cross section for energy below 20 MeV, these are relatively short-lived, implying that the gold backing could be reused after a significantly shorter decay time than for a copper backing (the contaminant with the longest half-life is  $^{65}\text{Zn}$ : 244 d [1.12 MeV ( $I_\gamma$ , 50%)]), making gold ideal as a backing material.

To compare the difference between electroplated thallium targets using gold and copper backings, high-purity germanium spectra (Supplemental Fig. 2) and ICP-MS analysis (Table 2) results were compared for the dissolved thallium target. ICP-MS analysis from previous studies by McNeil et al. (11) indicated  $1.5 \pm 0.7$   $\mu\text{g}$  of stable lead and  $175 \pm 105$   $\mu\text{g}$  of thallium in the final elution. Higher amounts of trace metal contaminants, specifically stable lead, can affect the molar activity of  $^{203}\text{Pb}$ . Our separation resulted in  $0.2 \pm 0.1$   $\mu\text{g}$  of stable lead in a 400- $\mu\text{L}$  final volume, yielding a high molar activity of  $4,745 \pm 2,657$  TBq/g ( $\sim 5$  TBq/ $\mu\text{mol}$ ) ( $n = 3$ ). Previous reports of specific activity range include 52 TBq/g (32 GBq/ $\mu\text{mol}$ ) by McNeil et al. (calculated on the basis of the data provided) (11),  $405 \pm 108$  TBq/g by Li et al. (19), and 4,150 TBq/g (2.1 TBq/ $\mu\text{mol}$ ) by Nelson et al. (18). Using ICP-MS, molar activity of 266.4 MBq/ $\mu\text{mol}$  (7.2 mCi/ $\mu\text{mol}$ ) was reported by Máthé et al. (20) and 15 MBq/ $\mu\text{mol}$  (0.4 mCi/ $\mu\text{mol}$ ) by Yao et al. (21), compared with a molar activity of about 5 TBq/ $\mu\text{mol}$  reported in the present study.

The molar activity numbers were not close to the theoretic specific activity of  $1.1 \times 10^5$  TBq/g ( $3 \times 10^6$  Ci/g), but the numbers reported in this work are the highest yet reported to our knowledge. It is also worth mentioning that the molar activity calculations were performed for small batch sizes of about 3.7 GBq ( $\sim 100$  mCi), and we anticipate improvement in these numbers as the batch size increases. AMA was also analyzed using a titration analysis with DO3A chelator, yielding a result of  $37.7 \pm 5.4$  GBq/ $\mu\text{mol}$  ( $1.1 \pm 0.1$  Ci/ $\mu\text{mol}$ ).

## CONCLUSION

This project aimed to develop a robust target preparation method for production of high-specific-activity  $^{203}\text{Pb}$  via proton irradiation and an accompanying separation method to address the high demand for  $^{203}\text{Pb}$  as an imaging-compatible surrogate for

the in vivo  $\alpha$ -particle generator  $^{212}\text{Pb}$ . With a suitable half-life (51.8 h), large production batches could be shipped to a large geographic area to fulfill the needs for preclinical and clinical studies. We established a production method using enriched  $^{205}\text{Tl}$  and electroplated targets that can withstand beam currents of up to 40  $\mu\text{A}$ . With a 3-h irradiation, an average production yield of  $4.6 \pm 0.43$  GBq ( $126 \pm 11.8$  mCi) was obtained. The separation method for  $^{203}\text{Pb}$  was developed, and more than 95% overall separation yields were achieved in less than a 400- $\mu\text{L}$  final volume, indicating a robust separation method. A standard operating procedure was also optimized for determining the AMA using DO3A chelator, and a high molar activity of about 37 GBq/ $\mu\text{mol}$  (1 Ci/ $\mu\text{mol}$ ) was routinely achieved.

## DISCLOSURE

This work was supported by the Department of Energy isotope program through grant DESC0020197 (principal investigator, Suzanne Lapi). This work was also supported in part by Viewpoint Molecular Targeting, now Perspective Therapeutics, of which Nicholas Baumhover and Michael Schultz are employees. No other potential conflict of interest relevant to this article was reported.

## KEY POINTS

**QUESTION:** Is it feasible to produce significant amounts of  $^{203}\text{Pb}$  with high molar activity using enriched  $^{205}\text{Tl}$  target material?

**PERTINENT FINDINGS:** An electroplating method was developed to prepare target material ( $^{205}\text{Tl}$ ) that could withstand a 24-MeV incident beam and high current without using a degrader. A separation method was developed to achieve approximately 95% recovery yields of  $^{203}\text{Pb}$  with a processing time of less than 1.5 h.  $^{203}\text{Pb}$  production batches of 9.2 GBq/mL were achieved using a small amount of target material.

**IMPLICATIONS FOR PATIENT CARE:** This work addresses a shortage in the availability of the theranostic matched pair  $^{203}\text{Pb}/^{212}\text{Pb}$  for clinical applications.

## REFERENCES

- Funkhouser J. Reinventing pharma: the theranostic revolution. *Curr Drug Discov*. 2002;2:17–19.
- Gomes Marin JF, Nunes RF, Coutinho AM, et al. Theranostics in nuclear medicine: emerging and re-emerging integrated imaging and therapies in the era of precision oncology. *Radiographics*. 2020;40:1715–1740.
- Elgqvist J, Frost S, Pouget J-P, Albertsson P. The potential and hurdles of targeted alpha therapy: clinical trials and beyond. *Front Oncol*. 2014;3:324.
- FDA approves new diagnostic imaging agent to detect rare neuroendocrine tumors. News release. U.S. Food and Drug Administration; June 1, 2016
- Raedler LA. Lutathera (Lutetium Lu 177 Dotatate) First Radioactive Drug Approved for Gastroenteropancreatic Neuroendocrine Tumors. *J Oncol Navig Surviv*. 2019;9:37–39.
- Fani M, Braun F, Waser B, et al. Unexpected sensitivity of sst2 antagonists to N-terminal radiometal modifications. *J Nucl Med*. 2012;53:1481–1489.
- Fani M, Del Pozzo L, Abiraj K, et al. PET of somatostatin receptor-positive tumors using  $^{64}\text{Cu}$ - and  $^{68}\text{Ga}$ -somatostatin antagonists: the chelate makes the difference. *J Nucl Med*. 2011;52:1110–1118.
- Horlock P, Thakur M, Watson I. Cyclotron produced lead-203. *Postgrad Med J*. 1975;51:751–754.
- Kratochwil C, Giesel FL, Stefanova M, et al. PSMA-targeted radionuclide therapy of metastatic castration-resistant prostate cancer with  $^{177}\text{Lu}$ -labeled PSMA-617. *J Nucl Med*. 2016;57:1170–1176.
- Kratochwil C, Bruchertseifer F, Giesel FL, et al.  $^{225}\text{Ac}$ -PSMA-617 for PSMA-targeted  $\alpha$ -radiation therapy of metastatic castration-resistant prostate cancer. *J Nucl Med*. 2016;57:1941–1944.
- McNeil BL, Robertson AK, Fu W, et al. Production, purification, and radiolabeling of the  $^{203}\text{Pb}/^{212}\text{Pb}$  theranostic pair. *EJNMMI Radiopharm Chem*. 2021;6:6.
- Suparman I. Proposal on “standardized high current solid targets for cyclotron production of diagnostic and therapeutic radionuclides.” In: *Research Co-ordination Meeting of the Co-ordinated Research Project on Standardized High Current Solid Targets for Cyclotron Production of Diagnostic and Therapeutic Radionuclides*. International Atomic Energy Agency; 2000:52–53.
- Queern SL, Aweda TA, Massicano AVF, et al. Production of Zr-89 using sputtered yttrium coin targets. *Nucl Med Biol*. 2017;50:11–16.
- Li M, Baumhover NJ, Liu D, et al. Preclinical evaluation of a lead specific chelator (PSC) conjugated to radiopeptides for  $^{203}\text{Pb}$  and  $^{212}\text{Pb}$ -based theranostics. *Pharmaceutics*. 2023;15:414.
- Zou Y, Cheng H, Wang H, et al. Thallium (I) oxidation by permanganate and chlorine: kinetics and manganese dioxide catalysis. *Environ Sci Technol*. 2020;54:7205–7216.
- Keith L, Telliard W. ES&T special report: priority pollutants—la perspective view. *Environ Sci Technol*. 1979;13:416–423.
- Garmestani K, Milenic DE, Brady ED, Plascjak PS, Brechbiel MW. Purification of cyclotron-produced  $^{203}\text{Pb}$  for labeling Herceptin. *Nucl Med Biol*. 2005;32:301–305.
- Nelson BJ, Wilson J, Schultz MK, Andersson JD, Wuest F. High-yield cyclotron production of  $^{203}\text{Pb}$  using a sealed  $^{205}\text{Tl}$  solid target. *Nucl Med Biol*. 2023;Jan–Feb:108314.
- Li M, Sagastume EA, Lee D, et al.  $^{203}/^{212}\text{Pb}$  theranostic radiopharmaceuticals for image-guided radionuclide therapy for cancer. *Curr Med Chem*. 2020;27:7003–7031.
- Máthé D, Szigeti K, Hegedűs N, et al. Production and in vivo imaging of  $^{203}\text{Pb}$  as a surrogate isotope for in vivo  $^{212}\text{Pb}$  internal absorbed dose studies. *Appl Radiat Isot*. 2016;114:1–6.
- Yao Z, Garmestani K, Wong KJ, et al. Comparative cellular catabolism and retention of astatine-, bismuth-, and lead-radiolabeled internalizing monoclonal antibody. *J Nucl Med*. 2001;42:1538–1544.
- Yong K, Brechbiel MW. Towards translation of  $^{212}\text{Pb}$  as a clinical therapeutic; getting the lead in! *Dalton Trans*. 2011;40:6068–6076.
- Cutler CS, Hennkens HM, Sisay N, Huclier-Markai S, Jurisson SS. Radiometals for combined imaging and therapy. *Chem Rev*. 2013;113:858–883.
- Smith NA, Bowers DL, Eht DA. The production, separation, and use of  $^{67}\text{Cu}$  for radioimmunotherapy: a review. *Appl Radiat Isot*. 2012;70:2377–2383.
- Reischl G, Rösch F, Machulla H-J. Electrochemical separation and purification of yttrium-86. *Radiochim Acta*. 2002;90:225–228.
- Geschwind JFH, Salem R, Carr BI, et al. Yttrium-90 microspheres for the treatment of hepatocellular carcinoma. *Gastroenterology*. 2004;127(suppl 1):S194–S205.
- Koehler L, Gagnon K, McQuarrie S, Wuest F. Iodine-124: a promising positron emitter for organic PET chemistry. *Molecules*. 2010;15:2686–2718.
- Kayano D, Kinuya S. Current consensus on I-131 MIBG therapy. *Nucl Med Mol Imaging*. 2018;52:254–265.
- Lehenberger S, Barkhausen C, Cohrs S, et al. The low-energy  $\beta^-$  and electron emitter  $^{161}\text{Tb}$  as an alternative to  $^{177}\text{Lu}$  for targeted radionuclide therapy. *Nucl Med Biol*. 2011;38:917–924.
- Baum RP, Singh A, Benešová M, et al. Clinical evaluation of the radiolanthanide terbium-152: first-in-human PET/CT with  $^{152}\text{Tb}$ -DOTATOC. *Dalton Trans*. 2017;46:14638–14646.
- Carzaniga TS, Auger M, Braccini S, et al. Measurement of  $^{43}\text{Sc}$  and  $^{44}\text{Sc}$  production cross-section with an 18 MeV medical PET cyclotron. *Appl Radiat Isot*. 2017;129:96–102.
- Rösch F, Baum RP. Generator-based PET radiopharmaceuticals for molecular imaging of tumours: on the way to THERANOSTICS. *Dalton Trans*. 2011;40:6104–6111.
- Singh A, van der Meulen NP, Müller C, et al. First-in-human PET/CT imaging of metastatic neuroendocrine neoplasms with cyclotron-produced  $^{44}\text{Sc}$ -DOTATOC: a proof-of-concept study. *Cancer Biother Radiopharm*. 2017;32:124–132.
- Mamtimin M, Harmon F, Starovoitova VN. Sc-47 production from titanium targets using electron linacs. *Appl Radiat Isot*. 2015;102:1–4.
- Domnanich KA, Eichler R, Müller C, et al. Production and separation of  $^{43}\text{Sc}$  for radiopharmaceutical purposes. *EJNMMI Radiopharm Chem*. 2017;2:14.

---

---

# Biostatistical Estimation of Tau Threshold Hallmarks (BETTH) Algorithm for Human Tau PET Imaging Studies

Alexandra Gogola<sup>1</sup>, Brian J. Lopresti<sup>1</sup>, Dana Tudorascu<sup>2</sup>, Beth Snitz<sup>3</sup>, Davneet Minhas<sup>1</sup>, Vincent Doré<sup>4,5</sup>, Milos D. Ikonovic<sup>3,6</sup>, C. Elizabeth Shaaban<sup>7</sup>, Cristy Matan<sup>1</sup>, Pierrick Bourgeat<sup>5</sup>, N. Scott Mason<sup>1</sup>, Howard Aizenstein<sup>2</sup>, Chester A. Mathis<sup>1</sup>, William E. Klunk<sup>2</sup>, Christopher C. Rowe<sup>4</sup>, Oscar L. Lopez<sup>3</sup>, Ann D. Cohen<sup>2</sup>, and Victor L. Villemagne<sup>2,4</sup> for the Alzheimer's Disease Neuroimaging Initiative

<sup>1</sup>Department of Radiology, University of Pittsburgh, Pittsburgh, Pennsylvania; <sup>2</sup>Department of Psychiatry, University of Pittsburgh, Pittsburgh, Pennsylvania; <sup>3</sup>Department of Neurology, University of Pittsburgh, Pittsburgh, Pennsylvania; <sup>4</sup>Department of Molecular Imaging and Therapy, Austin Health, Melbourne, Victoria, Australia; <sup>5</sup>Health and Biosecurity, Commonwealth Scientific and Industrial Research Organisation, Melbourne, Victoria, Australia; <sup>6</sup>Geriatric Research Education and Clinical Center, Veterans Affairs Pittsburgh Healthcare System, Pittsburgh, Pennsylvania; and <sup>7</sup>Department of Epidemiology, University of Pittsburgh, Pittsburgh, Pennsylvania

---

A methodology for determining tau PET thresholds is needed to confidently detect early tau deposition. We compared multiple threshold-determining methods in participants who underwent either <sup>18</sup>F-flortaucipir or <sup>18</sup>F-MK-6240 PET scans. **Methods:** <sup>18</sup>F-flortaucipir ( $n = 798$ ) and <sup>18</sup>F-MK-6240 ( $n = 216$ ) scans were processed and sampled to obtain regional SUV ratios. Subsamples of the cohorts were based on participant diagnosis, age, amyloid- $\beta$  status (positive or negative), and neurodegeneration status (positive or negative), creating older-adult (age  $\geq 55$  y) cognitively unimpaired (amyloid- $\beta$ -negative, neurodegeneration-negative) and cognitively impaired (mild cognitive impairment/Alzheimer disease, amyloid- $\beta$ -positive, neurodegeneration-positive) groups, and then were further subsampled via matching to reduce significant differences in diagnostic prevalence, age, and Mini-Mental State Examination score. We used the biostatistical estimation of tau threshold hallmarks (BETTH) algorithm to determine sensitivity and specificity in 6 composite regions. **Results:** Parametric double receiver operating characteristic analysis yielded the greatest joint sensitivity in 5 of the 6 regions, whereas hierarchic clustering, gaussian mixture modeling, and k-means clustering all yielded perfect joint specificity (2.00) in all regions. **Conclusion:** When <sup>18</sup>F-flortaucipir and <sup>18</sup>F-MK-6240 are used, Alzheimer disease-related tau status is best assessed using 2 thresholds, a sensitivity one based on parametric double receiver operating characteristic analysis and a specificity one based on gaussian mixture modeling, delimiting an uncertainty zone indicating participants who may require further evaluation.

**Key Words:** tau; PET; Alzheimer disease; <sup>18</sup>F-flortaucipir; <sup>18</sup>F-MK-6240

**J Nucl Med 2023; 64:1798–1805**

DOI: 10.2967/jnumed.123.265941

---

**A**lzheimer disease (AD) pathology, characterized by amyloid- $\beta$  ( $A\beta$ ) and hyperphosphorylated tau aggregation, starts accumulating decades before the onset of the clinical dementia phenotype (*1*). The

development of imaging and fluid biomarkers has facilitated noninvasive detection and disease progression monitoring. Additionally, such biomarkers have proven useful for predicting clinical progression and the risk of cognitive decline, as well as for determining inclusion, target engagement, and outcome measures in clinical trials.

The  $A\beta$  (A), tau (T), and neurodegeneration (N) framework was developed to take advantage of these available imaging and fluid biomarkers and dichotomize them (as positive [+ ] or negative [– ]) to discriminate between non-AD and AD continuum participants (*2*). The establishment of biomarker thresholds depends on the clinical or research question posed, which may benefit from a threshold that favors sensitivity or specificity. For example, if the research question aims at detecting early cortical tau deposition, it would be preferable to adopt a more sensitive threshold. On the other hand, if, for example, there is an antitau therapeutic trial, a more specific threshold would be preferable to ascertain robust levels of cortical tau to evaluate both target engagement and treatment efficacy. Previous work has defined biomarker thresholds for classifying cases as A+ or A– and as N+ or N–, examples of which include dichotomizing neuroimaging measures or cerebral spinal fluid or plasma measures of  $A\beta$  and either glucose metabolism or cortical thickness, respectively (*3*).

Although tau accumulation is associated with short-term clinical progression and cognitive decline rate in A+ individuals (*4,5*), a consensus method for tau threshold determination remains elusive (*6*). Another important aspect to consider is that clinical studies use many different tau PET tracers, which vary in degree of nonspecific binding, off-target binding, dynamic range, and kinetic behavior (*7*). These tau tracers include <sup>18</sup>F-flortaucipir (Tauvid [Eli Lilly and Co.], previously known as <sup>18</sup>F-AV-1451 and <sup>18</sup>F-T807) (*8*), <sup>18</sup>F-MK-6240 (*9*), <sup>18</sup>F-THK-5317, <sup>18</sup>F-THK-5351, <sup>11</sup>C-PBB3, <sup>18</sup>F-RO-948, <sup>18</sup>F-PI-2620, <sup>18</sup>F-GTP1, and <sup>18</sup>F-PM-PBB3 (*7*). This diversity complicates imaging result interpretation, tau load measure comparison, and tau PET signal standardization for determining tau status.

There are several potential methods for determining the appropriate tau PET threshold: cluster analysis, receiver operating characteristic (ROC) analysis, iterative outlier detection,  $z$  scores (as with CenTauR <sub>$z$</sub>  (*10*)), gaussian mixture modeling, and control group percentiles (*3,11*). Although it would be ideal to establish a single tau status threshold based on a universal tau load scale, as with centiloids for  $A\beta$  (*12*), there have been few head-to-head studies of tau tracers on which to base such a scale (*13,14*). One proposed

---

Received Apr. 26, 2023; revision accepted Aug. 3, 2023.

For correspondence or reprints, contact Alexandra Gogola (alexandra.gogola@pitt.edu).

Published online Sep. 14, 2023.

COPYRIGHT © 2023 by the Society of Nuclear Medicine and Molecular Imaging.



scale, termed CenTauR (10), defines a universal mask for sampling across tracers and a method for standardizing tau load indices to a common scale. Until a universal scale is adopted, it may be best to establish a methodology for tau threshold determination.

Varying regional sampling strategies have been used to identify pathologic tau accumulation considering the various tau pathologic phenotypes and tracer-specific off-target binding patterns. Previously suggested regions involve combinations of the entorhinal, parahippocampal, middle and inferior temporal, lateral occipital, fusiform, supramarginal gyrus, and inferior parietal regions as well as the amygdala and banks of the superior temporal sulcus (3,15,16). One proposed composite region, based on its being a locus of early AD-related tau deposition, even in the absence of A $\beta$  (17), is the mesial temporal lobe, which comprises the entorhinal, parahippocampal, fusiform, and amygdala regions. Because mesial temporal lobe tau deposition is associated with primary age-related tauopathy (18), a common pathology in older adults, other composite regions have been proposed that may be more specific for early AD-related tau deposition. One example, the meta temporal region proposed by Jack et al. (2), combines the mesial temporal lobe subregions with the middle and inferior temporal gyri.

The present work describes the biostatistical estimation of tau threshold hallmarks (BETTH) algorithm: our examination of different biostatistical approaches to establish tau thresholds for the 2 most widely used tau agents, <sup>18</sup>F-flortaucipir and <sup>18</sup>F-MK-6240, as tested in 6 composite regions and against clinically diagnosed test cases with the goal of identifying the threshold-determining methods that yield the greatest regional sensitivity and specificity for early AD-related tau deposition. Specifically, we aim at potentially detecting cortical tau deposition at the pre-symptomatic stages of the disease.

## MATERIALS AND METHODS

### Human Participants

This study was approved by the Institutional Review Boards of all participating institutions. Informed written consent was obtained from all participants at each site.

The <sup>18</sup>F-flortaucipir data used in the preparation of this article were obtained from the Alzheimer's Disease Neuroimaging Initiative (ADNI) database (<https://adni.loni.usc.edu/>). This dataset was collected by 42 participating sites using 30 different PET scanner models (19). The identification numbers of the ADNI participants can be found in Supplemental Table 1 (supplemental materials are available at <http://jnm.snmjournals.org>). The <sup>18</sup>F-MK-6240 dataset was acquired from Cerveau Technologies, Inc., and collected by 4 participating sites using 2 PET scanner models.

All participants were at least 55 y old; underwent <sup>18</sup>F-flortaucipir or <sup>18</sup>F-MK-6240 tau PET, A $\beta$  PET, structural T1 MRI, and cognitive testing; and received a consensus clinical diagnosis. For the <sup>18</sup>F-flortaucipir cohort, A $\beta$  load was reported in centiloids and A $\beta$  status was determined with a cutoff of 20 centiloids for optimal sensitivity (20). For the <sup>18</sup>F-MK-6240 cohort, categoric A $\beta$  status (A+ or A-) was reported by each participating site. For all participants, neurodegeneration status was

determined using MRI-based composite cortical thickness measures (CT composite) applying a cutoff of 2.7 mm for optimal sensitivity (3). Cognition was reported as the Mini-Mental State Examination score, and clinical diagnosis was reported as normal cognition with no subjective cognitive complaint, mild cognitive impairment, or AD.

### Data Selection

Dichotomized samples of participants from the cohorts were selected to maximize the likelihood that they would be T- or T+. Cognitively unimpaired (CU) individuals were clinically categorized as no-subjective-cognitive-complaint participants who were A- and N-. Cognitively impaired (CI) individuals were clinically categorized as AD or mild-cognitive-impairment participants who were A+ and N+. To limit potential bias from the significant differences ( $P < 0.05$ ) in age, cognition, and clinical diagnosis between the dichotomized samples (Supplemental Table 2), we subsampled the dichotomized <sup>18</sup>F-MK-6240 set by selecting only participants who had continuous measures of A $\beta$  load (centiloid scores), collected under the Australian Imaging, Biomarkers and Lifestyle Flagship Study of Ageing. Then, using the R (version 4.2.1) (21) MatchIt tool (22) and variable ratio matching, we drew participants from the dichotomized <sup>18</sup>F-flortaucipir set to match the subsampled <sup>18</sup>F-MK-6240 set on the basis of age, Mini-Mental State Examination score, global centiloid indices, and CT composite indices, with secondary consideration given to the distributions of sex and diagnostic prevalence. Figure 1 shows the subsampling process.

### Data Analyses

Brain parcellation atlases for PET image sampling were obtained from the MR images as previously described (23,24) using FreeSurfer

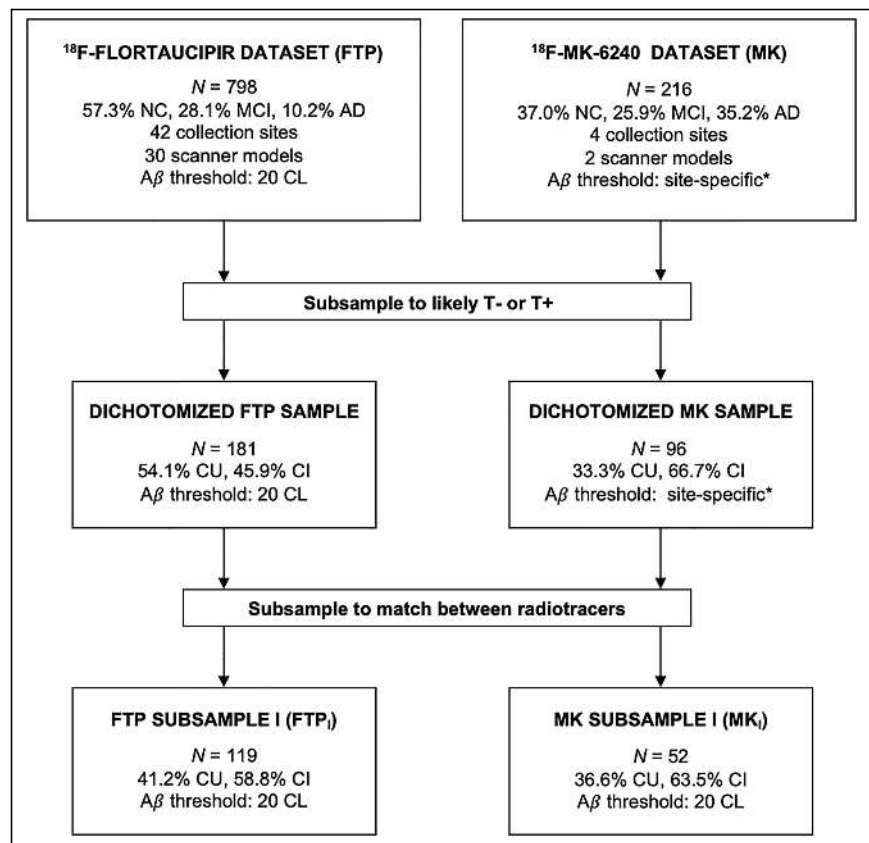


**FIGURE 1.** Subsampling process for threshold testing. \*A $\beta$  status was reported by each site depending on its individual method for threshold determination. CL = centiloids; MCI = mild cognitive impairment; NC = normal cognition with no subjective cognitive complaint.



version 7.1. Images were summed over 80–100 min for  $^{18}\text{F}$ -flortaucipir (25,26) and 90–110 min for  $^{18}\text{F}$ -MK-6240 (27).  $^{18}\text{F}$ -flortaucipir images, processed by the Commonwealth Scientific and Industrial Research Organization Health and Biosecurity Business Unit, Department of Industry Innovation and Science, Australian Government, were rigidly aligned to their corresponding MR images using the robust block-matching registration software Mirorr (28).  $^{18}\text{F}$ -MK-6240 images were registered to their corresponding MR images using rigid-body registration with the normalized mutual information cost function (29). All registrations were manually inspected for accuracy. The FreeSurfer parcellation template (Desikan-Killiany-Tourville atlas (30)) was used to sample summed PET images, and a volume-weighted average of FreeSurfer region counterparts (Table 1) was calculated for each of the 6 composite regions investigated: amygdala, inferior temporal region, lateral occipital region, lateral temporal region, mesial temporal region, and meta temporal region (3,15,16). SUV ratios were calculated using cerebellar gray matter as a reference (9,31). A CT composite was calculated as a surface area-weighted composite of the FreeSurfer-derived entorhinal, fusiform, inferior temporal, and middle temporal lobe CT values (3). To preserve the raw image data, no harmonization methods were applied to the reported data. However, to evaluate potential site- and scanner-specific effects, we conducted the same analyses on adjusted SUV ratios from the dichotomized subsample adjusted using the R ComBat tool (32), a harmonization tool designed to minimize scanner effects.

#### Methods for Tau Threshold Determination

Each subsample (subsampling  $^{18}\text{F}$ -flortaucipir set, subsampling  $^{18}\text{F}$ -MK-6240 set) was randomly split into training and testing sets, preserving matching, using R (70% and 30%, respectively) to avoid overfitting. Using the training set, we evaluated several approaches to determine and compare thresholds for both radiotracers: 90th percentile of CU participants, 95th percentile of CU participants,  $\text{CenTauR}_z$  1.5 (mean + 1.5 SDs of the CU group mean) (10),  $\text{CenTauR}_z$  2.0 (mean + 2 SDs of the CU group mean) (10), gaussian mixture modeling (33), hierarchic clustering (34), iterative outlier detection (35), k-means clustering (36), ROC method (37), nonparametric and parametric double ROC method (38), and Youden index (39).

#### Statistical Methods

All statistics were calculated using R. Statistical differences were assessed using a Mann–Whitney  $U$  test. The ability to discriminate tau signal between CU and CI participants was assessed using effect size (Cohen  $d$ ). Each threshold-determining approach was assessed using sensitivity and specificity by applying the determined thresholds to the testing set.

#### RESULTS

Table 2 shows the participant characteristics. After matching, there were no statistically significant differences in distributions or between metrics.

Regional SUV ratio means, SDs, and effect sizes are shown in Table 3. For both tracers, the amygdala and the mesial temporal region showed the greatest effect sizes, or differences between the CI and CU means.

Figure 2 displays each tracer’s sensitivities—and Figure 3, each tracer’s specificities—for the combinations of 12 threshold-determining methods and 6 composite region pairs. When considering joint (subsampling  $^{18}\text{F}$ -flortaucipir set plus subsampling  $^{18}\text{F}$ -MK-6240 set) sensitivity and specificity, we found that different methods performed optimally for each region. The 90th percentile and parametric double ROC methods in the mesial temporal region yielded the highest joint sensitivity (1.86). The 90th percentile,  $\text{CenTauR}_z$  1.5, nonparametric and parametric double ROC methods in the amygdala, and the parametric double ROC method in the inferior temporal region were slightly lower (1.81), followed by the parametric double ROC method in the meta temporal region (1.71), the Youden index in the lateral temporal region (1.70), and the parametric double ROC method in the lateral occipital region (1.65). Gaussian mixture modeling, hierarchic clustering, and k-means clustering each had a joint sensitivity of 2.00 in all regions with the addition of  $\text{CenTauR}_z$  2 in the amygdala and iterative outlier detection in the amygdala, mesial temporal region, and meta temporal region.

Application of the parametric double ROC method for a sensitivity threshold and gaussian mixture modeling for a specificity

**TABLE 1**  
Composite Regions of Interest

Composite region	Region	Sub-region	FreeSurfer region
Meta temporal	Mesial temporal	Amygdala	L amygdala
			R amygdala
			L entorhinal
			R entorhinal
			L fusiform
			R fusiform
	Lateral temporal	Inferior temporal	L parahippocampal
			R parahippocampal
			L inferior temporal
			R inferior temporal
			L middle temporal
			R middle temporal
Lateral occipital	Lateral occipital	L lateral occipital	
		R lateral occipital	

**TABLE 2**  
 Characteristics of CU and CI Participants for <sup>18</sup>F-Flortaucipir and <sup>18</sup>F-MK-6240 Matched Subsamples

Characteristic	Subsampled <sup>18</sup> F-flortaucipir set		Subsampled <sup>18</sup> F-MK-6240 set	
	A-N- CU	A+N+ CI	A-N- CU	A+N+ CI
<i>n</i>	49 (41.2%)	70 (58.8%)	19 (36.5%)	33 (63.5%)
Sex	49.0% F; 51.0% M	42.9% F; 57.1% M	47.4% F; 52.6% M	45.5% F; 54.5% M
AD/MCI	—	47.1% AD; 52.9% MCI	—	51.5% AD; 48.5% MCI
Age (y)	72.78 ± 4.79	76.70 ± 7.85	73.89 ± 4.76	74.06 ± 6.84
Mini-Mental State Examination score	29.12 ± 1.00	24.46 ± 4.02	28.47 ± 1.27	24.61 ± 2.95
CT composite (mm)	2.79 ± 0.07	2.54 ± 0.11	2.78 ± 0.07	2.56 ± 0.11
Centiloids	2.84 ± 8.61	88.54 ± 28.70	2.82 ± 8.09	98.92 ± 26.29

MCI = mild cognitive impairment.

threshold yielded the following respective threshold pairs: 1.30 and 1.58 for <sup>18</sup>F-flortaucipir and 0.78 and 1.29 for <sup>18</sup>F-MK-6240 in the amygdala, 1.26 and 1.48 for <sup>18</sup>F-flortaucipir and 1.09 and 1.63 for <sup>18</sup>F-MK-6240 in the inferior temporal region, 1.15 and 1.42 for <sup>18</sup>F-flortaucipir and 1.11 and 1.73 for <sup>18</sup>F-MK-6240 in the lateral occipital region, 1.24 and 1.49 for <sup>18</sup>F-flortaucipir and 1.07 and 1.63 for <sup>18</sup>F-MK-6240 in the lateral temporal region, 1.23 and 1.33 for <sup>18</sup>F-flortaucipir and 1.01 and 1.46 for <sup>18</sup>F-MK-6240 in the mesial temporal region, and 1.18 and 1.36 for <sup>18</sup>F-flortaucipir and 1.04 and 1.53 for <sup>18</sup>F-MK-6240 in the meta temporal region.

When all 72 combinations of thresholding methods and sample regions were considered, neither tracer showed a sensitivity advantage, with <sup>18</sup>F-flortaucipir showing a higher sensitivity than <sup>18</sup>F-MK-6240 in 34 of 72 (47.2%) comparisons, <sup>18</sup>F-MK-6240 showing a higher sensitivity than <sup>18</sup>F-flortaucipir in 33 of 72 (45.8%), and the two being equivalent in 5 of 72 (6.9%). <sup>18</sup>F-flortaucipir outperformed

<sup>18</sup>F-MK-6240 in specificity, showing an advantage in 39 of 72 (54.2%) comparisons, but the specificity was evenly matched in 23 of 72 (31.4%) comparisons.

The relative performance of threshold method sensitivities or specificities was not modified in either the unmatched dichotomized samples (Supplemental Table 3; Supplemental Figs. 1 and 2) or the ComBat harmonized samples (Supplemental Table 4; Supplemental Figs. 3 and 4).

#### DISCUSSION

When considering AD biomarker thresholds, it is important to note that the same threshold may not be optimal in all circumstances (11). Indeed, for the centiloid scale, a value of approximately 20 centiloids results in the greatest sensitivity for detecting early Aβ pathology (sensitivity threshold), but a threshold of

**TABLE 3**  
 Matched Composite Region Summary

Region	CU SUV ratio		CI SUV ratio		<i>d</i>
	Mean	$\sigma^2$	Mean	$\sigma^2$	
Subsampled <sup>18</sup> F-flortaucipir set					
Amygdala	1.18	0.11	1.64	0.33	1.87
Inferior temporal	1.18	0.09	1.67	0.47	1.43
Lateral occipital	1.10	0.09	1.35	0.38	0.90
Lateral temporal	1.17	0.08	1.63	0.46	1.39
Mesial temporal	1.15	0.08	1.52	0.31	1.63
Meta temporal	1.13	0.08	1.40	0.32	1.19
Subsampled <sup>18</sup> F-MK-6240 set					
Amygdala	0.67	0.06	1.770	0.67	2.30
Inferior temporal	1.06	0.07	1.936	0.88	1.41
Lateral occipital	1.12	0.11	1.673	0.84	0.93
Lateral temporal	1.04	0.07	1.834	0.83	1.35
Mesial temporal	0.94	0.07	1.808	0.68	1.80
Meta temporal	1.00	0.07	1.821	0.75	1.54

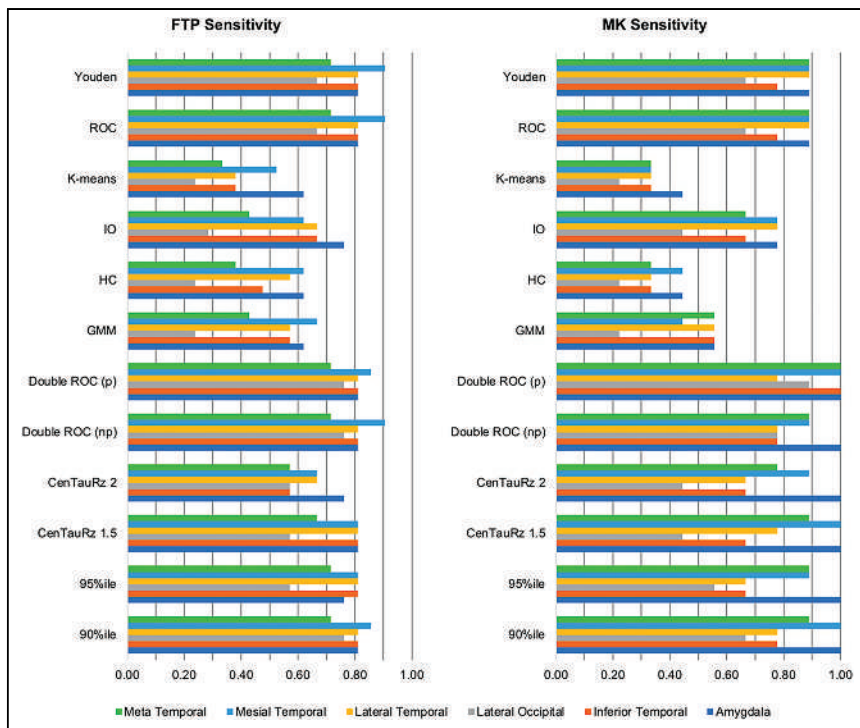


**FIGURE 2.** Matched threshold sensitivities for 6 composite regions when using each of 12 threshold-determining methods. CenTauR<sub>z</sub> 1.5 = mean + 1.5 SDs of CU group mean; CenTauR<sub>z</sub> 2.0 = mean + 2 SDs of CU group mean; GMM = gaussian mixture modeling; HC = hierarchic clustering; IO = iterative outlier detection.

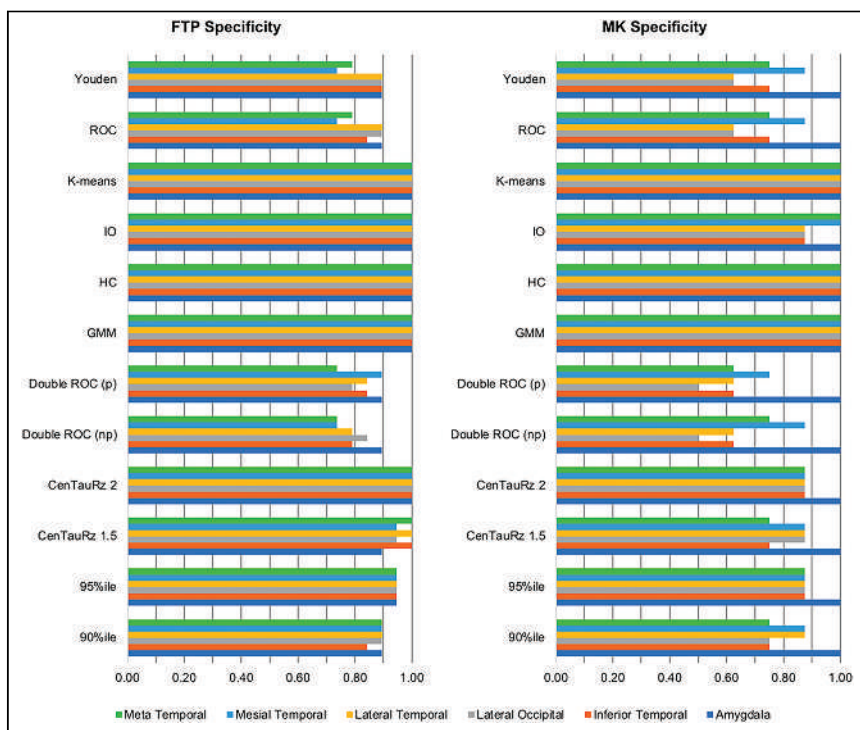


**FIGURE 3.** Matched threshold sensitivities and specificities for 6 composite regions when using each of 12 threshold-determining methods. CenTauR<sub>z</sub> 1.5 = mean + 1.5 SDs of CU group mean; CenTauR<sub>z</sub> 2.0 = mean + 2 SDs of CU group mean; GMM = gaussian mixture modeling; HC = hierarchic clustering; IO = iterative outlier detection.

approximately 50 centiloids better predicts the neuropathologic and clinical diagnosis of AD (specificity threshold) (40). Because the initial goal of the present work was to identify the threshold-determining methods that yield the greatest sensitivity and specificity for early AD-related tau deposition, and given the level of disagreement between the sensitivities and specificities of the various threshold-determining methods, it may be prudent to adopt distinct tau thresholds optimized for either sensitivity or specificity for AD-related tau as demanded by the application, similar to what has been proposed for establishing A $\beta$  positivity thresholds using the centiloid scale (41).

In assessing the 72 threshold-determining-method and composite-region pairs for joint sensitivity between tracers, we found that none of the threshold methods yielded the highest sensitivity for every region, although the parametric double ROC method showed the highest joint sensitivity for all but the lateral temporal region, where it was slightly lower (0.11) than the Youden or ROC method (Fig. 2). For joint specificity, there was even more overlap in optimal methods for each region. Gaussian mixture modeling, hierarchic clustering, and k-means clustering all yielded perfect joint specificities (2.0) for all 6 regions examined. We believe that the difference in optimal sensitivity and specificity threshold-determining methods can be attributed, in part, to the regional SUV ratio distributions between the CU and CI samples for each tracer (Supplemental Figs. 5 and 6). Given that a sizeable proportion of CI participants presents with low tau, as previously reported (42,43), even after dichotomizing and matching of samples, there was significant overlap in SUV ratios between CU and CI participants, with clearly identifiable groups of lower and higher tau load within the CI participants. These distributions pose a challenge in fully separating the CI participants from the CU participants. Compared with the other methods tested, the parametric double ROC method is well positioned to set the optimal sensitivity threshold because it does not rely solely on the CU group, as many others do, which ultimately favors specificity. Further, the threshold in this specific instance was based on achieving an accuracy of 95%, and given the increased prevalence of the CI participants here (>58%), sensitivity was inherently targeted over specificity. Between the success of the parametric double ROC method across regions and its innate advantages, this method can be used to set the sensitivity

threshold regardless of region. Conversely, gaussian mixture modeling, hierarchic clustering, and k-means clustering—being clustering methods—proved advantageous for specificity. They cluster lower tau load as one group and higher tau load as a second group, setting the threshold at the split between low- and high-tau-load CI participants, grouping all CU participants with the low-tau CI participants. Although gaussian mixture modeling, hierarchic clustering, and k-means clustering all yield perfect specificity, gaussian mixture modeling may be the best single method to use across all regions because it sets the lowest perfect specificity threshold.

Several composites have been suggested as potential sampling regions for determining tau status. Although the algorithm used in this work—BETTH—does not determine the optimal region for evaluating tau status, it does highlight their differences, particularly with respect to the chosen sensitivity method (parametric double ROC method). The mesial temporal region yielded the greatest sensitivity, closely followed by the amygdala and the inferior temporal region. As shown in Table 1, the mesial temporal region comprises a combination of Braak I and III regions, and the amygdala is one of the Braak III regions. Thus, it is unsurprising that they would have greater effect sizes as shown in Table 3, given that these regions start accumulating tau earlier than do the inferior temporal region, lateral temporal region, and meta temporal region (regions included in Braak IV) or the lateral occipital region (Braak V). In fact, the mesial temporal lobe is frequently a site of early tau deposition in the AD pathologic process, before the development of cognitive symptoms (17). However, its association with primary age-related tauopathy raises concerns about its ability to differentiate AD-related from age-related tau deposition (18). Further, the Braak and Delacourte stages capture, to varying degrees, the neuropathologic distribution of tau (44,45), but their application to PET studies may fail to consistently capture tau deposition because the regions are either too small and subject to partial-volume effects (46,47), as may be of concern for the amygdala, or too large and subject to dilution of focal specific PET signal (47). Although the meta temporal region (3) may not be able to capture some atypical AD presentations such as posterior cortical atrophy (48), it seems capable of detecting early tau deposition and discriminating between AD-related and age-related tau deposition through its combination of the mesial temporal lobe and the inferior and middle temporal neocortical regions (43), the latter of which is associated with cortical AD tau pathology (Braak IV and later) but not primary age-related tauopathy. Further, the meta temporal region captures the 3 AD pathologic subtypes (49), as well as nonstereotypic tau deposition (50), while discriminating AD from non-AD neurodegeneration (43) and is the most sensitive for longitudinal analysis of tau deposition (51,52).

Our previous work compared the relative performance of  $^{18}\text{F}$ -flortaucipir and  $^{18}\text{F}$ -MK-6240 in terms of visual assessments, off-target binding, and dynamic range, where we found  $^{18}\text{F}$ -MK-6240 to have approximately a 2-fold greater dynamic range and lower nonspecific binding than  $^{18}\text{F}$ -flortaucipir across Braak pathologic stage regions (14), suggesting that  $^{18}\text{F}$ -MK-6240 may be more useful for detecting early tau signal and small interval changes (53). The differences in dynamic range are of particular interest for the determination of tau thresholds. When comparing the 2 tracers' performance in differentiating between high and low tau load using the optimal specificity threshold, as set by gaussian mixture modeling, we found that  $^{18}\text{F}$ -flortaucipir and  $^{18}\text{F}$ -MK-6240 performed equivalently, each yielding perfect specificities. However, when comparing sensitivities, as determined using the parametric double ROC method, we found that  $^{18}\text{F}$ -MK-6240 outperformed

$^{18}\text{F}$ -flortaucipir by a mean sensitivity of  $0.15 \pm 0.10$  in all regions but the lateral temporal. This characteristic may support the use of  $^{18}\text{F}$ -MK-6240 over  $^{18}\text{F}$ -flortaucipir, particularly when sensitivity to early tau deposition is paramount.

The implementation of the BETTH threshold-determining approach in the present study has the benefit of being evaluated for 2 tau tracers (in datasets selected to be as clearly impaired or unimpaired as possible) and for matched samples. However, the present study has some limitations. In subsampling the CU and CI participants and matching, we reduced the sample sizes 2-fold and eliminated more ambiguously classified participants. Additionally, part of the selection process relied on third-party reporting either of clinical diagnosis or A $\beta$  status, which likely used different criteria and methods for determination. Future work will need to assess the BETTH approach in expanded datasets without selection bias. Because race, ethnicity, education, and apolipoprotein E status were not provided with the original data, those factors could not be considered in our matching process, leaving any existing bias in our matched cohorts. Future work should conduct the same analyses on datasets in which those demographics are included and can be accounted for. The success of the thresholds was evaluated relative to the assumption that CU participants were T $-$  and CI participants were T $+$ . Future work would benefit from evaluating the success of the thresholds relative to visual reads, although visual identification of early tau deposits, while more sensitive (54), may be complicated by off-target signal (55). The goal of the present work was to establish a universal method for determining tau thresholds, but only  $^{18}\text{F}$ -flortaucipir and  $^{18}\text{F}$ -MK-6240 were included in our evaluation. To ensure the generalizability of our methods, it will be necessary to extend BETTH to other tau tracers to validate the conclusions drawn here. Further, these thresholds reflect the idiosyncratic pharmacokinetic and pharmacologic properties (affinity, nonspecific binding, etc.) of the tracers used, as well as small differences introduced using PET scanners with different sensitivities and resolutions, reflecting the situation today and for these 2 tau tracers. The introduction and implementation of digital PET scanners, with greater sensitivities and higher resolutions, will require the revision of these thresholds under the new conditions. Finally, the whole cerebellar gray matter was used as a reference region, to keep processing uniform between both radiotracers. However, the calculated SUV ratios may be impacted by the off-target binding characteristics of each tracer. As progress is made toward a common scale indexing tau load, it will be necessary to investigate the effects that universal tau cortical and reference regions that account for the off-target binding of tracers (56) have on the resultant thresholds.

## CONCLUSION

Given that cortical tau is intimately and imminently associated with subsequent neurodegeneration and cognitive decline, it is imperative to detect AD-related cortical tau accumulation as early as possible. We have proposed the BETTH algorithm for assessing different approaches in various composite regions for determination of the optimal threshold to detect early tau deposition. Although the present work evaluated several threshold-determining methods and tissue-sampling strategies, BETTH is extensible and can be applied to other biomarkers. At this time, the present study suggests that AD-related tau status is best determined using a parametric double ROC-determined sensitivity threshold and a gaussian mixture modeling-determined specificity threshold. Each pair represents an uncertainty zone indicating participants who may need further evaluation.

## DISCLOSURE

This work was supported financially by National Institute of Aging grants P50 AG005133, RF1 AG025516, R01 AG052446, R01 AG052521, and P01 AG025204. <sup>18</sup>F-flortaucipir data collection and sharing for this project were funded by the ADNI (National Institutes of Health grant U01 AG024904) and DOD ADNI (Department of Defense award W81XWH-12-2-0012). ADNI is funded by the National Institute on Aging, the National Institute of Biomedical Imaging and Bioengineering, and through generous contributions from the following: AbbVie, Alzheimer's Association, Alzheimer's Drug Discovery Foundation, Araclon Biotech, BioClinica, Inc., Biogen, Bristol-Myers Squibb Company, CereSpir, Inc., Cogstate, Eisai Inc., Elan Pharmaceuticals, Inc., Eli Lilly and Company, EuroImmun, F. Hoffmann-La Roche Ltd. and its affiliated company Genentech, Inc., Fujirebio, GE Healthcare, IXICO Ltd., Janssen Alzheimer Immunotherapy Research & Development, LLC, Johnson & Johnson Pharmaceutical Research & Development, LLC, Lumosity, Lundbeck, Merck & Co., Inc., Meso Scale Diagnostics, LLC, NeuroRx Research, Neurotrack Technologies, Novartis Pharmaceuticals Corporation, Pfizer Inc., Piramal Imaging, Servier, Takeda Pharmaceutical Company, and Transition Therapeutics. The Canadian Institutes of Health Research is providing funds to support ADNI clinical sites in Canada. Private sector contributions are facilitated by the Foundation for the National Institutes of Health ([www.fnih.org](http://www.fnih.org)). The grantee organization is the Northern California Institute for Research and Education, and the study is coordinated by the Alzheimer's Therapeutic Research Institute at the University of Southern California. ADNI data are disseminated by the Laboratory for Neuro Imaging at the University of Southern California. <sup>18</sup>F-MK-6240 data were supplied by Cerveau Technologies. No other potential conflict of interest relevant to this article was reported.

## ACKNOWLEDGMENTS

Data used in preparation of this article were obtained from the ADNI database ([adni.loni.usc.edu](http://adni.loni.usc.edu)). The investigators within the ADNI contributed to the design and implementation of ADNI or provided data but did not participate in analysis or writing of this report. A complete listing of ADNI investigators is available online ([https://adni.loni.usc.edu/wp-content/uploads/how\\_to\\_apply/ADNI\\_Acknowledgement\\_List.pdf](https://adni.loni.usc.edu/wp-content/uploads/how_to_apply/ADNI_Acknowledgement_List.pdf)).

## KEY POINTS

**QUESTION:** Can a single threshold-determining method yield optimal sensitivity and specificity for both <sup>18</sup>F-flortaucipir and <sup>18</sup>F-MK-6240?

**PERTINENT FINDINGS:** A comparison of 12 threshold-determining methods in 6 composite regions revealed that no method performed optimally in terms of both sensitivity and specificity. In most cases, doing particularly well in terms of sensitivity meant doing poorly in terms of specificity and vice versa, likely because of the degree of overlap in the unimpaired and impaired participant groups.

**IMPLICATIONS FOR PATIENT CARE:** Given the prevalence of low tau in Aβ-positive CI individuals, no single threshold for tau can be both highly sensitive and highly specific. Therefore, the threshold selected will depend on the clinical or research question posed.

## REFERENCES

1. Villemagne VL, Burnham S, Bourgeat P, et al. Amyloid β deposition, neurodegeneration, and cognitive decline in sporadic Alzheimer's disease: a prospective cohort study. *Lancet Neurol*. 2013;12:357–367.
2. Jack CR, Bennett DA, Blennow K, et al. A/T/N: an unbiased descriptive classification scheme for Alzheimer disease biomarkers. *Neurology*. 2016;87:539–547.
3. Jack CR, Wiste HJ, Weigand SD, et al. Defining imaging biomarker cut points for brain aging and Alzheimer's disease. *Alzheimers Dement*. 2017;13:205–216.
4. Ossenkoppele R, Pichet Binette A, Groot C, et al. Amyloid and tau PET-positive cognitively unimpaired individuals are at high risk for future cognitive decline. *Nat Med*. 2022;28:2381–2387.
5. Strikwerda-Brown C, Hobbs DA, Gonneaud J, et al. Association of elevated amyloid and tau positron emission tomography signal with near-term development of Alzheimer disease symptoms in older adults without cognitive impairment. *JAMA Neurol*. 2022;79:975–985.
6. Schöll M, Lockhart SN, Schonhaut DR, et al. PET imaging of tau deposition in the aging human brain. *Neuron*. 2016;89:971–982.
7. Leuzy A, Chiotis K, Lemoine L, et al. Tau PET imaging in neurodegenerative tauopathies: still a challenge. *Mol Psychiatry*. 2019;24:1112–1134.
8. Chien WT, Leung SF, Yeung FK, Wong WK. Current approaches to treatments for schizophrenia spectrum disorders, part II: psychosocial interventions and patient-focused perspectives in psychiatric care. *Neuropsychiatr Dis Treat*. 2013;9:1463–1481.
9. Hostetler ED, Walji AM, Zeng Z, et al. Preclinical characterization of <sup>18</sup>F-MK-6240, a promising PET tracer for in vivo quantification of human neurofibrillary tangles. *J Nucl Med*. 2016;57:1599–1606.
10. Villemagne VL, Leuzy A, Bohorquez SS, et al. CenTauR: toward a universal scale and masks for standardizing tau imaging studies. *Alzheimers Dement (Amst)*. 2023;15:e12454.
11. Villemagne VL, Lopresti BJ, Doré V, et al. What Is T+? A Gordian Knot of Tracers, Thresholds, and Topographies. *J Nucl Med*. 2021;62:614–619.
12. Klunk WE, Koeppe RA, Price JC, et al. The centiloid project: standardizing quantitative amyloid plaque estimation by PET. *Alzheimers Dement*. 2015;11:1–15.e4.
13. Smith R, Schöll M, Leuzy A, et al. Head-to-head comparison of tau positron emission tomography tracers [<sup>18</sup>F]flortaucipir and [<sup>18</sup>F]RO948. *Eur J Nucl Med Mol Imaging*. 2020;47:342–354.
14. Gogola A, Minhas DS, Villemagne VL, et al. Direct comparison of the tau PET tracers <sup>18</sup>F-flortaucipir and <sup>18</sup>F-MK-6240 in human subjects. *J Nucl Med*. 2022;63:108–116.
15. Mishra S, Gordon BA, Su Y, et al. AV-1451 PET imaging of tau pathology in preclinical Alzheimer disease: defining a summary measure. *Neuroimage*. 2017;161:171–178.
16. Maass A, Landau S, Baker SL, et al. Comparison of multiple tau-PET measures as biomarkers in aging and Alzheimer's disease. *Neuroimage*. 2017;157:448–463.
17. Weigand AJ, Bangen KJ, Thomas KR, et al. Is tau in the absence of amyloid on the Alzheimer's continuum? A study of discordant PET positivity. *Brain Commun*. 2020;2:fcz046.
18. Cray JF, Trojanowski JQ, Schneider JA, et al. Primary age-related tauopathy (PART): a common pathology associated with human aging. *Acta Neuropathol (Berl)*. 2014;128:755–766.
19. Weiner MW, Veitch DP, Aisen PS, et al. The Alzheimer's Disease Neuroimaging Initiative 3: continued innovation for clinical trial improvement. *Alzheimers Dement*. 2017;13:561–571.
20. Rowe C, Amadoru S, Dore V, et al. Correlation of amyloid PET in centiloid units with neuropathological findings in Alzheimer's disease [abstract]. *J Nucl Med*. 2018;59(suppl 1):482.
21. R: a language and environment for statistical computing. The R Foundation website. <https://www.r-project.org/>. Accessed August 25, 2023.
22. Ho DEH, Imai K, King G, Stuart EA. Nonparametric preprocessing for parametric causal inference. *J Stat Softw*. 2011;42:1–28.
23. Okonkwo DO, Puffer RC, Minhas DS, et al. [<sup>18</sup>F]FDG, [<sup>11</sup>C]PiB, and [<sup>18</sup>F]AV-1451 PET imaging of neurodegeneration in two subjects with a history of repetitive trauma and cognitive decline. *Front Neurol*. 2019;10:831.
24. Fischl B, van der Kouwe A, Destrieux C, et al. Automatically parcellating the human cerebral cortex. *Cereb Cortex*. 2004;14:11–22.
25. Shcherbinin S, Schwarz AJ, Joshi A, et al. Kinetics of the tau PET tracer <sup>18</sup>F-AV-1451 (T807) in subjects with normal cognitive function, mild cognitive impairment, and Alzheimer disease. *J Nucl Med*. 2016;57:1535–1542.
26. Baker SL, Lockhart SN, Price JC, et al. Reference tissue-based kinetic evaluation of <sup>18</sup>F-AV-1451 for tau imaging. *J Nucl Med*. 2017;58:332–338.
27. Pascoal TA, Shin M, Kang MS, et al. In vivo quantification of neurofibrillary tangles with [<sup>18</sup>F]MK-6240. *Alzheimers Res Ther*. 2018;10:74.

28. Rivest-Hénault D, Dowson N, Greer PB, Fripp J, Dowling JA. Robust inverse-consistent affine CT-MR registration in MRI-assisted and MRI-alone prostate radiation therapy. *Med Image Anal.* 2015;23:56–69.
29. Studholme C, Hawkes DJ, Hill DLG. Normalized entropy measure for multimodality image alignment. Presented at: Medical Imaging 1998: Image Processing; June 24, 1998; San Diego, CA.
30. Klein A, Tourville J. 101 labeled brain images and a consistent human cortical labeling protocol. *Front Neurosci.* 2012;6:171.
31. Marquié M, Normandin MD, Vanderburg CR, et al. Validating novel tau positron emission tomography tracer [F-18]-AV-1451 (T807) on postmortem brain tissue. *Ann Neurol.* 2015;78:787–800.
32. Orlhac F, Eertink JJ, Cottreau AS, et al. A guide to ComBat harmonization of imaging biomarkers in multicenter studies. *J Nucl Med.* 2022;63:172–179.
33. Reynolds DA. Gaussian mixture models. In: *Encyclopedia of Biometrics.* Springer; 2009:741.
34. Murtagh F, Contreras P. Algorithms for hierarchical clustering: an overview. *WIREs Data Mining Knowl Discov.* 2012;2:86–97.
35. Aizenstein HJ, Nebes RD, Saxton JA, et al. Frequent amyloid deposition without significant cognitive impairment among the elderly. *Arch Neurol.* 2008;65:1509–1517.
36. Likas A, Vlassis N, Verbeek JJ. The global k-means clustering algorithm. *Pattern Recognit.* 2003;36:451–461.
37. Robin X, Turck N, Hainard A, et al. pROC: an open-source package for R and S+ to analyze and compare ROC curves. *BMC Bioinformatics.* 2011;12:77.
38. Greiner M, Sohr D, Göbel P. A modified ROC analysis for the selection of cut-off values and the definition of intermediate results of serodiagnostic tests. *J Immunol Methods.* 1995;185:123–132.
39. Thiele C, Hirschfeld G. cutpointr: improved estimation and validation of optimal cutpoints in R. *J Stat Softw.* 2021;98:1–27.
40. Amadoru S, Doré V, McLean CA, et al. Comparison of amyloid PET measured in centiloid units with neuropathological findings in Alzheimer’s disease. *Alzheimers Res Ther.* 2020;12:22.
41. van der Kall LM, Truong T, Bumham SC, et al. Association of  $\beta$ -amyloid level, clinical progression, and longitudinal cognitive change in normal older individuals. *Neurology.* 2021;96:e662–e670.
42. Rowe CC, Doré V, Krishnadas N, et al. Tau imaging with  $^{18}\text{F}$ -MK6240 across the Alzheimer’s disease spectrum. medRxiv website. <https://www.medrxiv.org/content/10.1101/2022.02.13.22270894v1>. Published February 15, 2022. Accessed August 25, 2023.
43. Ossenkoppele R, Rabinovici GD, Smith R, et al. Discriminative accuracy of [ $^{18}\text{F}$ ]flortaucipir positron emission tomography for Alzheimer disease vs other neurodegenerative disorders. *JAMA.* 2018;320:1151–1162.
44. Braak H, Braak E. Staging of Alzheimer’s disease-related neurofibrillary changes. *Neurobiol Aging.* 1995;16:271–278.
45. Delacourte A, David JP, Sergeant N, et al. The biochemical pathway of neurofibrillary degeneration in aging and Alzheimer’s disease. *Neurology.* 1999;52:1158–1165.
46. Schmidt ME, Chiao P, Klein G, et al. The influence of biological and technical factors on quantitative analysis of amyloid PET: points to consider and recommendations for controlling variability in longitudinal data. *Alzheimers Dement.* 2015;11:1050–1068.
47. Schwarz AJ, Shcherbinin S, Sliker LJ, et al. Topographic staging of tau positron emission tomography images. *Alzheimers Dement (Amst).* 2018;10:221–231.
48. Ossenkoppele R, Schonhaut DR, Schöll M, et al. Tau PET patterns mirror clinical and neuroanatomical variability in Alzheimer’s disease. *Brain.* 2016;139:1551–1567.
49. Murray ME, Graff-Radford NR, Ross OA, Petersen RC, Duara R, Dickson DW. Neuropathologically defined subtypes of Alzheimer’s disease with distinct clinical characteristics: a retrospective study. *Lancet Neurol.* 2011;10:785–796.
50. Seemiller J, Bischof GN, Hoenig MC, et al. Indication of retrograde tau spreading along Braak stages and functional connectivity pathways. *Eur J Nucl Med Mol Imaging.* 2021;48:2272–2282.
51. Schwarz C, Therneau T, Przybelski S, et al. Tau positivity: comparing flortaucipir meta-ROI vs. maximum of regional Z-scores. Presented at: 14th Human Amyloid Imaging; January 17, 2020; Miami, FL.
52. Schwarz CG, Therneau TM, Weigand SD, et al. Selecting software pipelines for change in flortaucipir SUVR: balancing repeatability and group separation. *Neuroimage.* 2021;238:118259.
53. Pascoal TA, Benedet AL, Tudorascu DL, et al. Longitudinal  $^{18}\text{F}$ -MK-6240 tau tangles accumulation follows Braak stages. *Brain.* 2021;144:3517–3528.
54. Provost K, Iaccarino L, Soleimani-Meigooni DN, et al. Comparing ATN-T designation by tau PET visual reads, tau PET quantification, and CSF PTau181 across three cohorts. *Eur J Nucl Med Mol Imaging.* 2021;48:2259–2271.
55. Fleisher AS, Pontecorvo MJ, Devous MD Sr, et al. Positron emission tomography imaging with [ $^{18}\text{F}$ ]flortaucipir and postmortem assessment of Alzheimer disease neuropathologic changes. *JAMA Neurol.* 2020;77:829–839.
56. Minhas D, Gogola A, Lopresti B, et al. Considerations for a universal tau PET reference region. Presented at: Alzheimer’s Association Tau 2022 Global Conference; February 22–23, 2022; online conference.



# Detection of IL12/23p40 via PET Visualizes Inflammatory Bowel Disease

Farzaneh Rezazadeh<sup>1</sup>, Nicholas Ramos<sup>1</sup>, Allen-Dexter Saliganan<sup>1</sup>, Najeeb Al-Hallak<sup>1</sup>, Kang Chen<sup>2</sup>, Bashar Mohamad<sup>3</sup>, Wendy N. Wiesend<sup>4</sup>, and Nerissa T. Viola<sup>1</sup>

<sup>1</sup>Department of Oncology, Karmanos Cancer Institute, Wayne State University, Detroit, Michigan; <sup>2</sup>Departments of Obstetrics and Gynecology, Wayne State University, Detroit, Michigan; <sup>3</sup>Department of Gastroenterology, Wayne State University, Detroit, Michigan; and <sup>4</sup>Department of Anatomic Pathology, Corewell Health William Beaumont University Hospital, Royal Oak, Michigan

Inflammatory bowel disease (IBD), which includes both Crohn disease and ulcerative colitis, is a relapsing inflammatory disease of the gastrointestinal tract. Long-term chronic inflammatory conditions elevate the patient's risk of colorectal cancer (CRC). Currently, diagnosis requires endoscopy with biopsy. This procedure is invasive and requires a bowel-preparatory regimen, adding to patient burden. Interleukin 12 (IL12) and interleukin 23 (IL23) play key roles in inflammation, especially in the pathogenesis of IBD, and are established therapeutic targets. We propose that imaging of IL12/23 and its p40 subunit in IBD via immuno-PET potentially provides a new noninvasive diagnostic approach. **Methods:** Our aim was to investigate the potential of immuno-PET to image inflammation in a chemically induced mouse model of colitis using dextran sodium sulfate by targeting IL12/23p40 with a <sup>89</sup>Zr-radiolabeled anti-IL12/23p40 antibody. **Results:** High uptake of the IL12/23p40 immuno-PET agent was exhibited by dextran sodium sulfate-administered mice, and this uptake correlated with increased IL12/23p40 present in the sera. Competitive binding studies confirmed the specificity of the radiotracer for IL12/23p40 in the gastrointestinal tract. **Conclusion:** These promising results demonstrate the utility of this radiotracer as an imaging biomarker of IBD. Moreover, IL12/23p40 immuno-PET can potentially guide treatment decisions for IBD management.

**Key Words:** immuno-PET; inflammatory bowel disease; IL12/23p40; colitis

J Nucl Med 2023; 64:1806–1814

DOI: 10.2967/jnumed.123.265649

**I**nflammatory bowel disease (IBD) is a chronic disorder of the gastrointestinal tract. It is believed to be caused by dysregulation of immune response to pathogens. IBD comprises 2 major forms: ulcerative colitis and Crohn disease (1). The global prevalence of IBD increased from 3.7 million in 1990 to more than 6.8 million in 2017 (2). The detailed etiology of IBD is still unclear, but genetic predisposition, intestinal dysbiosis, various proinflammatory cytokines, T-helper cells, and interleukins are implicated in its pathogenesis (3,4). In early-stage IBD, a loss of intestinal epithelial barrier function is observed, increasing bacterial translocation and thus activating the mucosal immune system and intestinal inflammation (5). If left

unmanaged, patients with ulcerative colitis have a 2% increased incidence of colorectal cancer (CRC) at 10 y after diagnosis, 8% at 20 y, and about 18% at 30 y, compared with those without IBD. So, careful monitoring of ulcerative colitis patients is recommended (6). IBD-associated CRC carries a particularly poor prognosis (mortality > 50%) (7) compared with sporadic CRC, for which the prognosis is improving. Unlike sporadic CRC, which progresses through an adenoma–carcinoma pathway, IBD CRC evolves from an inflammation–dysplasia–carcinoma sequence (8). Accordingly, there are currently no tools specifically designed to help clinicians track the initiation and progression of IBD CRC pathology.

Detecting and tracking chronic inflammation in the gastrointestinal tract is critical to improving outcomes among patients with IBD. Current diagnostic and surveillance methods for IBD involve clinical manifestations (e.g., bloody diarrhea) in conjunction with physical examination, endoscopy, and pathologic findings (9). Molecular assays that detect elevated biomarkers of inflammation in blood and stool samples reinforce its evaluation and diagnosis, albeit with no acquisition of locoregional information on inflamed areas (10). Currently, endoscopy with biopsy is the gold standard for the diagnosis of IBD and for staging its activity (11). However, endoscopy is invasive and can result in toxic megacolon if performed during exacerbation. Another drawback of endoscopy is that it is limited to imaging segmental areas of the intestine and the superficial mucosal surface. Furthermore, it cannot provide detailed molecular information on the disease (12). Less invasive imaging modalities, including CT, ultrasound, and MRI, are also used clinically for IBD diagnosis (13,14). However, these modalities provide information only on the anatomic integrity of gastrointestinal tissues. None of these available standard-of-care diagnostic tools, whether used alone or in combination, completely meets the need for safe, accessible, reliable, quantitative visualization of gastrointestinal inflammation with high spatial and molecular specificity. A less invasive and quantitative tool that can generate both molecular and morphologic information on specific pathologic processes would be useful in determining the extent of IBD activity (15).

Numerous studies have explored the utility of [<sup>18</sup>F]-FDG PET in the assessment of IBD. High uptake of [<sup>18</sup>F]-FDG in intestinal tissues due to increased immune metabolic activity allows the delineation of inflammatory sites in IBD patients (16,17). However, although [<sup>18</sup>F]-FDG has been shown to be sensitive in the detection of IBD, its specificity leaves much to be desired because of physiologic uptake in the normal bowel (18). To date, there are no specific PET tracers for imaging IBD that are Food and Drug Administration–approved. Other than [<sup>18</sup>F]-FDG, novel PET agents developed for IBD diagnosis are limited to preclinical studies (12,19–21), with only 3 new agents

Received Dec. 22 2022; revision accepted Jun. 20, 2023.  
For correspondence or reprints, contact Nerissa T. Viola (violan@karmanos.org).

Published online Jul. 20, 2023.

COPYRIGHT © 2023 by the Society of Nuclear Medicine and Molecular Imaging.

in patient trials (NCT03546868, NCT04507932, and NCT03414788). Thus, there is a clear need to develop a molecular imaging agent that can detect and visualize active inflammation on-site.

The cytokines interleukin 12 (IL12) and interleukin 23 (IL23) are associated with mediating inflammation. Both cytokines are members of the IL12 family and share the p40 subunit (22). IL12/23p40 has become a clinically relevant target in IBD treatment because of its central role in inducing and sustaining inflammation (23). For example, ustekinumab (Stelara; Janssen), an IL12/23p40 antagonist, has been Food and Drug Administration–approved for treatment, with clinical data showing that patients experienced symptom relief and achieved clinical remission (24,25). Thus, IL12/23p40 is an appealing target not only for treatment but also for diagnosis and surveillance of IBD.

Here, we present the development of an immuno-PET imaging agent by radiolabeling an antibody targeting IL12/23p40 with the radioisotope  $^{89}\text{Zr}$  (half-life,  $\sim 3.27$  d). We characterized the radiotracer's in vitro specificity and stability and evaluated its potential to visualize the cytokine in a dextran sodium sulfate (DSS)–induced acute model of gastrointestinal inflammation in immune-competent mice. We performed in vivo competitive binding studies to demonstrate the tracer's specificity and determined its whole-body tissue distribution. We also validated the uptake of the radiotracer from the genetic expression of IL12/23p40 from excised tissues. Finally, we explored the correlation between tracer uptake in gastrointestinal tissues and IL12/23p40 serum levels.

## MATERIALS AND METHODS

### General

All chemicals and supplies were purchased from commercial suppliers and used without further manipulation except when otherwise stated. [ $^{89}\text{Zr}$ ]Zr-oxalate was obtained from 3D Imaging, LLC. Anti-mouse IL12/23p40 monoclonal antibody (mAb) (rat IgG2a) was purchased from Bio X Cell (catalog number BE0051).

### Chemical Induction of Colitis via DSS

All animal experiments were conducted in compliance with the Institutional Animal Care and Use Committee at Wayne State University. Male and female BALB/c mice aged 10–14 wk (weight range, 20–30 g) were purchased from Charles River Laboratories. Colitis was induced by replacing normal drinking water with 3% (w/v) DSS (molecular mass, 40 kDa; Alfa Aesar) for 7 d alongside access to a chow diet (PicoLab Laboratory Rodent Diet 5L0D) ad libitum. The mice were weighed daily and assessed for clinical manifestations of colitis. The severity of the colitis was determined by a disease activity index according to Freise et al. (19): weight loss (0, none; 1, 1%–4%; 2, 5%–10%; 3, 11%–20%; 4, 0.20%), fecal blood (0, none; 2, blood present in stool; 4, gross bleeding from anus), and stool consistency (0, normal; 1, moist/sticky; 2, soft; 3, diarrhea; 4, bleeding).

### Antibody Conjugation and $^{89}\text{Zr}$ Radiolabeling

*p*-Benzyl-isothiocyanate-deferoxamine (DFO-Bz-SCN, Macrocylics) was conjugated to anti-IL12/23p40 by a similar protocol to that previously reported (26). Briefly, DFO-Bz-SCN in DMSO was added to the mAb at a ratio of 1:5 (mAb:DFO) in 0.9% saline, pH approximately 9, at 37°C for 1 h. Subsequent purification using a centrifugation column filter (molecular weight cutoff, 30 kDa) and 0.9% saline as the mobile phase eliminated unconjugated DFO-Bz-SCN.  $^{89}\text{Zr}$ -radioabeling of DFO-anti-IL12/23p40 antibody proceeded in a neutral pH environment in saline. Approximately 37 MBq (1 mCi) of [ $^{89}\text{Zr}$ ]Zr-oxalate previously neutralized to pH 7.0–7.2 were added to a solution of DFO-anti-IL12/23p40 (0.2 mg, 1.3 nmol) and incubated for 1 h at room temperature. The radiolabeling reaction and efficiency were monitored

via radio–instant thin-layer chromatography (Mini-Scan/FC; Eckert and Ziegler) using instant thin-layer chromatography glass microfiber chromatography paper impregnated with silica gel (Agilent Technologies, catalog number SGI0001) as the stationary phase and 50 mM ethylenediaminetetraacetic acid as the mobile phase. The reaction was quenched with 5  $\mu\text{L}$  of 50 mM ethylenediaminetetraacetic acid and purified through spin column centrifugation (molecular weight cutoff, 30 kDa) with sterile saline as the eluent. Stability studies of [ $^{89}\text{Zr}$ ]Zr-DFO-anti-IL12/23p40 were conducted in saline at 37°C and monitored over 96 h.

### In Vitro Binding and Blocking Studies

Saturation binding studies were conducted to determine the dissociation constant of the [ $^{89}\text{Zr}$ ]Zr-DFO-anti-IL12/23p40. Mouse IL12/23p40 protein (Bio-Techne) (5  $\mu\text{g}/\text{mL}$  in bicarbonate buffer) was coated onto a 96-well strip plate and incubated at 4°C overnight. The wells were then washed 3 times with 0.05% polysorbate-20 in  $\times 1$  phosphate-buffered saline and incubated for 2 h at room temperature with 200  $\mu\text{L}$  of blocking buffer (1% bovine serum albumin in wash buffer). The IL12/23p40-coated wells were incubated with varying concentrations of radiolabeled antibody (0.5–5,000 nM) or subjected to blocking by coinubation of the radiotracer with a 100-fold excess of unmodified IL12/23p40 antibody in triplicate. After 1 h at 37°C, the unbound radiotracer was removed and the bound activity for each well was measured with a  $\gamma$ -counter. The dissociation constant was calculated by nonlinear regression using GraphPad Prism, version 9.2. Specific binding was measured by subtracting nonspecific binding from total bound activity expressed as counts per minute. To evaluate specificity, a separate group of IL12/23p40-coated wells was treated with an excess of cold anti-IL12/23p40 mAb (500 nM) 30 min before the addition of the radiotracer (5 nM, 0.012 MBq [0.34  $\mu\text{Ci}$ ] per well) and incubation for 1 h at 37°C. Unbound radiotracer was removed, and the wells were washed twice with  $\times 1$  phosphate-buffered saline. All experiments were performed in triplicate. The bound activity for each well was measured by a  $\gamma$ -counter and expressed as counts per minute.

### PET/CT Imaging

[ $^{89}\text{Zr}$ ]Zr-DFO-anti-IL12/23p40 (6.66–9.25 MBq, 36–50  $\mu\text{g}$ , 0.24–0.33 nmol) in sterile saline was administered intravenously to mice (5 per sex) in the lateral tail vein 5 d after DSS treatment. A separate cohort of DSS-treated mice was injected with an  $^{89}\text{Zr}$ -labeled nonspecific isotype-matched IgG antibody to control for specificity. Images were then acquired using a Bruker Albira Si PET/CT scanner at 24, 48, and 96 h after injection while the mice were anesthetized with 2% isoflurane. Subsequent imaging scans were acquired at 48 h after injection, the time point that was identified to achieve optimum contrast. Corresponding CT scans were acquired at 45 kV and 400  $\mu\text{A}$  after each PET scan. Images were reconstructed through maximum-likelihood expectation maximization with 12 iterations and a 0.75-mm voxel resolution, registered on CT, and analyzed by PMOD software, version 4.3. Volumes of interest were acquired via isocontouring and are expressed as the mean percentage injected dose per  $\text{cm}^3$  of tissue (%ID/ $\text{cm}^3$ ). After imaging, the mice were euthanized, and the colons were excised and laid out for ex vivo PET imaging.

### Biodistribution and In Vivo Blocking Studies

The tissue distribution of [ $^{89}\text{Zr}$ ]Zr-DFO-anti-IL12/23p40 was assessed in healthy and DSS-treated mice by intravenous injection of 0.37–0.92 MBq (10–25  $\mu\text{Ci}$ , 2–5  $\mu\text{g}$ ) in the lateral tail vein of the mice. To assess the specificity of target binding, we performed an in vivo blocking study on a separate group of mice in which a  $\times 100$  excess of unlabeled anti-IL12/23p40 mAb was coinjected with the radiotracer. Euthanasia was performed via  $\text{CO}_2$  asphyxiation 48 h after injection. Blood was immediately collected via cardiac puncture. Select organs were collected and weighed. Bound radioactivity was measured using a  $\gamma$ -counter (2480 Wizard<sup>2</sup>; Perkin Elmer) and expressed as %ID/g.

### IL12/23p40 Enzyme-Linked Immunosorbent Assay

Blood was collected via the cheek vein before (baseline or day 0) and during (day 5) DSS treatment. Sera were obtained and stored at  $-80^{\circ}\text{C}$  to allow for decay before analysis. Levels of IL12/23p40 were evaluated using a commercial enzyme-linked immunosorbent assay kit (catalog number ELM-IL12p40p70; RayBiotech). Serum levels were then correlated with the radiotracer uptake data from the biodistribution studies.

### In Situ Hybridization

To investigate the expression of IL12/23p40 in DSS-treated mice, RNA in situ hybridization for IL12/23p40 messenger RNA (RNAscope probe Mm-IL12b; ACD Bio) was performed using an RNAscope 2.5 HD detection assay (ACD Bio). The RNA spatial expression of IL12p35 (*IL12a*; Mm IL12a; ACD Bio) and IFN- $\gamma$  (RNAscope Probe-Mm-Ifng-C2; ACD Bio) were also examined. In brief, intestinal tissues were harvested, fixed, and stored in 10% formalin until decayed. Once decayed, the formalin was removed and replaced with 70% ethanol before paraffin embedding and sectioning. Tissues were sliced into 5- $\mu\text{m}$  sections and mounted on glass slides. Paraffin-embedded tissue sections were deparaffinized and subjected to antigen retrieval using an RNAscope antigen retrieval kit (ACD Bio) followed by hybridization, signal amplification, and chromogenic detection procedures, which were performed according to the manufacturer's instructions (RNAscope 2.5 HD duplex detection; ACD Bio). The messenger RNA for IL12/23p40 and IFN- $\gamma$  was detected using red chromogen and that of IL12p35 was detected using green chromogen. Images ( $\times 40$  objective) were captured under an optical microscope (Carl Zeiss), and signal quantification was analyzed by HALO software, version 4.1.1 (Indica Labs). At least 5 fields per section were analyzed.

### Statistical Analysis

GraphPad Prism, version 9.02, was used to perform statistical analyses unless otherwise stated. Data are presented as the mean  $\pm$  SD. Mann-Whitney *t* tests were performed for the tumor-blocking competitive studies. Two-way ANOVA multiple-comparison analyses were performed for the tissue distribution studies. The significance of correlations was determined by Pearson analysis. A *P* value of less than 0.05 was considered statistically significant.

## RESULTS

### Successful Labeling and Target Binding of [ $^{89}\text{Zr}$ ]Zr-DFO-Anti-IL12/23p40

Radiolabeling of the DFO immunoconjugate was straightforward, with radiolabeling yields of more than 95%. A specific

activity of  $180 \pm 10$  MBq/mg was established. The radiotracer remained moderately intact ( $>90\%$ ) in saline over a 96-h incubation period (Supplemental Fig. 1). The binding of [ $^{89}\text{Zr}$ ]Zr-DFO-anti-IL12/23p40 to mouse IL12/23p40 protein was evaluated by saturation binding assays, showing total and nonspecific binding (Supplemental Fig. 2), which confirmed the high affinity (dissociation constant,  $\sim 9.8 \pm 1.9$  nM) of the radiolabeled mAb for its target (Fig. 1A). The in vitro blocking study, in which [ $^{89}\text{Zr}$ ]Zr-DFO-anti-IL12/23p40 was incubated with a 100-fold mass excess of the unmodified nonradiolabeled antibody, demonstrated significantly decreased binding of [ $^{89}\text{Zr}$ ]Zr-DFO-anti-IL12/23p40 to IL12/23p40 protein (*P* = 0.0001) (Fig. 1B), confirming the in vitro specificity of the radiotracer.

### Induction and Confirmation of Colitis

Colitis was induced in BALB/c mice by providing DSS ad libitum for 7 d, followed by recovery with regular drinking water on day 8 (Fig. 2A). DSS-treated mice showed weight loss on day 5 (Fig. 2B). Disease activity index scores for stool consistency and fecal bleeding were higher in the DSS-treated mice than in the healthy mice (Supplemental Table 1). On day 8, scores of more than 2 were recorded for DSS-treated mice according to the presence of diarrhea and blood in their stools.

### In Vivo Delineation of Intestinal Inflammation by IL12/23p40 Immuno-PET

[ $^{89}\text{Zr}$ ]Zr-DFO-anti-IL12/23p40 delineated the intestinal tract of a mouse with severe gastrointestinal inflammation, whereas no clear delineation was observed in healthy control mice (Fig. 3A). The planar sections of the PET images for these mice and those with mild IBD are shown in Supplemental Figures 3A and 3B. Uptake of the radiotracer in the colons of both healthy and DSS-treated mice was recorded and classified according to sex (Fig. 3B). For both male mice (DSS,  $5.99 \pm 0.65$  %ID/ $\text{cm}^3$ , vs. healthy,  $3.98 \pm 0.58$  %ID/ $\text{cm}^3$ ; *P* = 0.0002) and female mice (DSS,  $8.53 \pm 1.47$  %ID/ $\text{cm}^3$ , vs. healthy,  $6.56 \pm 0.85$  %ID/ $\text{cm}^3$ ; *P* = 0.014), DSS treatment led to higher uptake in the colon than that for the healthy group at 24 h after injection or day 6. A comparative analysis between the sexes in healthy and DSS mice revealed significant differences in radiotracer uptake between male and female (Fig. 3C). The time-activity curve of [ $^{89}\text{Zr}$ ]Zr-DFO-anti-IL12/23p40 taken from volumes of interest of the heart, liver, and muscle uptake from 24 to 96 h after injection (days 6–9) showed decreasing nonspecific binding of the radiotracer over time (Fig. 3D).

The specificity of the cytokine radiotracer was assessed by imaging a separate cohort of DSS-treated mice with a  $^{89}\text{Zr}$ -radiolabeled isotype control antibody. Unlike colitis mice imaged with [ $^{89}\text{Zr}$ ]Zr-DFO-anti-IL12/23p40, colitis mice imaged with [ $^{89}\text{Zr}$ ]Zr-DFO-IgG did not show specific accumulation in the colon (Fig. 3E). Colitis mice injected with [ $^{89}\text{Zr}$ ]Zr-DFO-IgG showed lower uptake in the colon at 48 h after injection (day 7) of the radiotracer than did DSS mice injected with [ $^{89}\text{Zr}$ ]Zr-DFO-anti-IL12/23p40 (Fig. 3F). Selected healthy organs (e.g., heart, liver, and muscle) displayed lower binding of [ $^{89}\text{Zr}$ ]Zr-DFO-IgG than of the IL12/23p40-specific radiotracer (Supplemental Figs. 3C–3D).

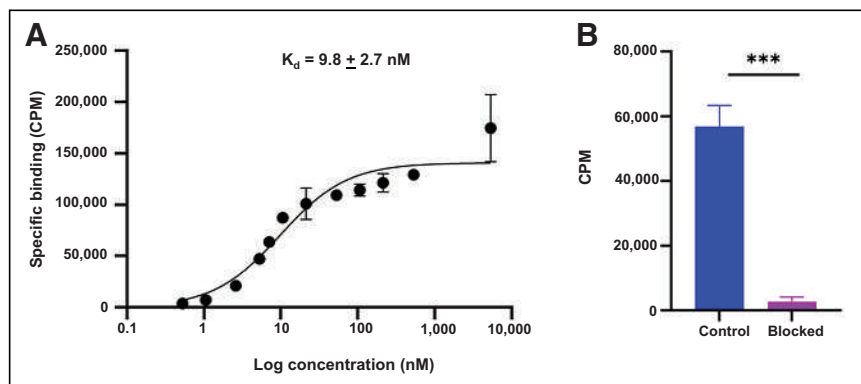


**FIGURE 1.** In vitro characterization of [ $^{89}\text{Zr}$ ]Zr-DFO-anti-IL12/23p40. (A) Nonlinear regression analysis determination of binding affinity (dissociation constant [ $K_d$ ]) of tracer for IL12/23p40. (B) Competitive inhibition with  $\times 100$  excess of unmodified antibody coadministered with radiotracer in IL12/23p40-coated wells. CPM = counts per minute. \*\*\**P* < 0.001.

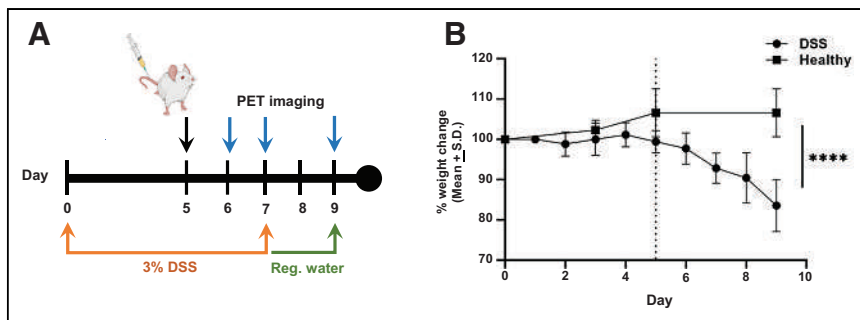


**FIGURE 2.** (A) Scheme showing days of DSS treatment, injection of [ $^{89}\text{Zr}$ ]Zr-DFO-anti-IL12/23p40, and PET imaging. (B) Changes in body weight after 5 d of DSS treatment (5 per sex). Vertical dashed line indicates beginning of body weight loss. \*\*\*\* $P = 0.0001$ .

### Ex Vivo Imaging of Excised Colons

We next performed ex vivo imaging to assess the specific focal uptake of the tracer in the colon. Tracer uptake was increased in the cecum, proximal colon, and mid colon of DSS-treated mice

### Tissue Biodistribution and Competitive Binding

Tissue biodistribution of [ $^{89}\text{Zr}$ ]Zr-DFO-anti-IL12/23p40 was analyzed in both healthy and DSS-treated mice at 48 h after injection (Fig. 4D). Uptake in the large intestine was higher in the DSS group than in the healthy mice ( $3.0 \pm 0.4$  %ID/g vs.  $1.7 \pm 0.35$  %ID/g,  $P = 0.0008$ ), whereas no significant differences in the cecum and small intestines were observed between the 2 cohorts.

To confirm specificity, blocking experiments were performed in which at least a 100-fold excess of the unmodified, nonradioactive mAb was coinjected with the radiotracer into DSS-treated mice. Blocking significantly decreased uptake in the small intestines ( $1.3 \pm 0.2$  %ID/g vs.  $0.4 \pm 0.1$  %ID/g,  $P < 0.0001$ ), colon ( $3.0 \pm 0.4$  %ID/g vs.  $0.8 \pm 0.2$  %ID/g,  $P < 0.0001$ ), and cecum ( $1.6 \pm 0.5$  %ID/g vs.  $1.0 \pm 0.3$  %ID/g,  $P = 0.0132$ ) (Fig. 4E). We also observed a decrease in accumulation of the radiotracer in the nontarget tissues of the blocked versus unblocked DSS cohorts (Fig. 4D), suggesting that the excess mAb attenuated the binding of the radiotracer in endogenously expressed and systemically circulating IL12/23p40. Furthermore, another rationale for the observed decreased binding is the fact that the mAb is inherently therapeutic, suggesting that the mass injected for blocking ( $\sim 200$   $\mu\text{g}$ ) may have depleted the cytokine at 48 h after injection, resulting in lower tracer binding.

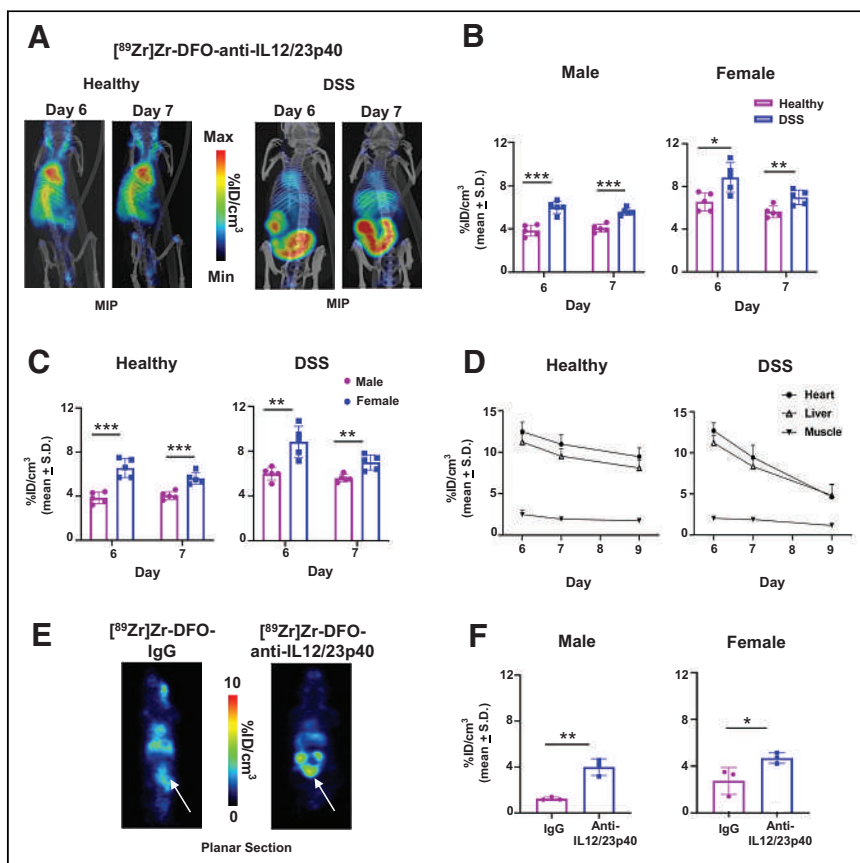


**FIGURE 3.** IL12/23p40 immuno-PET/CT imaging of healthy and DSS-treated mice. (A) Representative maximum-intensity projection images of healthy (left) and DSS-treated (right) mice acquired at 24 h (day 6) and 48 h (day 7) after injection of [ $^{89}\text{Zr}$ ]Zr-DFO-anti-IL12/23p40. (B) Plotted volumes of interest of animals administered [ $^{89}\text{Zr}$ ]Zr-DFO-anti-IL12/23p40 exhibiting higher uptake in colons of male and female mice treated with DSS than in healthy mice. (C) Sex differences in pooled analysis of uptake of IL12/23p40 radiotracer ( $n = 5$  per sex) in both healthy and DSS-treated groups. (D) Time-activity curves of [ $^{89}\text{Zr}$ ]Zr-DFO-anti-IL12/23p40 binding in heart, liver, and muscle in healthy and DSS-treated groups. (E) Planar section of DSS-treated mice imaged with [ $^{89}\text{Zr}$ ]Zr-DFO-IgG (3 per sex) vs. [ $^{89}\text{Zr}$ ]Zr-DFO-anti-IL12/23p40 demonstrating minimal binding of nonspecific radiotracer in colon at day 7 (arrows). (F) Higher colon uptake of [ $^{89}\text{Zr}$ ]Zr-DFO-anti-IL12/23p40 (anti-IL12/23p40) in male ( $n = 3$ ) and female groups ( $n = 3$ ) than in those imaged with [ $^{89}\text{Zr}$ ]Zr-DFO-IgG (IgG) at 48 h after injection. All cohorts were 5 per sex unless otherwise stated. MIP = maximum-intensity projection. \* $P < 0.05$ . \*\* $P < 0.01$ . \*\*\* $P < 0.001$ .

### Correlation Between Tracer Uptake and Serum Expression of IL12/23p40

To confirm expression of IL12/23p40 in colitis mice, sera were sequentially collected on day 0 before radiotracer injection (the baseline before DSS treatment) and on day 5. Enzyme-linked immunosorbent assay results showed elevated total IL12/23p40 on day 5 compared with day 0 for both male and female groups (Fig. 5A) (male,  $1.85 \pm 0.28$  vs.  $1.22 \pm 0.33$  ng/mL



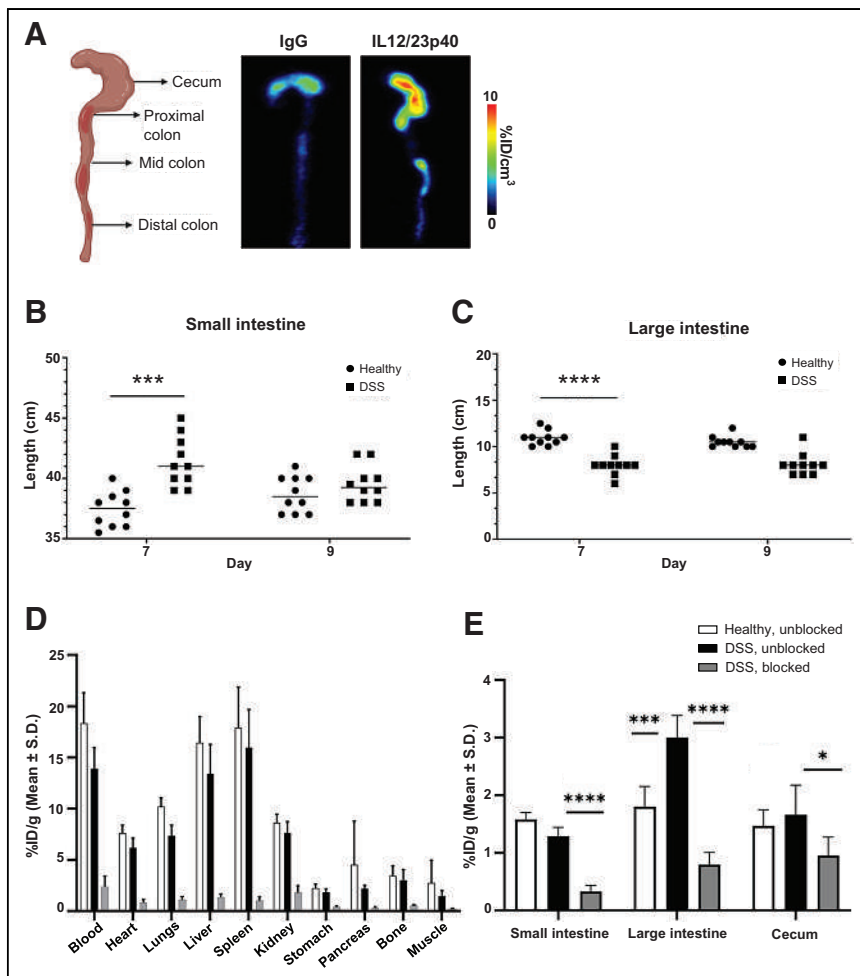


**FIGURE 4.** Ex vivo immuno-PET and tissue distribution studies. (A) Representative PET images of excised intestinal tissues from DSS-administered mice demonstrating increased accumulation of IL12/23p40 tracer (middle) in cecum, proximal colon, and mid colon vs. radiolabeled nonspecific isotype antibody (right). Schematic representation of mouse colon depicts colon sections (left) (created via Biorender). (B and C) Lengths of small (B) and large (C) intestines from separate cohorts were measured on last day of DSS treatment (day 7) and 2 d after switching to regular drinking water (day 9) (5 per sex). Small intestines in DSS-treated group were longer than those in healthy controls. Colons from DSS-treated mice were significantly shorter than those from healthy group on day 7, but there was no significant difference in length after switching to normal drinking water on day 9. (D) Tissue distribution of IL12/23p40 radiotracer in healthy and DSS-treated mice at 48 h after injection. Separate DSS-treated cohort was coinjected with excess of unmodified anti-IL23p40 for competitive binding with radiotracer (5 female animals per cohort). (E) Uptake of tracer in small intestines, colon, and cecum. \* $P < 0.05$ . \*\*\* $P < 0.001$ . \*\*\*\* $P < 0.0001$ .

[ $P = 0.0125$ ]; female,  $3 \pm 0.58$  vs.  $2.04 \pm 0.05$  ng/mL [ $P = 0.0473$ ]). A correlation between IL12/23p40 levels in sera on day 5 and [ $^{89}\text{Zr}$ ]Zr-DFO-anti-IL12/23p40 uptake in the small intestine and cecum (measured from the ex vivo distribution study) indicated a direct relationship between IL12/23p40 concentration and radiotracer uptake in the male group (Fig. 5B). A positive correlation, albeit not significant, was observed between IL12/23p40 in the serum and radiotracer uptake in the colon (Supplemental Fig. 4A; supplemental materials are available at <http://jnm.snmjournals.org>). In the female group, correlations between the serum level of IL12/23p40 and radiotracer uptake in the colon, cecum, and small intestine were not significant (Supplemental Fig. 4B).

### High Transcript Expression of IL12/23p40 in the Intestinal Tissues Validating PET Radiotracer Uptake

To further detect IL12/23p40 cytokine in healthy and DSS mice, in situ hybridization was performed to visualize RNA expression per cell (Fig. 6A). A high percentage of cells showed increased expression of *IL12b*, the gene for IL12/23p40 (percentage of cells positive for *IL12b*,  $27\% \pm 7.5\%$ ), in the cecum of DSS-treated mice compared with healthy tissue (Fig. 6B). To show that the p40 subunit is the main driver of inflammation, we examined for IL12p35 (*IL12a*), the other subunit specific to IL12 alone. *IL12a* was not as markedly expressed in inflamed tissues (percentage of cells positive for *IL12a*,  $2.75\% \pm 0.22\%$ ;  $P = 0.0012$ ) (Supplemental Fig. 5), suggesting that the inflammation in this mouse model is mediated by the p40 subunit. Interestingly, IFN- $\gamma$ , a downstream molecule produced by both IL12 and IL23 that is considered to stimulate massive leukocyte infiltration and mucosal damage in IBD (5), showed elevated transcript expression in the DSS-treated intestines but was not as elevated as IL12/23p40.

### DISCUSSION

The global increase in IBD incidence is anticipated to impose increasing health and economic burdens (2). Patients from industrialized western countries are those primarily affected by IBD. However, the prevalence and incidence are increasing worldwide, specifically in newly industrialized countries (2). On ultrasound alone, approximately 3.1 million adults were diagnosed with this autoimmune condition in 2015, with an increased prevalence observed for people over 45 y old, Hispanic and non-Hispanic white people, and those with low levels of education (27). Thus, addressing this autoimmune condition before it becomes a global issue is

critical. In addition, management and surveillance of IBD are crucial because it predisposes patients to a higher risk of CRC (28). Colitis is further observed as an immune-related adverse event associated with immune checkpoint inhibitors (29) and can be life-threatening at higher grades (30).

The current diagnostic standard of care is reliant on endoscopy or colonoscopy to assess mucosal inflammation. However, endoscopy or colonoscopy can image only superficial tissue architectures. These approaches reveal very little about the molecular characteristics of a patient's disease, especially when inflammation is occurring deep within the mucosal layer before anatomic changes are observed (31). Moreover, this approach carries the

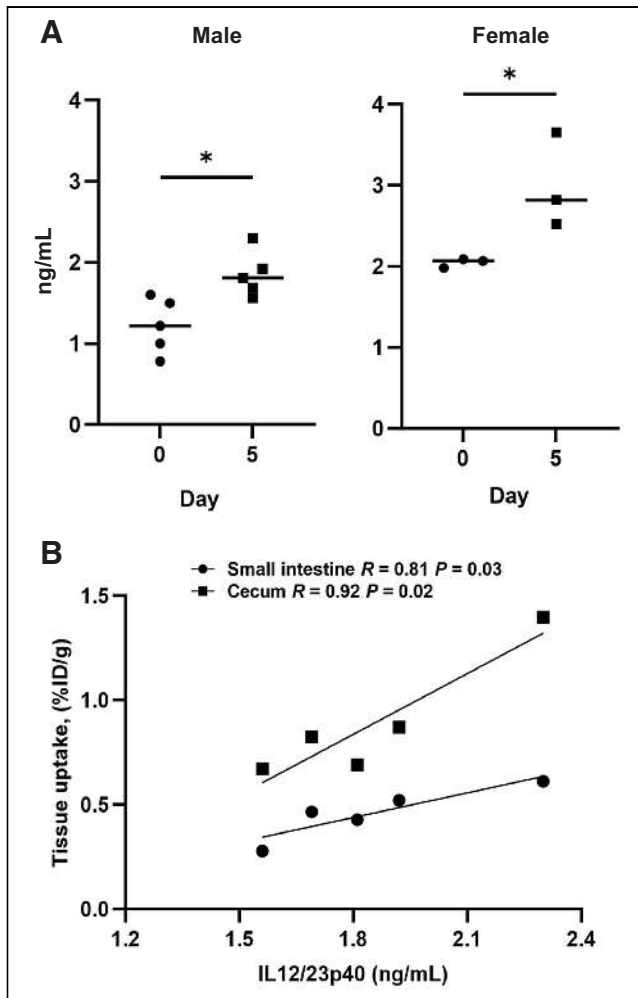


**FIGURE 5.** Correlation of serum IL12/23p40 with [<sup>89</sup>Zr]Zr-DFO-anti-IL12/23p40 tissue uptake. (A) IL12/23p40 in serum showing increased expression 5 d after DSS administration in male ( $n = 5$ ) and female ( $n = 3$ ) mice. (B) Strong positive correlation between IL12/23p40 serum concentration and radiotracer uptake in male group.  $*P < 0.05$ .

risk of bowel perforation, which can lead to bleeding. Noninvasive molecular imaging techniques can potentially overcome these limitations and improve IBD staging and diagnosis.

Here, we have presented the development of a noninvasive and quantitative imaging agent via immuno-PET that is directed against IL12/23p40, successfully achieving detection of acute inflammation in a DSS-induced mouse model of colitis. We have shown that [<sup>89</sup>Zr]Zr-DFO-anti-IL12/23p40 was able to detect IL12/23p40 in the colons of DSS-treated mice. We have demonstrated the radiotracer's specificity in both in vitro and in vivo competitive binding studies as well as when compared with a radiolabeled nonspecific antibody, which failed to delineate intestinal inflammation. The results of the biodistribution study clearly demonstrated increased uptake in the gastrointestinal tissues of the colitis mice, reflecting the PET imaging results.

In our hands, intestinal inflammation developed in the mice 5 d after administration of DSS, as marked by significant weight loss and high disease activity index scores. Different small- and large-intestine lengths in healthy versus DSS mice confirmed the intestinal inflammatory status of the latter, with measurements that agree

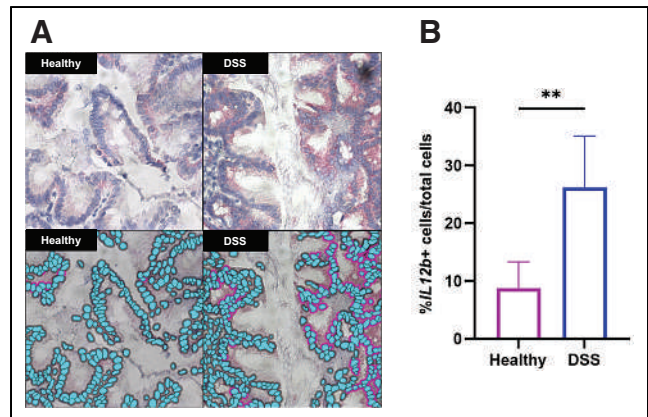


**FIGURE 6.** In situ hybridization to detect transcripts of IL12/23p40 (*IL12b*) in intestinal tissues of healthy and DSS mice. (A) Higher *IL12b* expression (red staining) in DSS-treated mice (top left) than in healthy mice (top right). Bottom figures represent individual cells analyzed by HALO software of healthy (left) and DSS-treated (right) colons. Purple outlines represent positive cells expressing *IL12b*, and cell nuclei are marked in blue. (B) Quantitative analysis of messenger RNA levels of IL12/23p40 ( $\geq 5$  fields of view from 1 tissue section). Cytokine expression is higher in DSS-treated than healthy mice.  $**P < 0.01$ .

well with prior reports (19). The radiotracer [<sup>89</sup>Zr]Zr-DFO-anti-IL12/23p40 was injected on day 5. We have determined that the optimum imaging time point at which a high signal-to-noise ratio can be achieved is between 24 h (day 6) and 48 h (day 7) after injection. The ex vivo imaging of excised large intestines displayed sporadic accumulation in the cecum and in different sections of the colon. We first endeavored to remove the feces. However, on removal, the PET signal decreased to almost background. We posit that the tracer is not bound to the gastrointestinal wall because it binds to soluble IL12/23p40, released in the extracellular milieu. Moreover, the cytokine binds to its receptor, which is present on trafficking immune cells. Thus, the PET signal from the images taken on different days is not localized (Fig. 3A).

One of the challenges we encountered in this study lies in the fact that inflammation is a dynamic immune event. The immune microenvironment during a state of inflammation is transient, with immune cells trafficking between the gut and peripheral lymphoid tissues to initiate and sustain inflammatory activity (32). Moreover, the severity of inflammation can vary in location and per animal, despite ensuring similar age and environmental conditions. This was evidenced through ex vivo images of the large intestines (Supplemental Fig. 3D) and through the disease activity index, where clinical manifestations (e.g., fecal blood, stool consistency) varied per mouse (Supplemental Table 1). As a result, discrepancies in radiotracer uptake between separate groups of animals used for imaging and those used for biodistribution can be misappropriated as discordant.

A growing body of evidence indicates that circulating IL23 may be a biomarker of disease severity in patients with IBD (33). Luca-ciu et al. have shown that for differentiating mild from severe inflammation, IL23 (from serum) is a diagnostic marker superior to current standard-of-care inflammation markers such as C-reactive protein and fecal calprotectin (34). Another study has shown that the enhanced serum levels of IL12p40 significantly correlate with clinical and endoscopic disease activity in patients with IBD (35).



In our study, we showed that elevated IL12/23p40 was detected by the radiotracer within the intestinal site and displayed a positive correlation between the ceca and small intestines with serum IL12/23p40 in male mice. We did not find a correlation between serum levels of IL12/23p40 and uptake of [<sup>89</sup>Zr]Zr-DFO-anti-IL12/23p40 in the colons of DSS-treated male mice, although a positive but nonsignificant trend was observed (Supplemental Fig. 3A). This is likely due to heterogeneity in immune activity and varying severities of inflammatory response, which can differ among mice despite their similar genetic backgrounds and housing conditions.

A sex disparity in inflammatory response to mucosal injury was evident in our study, and it was clearly delineated by the radiotracer. DSS-induced colitis in male mice resulted in significantly higher inflammation than that in female rodents, as demonstrated by disease activity index scores, a finding that parallels findings by others (36). Sex differences have long been recognized in IBD susceptibility and disease severity, but they remain poorly understood (37). The estrus cycle has been shown to influence IBD pathogenesis by controlling intestinal permeability, which is lower at the proestrus stage when estrogen peaks (38). Ogawa et al. reported that the gut of female rodents withstands the damaging effects of hypoxia and acidosis better than the gut of male rodents, but this disparity was eliminated on administration of estradiol to male rats, demonstrating the protective role of estrogen (33). Moreover, estrogen has been shown to exert an antiinflammatory function in the gut by reducing immune infiltration and cytokine secretion during colitis, which leads to significantly lower inflammation, as demonstrated by Houdeau et al. and Harnish et al. (39,40).

Other molecular agents to image IBD have been investigated. To date, clinical SPECT and PET imaging of IBD is restricted to using <sup>111</sup>In- or <sup>99m</sup>Tc-radiolabeled leukocytes and [<sup>18</sup>F]-FDG, none of which provides clinical information (17,41). Leukocyte SPECT imaging suffers from poor-quality images, and the radiolabeling is a time-consuming process (42). [<sup>18</sup>F]-FDG PET can identify inflammation, but its highly variable tissue uptake limits its utility as a diagnostic tool (43). [<sup>18</sup>F]-FDG marks cellular metabolism, providing information about the energy consumption of mucosal-layer-infiltrating immune cells within the inflamed tissue. This information can be useful for imaging glycolytic activity of immune cells but not for assessing mediators of inflammation (16). A significant drawback of using [<sup>18</sup>F]-FDG in IBD is that many individuals have progressive physiologic uptake in the gut, particularly in the large bowel, which may make it difficult to diagnose IBD in colonic segments (44). Additionally, patients with diabetes who use antidiabetic medications (such as metformin) may experience significant absorption in the large bowel, affecting the inflammatory readout from the tracer (45). New immuno-PET agents were developed and have shown excellent target selectivity; however, to date, their application to IBD detection is limited to preclinical studies. Freise et al. showed delineation of CD4<sup>+</sup> T cells that are present in inflamed colons of DSS mice using a murine CD4 diabody (GK1.5) radiolabeled with <sup>89</sup>Zr (19). Imaging CD4 precludes assessment of other proinflammatory immune cell phenotypes that contribute to this autoimmune condition (46,47). The innate immune markers CD11b and IL-1β were detected by <sup>89</sup>Zr-conjugated antibodies targeting these molecules. Both immuno-PET agents detected colonic inflammation, but [<sup>89</sup>Zr]Zr-anti-IL-1β was more specifically accumulated in the

gastrointestinal tract than was [<sup>89</sup>Zr]Zr-anti-CD11b, which was dispersed to other tissues (12). However, the role of IL-1β in IBD is far from clear, stemming from the lack of positive response in patients given the targeted blockade (12). Recently, an immuno-PET agent was developed for targeting tumor necrosis factor-α in DSS-induced colitis mice using <sup>89</sup>Zr-labeled mAb infliximab. Elevated levels of [<sup>89</sup>Zr]Zr-DFO-infliximab were observed in the colon of colitis mice compared with the healthy control and blocked groups (21). However, 30%–50% of patients eventually relapse from tumor necrosis factor-α blockade due to IL23-mediated resistance, which makes this new radiotracer more relevant as a predictive biomarker of response to therapy (48).

Our previous work developed and assessed an immuno-PET imaging agent specific for IL12p70 that detected the cytokine globally in an induced inflammation model (49). Compelling studies have shown that IL23 rather than IL12 plays a major proinflammatory role in IBD, which eliminates the targeting of IL12p70 as a method for imaging IBD. In this regard, the p40 subunit shared between IL12 and IL23 was demonstrated to be one of the mediators of inflammation and may be an appealing target for diagnosis and treatment of IBD. In fact, ustekinumab is an antihuman IL12/23p40 mAb currently deployed as the standard of care for Crohn disease patients and those with moderate to severe ulcerative colitis. Thus, the development of a companion diagnostic is an apparent rational next step (23).

Mouse IL12/23p40 is only 70% homologous to the human version (50). Consequently, we rationalize that proof-of-concept studies—as for all immunologic studies that use antibodies—will be better achieved if we use antibodies that target the host's protein (e.g., mouse IL12/23p40) and will eliminate variables that can confound the study. Indeed, using an antimouse IL12/23p40 antibody to target mouse IL12/23p40 precludes a straightforward application of the tracer in humans and limits the application in mice. However, our data establish proof that the tracer can delineate gastrointestinal inflammation, laying the groundwork for developing a tracer for human application.

A clear limitation of this radiotracer is its bispecificity for IL12 and IL23 because both share the p40 subunit, making it difficult to provide an absolute measure of IL23. IL12 (through *IL12a*) expression is 10-fold lower than that of IL23, suggesting that it is indeed IL23 that mediates the inflammation in this mouse model. Another limitation lies in the potential of the antibody to neutralize IL12/23p40, consequently decreasing IL12 and IL23 expression, which we have observed during *in vivo* competitive binding studies and during imaging studies. To address this, work is under way to develop nonneutralizing second-generation mAb fragments that are specific to IL23.

Our findings demonstrate that our IL12/23p40 tracer constitutes a novel approach to delineate IBD selectively and robustly in this model of acute inflammation. The promising findings from this study have major implications in IBD treatment as a noninvasive, quantitative, and molecular technique for its diagnosis, potentially improving the standard of care. Although there is a risk associated with radiation produced by radiopharmaceuticals agents, the advantages of PET imaging—in this case, informing inflammatory activity by imaging IL12/23p40—far outweigh exposure of patients to radiation, which can easily be mitigated by administering safe doses. Furthermore, IL12/23p40 immuno-PET can provide useful insight for patient treatment, including those who will potentially respond to its blockade.

## CONCLUSION

To the best of our knowledge, this is the first report illustrating the preliminary development of an IBD immuno-PET imaging tool specific for IL12/23p40. This new imaging technology can potentially facilitate detection and accurate staging of IBD in patients via generation of a global in vivo inflammation map of the entire gastrointestinal tract.

## DISCLOSURE

The study was supported by NIH/NCI R37 CA220482 (Nerissa Viola). The Microscopy, Imaging, and Cytometry Resources Core (MICR) and the Animal Modeling and Therapeutics Core, which provided technical assistance, are supported, in part, by NIH Cancer Center grant P30 CA022453 to the Karmanos Cancer Institute at Wayne State University. No other potential conflict of interest relevant to this article was reported.

## ACKNOWLEDGMENTS

We thank Dr. Lisa Polin and Michael Bradley for suggestions and advice on animal studies. We are further grateful to Dr. Freddy Escorcía for helpful discussions and review of the manuscript. We also thank Dr. Todd Sasser for assistance in the PET/CT image analysis.

## KEY POINTS

**QUESTION:** What is the potential of IL12/23p40 immuno-PET to visualize IBD?

**PERTINENT FINDINGS:** IL12/23p40 immuno-PET selectively and robustly delineated acute inflammation in an induced-colitis mouse model via monitoring IL12/23p40, making it a novel imaging technology that can potentially facilitate early detection of IBD.

**IMPLICATIONS FOR PATIENT CARE:** The findings of this study are significant because it potentially represents a new category of diagnostic tool for surveillance and diagnosis of IBD. Imaging IL12/23p40 is an innovative and minimally invasive approach for identifying the dominant signaling pathway to guide clinical decisions on appropriate treatment.

## REFERENCES

- Silva FA, Rodrigues BL, Ayriso ML, Leal RF. The immunological basis of inflammatory bowel disease. *Gastroenterol Res Pract*. 2016;2016:2097274.
- GBD 2017 Inflammatory Bowel Disease Collaborators. The global, regional, and national burden of inflammatory bowel disease in 195 countries and territories, 1990–2017: a systematic analysis for the Global Burden of Disease Study 2017. *Lancet Gastroenterol Hepatol*. 2020;5:17–30.
- Fiocchi C. Inflammatory bowel disease: etiology and pathogenesis. *Gastroenterology*. 1998;115:182–205.
- Hanauer SB. Inflammatory bowel disease: epidemiology, pathogenesis, and therapeutic opportunities. *Inflamm Bowel Dis*. 2006;12(suppl 1):S3–S9.
- Langer V, Vivi E, Regensburger D, et al. IFN- $\gamma$  drives inflammatory bowel disease pathogenesis through VE-cadherin-directed vascular barrier disruption. *J Clin Invest*. 2019;129:4691–4707.
- Lakatos PL, Lakatos L. Risk for colorectal cancer in ulcerative colitis: changes, causes and management strategies. *World J Gastroenterol*. 2008;14:3937–3947.
- Van Der Kraak L, Gros P, Beauchemin N. Colitis-associated colon cancer: is it in your genes? *World J Gastroenterol*. 2015;21:11688–11699.
- Porter RJ, Arends MJ, Churchhouse AM, Din S. Inflammatory bowel disease-associated colorectal cancer: translational risks from mechanisms to medicines. *J Crohns Colitis*. 2021;15:2131–2141.
- Kilcoyne A, Kaplan JL, Gee MS. Inflammatory bowel disease imaging: current practice and future directions. *World J Gastroenterol*. 2016;22:917–932.
- Loftus EV. Emerging diagnostic methods in inflammatory bowel disease. *Gastroenterol Hepatol (N Y)*. 2007;3:284–286.
- Spiceland CM, Lodhia N. Endoscopy in inflammatory bowel disease: role in diagnosis, management, and treatment. *World J Gastroenterol*. 2018;24:4014–4020.
- Dmochowska N, Tieu W, Keller MD, et al. Immuno-PET of innate immune markers CD11b and IL-1 $\beta$  detects inflammation in murine colitis. *J Nucl Med*. 2019;60:858–863.
- Le Fur M, Zhou IY, Catalano O, Caravan P. Toward molecular imaging of intestinal pathology. *Inflamm Bowel Dis*. 2020;26:1470–1484.
- Dmochowska N, Wardill HR, Hughes PA. Advances in imaging specific mediators of inflammatory bowel disease. *Int J Mol Sci*. 2018;19:2471.
- Caobelli F, Evangelista L, Quartuccio N, et al. Role of molecular imaging in the management of patients affected by inflammatory bowel disease: state-of-the-art. *World J Radiol*. 2016;8:829–845.
- Gelston D, Brosler SC, Vazquez J, et al. Utility of FDG PET/CT in assessing bowel inflammation. *Am J Nucl Med Mol Imaging*. 2021;11:271–279.
- Treglia G, Quartuccio N, Sadeghi R, et al. Diagnostic performance of fluorine-18-fluorodeoxyglucose positron emission tomography in patients with chronic inflammatory bowel disease: a systematic review and a meta-analysis. *J Crohns Colitis*. 2013;7:345–354.
- Aarntzen EH, Hermsen R, Drenth JP, Boerman OC, Oyen WJ.  $^{99m}\text{Tc}$ -CXCL8 SPECT to monitor disease activity in inflammatory bowel disease. *J Nucl Med*. 2016;57:398–403.
- Freise AC, Zettlitz KA, Salazar FB, et al. Immuno-PET in inflammatory bowel disease: imaging CD4-positive T cells in a murine model of colitis. *J Nucl Med*. 2018;59:980–985.
- Dmochowska N, Tieu W, Keller MD, et al.  $^{89}\text{Zr}$ -pro-MMP-9 F(ab')<sub>2</sub> detects colitis induced intestinal and kidney fibrosis. *Sci Rep*. 2020;10:20372.
- Yan G, Wang X, Fan Y, et al. Immuno-PET Imaging of TNF- $\alpha$  in colitis using  $^{89}\text{Zr}$ -DFO-infliximab. *Mol Pharm*. 2022;19:3632–3639.
- Neurath MF. IL-12 family members in experimental colitis. *Mucosal Immunol*. 2008;1(suppl 1):S28–S30.
- Kashani A, Schwartz DA. The expanding role of anti-IL-12 and/or anti-IL-23 antibodies in the treatment of inflammatory bowel disease. *Gastroenterol Hepatol (N Y)*. 2019;15:255–265.
- Krugliak NC, Inessa N, Anthony B, et al. Ustekinumab provides steroid-sparing and perianal improvement in IBD patients: single center experience: P-031. *Am J Gastroenterol*. 2018;113:S8.
- Sands BE, Sandborn WJ, Panaccione R, et al. Ustekinumab as induction and maintenance therapy for ulcerative colitis. *N Engl J Med*. 2019;381:1201–1214.
- Viola-Villegas NT, Sevak KK, Carlin SD, et al. Noninvasive imaging of PSMA in prostate tumors with  $^{89}\text{Zr}$ -labeled huJ591 engineered antibody fragments: the faster alternatives. *Mol Pharm*. 2014;11:3965–3973.
- Dahlhamer JM, Zammitti EP, Ward BW, Wheaton AG, Croft JB. Prevalence of inflammatory bowel disease among adults aged  $\geq 18$  years: United States, 2015. *MMWR Morb Mortal Wkly Rep*. 2016;65:1166–1169.
- Zhou Q, Shen Z-F, Wu B-S, et al. Risk of colorectal cancer in ulcerative colitis patients: a systematic review and meta-analysis. *Gastroenterol Res Practice*. 2019;2019:5363261.
- Tang L, Wang J, Lin N, et al. Immune checkpoint inhibitor-associated colitis: from mechanism to management. *Front Immunol*. 2021;12:800879.
- Gong Z, Wang Y. Immune checkpoint inhibitor-mediated diarrhea and colitis: a clinical review. *JCO Oncol Pract*. 2020;16:453–461.
- Mohammed Vahist N, Samaan M, Mosli MH, et al. Endoscopic scoring indices for evaluation of disease activity in ulcerative colitis. *Cochrane Database Syst Rev*. 2018;1:CD011450.
- Lu Q, Yang M-F, Liang Y-J, et al. Immunology of inflammatory bowel disease: molecular mechanisms and therapeutics. *J Inflamm Res*. 2022;15:1825–1844.
- Ogawa K, Matsumoto T, Esaki M, Torisu T, Iida M. Profiles of circulating cytokines in patients with Crohn's disease under maintenance therapy with infliximab. *J Crohns Colitis*. 2012;6:529–535.
- Lucaci LA, Iliş M, Vesa ŞC, et al. Serum interleukin (IL)-23 and IL-17 profile in inflammatory bowel disease (IBD) patients could differentiate between severe and non-severe disease. *J Pers Med*. 2021;11:1130.
- Lee HW, Chung SH, Moon CM, et al. The correlation of serum IL-12B expression with disease activity in patients with inflammatory bowel disease. *Medicine (Baltimore)*. 2016;95:e3772.
- Bábícková J, Tóthová L, Lengyelová E, et al. Sex differences in experimentally induced colitis in mice: a role for estrogens. *Inflammation*. 2015;38:1996–2006.
- Zelinková Z, Woude CJ. Gender and inflammatory bowel disease. *J Clin Cell Immunol*. 2014;5:1–6.

38. Braniste V, Leveque M, Buisson-Brenac C, Bueno L, Fioramonti J, Houdeau E. Oestradiol decreases colonic permeability through oestrogen receptor  $\beta$ -mediated up-regulation of occludin and junctional adhesion molecule-A in epithelial cells. *J Physiol (Lond)*. 2009;587:3317–3328.
39. Houdeau E, Moriez R, Leveque M, et al. Sex steroid regulation of macrophage migration inhibitory factor in normal and inflamed colon in the female rat. *Gastroenterology*. 2007;132:982–993.
40. Harnish DC, Albert LM, Leathurby Y, et al. Beneficial effects of estrogen treatment in the HLA-B27 transgenic rat model of inflammatory bowel disease. *Am J Physiol Gastrointest Liver Physiol*. 2004;286:G118–G125.
41. Tsopelas C. The radiopharmaceutical chemistry of  $^{99m}\text{Tc}$ -tin fluoride colloid-labeled-leukocytes. *Q J Nucl Med Mol Imaging*. 2005;49:319–324.
42. Palestro CJ, Love C, Bhargava K. Labeled leukocyte imaging: current status and future directions. *Q J Nucl Med Mol Imaging*. 2009;53:105–123.
43. Malham M, Hess S, Nielsen RG, Husby S, Høilund-Carlsen PF. PET/CT in the diagnosis of inflammatory bowel disease in pediatric patients: a review. *Am J Nucl Med Mol Imaging*. 2014;4:225–230.
44. Glaudemans AW, de Vries EF, Galli F, Dierckx RA, Slart RH, Signore A. The use of F-FDG-PET/CT for diagnosis and treatment monitoring of inflammatory and infectious diseases. *Clin Dev Immunol*. 2013;2013:623036.
45. Das CJ, Makharia GK, Kumar R, et al. PET/CT colonography: a novel non-invasive technique for assessment of extent and activity of ulcerative colitis. *Eur J Nucl Med Mol Imaging*. 2010;37:714–721.
46. Raphael I, Joern RR, Forsthuber TG. Memory CD4+ T cells in immunity and autoimmune diseases. *Cells*. 2020;9:531.
47. Skapenko A, Leipe J, Lipsky PE, Schulze-Koops H. The role of the T cell in autoimmune inflammation. *Arthritis Res Ther*. 2005;7(suppl 2):S4–S14.
48. Atreya R, Neurath MF. IL-23 blockade in anti-TNF refractory IBD: from mechanisms to clinical reality. *J Crohns Colitis*. 2022;16:ii54–ii63.
49. Viola NT, Glassbrook JE, Kalluri JR, et al. Evaluation of an immunoPET tracer for IL-12 in a preclinical model of inflammatory immune responses. *Front Immunol*. 2022;13:870110.
50. Walter MJ. Interleukins | IL-12. In: Janes SM, ed. *Encyclopedia of Respiratory Medicine*. 2006;377–382.

---

---

# Long Versus Short Axial Field of View Immuno-PET/CT: Semiquantitative Evaluation for $^{89}\text{Zr}$ -Trastuzumab

Philipp Mohr<sup>1</sup>, Joyce van Sluis<sup>1</sup>, Laura Providência<sup>1</sup>, Johannes H. van Snick<sup>1</sup>, Marjolijn N. Lub-de Hooge<sup>2</sup>, Antoon T. Willemssen<sup>1</sup>, Andor W.J.M. Glaudemans<sup>1</sup>, Ronald Boellaard<sup>1,3</sup>, Adriaan A. Lammertsma<sup>1</sup>, Adrienne H. Brouwers<sup>1</sup>, and Charalampos Tsoumpas<sup>1</sup>

<sup>1</sup>Department of Nuclear Medicine and Molecular Imaging, University Medical Center Groningen, University of Groningen, Groningen, The Netherlands; <sup>2</sup>Department of Clinical Pharmacy and Pharmacology, University Medical Center Groningen, University of Groningen, Groningen, The Netherlands; and <sup>3</sup>Department of Radiology and Nuclear Medicine, Amsterdam University Medical Centers, Location VUmc, Amsterdam, The Netherlands

---

The purpose of this study was to quantify any differences between the SUVs of  $^{89}\text{Zr}$  immuno-PET scans obtained using a PET/CT system with a long axial field of view (LAFOV; Biograph Vision Quadra) compared to a PET/CT system with a short axial field of view (SAFOV; Biograph Vision) and to evaluate how LAFOV PET scan duration affects image noise and SUV metrics. **Methods:** Five metastatic breast cancer patients were scanned consecutively on SAFOV and LAFOV PET/CT scanners. Four additional patients were scanned using only LAFOV PET/CT. Scans on both systems lasted approximately 30 min and were acquired 4 d after injection of 37 MBq of  $^{89}\text{Zr}$ -trastuzumab. LAFOV list-mode data were reprocessed to obtain images acquired using shorter scan durations (15, 10, 7.5, 5, and 3 min). Volumes of interest were placed in healthy tissues, and tumors were segmented semi-automatically to compare coefficients of variation and to perform Bland-Altman analysis on SUV metrics ( $\text{SUV}_{\text{max}}$ ,  $\text{SUV}_{\text{peak}}$ , and  $\text{SUV}_{\text{mean}}$ ). **Results:** Using 30-min images, 2 commonly used lesion SUV metrics were higher for SAFOV than for LAFOV PET ( $\text{SUV}_{\text{max}}$ ,  $16.2\% \pm 13.4\%$ , and  $\text{SUV}_{\text{peak}}$ ,  $10.1\% \pm 7.2\%$ ), whereas the  $\text{SUV}_{\text{mean}}$  of healthy tissues showed minimal differences ( $0.7\% \pm 5.8\%$ ). Coefficients of variation in the liver derived from 30-min SAFOV PET were between those of 3- and 5-min LAFOV PET. The smallest  $\text{SUV}_{\text{max}}$  and  $\text{SUV}_{\text{peak}}$  differences between SAFOV and LAFOV were found for 3-min LAFOV PET. **Conclusion:** LAFOV  $^{89}\text{Zr}$  immuno-PET showed a lower  $\text{SUV}_{\text{max}}$  and  $\text{SUV}_{\text{peak}}$  than SAFOV because of lower image noise. LAFOV PET scan duration may be reduced at the expense of increasing image noise and bias in SUV metrics. Nevertheless,  $\text{SUV}_{\text{peak}}$  showed only minimal bias when reducing scan duration from 30 to 10 min.

**Key Words:** immuno-PET; zirconium; scan duration; LAFOV; PET/CT

**J Nucl Med 2023; 64:1815–1820**

DOI: 10.2967/jnumed.123.265621

---

**I**mmuno-PET refers to imaging of radiolabeled monoclonal antibodies (mAbs) by means of PET, which makes it possible to study their biodistribution and tumor targeting. This molecular imaging technique has shown promise in improving and tailoring therapy with existing mAbs, as well as in developing novel mAbs more efficiently (1–6). To match the slow kinetics of mAbs, radionuclides

with a long half-life are used, such as  $^{89}\text{Zr}$ , thereby enabling PET measurements over several days. The longer half-life, however, is associated with a higher radiation dose than for short-lived radionuclides, and thus, the amount of activity that can be administered to patients is limited (7,8). As a result, longer scan durations are required to obtain adequate image quality, especially at later imaging time points.

The introduction of PET/CT systems with silicon photomultipliers and time-of-flight image reconstruction capabilities already has improved the signal-to-noise ratio of PET measurements, which, in turn, has led to a reduction in scan duration or activity administration (9–12). The more recent introduction of PET systems with a long axial field of view (LAFOV), with their increased sensitivity (13), further improves the signal-to-noise ratio (14,15), leading to several new opportunities in clinical practice and research (16–18). To use these new-generation of PET/CT systems efficiently, it is necessary to optimize scan protocols and understand the impact of various parameters on SUVs.

In the case of  $^{89}\text{Zr}$  immuno-PET, typical scan durations for standard axial field of view (SAFOV) PET/CT systems at 4 d after injection of 37 MBq of a labeled mAb are 30 min for a PET/CT system with 210-ps (10) time-of-flight and 45 min for an earlier-generation system with poorer time-of-flight resolution (527 ps (19)) (20). For later imaging time points, such as on day 7 after injection, with an earlier-generation system, scan duration may have to be increased to 2 h to obtain adequate count statistics for reasonable image quality (21).

The increased sensitivity of LAFOV PET/CT systems provides several options for  $^{89}\text{Zr}$  immuno-PET. First, it improves the signal-to-noise ratio of the PET measurement and thereby leads to better image quality. Furthermore, the scan duration may be shortened, resulting in greater patient comfort and a lower demand on scanner time. Finally, there is the possibility to lower the injected dose of a  $^{89}\text{Zr}$ -labeled mAb, thereby enabling immuno-PET studies in nononcologic and younger patients.

In this study, SUV and coefficient of variation (COV) as obtained with a 106-cm LAFOV Biograph Vision Quadra PET/CT system (Siemens Healthineers) versus a 26.3-cm SAFOV Biograph Vision PET/CT system (Siemens Healthineers) were compared for  $^{89}\text{Zr}$  immuno-PET. In addition, the possibility of shortening the scan duration and its effect on SUV and COV were assessed, as this has not yet been explored for  $^{89}\text{Zr}$ -labeled tracers imaged with LAFOV PET/CT.

---

Received Feb. 21, 2023; revision accepted Jun. 20, 2023.  
For correspondence or reprints, contact Philipp Mohr (p.mohr@umcg.nl).  
Published online Aug. 3, 2023.  
COPYRIGHT © 2023 by the Society of Nuclear Medicine and Molecular Imaging.

## MATERIALS AND METHODS

### Patient Population

Nine patients diagnosed with metastatic human epidermal growth factor receptor 2–positive breast cancer were included. PET scans with 37 MBq (range, 35–39 MBq; effective dose, ~17 mSv (22)) of  $^{89}\text{Zr}$ -trastuzumab (50-mg protein dose) were performed to assist in clinical decision-making (23). Patients (female; weight range, 59–80 kg) were enrolled in this study between November 2021 and January 2023. Five patients underwent 2 scans, first with SAFOV PET/CT and then with LAFOV PET/CT. The 4 remaining patients were scanned with LAFOV PET/CT only.

The medical ethics review committee of the University Medical Center Groningen waived the need for a formal ethical review of the validation protocol for the Biograph Vision Quadra PET/CT system (waiver METc2020/554). Patients were informed about the study aims and procedures and the need to acquire an additional low-dose CT scan (average effective dose, ~2 mSv). All subjects gave written informed consent.

### Imaging and Reconstruction Protocol

Scans on both PET/CT systems, each lasting approximately 30 min, were acquired 4 d after injection of  $^{89}\text{Zr}$ -trastuzumab. The average time difference between scans on the 2 systems was 38 min (range, 31–49 min). On the SAFOV system, the data were acquired with continuous bed motion (24) for approximately 30 min (slightly varying with patient length) and with a variable number of passes (either 1 or 4). On the LAFOV system, data were acquired in list mode for 30 min using a single bed position with a fixed field of view of 106 cm. The axial length of the SAFOV images was variable and slightly shorter (on average, 7%) than that of the LAFOV images.

For both scanners, PET data were reconstructed using 3 different protocols. First, a local clinical reconstruction protocol (hereafter referred to as CLIN) was applied, which was an ordinary Poisson ordered-subset expectation maximization 3-dimensional iterative time-of-flight algorithm (25) using 4 iterations and 5 subsets, with point spread function incorporated (26) and with no filtering. The resulting image size was  $440 \times 440$  with a voxel size of  $1.65 \times 1.65 \times 1.50 \text{ mm}^3$ . In addition, European Association of Nuclear Medicine Research Ltd. (EARL)–compliant images were obtained using the same reconstruction algorithm with 4 iterations and 5 subsets but with a matrix size of  $220 \times 220$ , a voxel size of  $3.3 \times 3.3 \times 1.5 \text{ mm}^3$ , and a postreconstruction isotropic gaussian filter of 5 mm (in full width at half maximum) for EARL standard 2 (EARL2 (27)) and 7 mm for EARL standard 1 (EARL1 (28)). Data acquired with LAFOV PET/CT were reconstructed with a maximum ring difference of 85 (13) because reconstruction with a larger maximum ring difference was not available in the current system software.

For the comparison of LAFOV and SAFOV systems, the following images were obtained per patient ( $n = 5$ ): SAFOV-CLIN, SAFOV-EARL1, SAFOV-EARL2, LAFOV-CLIN, LAFOV-EARL1, and LAFOV-EARL2. For the investigation of lowering scan duration, the following images were obtained per patient ( $n = 9$ ) for both EARL1 and EARL2 settings: LAFOV-15, LAFOV-10, LAFOV-7.5, LAFOV-5, and LAFOV-3, corresponding to reduced scan durations of 15, 10, 7.5, 5, and 3 min, respectively.

### Semiquantitative Image Analysis

Reconstructed PET images were analyzed using the quAntitative onCology moleCulaR Analysis suiTE (ACCURATE), version 06022022 (29). Spherical volumes of interest (VOIs) were placed in the blood pool (ascending aorta), kidney cortex, spleen (diameter of 1.5 cm), and liver (diameter of 3 cm (30)) to assess the SUV metrics of healthy tissues. In addition, COVs were calculated for liver VOIs using SD and mean activity concentration in the VOI. VOIs for healthy tissues were placed individually per system and reconstruction type for the total-scan-duration images and subsequently were reused for the lower scan durations of LAFOV PET after visually verifying their position. For lesion segmentation, the semiautomated method A50P was used, which uses 50% of the lesion  $\text{SUV}_{\text{peak}}$  while correcting for local background activity around the lesion (31). This lesion segmentation was performed individually on each reconstructed image. A maximum of 5 lesions per patient were included to avoid a bias toward 1 patient. In general, lesions with the highest uptake were selected, and small lymph nodes with a volume of less than 0.5 mL were excluded to avoid partial-volume effects (32).

### Statistical Analysis

For tumors,  $\text{SUV}_{\text{max}}$  and  $\text{SUV}_{\text{peak}}$  were compared between the 2 PET/CT systems, whereas for healthy tissues,  $\text{SUV}_{\text{max}}$ ,  $\text{SUV}_{\text{peak}}$ , and  $\text{SUV}_{\text{mean}}$  were compared. Comparison between the systems was performed using Bland–Altman plots (33). LAFOV measurements were selected as baseline measurements, and the relative difference ( $d$ ) between SUVs measured using the 2 systems was defined as

$$d = \frac{\text{SUV}_{\text{SAFOV}} - \text{SUV}_{\text{LAFOV}}}{\text{SUV}_{\text{LAFOV}}} \times 100\%.$$

These differences were expressed as percentages to account for variations in the absolute magnitude of SUVs in different tissues.

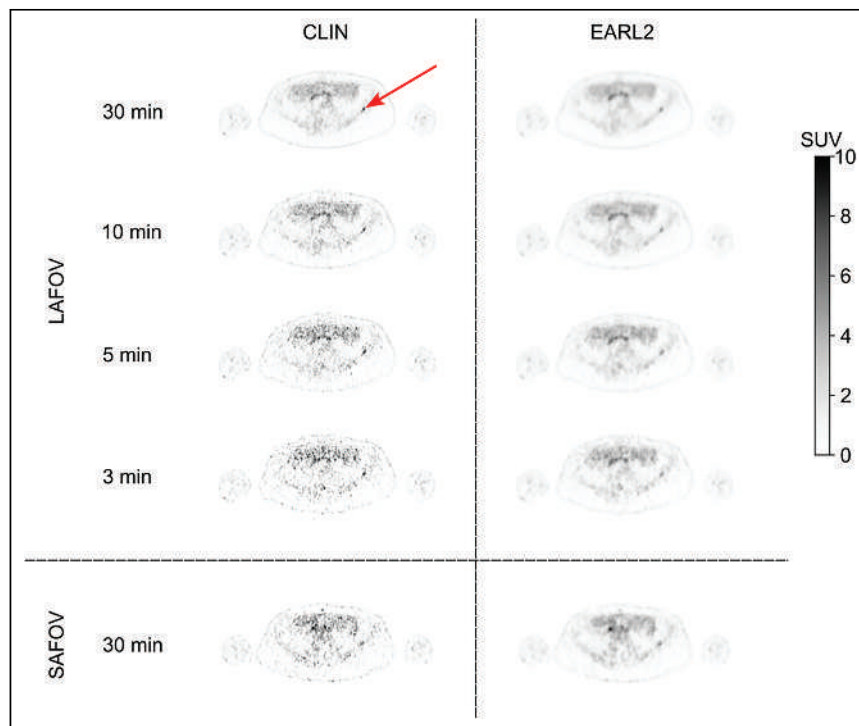


**FIGURE 1.** Axial images of patient scanned on both scanners for approximately 30 min (LAFOV: Biograph Vision Quadra, SAFOV: Biograph Vision) on day 4 after injection of 37 MBq of  $^{89}\text{Zr}$ -trastuzumab, showing small metastasis in iliac bone (arrow). Images are shown for 2 reconstruction protocols and for reduced scan durations of 10, 5, and 3 min for LAFOV PET.

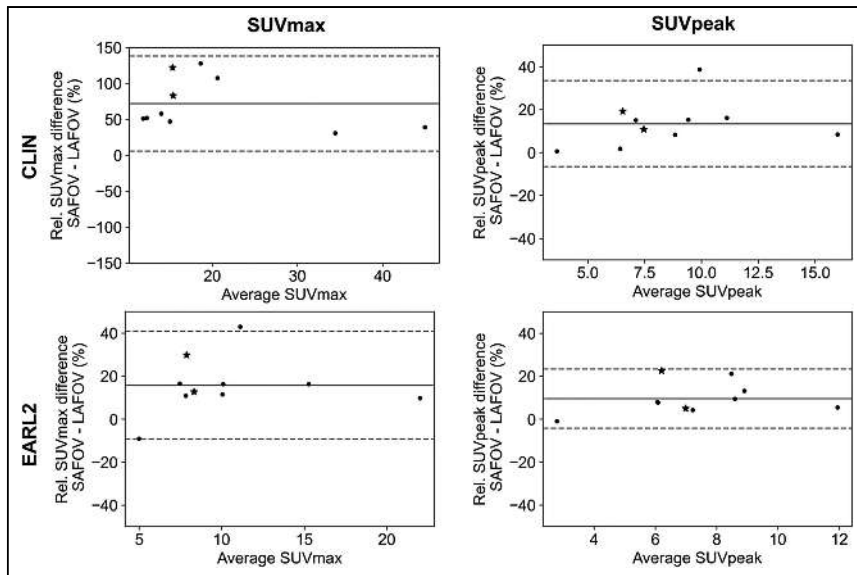


**FIGURE 2.** Relative differences between SAFOV and LAFOV lesion  $SUV_{max}$  and  $SUV_{peak}$  for CLIN- and EARL2-reconstructed images based on 5 patients with total of 10 lesions. Different marker (star) was used for 1 patient, because LAFOV scan duration was only 10 min instead of 30 min. CLIN  $SUV_{max}$  subplot has larger y-axis limits.

For investigating lower LAFOV PET scan durations, SUVs acquired with shorter scan durations (15, 10, 7.5, 5, and 3 min) were compared with corresponding values of the full scan duration (30 min). Bias was expressed as

$$\text{bias (\%)} = \frac{SUV_{LAFOV, t} - SUV_{LAFOV, 30 \text{ min}}}{SUV_{LAFOV, 30 \text{ min}}} \times 100\%,$$

where  $SUV_{LAFOV, t}$  is the SUV acquired with a reconstructed scan duration of  $t = 15, 10, 7.5, 5,$  and 3 min, and  $SUV_{LAFOV, 30 \text{ min}}$  is the SUV acquired using the full scan duration.

SUV metrics between systems and between LAFOV PET scan durations were compared using Wilcoxon signed-rank tests, as, in general, these differences were not normally distributed.

## RESULTS

Figure 1 shows example axial PET images from a patient scanned on both systems for 2 reconstruction protocols and 3 reduced LAFOV PET scan durations (10, 5, and 3 min). Supplemental Figure 1 provides another patient example with sagittal images (supplemental materials are available at <http://jnm.snmjournals.org>). In total, 10 lesions were included across the 5 double-scanned patients, and 27 lesions were included across all 9 patients who were scanned on the

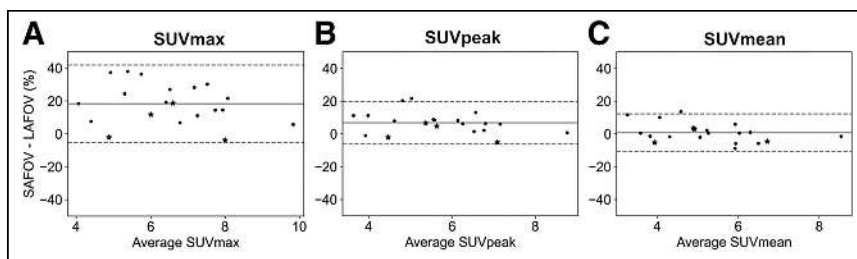


**FIGURE 3.** Relative differences between  $SUV_{max}$  (A),  $SUV_{peak}$  (B), and  $SUV_{mean}$  (C) of healthy-tissue VOIs for SAFOV compared with LAFOV EARL2-reconstructed images. Different marker (star) was used for 1 patient, because scan duration was only 10 min instead of 30 min on LAFOV.

LAFOV PET system. One of the double-scanned patients could be scanned for only 10 min on the LAFOV PET/CT system, instead of the intended 30 min, because of patient discomfort.

## Semiquantitative Image Analysis

Comparisons of tumor lesion  $SUV_{max}$  and  $SUV_{peak}$  between the 2 different systems (i.e., 30 min on both scanners) are shown in Figure 2. In general, both the  $SUV_{max}$  and the  $SUV_{peak}$  of the lesions were lower for LAFOV than for SAFOV PET. Comparing images reconstructed according to the CLIN protocol, we found that the mean difference between SAFOV and LAFOV PET was  $71.9\% \pm 33.8\%$  for  $SUV_{max}$  and  $13.4\% \pm 10.2\%$  for  $SUV_{peak}$ . These differences were less pronounced for EARL2-reconstructed images, that is,  $15.7\% \pm 12.8\%$  for  $SUV_{max}$  and  $9.5\% \pm 7.0\%$  for  $SUV_{peak}$ . All reported differences were statistically significant ( $P < 0.01$ ). In this comparison, the 2 lesions from the patient scanned for only 10 min with the LAFOV PET/CT system were included.

The SUVs for these lesions were lower with 10 min of LAFOV than with 30 min of SAFOV PET.

The large differences in  $SUV_{max}$  and  $SUV_{peak}$  between the 2 systems when using the CLIN reconstruction protocol support the recommendation that quantification should be performed with EARL-compliant image reconstructions to allow harmonization between different scanners (27,34). Therefore, the following results focus on EARL2-reconstructed images. Since EARL1 is still recommended for  $^{89}\text{Zr}$  immuno-PET using the Vision (35), results for EARL1-reconstructed images can be found in Supplemental Figures 2–6.

Although for healthy tissues only  $SUV_{mean}$  is usually reported, normal-tissue  $SUV_{max}$  and  $SUV_{peak}$  differences between the 2 scanners can complement the above observations for the lesions. The  $SUV_{max}$  and  $SUV_{peak}$  of healthy tissues were also lower with LAFOV than with SAFOV (Fig. 3). The mean and SD were  $18.6\% \pm 11.4\%$  for  $SUV_{max}$  and  $7.2\% \pm 6.7\%$  for  $SUV_{peak}$ . On the other hand, the  $SUV_{mean}$  of healthy tissues showed only a minimal difference of  $0.7\% \pm 5.8\%$ .  $SUV_{max}$  and  $SUV_{peak}$  were statistically significantly different ( $P < 0.01$ ), whereas  $SUV_{mean}$  was not ( $P = 0.98$ ).

COVs derived from the liver VOIs on EARL2-reconstructed images of patients who were scanned twice are shown in Figure 4 and were, on average, 13.4% for 30-min SAFOV ( $n = 5$ ); 5.6% and 6.8% for 30- and 15-min LAFOV ( $n = 4$ ), respectively; and 7.9%, 9.3%, 12.2%, and 15.4% for 10-, 7.5-, 5-, and 3-min LAFOV ( $n = 5$ ), respectively. Since COV is an indicator of image noise, the noise level of 30-min SAFOV images seems to be between that of 3- and 5-min LAFOV images.

Figure 5 shows the effect of reducing LAFOV PET scan duration on lesion  $SUV_{max}$  and  $SUV_{peak}$  and on healthy-tissue  $SUV_{mean}$ , expressed as a percentage



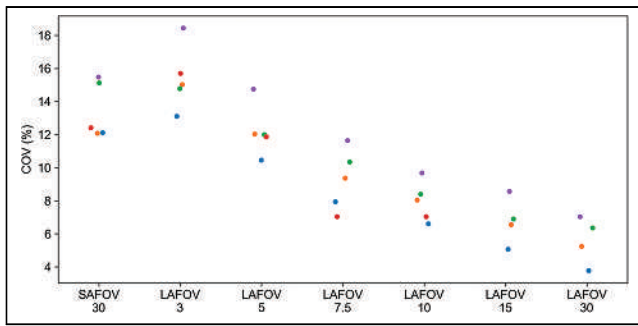


**FIGURE 4.** COV in spheric liver VOI (3-cm diameter) in EARL2-reconstructed images for 5 patients (visualized with different colors) scanned on both SAFOV and LAFOV PET systems for approximately 30 min. One patient was scanned for only 10 min on LAFOV system, resulting in 4 patients for LAFOV-30 and LAFOV-15.

difference relative to the values of the full scan duration (30 min). Lesion  $SUV_{max}$  was, on average, higher for lower scan durations, with differences of 1.3%, 4.2%, 6.1%, 11.1%, and 16.7% for 15, 10, 7.5, 5, and 3 min, respectively; 15-min  $SUV_{max}$  was not significantly different ( $P = 0.44$ ), but significant differences were found in the 10-min scans ( $P < 0.05$ ), as well as in the lower scan durations ( $P < 0.01$ ). Lesion  $SUV_{peak}$  also showed, on average, a positive, although less pronounced, bias for lower scan durations, with 0.4%, 1.4%, 2.3%, 3.0%, and 5.1% for the progressively decreasing scan durations. Significant differences were not found for 15 min ( $P = 0.73$ ) and 10 min ( $P = 0.11$ ) but were found for 7.5 min and 5 min ( $P < 0.05$ ), as well as 3 min ( $P < 0.01$ ). For individual lesions, the bias can be higher than these average values, given that corresponding SDs were 5.2%, 7.4%, 8.9%, 12.4%, and 14.2% for  $SUV_{max}$  and 2.6%, 3.1%, 4.0%, 5.3%, and 6.8% for  $SUV_{peak}$  for 15, 10, 7.5, 5, and 3 min, respectively. A small, statistically significant ( $P < 0.01$ ) positive bias of 1.3%, 2.0%, 1.8%, 2.4%, and 3.0% in the  $SUV_{mean}$  of healthy tissues was also observed with reducing scan durations (Fig. 5, right). This bias, in addition to the noise component, contributes to the reported differences in  $SUV_{max}$  and  $SUV_{peak}$  for lower scan durations.

Considering the increasing SUV metrics with decreasing scan duration, we also compared the lesion SUV of SAFOV PET with that of 3-min LAFOV (Fig. 6). The smallest difference in lesion SUVs between SAFOV and any of the LAFOV PET images was found for 3-min LAFOV, with a mean ( $\pm$ SD) difference of  $2.8\% \pm 16.1\%$  for  $SUV_{max}$  and  $7.1\% \pm 9.0\%$  for  $SUV_{peak}$ .

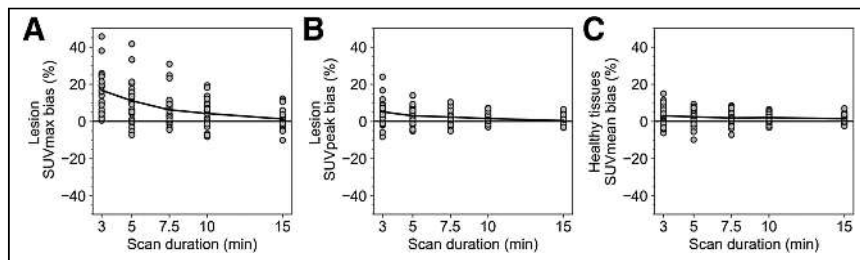


**FIGURE 5.** (A and B) Tumor  $SUV_{max}$  (A) and  $SUV_{peak}$  (B) bias of lower scan durations compared with full scan duration of 30 min for EARL2 LAFOV PET, based on 25 lesions across 8 patients. (C) Healthy-tissue  $SUV_{mean}$  bias, based on 8 patients each with 4 healthy tissue types. Solid line joins averages between scan durations.

## DISCUSSION

This study confirmed that also for  $^{89}Zr$  immuno-PET images, the increased sensitivity of a LAFOV PET/CT system results in better image quality than does a state-of-the-art SAFOV PET/CT system. The focus of the present study was, however, on the semiquantitative performance of the 2 systems for  $^{89}Zr$  immuno-PET/CT imaging and the possibility of reducing scan duration with LAFOV PET.

SAFOV immuno-PET showed a significantly higher lesion  $SUV_{max}$  and  $SUV_{peak}$  than did LAFOV immuno-PET for both the CLIN and the EARL reconstruction protocols. For the CLIN reconstruction protocol, the mean differences in lesion SUV were as high as 62% for  $SUV_{max}$  and 16% for  $SUV_{peak}$ , and they were associated with a large SD. These differences were less pronounced in the EARL2-reconstructed images. However, even  $SUV_{peak}$  derived from EARL2-reconstructed images showed a mean difference of  $9.5\% \pm 7.0\%$  ( $6.6\% \pm 7.1\%$  for EARL1, Supplemental Fig. 2). Nevertheless, these results strongly support the use of EARL reconstruction protocols and  $SUV_{peak}$  for comparison of SUVs between different scanner types, as this combination provides the smallest differences. In addition, these results suggest that for  $^{89}Zr$  immuno-PET applications, on average, there may be, even with EARL reconstruction protocols and  $SUV_{peak}$ , slightly higher values with SAFOV than with LAFOV.

Differences in  $SUV_{max}$  and  $SUV_{peak}$  most likely are due to different noise levels in the images, as both metrics are noise-sensitive, resulting in upward bias, as shown by earlier studies (36–38). This explanation is also supported by the fact that no significant differences in  $SUV_{mean}$  (with better statistics) were found between healthy-tissue VOIs. Therefore, a higher  $SUV_{max}$  and  $SUV_{peak}$  can be attributed to noise in the underlying data rather than to inherent bias.

The reported sensitivities according to the standard National Electrical Manufacturers Association protocol are 16.4 cps/kBq for the Biograph Vision (10) and 83 cps/kBq (maximum ring difference, 85) for the Biograph Vision Quadra (13), both measured with a 70-cm line source at 1 bed position, resulting in a factor of approximately 5 between the 2 scanners. However, the necessary field of view for the clinical immuno-PET acquisition reaches from the patient's skull base to the mid thighs (approximately 1 m), which requires a continuous-bed-motion acquisition with the SAFOV PET/CT scanner, different from the National Electrical Manufacturers Association sensitivity measurements.

A similar direct comparison of the 2 systems has shown that, for shorter-lived tracers (labeled with  $^{18}F$  or  $^{68}Ga$ ), LAFOV PET provided a liver signal-to-noise ratio equivalent to that of SAFOV PET

but with an approximately 8–9 times reduction in scan duration (14). The intraindividual comparison of the 5 double-scanned patients in the present study confirms this result for a long-lived  $^{89}Zr$ -labeled tracer, as the COV for a liver VOI of the 30-min SAFOV scans was in the same range as that of 3- and 5-min LAFOV scans.

Investigation of the effects of reducing LAFOV PET scan duration on semiquantitative metrics was restricted to EARL-reconstructed images, as EARL reconstruction settings are preferable for harmonization between different PET/CT systems (27). Previously, it was shown that

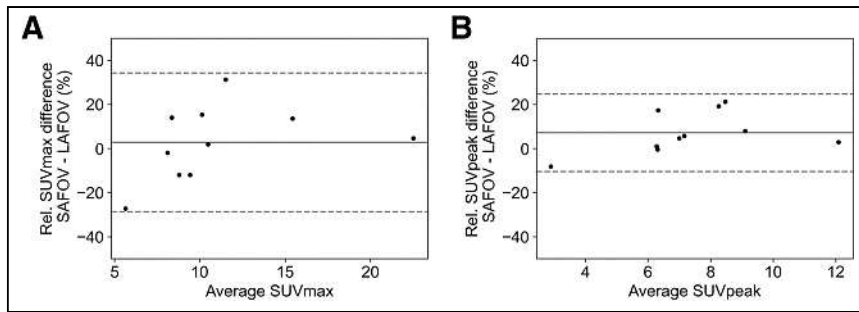


**FIGURE 6.** Relative differences between SAFOV (~30 min) and LAFOV-3 (3 min)  $SUV_{max}$  (A) and  $SUV_{peak}$  (B) of lesions for EARL2-reconstructed images, based on 5 patients with total of 10 lesions.

EARL2 was the preferred reconstruction protocol for [ $^{18}F$ ]FDG scans acquired on a LAFOV PET/CT system (34). For the present comparison of  $^{89}Zr$ -immuno-PET scans, EARL1-reconstructed images were also considered (supplemental materials). EARL1 images resulted in only slightly smaller differences between LAFOV and SAFOV scanners than EARL2 images. This finding can be attributed to the higher degree of smoothing using a 7-mm rather than a 5-mm postreconstruction filter.

For EARL2-reconstructed images, scan duration could be reduced to 10 min (reduction by a factor of 3), leading to only a very small bias of  $1.4\% \pm 3.1\%$  in  $SUV_{peak}$ , whereas lower scan durations, especially in combination with  $SUV_{max}$ , resulted in larger bias. A reduction in scan duration is associated with an increase in image noise, but for a 10-min LAFOV scan, this is still lower than for a 30-min SAFOV scan. It should also be noted that the lower noise levels of LAFOV PET images reconstructed using the CLIN protocol, compared with SAFOV PET CLIN images (Fig. 1), may be beneficial for visual assessment of small lesions.

On the basis of noise levels in the liver, the SUV metrics of SAFOV best matched those of 3-min LAFOV acquisitions. However, when the large SD of the SUV differences is also taken into account, matching the noise level of LAFOV to that of SAFOV is not the preferred solution for  $^{89}Zr$  immuno-PET, as it leads to less repeatable SUV quantification, which may compromise its use as a potential biomarker for treatment response (39).

As an alternative to reducing the scan duration, the injected dose can be reduced by the same factor while keeping the original scan duration. Current immuno-PET protocols, based on the administration of 37 MBq of a  $^{89}Zr$ -labeled tracer, have an effective radiation dose of around 17 mSv (22). So, a reduction of the injected activity by a factor of 3 would give a radiation dose well below 10 mSv and therefore opens up  $^{89}Zr$ -immuno-PET applications in nononcologic diseases and young patients (e.g., inflammatory targets (40)). The third direction in which the increased sensitivity can be exploited concerns scanning later than day 4 or 7 (41) with reasonable scan durations.

The average total coincidence rate of the LAFOV acquisitions was approximately  $7 \times 10^4$  coincidences per second, including about 23% random coincidences. A blank scan provided an overall coincidence rate (due to the lutetium orthosilicate background) of about  $5 \times 10^3$  coincidences per second (7% of the immuno-PET coincidence rate) with more than 99% random coincidences. Therefore, lutetium orthosilicate activity should not be problematic for a dose reduction by a factor of 3–4. However, when the dose is reduced further or scans are performed at substantially later time points (e.g., 10 d after injection), the lutetium orthosilicate background could become more significant.

One of the limitations of the present work is the small sample size; therefore, the results presented can only give an indication of differences between systems and scan durations. In addition, other factors may affect SUVs, in particular effects of motion and, potentially, tracer kinetics. The effect of the latter is expected to be minimal because of the relatively slow kinetics of mAb tracers. The results for this specific mAb tracer,  $^{89}Zr$ -trastuzumab, are expected to be valid also for other  $^{89}Zr$ -labeled full mAbs with similar biologic behavior. However, further studies including a broader patient population and using different  $^{89}Zr$  immuno-PET tracers will be useful to optimize LAFOV immuno-PET scan protocols.

## CONCLUSION

$^{89}Zr$  immuno-PET  $SUV_{max}$  and  $SUV_{peak}$  were lower for LAFOV than for SAFOV because of lower image noise. With LAFOV PET/CT, the scan duration for  $^{89}Zr$ -labeled mAbs may be reduced by up to a factor of 3 and still achieve lower levels of image noise than with state-of-the-art SAFOV PET/CT or may be reduced by a factor of approximately 8 to match noise levels. Lesion  $SUV_{peak}$  derived from EARL-reconstructed images is the preferred metric for comparison between the 2 system types or different LAFOV scan durations.

## DISCLOSURE

Andor W.J.M. Glaudemans, Ronald Boellaard, and Charalampos Tsoumpas received research grants from Siemens Healthineers. No other potential conflict of interest relevant to this article was reported.

## KEY POINTS

**QUESTION:** How do SUVs differ between SAFOV and LAFOV in  $^{89}Zr$  immuno-PET imaging, and how does LAFOV scan duration affect them?

**PERTINENT FINDINGS:** Patients were scanned consecutively with SAFOV and LAFOV PET/CT scanners 4 d after injection of 37 MBq of  $^{89}Zr$ -trastuzumab, and various SUV metrics were compared. SAFOV resulted, on average, in 16% and 10% higher values for lesion  $SUV_{max}$  and  $SUV_{peak}$ , respectively, than LAFOV. LAFOV scan duration can be reduced by a factor of 2 or 3 without significant bias for  $SUV_{max}$  or  $SUV_{peak}$  and still result in a lower liver COV (7.9% vs. 13.4%).

**IMPLICATIONS FOR PATIENT CARE:** LAFOV in  $^{89}Zr$  immuno-PET imaging allows a substantial reduction of scan duration or activity administration while maintaining SUV accuracy and precision.

## REFERENCES

- Jauw YW, Menke-van der Houven van Oordt CW, Hoekstra OS, et al. Immuno-positron emission tomography with zirconium-89-labeled monoclonal antibodies in oncology: what can we learn from initial clinical trials? *Front Pharmacol.* 2016; 7:131.

2. McKnight BN, Viola-Villegas NT.  $^{89}\text{Zr}$ -immunoPET companion diagnostics and their impact in clinical drug development. *J Labelled Comp Radiopharm*. 2018;61:727–738.
3. Yoon J-K, Park B-N, Ryu E-K, An Y-S, Lee S-J. Current perspectives on  $^{89}\text{Zr}$ -PET imaging. *Int J Mol Sci*. 2020;21:4309.
4. Van Dongen GA, Beaino W, Windhorst AD, et al. The role of  $^{89}\text{Zr}$ -immuno-PET in navigating and derisking the development of biopharmaceuticals. *J Nucl Med*. 2021;62:438–445.
5. Wu AM, Pandit-Taskar N. ImmunoPET: harnessing antibodies for imaging immune cells. *Mol Imaging Biol*. 2022;24:181–197.
6. van Dongen GA, Huisman M, Boellaard R, et al.  $^{89}\text{Zr}$ -immuno-PET for imaging of long circulating drugs and disease targets: why, how and when to be applied? *Q J Nucl Med Mol Imaging*. 2015;59:18–38.
7. Börjesson PKE, Jauw YWS, de Bree R, et al. Radiation dosimetry of  $^{89}\text{Zr}$ -labeled chimeric monoclonal antibody U36 as used for immuno-PET in head and neck cancer patients. *J Nucl Med*. 2009;50:1828–1836.
8. Conti M, Eriksson L. Physics of pure and non-pure positron emitters for PET: a review and a discussion. *EJNMMI Phys*. 2016;3:8.
9. Hsu DFC, Ilan E, Peterson WT, Uribe J, Lubberink M, Levin CS. Studies of a next-generation silicon-photomultiplier-based time-of-flight PET/CT system. *J Nucl Med*. 2017;58:1511–1518.
10. van Sluis J, de Jong J, Schaar J, et al. Performance characteristics of the digital Biograph Vision PET/CT system. *J Nucl Med*. 2019;60:1031–1036.
11. Nguyen NC, Vercher-Conejero JL, Sattar A, et al. Image quality and diagnostic performance of a digital PET prototype in patients with oncologic diseases: initial experience and comparison with analog PET. *J Nucl Med*. 2015;56:1378–1385.
12. Rausch I, Ruiz A, Valverde-Pascual I, Cal-González J, Beyer T, Carrio I. Performance evaluation of the Vereos PET/CT system according to the NEMA NU-2-2012 standard. *J Nucl Med*. 2019;60:561–567.
13. Prenosil GA, Sari H, Fürstner M, et al. Performance characteristics of the Biograph Vision Quadra PET/CT system with long axial field of view using the NEMA NU 2-2018 standard. *J Nucl Med*. 2022;63:476–484.
14. Alberts I, Hünermund J-N, Prenosil G, et al. Clinical performance of long axial field of view PET/CT: a head-to-head intra-individual comparison of the Biograph Vision Quadra with the Biograph Vision PET/CT. *Eur J Nucl Med Mol Imaging*. 2021;48:2395–2404.
15. Badawi RD, Shi H, Hu P, et al. First human imaging studies with the EXPLORER total-body PET scanner. *J Nucl Med*. 2019;60:299–303.
16. Slart RHJA, Tsoumpas C, Glaudemans AJWM, et al. Long axial field of view PET scanners: a road map to implementation and new possibilities. *Eur J Nucl Med Mol Imaging*. 2021;48:4236–4245.
17. de Vries EFJ, Elsinga PH, Tsoumpas C. Will extended field-of-view PET/CT depopulate the graveyard of failed PET radiopharmaceuticals? *Cancer Imaging*. 2022;22:70.
18. van Sluis J, Borra R, Tsoumpas C, et al. Extending the clinical capabilities of short- and long-lived positron-emitting radionuclides through high sensitivity PET/CT. *Cancer Imaging*. 2022;22:69.
19. Jakoby BW, Bercier Y, Conti M, Casey ME, Bendriem B, Townsend DW. Physical and clinical performance of the mCT time-of-flight PET/CT scanner. *Phys Med Biol*. 2011;56:2375–2389.
20. Brouwers AH, van Sluis J, van Snick JH, et al. First-time imaging of [ $^{89}\text{Zr}$ ]trastuzumab in breast cancer using a long axial field-of-view PET/CT scanner. *Eur J Nucl Med Mol Imaging*. 2022;49:3593–3595.
21. Bensch F.  $^{89}\text{Zr}$ -atezolizumab imaging as a non-invasive approach to assess clinical response to PD-L1 blockade in cancer. *Nat Med*. 2018;24:1852–1858.
22. Laforest R, Lapi SE, Oyama R, et al. [ $^{89}\text{Zr}$ ]trastuzumab: evaluation of radiation dosimetry, safety, and optimal imaging parameters in women with HER2-positive breast cancer. *Mol Imaging Biol*. 2016;18:952–959.
23. Bensch F.  $^{89}\text{Zr}$ -trastuzumab PET supports clinical decision making in breast cancer patients, when HER2 status cannot be determined by standard work up. *Eur J Nucl Med Mol Imaging*. 2018;45:2300–2306.
24. Siman W, Kappadath SC. Comparison of step-and-shoot and continuous-bed-motion PET modes of acquisition for limited-view organ scans. *J Nucl Med Technol*. 2017;45:290–296.
25. Varrone A, Sjöholm N, Eriksson L, Gulyás B, Halldin C, Farde L. Advancement in PET quantification using 3D-OP-OSEM point spread function reconstruction with the HRRT. *Eur J Nucl Med Mol Imaging*. 2009;36:1639–1650.
26. Panin VY, Kehren F, Michel C, Casey M. Fully 3-D PET reconstruction with system matrix derived from point source measurements. *IEEE Trans Med Imaging*. 2006;25:907–921.
27. Boellaard R, Delgado-Bolton R, Oyen WJG, et al. FDG PET/CT: EANM procedure guidelines for tumour imaging—version 2.0. *Eur J Nucl Med Mol Imaging*. 2015;42:328–354.
28. Boellaard R, O'Doherty MJ, Weber WA, et al. FDG PET and PET/CT: EANM procedure guidelines for tumour PET imaging—version 1.0. *Eur J Nucl Med Mol Imaging*. 2010;37:181–200.
29. Boellaard R. Quantitative oncology molecular analysis suite: ACCURATE [abstract]. *J Nucl Med*. 2018;59(suppl 1):1753.
30. Wahl RL, Jacene H, Kasamon Y, Lodge MA. From RECIST to PERCIST: evolving considerations for PET response criteria in solid tumors. *J Nucl Med*. 2009;50(suppl 1):122S–150S.
31. Kolinger GD, Vázquez García D, Kramer GM, et al. Repeatability of [ $^{18}\text{F}$ ]FDG PET/CT total metabolic active tumour volume and total tumour burden in NSCLC patients. *EJNMMI Res*. 2019;9:14.
32. Soret M, Bacharach SL, Buvat I. Partial-volume effect in PET tumor imaging. *J Nucl Med*. 2007;48:932–945.
33. Bland JM, Altman DG. Statistical methods for assessing agreement between two methods of clinical measurement. *Lancet*. 1986;1:307–310.
34. van Sluis J, van Snick JH, Brouwers AH, et al. EARL compliance and imaging optimisation on the Biograph Vision Quadra PET/CT using phantom and clinical data. *Eur J Nucl Med Mol Imaging*. 2022;49:4652–4660.
35. Van Sluis J, Boellaard R, Dierckx RAJO, et al. Optimisation of scan duration and image quality in oncological  $^{89}\text{Zr}$  immunoPET imaging using the Biograph Vision PET/CT. *EJNMMI*. 2023;50:2258–2270.
36. Lodge MA, Chaudhry MA, Wahl RL. Noise considerations for PET quantification using maximum and peak standardized uptake value. *J Nucl Med*. 2012;53:1041–1047.
37. Sher A, Lacoëuille F, Fosse P, et al. For avid glucose tumors, the SUV peak is the most reliable parameter for [ $^{18}\text{F}$ ]FDG-PET/CT quantification, regardless of acquisition time. *EJNMMI Res*. 2016;6:21.
38. Boellaard R, Krak NC, Hoekstra OS, Lammertsma AA. Effects of noise, image resolution, and ROI definition on the accuracy of standard uptake values: a simulation study. *J Nucl Med*. 2004;45:1519–1527.
39. Kist de Ruijter L, van de Donk PP, Hooiveld-Noeken JS, et al. Whole-body CD8+ T cell visualization before and during cancer immunotherapy: a phase 1/2 trial. *Nat Med*. 2022;28:2601–2610.
40. van der Geest KSM, Sandovici M, Nienhuis PH, et al. Novel PET imaging of inflammatory targets and cells for the diagnosis and monitoring of giant cell arteritis and polymyalgia rheumatica. *Front Med (Lausanne)*. 2022;9:902155.
41. Berg E, Gill H, Marik J, et al. Total-body PET and highly stable chelators together enable meaningful  $^{89}\text{Zr}$ -antibody PET studies up to 30 days after injection. *J Nucl Med*. 2020;61:453–460.

---

---

# Total-Body Multiparametric PET Quantification of $^{18}\text{F}$ -FDG Delivery and Metabolism in the Study of Coronavirus Disease 2019 Recovery

Yiran Wang<sup>1,2</sup>, Lorenzo Nardo<sup>1</sup>, Benjamin A. Spencer<sup>1,2</sup>, Yasser G. Abdelhafez<sup>1,3</sup>, Elizabeth J. Li<sup>2</sup>, Negar Omidvari<sup>2</sup>, Abhijit J. Chaudhari<sup>1</sup>, Ramsey D. Badawi<sup>1,2</sup>, Terry Jones<sup>1</sup>, Simon R. Cherry<sup>1,2</sup>, and Guobao Wang<sup>1</sup>

<sup>1</sup>Department of Radiology, Davis Medical Center, University of California, Sacramento, California; <sup>2</sup>Department of Biomedical Engineering, University of California, Davis, Davis, California; and <sup>3</sup>Nuclear Medicine Unit, South Egypt Cancer Institute, Assiut University, Assiut, Egypt

---

Conventional whole-body static  $^{18}\text{F}$ -FDG PET imaging provides a semi-quantitative evaluation of overall glucose metabolism without insight into the specific transport and metabolic steps. Here we demonstrate the ability of total-body multiparametric  $^{18}\text{F}$ -FDG PET to quantitatively evaluate glucose metabolism using macroparametric quantification and assess specific glucose delivery and phosphorylation processes using microparametric quantification for studying recovery from coronavirus disease 2019 (COVID-19). **Methods:** The study included 13 healthy subjects and 12 recovering COVID-19 subjects within 8 wk of confirmed diagnosis. Each subject had a 1-h dynamic  $^{18}\text{F}$ -FDG scan on the uEXPLORER total-body PET/CT system. Semiquantitative SUV and the SUV ratio relative to blood (SUV<sub>R</sub>) were calculated for different organs to measure glucose utilization. Tracer kinetic modeling was performed to quantify the microparametric blood-to-tissue  $^{18}\text{F}$ -FDG delivery rate  $K_1$  and the phosphorylation rate  $k_3$ , as well as the macroparametric  $^{18}\text{F}$ -FDG net influx rate ( $K_i$ ). Statistical tests were performed to examine differences between healthy subjects and recovering COVID-19 subjects. The effect of COVID-19 vaccination was also investigated. **Results:** We detected no significant difference in lung SUV but significantly higher lung SUV<sub>R</sub> and  $K_i$  in COVID-19 recovery, indicating improved sensitivity of kinetic quantification for detecting the difference in glucose metabolism. A significant difference was also observed in the lungs with the phosphorylation rate  $k_3$  but not with  $K_1$ , which suggests that glucose phosphorylation, rather than glucose delivery, drives the observed difference of glucose metabolism. Meanwhile, there was no or little difference in bone marrow  $^{18}\text{F}$ -FDG metabolism measured with SUV, SUV<sub>R</sub>, and  $K_i$  but a significantly higher bone marrow  $K_1$  in the COVID-19 group, suggesting a difference in glucose delivery. Vaccinated COVID-19 subjects had a lower lung  $K_i$  and a higher spleen  $K_i$  than unvaccinated COVID-19 subjects. **Conclusion:** Higher lung glucose metabolism and bone marrow glucose delivery were observed with total-body multiparametric  $^{18}\text{F}$ -FDG PET in recovering COVID-19 subjects than in healthy subjects, implying continued inflammation during recovery. Vaccination demonstrated potential protection effects. Total-body multiparametric PET of  $^{18}\text{F}$ -FDG can provide a more sensitive tool and more insights than conventional whole-body static  $^{18}\text{F}$ -FDG imaging to evaluate metabolic changes in systemic diseases such as COVID-19.

**Key Words:**  $^{18}\text{F}$ -FDG PET; tracer kinetic modeling; total-body dynamic PET; COVID-19

**J Nucl Med 2023; 64:1821–1830**

DOI: 10.2967/jnumed.123.265723

---

**P**ET with the radiotracer  $^{18}\text{F}$ -FDG is a noninvasive in vivo molecular imaging technique that reflects glucose metabolism. Conventional whole-body static  $^{18}\text{F}$ -FDG PET imaging can provide an overall evaluation of glucose utilization throughout the body, but it mixes the specific glucose transport and metabolic steps. Identification and quantification of these specific processes separately require a fast dynamic scanning protocol; however, it is limited to a single organ or a confined region by a PET scanner with a short axial field of view. The advent of total-body PET/CT systems such as uEXPLORER (United Imaging Healthcare) (1) and other PET scanners with a long axial field of view (2,3) has brought new opportunities for total-body dynamic PET imaging, with increased detection sensitivity and simultaneous dynamic imaging of multiple organs (4). Combined with tracer kinetic modeling (5), total-body dynamic  $^{18}\text{F}$ -FDG PET enables a multiparametric quantification method (6) that allows quantitative measurement of not only overall glucose utilization but also microparametric rates of glucose delivery and phosphorylation (7) over the entire body.

Although mostly used in oncology,  $^{18}\text{F}$ -FDG PET has the potential to characterize inflammatory diseases such as vasculitis (8), hepatitis (9), osteomyelitis (10), and the recent coronavirus disease 2019 (COVID-19) (11–14). COVID-19 primarily attacks the respiratory system, leading to conditions varying from mild manifestations to acute, high-mortality symptoms (15). Meanwhile, it can affect multiple organs associated with different body systems, including the nervous (16), cardiovascular (17), and immune systems (18). In addition, various prolonged effects of COVID-19 have been reported (19–22). However, investigations of the whole-body consequences and prolonged effects from COVID-19 are limited, partially because of the lack of an approach for in-depth total-body evaluation.

For this article, we conducted a quantitative evaluation of glucose utilization in multiple organs of healthy subjects and recovering COVID-19 subjects using total-body multiparametric  $^{18}\text{F}$ -FDG PET imaging. We analyzed overall glucose metabolism and, more subtly, the blood-to-tissue glucose delivery and glucose phosphorylation to gain insight into the metabolic differences induced by COVID-19.

---

Received Mar. 15, 2023; revision accepted Jul. 5, 2023.

For correspondence or reprints, contact Yiran Wang (yrdwang@ucdavis.edu).

Published online Aug. 17, 2023.

Immediate Open Access: Creative Commons Attribution 4.0 International License (CC BY) allows users to share and adapt with attribution, excluding materials credited to previous publications. License: <https://creativecommons.org/licenses/by/4.0/>. Details: <http://jnm.snmjournals.org/site/misc/permission.xhtml>

COPYRIGHT © 2023 by the Society of Nuclear Medicine and Molecular Imaging.

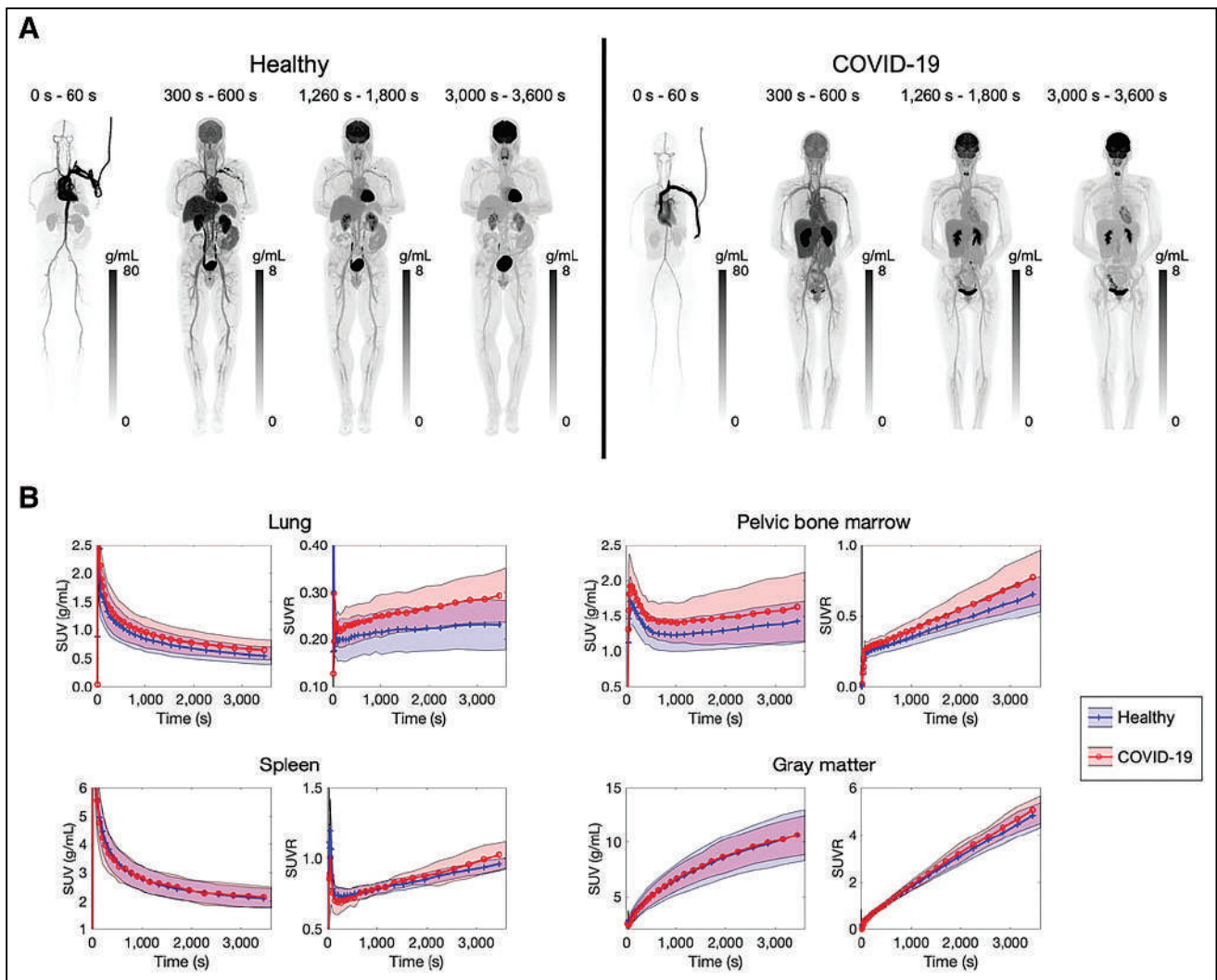


**FIGURE 1.** (A) Total-body dynamic  $^{18}\text{F}$ -FDG PET images of a healthy subject and a recovering COVID-19 subject. Maximum-intensity projections are shown. (B) Averaged time-activity curves (shown as SUV and SUVR) of 4 organs of interest (lung, pelvic bone marrow, spleen, and gray matter) of 13 healthy and 12 recovering COVID-19 subjects. Averaged values are shown as solid lines, and SDs are shown as bands.

## MATERIALS AND METHODS

### Study Participants and Data Acquisition

With Institutional Review Board approval and written informed consent at University of California Davis Health, the study included a cohort of 13 healthy subjects and 12 COVID-19 subjects. The healthy subjects were scanned between May 2019 and January 2020. They had no history of major disease (e.g., cancer or myocardium infarction) over the previous 5 y and lacked ongoing acute inflammation. The COVID-19 subjects had mild to moderate symptoms, as summarized in Supplemental Table 1 (supplemental materials are available at <http://jnm.snmjournals.org>), and none of them were hospitalized. Seven COVID-19 subjects had 1–3 doses of COVID-19 vaccines before PET imaging, and the other 5 were not vaccinated. Each subject had a total-body 1-h  $^{18}\text{F}$ -FDG dynamic scan on the uEXPLORER PET/CT system (23,24). The PET/CT scans for the COVID-19 subjects were performed within 8 wk ( $37 \pm 16$  d) of confirmed diagnosis. All COVID-19 subjects tested negative for COVID-19  $11 \pm 7$  d before the PET scan (inclusion and exclusion criteria are summarized in the supplemental materials). The subjects were injected with  $333 \pm 45$  MBq of  $^{18}\text{F}$ -FDG intravenously immediately after initiating list-mode data acquisition.

A total-body ultra-low-dose CT scan with settings of 140 kVp and 5 mAs was performed before the PET scan for attenuation correction. Dynamic PET data were reconstructed into 29 frames ( $6 \times 10$  s,  $2 \times 30$  s,  $6 \times 60$  s,  $5 \times 120$  s,  $4 \times 180$  s, and  $6 \times 300$  s) with a voxel size of  $4 \times 4 \times 4$  mm<sup>3</sup> using the vendor-provided ordered-subset expectation maximization algorithm with 4 iterations and 20 subsets (23).

### Total-Body Kinetic Modeling

Regions of interest (ROIs) were placed in various organs and tissues (e.g., brain, liver, lungs, spleen, and bone marrow) throughout the entire body on the dynamic images of each subject (details of ROI placement are in Supplemental Table 2 and Supplemental Fig. 1). Time-activity curves were then extracted from the organ ROIs. In addition, ROI placement and time-activity curve extraction were done for the ascending aorta and right ventricle to acquire image-derived input functions.

A 2-tissue irreversible compartmental model, shown in Supplemental Figure 2, was used to model the dynamic  $^{18}\text{F}$ -FDG data with time delay correction included (6). The measured tissue time-activity curve  $C_T(t)$  was modeled as follows:

$$C_T(t) = (1 - v_b)(C_f(t) + C_m(t)) + v_b C_{wb}(t), \quad \text{Eq. 1}$$

**TABLE 1**  
Comparison of  $^{18}\text{F}$ -FDG Metabolic Metrics SUV, SUVR, and  $K_i$  Between Healthy Subjects and Recovering COVID-19 Subjects in Multiple Organs and Tissues

Organ or tissue	Metric	Healthy group	Recovering COVID-19 group	$P_T$	$P_U$
Lung	SUV	$0.54 \pm 0.16$	$0.64 \pm 0.18$	0.15	0.22
	SUVR	$0.230 \pm 0.055$	$0.293 \pm 0.060$	0.012	0.018
	$K_i$	$0.00038 \pm 0.00033$	$0.00084 \pm 0.00045$	0.0075	0.011
Myocardium	SUV	$7.5 \pm 3.5$	$5.8 \pm 2.8$	0.21	0.20
	SUVR	$3.4 \pm 1.6$	$2.8 \pm 1.4$	0.38	0.34
	$K_i$	$0.055 \pm 0.033$	$0.043 \pm 0.025$	0.31	0.37
Liver	SUV	$2.64 \pm 0.44$	$2.56 \pm 0.40$	0.65	0.61
	SUVR	$1.208 \pm 0.060$	$1.218 \pm 0.061$	0.69	0.68
	$K_i$	$0.00279 \pm 0.00094$	$0.00330 \pm 0.00086$	0.17	0.17
Spleen	SUV	$2.11 \pm 0.35$	$2.15 \pm 0.36$	0.74	0.93
	SUVR	$0.963 \pm 0.041$	$1.024 \pm 0.097$	0.048	0.053
	$K_i$	$0.0037 \pm 0.0010$	$0.0049 \pm 0.0018$	0.055	0.087
Spine bone marrow	SUV	$2.06 \pm 0.38$	$2.21 \pm 0.59$	0.43	0.57
	SUVR	$0.95 \pm 0.17$	$1.05 \pm 0.21$	0.21	0.22
	$K_i$	$0.0072 \pm 0.0015$	$0.0080 \pm 0.0023$	0.35	0.50
Pelvic bone marrow	SUV	$1.42 \pm 0.31$	$1.63 \pm 0.51$	0.22	0.43
	SUVR	$0.65 \pm 0.13$	$0.77 \pm 0.20$	0.087	0.13
	$K_i$	$0.0050 \pm 0.0012$	$0.0059 \pm 0.0019$	0.19	0.24
Thigh muscle	SUV	$0.57 \pm 0.16$	$0.58 \pm 0.12$	0.92	0.93
	SUVR	$0.262 \pm 0.056$	$0.279 \pm 0.065$	0.50	0.72
	$K_i$	$0.00168 \pm 0.00057$	$0.00179 \pm 0.00059$	0.65	0.89
Gray matter	SUV	$10.7 \pm 2.4$	$10.7 \pm 1.9$	0.99	0.76
	SUVR	$4.84 \pm 0.54$	$5.07 \pm 0.60$	0.33	0.31
	$K_i$	$0.0476 \pm 0.0062$	$0.0487 \pm 0.0061$	0.65	0.68
White matter	SUV	$4.5 \pm 1.6$	$3.9 \pm 1.0$	0.28	0.22
	SUVR	$2.03 \pm 0.45$	$1.85 \pm 0.31$	0.26	0.46
	$K_i$	$0.0168 \pm 0.0051$	$0.0148 \pm 0.0046$	0.33	0.50
Brain stem	SUV	$6.1 \pm 1.3$	$5.84 \pm 0.82$	0.55	0.68
	SUVR	$2.78 \pm 0.24$	$2.79 \pm 0.34$	0.90	0.85
	$K_i$	$0.0247 \pm 0.0023$	$0.0241 \pm 0.0033$	0.62	0.46
Cerebellum	SUV	$7.3 \pm 1.3$	$6.99 \pm 0.77$	0.49	0.50
	SUVR	$3.34 \pm 0.28$	$3.35 \pm 0.27$	0.93	0.89
	$K_i$	$0.0300 \pm 0.0033$	$0.0300 \pm 0.0030$	1.0	1.0

$P_T = P$  value of  $t$  test;  $P_U = P$  value of Mann–Whitney  $U$  test.  
Groups are mean  $\pm$  SD, SUV is in g/mL, and  $K_i$  is in mL/min/cm<sup>3</sup>.

where  $C_{wb}(t)$ ,  $C_f(t)$ , and  $C_m(t)$  represent the concentrations of whole blood  $^{18}\text{F}$ -FDG, tissue free-state  $^{18}\text{F}$ -FDG, and tissue-metabolized  $^{18}\text{F}$ -FDG-6P, respectively, and  $v_b$  is the fractional blood volume. Details of the compartmental model are described in the supplemental materials.

All kinetic parameters ( $K_1$ , blood-to-tissue  $^{18}\text{F}$ -FDG delivery rate;  $k_2$ , tissue-to-blood delivery rate; and  $k_3$ ,  $^{18}\text{F}$ -FDG phosphorylation rate, fractional blood volume  $v_b$ , and the time delay for input function  $t_d$ ) were jointly estimated through a nonlinear least-square fitting method (6) with a weighting factor that considers the time length of each frame and nuclear decay (25).

#### Macroparametric and Microparametric Quantification

The macroparameter  $K_i$ , denoting the  $^{18}\text{F}$ -FDG net influx rate, is commonly used to characterize overall glucose metabolism and is calculated as follows:

$$K_i = \frac{K_1 k_3}{k_2 + k_3} \quad \text{Eq. 2}$$

We also applied semiquantitative SUV (26) and the SUV ratio relative to blood (SUVR) (27) using the last dynamic frame (55–60 min) to evaluate overall glucose metabolism. As described in the supplemental materials, the right ventricle was used to extract the image-derived



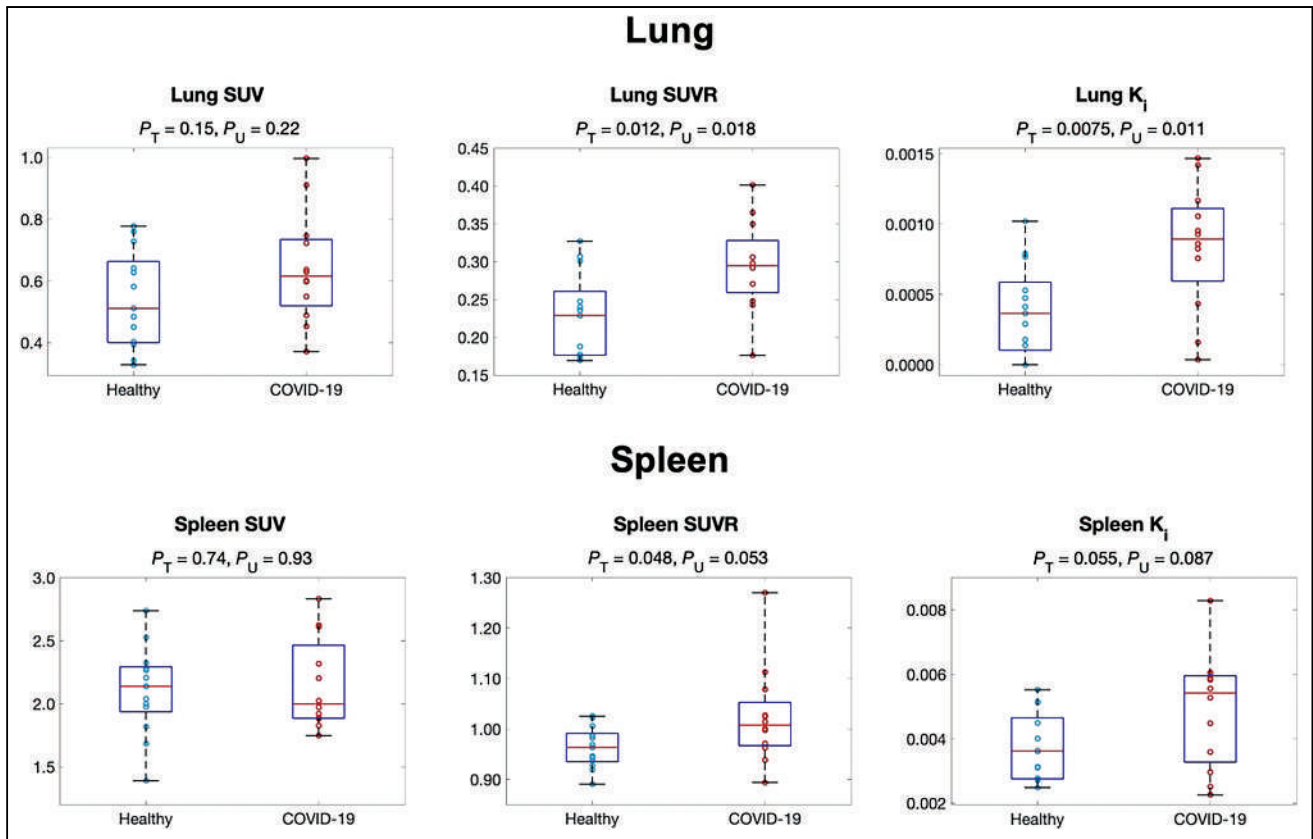


**FIGURE 2.** Comparison of  $^{18}\text{F}$ -FDG metabolism in lung (top) and spleen (bottom) between healthy and recovering COVID-19 groups using SUV, SUVR (both from 55 to 60 min), and  $K_i$ .  $P_T = P$  value of  $t$  test;  $P_U = P$  value of Mann–Whitney  $U$  test.

input function for the lung SUVR calculation, and the ascending aorta was used for the SUVR calculation of all other organs (28).

In addition to the measures of overall  $^{18}\text{F}$ -FDG metabolism by SUV, SUVR, and  $K_i$ , we used the microparameters of the 2-tissue irreversible kinetic model, specifically  $K_1$  and  $k_3$ , to gain insight into the individual molecular processes of glucose utilization. The ability of this microparametric quantification is a feature that distinguishes compartmental modeling from whole-body static imaging or whole-body dynamic imaging with a simplified graphical analysis method (e.g., the Patlak plot).

### Statistical Analysis

Statistical analysis in this study was performed using an unpaired, 2-tailed  $t$  test and the Mann–Whitney  $U$  test on SUV, SUVR, and parametric PET metrics to investigate metabolic differences in the recovering COVID-19 subjects compared with the healthy subjects. In addition, the tests were performed on lung CT ROI quantitation for complementary information. Effect of vaccination was also investigated when appropriate between the vaccinated and the unvaccinated COVID-19 groups (29,30). All statistical data analyses were conducted using MATLAB (MathWorks).  $P$  values of less than 0.05 were considered statistically significant.

**TABLE 2**  
Comparison of Lung Microkinetic Parameters  $K_1$ ,  $k_2$ , and  $k_3$  Between Healthy Subjects and Recovering COVID-19 Subjects, and Correlation Between Microparameters and Lung  $K_i$  Using Pearson and Spearman Analyses

Kinetic parameter	Comparison				Correlation with $K_i$			
	Healthy group	Recovering COVID-19 group	$P_T$	$P_U$	Pearson		Spearman	
					$r$	$P$	$\rho$	$P_S$
$K_1$ (mL/min/cm <sup>3</sup> )	0.018 ± 0.022	0.017 ± 0.019	0.89	0.98	0.23	0.26	0.44	0.028
$k_2$ (min <sup>-1</sup> )	0.32 ± 0.33	0.26 ± 0.25	0.61	0.81	0.17	0.42	0.36	0.075
$k_3$ (min <sup>-1</sup> )	0.0079 ± 0.0071	0.021 ± 0.023	0.049	0.011	0.56	0.0035	0.87	1.7 e-08

$P_T = P$  value of  $t$  test;  $P_U = P$  value of Mann–Whitney  $U$  test;  $P_S = P$  value of Spearman rank correlation. Groups are mean ± SD.

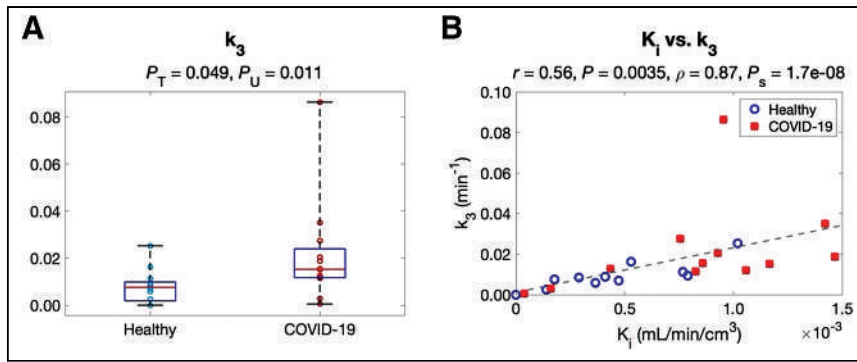


**FIGURE 3.** Study of lung kinetic parameters in the healthy and the recovering COVID-19 groups. (A) Comparison of  $k_3$  between 2 groups. (B) Correlation between  $k_3$  and  $K_1$  among subjects.  $P_T = P$  value of Spearman rank correlation;  $P_U = P$  value of  $t$  test;  $P_s = P$  value of Mann-Whitney  $U$  test.

For organs that showed a trend of differences in glucose metabolism between the healthy and the COVID-19 groups, Pearson correlation analysis and Spearman rank correlation analysis between  $K_i$  and microparameters  $K_1$ ,  $k_2$ , and  $k_3$  were also calculated to understand the association among the delivery, phosphorylation, and overall metabolism of  $^{18}\text{F}$ -FDG.

### Parametric Imaging of COVID-19

In addition to the ROI-based analysis, voxelwise parametric images were generated for the healthy subjects and the recovering COVID-19 subjects using the 2-tissue irreversible compartmental model (31,32). Kernel smoothing was applied to both the dynamic images and the parametric images for noise reduction (6). To focus the comparison of parametric images on organs of interest, masking was used to visualize individual organs or tissues (e.g., lung or bone marrow) within the parametric images for intersubject comparisons.

## RESULTS

### Subject Characteristics

A summary of subject characteristics is provided in Supplemental Table 1. The healthy subjects consisted of 6 men and 7 women of age  $49 \pm 15$  y and weight  $82 \pm 18$  kg. The COVID-19 subjects consisted of 3 men and 9 women of age  $41 \pm 10$  y and weight

$84 \pm 25$  kg. There was no statistical difference between the 2 groups in age, weight, body mass index, blood glucose level, or fasting time before the PET scan using the unpaired  $t$  test and the  $U$  test. In addition, there were no statistical differences in lung CT values and in the SUV of the input functions between the 2 groups.

### Dynamic Images and Time-Activity Curves

Total-body dynamic  $^{18}\text{F}$ -FDG PET images of a representative healthy subject and a recovering COVID-19 subject are shown in Figure 1A. Figure 1B shows 4 examples of the time-activity curves in the form of SUV and SUVR over time. The most notable finding was the increased lung SUVR in the recovering COVID-19 group compared with the healthy group, whereas the bone marrow SUVR and spleen SUVR of recovering COVID-19 group also tended to be higher.

### Comparison of Overall Glucose Utilization in Multiple Organs

Table 1 summarizes the SUV, SUVR, and  $K_i$  of the healthy and the recovering COVID-19 groups, along with group comparison results for 11 organ ROIs. There was no significant difference in lung SUV between the 2 groups ( $P > 0.1$ ) (Fig. 2). However, there was a statistically significant increase of approximately 120% in lung  $K_i$  in the COVID-19 group ( $P \approx 0.01$ ). SUVR showed a difference ( $\sim 25\%$  increase) but to a lower degree.

The  $^{18}\text{F}$ -FDG metabolism of the spleen was higher in the COVID-19 group, as shown in Table 1 and the box plots in Figure 2.  $K_i$  produced a larger group difference than SUV, whereas SUVR was comparable to  $K_i$ . The  $^{18}\text{F}$ -FDG metabolism of the pelvic bone marrow also tended to increase ( $P \approx 0.1$ ), as shown by the SUVR measures in Table 1 and Supplemental Figure 3. We did not observe a statistically significant difference with SUV, SUVR, and  $K_i$  in other organs (e.g., brain and liver).

On the basis of the preceding analyses, the lung, bone marrow, and spleen were selected for further study of microparametric quantification.

**TABLE 3**

Comparison of Bone Marrow Microkinetic Parameters  $K_1$ ,  $k_2$ , and  $k_3$  Between Healthy Subjects and Recovering COVID-19 Subjects, and Correlation Between Microparameters and Bone Marrow  $K_i$  Using Pearson and Spearman Analyses

Bone marrow type	Kinetic parameter	Comparison				Correlation with $K_i$			
		Healthy group	Recovering COVID-19 group	$P_T$	$P_U$	Pearson		Spearman	
						$r$	$P$	$\rho$	$P_s$
Spine	$K_1$	$0.221 \pm 0.055$	$0.285 \pm 0.089$	0.041	0.068	0.46	0.020	0.39	0.056
	$k_2$	$0.76 \pm 0.19$	$0.92 \pm 0.31$	0.14	0.20	0.45	0.023	0.35	0.091
	$k_3$	$0.0261 \pm 0.0061$	$0.027 \pm 0.013$	0.73	0.76	0.78	$3.5 \times 10^{-6}$	0.82	$2.2 \times 10^{-6}$
Pelvic	$K_1$	$0.122 \pm 0.026$	$0.149 \pm 0.037$	0.042	0.047	0.66	0.00032	0.71	$9.5 \times 10^{-5}$
	$k_2$	$0.573 \pm 0.081$	$0.64 \pm 0.14$	0.17	0.26	0.51	0.0090	0.51	0.011
	$k_3$	$0.0246 \pm 0.0060$	$0.0262 \pm 0.0088$	0.61	0.81	0.85	$9.1 \times 10^{-8}$	0.77	$1.3 \times 10^{-5}$

$P_T = P$  value of  $t$  test;  $P_U = P$  value of Mann-Whitney  $U$  test;  $P_s = P$  value of Spearman rank correlation. Groups are mean  $\pm$  SD,  $K_1$  is in  $\text{mL}/\text{min}/\text{cm}^3$ , and  $k_2$  and  $k_3$  are in  $\text{min}^{-1}$ .

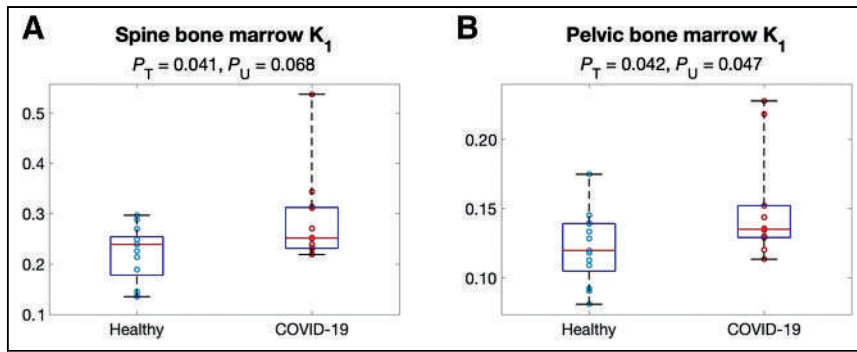


**FIGURE 4.** Comparison of  $K_1$  of spine bone marrow (A) and pelvic bone marrow (B) between the healthy and the recovering COVID-19 groups.  $P_T$  =  $P$  value of  $t$  test;  $P_U$  =  $P$  value of Mann–Whitney  $U$  test.

### Microparametric Quantification of the Lungs

Table 2 shows the analysis of microparametric quantification of the lungs. The correlation between each microparameter and lung  $K_i$  is also included using all subject data. Neither  $K_1$  nor  $k_2$  detected any group difference ( $P > 0.6$ ).  $k_3$  was higher in the COVID-19 group ( $P < 0.05$ ), as further shown in Figure 3A. In addition,  $k_3$  had the strongest correlation with  $K_i$  ( $P < 0.01$ ) among the 3 microparameters (Fig. 3B), whereas the correlations of  $K_1$  and  $k_2$  with  $K_i$  were weaker ( $P > 0.25$ ). The findings suggested that increased  $^{18}\text{F}$ -FDG phosphorylation (as quantified by  $k_3$ ) might be the main driving factor for the increased lung  $^{18}\text{F}$ -FDG metabolism (assessed by  $K_i$ ) in COVID-19 recovery.

### Microparametric Quantification of Bone Marrow

The microparametric quantification results for bone marrow are summarized in Table 3. While bone marrow metabolism did not show a statistically significant difference between the 2 groups as measured with SUV, SUVR, or  $K_i$  (Table 1), bone marrow  $K_1$  was approximately 20% higher in the COVID-19 subjects with a statistical difference ( $P < 0.05$ ), as shown in Figure 4 and Table 3. In comparison, no statistical significance was observed in  $k_2$  or  $k_3$ . In contrast to the results in the lungs, the bone marrow microparameters  $K_1$ ,  $k_2$ , and  $k_3$  all had strong correlations with  $K_i$ , although the correlation of  $K_1$  with  $K_i$  remained relatively weak (Table 3).

### Microparametric Quantification of the Spleen

Table 4 shows the microparametric quantification results for the spleen.  $k_3$  was approximately 45% higher in the COVID-19

group (Fig. 5A), whereas  $K_1$  and  $k_2$  did not show a significant group difference ( $P > 0.3$ ).  $k_3$  correlated the most strongly with  $K_i$  among the 3 microparameters (Fig. 5B), indicating that the increased trend in spleen  $^{18}\text{F}$ -FDG metabolism (represented by SUVR and  $K_i$ ) was dominated by increased phosphorylation. Overall, the observed changes in the spleen were similar to those of the lungs but with weaker statistical significance.

### Effect of Vaccination

Among the COVID-19 subjects, 5 subjects were unvaccinated and 7 subjects were vaccinated before their PET scans (Supplemental Table 1). There was no statistical difference in age, body mass index, or blood sugar level between the unvaccinated and the vaccinated COVID-19 subjects ( $P > 0.2$ ). Lung  $K_i$  was higher in unvaccinated COVID-19 subjects than in healthy subjects ( $P < 0.001$ ), as shown in Figure 6. Lung  $K_i$  was reduced in vaccinated COVID-19 subjects but still slightly higher than in the healthy group. Spine bone marrow  $K_1$  of both unvaccinated and vaccinated COVID-19 subjects was higher than that of healthy subjects, but it differed little between unvaccinated and vaccinated COVID-19 subjects. Figure 6 also shows that the spleen  $K_i$  of the vaccinated subjects tended to have a larger difference from the healthy subjects than the spleen  $K_i$  of the unvaccinated ones. No effect of vaccination was noted in other organs of recovering COVID-19 subjects.

### Parametric Imaging of Recovering COVID-19 Subjects

Figure 7 shows the parametric images of the lungs and bone marrow from healthy subjects and COVID-19 subjects. The lung images of SUVR,  $K_i$ , and  $k_3$  showed enhanced contrast between the healthy and the recovering COVID-19 subjects compared with SUV (Fig. 7A) through visual inspection, supporting the ROI-based analyses. The demonstrated spatial heterogeneity across different lung lobes (Fig. 7A) is consistent with the lobe-based results of lung SUV and  $K_i$ , as reported in Supplemental Figure 4. In all 5 individual lung lobes,  $K_i$  produced a larger statistical group difference than SUV.

The spine bone marrow (Fig. 7B) and pelvic bone marrow (Supplemental Fig. 5A) images of  $K_i$  and  $K_1$  showed increased contrast between the 2 subjects compared with SUV. The SUVR and  $K_i$

**TABLE 4**  
Comparison of Spleen Microkinetic Parameters  $K_1$ ,  $k_2$ , and  $k_3$  Between Healthy Subjects and Recovering COVID-19 Subjects, and Correlation Between Microparameters and Spleen  $K_i$  Using Pearson and Spearman Analyses

Kinetic parameter	Comparison				Correlation with $K_i$			
	Healthy group	Recovering COVID-19 group	$P_T$	$P_U$	Pearson		Spearman	
					$r$	$P$	$\rho$	$P_S$
$K_1$ (mL/min/cm <sup>3</sup> )	1.61 ± 0.75	1.31 ± 0.88	0.37	0.40	-0.55	0.0044	-0.65	0.00052
$k_2$ (min <sup>-1</sup> )	2.5 ± 1.0	2.1 ± 1.2	0.34	0.40	-0.43	0.034	-0.46	0.021
$k_3$ (min <sup>-1</sup> )	0.0062 ± 0.0024	0.0090 ± 0.0041	0.047	0.097	0.98	9.6 e-17	0.98	6.3 e-07

$P_T$  =  $P$  value of  $t$  test;  $P_U$  =  $P$  value of Mann–Whitney  $U$  test;  $P_S$  =  $P$  value of Spearman rank correlation.  
Groups are mean ± SD.

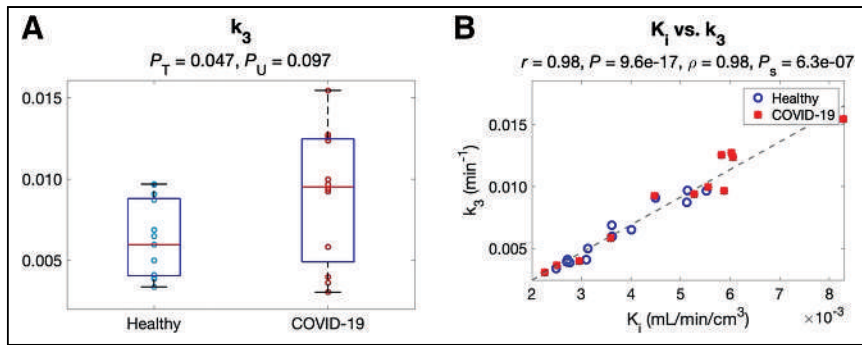


**FIGURE 5.** Study of microparametric quantification in spleen. (A) Comparison of  $k_3$  between 2 groups. (B) Correlation between  $k_3$  and  $K_i$  among subjects.  $P_S = P$  value of Spearman rank correlation;  $P_T = P$  value of  $t$  test;  $P_U = P$  value of Mann-Whitney  $U$  test.

images of the spleen also tended to have higher contrast than the SUV images (Supplemental Fig. 5B). These observations are consistent with the ROI-based findings.

## DISCUSSION

In this pilot study, we evaluated the metabolic differences in multiple organs between recovering COVID-19 subjects and healthy subjects using total-body dynamic  $^{18}\text{F}$ -FDG PET combined with kinetic modeling. This article focuses on establishing the technical foundation for quantitative measurements of glucose metabolism using total-body dynamic PET within the context of COVID-19, which helps inform and guide future research that

involves subtle systemic changes, such as longitudinal tracking of long COVID-19.

We detected increased metabolism using  $K_i$  in the lungs, whereas SUV or CT values gave no group differentiation (Table 1; Fig. 2), indicating the ability of lung  $K_i$  to detect a subtle difference that is undetectable with SUV or CT. The inability of SUV to distinguish the groups likely occurs because of its semiquantitative nature and because it is susceptible to confounding factors (26). The results suggest the power of kinetic quantification for assessing glucose metabolism. The increased lung metabolism in the COVID-19 group may indicate continued inflammation during the early stages of recovery. Previous dynamic lung  $^{18}\text{F}$ -FDG PET studies have associated increased lung  $K_i$  with pulmonary inflammation in multiple conditions, such as acute lung injury (33) and chronic obstructive pulmonary disease (34). Meanwhile, prolonged lung inflammation caused by COVID-19 has been reported; it can last more than 60 d after infection, even for asymptomatic patients and those with mild cases (35,36). The detected difference in lung glucose metabolism might potentially be related to the increased metabolism of immune cells, such as neutrophils (33,37,38) and macrophages (39,40), because of their accumulation and activation in the lungs.

Another advantage of compartmental modeling is microparametric quantification. According to the analysis in the lungs,  $k_3$  is the parameter that was responsible for the healthy versus COVID-19

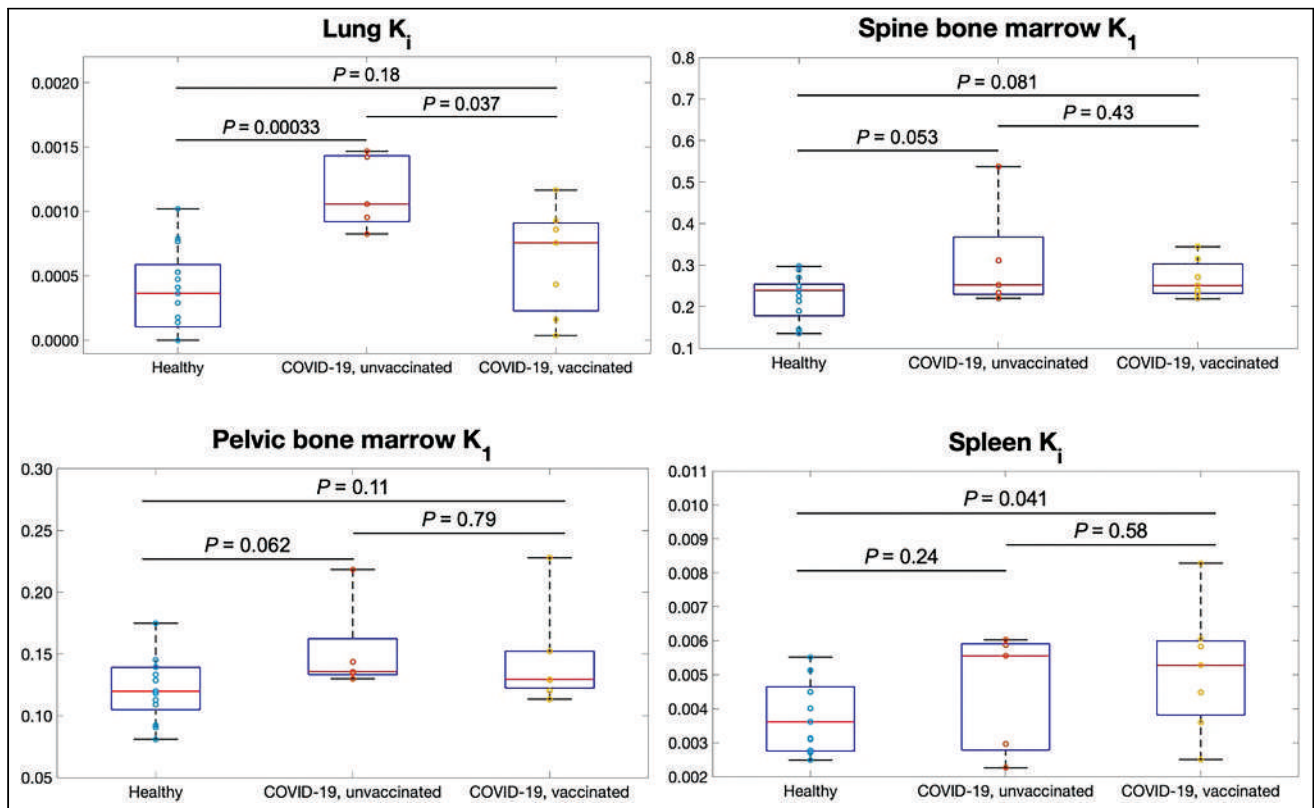


**FIGURE 6.** Evaluation of unvaccinated and vaccinated COVID-19 subjects compared with healthy subjects using kinetic parameters of interest: lung  $K_i$ , spine bone marrow  $K_i$ , pelvic bone marrow  $K_i$ , and spleen  $K_i$ .  $P$  values were calculated using unpaired  $t$  test.



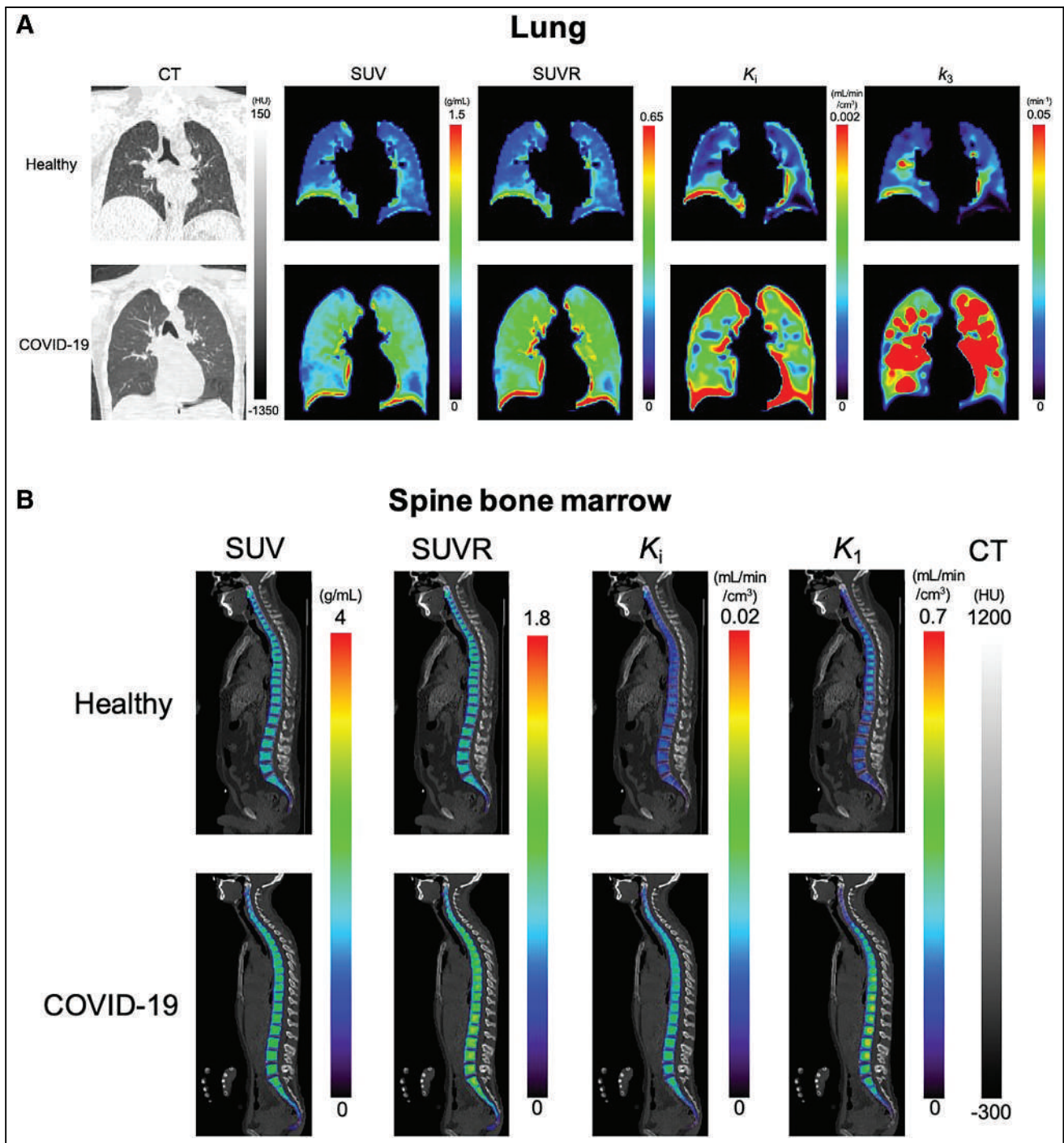


**FIGURE 7.** Parametric images of example healthy subjects and COVID-19 subjects. (A) Lung CT, <sup>18</sup>F-FDG SUV, SUVR, and parametric images of  $K_1$  and  $k_3$ . Coronal slices are selected as middle of trachea carina. (B) Spine bone marrow images of <sup>18</sup>F-FDG SUV, SUVR, and parametric image  $K_1$  and  $K_1$ . PET images are masked for bone marrow region and overlaid on CT images. HU = Hounsfield unit.

group difference in  $K_1$  (Figs. 3 and 7A) and correlated best with  $K_1$  among different microparameters (Table 2). The result implies that increased glucose phosphorylation, rather than glucose delivery, may be the main driving factor for increased lung metabolism. These findings are consistent with previous animal studies that observed  $k_3$  increases in lung inflammation and the association between  $K_1$  and  $k_3$  (31–33,41).

Bone marrow demonstrated a significant change of  $K_1$  in the recovering COVID-19 group compared with healthy subjects (Figs. 4 and 7B), but no differences were observed with SUV, SUVR, or  $K_1$  that reflect overall <sup>18</sup>F-FDG metabolism (Table 1). This result indicates the substantial importance of microparametric quantification. Bone marrow is essential for immunoregulation and is the origin of immune cells (42). Animal studies have

reported that bone marrow cells play an important role in the repair of the injured lung during lung inflammation (43,44). Hence, the increased  $^{18}\text{F}$ -FDG delivery represented by  $K_1$  may be associated with immune system response during COVID-19 recovery. Given that  $^{18}\text{F}$ -FDG  $K_1$  of liver was also demonstrated to associate with hepatic inflammation in fatty liver disease (9,45), the interplay between  $K_1$  and inflammation reaction and the potential of  $K_1$  as a biomarker of disease are worth more studies to explore clinical applications.

The spleen tended to have higher glucose metabolism in the COVID-19 group, as represented by  $K_i$  or SUV<sub>R</sub> (Table 1). This observation is consistent with the splenic  $^{18}\text{F}$ -FDG uptake increase reported in previous studies of COVID-19 (14) and other infectious diseases (46). As an immune organ, the spleen plays an important role in response to COVID-19 (47), and the immune response may lead to increased metabolism.

Our study also separated the unvaccinated and vaccinated COVID-19 groups to evaluate the potential effect of vaccination. The results from the unvaccinated COVID-19 subjects alone (Fig. 6) confirmed that COVID-19 is likely responsible for the observed differences in the lungs and bone marrow between the recovering COVID-19 group and the healthy group. Nonetheless, vaccination showed a combined effect on top of the impact of COVID-19. The lower lung  $K_i$  in the vaccinated group may indicate reduced lung inflammation because of a protecting effect of vaccination. The higher spleen  $K_i$  in the vaccinated subjects (Fig. 6) could also suggest increased immune response because of vaccination. These results are complicated by different vaccination conditions, such as the type, dose, and vaccination date before the PET scan.

This work has several limitations. First, the pilot study cohort is relatively small, especially in the comparison of unvaccinated (5 subjects) versus vaccinated (7 subjects). Therefore, the results, particularly concerning physiologic insights, should be interpreted with caution and warrant confirmation with future hypothesis-driven studies. With an increased sample size, it may be possible to observe some group differences that were not statistically significant in the current study. Second, the healthy and the COVID-19 groups are not exactly matched in this pilot study. Although there is no statistical difference in age, weight, body mass index, or blood sugar level between healthy subjects and recovering COVID-19 subjects, the unpaired age and the time variability between the COVID-19 diagnosis and the PET/CT scan could introduce potential bias. The percentage of women is higher in the COVID-19 group and further separated the analyses according to sex. Example results for lung SUV and  $K_i$  are provided in Supplemental Figure 6 to indicate that the major findings of this work remained valid, although the statistical difference of  $K_i$  became lower, primarily because of the limited sample size. Third, the study lacks histopathology or clinical laboratory data to elaborate on the reason for the differences in  $^{18}\text{F}$ -FDG kinetics between the 2 groups, and the potential impact of COVID-19 treatment on PET quantification was not analyzed because of the inaccessibility of medical records. In addition, some of the healthy cohort, although recruited between May 2019 and January 2020, before the COVID-19 pandemic (the first confirmed U.S. case was January 18, 2020), might have been exposed to COVID-19. Fourth, the statistical analysis in this pilot study was not corrected for possible familywise error rate, because the focus of this work is on comparing parametric metrics with SUV. Confirmation of the physiologic findings from this study will require a larger sample size with an appropriate correction for multiple comparisons.

Finally, the kinetic model for ROI-based analysis and parametric imaging (31,32) used in this work followed a commonly used 2-tissue model for analyzing  $^{18}\text{F}$ -FDG data and considered time delay and organ-specific input functions. More advanced and organ-specific compartmental models could be investigated, for example, the 3-tissue model (33) and the recent high-temporal resolution model (48) for the lungs. We are investigating such models.

Our next steps are to use a similar methodology and more advanced models to study the impact of long COVID-19 on individual subjects. The interplay and correlation of tracer kinetics among different organs will be of interest. In addition, the results from this pilot work suggest future study designs should focus more on immune-related metabolic changes, for example, by tracking macrophage (49) or neutrophil (50) recruitment or monitoring serum inflammatory factors, to gain a deeper understanding of the prolonged impact of COVID-19 on glucose metabolism.

## CONCLUSION

With total-body multiparametric PET, increased lung  $^{18}\text{F}$ -FDG metabolism (measured by  $K_i$ ) and increased bone marrow  $^{18}\text{F}$ -FDG delivery (measured by  $K_1$ ) were detected in recovering COVID-19 subjects compared with healthy subjects. The changes may be associated with continued inflammation and immune response during the early stages of recovery from COVID-19. Vaccination may have a protection effect. These findings are missed or not possible to find if standard SUV measures are used. Total-body multiparametric  $^{18}\text{F}$ -FDG PET can be a more sensitive tool than conventional whole-body static  $^{18}\text{F}$ -FDG imaging for detecting subtle changes and may be used to study postacute sequelae of COVID-19.

## DISCLOSURE

This research is supported in part by National Institutes of Health grants R01 CA206187, R01 DK124803, and R01 AR076088. University of California, Davis, has a research agreement and revenue-sharing agreement with United Imaging Healthcare. No other potential conflict of interest relevant to this article was reported.

## ACKNOWLEDGMENTS

We thank technologists and staff, particularly Lynda E. Painting, of the EXPLORER Molecular Imaging Center, for their assistance in patient consent and data acquisition.

## KEY POINTS

**QUESTION:** Compared with standard whole-body  $^{18}\text{F}$ -FDG PET imaging, is there benefit from using total-body multiparametric  $^{18}\text{F}$ -FDG PET to study COVID-19 recovery?

**PERTINENT FINDINGS:** Higher  $^{18}\text{F}$ -FDG net influx and phosphorylation in the lungs and higher  $^{18}\text{F}$ -FDG blood-to-tissue delivery in bone marrow were detected in recovering COVID-19 subjects than in healthy subjects, whereas no statistical difference was detected using SUV.

**IMPLICATIONS FOR PATIENT CARE:** Total-body multiparametric  $^{18}\text{F}$ -FDG PET may offer a more sensitive tool than SUV for quantitative assessment of multiorgan effects in COVID-19 recovery and may be used to study long COVID-19.



## REFERENCES

- Cherry SR, Badawi RD, Karp JS, Moses WW, Price P, Jones T. Total-body imaging: transforming the role of positron emission tomography. *Sci Transl Med*. 2017; 9:eaa6169.
- Pantel AR, Viswanath V, Daube-Witherspoon ME, et al. PennPET Explorer: human imaging on a whole-body imager. *J Nucl Med*. 2020;61:144–151.
- Alberts I, Hünermund J-N, Prenosil G, et al. Clinical performance of long axial field of view PET/CT: a head-to-head intra-individual comparison of the Biograph Vision Quadra with the Biograph Vision PET/CT. *Eur J Nucl Med Mol Imaging*. 2021;48:2395–2404.
- Wang Y, Li E, Cherry SR, Wang G. Total-body PET kinetic modeling and potential opportunities using deep learning. *PET Clin*. 2021;16:613–625.
- Carson RE. Tracer kinetic modeling in PET. In: Bailey DL, Townsend DW, Valk PE, Maisey MN, eds. *Positron Emission Tomography*. Springer; 2005:127–159.
- Wang G, Nardo L, Parikh M, et al. Total-body PET multiparametric imaging of cancer using a voxel-wise strategy of compartmental modeling. *J Nucl Med*. 2022; 63:1274–1281.
- Sundaram SM, Doughty LA, Sereda MW. Location matters: hexokinase 1 in glucose metabolism and inflammation. *Trends Endocrinol Metab*. 2022;33:665–667.
- Zerizer I, Tan K, Khan S, et al. Role of FDG-PET and PET/CT in the diagnosis and management of vasculitis. *Eur J Radiol*. 2010;73:504–509.
- Wang G, Corwin MT, Olson KA, Badawi RD, Sarkar S. Dynamic PET of human liver inflammation: impact of kinetic modeling with optimization-derived dual-blood input function. *Phys Med Biol*. 2018;63:155004.
- Wenter V, Müller J-P, Albert NL, et al. The diagnostic value of [<sup>18</sup>F]FDG PET for the detection of chronic osteomyelitis and implant-associated infection. *Eur J Nucl Med Mol Imaging*. 2016;43:749–761.
- Zou S, Zhu X. FDG PET/CT of COVID-19. *Radiology*. 2020;296:E118.
- Afshar-Oromieh A, Prosch H, Schaefer-Prokop C, et al. A comprehensive review of imaging findings in COVID-19: status in early 2021. *Eur J Nucl Med Mol Imaging*. 2021;48:2500–2524.
- Fields BKK, Demirjian NL, Dadgar H, Gholamrezanezhad A. Imaging of COVID-19: CT, MRI, and PET. *Semin Nucl Med*. 2021;51:312–320.
- Dietz M, Chironi G, Claessens Y-E, et al. COVID-19 pneumonia: relationship between inflammation assessed by whole-body FDG PET/CT and short-term clinical outcome. *Eur J Nucl Med Mol Imaging*. 2021;48:260–268.
- Hu B, Guo H, Zhou P, Shi Z-L. Characteristics of SARS-CoV-2 and COVID-19. *Nat Rev Microbiol*. 2021;19:141–154.
- Soltani Zangbar H, Gorji A, Ghadiri T. A review on the neurological manifestations of COVID-19 infection: a mechanistic view. *Mol Neurobiol*. 2021;58:536–549.
- Zaim S, Chong JH, Sankaranarayanan V, Harky A. COVID-19 and multiorgan response. *Curr Probl Cardiol*. 2020;45:100618.
- Yazdanpanah F, Hamblin MR, Rezaei N. The immune system and COVID-19: friend or foe? *Life Sci*. 2020;256:117900.
- Crook H, Raza S, Nowell J, Young M, Edison P. Long COVID: mechanisms, risk factors, and management. *BMJ*. 2021;374:n1648.
- Guedj E, Campion JY, Dudouet P, et al. <sup>18</sup>F-FDG brain PET hypometabolism in patients with long COVID. *Eur J Nucl Med Mol Imaging*. 2021;48:2823–2833.
- Sollini M, Morbelli S, Ciccarelli M, et al. Long COVID hallmarks on [<sup>18</sup>F]FDG-PET/CT: a case-control study. *Eur J Nucl Med Mol Imaging*. 2021;48:3187–3197.
- Sollini M, Ciccarelli M, Ceconi M, et al. Vasculitis changes in COVID-19 survivors with persistent symptoms: an [<sup>18</sup>F]FDG-PET/CT study. *Eur J Nucl Med Mol Imaging*. 2021;48:1460–1466.
- Spencer BA, Berg E, Schmall JP, et al. Performance evaluation of the uEXPLORER total-body PET/CT scanner based on NEMA NU 2-2018 with additional tests to characterize PET scanners with a long axial field of view. *J Nucl Med*. 2021;62:861–870.
- Badawi RD, Shi H, Hu P, et al. First human imaging studies with the EXPLORER total-body PET scanner. *J Nucl Med*. 2019;60:299–303.
- Thiele F, Buchert R. Evaluation of non-uniform weighting in non-linear regression for pharmacokinetic neuroreceptor modelling. *Nucl Med Commun*. 2008;29:179–188.
- Thie JA. Understanding the standardized uptake value, its methods, and implications for usage. *J Nucl Med*. 2004;45:1431–1434.
- van den Hoff J, Oehme L, Schramm G, et al. The PET-derived tumor-to-blood standard uptake ratio (SUR) is superior to tumor SUV as a surrogate parameter of the metabolic rate of FDG. *EJNMMI Res*. 2013;3:77.
- Schroeder T, Vidal Melo MF, Musch G, Harris RS, Venegas JG, Winkler T. Image-derived input function for assessment of <sup>18</sup>F-FDG uptake by the inflamed lung. *J Nucl Med*. 2007;48:1889–1896.
- McIntosh LJ, Bankier AA, Vijayaraghavan GR, Licho R, Rosen MP. COVID-19 vaccination-related uptake on FDG PET/CT: an emerging dilemma and suggestions for management. *AJR*. 2021;217:975–983.
- Keshavarz P, Yazdanpanah F, Rafiee F, Mizandari M. Lymphadenopathy following COVID-19 vaccination: imaging findings review. *Acad Radiol*. 2021;28:1058–1071.
- Wellman TJ, Winkler T, Costa ELV, et al. Effect of local tidal lung strain on inflammation in normal and lipopolysaccharide-exposed sheep. *Crit Care Med*. 2014;42:e491–e500.
- de Prost N, Costa EL, Wellman T, et al. Effects of surfactant depletion on regional pulmonary metabolic activity during mechanical ventilation. *J Appl Physiol*. 2011; 111:1249–1258.
- de Prost N, Feng Y, Wellman T, et al. <sup>18</sup>F-FDG kinetics parameters depend on the mechanism of injury in early experimental acute respiratory distress syndrome. *J Nucl Med*. 2014;55:1871–1877.
- Subramanian DR, Jenkins L, Edgar R, Quraishi N, Stockley RA, Parr DG. Assessment of pulmonary neutrophilic inflammation in emphysema by quantitative positron emission tomography. *Am J Respir Crit Care Med*. 2012;186:1125–1132.
- Doikov I, Hällqvist J, Gilmour KC, Grandjean L, Mills K, Heywood WE. “The long tail of COVID-19”: the detection of a prolonged inflammatory response after a SARS-CoV-2 infection in asymptomatic and mildly affected patients. *F1000Res*. 2020;9:1349.
- Albano D, Bertagna F, Bertoli M, et al. Incidental findings suggestive of COVID-19 in asymptomatic patients undergoing nuclear medicine procedures in a high-prevalence region. *J Nucl Med*. 2020;61:632–636.
- de Prost N, Tucci MR, Melo MFV. Assessment of lung inflammation with <sup>18</sup>F-FDG PET during acute lung injury. *AJR*. 2010;195:292–300.
- Zuo Y, Yalavarthi S, Shi H, et al. Neutrophil extracellular traps in COVID-19. *JCI Insight*. 2020;5:e138999.
- Chen DL, Agapov E, Wu K, et al. Selective imaging of lung macrophages using [<sup>11</sup>C]PBR28-based positron emission tomography. *Mol Imaging Biol*. 2021;23:905–913.
- McGonagle D, Sharif K, O’Regan A, Bridgewood C. The role of cytokines including interleukin-6 in COVID-19 induced pneumonia and macrophage activation syndrome-like disease. *Autoimmun Rev*. 2020;19:102537.
- Chen DL, Mintun MA, Schuster DP. Comparison of methods to quantitate <sup>18</sup>F-FDG uptake with PET during experimental acute lung injury. *J Nucl Med*. 2004; 45:1583–1590.
- Zhao E, Xu H, Wang L, et al. Bone marrow and the control of immunity. *Cell Mol Immunol*. 2012;9:11–19.
- Rojas M, Xu J, Woods CR, et al. Bone marrow-derived mesenchymal stem cells in repair of the injured lung. *Am J Respir Cell Mol Biol*. 2005;33:145–152.
- Yamada M, Kubo H, Kobayashi S, et al. Bone marrow-derived progenitor cells are important for lung repair after lipopolysaccharide-induced lung injury. *J Immunol*. 2004;172:1266–1272.
- Sarkar S, Corwin MT, Olson KA, et al. Pilot study to diagnose nonalcoholic steatohepatitis with dynamic <sup>18</sup>F-FDG PET. *AJR*. 2019;212:529–537.
- Liu Y. Clinical significance of diffusely increased splenic uptake on FDG-PET. *Nucl Med Commun*. 2009;30:763–769.
- Kaneko N, Kuo H-H, Boucau J, et al. Loss of Bcl-6-expressing T follicular helper cells and germinal centers in COVID-19. *Cell*. 2020;183:143–157.e13.
- Wang Y, Spencer BA, Schmall J, et al. High-temporal-resolution lung kinetic modeling using total-body dynamic PET with time-delay and dispersion corrections. *J Nucl Med*. 2023;64:1154–1161.
- Kim EJ, Kim S, Seo HS, et al. Novel PET imaging of atherosclerosis with <sup>68</sup>Galabeled NOTA-neomannosylated human serum albumin. *J Nucl Med*. 2016;57: 1792–1797.
- Antoni G, Lubberink M, Sörensen J, et al. In vivo visualization and quantification of neutrophil elastase in lungs of COVID-19 patients: a first-in-humans PET study with <sup>11</sup>C-NES. *J Nucl Med*. 2023;64:145–148.

---

---

# Total-Body Perfusion Imaging with [<sup>11</sup>C]-Butanol

Elizabeth J. Li<sup>1</sup>, Javier E. López<sup>2</sup>, Benjamin A. Spencer<sup>1</sup>, Yasser Abdelhafez<sup>3</sup>, Ramsey D. Badawi<sup>1,3</sup>, Guobao Wang<sup>3</sup>, and Simon R. Cherry<sup>1,3</sup>

<sup>1</sup>Department of Biomedical Engineering, UC Davis, Davis, California; <sup>2</sup>Department of Internal Medicine, Division of Cardiovascular Medicine, UC Davis Health, UC Davis, Sacramento, California; and <sup>3</sup>Department of Radiology, UC Davis Health, UC Davis, Sacramento, California

---

Tissue perfusion can be affected by physiology or disease. With the advent of total-body PET, quantitative measurement of perfusion across the entire body is possible. [<sup>11</sup>C]-butanol is a perfusion tracer with a superior extraction fraction compared with [<sup>15</sup>O]-water and [<sup>13</sup>N]-ammonia. To develop the methodology for total-body perfusion imaging, a pilot study using [<sup>11</sup>C]-butanol on the uEXPLORER total-body PET/CT scanner was conducted. **Methods:** Eight participants (6 healthy volunteers and 2 patients with peripheral vascular disease [PVD]) were injected with a bolus of [<sup>11</sup>C]-butanol and underwent 30-min dynamic acquisitions. Three healthy volunteers underwent repeat studies at rest (baseline) to assess test–retest reproducibility; 1 volunteer underwent paired rest and cold pressor test (CPT) studies. Changes in perfusion were measured in the paired rest–CPT study. For PVD patients, local changes in perfusion were investigated and correlated with patient medical history. Regional and parametric kinetic analysis methods were developed using a 1-tissue compartment model and leading-edge delay correction. **Results:** Estimated baseline perfusion values ranged from 0.02 to 1.95 mL·min<sup>-1</sup>·cm<sup>-3</sup> across organs. Test–retest analysis showed that repeat baseline perfusion measurements were highly correlated (slope, 0.99; Pearson  $r = 0.96$ ,  $P < 0.001$ ). For the CPT subject, the largest regional increases were in skeletal muscle (psoas, 142%) and the myocardium (64%). One of the PVD patients showed increased collateral vessel growth in the calf because of a peripheral stenosis. Comorbidities including myocardial infarction, hypothyroidism, and renal failure were correlated with variations in organ-specific perfusion. **Conclusion:** This pilot study demonstrates the ability to obtain reproducible measurements of total-body perfusion using [<sup>11</sup>C]-butanol. The methods are sensitive to local perturbations in flow because of physiologic stressors and disease.

**Key Words:** dynamic PET; kinetic modeling; perfusion and blood flow; [<sup>11</sup>C]-butanol; total-body PET

**J Nucl Med 2023; 64:1831–1838**  
DOI: 10.2967/jnumed.123.265659

---

**P**erfusion imaging using PET has been clinically used to assess single-organ, flow-related diseases such as cerebral stroke and myocardial ischemia (1,2). With the advent of total-body PET/CT, blood flow to all tissues in the body can be measured simultaneously, along with the image-derived input function (IDIF). This allows quantitative total-body perfusion measurements to be made

with minimal invasiveness. Tissues of interest across the body have a range of perfusion values. However, commonly used tracers such as [<sup>15</sup>O]-water, [<sup>82</sup>Rb]-RbCl, and [<sup>13</sup>N]-ammonia underestimate perfusion as flow increases because of their flow- and tissue-dependent extraction fraction (3–5). This is a challenge for measuring high flow rates, which can occur either inherently in some organs or in response to an external pressor, such as exercise, injection of adenosine, or increased partial pressure of CO<sub>2</sub> (2,3,6). Thus, accurate perfusion measurements require a highly extracted tracer that can be used to quantify perfusion over the range encountered in the human body in health and disease.

Butanol, labeled with <sup>11</sup>C or <sup>15</sup>O, has been used as a perfusion agent in both human (3,7) and preclinical (8,9) settings. It has the key advantage of having an approximately 100% extraction fraction in the brain for flows at least as high as 1.7 mL·min<sup>-1</sup>·g<sup>-1</sup> (4). Furthermore, labeling with <sup>11</sup>C reduces positron range blurring relative to <sup>15</sup>O, <sup>82</sup>Rb, and <sup>13</sup>N (10) and, with its longer half-life, gives a wider time window to accommodate delays in administration. However, the metabolism- and tissue-dependent permeability of [<sup>11</sup>C]-butanol presents challenges. [<sup>11</sup>C]-butanol is metabolized in a manner similar to ethanol (9). Metabolism mainly occurs in the liver, where alcohol dehydrogenases break down [<sup>11</sup>C]-butanol into [<sup>11</sup>C]-butyric aldehyde and [<sup>11</sup>C]-butyric acid, the latter of which can undergo β-oxidation to form [<sup>11</sup>C]-CO<sub>2</sub> (9). Because these metabolites do not significantly affect the first-pass kinetics of [<sup>11</sup>C]-butanol (9), it is possible to perform first-pass perfusion imaging of the entire body without the need for metabolite correction.

Because of the short acquisition time (AT), the improved sensitivity and extended axial field of view of total-body PET (11) are vital to multiorgan first-pass perfusion imaging with freely diffusible and reversible tracers such as [<sup>11</sup>C]-butanol and [<sup>15</sup>O]-water. In this work, we focused on developing a reliable methodology for quantifying perfusion across the body using kinetic modeling and demonstrating that these methods are sensitive to indications that alter perfusion. Baseline studies were conducted to establish the modeling approach and to determine quantitative perfusion values in a range of tissues. Reproducibility was assessed through resting test–retest studies. The sensitivity of the methods to changes in perfusion was assessed in 1 subject through a rest–stress paradigm generated via the cold pressor test (CPT) and by assessing regional ischemia and visualization of comorbidities in patients with peripheral vascular disease (PVD). These examples illustrate a few of the possible applications for total-body perfusion imaging. Although the short half-life of [<sup>11</sup>C]-butanol may not be ideal for clinical use, it is an attractive tracer for systems-level physiologic research and studies of systemic chronic medical conditions such as heart, kidney, or liver failure. These methods can also be applied to studies with [<sup>15</sup>O]-water.

---

Received Mar. 2, 2023; revision accepted Jul. 17, 2023.  
For correspondence or reprints, contact Simon R. Cherry (srcherry@ucdavis.edu)  
Published online Aug. 31, 2023.  
COPYRIGHT © 2023 by the Society of Nuclear Medicine and Molecular Imaging.

## MATERIALS AND METHODS

### [<sup>11</sup>C]-Butanol Synthesis

[<sup>11</sup>C]-butanol was synthesized using an uninterrupted process beginning with radioactive [<sup>11</sup>C]-CO<sub>2</sub>, *n*-propyl magnesium chloride (Grignard solution) in ether, lithium aluminum hydride, and hydrochloric acid. The 20-min in situ process simultaneously purified [<sup>11</sup>C]-butanol, formulated the final product solution, and sterilized and filtered the product solution into the vial after synthesis completion. Typical yields were 5,000 MBq (200–1,200 MBq/mL) at the end of synthesis, obtained from 60,000 MBq of [<sup>11</sup>C]-CO<sub>2</sub>. Radiochemical purity was in the range of 91%–97%.

### Data Acquisition

With Institutional Review Board approval and written informed consent, 6 healthy volunteers (1 man, 5 women; body mass index, 20.9–30.4 kg/m<sup>2</sup>; age, 23–64 y) and 2 patients with PVD (body mass index, 27.5 and 28.4 kg/m<sup>2</sup>; 66-y-old man and 69-y-old woman, respectively) were imaged on the uEXPLORER PET/CT scanner (United Imaging Healthcare). A low-dose, total-body CT scan (140 kVp and 50 mAs with automatic dose modulation) was acquired for attenuation and scatter correction before bolus injection of [<sup>11</sup>C]-butanol (mean, 281 MBq; range, 191–349 MBq). List-mode acquisitions on the uEXPLORER scanner (11) lasted about 30 min.

All 6 healthy volunteers received a baseline scan to measure resting perfusion across the body. One baseline visit from each of the 6 healthy volunteers (baseline healthy volunteers [BHV<sub>s</sub>]) was used to investigate total image-derived activity (TIDA) and optimize AT, as well as to report baseline perfusion values. Three healthy volunteers underwent a second baseline scan to assess test–retest reproducibility. One healthy volunteer underwent a paired resting and CPT study to measure effects of CPT. For subjects receiving 2 scans, visits occurred within 2 wk (9.0 ± 3.4 d). PVD patients had a single resting scan.

For the CPT, foot therapy pads (Polar Products) were placed on both feet before the CT acquisition. Starting after the CT scan but about 60 s before the start of the PET acquisition, ice water was continuously pumped through the conformable boots for 5 min.

### Image Reconstruction

Reconstruction software, provided by the vendor, was used to perform time-of-flight ordered-subset expectation maximization (20 subsets and 4 iterations), with corrections for attenuation, scatter, randoms, dead time, and decay (12). No modeling of the point spread function or smoothing after reconstruction was applied. Images were reconstructed with 4.0 × 4.0 × 4.0 mm<sup>3</sup> voxels (matrix size, 150 × 150 × 486) and 57 frames (30 × 2, 12 × 5, 6 × 10, 4 × 30, and 5 × 300 s). The full 30-min dynamic reconstruction was used to measure TIDA and thus assess tracer metabolism. Only the first 5 min were used for kinetic modeling and perfusion estimation.

### Region Delineation

Tissue time–activity curves were derived from 20 large or whole-organ volumetric regions of interest (ROIs) using PMOD software (PMOD Technologies), as listed in Supplemental Table 1 (supplemental materials are available at <http://jnm.snmjournals.org>). All bilateral regions were drawn separately (e.g., left and right kidneys) and averaged for kinetic modeling except for the deltoid, which demonstrated high spillover from the vessels in the arm in which the bolus was delivered; thus, only the contralateral deltoid was included. The CT scan was used for initial ROI delineation. ROIs were modified to account for the effects of subject motion in a tissue-dependent manner (Supplemental Table 1) through 2 image visualization strategies: use of a 0- to 5-min average PET image and avoidance of visible motion or spillover effects in high-contrast frames.

Volumetric ROIs were drawn in the descending aorta and the right ventricle (RV) to measure the IDIFs. For ROI-based time–activity curves, the descending aorta IDIF was used for all tissues except for the lungs, where the RV IDIF was used, because the dominant lung blood supply is via the pulmonary vein, not the bronchial artery (13–15). Parametric images were generated using the descending aorta IDIF for all voxels except for lung voxels, where the RV IDIF was used instead (supplemental materials, particularly Supplemental Fig. 1).

### TIDA

Knapp et al. (9) found no metabolites in the blood during the first pass of [<sup>11</sup>C]-butanol in a rabbit study. Because no blood sampling was performed in this study, TIDA curves for [<sup>11</sup>C]-butanol were measured to assess end metabolism of [<sup>11</sup>C]-butanol (characterized by expired [<sup>11</sup>C]-CO<sub>2</sub> and loss of activity from the subject) during the first few minutes of acquisition used for kinetic modeling. Total-body PET can measure the total activity in the subject over time because the whole body is within the field of view. TIDA for each PET image frame *m* was defined as follows (12):

$$\text{TIDA}(m) = V \times \sum_i A_i(m), \quad \text{Eq. 1}$$

where *V* is the voxel volume (mL) and *A<sub>i</sub>(m)* (MBq/mL) is the decay-corrected activity concentration of voxel *i* in frame *m*. For each study, TIDA(*m*) was normalized by injected dose. To account for timing variation of the bolus delivery, delay correction was performed on the TIDA curves using the leading-edge method (16), with a 1% threshold of the RV time–activity curve.

### Kinetic Modeling

Three models were used in this work: a 0-tissue, 2-parameter model (*v<sub>b</sub>* and delay); a 1-tissue, 4-parameter (1T4P) model (*v<sub>b</sub>*, *K<sub>1</sub>*, *k<sub>2</sub>*, and delay); and a 1-tissue, 6-parameter (1T6P) model (*v<sub>b</sub>*, *K<sub>1</sub>*, *k<sub>2</sub>*, delay, dispersion, and fraction contributed from a second blood input function) (17). *v<sub>b</sub>* (mL·cm<sup>-3</sup>) is the blood volume fraction, *K<sub>1</sub>* (mL·min<sup>-1</sup>·cm<sup>-3</sup>) represents perfusion, and *k<sub>2</sub>* (min<sup>-1</sup>) represents the washout rate constant from the tissue back into systemic circulation. The partition coefficient *p* is *K<sub>1</sub>/k<sub>2</sub>*. After implementing leading-edge delay correction (16), modeling was performed using nonlinear least-squares fitting (18).

On the basis of preliminary fitting results and comparison of the Akaike information criterion for 1T4P and 1T6P models (with correction for small sample size), a 1T4P model was implemented for all ROI-based tissue time–activity curves except for the liver time–activity curve, for which the 1T6P model was used to account for the portal vein blood supply (Supplemental Table 2). No correction for lung tissue fraction was applied. Parameter identifiability and AT were investigated using these fixed models for ROI-based time–activity curves.

For parametric imaging, all 3 compartment models were considered for each voxel time–activity curve, where the 0-tissue, 2-parameter and 1T6P models were used to account for the blood pool and liver, respectively. Model selection was performed at the voxel level using the Akaike information criterion with correction for small sample size (supplemental materials).

### AT

Because the Akaike information criterion depends on the number of image frames, we first compared the Akaike information criterion for each tissue with a constant AT of 180 s. After determining the most appropriate model based on an AT of 180 s, we explored how AT, or the delay-corrected total time of the time–activity curve used for kinetic modeling, affected the fitted parameters. Optimal AT was guided by the stability of the mean *K<sub>1</sub>*, *v<sub>b</sub>*, and *p* across ATs and the magnitude of the SD, as well as their relation to previously published literature values in Supplemental Table 3 (3,6,13,14,19–43). Time 0 was defined as the bolus arrival time in the ROI. ATs ranging from 60

to 270 s in 30-s increments were studied across all baseline acquisitions. For tissues that showed stability across ATs, 180 s was selected as the default.

### Parameter Estimation

Using the appropriate model and AT, kinetic parameter estimates for ROI-based time–activity curves were obtained. Bilateral parameter estimates in the lungs and kidneys, as well as parameter estimates in most skeletal muscle regions (splenius capitis, psoas, thigh, and calf), were averaged to give a single value for each tissue. An identifiability analysis (44–47) for parameter identification also was performed (Supplemental Table 4).

For voxelwise kinetic modeling, image data were smoothed (48). An AT of 180 s was used with a leading-edge threshold of 7.5% to correct for delay (16) across all voxels. Further details are provided in the supplemental materials, particularly Supplemental Figure 2 and Supplemental Table 5.

### Comparative Analysis

For the 3 BHV subjects with repeat scans, test–retest reproducibility was assessed first using Pearson *r*. A 1-sample Kolmogorov–Smirnov test was used to assess normality. After determining normality, Bland–Altman plots were generated with limits of agreement of 1.96 times the SD. A significance level of 0.05 was used. Additional test–retest assessments (the intraclass correlation coefficient and intrasubject coefficient of variation) are included in the supplemental materials.

For the rest–CPT study, intrasubject regional parameter estimates were compared. Assessments for the 2 PVD patients were made on the basis of clinical history and comorbidities.

## RESULTS

IDIFs and ROI-based time–activity curves showed consistency in shape for a given tissue, whereas the magnitude varied across subjects (Fig. 1A). The time–activity curves of the 2 PVD subjects (Fig. 1A, red) were quite different in several tissues from those of the healthy subjects and were different from each other, indicating the heterogeneity of the perfusion patterns across disease states.

### TIDA

As shown in Figure 1B, the normalized BHV TIDA curve decreased slowly over the course of the 30-min acquisition (~10% average drop overall), reflecting the expected loss of activity through the exhalation of [<sup>11</sup>C]-CO<sub>2</sub>. However, the curve remained quite flat over the first 5 min of the study (Fig. 1B, inset), confirming that metabolic losses of <sup>11</sup>C in the form of [<sup>11</sup>C]-CO<sub>2</sub> are negligible for the ATs used for kinetic modeling and agreeing with previous measurements in animal studies (9,49). A small positive bias (<8%) was observed from 10 to 20 s—a previously noted effect that has been attributed to the injection of the bolus and small errors in correction factors with rapidly changing tracer distribution (12).

### Impact of AT on Parameter Estimates

Figure 2 shows the stability of BHV estimates of  $K_1$ ,  $v_b$ , and  $p$  as a function of the AT used for kinetic modeling for a subset of tissues. For most tissues, parameters were stable across ATs or reached stability by around 180–210 s after bolus arrival. A notable exception was the kidney, where  $K_1$  was inversely related to  $p$  across ATs. Gray matter and skeletal muscle estimates of  $p$  were highly variable at shorter ATs but showed stabilization at longer ATs.

Using data similar to those in Figure 2, optimal ATs for all tissues were identified and fixed for each region for further analyses. All subsequent fitting at the ROI level was performed with the tissue-specific ATs listed in Table 1.

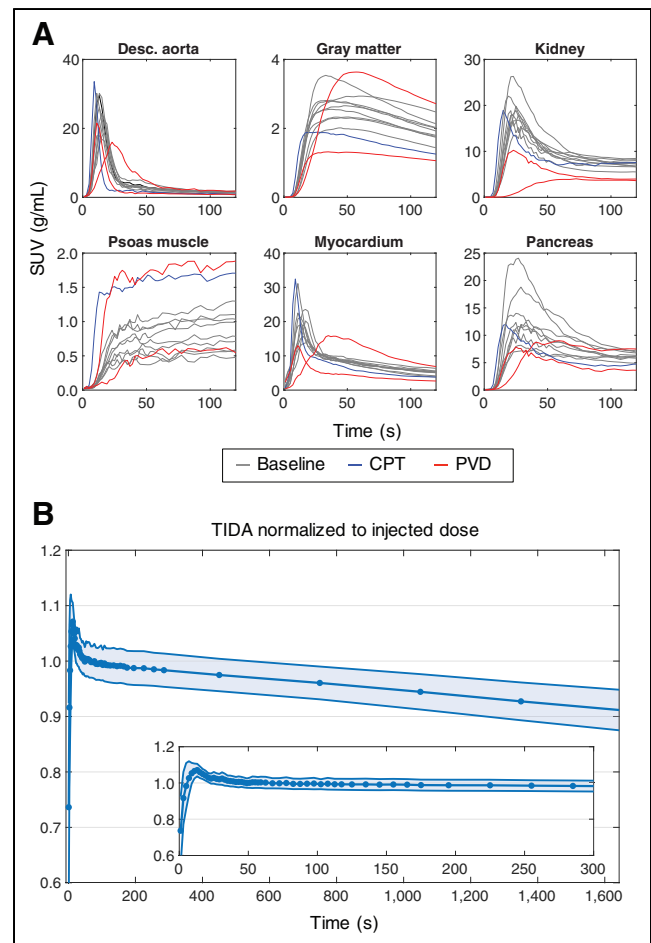


**FIGURE 1.** (A) Representative [<sup>11</sup>C]-butanol time–activity curves (0–150 s) for subset of tissue types. (B) Normalized TIDA (mean ± SD) for BHV 30-min dynamic acquisitions. Desc. = descending.

### Baseline Parameter Estimates in Healthy Volunteers

When the optimal AT was used (Table 1), all tissues except for the liver were fit with the 1T4P model, whereas the liver was fit with the 1T6P model (Supplemental Table 2). The leading-edge method failed to provide reasonable delay estimates for the liver; thus, delay correction in the liver was performed using joint estimation. The BHV results (Table 1, bold; Fig. 3) demonstrate the range of perfusion values ( $K_1$ ) found across organs and tissues. One healthy subject showed abnormally low hepatic perfusion; after further investigation of the CT image, fatty infiltration of the liver was noted. Thus, the liver values for this subject were excluded from Table 1 and Figure 3. Tissue-specific BHV parameter estimates were compared with previously published literature values for individual organs (mostly obtained using [<sup>15</sup>O]-water) as listed in Supplemental Table 3. Values were generally in good agreement, although direct comparison is difficult because of differences in the tracer used, modeling methodology, and imaging technology.

### Test–Retest Assessments

Correlation analysis of the 3 test–retest subjects showed good agreement of  $K_1$  (Fig. 4A; slope, 0.99;  $r = 0.96$ ,  $P < 0.001$ ),  $v_b$  (Fig. 4B; slope, 0.90;  $r = 0.92$ ,  $P < 0.001$ ), and delay (slope, 0.95;  $r = 0.94$ ,  $P < 0.001$ ) across all 16 tissue types, where the muscle regions were averaged. The partition coefficient  $p$  was also in agreement between visits (slope, 0.90;  $r = 0.91$ ,  $P < 0.001$ ). The Kolmogorov–Smirnov

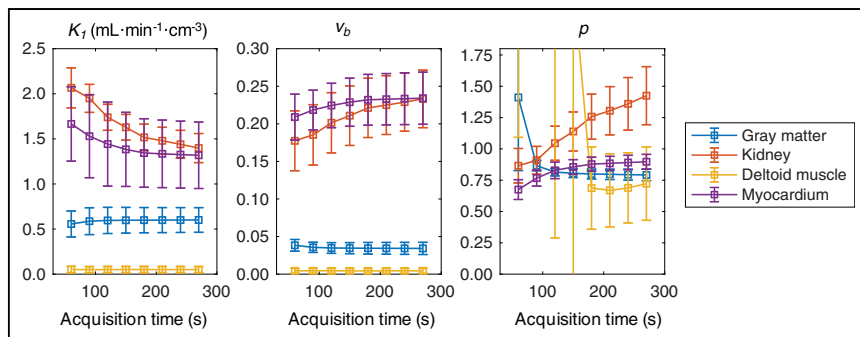


**FIGURE 2.** Impact of AT on BHV parameter estimates (mean  $\pm$  SD) as assessed by fitting time-activity curves across ATs of 60–270 s in 30-s increments.

tests of the data showed a lack of normality, whereas the log-transformed data showed normality (Fig. 4). There were a range of intrasubject coefficient of variation and intraclass correlation coefficient values of  $K_1$  across organs (Supplemental Table 6).

### Parametric Imaging

The dynamic [ $^{11}\text{C}$ ]-butanol data were of sufficient quality to produce low-noise parametric maps across the whole body. A representative baseline study is shown in Figure 5.

### Effects of CPT

Compared with the corresponding resting scan, large increases in perfusion were observed after CPT in skeletal muscle, for which average  $K_1$  increased from 0.06 to 0.14  $\text{mL}\cdot\text{min}^{-1}\cdot\text{cm}^{-3}$ . The overall range of  $K_1$  after CPT was 0.07  $\text{mL}\cdot\text{min}^{-1}\cdot\text{cm}^{-3}$  in the calves to 0.21  $\text{mL}\cdot\text{min}^{-1}\cdot\text{cm}^{-3}$  in the deltoid. At rest,  $K_1$  ranged from

0.04  $\text{mL}\cdot\text{min}^{-1}\cdot\text{cm}^{-3}$  in the calves to 0.10  $\text{mL}\cdot\text{min}^{-1}\cdot\text{cm}^{-3}$  in the deltoid. Regionally, the highest increase with CPT was in the psoas (142%), followed by the thigh muscles (137%), deltoid (111%), splenius capitis (106%), and calf muscles (71%). An increase in perfusion also was observed in the myocardium (rest, 1.48  $\text{mL}\cdot\text{min}^{-1}\cdot\text{cm}^{-3}$ ; CPT, 2.43  $\text{mL}\cdot\text{min}^{-1}\cdot\text{cm}^{-3}$ ). There was also a small increase in gray matter  $K_1$  (rest, 0.47  $\text{mL}\cdot\text{min}^{-1}\cdot\text{cm}^{-3}$ ; CPT, 0.56  $\text{mL}\cdot\text{min}^{-1}\cdot\text{cm}^{-3}$ ). Thyroid perfusion showed a large decrease (rest, 1.64  $\text{mL}\cdot\text{min}^{-1}\cdot\text{cm}^{-3}$ ; CPT, 0.92  $\text{mL}\cdot\text{min}^{-1}\cdot\text{cm}^{-3}$ ). For the pancreas, spleen, and thyroid,  $v_b$  was lower for

the CPT study. Regional differences from BHVs are shown in Supplemental Figure 3. There were also reductions in delay estimates of 1–3 s with CPT except for in the lungs, which showed the same delay estimate for both acquisitions.

These trends are visible in the parametric images (Fig. 6). Figure 6A shows changes in parametric  $K_1$  images of the brain (increase in  $K_1$  in gray matter and decrease in white matter). Short-axis, horizontal long-axis, and vertical long-axis views of the myocardium (Fig. 6B) and axial views of skeletal muscles in the thighs (Fig. 6C) show increased  $K_1$ .

### PVD Patients

Results for the 2 PVD patients are shown in Figure 7. Patient 1 had a chronic and symptomatic left popliteal arterial stenosis and a prior myocardial infarction (Fig. 7A). Downstream of the popliteal stenosis, parametric assessment revealed an area of increased

**TABLE 1**  
Tissue-Specific BHV Parameters ( $n = 6$ )

Category	Tissue	AT (s)	LE threshold (%)	Delay (s)	$K_1$	$v_b$	$p$
Brain	Gray matter	180	1.75	4.50 (0.84)	<b>0.60 (0.14)</b>	0.034 (0.008)	0.80 (0.04)
	White matter	180	2.00	4.67 (0.82)	<b>0.27 (0.05)</b>	0.016 (0.004)	0.65 (0.05)
Intestines	Large intestine	180	2.00	5.50 (2.74)	<b>0.11 (0.02)</b>	0.009 (0.008)	0.40 (0.11)
	Small intestine	180	2.00	7.00 (1.10)	<b>0.35 (0.06)</b>	0.039 (0.012)	1.18 (0.36)
Kidneys		90	1.50	4.92 (0.80)	<b>1.95 (0.16)</b>	0.185 (0.040)	0.91 (0.11)
Liver*		120	—	1.17 (1.33)	<b>1.23 (0.36)</b>	0.026 (0.054)	1.80 (0.43)
Lungs		60	2.50	3.50 (0.63)	<b>1.72 (0.32)</b>	0.089 (0.043)	0.16 (0.02)
Skeletal muscle <sup>†</sup>		240 (33)	3.56	8.50 (1.85)	<b>0.05 (0.02)</b>	0.003 (0.002)	1.71 (1.70)
Marrow and bone	Red marrow	180	2.00	2.17 (0.98)	<b>0.18 (0.07)</b>	0.009 (0.005)	0.67 (0.13)
	Trabecular bone	180	1.00	2.17 (2.56)	<b>0.02 (0.01)</b>	0.000 (0.001)	0.17 (0.13)
	Cortical bone	180	1.00	8.50 (3.94)	<b>0.03 (0.01)</b>	0.002 (0.002)	0.24 (0.12)
Myocardium		180	0.25	−3.17 (0.75)	<b>1.34 (0.38)</b>	0.232 (0.034)	0.88 (0.06)
Pancreas		120	3.00	5.00 (1.10)	<b>1.26 (0.60)</b>	0.096 (0.052)	0.93 (0.10)
Spleen		90	2.00	4.50 (0.55)	<b>1.65 (0.18)</b>	0.086 (0.028)	1.04 (0.03)
Stomach		120	5.00	4.17 (2.79)	<b>0.58 (0.15)</b>	0.028 (0.020)	0.81 (0.32)
Thyroid		180	3.00	5.00 (2.10)	<b>1.36 (0.34)</b>	0.220 (0.151)	0.78 (0.22)

\* $n = 5$  (see text).

<sup>†</sup>Reported values are averaged.

LE = leading edge.

Data are mean followed by SD in parentheses. Units for  $K_1$  are  $\text{mL}\cdot\text{min}^{-1}\cdot\text{cm}^{-3}$ .



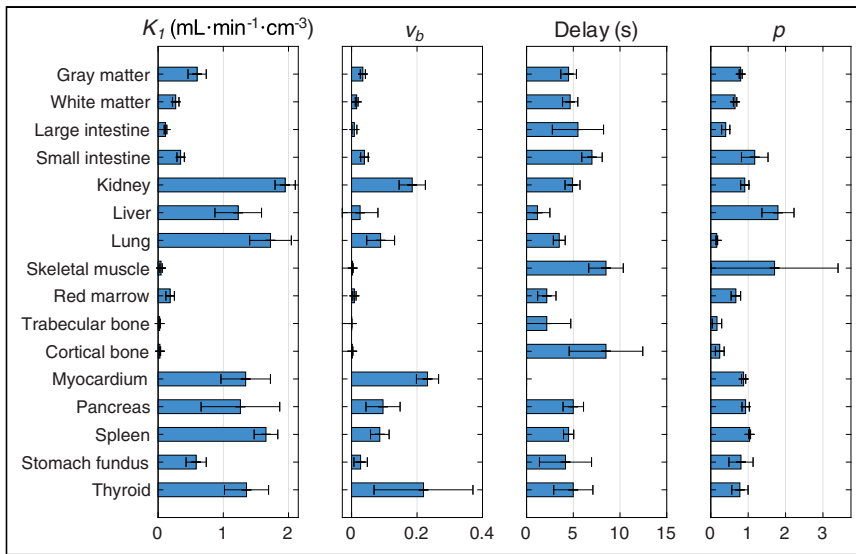


**FIGURE 3.** BHV ROI-based kinetic parameter estimates (mean  $\pm$  SD). AT was fixed for individual tissues (Table 1).

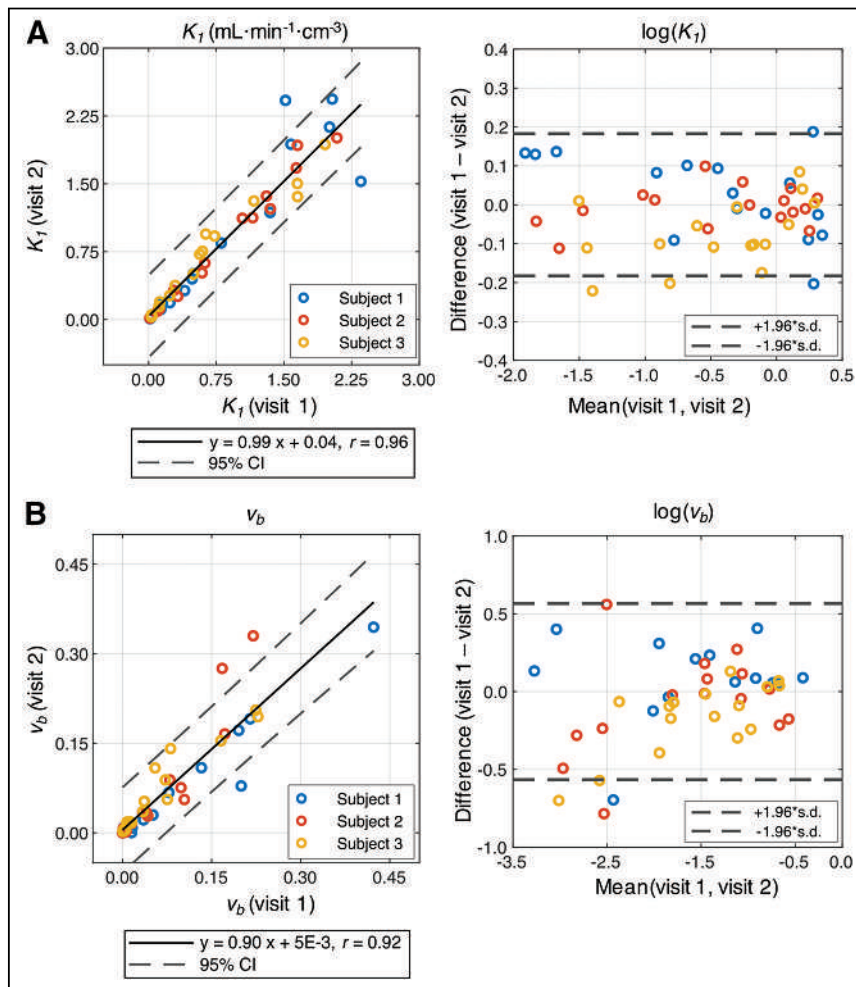


**FIGURE 4.** Correlation analysis and Bland–Altman plots of test–retest studies.  $K_1$  (A) and  $v_b$  (B) showed strong agreement between 2 visits. Normality was observed for log-transformed data points shown in Bland–Altman plots for  $K_1$  and  $v_b$ .

perfusion, with a 70% increase in  $K_1$  relative to the right calf (0.074 vs. 0.044 mL·min<sup>-1</sup>·cm<sup>-3</sup>). Average skeletal muscle  $K_1$  (0.11 mL·min<sup>-1</sup>·cm<sup>-3</sup>) was 146% higher than in BHV studies. Figure 7A includes myocardial short-axis, horizontal long-axis, and vertical long-axis parametric images. Whole myocardial perfusion for this PVD patient was 29% lower than BHV results (0.96 vs. 1.34 mL·min<sup>-1</sup>·cm<sup>-3</sup>).

The influence of known comorbidities—including renal failure, hypothyroidism, and right ventricular dilation—of PVD patient 2 were reflected in the parametric  $K_1$  image (Fig. 7B) and the large regional differences compared with those of BHVs (Supplemental Fig. 4). In the kidney and thyroid, respectively, there were 85% and 71% reductions in  $K_1$  compared with BHV studies (0.30 vs. 1.95 and 0.39 vs. 1.36 mL·min<sup>-1</sup>·cm<sup>-3</sup>). Patient 2 also had evidence of pulmonary hypertension in prior imaging studies (World Health Organization grade 2) and exhibited low lung  $K_1$ —with a dilated RV—compared with those of BHVs (94% drop; Supplemental Fig. 4).

## DISCUSSION

We have presented methods and analyses for dynamic [<sup>11</sup>C]-butanol total-body PET imaging to quantify tissue perfusion. An advantage of total-body PET is that perfusion and the tracer partition coefficient can be estimated simultaneously in every organ and tissue in the body (not possible with conventional scanners because of the fast kinetics of freely diffusible perfusion tracers). The high detection sensitivity of total-body PET allows high-quality, high-temporal-resolution (2-s frames) data to better capture the tissue time–activity curves and the input function, along with the potential for voxelwise kinetic modeling. Total ATs of approximately 5 min are sufficient for bolus delivery and capture of time–activity curves for all tissues and organs in the body, which then can be used to quantify perfusion using ROIs. An AT of 180 s from bolus arrival was suitable for most tissues. Average BHV parameter estimates were in broad agreement with single-organ literature values.

It is also possible to acquire whole-body perfusion images on conventional scanners with trapped perfusion tracers such as [<sup>13</sup>N]-NH<sub>3</sub> and [<sup>62</sup>Cu]-ethylglyoxal bis(thiosemicarbazonato)copper(II) (43). However, these tracers can have flow- or tissue-dependent extraction, which may make absolute quantification difficult



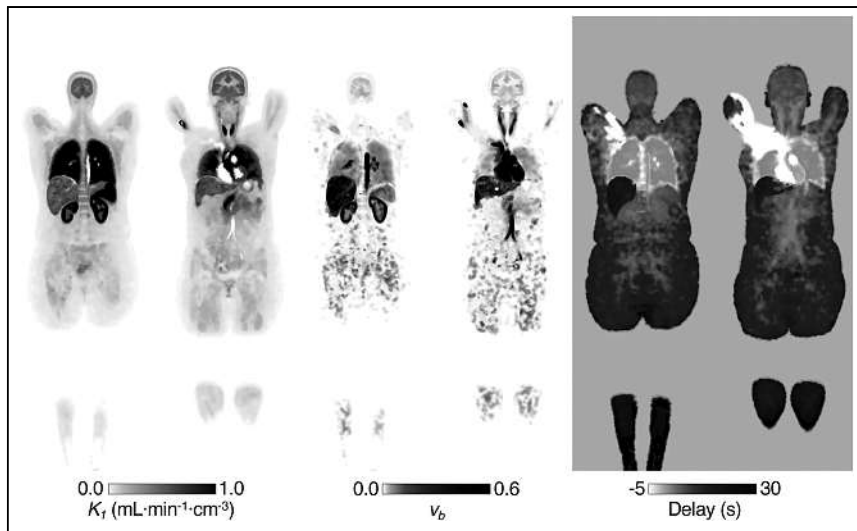


**FIGURE 5.** Example parametric images of 2 coronal slices (baseline). Grayscale bars have been manually adjusted to allow visualization across full range of values.

across all tissue types and blood flow ranges encountered in the body.

Baseline test–retest reproducibility in 3 healthy volunteers indicated that estimates of perfusion,  $v_b$ , and delay are all highly reproducible (Pearson  $r > 0.9$ ,  $P < 0.001$ ) between visits. The  $K_1$  intrasubject coefficient of variation and intraclass correlation coefficient exhibited no clear pattern, although the kidney and spleen showed a particularly low intraclass correlation coefficient ( $<0$ ) despite a high  $K_1$ . These highly perfused tissues may experience variable  $K_1$  because of normal changes in function throughout the day (50) or stress-related effects linked to the imaging procedure. Estimates of  $p$  for the lung demonstrate that the RV IDIF and 1T4P

shorter with CPT, indicative of an increased heart rate because of sympathetic nervous system stimulation. Although conclusions cannot be drawn from a single subject, the changes with CPT noted earlier are greater than the baseline test–retest range (Fig. 4). This demonstrates the sensitivity of total-body perfusion imaging with [ $^{11}\text{C}$ ]-butanol in identifying multiorgan alterations in perfusion.

Similarly, larger changes in perfusion were observed in the PVD patients than in BHVs (Supplemental Fig. 4). PVD is a heterogeneous condition, typically affecting multiple organs and accompanied by other comorbidities. Both patients exhibited perfusion patterns that are consistent with their clinical symptoms and histories. These results highlight the potential utility of total-body perfusion imaging in assessing perfusion patterns across the entire body in systemic cardiovascular disease and support carefully designed imaging trials that can take advantage of this methodology.

This study has several limitations. First, full testing and validation of TIDA as a surrogate for assessment of metabolism of [ $^{11}\text{C}$ ]-butanol in humans is necessary through measurement of circulating metabolites, including [ $^{11}\text{C}$ ]- $\text{CO}_2$  and [ $^{11}\text{C}$ ]-bicarbonate. Second, [ $^{11}\text{C}$ ]-butanol has not been extensively used outside research applications in the brain and myocardium. Direct comparison with [ $^{15}\text{O}$ ]-water (for which our methods would also be applicable) would be helpful in other tissues to assess the effects of tissue-dependent permeability and the extent to which tissues known to metabolize alcohols (e.g., liver) or alcohol metabolites (e.g., muscle) need to be considered when using first-pass kinetic data to estimate perfusion. Third, the small positive TIDA bias present in early frames of the acquisition may affect the IDIF (and thereby introduce a small negative bias in  $K_1$ ); thus, additional studies investigating this bias are warranted. However, given the

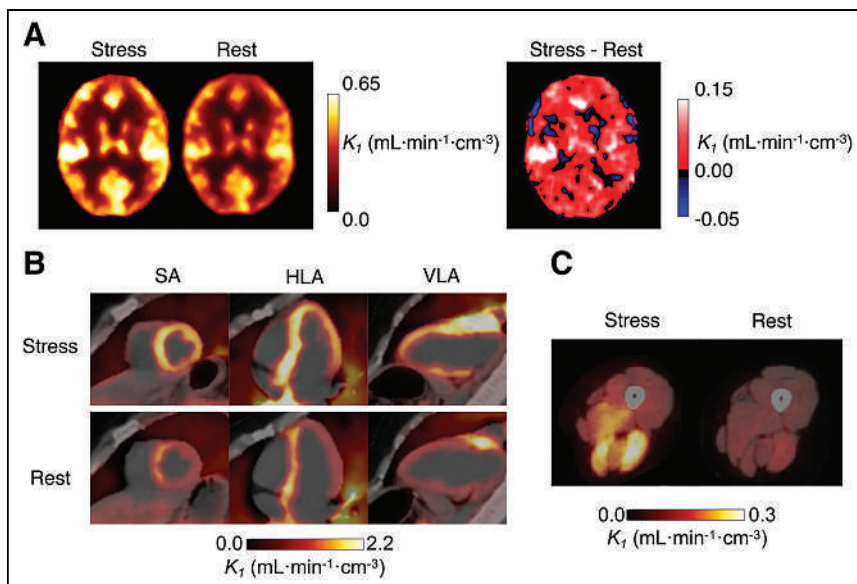


**FIGURE 6.** Intrasubject comparison between rest and stress (CPT) parametric images of  $K_1$ . Increases in gray matter (A), myocardial (B), and skeletal muscle (C) perfusion were observed with CPT, relative to rest. (B) Short-axis (SA), horizontal long-axis (HLA), and vertical long-axis (VLA) views show increased myocardial perfusion with CPT. (C) Similarly, axial cross section of thigh shows increased  $K_1$  in specific muscle groups.

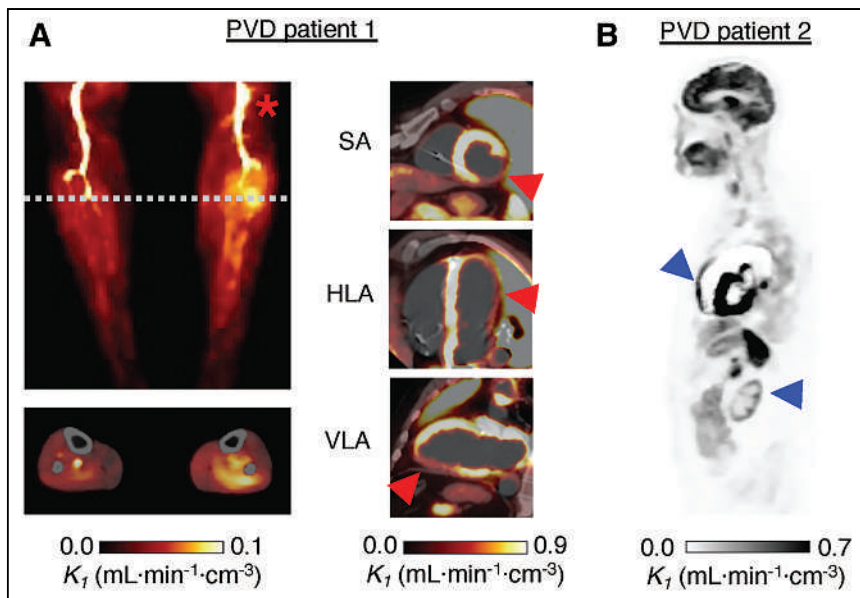


**FIGURE 7.** (A) Parametric  $K_1$  images of PVD in patient 1. Maximum intensity projection showed increased perfusion in left calf, below popliteal occlusion (asterisk). Below, cross-sectional perfusion image was obtained at dashed line and overlaid on CT. Short-axis (SA), horizontal long-axis (HLA), and vertical long-axis (VLA) views show reduced perfusion at site of earlier myocardial infarction (arrowheads). (B) Perfusion image for PVD patient 2 showed several abnormalities—including enlarged RV and low renal cortex perfusion (arrowheads)—relative to BHVs (Table 1; Supplemental Fig. 4).

small magnitude and short duration of this bias, effects are not expected to be large, and similar effects are likely present in any dynamic PET acquisition with short image frames.

Fourth, because of the limited number of enrolled subjects, known heterogeneity of response to CPT challenges, and heterogeneous presentation of PVD, broader interpretations of perfusion differences or their significance are not possible. Fifth, although subjects abstained from caffeine 2 h before imaging, other factors may affect perfusion estimates—such as recent exercise, time of day, and stress imposed by the procedure—and thus may contribute to differences between scans. It is therefore likely that close attention to these factors could further improve test–retest reproducibility and reliability. Strategies to allow a pair of studies (baseline–intervention) to be performed in close succession (within 1 h) are being investigated.

Nonetheless, this work sets forth the methodology for dynamic total-body [ $^{11}\text{C}$ ]-butanol imaging to quantify tissue perfusion. By providing measurements of baseline values in healthy volunteers, assessing test–retest reproducibility and reliability, and demonstrating changes in perfusion under a challenge (CPT) or with disease (PVD), this study lays the groundwork for application of total-body PET perfusion imaging in a range of physiologic research and in systemic cardiovascular diseases.

## CONCLUSION

In this pilot study, we conducted total-body studies using [ $^{11}\text{C}$ ]-butanol and developed analysis and kinetic modeling methodology for ROI-based measurement and parametric imaging of perfusion in all organs simultaneously. Reproducible measurements were obtained from tissues throughout the body. In addition, this work

established that these methods were sensitive to changes in perfusion because of physiologic challenge and disease. This study sets the foundation for using total-body perfusion imaging with [ $^{11}\text{C}$ ]-butanol in a range of physiologic research and in studying systemic cardiovascular disease.

## DISCLOSURE

This work was supported by NIH R01 CA206187 and R35 CA197608. UC Davis has a sales-based revenue-sharing agreement with United Imaging Healthcare. Ramsey Badawi and Simon Cherry are principal investigators on a research agreement with United Imaging Healthcare. No other potential conflict of interest relevant to this article was reported.

## ACKNOWLEDGMENTS

We thank the EXPLORER team members, clinical research staff (particularly Lynda Painting), and technologists for their contributions to this work and Optimal Tracers for synthesizing [ $^{11}\text{C}$ ]-butanol.

## KEY POINTS

**QUESTION:** Can [ $^{11}\text{C}$ ]-butanol be used for the assessment of perfusion with total-body PET?

**PERTINENT FINDINGS:** Baseline perfusion measurements were reproducible, and these methods were sensitive to variations in perfusion because of physiologic perturbation and disease.

**IMPLICATIONS FOR PATIENT CARE:** Local changes and heterogeneity of flow across organs may be indications of disease. This study demonstrated that [ $^{11}\text{C}$ ]-butanol can be used for quantitative assessment of perfusion through total-body PET, with potential application for systemic cardiovascular disease.

## REFERENCES

- Wang Z, Mascarenhas C, Jia X. Positron emission tomography after ischemic brain injury: current challenges and future developments. *Transl Stroke Res.* 2020;11:628–642.
- Murthy VL, Bateman TM, Beanlands RS, et al. Clinical quantification of myocardial blood flow using PET: joint position paper of the SNMMI cardiovascular council and the ASNC. *J Nucl Cardiol.* 2018;25:269–297.
- Berridge MS, Adler LP, Nelson AD, et al. Measurement of human cerebral blood flow with [ $^{15}\text{O}$ ]-butanol and positron emission tomography. *J Cereb Blood Flow Metab.* 1991;11:707–715.
- Herscovich P, Raichle ME, Kilbourne MR, Welch MJ. Positron emission tomographic measurement of cerebral blood flow and permeability–surface area product of water using [ $^{15}\text{O}$ ]water and [ $^{11}\text{C}$ ]butanol. *J Cereb Blood Flow Metab.* 1987;7:527–542.
- Phelps ME, Huang SC, Hoffman EJ, Selin C, Kuhl DE. Cerebral extraction of N-13 ammonia: its dependence on cerebral blood flow and capillary permeability–surface area product. *Stroke.* 1981;12:607–619.
- Quarles RP, Mintun MA, Larson KB, Markham J, Macleod AM, Raichle ME. Measurement of regional cerebral blood flow with positron emission tomography: a

- comparison of [<sup>15</sup>O]-water to [<sup>11</sup>C]-butanol with distributed-parameter and compartmental models. *J Cereb Blood Flow Metab.* 1993;13:733–747.
7. Hack SN, Bergmann SR, Eichling JO, Sobel BE. Quantification of regional myocardial perfusion by exponential infusion of [<sup>11</sup>C]-butanol. *IEEE Trans Biomed Eng.* 1983;30:716–722.
  8. Gjedde A, Hansen AJ, Siemkowitz E. Rapid simultaneous determination of regional blood flow and blood-brain glucose transfer in brain of rat. *Acta Physiol Scand.* 1980;108:321–330.
  9. Knapp WH, Helus F, Oberdorfer F, et al. [<sup>11</sup>C]-butanol for imaging of the blood-flow distribution in tumor-bearing animals. *Eur J Nucl Med.* 1985;10:540–548.
  10. Sánchez-Crespo A, Andreo P, Larsson SA. Positron flight in human tissues and its influence on PET image spatial resolution. *Eur J Nucl Med Mol Imaging.* 2004;31:44–51.
  11. Spencer BA, Berg E, Schmall JP, et al. Performance evaluation of the uEXPLORER total-body PET/CT scanner based on NEMA NU 2-2018 with additional tests to characterize PET scanners with a long axial field of view. *J Nucl Med.* 2021;62:861–870.
  12. Leung EK, Berg E, Omidvari N, et al. Quantitative accuracy in total-body imaging using the uEXPLORER PET/CT scanner. *Phys Med Biol.* 2021;66:205008.
  13. Schuster DP, Kaplan JD, Gauvain K, Welch MJ, Markham J. Measurement of regional pulmonary blood flow with PET. *J Nucl Med.* 1995;36:371–377.
  14. Matsunaga K, Yanagawa M, Otsuka T, et al. Quantitative pulmonary blood flow measurement using [<sup>15</sup>O]-H<sub>2</sub>O PET with and without tissue fraction correction: a comparison study. *EJNMMI Res.* 2017;7:102.
  15. Wang Y, Spencer BA, Schmall J, et al. High-temporal-resolution lung kinetic modeling using total-body dynamic PET with time-delay and dispersion corrections. *J Nucl Med.* 2023;64:1154–1161.
  16. Li EJ, Spencer BA, Schmall JP, et al. Efficient delay correction for total-body PET kinetic modeling using pulse timing methods. *J Nucl Med.* 2022;63:1266–1273.
  17. Wang G, Corwin MT, Olson KA, Badawi RD, Sarkar S. Dynamic PET of human liver inflammation: impact of kinetic modeling with optimization-derived dual-liver input function. *Phys Med Biol.* 2018;63:155004.
  18. Wang G, Qi J. Generalized algorithms for direct reconstruction of parametric images from dynamic PET data. *IEEE Trans Med Imaging.* 2009;28:1717–1726.
  19. Leenders KL, Perani D, Lammertsma AA, et al. Cerebral blood flow, blood volume and oxygen utilization: normal values and effect of age. *Brain.* 1990;113:27–47.
  20. Herzog H, Seitz RJ, Tellmann L, et al. Quantitation of regional cerebral blood flow with [<sup>15</sup>O]-butanol and positron emission tomography in humans. *J Cereb Blood Flow Metab.* 1996;16:645–649.
  21. Ito H, Kanno I, Iida H, et al. Arterial fraction of cerebral blood volume in humans measured by positron emission tomography. *Ann Nucl Med.* 2001;15:111–116.
  22. Yamashita M, Inaba T, Oda Y, Mizukawa N. Renal blood volume vs. glomerular filtration rate: evaluation with [<sup>15</sup>O]-CO and [<sup>68</sup>Ga]-ethylenediaminetetraacetic acid (EDTA) study. *Radioisotopes.* 1989;38:373–376.
  23. Kudomi N, Koivuviita N, Liukko KE, et al. Parametric renal blood flow imaging using [<sup>15</sup>O]-H<sub>2</sub>O and PET. *Eur J Nucl Med Mol Imaging.* 2009;36:683–691.
  24. Taniguchi H, Masuyama M, Koyama H, Oguro A, Takahashi T. Quantitative measurement of human tissue hepatic blood volume by [<sup>15</sup>O]-CO inhalation with positron-emission tomography. *Liver.* 1996;16:258–262.
  25. Taniguchi H, Yamaguchi A, Kunishima S, et al. Using the spleen for time-delay correction of the input function in measuring hepatic blood flow with oxygen-15 water by dynamic PET. *Ann Nucl Med.* 1999;13:215–221.
  26. Schober OH, Meyer GJ, Bossaller C, Creutzig H, Lichtlen PR, Hundeshagen H. Quantitative determination of regional extravascular lung water and regional blood volume in congestive heart failure. *Eur J Nucl Med.* 1985;10:17–24.
  27. Brudin LH, Rhodes CG, Valind SO, Wollmer P, Hughes JMB. Regional lung density and blood volume in nonsmoking and smoking subjects measured by PET. *J Appl Physiol.* 1987;63:1324–1334.
  28. Iida S, Harada Y, Ikenoue S, Moriya H. Measurement of bone marrow blood volume in the knee by positron emission tomography. *J Orthop Sci.* 1999;4:216–222.
  29. Liu YJ, Yang HT, Yao MMS, et al. Quantifying lumbar vertebral perfusion by a Tofts model on DCE-MRI using segmental versus aortic arterial input function. *Sci Rep.* 2021;11:2920.
  30. Martiat P, Ferrant A, Cogneau M, et al. Assessment of bone marrow blood flow using positron emission tomography: no relationship with bone marrow cellularity. *Br J Haematol.* 1987;66:307–310.
  31. Kahn D, Weiner GJ, Ben-Haim S, et al. Positron emission tomographic measurement of bone marrow blood flow to the pelvis and lumbar vertebrae in young normal adults. *Blood.* 1994;83:958–963.
  32. Raitakari M, Knuuti MJ, Ruotsalainen U, et al. Insulin increases blood volume in human skeletal muscle: studies using [<sup>15</sup>O]CO and positron emission tomography. *Am J Physiol.* 1995;269:E1000–5.
  33. Nuutila P, Raitakari M, Laine H, et al. Role of blood flow in regulating insulin-stimulated glucose uptake in humans: studies using bradykinin, [<sup>15</sup>O]-water, and [<sup>18</sup>F]-fluoro-deoxy-glucose and positron emission tomography. *J Clin Invest.* 1996;97:1741–1747.
  34. Burchert W, Schellong S, Van Den Hoff J, Meyer GJ, Alexander K, Hundeshagen H. Oxygen-15-water PET assessment of muscular blood flow in peripheral vascular disease. *J Nucl Med.* 1997;38:93–98.
  35. Iida H, Rhodes CG, De Silva R, et al. Myocardial tissue fraction correction for partial volume effects and measure of tissue viability. *J Nucl Med.* 1991;32:2169–2175.
  36. Kaufmann PA, Gnecci-Ruscione T, Yap JT, Rimoldi O, Camici PG. Assessment of the reproducibility of baseline and hyperemic myocardial blood flow measurements with [<sup>15</sup>O]-labeled water and PET. *J Nucl Med.* 1999;40:1848–1856.
  37. Delrue L, Blanckaert P, Mertens D, Van Meerbeeck S, Ceelen W, Duyck P. Tissue perfusion in pathologies of the pancreas: assessment using 128-slice computed tomography. *Abdom Imaging.* 2012;37:595–601.
  38. Komar G, Kauhaneen S, Liukko K, et al. Decreased blood flow with increased metabolic activity: a novel sign of pancreatic tumor aggressiveness. *Clin Cancer Res.* 2009;15:5511–5517.
  39. Horsager J, Okkels N, Van Den Berge N, et al. In vivo vesicular acetylcholine transporter density in human peripheral organs: an [<sup>18</sup>F]-FE0BV PET/CT study. *EJNMMI Res.* 2022;12:17.
  40. Yan C, Han X, Liang X, Jia J, Xu Y, Zhao L. Non-invasive evaluation of esophageal varices in patients with liver cirrhosis using low-dose splenic perfusion CT. *Eur J Radiol.* 2022;152:110326.
  41. Oguro A, Taniguchi H, Koyama H, et al. Quantification of human splenic blood flow (quantitative measurement of splenic blood flow with [<sup>15</sup>O]-H<sub>2</sub>O and a dynamic state method: 1). *Ann Nucl Med.* 1993;7:245–250.
  42. Rumboldt Z, Al-Okaili R, Deveikis JP. Perfusion CT for head and neck tumors: pilot study. *AJNR.* 2005;26:1178–1185.
  43. Fletcher JW, Logan TF, Eitel JA, et al. Whole-body PET/CT evaluation of tumor perfusion using generator-based [<sup>62</sup>Cu]-ethylglyoxal bis(thiosemicarbazonato) copper(II): validation by direct comparison to [<sup>15</sup>O]-water in metastatic renal cell carcinoma. *J Nucl Med.* 2015;56:56–62.
  44. Mankoff DA, Shields AF, Graham MM, Link JM, Eary JF, Krohn KA. Kinetic analysis of 2-[<sup>11</sup>C]-thymidine PET imaging studies: compartmental model and mathematical analysis. *J Nucl Med.* 1998;39:1043–1055.
  45. Wells JM, Mankoff DA, Muzi M, et al. Kinetic analysis of 2-[<sup>11</sup>C]-thymidine PET imaging studies of malignant brain tumors: compartmental model investigation and mathematical analysis. *Mol Imaging.* 2002;1:151–159.
  46. Muzi M, Mankoff DA, Grierson JR, Wells JM, Vesselle H, Krohn KA. Kinetic modeling of 3'-deoxy-3'-fluorothymidine in somatic tumors: mathematical studies. *J Nucl Med.* 2005;46:371–380.
  47. Zuo Y, Sarkar S, Corwin MT, Olson K, Badawi RD, Wang G. Structural and practical identifiability of dual-input kinetic modeling in dynamic PET of liver inflammation. *Phys Med Biol.* 2019;64:175023.
  48. Wang G, Nardo L, Parikh M, et al. Total-body PET multiparametric imaging of cancer using a voxelwise strategy of compartmental modeling. *J Nucl Med.* 2022;63:1274–1281.
  49. DiVincenzo GD, Hamilton ML. Fate of n-butanol in rats after oral administration and its uptake by dogs after inhalation or skin application. *Toxicol Appl Pharmacol.* 1979;48:317–325.
  50. Dibner C, Schibler U. Circadian timing of metabolism in animal models and humans. *J Intern Med.* 2015;277:513–527.
  51. Schindler TH, Nitzsche EU, Olschewski M, et al. PET-measured responses of MBF to cold pressor testing correlate with indices of coronary vasomotion on quantitative coronary angiography. *J Nucl Med.* 2004;45:419–428.
  52. Petrovic P, Petersson KM, Ghatan PH, Stone-Elander S, Ingvar M. Pain-related cerebral activation is altered by a distracting cognitive task. *Pain.* 2000;85:19–30.
  53. Keramida G, Gregg S, Peters AM. Stimulation of the hepatic arterial buffer response using exogenous adenosine: hepatic rest/stress perfusion imaging. *Eur Radiol.* 2020;30:5852–5861.
  54. Galea N, Cundari G, Borrazzo C, et al. Splenic blood flow increases after hypothermic stimulus (cold pressor test): a perfusion magnetic resonance study. *BioMed Res Int.* 2019;2019:8437927.
  55. Kannerkeril D, Janka R, Bosch A, et al. Detection of changes in renal blood flow using arterial spin labeling MRI. *Am J Nephrol.* 2021;52:69–75.



# Obstructive Sialadenitis from Oral Squamous Cell Carcinoma: [<sup>68</sup>Ga]Ga-FAPI-46 PET–Positive and [<sup>18</sup>F]FDG PET–Negative

Peter George Maliha<sup>1</sup>, Abie H. Mendelsohn<sup>2</sup>, Johannes Czernin<sup>1</sup>, Taylor Howard<sup>3</sup>, Jeremie Calais<sup>\*1</sup>, and Masatoshi Hotta<sup>\*1</sup>

<sup>1</sup>Ahmanson Translational Theranostics Division, Department of Molecular and Medical Pharmacology, UCLA, Los Angeles, California; <sup>2</sup>Department of Head and Neck Surgery, UCLA, Los Angeles, California; and <sup>3</sup>Department of Pathology, UCLA, Los Angeles, California

**A** 67-y-old nonsmoker woman with no prior history of head or neck surgery or radiation therapy presented with a growing ulcerative right floor-of-mouth mass with increasing tenderness, otalgia, and minimal intermittent bleeding. The floor-of-mouth mass biopsy was consistent with squamous cell carcinoma, and the patient underwent a preoperative <sup>68</sup>Ga-fibroblast activation protein inhibitor ([<sup>68</sup>Ga]Ga-FAPI)-46 PET/CT study (injected activity, 151.7 MBq [4.1 mCi]) under the prospective study NCT04147494. The preoperative [<sup>18</sup>F]FDG PET/CT study (injected activity, 407 MBq [11.0 mCi]) revealed intense uptake (SUV<sub>max</sub>, 12.8) in the anterior paramedian right primary tumor and mild uptake (SUV<sub>max</sub>, 1.6–3.4) in several subcentimeter bilateral neck nodes (stage T2N2cM0). The subsequent [<sup>68</sup>Ga]Ga-FAPI-46 PET/CT study revealed intense uptake (SUV<sub>max</sub>, 12.6) in the primary lesion and moderate uptake (SUV<sub>max</sub>, 5.4) in 1 right neck node (also [<sup>18</sup>F]FDG-avid; SUV<sub>max</sub>, 2.4).

Interestingly, there was markedly increased [<sup>68</sup>Ga]Ga-FAPI-46 uptake (SUV<sub>max</sub>, 8.1) in the right submandibular gland (SMG) and mildly increased uptake in the left SMG (SUV<sub>max</sub>, 4.0), with no associated abnormal [<sup>18</sup>F]FDG uptake. The patient did not report salivary gland tenderness or xerostomia. The oral squamous cell carcinoma was located along the course of both Wharton ducts, more pronounced on the right side. The increased [<sup>68</sup>Ga]Ga-FAPI-46 uptake in the SMGs reflected changes

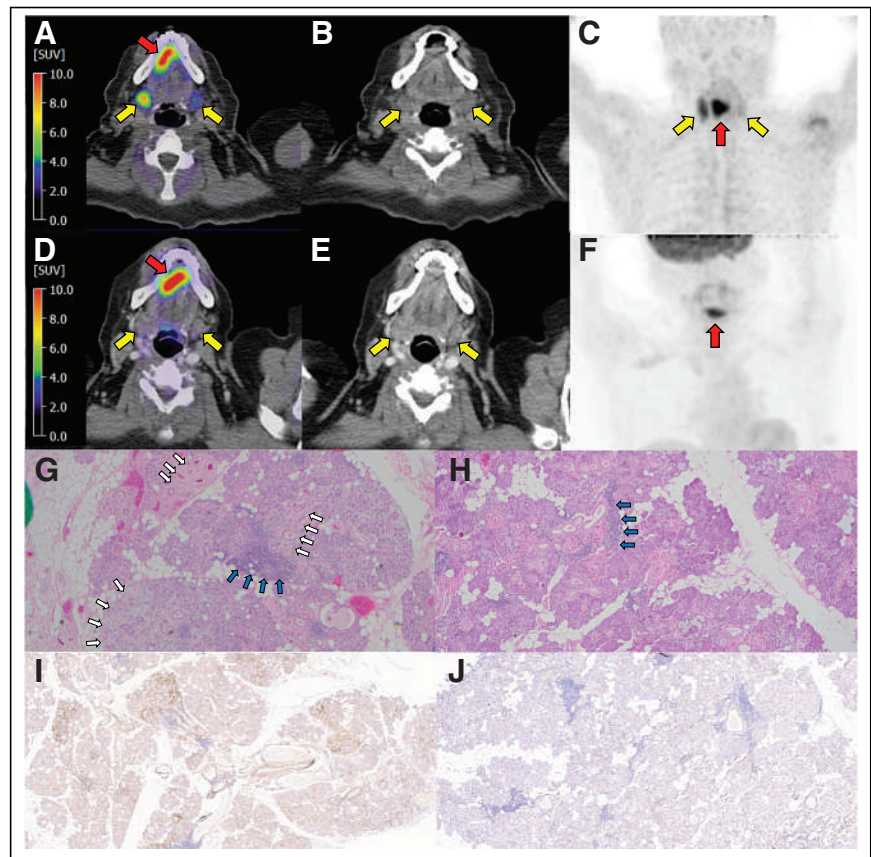


**FIGURE 1.** (A–F) Axial fused (A and D), axial CT (B and E), and maximum-intensity-projection (C and F) [<sup>68</sup>Ga]Ga-FAPI-46 PET/CT (A–C) and [<sup>18</sup>F]FDG PET/CT (D–F) images demonstrating increased [<sup>68</sup>Ga]Ga-FAPI-46 uptake in both SMGs, right more than left, and normal [<sup>18</sup>F]FDG uptake in both SMGs (yellow arrows). Primary SCC was intensely avid for [<sup>68</sup>Ga]Ga-FAPI-46 and [<sup>18</sup>F]FDG (red arrows). (G and H) Hematoxylin and eosin staining of right (G) and left (H) SMGs revealing lymphoplasmocytic infiltration bilaterally (blue arrows) and fibrosis in right SMG (white arrows). (I and J) Immunohistochemistry of SMGs revealing strong fibroblast activation protein expression in right gland (I) and overall weak expression in left gland (J).

Received Jan. 24, 2023; revision accepted Mar. 30, 2023.  
For correspondence or reprints, contact Jeremie Calais (jcalais@mednet.ucla.edu).

\*Contributed equally to this work.

Guest Editor: David A. Mankoff, University of Pennsylvania

Published online May 25, 2023.

COPYRIGHT © 2023 by the Society of Nuclear Medicine and Molecular Imaging.

DOI: 10.2967/jnumed.123.265498

caused by obstructive sialadenitis, confirmed on histopathology after resection of the oral squamous cell carcinoma and bilateral neck dissections, including total right and partial left SMG resections (Fig. 1). Immunohistochemistry of the SMGs revealed strong fibroblast activation protein expression in the right gland and overall weak expression in the left gland.

Histologically, chronic obstructive sialadenitis is characterized by acinar atrophy, lymphocytic infiltrates, and fibrosis (1). In this case, inflammatory cells were observed in both SMGs. Fibrotic cells were also observed bilaterally but predominantly in the right SMG. The [<sup>68</sup>Ga]Ga-FAPI-46-positive/[<sup>18</sup>F]FDG-negative pattern observed in the SMGs may be explained by an active fibrotic process with fibroblast activation protein expression (2) rather than an active inflammatory process. Chronic sialadenitis appears to be an additional oncologic imaging pitfall on [<sup>68</sup>Ga]Ga-FAPI-46-targeting radiopharmaceutical PET, potentially mimicking metastases.

## DISCLOSURE

No potential conflict of interest relevant to this article was reported.

## REFERENCES

1. Teymoortash A, Tiemann M, Schrader C, Werner JA. Characterization of lymphoid infiltrates in chronic obstructive sialadenitis associated with sialolithiasis. *J Oral Pathol Med.* 2004;33:300–304.
2. Hotta M, Rieger AC, Jafarvand MG, et al. Non-oncologic incidental uptake on FAPI PET/CT imaging. *Br J Radiol.* 2023;96:20220463.

## HER2-Low Breast Cancer Can Be Visualized by HER2 PET

**TO THE EDITOR:** We would like to comment on the letter from Seban et al. to the editor of *The Journal of Nuclear Medicine* in the July issue (1).

The results from the DESTINY-Breast04 trial, receiving a standing ovation during the presidential symposium at the annual conference of the American Society of Clinical Oncology in June 2022, have had a practice-changing impact on oncologists' views on the role of human epidermal growth factor receptor 2 (HER2) as a therapy-predictive biomarker. Not only have promising treatment results with trastuzumab deruxtecan (Enhertu; Daiichi Sankyo Company, Limited) been found for HER2-low breast cancer, but even patients with HER2-low gastroesophageal cancer and uterine carcinosarcoma have been demonstrated to derive a clinical benefit from treatment with this drug (2,3).

Several challenges exist in identifying patients with HER2-low metastatic breast cancer who benefit from treatment with a HER2 antibody–drug conjugate, related to both pathologic reporting (4,5) and a deepened understanding of disease heterogeneity (6). This has profound implications, as selection for trastuzumab deruxtecan (or, in the future, other HER2 antibody–drug conjugates) is based on the results from tumor biopsies from single metastatic lesions. Performing repeated biopsies, especially from sanctuary sites such as the lungs or central nervous system, is burdensome for patients and not always technically and logistically feasible.

We fully agree with the authors that HER2 PET imaging holds great promise for the molecular characterization, treatment planning, and biologic understanding of HER2-low breast cancer. Therefore, we initiated a pilot study to investigate the potential of PET/CT imaging with the Affibody (Affibody AB)-based tracer [<sup>68</sup>Ga]Ga-ABY-025 in patients with HER2-low metastatic breast cancer. This proof-of-concept investigator-initiated trial is part of the larger basket trial “Phase II Study of [<sup>68</sup>Ga]Ga-ABY-025 PET for Noninvasive Quantification of HER2-Status in Solid Tumors,” which is registered at Clinicaltrials.gov with number NCT05619016 and has been approved by the Swedish Medical Product Agency and Ethical Review Authority.

Ten patients with previously biopsy-confirmed HER2-low metastatic breast cancer were included in this pilot study, and all underwent HER2 PET with [<sup>68</sup>Ga]Ga-ABY-025 followed by a tumor biopsy, with the biopsy site being guided by the results from the PET images. The results of our study are currently being analyzed, and independent reviews of both the PET images and the study biopsy samples by nuclear medicine physicians and pathologists, respectively, are ongoing. Preliminary conclusions reveal that the technique is feasible, with [<sup>68</sup>Ga]Ga-ABY-025-avid lesions in all patients with HER2-low metastatic breast cancer, and without any new safety concerns. Interesting signals relating to disease heterogeneity have been noted, as well as hypothesis-generating findings that will provide the basis for a prospective phase II clinical trial that our group is currently planning.

In conclusion, HER2-low breast cancer is, as Seban et al. stated, a clinically relevant entity for which molecular imaging with HER2 PET potentially provides a precision medicine tool that enables a minimally invasive, real-time, whole-body assessment of the presence of the target of treatment. Expansion of molecular imaging trials to other tumor types with HER2-low status (e.g., gastroesophageal and uterine carcinosarcoma), as well as with tracers representing other disease characteristics that are used for treatment selection (i.e., programmed death ligand 1), holds great promise for further clinical implementation of molecular imaging strategies.

### REFERENCES

1. Seban RD, Champion L, Bellesoeur A, Vincent-Salomon A, Bidard FC. Clinical potential of HER2 PET as a predictive biomarker to guide the use of trastuzumab deruxtecan in breast cancer patients. *J Nucl Med*. 2023;64:1164–1165.
2. Yamaguchi K, Bang YL, Iwasa I, et al. Trastuzumab deruxtecan in anti-human epidermal growth factor receptor 2 treatment-naïve patients with human epidermal growth factor receptor 2–low gastric or gastroesophageal junction adenocarcinoma: exploratory cohort results in a phase II trial. *J Clin Oncol*. 2023;41:816–825.
3. Nishikawa T, Hasegawa K, Matsumoto K, et al. Trastuzumab deruxtecan for human epidermal growth factor receptor 2–expressing advanced or recurrent uterine carcinosarcoma (NCCH1615): the STATICE trial. *J Clin Oncol*. 2023;41:2789–2799.
4. Schettini F, Chic N, Brasó-Maristany F, et al. Clinical, pathological, and PAM50 gene expression features of HER2-low breast cancer. *NPJ Breast Cancer*. 2021;7:1.
5. Fernandez AI, Liu M, Bellizzi A, et al. Examination of low ERBB2 protein expression in breast cancer tissue. *JAMA Oncol*. 2022;8:1–4.
6. Geukens T, De Sveper M, Richard F, et al. Intra-patient and inter-metastasis heterogeneity of HER2-low status in metastatic breast cancer. *Eur J Cancer*. 2023;188:152–160.

Renske Altena\*

Siri af Burén

Thuy Tran

Rimma Axelsson

\*Karolinska University Hospital

Stockholm, Sweden

E-mail: renske.altena@ki.se

Published online Sep. 14, 2023.  
DOI: 10.2967/jnumed.123.266101

**REPLY:** I extend my gratitude to Altena et al. for their insightful response to our letter to the editor (1) regarding human epidermal growth factor receptor 2 (HER2)-targeted PET imaging in breast cancer patients. It is with great enthusiasm that I acknowledge the pivotal role their work holds in propelling the field of nuclear medicine forward.

The pursuit of HER2-targeted therapies will probably transform the landscape of oncology, analogous to the paradigm shift brought about by HER2-targeted antibody–drug conjugates in HER2-positive and HER2-low metastatic breast cancer (with trastuzumab-deruxtecan as the best example right now) (2). Similarly, the introduction of HER2-targeted PET imaging could mark a vital turning point for the nuclear medicine community (3,4). This approach not only holds promise for metastatic breast cancer but also extends its implications to broader horizons, encompassing conditions such as gastroesophageal cancer and uterine carcinosarcoma (5,6).

Undoubtedly, their ongoing clinical trial entitled “[<sup>68</sup>Ga]Ga-ABY-025 PET for Quantification of HER2-Status in Solid Tumors”



(ClinicalTrials.gov identifier NCT05619016) aligns perfectly with the pressing concerns of our time, bearing in mind developments with HER2-low as a novel category of breast cancer. These data will shed light on the potential of HER2-targeted PET imaging in addressing diagnostic and therapeutic challenges across a spectrum of solid tumors. The authors' endeavors naturally resonate with the evolving therapeutic landscape, validating the need for precise and individualized treatment strategies.

In conclusion, I commend the authors for their pioneering work in the realm of HER2-targeted PET imaging. Their dedication holds the promise of reshaping how we approach diagnosis and treatment using PET imaging for breast cancer and beyond. It is my sincere hope that their research will serve as a cornerstone for innovation and collaboration in the field of nuclear medicine in oncology.

## REFERENCES

1. Seban R-D, Champion L, Bellesoeur A, Vincent-Salomon A, Bidard F-C. Clinical potential of HER2 PET as a predictive biomarker to guide the use of trastuzumab deruxtecan in breast cancer patients. *J Nucl Med.* 2023;64:1164–1165.

2. Rassy E, Rached L, Pistilli B. Antibody drug conjugates targeting HER2: clinical development in metastatic breast cancer. *Breast.* 2022;66:217–226.
3. McGale J, Khurana S, Huang A, et al. PET/CT and SPECT/CT imaging of HER2-positive breast cancer. *J Clin Med.* 2023;12:4882.
4. Altena R, Tzortzakakis A, Af Burén S, et al. Current status of contemporary diagnostic radiotracers in the management of breast cancer: first steps toward theranostic applications. *EJNMMI Res.* 2023;13:43.
5. Yamaguchi K, Bang Y-J, Iwasa S, et al. Trastuzumab deruxtecan in anti-human epidermal growth factor receptor 2 treatment-naive patients with human epidermal growth factor receptor 2-low gastric or gastroesophageal junction adenocarcinoma: exploratory cohort results in a phase II Trial. *J Clin Oncol.* 2023;41:816–825.
6. Nishikawa T, Hasegawa K, Matsumoto K, et al. Trastuzumab deruxtecan for human epidermal growth factor receptor 2-expressing advanced or recurrent uterine carcinosarcoma (NCCH1615): the STATICE trial. *J Clin Oncol.* 2023;41:2789–2799.

**Romain-David Seban**

*Institut Curie*

*E-mail: romain.seban@gmail.com*

---

Published online Sep. 14, 2023.  
DOI: 10.2967/jnumed.123.266490



Innovate. Illuminate.

June 8-11  
2024

**SNMMI**  
**ANNUAL MEETING**

CANADA  
TORONTO

 **CALL FOR ABSTRACTS**

Attention nuclear medicine and molecular imaging professionals! Submit your abstract for SNMMI's 2024 Annual Meeting to present your research to a global audience and increase your professional recognition.

Original abstracts will be accepted on the following scientific tracks:

- Cardiovascular
- Educational Exhibits
- General Clinical Specialties
- Molecular Targeting Probes
- Neurosciences
- Oncology – Basic
- Oncology – Clinical Diagnosis and Therapy
- Physics, Instrumentation and Data Sciences
- Technologist/Technologist Student

**ABSTRACT  
SUBMISSION  
DEADLINE:  
JANUARY 5, 2024**







**SNM** SOCIETY OF  
**MI** NUCLEAR MEDICINE &  
MOLECULAR IMAGING  
**ANNUAL MEETING**



# MY SNMMI

## Get Ready for 2024 by Updating Your Member Profile

Your **"My SNMMI"** dashboard is an easy way to navigate the many member benefits available to you. Take 5 minutes to customize your member experience through SNMMI profile options.

-  Access the SNMMI Member Directory to begin expanding your professional network
-  Manage your credit history, see your transcript, and access the SNMMI Learning Center
-  Manage your email and publication preferences to ensure you get the latest news from SNMMI
-  Review and update new demographic questions and professional certifications
-  Choose your journal preferences for both JNM and JNMT online or print issues
-  Stay up-to-date by updating your email and mailing address as needed

[www.snmmi.org/MySNMMI](http://www.snmmi.org/MySNMMI)

*We encourage you to bookmark this page for future use*

**SNMMI** SOCIETY OF  
NUCLEAR MEDICINE &  
MOLECULAR IMAGING

# SNMMI Ones to Watch for 2024

## The Search Is Underway!

SNMMI is now accepting nominations for our **2024 Ones to Watch** selections. As the field continues to expand, a new wave of talent is at the forefront of this cutting-edge specialty. We hope you'll help us identify those early career professionals working to shape the future of nuclear medicine and molecular imaging.

Members can nominate someone they know—currently in training or who have completed their training within the last 5 years—whose actions, work, or studies have set them apart as a future thought leader in the field.

Nominations Must Include:

- Name and credentials
- Years in nuclear medicine/molecular imaging/radiology profession
- Occupation and employer \*Substitute program name if still in training\*
- 250 (maximum) words about their achievements or demonstrated potential in the field of nuclear medicine or molecular imaging
- A headshot of the nominee

Submit your **Ones to Watch** nomination by **December 31, 2023** for consideration.

**Self nominations are no longer permitted.**





# TECHNEGAS<sup>®</sup>



Kit for the preparation of technetium Tc 99m-labeled carbon inhalation aerosol



The wait is over...  
Cyclomedica is proud to bring its innovative technology, Technegas<sup>®</sup>, to the United States.

Technegas<sup>®</sup>, referenced in both the European<sup>1</sup> and Canadian<sup>2</sup> Associations of Nuclear Medicine guidelines for diagnosing Pulmonary Embolism, is now available to patients in the USA.

Join us in our advance into a new era and experience nuclear pulmonary imaging with Technegas<sup>®</sup>!

 [info@cyclomedica.com](mailto:info@cyclomedica.com)

 [cyclomedica.com](http://cyclomedica.com)

**JOIN OUR GROWING U.S. TEAM:**  
SERVICE ENGINEERS & APPLICATIONS  
SPECIALISTS POSITIONS AVAILABLE

 [cyclomedica.com/careers](http://cyclomedica.com/careers)

## HIGHLIGHTS TO PRESCRIBING INFORMATION<sup>3</sup>

These highlights do not include all the information needed to use TECHNEGAS safely and effectively. See full prescribing information for TECHNEGAS.

## INDICATIONS & USAGE

TECHNEGAS<sup>®</sup>, when used with sodium pertechnetate Tc 99m in the Technegas<sup>®</sup> Plus System, provides technetium Tc 99m-labeled carbon inhalation aerosol (Technegas<sup>®</sup> Aerosol), a radioactive diagnostic agent for use in adults and pediatric patients aged 6 years and older for:

- visualization of pulmonary ventilation
- evaluation of pulmonary embolism when paired with perfusion imaging

## DOSAGE & ADMINISTRATION

- For adult patients, the recommended activity of sodium pertechnetate Tc 99m injection to be loaded in the Technegas Crucible is 400 MBq to 1,000 MBq (10.8 mCi to 27 mCi) to achieve a lung count rate between 1,500 counts per second (cps) and 2,500 cps at the end of the last respiration. (2.2)

- For pediatric patients aged 6 years and older, a sufficient amount of Technegas Aerosol should be inhaled to achieve between 500 cps and 1,000 cps at the end of last respiration. The radioactivity to be loaded in the Technegas Crucible is a fraction of the recommended activity for adults adjusted by body weight. (2.2)
- Administer as soon as possible following preparation and complete inhalation within 10 minutes of preparation. (2.2)
- For drug handling, breathing techniques, preparation, and dosimetry information, see the full prescribing information. (2.1, 2.3, 2.4, 2.5)

## DOSAGE FORMS & STRENGTH

TECHNEGAS (kit for the preparation of technetium Tc 99m labeled carbon inhalation aerosol) is a 1.25 gram single-use black to dark grey oval shaped graphite carbon crucible (Technegas Crucible). Upon addition of sodium pertechnetate Tc 99m injection, USP to the Technegas Crucible, the Technegas Plus System provides Technegas Aerosol for oral inhalation. (3)

## CONTRAINDICATIONS

None. (4)

## WARNINGS & PRECAUTIONS

**Decreased Oxygen Saturation:** Monitor oxygen saturation with continuous pulse oximetry. If clinically indicated, allow patients to breathe room air throughout the procedure and consider administration of supplemental oxygen before and at any time during the procedure. (5.1)

**Radiation Exposure Risk:** Ensure safe handling and preparation procedures to protect patients and health care providers from unintentional radiation exposure. (2.1, 5.2)

## ADVERSE REACTIONS

The most common adverse reaction ( $\geq 1\%$ ) was hypoxia. (6.1)

**To report SUSPECTED ADVERSE REACTIONS, contact Cyclomedica Australia Pty Ltd at toll free phone number 1-888-8-586-4396 or FDA at 1-800-FDA-1088 or [www.fda.gov/medwatch](http://www.fda.gov/medwatch).**

## USE IN SPECIFIC POPULATIONS

**Lactation:** Temporarily discontinue breastfeeding. A lactating woman should pump and discard breastmilk for at least 4 hours after Technegas Aerosol inhalation to minimize exposure to the breastfed infant. (8.2)

<sup>1</sup> Bajc M, et al, Eur J Nucl Med Mol Imaging (2019) 46:2429–2451

<sup>2</sup> Leblanc M, et al. CANM Guidelines for V/P SPECT in PE. CANM Nov 2018

<sup>3</sup> [https://www.accessdata.fda.gov/drugsatfda\\_docs/label/2023/022335s000lbl.pdf](https://www.accessdata.fda.gov/drugsatfda_docs/label/2023/022335s000lbl.pdf)

**Journal of Nuclear Medicine** | November 2023 | Vol. 64 | Pages 1671-1842